COMPUTATIONAL MODELING FOR THE ASSESSMENT OF THE BIOMECHANICAL PROPERTIES OF THE HEALTHY, DISEASED AND TREATED SPINE

EDITED BY: Enrico Dall'Ara, Fabio Galbusera, Hendrik Schmidt, Marwan El-Rich and Grace D. O'Connell

PUBLISHED IN: Frontiers in Bioengineering and Biotechnology

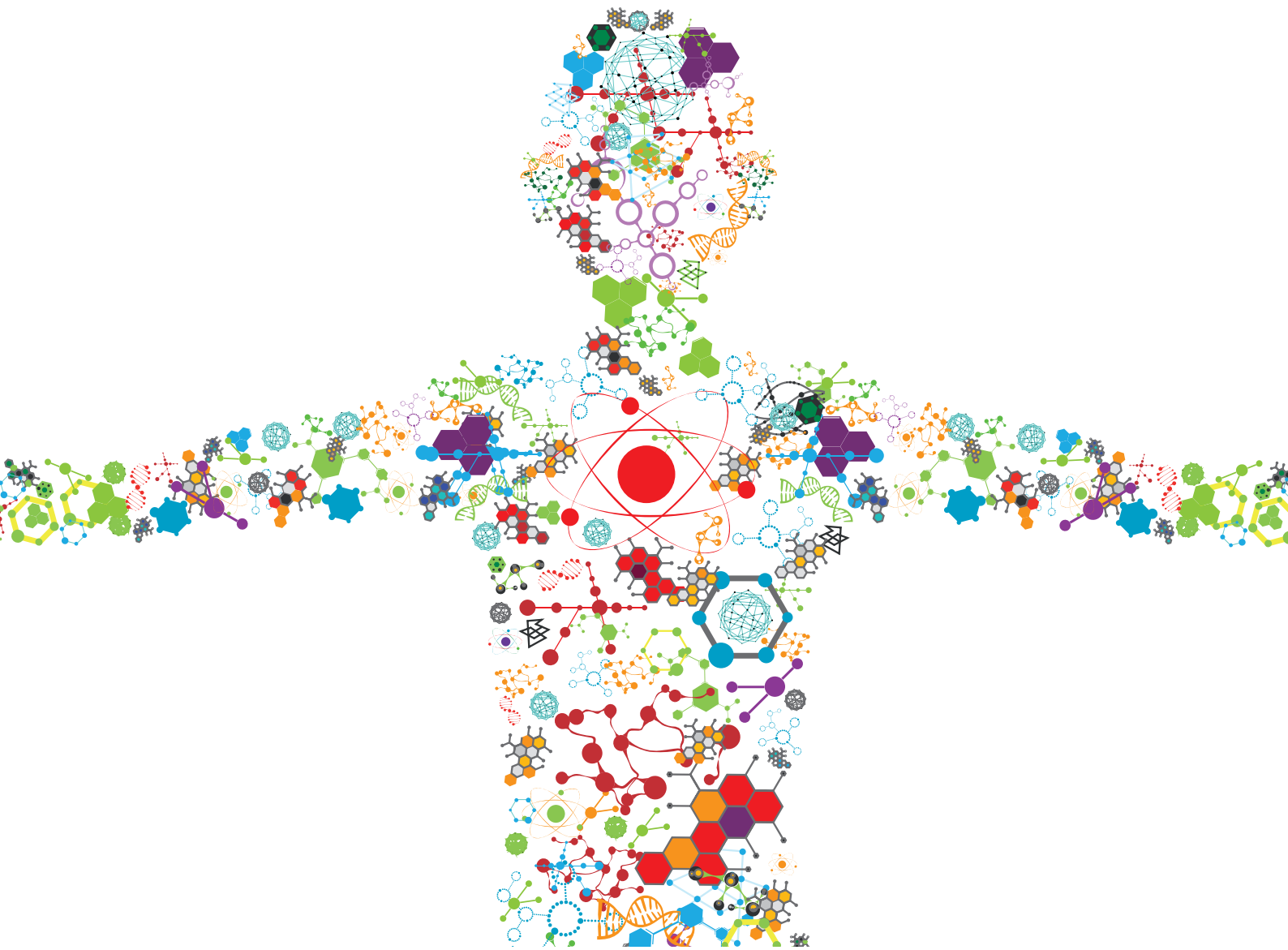

frontiers Research Topics

frontiers

ISSN 1664-8714
ISBN 978-2-83250-038-5
DOI 10.3389/978-2-83250-038-5

About Frontiers

Frontiers is more than just an open-access publisher of scholarly articles: it is a pioneering approach to the world of academia, radically improving the way scholarly research is managed. The grand vision of Frontiers is a world where all people have an equal opportunity to seek, share and generate knowledge. Frontiers provides immediate and permanent online open access to all its publications, but this alone is not enough to realize our grand goals.

Frontiers Journal Series

The Frontiers Journal Series is a multi-tier and interdisciplinary set of open-access, online journals, promising a paradigm shift from the current review, selection and dissemination processes in academic publishing. All Frontiers journals are driven by researchers for researchers; therefore, they constitute a service to the scholarly community. At the same time, the Frontiers Journal Series operates on a revolutionary invention, the tiered publishing system, initially addressing specific communities of scholars, and gradually climbing up to broader public understanding, thus serving the interests of the lay society, too.

Dedication to Quality

Each Frontiers article is a landmark of the highest quality, thanks to genuinely collaborative interactions between authors and review editors, who include some of the world's best academicians. Research must be certified by peers before entering a stream of knowledge that may eventually reach the public - and shape society; therefore, Frontiers only applies the most rigorous and unbiased reviews.
Frontiers revolutionizes research publishing by freely delivering the most outstanding research, evaluated with no bias from both the academic and social point of view. By applying the most advanced information technologies, Frontiers is catapulting scholarly publishing into a new generation.

What are Frontiers Research Topics?

Frontiers Research Topics are very popular trademarks of the Frontiers Journals Series: they are collections of at least ten articles, all centered on a particular subject. With their unique mix of varied contributions from Original Research to Review Articles, Frontiers Research Topics unify the most influential researchers, the latest key findings and historical advances in a hot research area! Find out more on how to host your own Frontiers Research Topic or contribute to one as an author by contacting the Frontiers Editorial Office: frontiersin.org/about/contact

COMPUTATIONAL MODELING FOR THE ASSESSMENT OF THE BIOMECHANICAL PROPERTIES OF THE HEALTHY, DISEASED AND TREATED SPINE

Topic Editors:
Enrico Dall'Ara, The University of Sheffield, United Kingdom
Fabio Galbusera, Schulthess Klinik, Switzerland
Hendrik Schmidt, Charité Medical University of Berlin, Germany
Marwan El-Rich, Khalifa University, United Arab Emirates
Grace D. O'Connell, University of California, Berkeley, United States

Citation: Dall'Ara, E., Galbusera, F., Schmidt, H., El-Rich, M., O'Connell, G. D., eds. (2022). Computational Modeling for the Assessment of the Biomechanical Properties of the Healthy, Diseased and Treated Spine. Lausanne: Frontiers Media SA. doi: 10.3389/978-2-83250-038-5

Table of Contents

05 ***Editorial: Computational Modeling for the Assessment of the Biomechanical Properties of the Healthy, Diseased and Treated Spine***
Enrico Dall'Ara, Hendrik Schmidt, Marwan El-Rich, Grace D. O'Connell and Fabio Galbusera

09 ***Automated Pipeline to Generate Anatomically Accurate Patient-Specific Biomechanical Models of Healthy and Pathological FSUs***
Sebastiano Caprara, Fabio Carrillo, Jess G. Snedeker, Mazda Farshad and Marco Senteler

24 ***Toward Patient Specific Models of Pediatric IVDs: A Parametric Study of IVD Mechanical Properties***
Edmund Pickering, Peter Pivonka and J. Paige Little

36 ***Patient-Specific Finite Element Models of Posterior Pedicle Screw Fixation: Effect of Screw's Size and Geometry***
Marco Sensale, Tanguy Vendeuvre, Christoph Schilling, Thomas Grupp, Michel Rochette and Enrico Dall'Ara

50 ***Maintaining Bone Health in the Lumbar Spine: Routine Activities Alone Are Not Enough***
Clément D. Favier, Alison H. McGregor and Andrew T. M. Phillips

66 ***Biomechanical Effects of a Cross Connector in Sacral Fractures – A Finite Element Analysis***
Meike Gierig, Fangrui Liu, Lukas Weiser, Wolfgang Lehmann, Peter Wriggers, Michele Marino and Dominik Saul

81 ***Experimental and Computational Comparison of Intervertebral Disc Bulge for Specimen-Specific Model Evaluation Based on Imaging***
Marlène Mengoni, Fernando Y. Zapata-Cornelio, Vithanage N. Wijayathunga and Ruth K. Wilcox

93 ***Biomechanical Investigation Between Rigid and Semirigid Posterolateral Fixation During Daily Activities: Geometrically Parametric Poroelastic Finite Element Analyses***
Mohammad Nikkhoo, Meng-Ling Lu, Wen-Chien Chen, Chen-Ju Fu, Chi-Chien Niu, Yang-Hua Lin and Chih-Hsiu Cheng

107 ***A Robust Multiscale and Multiphasic Structure-Based Modeling Framework for the Intervertebral Disc***
Minhao Zhou, Shiyin Lim and Grace D. O'Connell

126 ***Quantitative MRI to Characterize the Nucleus Pulposus Morphological and Biomechanical Variation According to Sagittal Bending Load and Radial Fissure, an* ex vivo *Ovine Specimen Proof-of-Concept Study***
Jean-Philippe Deneuville, Maksym Yushchenko, Tanguy Vendeuvre, Arnaud Germaneau, Maxime Billot, Manuel Roulaud, Mathieu Sarracanie, Najat Salameh and Philippe Rigoard

139 ***Load Distribution in the Lumbar Spine During Modeled Compression Depends on Lordosis***
Andreas Müller, Robert Rockenfeller, Nicolas Damm, Michael Kosterhon, Sven R. Kantelhardt, Ameet K. Aiyangar and Karin Gruber

151 ***Sensitivity of Intervertebral Disc Finite Element Models to Internal Geometric and Non-geometric Parameters***
Yuekang Du, Saman Tavana, Tamanna Rahman, Nicoleta Baxan, Ulrich N. Hansen and Nicolas Newell

163 ***Biomechanical Analysis of Cervical Artificial Disc Replacement Using Cervical Subtotal Discectomy Prosthesis***
Jin Wo, Zhenjing Lv, Jing Wang, Kui Shen, Haoran Zhu, Yang Liu, Yuen Huang, Guodong Sun and Zhizhong Li

178 ***The Influence of Kinematic Constraints on Model Performance During Inverse Kinematics Analysis of the Thoracolumbar Spine***
Mohammad Mehdi Alemi, Katelyn A. Burkhart, Andrew C. Lynch, Brett T. Allaire, Seyed Javad Mousavi, Chaofei Zhang, Mary L. Bouxsein and Dennis E. Anderson

193 ***Biomechanical Evaluation of Different Surgical Approaches for the Treatment of Adjacent Segment Diseases After Primary Anterior Cervical Discectomy and Fusion: A Finite Element Analysis***
Wencan Ke, Chao Chen, Bingjin Wang, Wenbin Hua, Saideng Lu, Yu Song, Rongjin Luo, Zhiwei Liao, Gaocai Li, Liang Ma, Yunsong Shi, Kun Wang, Shuai Li, Xinghuo Wu, Yukun Zhang and Cao Yang

204 ***Surgical Outcome Prediction Using a Four-Dimensional Planning Simulation System With Finite Element Analysis Incorporating Pre-bent Rods in Adolescent Idiopathic Scoliosis: Simulation for Spatiotemporal Anatomical Correction Technique***
Hiroyuki Tachi, Koji Kato, Yuichiro Abe, Terufumi Kokabu, Katsuhisa Yamada, Norimasa Iwasaki and Hideki Sudo

216 ***Biomechanics of Lumbar Spine Injury in Road Barrier Collision—Finite Element Study***
L. Pachocki, K. Daszkiewicz, P. Łuczkiewicz and W. Witkowski

226 ***Sex-Dependent Estimation of Spinal Loads During Static Manual Material Handling Activities—Combined* in vivo *and* in silico *Analyses***
Ali Firouzabadi, Navid Arjmand, Fumin Pan, Thomas Zander and Hendrik Schmidt

240 ***Stability Evaluation of Different Oblique Lumbar Interbody Fusion Constructs in Normal and Osteoporotic Condition – A Finite Element Based Study***
Ferenc Bereczki, Mate Turbucz, Rita Kiss, Peter Endre Eltes and Aron Lazary

252 ***The Simulation of Muscles Forces Increases the Stresses in Lumbar Fixation Implants with Respect to Pure Moment Loading***
Matteo Panico, Tito Bassani, Tomaso Maria Tobia Villa and Fabio Galbusera

259 ***Sensitivity of the Cervical Disc Loads, Translations, Intradiscal Pressure, and Muscle Activity Due to Segmental Mass, Disc Stiffness, and Muscle Strength in an Upright Neutral Posture***
Rizwan Arshad, Hendrik Schmidt, Marwan El-Rich and Kodjo Moglo

frontiers | Frontiers in Bioengineering and Biotechnology

TYPE Editorial
PUBLISHED 11 October 2022
DOI 10.3389/fbioe.2022.1016311

OPEN ACCESS

EDITED AND REVIEWED BY
Markus O. Heller,
University of Southampton,
United Kingdom

*CORRESPONDENCE
Enrico Dall'Ara,
e.dallara@sheffield.ac.uk

SPECIALTY SECTION
This article was submitted to Biomechanics, a section of the journal Frontiers in Bioengineering and Biotechnology

RECEIVED 10 August 2022
ACCEPTED 27 September 2022
PUBLISHED 11 October 2022

CITATION
Dall'Ara E, Schmidt H, El-Rich M, O'Connell GD and Galbusera F (2022), Editorial: Computational modeling for the assessment of the biomechanical properties of the healthy, diseased and treated spine.
Front. Bioeng. Biotechnol. 10:1016311.
doi: 10.3389/fbioe.2022.1016311

Editorial: Computational modeling for the assessment of the biomechanical properties of the healthy, diseased and treated spine

Enrico Dall'Ara[1,2]*, Hendrik Schmidt[3], Marwan El-Rich[4], Grace D. O'Connell[5] and Fabio Galbusera[6]

[1]Department of Oncology and Metabolism, Mellanby Centre for Bone Research, University of Sheffield, Sheffield, United Kingdom, [2]INSIGNEO Institute for in Silico Medicine, University of Sheffield, Sheffield, United Kingdom, [3]Julius Wolff Institute, Charité—Universitätsmedizin Berlin, Corporate Member of Freie Universität Berlin and Humboldt-Universität zu Berlin, and Berlin Institute of Health, Berlin, Germany, [4]Healthcare Engineering Innovation Center, Department of Mechanical Engineering, Khalifa University, Abu Dhabi, United Arab Emirates, [5]Department of Mechanical Engineering, University of California-Berkeley, Berkeley, CA, United States, [6]Spine Center, Schulthess Clinic, Zürich, Switzerland

KEYWORDS

spine, spinal fractures, posterior fixation, finite element, musculoskeletal model, implants

Editorial on the Research Topic
Computational modeling for the assessment of the biomechanical properties of the healthy, diseased and treated spine

The human spine has been optimised through the evolutionary process resulting in a unique structural combination of hard (i.e., bone) and soft tissues (i.e., intervertebral disc, tendons, ligaments, cartilage). The spine and surrounding musculature provide flexibility and structural stability while subjected to loads of varying magnitudes and directions during daily activities and protect the spinal cord and nerve roots from excessive strain. These biological tissues have complex heterogeneous, anisotropic, nonlinear, and hierarchical properties, making their biomechanical characterization challenging. Moreover, aging, diseases, and injuries may affect biomechanical stability, leading to vertebral fractures and/or intervertebral disc (IVD) degeneration, which may induce pain and disability. Different interventions are available to fix or slow the damage progression of the affected tissues, from pharmacological and conservative treatments to surgeries. However, due to the complexity of the microstructure and material properties of the tissues that compose the spine, assessing disease progression or treatment effects on the spine's biomechanical properties are not trivial.

Experimental assessments such as motion capture, complex mechanical loading using dedicated multi-axial rigs, strain analyses with strain gauges, and digital image or volume correlation have been used to characterize biomechanical properties of the spine at

different dimensional levels, but they lack the flexibility of testing the same structure in different loading conditions until failure. Moreover, the intrinsic variability of the geometrical, structural, and material properties due to sex, age, size, disease progression, treatments, etc. makes it difficult to test all possible scenarios experimentally. In particular, it is very challenging to measure the influence of the properties of the microstructural components (e.g., remodelled bone, fibers in the annulus fibrosus) on bulk tissue material properties. Moreover, damage accumulation of these viscoelastic and poroelastic tissues with age or disease also contributes to experimental challenges in the characterisation of their material behaviour. Therefore, computational models of spine segments and entire lumbar, thoracolumbar, and cervical spines have been developed to evaluate the biomechanical properties of healthy and diseased spines (e.g., patients with osteoporosis, osteoarthritis, bone metastases, traumatic fractures), and to optimize spinal treatment. While generic or subject-specific computational models can be parameterized, efficiently test several loading conditions and comprehensively study the spine biomechanics, the experimental studies remain invaluable to inform, calibrate and validate the models. In fact, increasing the model credibility, based on model verification, validation, sensitivity analyses, and uncertainty quantification is fundamental for developing tools that can be used to support clinical decisions (The American Society of Mechanical Engineers (ASME), 2018).

The current Research Topic presents a unique collection of studies that increase our knowledge about spine biomechanics and stimulate discussions for the improvement of techniques used for computational model development and validation.

Four studies have used multi-body dynamics (MDB) models for evaluation of ROM, load distribution, muscle forces, and activation on both thoracolumbar and cervical spine. Müller et al. have used MBD models with subject-specific geometry to predict the load distribution in a healthy lumbar spine as function of the lordosis angle. They confirm earlier assumptions by Roussouly and Pinheiro-Franco (Roussouly and Pinheiro-Franco, 2011) that large lordosis angles generate more stress on the facet joints but less stress on the vertebral bodies and intervertebral discs. This result is important both for optimising therapeutic measures and for identifying boundary conditions for computational models at lower dimensional scales (e.g., Finite Element (FE) models). Alemi et al. have used inverse kinematics, informed from motion analyses of seven healthy participants, to evaluate the effect of different kinematic constraints on the performance of thoracolumbar spine MBD models. They concluded that kinematic constraints with 5 degrees of freedom was the best compromise to track measurements and produce smooth spine motion. Arshad et al. have developed an inverse dynamic model of the head-neck complex, including the head, C1-T1 vertebrae, and detailed soft tissues (517 nonlinear ligament fibers and 258 muscle fascicles). A comprehensive sensitivity analysis showed that increased segment mass led to increased disc loads and muscle activity, that disc stiffness affected only disc translation, and that by increasing muscle strength, the muscle activity largely decreased. These results show that these models can be used to study the effect of diseases and treatments, after appropriate model validation. Firouzabadi et al. have compared spine loads during static manual material handling activities for males and female subjects, using a whole body MBD model. Female subjects had larger compressive and shear loads when normalized to the body weight and larger forces in the oblique abdominal muscles, while male subjects had larger back extensor muscle forces. The study highlights the importance of considering sex-specific parameters.

Ten manuscripts have used detailed structural FE models to evaluate the mechanical properties of the IVD, single vertebra, or spine segments. While many FE models have been utilized to characterize biomechanical properties of vertebral bodies and spine segments, there are still challenges to accurately model of the IVD material, create efficient spinal segment models, and to using FE models predictions to optimise treatment strategies. Pickering et al. have developed a pipeline to create models of paediatric IVDs and performed a sensitivity analysis on the material model inputs. They found that IVD collagen fiber bundles are the main contributors of IVD mechanical behaviour and should therefore be integrated in patient specific FE models of the paediatric spine. In another study, Du et al. have created FE models of the IVD based on magnetic resonance imaging (MRI) data from bovine spine and evaluated the model sensitivity to different geometrical and material input parameters, highlighting that it is fundamental to model well the geometry of the vertebral endplates. It should be noted that while FE models have great potential in assessing the biomechanical behaviour of spine segments, process automation is needed to improve the efficiency and reduce operator dependency for clinical application. Caprara et al. have developed an automatic pipeline to create subject-specific FE models of the lumbar spine from CT images by using deep learning techniques to segment the geometries, statistical shape models to create the meshes, and FE models to simulate different loading conditions and predict ROM of the segments. This automatic tool, the results of which agreed with literature data, has the potential of improving the clinical applicability of biomechanical simulations. FE models have been widely used to test the effect of spine fixation for treating vertebral fractures, IVD degeneration, spine deformities and other diseases as well. Sensale et al. have performed a verification and sensitivity analysis for subject-specific FE models of a single vertebra implanted with two pedicle screws. They have reported that the diameter of the screw is more important than its length for minimising screw and bone deformations. Moreover, they highlighted the importance of modelling realistic screw geometry. Bereczki et al. have developed an L2-L4 spine segment FE model to study the stability of different implants

for oblique lumbar interbody fusion when implanted in healthy or osteoporotic bone. They showed that spine segment stability was affected by the used implant and that osteoporosis increases the ROM for all tested constructs. Gierig et al. have used a large FE model of the lumbar spine that also included the pelvis and spinopelvic devices to study the best configuration in fixing spinopelvic fractures and to show its superiority compared to non-surgical treatment. Ke et al. have used an FE model of C2-T1 spine segments to evaluate different surgical treatments of adjacent diseased segment (ADS) after a primary anterior cervical discectomy and fusion (ACDF). The model suggests that a second ACDF leads to better outcomes compared to laminoplasty in the tested case. In another study, Wo et al. have used a combination of an FE model of C2-C7 cervical segment, wear tests and animal study on non-human primate, to study the biomechanics of cervical subtotal discectomy prosthesis (CSDP) as an alternative for ACDF. The FE models showed the influence of the implant position on the CSDP performance including ROM, bone-implant stress, and forces at the facet joints. Nikkhoo et al. have used poro-elastic FE models to study the biomechanical stability of rigid (Ti rods) or semi-rigid (PEEK) posterolateral fixation for ADS. They showed that, compared with Ti constructs, the PEEK prosthesis may be preferable as it is associated with a slightly higher ROM at the instrumented level and lower IVD height loss, fluid loss, axial stress, and collagen fiber strain in the adjacent disc. Tachi et al. have used an FE model of the spine of patients with adolescent idiopathic scoliosis to pre-plan the surgical correction procedure with pre-bent spinal rods. This preplanning system can be used to optimize which spine levels to instrument and the rod shape.

The above-mentioned studies showed how FE models can assist surgeons in identifying the best prosthesis in cases of different spine diseases. However, there are still challenges in creating more realistic computational models accounting for the hierarchical properties of the spine with multi-scale approaches, that for example, better estimate the loading scenarios or the effect of bone remodelling over time, and in validating the outputs of the models to improve their credibility and their future clinical applicability. Favier et al. coupled L1-L5 spine FE model with lower strain-driven algorithm to predict local bone changes induced by physiological loading conditions calculated from a previously developed full-body MBD model. They showed that in order to maintain trabecular and cortical bone health, a combination of moderate and more demanding activities (large spine movement and lifting tasks) are needed. In fact, moderate intensity activities alone were not found to be sufficient to maintain bone health in the vertebrae. Panico et al. have tested the effect of simulating realistic muscle forces in FE models of lumbar fixation implants. They coupled a previously developed MBD model of the thoraco-lumbar spine with articulated ribcage with a detailed FE model of T10-T12 segments to compare the results of models with realistic and simplified (pure moments) loading. Intact spine segments and instrumented spine segments with rods and screws were simulated. The realistic FE models showed similar ROM but higher stresses in the pedicle screws and in the posterior rods compared to the simplified models, showing the importance of using realistic loading when evaluating implant stresses. Pachocki et al. have used a global FE model that includes a concrete road safety barrier, an impacting vehicle, and an occupant. The occupant model includes a lumbar spine FE model to study the biomechanics of injuries during road barrier collision. The two-scales model estimated the loading condition on the spine model from a larger FE dynamic model of the subject in the impacting vehicle. They have shown that during the crash the loading on the lumbar spine is eccentric and leads to high axial loads and flexion bending moments on L1-L5, explaining why fractures are associated with this loading scenario.

Three manuscripts in the Research Topic have collected *ex vivo* or *in vivo* experimental data to inform and validate FE models of the IVD. Deneuville et al. have performed a proof-of-concept study using *ex vivo* MRI imaging of an L1-L3 ovine spine segment under different loading conditions before and after inducing damage of the IVD to evaluate its effect on the deformation of the nucleus pulposus. They combined this experiment with an FE model of the spine segments to evaluate the effect of the IVD damage on the stress field, showing the potential of this approach to study IVD biomechanics from MR images. Mengoni et al. have validated the outputs of MRI based FE models of the IVD, against *ex vivo* experiments performed on bovine specimens to measure the IVD bulge. The results showed that including subject-specific geometrical and material properties of the IVD in the FE models does not improve substantially the predictions of IVD stiffness and bulge. Finally, Zhou et al. Have developed a multiscale and multiphasic FE model of the IVD and validated it against experiments for the bovine caudal vertebra. In most cases the multiscale model, developed from experimental data of fiber and matrix mechanical behaviour, accurately predicted the structural response of the IVD, highlighting the importance of modelling the fibers, matrix-fiber interactions, and the fluid-based load bearing mechanism of this complex structure.

This Research Topic includes 20 peer-reviewed papers tackling different challenges in the topic of development and validation of computational modelling of spine biomechanics. Every paper reports the potential and current limitations of the developed approaches, highlighting progress that the research community has done in this area, and where we should focus to improve clinical applicability. We would like to emphasise that, while the presented research is fundamental for understanding the biomechanics of the spine and further develop computational models to support clinical decision making, a lot of work needs to be done to see these approaches used routinely. We anticipate that future studies that use biomechanical models of the human spine will be even more realistic and biofidelic (e.g., considering complex individualized loading and boundary conditions taking into account the everyday behaviour, functional behaviours and adaptations after surgical procedures or pain experiences, activation patterns, individualized material properties, *etc.*), more credible through

comprehensive and systematic validation process using *ex vivo* and *in vivo* data, certifiable by regulatory bodies, adaptable to study a single subject or generic to study a patient population. To conclude, while there is no doubt that research in this exciting area will keep progressing and improving our knowledge of the Biomechanical Properties of the Healthy, Diseased and Treated Spine as demonstrated in this Research Topic, the research community should encourage and strengthen interdisciplinary collaborative research involving bioengineering, biology, and medicine.

Author contributions

ED'A has prepared the draft of the editorial and all other authors have critically revised it. All authors have approved the final version of the manuscript.

Conflict of interest

The authors declare that the research was conducted in the absence of any commercial or financial relationships that could be construed as a potential conflict of interest.

Publisher's note

References

Roussouly, P., and Pinheiro-Franco, J. L. (2011). Biomechanical analysis of the spino-pelvic organization and adaptation in pathology. *Eur. Spine J.* 20, 609–618. doi:10.1007/s00586-011-1928-x

The American Society of Mechanical Engineers (ASME) (2018). Assessing credibility of computational modeling through verification and validation: Application to medical devices VV40. Available at https://www.asme.org/products/codes-standards/v-v-40-2018-assessing-credibility-computational (Accessed January 24, 2021).

frontiers in Bioengineering and Biotechnology

ORIGINAL RESEARCH
published: 28 January 2021
doi: 10.3389/fbioe.2021.636953

Automated Pipeline to Generate Anatomically Accurate Patient-Specific Biomechanical Models of Healthy and Pathological FSUs

Sebastiano Caprara[1,2], Fabio Carrillo[2,3], Jess G. Snedeker[1,2], Mazda Farshad[1] and Marco Senteler[1,2]*

[1] Department of Orthopedics, University Hospital Balgrist, University of Zurich, Zurich, Switzerland, [2] Institute for Biomechanics, Swiss Federal Institute of Technology (ETH), Zurich, Switzerland, [3] Research in Orthopedic Computer Science, University Hospital Balgrist, Zurich, Switzerland

OPEN ACCESS

Edited by:
Fabio Galbusera, Galeazzi Orthopedic Institute (IRCCS), Italy

Reviewed by:
Navid Arjmand, Sharif University of Technology, Iran
René Jonas, University of Ulm, Germany

***Correspondence:**
Sebastiano Caprara
sebastiano.caprara@hest.ethz.ch

Specialty section:
This article was submitted to Biomechanics, a section of the journal Frontiers in Bioengineering and Biotechnology

Received: *02 December 2020*
Accepted: *11 January 2021*
Published: *28 January 2021*

Citation:
Caprara S, Carrillo F, Snedeker JG, Farshad M and Senteler M (2021) Automated Pipeline to Generate Anatomically Accurate Patient-Specific Biomechanical Models of Healthy and Pathological FSUs. Front. Bioeng. Biotechnol. 9:636953. doi: 10.3389/fbioe.2021.636953

State-of-the-art preoperative biomechanical analysis for the planning of spinal surgery not only requires the generation of three-dimensional patient-specific models but also the accurate biomechanical representation of vertebral joints. The benefits offered by computational models suitable for such purposes are still outweighed by the time and effort required for their generation, thus compromising their applicability in a clinical environment. In this work, we aim to ease the integration of computerized methods into patient-specific planning of spinal surgery. We present the first pipeline combining deep learning and finite element methods that allows a completely automated model generation of functional spine units (FSUs) of the lumbar spine for patient-specific FE simulations (FEBio). The pipeline consists of three steps: (a) multiclass segmentation of cropped 3D CT images containing lumbar vertebrae using the DenseVNet network, (b) automatic landmark-based mesh fitting of statistical shape models onto 3D semantic segmented meshes of the vertebral models, and (c) automatic generation of patient-specific FE models of lumbar segments for the simulation of flexion-extension, lateral bending, and axial rotation movements. The automatic segmentation of FSUs was evaluated against the gold standard (manual segmentation) using 10-fold cross-validation. The obtained Dice coefficient was 93.7% on average, with a mean surface distance of 0.88 mm and a mean Hausdorff distance of 11.16 mm (N = 150). Automatic generation of finite element models to simulate the range of motion (ROM) was successfully performed for five healthy and five pathological FSUs. The results of the simulations were evaluated against the literature and showed comparable ROMs in both healthy and pathological cases, including the alteration of ROM typically observed in severely degenerated FSUs. The major intent of this work is to automate the creation of anatomically accurate patient-specific models by a single pipeline allowing

functional modeling of spinal motion in healthy and pathological FSUs. Our approach reduces manual efforts to a minimum and the execution of the entire pipeline including simulations takes approximately 2 h. The automation, time-efficiency and robustness level of the pipeline represents a first step toward its clinical integration.

Keywords: deep learning, patient-specific 3D model, FE analysis, surgical planning and simulation, spine-pathology

INTRODUCTION

Patient-specific three-dimensional (3D) models are essential in computer-assisted surgical procedures. In spine surgery, computer-assisted techniques have been increasingly used in various stages of surgical planning and/or execution, e.g., to determine the optimal trajectory for the insertion of pedicle screws (Goerres et al., 2017; Knez et al., 2019; Mischler et al., 2020), but also to improve surgical navigation and allow an improved execution of the surgical plan (Liebmann et al., 2020; Müller et al., 2020). Biomechanical models can provide information on the preoperative pathological condition such as degenerative changes and their biomechanical consequences (Du et al., 2016; Cai et al., 2020). Patient-specific simulations can be used to analyze the effects of different surgical procedures on specific structures and pathologies. Potentially, the surgical plan can be improved based on the simulation output (Jiang and Li, 2019; Zhou and Willing, 2020). If included in the clinical workflow, such preoperative computational biomechanical analysis, in combination with precise intraoperative navigation, may improve patient outcomes. Finite element (FE) simulations of the lumbar spine have been employed in clinical applications to identify biomechanical parameters (Bernakiewicz and Viceconti, 2002; Little and Adam, 2012), evaluate surgical procedures, and analyze implants, e.g., for spinal fusion (Zhang et al., 2018) or total disc arthroplasty (Zhou and Willing, 2020). Such analyses may provide information on the expected bone and implant loads before surgery (Erbulut et al., 2015; Más et al., 2017; Özmen and Günay, 2019; Panico et al., 2020). Moreover, the biomechanical analysis of pathological spinal segments has the potential to provide indications on the degeneration process of intervertebral disc (IVD) and facet joints (FJs) (Rohlmann et al., 2006; Bashkuev et al., 2020; Cai et al., 2020), thus helping in the analysis of postoperative complications such as the development of adjacent segment degeneration (Li et al., 2015; Zhou and Willing, 2020). IVD and FJ degenerations alter the load transfer in the spine and are commonly associated with low back pain (Uçar et al., 2019; Bashkuev et al., 2020). Nevertheless, current standard clinical procedures lack the ability to perform such patient-specific biomechanical analysis on a daily basis, which hinders the possibility for optimizing the surgical plan.

Abbreviations: CT, Computed Tomography; CNN, Convolutional neural network; DOF, Degree of freedom; DC, Dice coefficient; FJ, Facet joint; FE, Finite element; FSU, Functional spine unit; HD, Hausdorff distance; IVD, Intervertebral disc; MSD, Mean surface distance; ROM, Range of motion; 3D, Three-dimensional.

One of the major challenges for inclusion of such methods in the clinical practice is the effort required to create patient-specific functional models from medical images. It includes several manual steps and is time-consuming even for experienced professionals (Sarkalkan et al., 2014; Campbell and Petrella, 2015). The time needed for the creation of patient-specific finite element (FE) models has rarely been reported, although critical for integrating biomechanical simulations in a clinical environment (Zadpoor and Weinans, 2015). To the best of our knowledge there is no complete automated pipeline for anatomically accurate FE simulations of the lumbar spine based on 3D CT images. A lot of work has been done on parametric FE models (Galbusera et al., 2008; Bashkuev et al., 2018, 2020; Lavecchia et al., 2018; Nikkhoo et al., 2020; Zhou and Willing, 2020) or a combination of statistical and FE models (Bonaretti et al., 2011, 2014; Rao et al., 2013; Campbell and Petrella, 2016). However, those models either neglect important patient-specific structures or their generation involve high amounts of manual work requiring certain types of operator expertise. Although efforts have been made to automate the generation of FE models of the healthy spine (Bah et al., 2009; Campbell and Petrella, 2015), hitherto this process has never been combined with deep learning-based segmentation methods and has not yet been applied to pathological cases. Nowadays, deep learning methods are employed in medical research to analyze images, extract structural information, and to localize and segment 3D structures (Glocker et al., 2012; Korez et al., 2015; Roth et al., 2016; Lessmann et al., 2019). They provide fast results in an automated fashion, with an accuracy comparable to those from manual human processing (Nikolov et al., 2018). Integrating these methods into the creation of patient-specific biomechanical models could drastically accelerate the process and enable a complete automated framework, which in turn would allow clinical routine applications of computational preoperative planning using 3D models (Zadpoor and Weinans, 2015). In previous studies, deformable models were added to a 3D convolutional neural network (CNN) (Korez et al., 2015) to perform segmentation of vertebral bodies from 3D magnetic resonance spine images, However, the method has not yet been applied to FE modeling. It has been also shown how the automatic creation of FE models could benefit from using a mesh-based registration method (Bonaretti et al., 2014).

In this work, we propose a combination of deep learning, statistical, and FE methods on lumbar 3D CT images to generate anatomically accurate patient-specific FE models of FSUs. A biomechanical investigation of spinal segments may be highly clinically relevant, hence our main aim is the automation

of the complete workflow (**Figure 1**). By saving time and reducing manual interaction for modeling and simulation, the main intent of the presented pipeline is a step toward a seamless clinical integration of such models. The goals are the ability to perform state-of-the-art segmentation of pathological (degenerative) lumbar spine's segments and the execution of FE simulations with reasonable results. Using clinically available dataset, the implemented pipeline should provide a basis for further developments toward the integration of patient-specific modeling in clinical planning of spinal surgery. The automation is achieved by the integration of state-of-the-art deep learning methods and a novel interface to FE modeling. The outputs are anatomically accurate patient-specific biomechanical models and results of FE simulations.

MATERIALS AND METHODS

We have combined multiple deep learning methods using two 3D CNNs allowing the automated segmentation of lumbar vertebrae and identification of corresponding point sets on the vertebral meshes. Multiple training datasets were prepared and used to train the different networks needed for the segmentation of the 3D CT images and for the identification of anatomical regions on vertebral models (**Figures 1A,B**). We re-trained the DenseVNet segmentation network presented in Gibson et al. (2018a) within the NiftyNet platform (Gibson et al., 2018b). The correspondence of anatomical points and regions between the segmentation and the template model is achieved by an automated identification of anatomical landmarks on the vertebral surfaces through semantic segmentation. This step acts as an interface to perform non-rigid fitting of the template SSMs and improves the following non-rigid registration results (Clogenson et al., 2015). The method for landmarks identification employed feature steered graph convolutions (FeaStNet) described in Verma et al. (2018). Meticulously prepared reference meshes of the SSMs were a requirement to enable automatic identification of soft tissue insertion points and surfaces. Subsequently, a functional patient specific FE model is automatically created for different lumbar segments based on deformable template models. The goal of the resulting pipeline is to eliminate the time-consuming procedure of preparing FE models (Bah et al., 2009; Taylor and Prendergast, 2015; Wu et al., 2019).

Some of the methods implemented and combined in this work exist as individual implementations. Major effort was spent for their combination and integration into a single pipeline, and developing required interfaces. The correspondence property of the registered template meshes was crucial for the automatic creation of the FE models, e.g., for healthy and degenerated discs (**Figure 1C**). The exclusion of manual steps may result in more reliable and robust pipelines. Furthermore, the ability to biomechanically analyze pathological cases in an automated fashion seems highly relevant for computational surgery planning in an efficient clinical workflow.

Multiclass Segmentation

Training Dataset

The preoperative clinical 3D CT images were selected from a larger dataset by exclusion of severe pathological vertebrae (ethics approval ID: BASEC: 2019-00698). The resulting dataset contains 52 3D CT images all acquired at Balgrist University Hospital between 2014 and 2019. The original field of view (FoV) was manually and systematically reduced by cropping the 3D images to contain the lumbar spine from level L2 until the sacrum. Final 3D images include 3 complete lumbar vertebrae (L5, L4, and L3). The resulting FoVs covered a range of 224–390 voxels (87–117 mm) transversely, and 107–402 voxels (107–141 mm) in the inferior-superior direction. Each cropped 3D image was manually segmented by a single trained radiologist to minimize variability, using the software Mimics 19.0 (Materialise Inc., Leuven, Belgium). Available region-growing and thresholding algorithms were used to generate 3D masks of the original 3D CT images. Distinctive labels were assigned to vertebrae of different levels. Similarly, the output of the trained network will

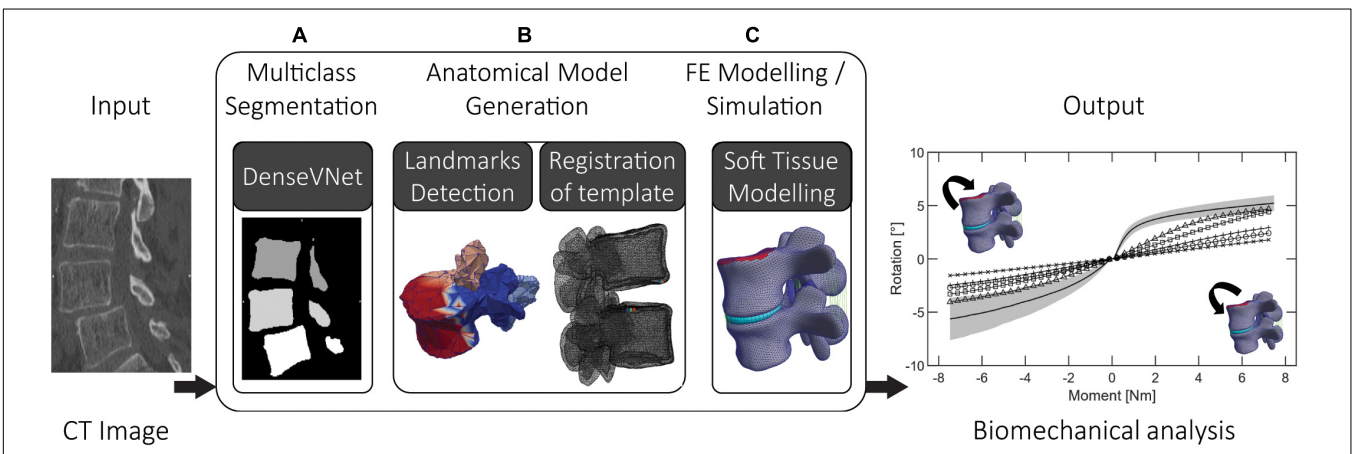

FIGURE 1 | The three steps of the proposed pipeline: **(A)** multiclass segmentation of the CT image dataset, **(B)** semantic segmentation and non-rigid registration of template model, **(C)** FE modeling and simulation, involving complementing the anatomical models with soft tissues (ligaments, IVD) using automatic landmarks detection.

not only contain the segmentation, but also a label discerning between vertebral levels. By cropping the images, we eliminated the class imbalance problem that could otherwise lead to a biased network (Hesamian et al., 2019), which occurs when the majority of the imaging dataset is occupied by background. After cropping, the 3D images were pre-processed by applying a histogram matching transformation (Woods and Gonzales, 1981), equalizing histograms with the reference histograms of an arbitrarily chosen CT image. This preprocessing step allowed the normalization of the intensity within the dataset and is easily applicable to any new image.

Training Process

The DenseVNet network was re-trained using NiftyNet framework (Gibson et al., 2018b) on the 52 3D CT images. This network was originally developed to perform multiclass segmentation of different organs in abdominal CT and offers the possibility to perform segmentation of different structures with improved boundary accuracy. This peculiarity offers an advantage for the definition of facet joints' boundaries between adjacent vertebral bones, particularly critical for the definition of contact surfaces for the FE analysis. The platform NiftyNet was explicitly designed for medical image analysis and it includes the DenseVNet network structure. We included the computation of the Dice-hinge coefficient (DC) losses for the segmentation of each vertebra as described in Gibson et al. (2018a) in the NiftyNet library. This loss function was chosen as it proved promising generalization properties thanks to the adapted weights for classes with low dice scores but significant gradients during training. As the training dataset included images of different dimensions and resolutions, the input volumes were resampled to a voxel dimension of [0.39, 0.39, 0.5]. The training was run for 4,000 iterations using the Adam optimizer with $\varepsilon = 0.001$ (Gibson et al., 2018a) on a Quadro P6000 GPU (NVIDIA Corporation, Los Alamitos, CA) and took 30 h. The output of the trained network is a 3D mask with four different classes, three for the vertebrae, and one for the background (**Figure 1A**). Using the different labels, each vertebral mask was post-processed by removing incorrectly segmented isolated regions with a significantly smaller area compared to the segmented vertebrae. Finally, three segmented models were generated, one for each vertebral level (**Figure 2A**), by performing three different triangulations in MATLAB R2019a (The MathWorks, Inc., United States) using the GIBBON package (Moerman, 2018).

Anatomical Model Generation

Semantic Segmentation of Segmented Vertebrae

Training dataset

The ground truth images used for the training of the DenseVNet network were used to prepare 3D meshes of single vertebral structures. The segmented masks were used to export 3D models of individual vertebrae in the form of triangular surfaces (stereolithographic files: STL). These models were manually divided into four semantic classes: the vertebral body, the left transverse with the left superior articular processes, the right transverse with the right superior articular processes, and the spinous process with the lamina (**Figure 2C**). The division was arbitrarily chosen to achieve satisfying registration of the template model prior to template mesh-fitting. The rationales behind the semantic segmentation step, and the consequent ability to select patient-specific anatomical landmarks, are multiple. Since the same landmarks were labeled on the SSMs, the transformation to place the deformable models can be found automatically. Additionally, initializing the non-rigid registration using landmarks has been shown to improve results (Clogenson et al., 2015). Since the training of the network needed each vertebral model within the dataset to have the same number of points (equal to N in **Figure 3**), the segmented vertebrae were preprocessed to prepare the training dataset. The complete set of vertebral 3D models was down- or up-sampled before the semantic division to match a defined number of points. To assure homogeneous meshes and an accurate representation of details, N was set to 2,947, with 4,000 triangular faces in each mesh. The final training dataset comprised 138 vertebral meshes that were manually segmented and semantically divided.

Training process

Regional information on the segmented meshes was needed to initialize the position of the template models. The Tensorflow Graphics (TG) framework uses revised CNNs to segment 3D models in semantic parts (Valentin et al., 2019), the network is referred as graph convolutional network and is able to process point cloud data (Verma et al., 2018). A simplified CNN version of the FeaStNet architecture was implemented in TG according to Valentin et al. (2019) and used to semantically divide the segmented models of the vertebrae into four parts. **Figure 3** shows the network structure: first, each vertex of the point was encoded by a mesh encoder into a $N \times 4$ logits, where N is the number of points and 4 the number of semantic classes. The mesh encoder consists in 1×1 convolutions linear layer to change the input dimensions, a sequence of feature steered graph convolutions was then followed by 1×1 convolutions to convert the output to a $N \times 4$ logits. The training was run using the Adam optimizer with $\varepsilon = 1e - 8$ and a learning rate equal to 0.001 (Valentin et al., 2019). The output of the mesh encoder was used to perform a soft-assignment of each vertex to one of the four classes (Verma et al., 2018).

The trained network was used to establish correspondence between vertebral 3D models according to the steps depicted in **Figure 2**. The division into semantic classes facilitated positioning of the template SSMs by the automatic identification of labeled anatomical locations. The landmarks were found by computing the center of mass of each semantic part, which was then projected on the surface mesh. A rigid transformation was defined using the identified landmarks on the 3D models and the corresponding points labeled on the SSMs. To account for the uncertainty in the identification of anatomical points, the iterative closest point method (Besl and McKay, 1992) was used to fine-tune the final position, providing an improved initialization for the morphing of the SSMs in the subsequent step.

Template Model's Fitting

Five SSMs were created, one for each lumbar vertebra. Each model was trained using manually segmented 3D meshes of

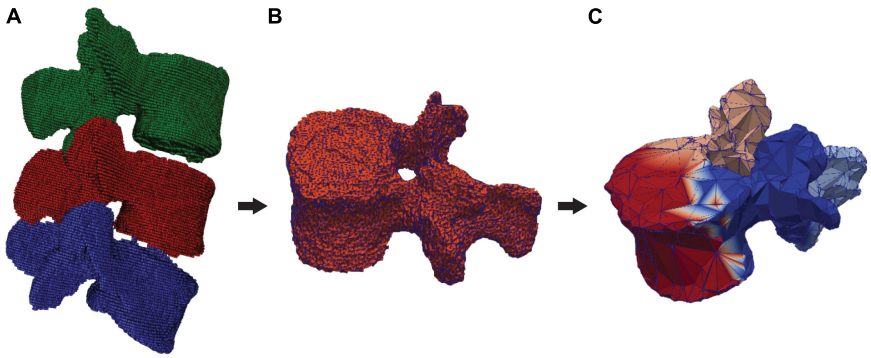

FIGURE 2 | Segmented and labeled vertebrae and division in semantic parts. **(A)** DenseVNet output (L3: green, L4: red, L5: blue), **(B)** 3D segmentation of one vertebra (L4), **(C)** Output of the semantic segmentation of four regions of a vertebra (front: red, left: blue, right: pink, back: azure).

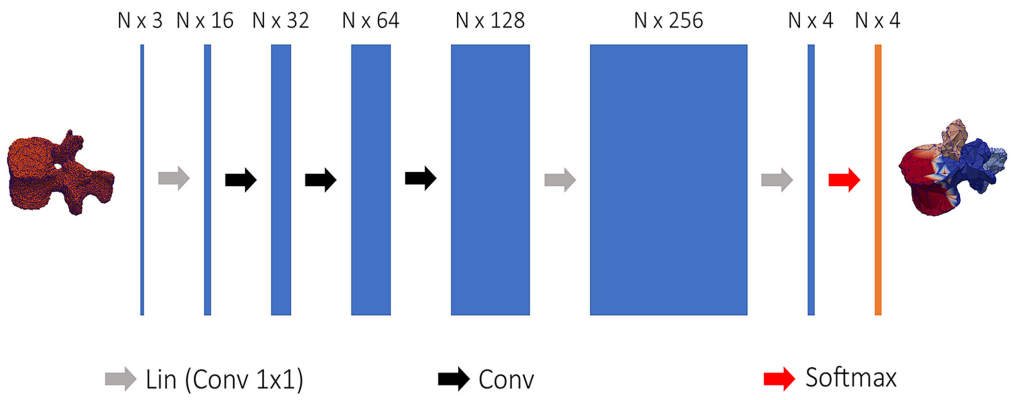

FIGURE 3 | Structure of the network used to semantically segment vertebral models. 3D coordinates of the vertebral point cloud are input to the first linear convolution layer, changing the input feature dimensions. The following layers are the feature steered graph convolutions preceding 1 × 1 convolution to N × 4 logits, used to soft-assign each point of the point cloud to one of the four classes.

lumbar vertebrae, which were not extracted from the images used for the training of the CNNs. The vertebral meshes were divided based on the spinal level and multiple training datasets were created consisting of 100 meshes pro lumbar level. The SSMs were built using a Procrustes Alignment to align each dataset, which was followed by a non-rigid registration as investigated in Clogenson et al. (2015). The resulting 3D models are used to construct the SSMs by finding the main shape variations with a principal component analysis (PCA). The manual creation of the reference meshes used as templates assures a smooth surface and a homogeneous triangularization of elements along the whole vertebral models. The preparation of the template, the training of the SSMs, and the registration framework were implemented in the Scalismo package (University of Basel, Switzerland) (Lüthi et al., 2012). The semantic division together with the positions of the 4 landmarks identified by the trained FeaStNet network provided an optimal initialization for the non-rigid registration of the template SSMs. The non-rigid registration was implemented according to Clogenson et al. (2015) and is based on a point set to image registration. The registrations of the SSMs were further constrained by the four landmarks which were identified on the templates in advance. An additional step was added to the framework presented in Clogenson et al. (2015) and consists in a projection of the SSMs points along the mesh's normal vectors toward the target surfaces. The correspondence of the landmarks together with the projection step increased the performance of the non-rigid registration as well as the precision of correspondence between registered vertebral structures. Constraining the registration allowed a reduction of the search space, leading to a more robust and faster registration process (Clogenson et al., 2015). To finalize the non-rigid registration, a projection of the template nodes was performed after the last iteration along the model's normal vectors on the target triangulated model resulting from the DenseVNet segmentation. This step enables the union of the correspondence property of SSMs with the precision of DL segmentation. The resulting patient-specific anatomical models have the same triangularization properties as the reference meshes of the SSMs but represent the patient's spinal structures.

Anatomical Model Evaluation

To evaluate the anatomical models, the training of the DenseVNet network was performed using 47 labeled 3D CT images while five were excluded for inference. Ten-fold

cross-validation was performed to assess the performance of the anatomical model generation. During each iteration, the network was trained anew and tested on the five excluded images (containing three vertebrae each). Thus, 150 ($10 \times 5 \times 3$) vertebral 3D models were automatically segmented and compared to manually segmented 3D models (ground truth).

The generation of the anatomical model was evaluated directly after the DenseVNet segmentation and after the non-rigid registration of the deformable model. This enables tracking of the segmentation performance throughout the pipeline. Both outputs were compared to the ground truth vertebrae. The evaluation criteria were: the DC, the mean surface distance (MSD), and the Hausdorff distance (HD).

Finite Element Modeling and Simulation

Model Validation Using Cross-Validation Healthy Data

The five images segmented in the last iteration of the cross-validation were used to create and run FE simulations of all L3L4 and L4L5 FSUs of each patient, respectively. The dimensions of the resulting healthy vertebrae were on average: 86.28 mm left-right, 88.43 mm anterior-posterior, and 48.35 mm inferior superior. The registration of the deformable templates ensures the correspondence of nodes across the fitted surface models (Verma et al., 2018; Wu et al., 2019). The correspondence property allows to label essential regions for the creation of the final FE model. The facet joints, the vertebral endplates, and the ligament attachment points were manually labeled on the template of each vertebra *a priori*, as shown in **Figure 4** for a model of L4, and used to define contacts and boundary conditions. The registered SSM resulted in patient-specific surface meshes allowing the personalization of insertion points and contact surfaces, adjusted according to the patient anatomies by the registration step. The resulting surface models were converted into volumetric meshes and divided into cortical and trabecular bone. The inter-subject variability of the material properties was not considered. All the material properties of the FE model were implemented according to Finley et al. (2018). The trabecular bone, the IVD nucleus, the vertebral endplates, and the facet cartilage were represented using a neo-Hookean model; the cortical bone is modeled as orthotropic elastic material, and the superior endplate of the upper vertebra (indicated in red in **Figure 4**) was rigidly modeled and used to apply the pure moment loading. To represent the annulus, a compressible Holmes-Mow material model was coupled with two fiber components. The material properties of the FE models are summarized in **Table 1**.

The anterior longitudinal ligament, posterior longitudinal ligament, supraspinous ligament, intertransverse ligament, ligamentum flavum, and interspinous ligament were modeled as non-linear and tension-only elements (Finley et al., 2018). The endplates of the superior and inferior vertebrae served as reference to place and fit the IVD. The superior endplate of the upper vertebra was used to apply the pure moment of 7.5 Nm in various directions to simulate flexion, extension, axial rotation, and lateral bending, whereas the inferior endplate remained constrained in all the degrees of freedom (DOF). Contact areas of the FJs were defined in facet's cartilage regions and implemented as sliding interfaces enforcing a non-penetration constraint. **Figure 4** shows how those regions and landmarks are marked on different template models. Using the endplates' nodes, a hexahedral mesh defining the IVD was created for each FSU and deformed to assure a tied contact with superior and inferior vertebrae. These steps defining the FSU FE model were implemented in the GIBBON package (Moerman, 2018) and the simulations were performed within the open-source tool FEBio 2.9 (Maas et al., 2012) using an implicit FE solver. The pipeline was implemented such that the creation of the FE models and the corresponding simulations were automatically run in sequence. In this study, only the geometrical inter-subject differences were considered; because automating the creation of FE models in a single pipeline was the primary goal.

For the simulation of flexion, extension, lateral bending, and axial rotation movements all the DOF of the inferior endplate were constrained and a pure moment of 7.5 Nm was applied to the superior endplate of the upper vertebra. To test the mesh convergence of the FE simulations, down-sampled deformable models (**Figure 4B**) were registered to the L4 and L5 vertebrae of one subject. The resulting range of motion (ROM) from axial rotation simulations was compared among the different down-sampled models to assess mesh-convergence of the FE simulations and to compare the results using different template models.

Evaluation on Pathological FSUs

The whole pipeline was further evaluated on 5 pathological cases, in addition to the five non-pathological cases from the training dataset. The 3D CT images were initially acquired as part of a previous study in our institution (Widmer et al., 2020a) with approval from local ethical authorities (BASEC Nr. 2017-00874). The specimens selected for this project were excluded in Widmer et al. (2020a) as they were classified as severely pathological by a medical professional. To evaluate the robustness of the pipeline, different lumbar spinal segments were included. The five pathological FSUs were composed of two L2L3, two L3L4, and one L1L2. The anatomical dimensions of the pathological vertebrae were similar to the ones of the healthy FSUs: 87.37 mm left-right, 95.9 mm anterior-posterior, and 53.3 mm inferior-superior. The pathological specimens originated from fresh frozen cadavers (**Table 2**). The classification of IVD degeneration was performed by Pfirrmann grade (Pfirrmann et al., 2001) based on the segmented 3D models, the CT, and the MR images. From the five pathological lumbar segments, 3 had Pfirrmann grade equal to 4, and in two cases the specimen was classified with a Pfirrmann grade equal to 5. The Weishaupt grade (Zhou et al., 2016) for FJ degeneration in the 5 pathological FSUs was between 2 (narrowing of the facet joint space), and 3 (narrowing of the facet joint space and/or moderate osteophytes, and/or moderate hypertrophy of the articular process, and/or mild subarticular bone erosions). In this study, the vertebral structures were segmented and fitted using the trained neural networks and the statistically deformable templates as described above, but the IVD was fitted between the labeled upper and lower vertebral endplates. The accuracy in the segmentation of

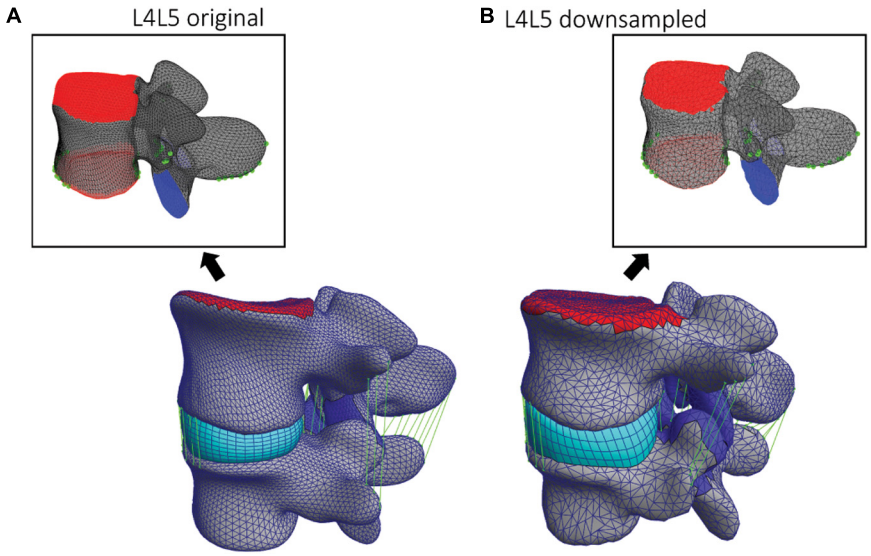

FIGURE 4 | (A) Original and **(B)** down-sampled template L4 models and corresponding L4L5 FSU FE models. On the two template models, the facets and endplates surfaces are labeled (blue and red) as well as the ligaments attachment points and paths (green).

TABLE 1 | Material properties used for the FE simulations of the healthy FSUs.

Structure	Material model	Young's modulus (MPa)	Poisson's ratio
Cortical bone	Orthotropic elastic	E_1 = 8,000	ν_{12} = 0.4
		E_2 = 8,000	ν_{23} = 0.3
		E_3 = 12,000	ν_{31} = 0.35
Trabecular bone	Neo-Hookean	E = 100	v = 0.2
Vertebral endplate	Neo-Hookean	E = 1,000	v = 0.3
Nucleus pulposus	Neo-Hookean	E = 1	v = 0.49
Annulus matrix	Holmes-Mow	E = 1	v = 0.4
		β = 3.4	
Annulus fibers	Fiber-exponential-power	α = 65	–
		β = 2	
		ξ = 0.296	
Facet cartilage	Neo-Hookean	E = 30	v = 0.4

the bony structures defined the shape of the IVD mesh that was enforced to be in contact with the vertebral endplates. To account for the existing pathology, the material parameters were corrected automatically. For the FSUs with Pfirrmann grade 4, the Young's modulus values of the nucleus pulposus and of the annulus matrix were changed to 1.4 and 4.5 MPa, respectively. The Poisson's ratio was changed to 0.42 in the nucleus pulposus. The remaining properties were as stated in **Table 1**. For Pfirrmann grade 5, the Young's modulus of the nucleus pulposus and the annulus matrix were set to 2.2 and 5.5 MPa, respectively. The Poisson's ratio of the nucleus pulposus was changed to 0.32 (Wang et al., 2012). The altered material properties reflect a stiffening of the IVD concomitant with a loss of fluid content as the degeneration progresses (Wang et al., 2012).

TABLE 2 | Demographics and degeneration state for the five pathological samples.

Specimen	Sex	Age (y)	Height (cm)	Weight (kg)	Pfirrmann
S182452	Male	62	173	79	4
S182664	Male	75	185	98	5
S181997	Male	82	185	91	4
S182571	Female	84	165	67	4
S181934	Male	75	188	79	5

Although material properties mapped from imaging data would be desirable, patient-specific material properties have not been included in this study. The main objective of this work is the automated generation of anatomically accurate FSUs models. Any material mapping method could then be implemented on these models. Nevertheless, we used our models to simulate ROM and evaluated the reasonability of results by comparing them to reported values from the literature.

RESULTS

Cross-Validation

We report the results of the cross-validation in terms of the segmentation resulting from the trained DenseVNet network, and precision of the 3D model after landmark-based template model fitting (section "Segmentation") corresponding to the 150 healthy vertebrae. The FE simulations' results are presented for the 10 FSUs resulting from the last iteration of the cross-validation (section "Finite Element Modeling"). The segmentation metrics before and after the deformation of the template model showed a slight decrease in performance in terms

of DC, on the other hand, the MSD and the HD were better after the template model deformation.

Segmentation

The evaluated metrics were computed for each vertebra in the 5 excluded images segmented during cross-validation. For each iteration, the metric values were averaged over the five images for each vertebral level. **Table 3** summarizes the average of the evaluation metrics for all the 3 vertebrae after 10 iterations of the cross-validation (N = 50 per vertebral level). The resulting metrics show how the trained network achieved state-of-the-art performance in the segmentation of lumbar vertebrae with average DC equal to 93.71%. The MSD was equal to 0.88 mm and the HD to 11.16 mm, on average among all the three vertebrae for all the five images excluded in each iteration of the cross-validation (N = 150, combining the three lumbar vertebrae). **Table 3A** shows the same metrics divided per level. After the non-rigid registration step, which was performed directly after each iteration of the cross-validation, the DC performance decreased by 3.05%, but the MSD and HD performances increased by 23.86 and 34.23%, respectively (**Table 3B**). The non-rigid registration of the template models acts as a smoothing filter on the segmented vertebrae, lowering the overall performance in terms of the DC, but improving the surface distance metrics of the segmented models by filtering out large HD values.

Finite Element Modeling

The FE simulations provide load-deformation behavior for flexion, extension, lateral bending, and axial rotation. The ROM values averaged over all the 5 subjects are shown in **Figure 5** for each type of motion and two lumbar FSUs.

These ROM values are depicted with reported values for single FSU models from two different studies (Dreischarf et al., 2014; Finley et al., 2018). **Figure 5** shows the average and the standard deviation of the intersegmental rotation angles vs. the change in the applied moment from −7.5 to 7.5 Nm. The results were in agreement with those from Finley et al. (2018) and with the reported values from the six computational models analyzed in Dreischarf et al. (2014). The ROMs resulting from the FE simulations in this study were 4.49°–6.45° and 3.64°–7.64° for flexion and extension, respectively, 4.39°–13.12° for lateral bending, and 3.31°–6.75° for axial rotation. The ranges of the flexion and extension angles obtained in Finley et al. (2018) were 3°–4° and 2.1°–3.8°, respectively, whereas the ranges for lateral bending and axial rotation were 2.3°–3.84° and 2.18°–3.75°, respectively. The ROMs reported in Dreischarf et al. (2014) from median *in vivo* values differed more to the simulated ones, they reported angles between 5.5° and 19.2° and −1° and 4° for flexion and extension, respectively. The ranges for lateral bending and axial rotation were independent of the rotational direction and equal to −2.3° and 10.3° and −1° and 4°, respectively.

The results of the mesh convergence analysis performed on an L4L5 FSU of one subject are summarized in **Figure 6**. The reference meshes of the SSMs representing the two vertebral levels were down-sampled by factors of 1.2, 1.5, 2, and 3 and registered to the DenseVNet outputs using the same landmark-based fitting method. The down-sampled models did not affect the non-rigid registration precision since it was constrained by the same landmarks identified using the FeaStNet network and were able to achieve patient-specific geometries. Large down-sampling factors lead to early non-convergence of the simulations, likely related to the adverse effect of large element size in contact modeling. As the original mesh size offers a good compromise between registration precision and computational costs, all following models were created with this mesh size.

Pathological FSUs

The pipeline was also evaluated on pathological 3D CT images and the same metrics were computed after the segmentation of the five pathological FSUs. The results show how the performance of the pipeline resulting from the cross-validation translates to clinically relevant cases. After segmentation, the average DC was equal to 90.4 ± 2.9%, the MSD was 0.66 ± 0.1 mm, and the average HD was 10.7 ± 4.4 mm. **Figure 7** shows a comparison between a healthy FSU FE model from the cross-validation and a pathological FSU with Pfirrmann grade equal to 5. The vertebral structures were segmented and fitted with the deformable templates as described above, but the elements of the IVD were reduced automatically according to the mean distance between the labeled endplates.

The FE simulations of the pathological cases are presented in **Figure 8** together with the ROMs of the healthy FSUs for flexion/extension, lateral bending, and axial rotation. The ROM values for pathological FSUs presented in two different studies (Rohlmann et al., 2006; Warren et al., 2020) are included in **Figure 8**. The resulting rotations decreased with the same moment of 7.5 Nm applied. From the FE simulations, a difference in intersegmental rotation between specimens presenting Pfirrmann grade equal to 4 and 5 was noticeable.

TABLE 3 | Mesh metrics from the cross-validation.

	(A) DenseVNet segmentation			(B) Non-rigid registration		
	DC (%)	AD (mm)	HD (mm)	DC (%)	AD (mm)	HD (mm)
L3	93.71 ± 8.2	1.02 ± 1.71	11.9 ± 11.61	92.54 ± 1.8	0.55 ± 0.14	6.39 ± 3.42
L4	93.68 ± 5.9	0.90 ± 1.24	11.1 ± 9.4	90.62 ± 2.5	0.70 ± 0.21	7.27 ± 2.51
L5	93.73 ± 4.9	0.72 ± 0.77	10.4 ± 7.03	89.38 ± 5.7	0.75 ± 0.33	8.30 ± 4.82

*The performance is evaluated directly after the DenseVNet Segmentation **(A)** and after the registration of the deformable models **(B)**. Each metric was evaluated on 50 vertebral models, for each lumbar level.*

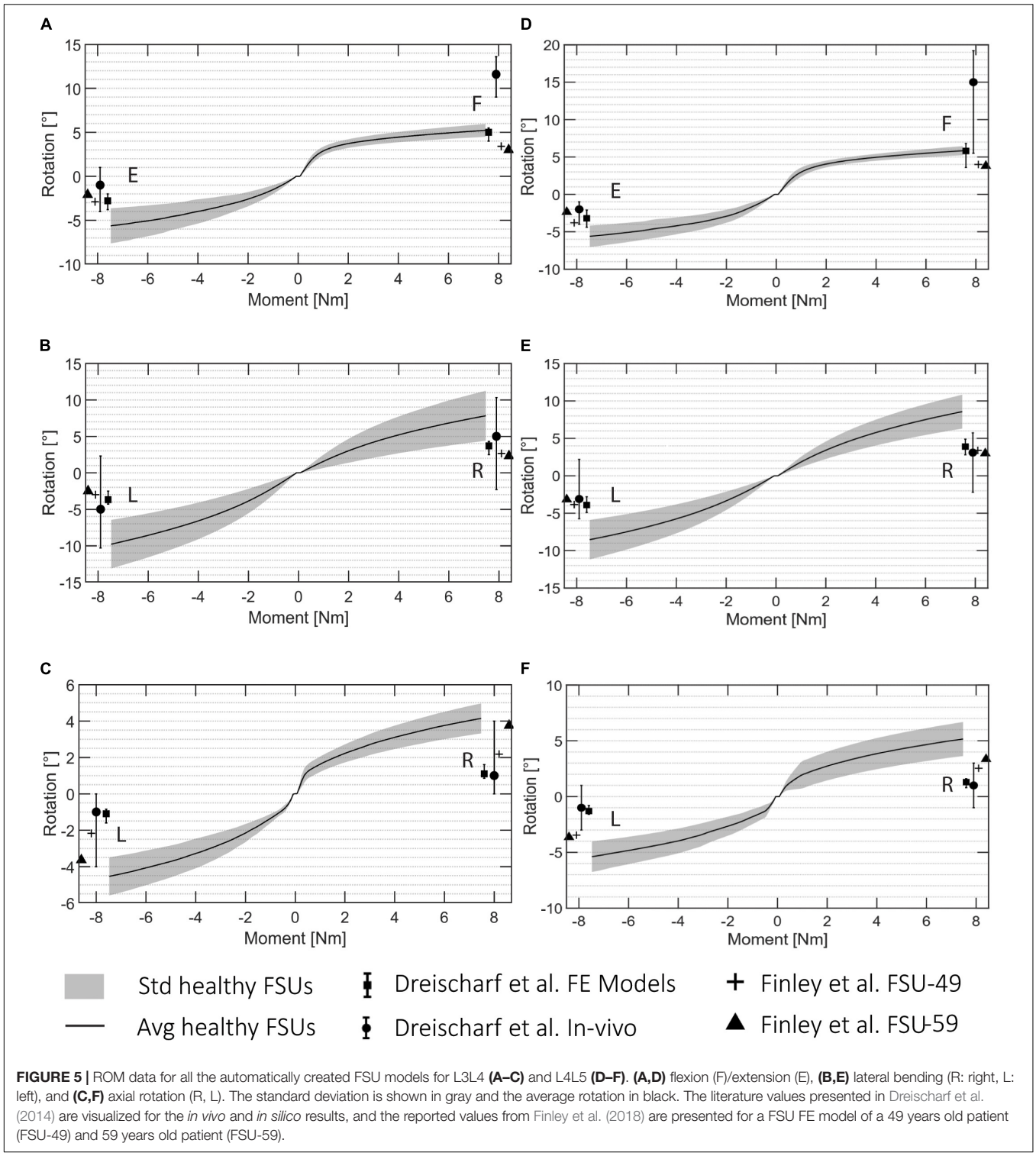

FIGURE 5 | ROM data for all the automatically created FSU models for L3L4 **(A–C)** and L4L5 **(D–F)**. **(A,D)** flexion (F)/extension (E), **(B,E)** lateral bending (R: right, L: left), and **(C,F)** axial rotation (R, L). The standard deviation is shown in gray and the average rotation in black. The literature values presented in Dreischarf et al. (2014) are visualized for the *in vivo* and *in silico* results, and the reported values from Finley et al. (2018) are presented for a FSU FE model of a 49 years old patient (FSU-49) and 59 years old patient (FSU-59).

The ranges resulting from the pathological simulations were on average 57.7% lower than the average angles resulted for the same simulations on the healthy FSUs. The flexion/extension simulations resulted in ranges of 1.79°–4.67°, and 1.56°–4.04°, respectively. Lateral bending was between 0.93°–3.76° in left and right directions, and axial rotation resulted in movements between 1.22° and 2.56° in left and right directions. The ROMs decreased with respect to the healthy ones according to the degeneration grades assigned during the classifications (Widmer et al., 2020a) the average ROM reduction for FSUs classified as Pfirrmann equal to 4 was 49.3%, and the reduction for FSU with Pfirrmann grade equal to 5 was 70.4%. Therefore, FSUs

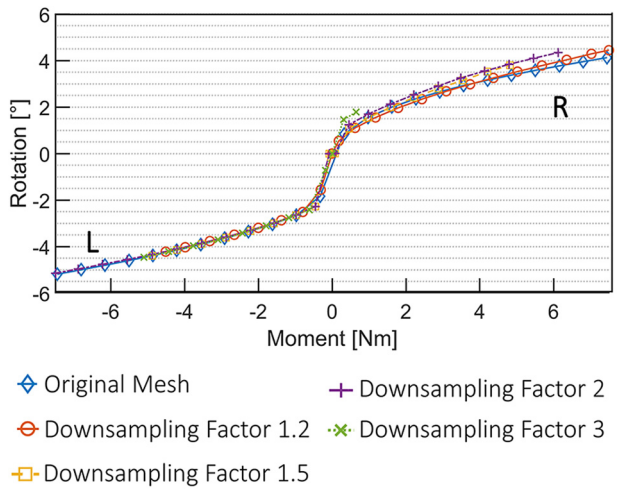

FIGURE 6 | Convergence analysis using five different 3D deformable models. An FSU of L4L5 was used for the simulation of axial rotational movement (R, right; L, left).

with a higher degenerative condition corresponded to a reduced ROM from the FE simulations. This was true for all the three simulated motions. Because of the asymmetrical FJs and/or IVD degenerations, lateral bending and axial rotation simulations resulted in different movements for the left and right sides.

DISCUSSION

The presented pipeline combines deep learning methods to perform image and semantic mesh segmentations, together with FE modeling to automatically generate and analyze patient-specific FSUs. The segmentation of vertebrae using the DenseVNet network produced highly accurate results comparable to the state-of-the-art automated segmentation methods (Sekuboyina et al., 2017; Janssens et al., 2018; Vania et al., 2019) for both healthy and pathological FSUs. The simulations using the open-source FE solver FEBio during cross-validation had comparable results to the ones reported in the literature (Dreischarf et al., 2014; Finley et al., 2018) and also for the simulated pathological cases (Rohlmann et al., 2006; Jiang and Li, 2019). The whole pipeline is based on a cropped 3D CT image of lumbar spinal segments of interest and does not require any other inputs or manual interaction to perform a biomechanical analysis of FSUs. The current time required to create a FE model of the spine is rarely reported but the state-of-the-art process includes using a software for the segmentation of volumetric images to obtain surface meshes. The latter are again imported in a second software to create volumetric models and perform the FE simulations including pre- and postprocessing steps (Bah et al., 2009; Haj-Ali et al., 2019; Jiang and Li, 2019; Özmen and Günay, 2019). From our empirical experience, the process of segmentation, meshing, FE model preparation and simulation can take up to several days. In addition, since many tedious manual steps are needed for the model's preparation, the robustness of the process could be affected. However, replicability is key when different FSU configurations have to be tested, to identify clinically relevant differences between patients' structures. With the proposed pipeline, we were able to simulate simple movements for many FSUs from a 3D CT image with a minimal amount of user interaction for cropping the input image, requiring a time effort of about 30 s. Both segmentation and FE simulations were evaluated on five healthy cases within the cross-validation, and on five pathological FSUs selected from a different dataset of images. The entire pipeline, from image cropping to the patient-specific biomechanical results for the FSUs of interest, is about 2 h. Compared to current state-of-the-art this represents a significant reduction in time and manual interaction.

The resulting ROMs of the healthy FSUs were within the range of other published FE models but slightly outside the range of *in vivo* measured ROMs (Dreischarf et al., 2014). The comparison between models is difficult since the patient-specific geometries are potentially affecting the ROM. The geometrical variability was mostly not considered in FE modeling, but different structures could lead to different ROM results. Patient-specific material properties were neither considered in the creation of the FE model, potentially introducing further deviation from *in vivo* behavior (Dreischarf et al., 2014). From the obtained results, we can observe the larger influence of the facet joints in the lateral bending and axial rotation simulations due to specificity of patient geometry when estimating joint motion. However, the different results between healthy and pathological cases were verified and the pipeline is able to capture different degenerated states automatically, as shown in **Figure 8**. The resulting ROMs obtained for the pathological cases were in line with the clinical degeneration grades, correctly showing a reduction in the intersegmental rotation angles in comparison to the healthy FSUs ROMs. Furthermore, the simulated ROMs partially agreed with the pathological values reported in the *in silico* studies from Rohlmann et al. (2006) and Warren et al. (2020). However, a direct comparison of values may be compromised due to simplified FE models in those studies.

The automatization of simulations for the proposed pathological cases may accelerate the inclusion of FE simulations in the planning of spinal surgery. It allows studying how different degrees of degeneration affect the FSU's motion patient-specifically. A biomechanically based preoperative assessment is needed for patients presenting signs of IVD and/or FJ degeneration, to obtain an optimal patient-specific surgical plan taking pre-existing conditions into account (Li et al., 2015; Perolat et al., 2018) and to customize corresponding patient treatment (Zhou et al., 2016). The selection of an FSU of interest is the only manual step within the suggested pipeline, making its integration into the surgical planning workflow easier.

Following, we discuss some of the limitations of this work. The implemented pipeline was not evaluated on publicly available datasets. However, it achieved state-of-the-art precision employing standard medical data. Our goal was not to outperform existing segmentation methods, but rather to combine different solutions for both segmentation and FE modeling tasks in a single automated pipeline. Biomechanical analysis has the potential to improve surgical planning but

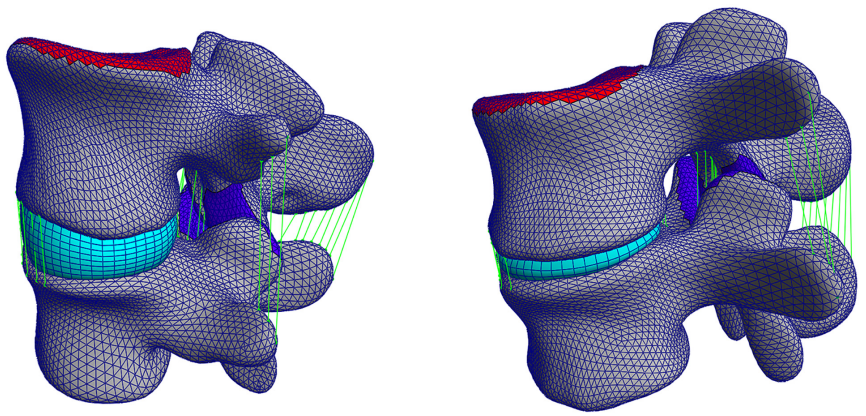

FIGURE 7 | Left: a healthy FSU FE model evaluated in the cross-validation, right: a pathological FSU FE model with Pfirrmann grade equal to 5.

its integration in the clinical workflow is essential. Hence, the acceleration of the time-consuming preparation of FE models was targeted using the proposed implementation. The input images must still be manually cropped by a user, yet this could be considered as a user control point to select the correct levels of interest. The cropping itself represents a very quick step for medical professionals and the pipeline functions with different cropping sizes and regions of the lumbar spine. This is one of the main differences to other semi-automatic approaches consisting of labor-intensive (and therefore costly) and time-consuming steps (Zadpoor and Weinans, 2015; Haj-Ali et al., 2019; Nikkhoo et al., 2020). Indeed, many training data used in this work were manually annotated, for example the segmentation of 3D CT images, or the anatomical landmarks defined on the reference meshes of the SSMs. Although manual annotation may be a possible insertion of errors, it is also comparable with the state-of-the-art creation of biomechanical models from CT data. We believe that the advantages are multiple and as a result of the different trainings, our pipeline is able to reduce inter-user variability which is normally intrinsic in the creation of biomechanical models mostly due to the inevitable involvement of manual work. The automation of multiple steps has the natural consequence of improving consistency and allowing comparisons between multiple patient-specific analysis. In addition, new training datasets may be created with a drastic decrease in manual efforts.

As another limitation, patient-specific material mapping was not implemented. This could be critical for a correct patient-specific model, since the inclusion of patient-specific material properties plays a crucial role in generating clinically relevant outputs. The lack of patient-specific material properties may influence the resulting ROMs. Different studies have shown how much biomechanical parameters vary between subjects (Van Rijsbergen et al., 2018; Sawa et al., 2020; Wawrose et al., 2020) and how the ROM is affected by these variations. The ROMs reported in this work were partially out of range as compared to other studies (Dreischarf et al., 2014). Also, minor inaccuracies in the vertebral geometry, and especially in the FJs, may influence the ROMs (O'Reilly and Whyne, 2008). In our pipeline, small errors resulting from the automated segmentation were predominantly concentrated in the FJ regions. On one hand, this has a negative impact on the performance metrics of the segmentation, yet a small one since the surface of the FJ regions are small as compared to the overall surface of a vertebra. On the other hand, this could further lead to penetrations between the vertebral meshes of different levels after SSM registration. In such cases the FJ gap is created automatically by making fine adjustments to mesh regions. The resulting small morphological deviations from the real patient's anatomy may have a significant effect on simulated motion, and are a potential explanation for the large ROM values observed in lateral bending and axial rotation. Particularly in these modes of spinal movement facet joints act to prevent from excessive motion, which may have been compromised on the current study. In addition to ROM, the FJ forces and intradiscal pressure may deliver insight on the validity of the presented model, and we intend to further improve the model by also evaluating these measures. In any case, a comprehensive validation of the desired outputs is required prior to any clinical application, as with any computational model.

The intent of this study, however, was to prove that a complete automated concept for the biomechanical analysis of lumbar 3D CT images is possible in a single pipeline. Our main objective was the implementation of a complete automated pipeline able to generate and simulate anatomically accurate FE models, also in pathological conditions. More complex FE models could contain patient-specific material mapping and implants could be also added. The improvement of the patient-specificity of the model using material mapping, together with an improved version of the material models in the FE simulations, are the next expected steps to improve our pipeline (Widmer et al., 2020a,b). Additionally, the identification of clinically relevant FSUs could be implemented automatically using existing techniques for image cropping, vertebrae localization (Chu et al., 2015; Korez et al., 2015; Sekuboyina et al., 2017), and segmentation of pathological (Ibragimov et al., 2017) or fractured vertebral structures (Roth et al., 2016) including the segmentation of the IVD (Zheng et al., 2017; Han et al., 2018). In its current implementation, the pipeline is not able to run

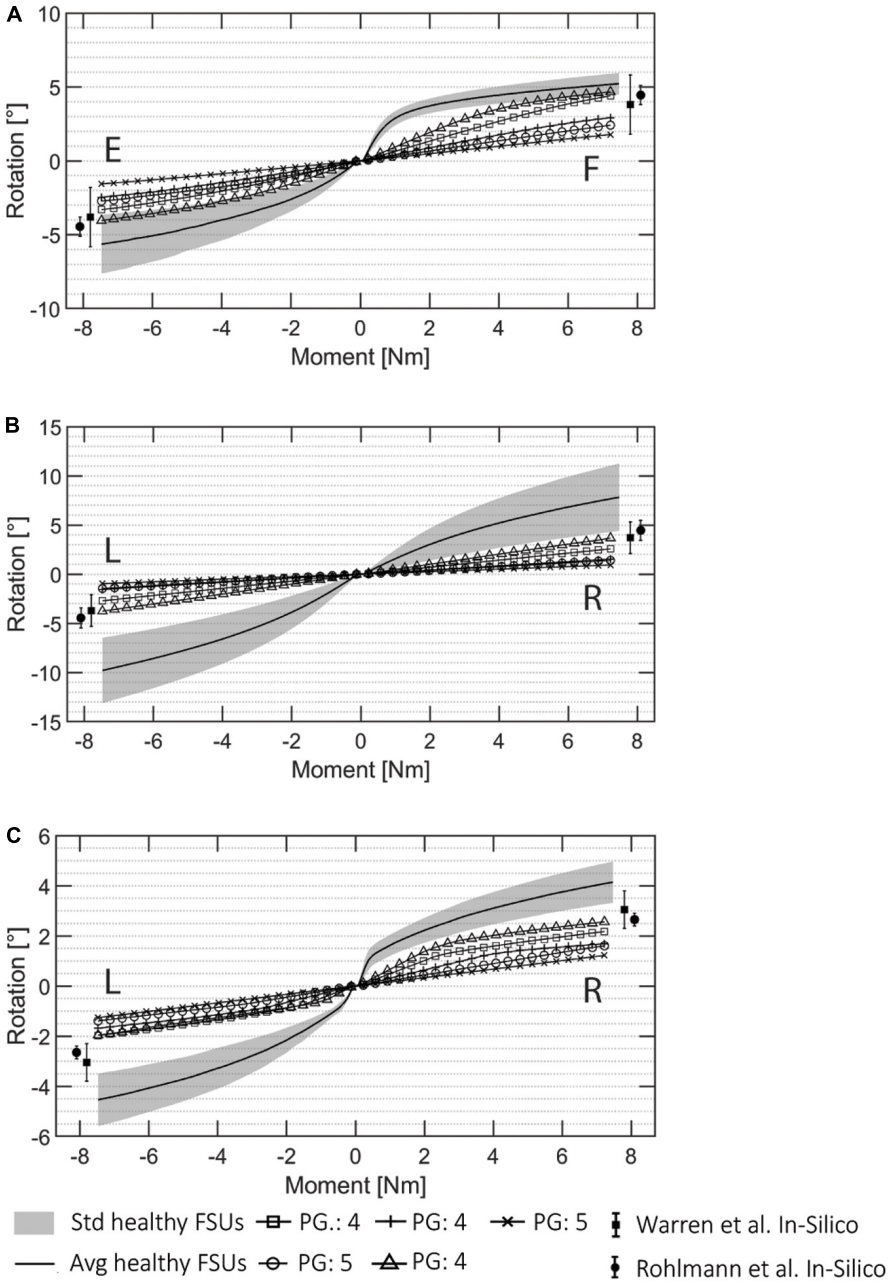

FIGURE 8 | ROM data for all the automatically created pathological FSU models for **(A)** flexion (F)/extension (E), **(B)** lateral bending (R: right, L: left), and **(C)** axial rotation (R, L). The Pfirrmann grade (PG) of each FSUs is marked in the image. The pathological results from the literature presented in Rohlmann et al. (2006) and Warren et al. (2020) are visualized.

the FE simulations for pathologies such as fused vertebrae or disc prolapse. An enlarged or additional training dataset will be needed to allow the accurate segmentation of pathological cases. These may then also include fractured or collapsed vertebral structures. The current pipeline is limited in that it is only able to create anatomical models of intact vertebral structures without osteophytes. The automatic identification and segmentation of such cases avoiding *biases* is one of the bottlenecks in medical images processing (Galbusera et al., 2019). However, in our group, the accelerated creation of anatomically accurate models has supported the preparation of instrumented FE models to investigate the bone-screw interface (Widmer et al., 2020b). Even if the current pipeline only accepts very specific types of deformities, it represents a first successful attempt for the automation of biomechanical analysis. The time saved for model preparation enables computational analysis at a low cost, which we believe is an important step toward their clinical integration.

CONCLUSION

The results obtained from the implemented pipeline demonstrate a novel and powerful approach for automatic generation of predictive models with results that are comparable to manually segmented and manually generated FE models, in both healthy and pathological FSUs. The approach reduces manual interaction to a minimum, involving only the cropping of the 3D CT image as input to the pipeline for fast generation of anatomically accurate FE models. The automatization of the labor-intensive steps of vertebrae segmentation, landmark identification, and finite element model generation reduces clock time by orders of magnitude as compared to manual preparation. Results of FE simulations are available in about 2 h from feeding cropped images into the pipeline. Notably, the approach allows modeling of pre-existing pathological conditions in an automatic fashion. The advances described in this work are a first step toward enabling substantial improvements for computer-assisted surgical planning of the spine thanks to the integration of patient-specific biomechanical analysis.

DATA AVAILABILITY STATEMENT

The data analyzed in this study is subject to the following licenses/restrictions: The dataset is under property of a third party. Requests to access these datasets should be directed to MF, Mazda.Farshad@balgrist.ch.

ETHICS STATEMENT

The studies involving human participants were reviewed and approved by ID: BASEC: 2019-00698. Written informed consent for participation was not required for this study in accordance with the national legislation and the institutional requirements.

AUTHOR CONTRIBUTIONS

SC developed the pipeline and was responsible for the technical details and designed the training and validation of the different CNNs and the implementation of the statistical models and analyzed the FE simulations results and wrote the manuscript and prepared the figures. FC contributed to the design of the models and to the presentation of the results and assisted with the simulations and supported the figures' creation and also contributed to the final manuscript. JS supervised the project and contributed to the interpretation and presentation of the results. JS, MF, and MS contributed to the final version of the manuscript. MF supervised the design of the research and contributed to the interpretation of the results from the clinical side. MS supervised the project and technical details and designed the structure of the pipeline and supported SC with the analysis of the results and the preparation of the figures. All authors contributed to the article and approved the submitted version.

FUNDING

This work is part of "SURGENT" under the umbrella of University Medicine Zurich/Hochschulmedizin Zürich.

ACKNOWLEDGMENTS

We would like to acknowledge A. Encinas Bartos for the help with the cross-validation, V. Gerber for the help with the FE simulations and convergence study, and Frédéric Cornaz and Jonas Widmer for providing the data of the pathological FSUs.

REFERENCES

Bah, M. T., Nair, P. B., and Browne, M. (2009). Mesh morphing for finite element analysis of implant positioning in cementless total hip replacements. *Med. Eng. Phys.* 31, 1235–1243. doi: 10.1016/j.medengphy.2009.08.001

Bashkuev, M., Reitmaier, S., and Schmidt, H. (2018). Effect of disc degeneration on the mechanical behavior of the human lumbar spine: a probabilistic finite element study. *Spine J.* 18, 1910–1920. doi: 10.1016/j.spinee.2018.05.046

Bashkuev, M., Reitmaier, S., and Schmidt, H. (2020). Relationship between intervertebral disc and facet joint degeneration: a probabilistic finite element model study. *J. Biomech.* 102:109518. doi: 10.1016/j.jbiomech.2019.109518

Bernakiewicz, M., and Viceconti, M. (2002). The role of parameter identification in finite element contact analyses with reference to Orthopaedic biomechanics applications. *J. Biomech.* 35, 61–67. doi: 10.1016/S0021-9290(01)00163-4

Besl, P. J., and McKay, N. D. (1992). "Method for registration of 3D shapes," in *Proceedings of the Sensor Fusion IV: Control Paradigms and Data Structures*, Boston, MA.

Bonaretti, S., Seiler, C., Boichon, C., and Philippe, B. (2011). "Mesh-based vs. Image-based statistical appearance model of the human femur. a preliminary comparison study for the creation of finite element meshes," in *Proceedings of the Mesh Processing in Medical Image Analysis Workshop, MICCAI*, Bern.

Bonaretti, S., Seiler, C., Boichon, C., Reyes, M., and Büchler, P. (2014). Image-based vs. mesh-based statistical appearance models of the human femur: implications for finite element simulations. *Med. Eng. Phys.* 36, 1626–1635. doi: 10.1016/j.medengphy.2014.09.006

Cai, X. Y., Sang, D., Yuchi, C. X., Cui, W., Zhang, C., Du, C. F., et al. (2020). Using finite element analysis to determine effects of the motion loading method on facet joint forces after cervical disc degeneration. *Comput. Biol. Med.* 116:103519. doi: 10.1016/j.compbiomed.2019.103519

Campbell, J., and Petrella, A. (2015). An automated method for landmark identification and finite element modeling of the lumbar Spine. *IEEE Trans. Biomed. Eng.* 62, 2709–2716. doi: 10.1109/TBME.2015.2444811

Campbell, J. Q., and Petrella, A. J. (2016). Automated finite element modeling of the lumbar spine: using a statistical shape model to generate a virtual population of models. *J. Biomech.* 49, 2593–2599. doi: 10.1016/j.jbiomech.2016.05.013

Chu, C., Belavı, D. L., Armbrecht, G., Bansmann, M., Felsenberg, D., and Zheng, G. (2015). Fully automatic localization and segmentation of 3D vertebral bodies from CT/MR images via a learning-based method. *PLoS One* 10:e0143327. doi: 10.1371/journal.pone.0143327

Clogenson, M., Duff, J. M., Luethi, M., Levivier, M., Meuli, R., Baur, C., et al. (2015). A statistical shape model of the human second cervical vertebra. *Int. J. Comput. Assist. Radiol. Surg.* 10, 1097–1107. doi: 10.1007/s11548-014-1121-x

Dreischarf, M., Zander, T., Shirazi-Adl, A., Puttlitz, C. M., Adam, C. J., Chen, C. S., et al. (2014). Comparison of eight published static finite element models of the intact lumbar spine: predictive power of models improves when combined together. *J. Biomech.* 47, 1757–1766. doi: 10.1016/j.jbiomech.2014.04.002

Du, C. F., Yang, N., Guo, J. C., Huang, Y. P., and Zhang, C. (2016). Biomechanical response of lumbar facet joints under follower preload: a finite element study. *BMC Musculoskelet. Disord.* 17:126. doi: 10.1186/s12891-016-0980-4

Erbulut, D. U., Zafarparandeh, I., Hassan, C. R., Lazoglu, I., and Ozer, A. F. (2015). Determination of the biomechanical effect of an interspinous process device on implanted and adjacent lumbar spinal segments using a hybrid testing protocol: a finite-element study. *J. Neurosurg. Spine* 23, 200–208. doi: 10.3171/2014.12.SPINE14419

Finley, S. M., Brodke, D. S., Spina, N. T., DeDen, C. A., and Ellis, B. J. (2018). FEBio finite element models of the human lumbar spine. *Comput. Methods Biomech. Biomed. Engin.* 21, 444–452. doi: 10.1080/10255842.2018.1478967

Galbusera, F., Bellini, C. M., Aziz, H. N., Raimondi, M. T., Brayda-Bruno, M., and Fornari, M. (2008). Parametric FE mesh generation: application to the cervical spine. *J. Appl. Biomater. Biomech.* 6, 95–103. doi: 10.1177/228080000800600205

Galbusera, F., Casaroli, G., and Bassani, T. (2019). Artificial intelligence and machine learning in spine research. *J. Spine* 2:e1044. doi: 10.1002/jsp2.1044

Gibson, E., Giganti, F., Hu, Y., Bonmati, E., Bandula, S., Gurusamy, K., et al. (2018a). Automatic multi-organ segmentation on abdominal CT with dense V-networks. *IEEE Trans. Med. Imag.* 37, 1822–1834. doi: 10.1109/TMI.2018.2806309

Gibson, E., Li, W., Sudre, C., Fidon, L., Shakir, D. I., Wang, G., et al. (2018b). NiftyNet: a deep-learning platform for medical imaging. *Comput. Methods Programs Biomed.* 158, 113–122. doi: 10.1016/j.cmpb.2018.01.025

Glocker, B., Feulner, J., Criminisi, A., Haynor, D. R., and Konukoglu, E. (2012). Automatic localization and identification of vertebrae in arbitrary field-of-view CT scans. *Med. Image Comput. Comput. Assist. Interv.* 15(Pt 3), 590–598. doi: 10.1007/978-3-642-33454-2_73

Goerres, J., Uneri, A., De Silva, T., Ketcha, M., Reaungamornrat, S., Jacobson, M., et al. (2017). Spinal pedicle screw planning using deformable atlas registration. *Phys. Med. Biol.* 62, 2871–2891. doi: 10.1088/1361-6560/aa5f42

Haj-Ali, R., Wolfson, R., and Masharawi, Y. (2019). A patient specific computational biomechanical model for the entire lumbosacral spinal unit with imposed spondylolysis. *Clin. Biomech.* 68, 37–44. doi: 10.1016/j.clinbiomech.2019.05.022

Han, Z., Wei, B., Mercado, A., Leung, S., and Li, S. (2018). Spine-GAN: semantic segmentation of multiple spinal structures. *Med. Image Anal.* 50, 23–35. doi: 10.1016/j.media.2018.08.005

Hesamian, M. H., Jia, W., He, X., and Kennedy, P. (2019). Deep learning techniques for medical image segmentation: achievements and challenges. *J. Digit. Imag.* 32, 582–596. doi: 10.1007/s10278-019-00227-x

Ibragimov, B., Korez, R., Likar, B., Pernus, F., Xing, L., and Vrtovec, T. (2017). Segmentation of pathological structures by landmark-assisted deformable models. *IEEE Trans. Med. Imag.* 36, 1457–1469. doi: 10.1109/TMI.2017.2667578

Janssens, R., Zeng, G., and Zheng, G. (2018). "Fully automatic segmentation of lumbar vertebrae from CT images using cascaded 3D fully convolutional networks," in *Proceedings of the IEEE 15th International Symposium on Biomedical Imaging (ISBI 2018)*, Washington, DC.

Jiang, S., and Li, W. (2019). Biomechanical study of proximal adjacent segment degeneration after posterior lumbar interbody fusion and fixation: a finite element analysis. *J. Orthop. Surg. Res.* 14, 1–7. doi: 10.1186/s13018-019-1150-9

Knez, D., Nahle, I. S., Vrtovec, T., Parent, S., and Kadoury, S. (2019). Computer-assisted pedicle screw trajectory planning using CT-inferred bone density: a demonstration against surgical outcomes. *Med. Phys.* 46, 3543–3554. doi: 10.1002/mp.13585

Korez, R., Ibragimov, B., Likar, B., Pernus, F., and Vrtovec, T. (2015). A framework for automated spine and vertebrae interpolation-based detection and model-based segmentation. *IEEE Trans. Med. Imag.* 34, 1649–1662. doi: 10.1109/TMI.2015.2389334

Lavecchia, C. E., Espino, D. M., Moerman, K. M., Tse, K. M., Robinson, D., Lee, P. V. S., et al. (2018). Lumbar model generator: a tool for the automated generation of a parametric scalable model of the lumbar spine. *J. R. Soc. Interf.* 15:829. doi: 10.1098/rsif.2017.0829

Lessmann, N., van Ginneken, B., de Jong, P. A., and Išgum, I. (2019). Iterative fully convolutional neural networks for automatic vertebra segmentation and identification. *Med. Image Anal.* 53, 142–155. doi: 10.1016/j.media.2019.02.005

Li, C., He, Q., Tang, Y., and Ruan, D. (2015). The fate of adjacent segments with pre-existing degeneration after lumbar posterolateral fusion: the influence of degenerative grading. *Eur. Spine J.* 24, 2468–2473. doi: 10.1007/s00586-015-3921-2

Liebmann, F., Roner, S., von Atzigen, M., Wanivenhaus, F., Neuhaus, C., Spirig, J., et al. (2020). Registration made easy – standalone orthopedic navigation with HoloLens. *arXiv* [Preprint]. Available online at: https://arxiv.org/abs/2001.06209 (accessed February 25, 2020).

Little, J. P., and Adam, C. (2012). Towards determining soft tissue properties for modelling spine surgery: current progress and challenges. *Med. Biol. Eng. Comput.* 50, 199–209. doi: 10.1007/s11517-011-0848-6

Lüthi, M., Blanc, R., Albrecht, T., Gass, T., Goksel, O., Büchler, P., et al. (2012). Statismo - A framework for PCA based statistical models. *Insight J.* 1, 1–18.

Maas, S. A., Ellis, B. J., Ateshian, G. A., and Weiss, J. A. (2012). FEBio: finite elements for biomechanics. *J. Biomech. Eng.* 134, 1–10. doi: 10.1115/1.4005694

Más, Y., Gracia, L., Ibarz, E., Gabarre, S., Peña, D., and Herrera, A. (2017). Finite element simulation and clinical followup of lumbar spine biomechanics with dynamic fixations. *PLoS One* 12:e0188328. doi: 10.1371/journal.pone.0188328

Mischler, D., Windolf, M., Gueorguiev, B., Nijs, S., and Varga, P. (2020). Computational optimisation of screw orientations for improved locking plate fixation of proximal humerus fractures. *J. Orthop. Transl.* 25, 1–128. doi: 10.1016/j.jot.2020.02.007

Moerman, K. (2018). GIBBON: the geometry and image-based bioengineering add-On. *J. Open Source Softw.* 3:506. doi: 10.21105/joss.00506

Müller, F., Roner, S., Liebmann, F., Spirig, J. M., Fürnstahl, P., and Farshad, M. (2020). Augmented reality navigation for spinal pedicle screw instrumentation using intraoperative 3D imaging. *Spine J.* 20, 621–628. doi: 10.1016/j.spinee.2019.10.012

Nikkhoo, M., Khoz, Z., Cheng, C. H., Niu, C. C., El-Rich, M., and Khalaf, K. (2020). Development of a novel geometrically-parametric patient-specific finite element model to investigate the effects of the lumbar lordosis angle on fusion surgery. *J. Biomech.* 102:109722. doi10.1016/j.jbiomech.2020.109722

Nikolov, S., Blackwell, S., Mendes, R., De Fauw, J., Meyer, C., Hughes, C., et al. (2018). Deep learning to achieve clinically applicable segmentation of head and neck anatomy for radiotherapy. *arXiv* [Preprint]. Available online at: https://arxiv.org/pdf/1809.04430.pdf (accessed January 23, 2020).

O'Reilly, M. A., and Whyne, C. M. (2008). Comparison of computed tomography based parametric and patient-specific finite element models of the healthy and metastatic spine using a mesh-morphing algorithm. *Spine* 33, 1876–1881. doi: 10.1097/BRS.0b013e31817d9ce5

Özmen, R., and Günay, M. (2019). Kinematical considerations related to prosthesis position and core radius on the biomechanics of the C5-C6 functional spinal unit. *Eng. Sci. Technol. Int. J.* 22, 786–793. doi: 10.1016/j.jestch.2018.12.017

Panico, M., Chande, R. D., Lindsey, D. P., Mesiwala, A., Villa, T. M. T., Yerby, S. A., et al. (2020). The use of triangular implants to enhance sacropelvic fixation: a finite element investigation. *Spine J.* 20, 1717–1724. doi: 10.1016/j.spinee.2020.05.552

Perolat, R., Kastler, A., Nicot, B., Pellat, J. M., Tahon, F., Attye, A., et al. (2018). Facet joint syndrome: from diagnosis to interventional management. *Insights Imag.* 9, 773–789. doi: 10.1007/s13244-018-0638-x

Pfirrmann, C. W. A., Metzdorf, A., Zanetti, M., Hodler, J., and Boos, N. (2001). Magnetic resonance classification of lumbar intervertebral disc degeneration. *Spine* 26, 1873–1878. doi: 10.1097/00007632-200109010-00011

Rao, C., Fitzpatrick, C. K., Rullkoetter, P. J., Maletsky, L. P., Kim, R. H., and Laz, P. J. (2013). A statistical finite element model of the knee accounting for shape and alignment variability. *Med. Eng. Phys.* 35, 1450–1456. doi: 10.1016/j.medengphy.2013.03.021

Rohlmann, A., Zander, T., Schmidt, H., Wilke, H. J., and Bergmann, G. (2006). Analysis of the influence of disc degeneration on the mechanical behaviour of a lumbar motion segment using the finite element method. *J. Biomech.* 39, 2484–2490. doi: 10.1016/j.jbiomech.2005.07.026

Roth, H. R., Wang, Y., Yao, J., Lu, L., Burns, J. E., and Summers, R. M. (2016). "Deep convolutional networks for automated detection of posterior-element fractures on spine CT," in *Proceedings of the Medical Imaging 2016: Computer-Aided Diagnosis*, (San Diego, CA), doi: 10.1117/12.2217146

Sarkalkan, N., Weinans, H., and Zadpoor, A. A. (2014). Statistical shape and appearance models of bones. *Bone* 60, 129–140. doi: 10.1016/j.bone.2013.12.006

Sawa, A. G. U., Lehrman, J. N., Crawford, N. R., and Kelly, B. P. (2020). Variations among human lumbar spine segments and their relationships to

in vitro biomechanics: a retrospective analysis of 281 motion segments from 85 cadaveric spines. *Int. J. Spine Surg.* 14, 140–150. doi: 10.14444/7021

Sekuboyina, A., Valentinitsch, A., Kirschke, J. S., and Menze, B. H. (2017). A localisation-segmentation approach for multi-label annotation of lumbar vertebrae using deep nets. *arXiv* [Preprint]. Available online at: https://arxiv.org/abs/1703.04347 (accessed March 3, 2020).

Taylor, M., and Prendergast, P. J. (2015). Four decades of finite element analysis of orthopaedic devices: where are we now and what are the opportunities? *J. Biomech.* 48, 767–778. doi: 10.1016/j.jbiomech.2014.12.019

Uçar, B. Y., Özcan, Ç, Polat, Ö, and Aman, T. (2019). Transforaminal lumbar interbody fusion for lumbar degenerative disease: patient selection and perspectives. *Orthop. Res. Rev.* 11, 183–189. doi: 10.2147/ORR.S204297

Valentin, J., Keskin, C., Pidlypenskyi, P., Makadia, A., Sud, A., and Bouaziz, S. (2019). *TensorFlow Graphics Computer Graphics Meets Deep Learning, in: TensorflowGraphicsIO2019*. Available online at: https://github.com/tensorflow/graphics (accessed July 2, 2020).

Van Rijsbergen, M., Van Rietbergen, B., Barthelemy, V., Eltes, P., Lazáry, Á, Lacroix, D., et al. (2018). Comparison of patient-specific computational models vs. clinical follow-up, for adjacent segment disc degeneration and bone remodelling after spinal fusion. *PLoS One* 13:899. doi: 10.1371/journal.pone.0200899

Vania, M., Mureja, D., and Lee, D. (2019). Automatic spine segmentation from CT images using convolutional neural network via redundant generation of class labels. *J. Comput. Des. Eng.* 6, 224–232. doi: 10.1016/j.jcde.2018.05.002

Verma, N., Boyer, E., and Verbeek, J. (2018). "FeaStNet: feature-steered graph convolutions for 3D shape analysis," in *Proceedings of the IEEE Conference on Computer Vision & Pattern Recognition*, (Salt Lake City), doi: 10.1109/CVPR.2018.00275

Wang, Y., Chen, H., Bin, L., Zhang, L. Y., Zhang, L. Y., Liu, J. C., et al. (2012). Influence of degenerative changes of intervertebral disc on its material properties and pathology. *Chin. J. Traumatol.* 15, 67–76. doi: 10.3760/cma.j.issn.1008-1275.2012.02.001

Warren, J. M., Mazzoleni, A. P., and Hey, L. A. (2020). Development and validation of a computationally efficient finite element model of the human lumbar spine: application to disc degeneration. *Int. J. Spine Surg.* 14, 502–510. doi: 10.14444/7066

Wawrose, R. A., LeVasseur, C. M., Byrapogu, V. K., Dombrowski, M. E., Donaldson, W. F., Shaw, J. D., et al. (2020). In vivo changes in adjacent segment kinematics after lumbar decompression and fusion. *J. Biomech.* 102:109515. doi: 10.1016/j.jbiomech.2019.109515

Widmer, J., Cornaz, F., Scheibler, G., Spirig, J. M., Snedeker, J. G., and Farshad, M. (2020a). Biomechanical contribution of spinal structures to stability of the lumbar spine - Novel biomechanical insights. *Spine J.* 20, 1705–1716. doi: 10.1016/j.spinee.2020.05.541

Widmer, J., Fasser, M. R., Croci, E., Spirig, J., Snedeker, J. G., and Farshad, M. (2020b). Individualized prediction of pedicle screw fixation strength with a finite element model. *Comput. Methods Biomech. Biomed. Engin.* 23, 155–167. doi: 10.1080/10255842.2019.1709173

Woods, R. E., and Gonzales, R. C. (1981). Real-time digital image enhancement. *Proc. IEEE* 69, 643–654.

Wu, J., Cai, M., Li, J., Cao, L., Xu, L., Li, N., et al. (2019). Development and validation of a semi-automatic landmark extraction method for mesh morphing. *Med. Eng. Phys.* 70, 62–71. doi: 10.1016/j.medengphy.2019.04.007

Zadpoor, A. A., and Weinans, H. (2015). Patient-specific bone modeling and analysis: the role of integration and automation in clinical adoption. *J. Biomech.* 48, 750–760. doi: 10.1016/j.jbiomech.2014.12.018

Zhang, Z., Fogel, G. R., Liao, Z., Sun, Y., and Liu, W. (2018). Biomechanical analysis of lumbar interbody fusion cages with various lordotic angles: a finite element study. *Comput. Methods Biomech. Biomed. Engin.* 21, 247–254. doi: 10.1080/10255842.2018.1442443

Zheng, G., Chu, C., Belavý, D. L., Ibragimov, B., Korez, R., Vrtovec, T., et al. (2017). Evaluation and comparison of 3D intervertebral disc localization and segmentation methods for 3D T2 MR data: a grand challenge. *Med. Image Anal.* 35, 327–344. doi: 10.1016/j.media.2016.08.005

Zhou, C., and Willing, R. (2020). Sensitivities of lumbar segmental kinematics and functional tissue loads in sagittal bending to design parameters of a ball-in-socket total disc arthroplasty prosthesis. *Comput. Methods Biomech. Biomed. Engin.* 23, 536–547. doi: 10.1080/10255842.2020.1745783

Zhou, X., Liu, Y., Zhou, S., Fu, X. X., Yu, X. L., Fu, C. L., et al. (2016). The correlation between radiographic and pathologic grading of lumbar facet joint degeneration. *BMC Med. Imag.* 16:27. doi: 10.1186/s12880-016-0129-9

Conflict of Interest: The authors disclose ties to Incremed AG, Zurich, Switzerland, which is developing solutions for the preoperative planning of spinal surgeries. MF was a board member and SC was an employee of Incremed AG.

frontiers in Bioengineering and Biotechnology

ORIGINAL RESEARCH
published: 15 February 2021
doi: 10.3389/fbioe.2021.632408

Toward Patient Specific Models of Pediatric IVDs: A Parametric Study of IVD Mechanical Properties

Edmund Pickering[1,2]*, *Peter Pivonka*[1,2] and *J. Paige Little*[1,2]

[1] School of Mechanical, Medical and Process Engineering, Queensland University of Technology, Brisbane, QLD, Australia, [2] Biomechanics and Spine Research Group, Centre for Children's Health Research, Queensland University of Technology, Brisbane, QLD, Australia

Patient specific finite element (FE) modeling of the pediatric spine is an important challenge which offers to revolutionize the treatment of pediatric spinal pathologies, for example adolescent idiopathic scoliosis (AIS). In particular, modeling of the intervertebral disc (IVD) is a unique challenge due to its structural and mechanical complexity. This is compounded by limited ability to non-invasively interrogate key mechanical parameters of a patient's IVD. In this work, we seek to better understand the link between mechanical properties and mechanical behavior of patient specific FE models of the pediatric lumbar spine. A parametric study of IVD parameter was conducted, coupled with insights from current knowledge of the pediatric IVD. In particular, the combined effects of parameters was investigated. Recommendations are made toward areas of importance in patient specific FE modeling of the pediatric IVD. In particular, collagen fiber bundles of the IVD are found to dominate IVD mechanical behavior and are thus recommended as an area of primary focus for patient specific FE models. In addition, areas requiring further experimental research are identified. This work provides a valuable building block toward the development of patient specific models of the pediatric spine.

Keywords: intervertebral disc, pediatric, finite element, patient specific, stiffness

OPEN ACCESS

Edited by:
Enrico Dall'Ara,
The University of Sheffield,
United Kingdom

Reviewed by:
Claudio Vergari,
ParisTech École Nationale Supérieure d'Arts et Métiers, France
André P. G. Castro,
Instituto Superior Técnico, Portugal

***Correspondence:**
Edmund Pickering
ei.pickering@qut.edu.au

Specialty section:
This article was submitted to Biomechanics, a section of the journal Frontiers in Bioengineering and Biotechnology

Received: *23 November 2020*
Accepted: *18 January 2021*
Published: *15 February 2021*

Citation:
Pickering E, Pivonka P and Little JP (2021) Toward Patient Specific Models of Pediatric IVDs: A Parametric Study of IVD Mechanical Properties. Front. Bioeng. Biotechnol. 9:632408. doi: 10.3389/fbioe.2021.632408

1. INTRODUCTION

Development of patient specific spine models is of increased interest in the treatment of pediatric spinal pathologies. Such models aim to revolutionize clinical practice by providing practitioners with detailed predictions of a patient's spinal biomechanics. For example, such models are already showing promise in predicting outcomes of corrective interventions for AIS (Little and Adam, 2011; Vergari et al., 2015; Aubin et al., 2018).

The accuracy of these models is underpinned by the fidelity in which the patient specific geometry and patient specific material parameters are represented. Here, patient specific geometry can be readily extracted from medical scans (Strickland et al., 2011; Finley et al., 2018) (including the use of pre-operative scans, Little and Adam, 2015). In contrast, patient specific material parameters cannot be directly interrogated and are thus a greater challenge. As a substitute, these are commonly extracted from experimental biomechanics studies. However, a majority of research on IVD biomechanics focuses on adult cases, thus there is a paucity of material data for pediatric IVDs. As such, most FE models of the pediatric IVD use material parameters extracted from studies on adult IVDs (for example Sairyo et al., 2006; Little et al., 2008; Cahill et al., 2012; Dong et al., 2013).

It thus becomes important to understand how the material parameters and related mechanics of the pediatric IVD differs from those of adults. We address this challenge by first understanding how pediatric IVD material parameters differ from adults, followed by exploring how this affects the overall IVD mechanics. Focus will be place on adolescents (i.e., minimum age of 10 year). Further, focus will be placed on the annulus fibrosus (AF) as this is the main source of variance in FE IVD models (it being well-accepted that in FE models of the young, healthy IVD, the nucleus pulposus (NP) can be treated as an incompressible fluid Fagan et al., 2002a; Rohlmann et al., 2006; Little et al., 2008; Dong et al., 2013). To achieve this, a detailed literature review on the biomechanics of the AF and those parameters which affect mechanical behavior was conducted. This was complemented by a parametric study which explored how AF parameters affected the stiffness of the IVD under axial rotation, flexion, extension and lateral bending. This cumulated in overall recommendations for FE modeling of pediatric IVDs.

2. THE PEDIATRIC IVD

While, most IVD research focuses on the case of healthy adults and/or degenerative IVDs, this work places a special focus on pediatric IVDs—an overlooked area. It thus becomes important to build an understanding of the biomechanics of the IVD, focusing on those parameters relevant for mechanical behavior. There however is a paucity of studies on those parameters relevant for modeling of pediatric IVDs. Below, we aim to highlight key findings, insights and hypothesis of the pediatric IVD biomechanics relevant for FE modeling. Focus will be placed on the AF fiber angle, AF fiber stiffness and AF ground matrix stiffness, as these are the key variables in such FE models. In addition, while the NP is not of focus in this study, development changes will be briefly addressed. Focus will not be placed on the geometry of the IVD as in patient specific models, these are derived from medical imaging. Finally, focus is not placed on the aged or degenerate IVD as these deviate from the healthy case and are outside of the scope of this research (Urban et al., 2000; Sharabi et al., 2018).

2.1. Embryology and IVD Development

The AF and NP have different embryonic origins; the AF deriving from the sclerotome while the NP derives from the notochord (Sivakamasundari and Lufkin, 2012). By full term however, the fetal IVD exhibits the structure of an adult IVD (Walmsley, 1953). Thus, it is reasonable to conclude that the modeling approach used in adult IVDs (Shirazi-Adl et al., 1986) is valid for pediatric IVDs.

2.2. Stiffness of Collagen Fiber Bundles

Collagen fiber bundles of the IVD are responsible for carrying tensile loads, thus the fiber stiffness becomes a key parameter. Fiber stiffness can be considered either by studying the elastic properties of individual fiber bundles (Holzapfel et al., 2005; Zhu et al., 2008), or by study the stiffness of larger IVD sections (i.e., multiple fiber bundles embedded in ground matrix) and extracting the fiber stiffness (Galante, 1967; Wu and Yao, 1976; Little et al., 2010).

During growth from a pediatric to adult IVD, several changes can be expected within individual collagen fiber bundles. The bundle thickness will increase (Marchand and Ahmed, 1990; Langlais et al., 2019), the number of individual bundles will increase (Marchand and Ahmed, 1990), and chemical changes can be expected (Galante, 1967; Buckwalter, 1995; Sharabi et al., 2018). These all link to the mechanical behavior of the fiber bundles, but provide limited information on the overall stiffness of the collagen fiber bundles themselves. Further, no study has explored the age-related stiffness of a single fiber bundle. Thus, it becomes relevant to consider the embodied stiffness of a larger section of the IVD.

The most detailed study on fiber stiffness and age was conducted by Galante (1967). In this, AF sections were tested to a set tensile load. No significant trends were observed for samples over 26 years of age, matching other findings (Ebara et al., 1996; Holzapfel et al., 2005). However, for ages under 26 years, sample elongation increased steadily. At 10 years of age, samples exhibited 50% greater elongation, in comparison to those over 26 years. This is equivalent to a 33% reduction in stiffness. Two key factors should be noted here. First, the AF consists of collagen fibers embedded in a ground matrix. The results presented are thus the combined stiffness of the collagen fibers and the ground matrix. However, under tension the fibers are significantly stiffer than the ground matrix, thus the results here can be assumed directly applicable to the fibers themselves. Second, the stiffness here is a combined effect of the fiber elastic modulus, fiber spacing and fiber cross-sectional area. This is in-fact beneficial as consideration need not be given to these individual parameters, rather the fiber stiffness can be considered on a whole. Thus, in summary, for IVDs over 26 year, fiber stiffness remains constant, however, for ages below 26 years, the fiber stiffness decreases gradually. For samples of 10 years age, the fiber stiffness can be 33% less than that of IVDs over 26 years.

2.3. Fiber Angle

In the adult lumbar IVD, fiber angle varies with both location and radial depth (Cassidy et al., 1989; Holzapfel et al., 2005), however it is generally accepted that the mean fiber angle is 30° (Holzapfel et al., 2005; Michalek, 2019). Holzapfel et al. (2005) reported a 95% prediction interval of approximately ±15° for fiber angle.

Considering average fiber angles during development, in a study of fetal IVDs, Hickey and Hukins (1980) observed no trend in fiber angles between a conception ages of 10–25 weeks. Further, the fiber angles observed by Hickey and Hukins aligned to studies of adult IVDs (Cassidy et al., 1989; Holzapfel et al., 2005). Thus, it is reasonable to argue that average the fiber angle does not change appreciably during development.

Adding weight to this argument, Michalek (2019) proposed a growth-based model to predict fiber angles. In this, Michalek assumed that growth of the AF initiates from a thin cylinder with constant angles and thus hypothesized that the fiber angles can be fully predicted based upon IVD geometry. The resulting model showed good alignment to experimental results. Crucially, it has been shown that during growth, the IVD height and

diameter increase at the same rate (Taylor, 1975). For this case, the Michalek model would predict the average fiber angles in the pediatric IVD to match that of an adult. A further advantage of the Michalek model is that it may predict patient-specific fiber orientation in IVDs with atypical geometries; for example in AIS patients which have increased disc height compared to the population average (Ponrartana et al., 2016).

Combining the facts that (1) fiber angle observations of fetuses (Hickey and Hukins, 1980) align with those of adults (Cassidy et al., 1989; Holzapfel et al., 2005), and (2) the IVD exhibits approximate linear scaling during growth (Taylor, 1975) for which the Michalek model (Michalek, 2019) would predict similar fiber angle, we conclude fiber angle distributions in the pediatric IVD would align to those of the adult IVD. Thus, the fiber angle in pediatric patients can be expected to be independent of age, with an mean angle of 30°, and with natural population variances inline with those observed by Holzapfel et al. (2005).

2.4. Ground Matrix

To our best knowledge, no study has explored age-dependent changes of ground matrix mechanical properties. This is a limitation in patient specific models of pediatric IVDs, which will require additional experimental work to address. An alternative approach would be to focus on changes in the biochemistry and composition of the ground matrix, and make inferences about the age-dependent mechanical properties. For example, the pediatric IVD has a lower concentration of glycoproteins (Galante, 1967). We however recommend against this approach. Mechanical behavior is function of both composition and structure. Thus, making assumptions on mechanical behavior based upon composition is an uncertain process.

2.5. Nucleus Pulposus

The NP is composed predominately of water (70–90%), proteoglycans (65% of dry weight), collagen (20% of dry weight), elastic fibers and other proteins (Bogduk, 2005). Due to its high water content and low resistance to shear (Iatridis et al., 1996, 1997), FE models of the NP generally considered it to behave like a hydrostatic fluid (Fagan et al., 2002a; Rohlmann et al., 2006; Little et al., 2008; Dong et al., 2013). During aging, the water content of the IVD degreases while the collagen content increases (Urban and McMullin, 1988; Urban et al., 2000). In turn, the pressure within the NP reduces (Urban and McMullin, 1988). Further, the transition from AF to NP becomes unclear (Urban et al., 2000). However, these changes occur in the aging IVD, while a lack of literature is present on how the pediatric NP differ from the healthy adult case. As the healthy adult NP approximates a hydrostatic fluid, it is reasonable to assume the young NP behaves in a similar nature. Although, the variance in hydrostatic pressure of the young NP remains an open question.

2.6. Summary

Based upon the above investigation, the following conclusions can be drawn. First, from an early age (i.e., full term fetus) the IVD exhibits the structure of an adult IVD (Walmsley, 1953), suggesting that modeling approaches used for adult IVDs will be valid for pediatric IVDs. Overall fiber stiffness increases with age in an approximately linear fashion up to 26 years. Stiffness of collagen fibers in a 10 year old IVD can be expected to be 33% less than that of a healthy adult (Galante, 1967). There is however little data on how fiber stiffness varies within particular age brackets, thus this remains an open question. Observations of fiber angles in fetal IVDs match those of adults (Hickey and Hukins, 1980; Cassidy et al., 1989; Holzapfel et al., 2005). This suggests little difference across age group and thus standard population variance can be assumed (Holzapfel et al., 2005). With respect to the ground matrix, no data was found on its stiffness in young age groups, thus this remains an open question. While, much detail is available on the biochemical changes (Galante, 1967; Sharabi et al., 2018), we advise caution in inferring mechanical properties from these as mechanical behavior is both a function of composition and structure. Finally, while numerous structural and composition changes occur in the NP during aging, it is reasonable to assume the pediatric IVD behaves in a similar nature to the young, healthy, adult IVD.

3. METHOD

3.1. Geometry

An FE model representative of the L1-2 IVD was generated from the computed 'tomography (CT) dataset of the Visible Man (The Visible Human Project, US National Library of Medicine). The IVD geometry was identified from CT by manually extracting keypoints of the superior and inferior surface using an in-house MATLAB code. These keypoints were then imported into an in-house Python code, which defined the IVD geometry based upon a parametric description of endplate geometry (Little et al., 2007). Further detail on this process is described in Little et al. (2007) and Little and Adam (2012).

As this study is focused on mechanical properties, we elected to use geometry extracted from the Visible Man, as this is a well-studied geometry (Cooper et al., 2001; Little et al., 2008; Lavecchia et al., 2018). Use of a commonly studied and publicly available geometry will increase translatability of findings. Further, in patient specific modeling, any influence of a patient's specific geometry can be extracted from medical images. As the adult and pediatric IVD show similar structure, we argue that any findings can be translated to the pediatric domain (incorporating patient specific geometry).

3.2. Finite Element Model

FE modeling of the IVD is a balance between model fidelity (i.e., how closely the model represents the true biological case) and model complexity. Introduction of higher fidelity representations increases the model complexity. In this work, we employ well-established methods of representing the AF ground matrix, AF collagen fibers and NP. Through this we seek to balance the needs of fidelity and complexity.

In this work, we use a previously validated IVD model (Little et al., 2008). As our process for modeling the IVD has been previously described in detail (Little et al., 2008), we will only provide a brief description here. A schematic representation of the FE mesh is shown in **Figure 1**, which follows the meshing

approach of most common IVD FE models (Shirazi-Adl et al., 1986; Smit et al., 1997; Little et al., 2008; Dreischarf et al., 2014). The AF was modeled as a ground matrix with reinforcing collagen fibers (Shirazi-Adl et al., 1986; Little et al., 2008; Dong et al., 2013). The AF ground matrix was modeled by three concentric rings of three dimensional (3D) solid continuum elements (see **Figure 1**). The collagen fibers were represented as tension-only rebar elements located on the hoop faces of the AF at an angle of θ (where θ represents the fiber angle from the horizontal plane as shown in **Figure 1**). Each hoop-face consisted of two-layers of alternate angled rebar elements, equivalent to eight lamellae (Shirazi-Adl et al., 1986; Little et al., 2008; Dong et al., 2013). The collagen fibers were assigned an elastic modulus of E with a cross-section selected such that the volume of the collagen fibers was 25% that of the AF (Marchand and Ahmed, 1990) The NP was represented using 3D hydrostatic elements (Fagan et al., 2002a; Rohlmann et al., 2006; Little et al., 2008; Dong et al., 2013) with a pressure of 0.25 MPa prior to loading (Wilke et al., 1999; Meir et al., 2007). Details of the NP, AF ground matrix and collagen fibers are given in **Table 1** including element type, material model and properties.

Replicating realistic loading on a model of a single the IVD is challenging as the deformation of the IVD is governed by the mechanics of the spinal column. Further, spinal motion is driven by the motion and mechanics of the facet joints and the intervertebral joint at each spinal motion segment. In simulating the IVD in isolation, it is important for the boundary and loading conditions to create motion in the IVD which mimics that observed in the full spine. Many studies have described the deformation of the IVD using the instentaneous axis of rotation (IAR). In this, the motion of the superior endplate is tracked relative to the inferior endplate and at each instant the center of rotation is found. *In vivo* (Pearcy and Bogduk, 1988), *ex vivo* (Cossette et al., 1971), and *in silico* (Schmidt et al., 2008) studies have all explored the IAR in IVDs of the lumbar spine.

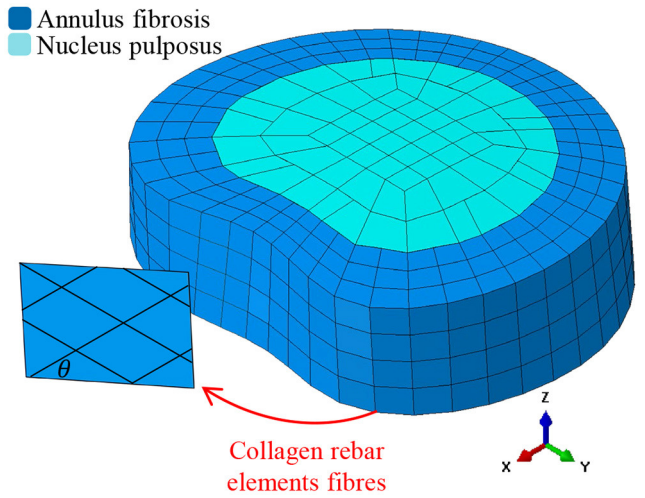

FIGURE 1 | Schematic representation of the IVD finite element model.

In this work, we take guidance from Schmidt et al. (2008) who explored the IAR of a lumbar functional spinal unit via FE modeling. Schmidt et al. found that for common motions (i.e., axial rotation, flexion, extension, and lateral bending) under low moments, the IAR locus was near the centroid of the IVD. For larger moments (up to 7.5 N), the IAR shifted, in a manner largely governed by spinous process interactions. Adapting this, it was assumed that the IAR was located at the centroid of the IVD. To replicate this, nodes of the inferior endplate were fixed, while nodes of the superior endplate were pinned via rigid beam elements to a nodes located at the centroid of the IVD. This node was then pin supported, causing the IVD to deform about the IAR. Four motions were investigated in this study; axial rotation, flexion, extension and lateral bending. In each case, these motions were produced through the application of a 7.5 Nm moment to the superior endplate, over 30 substeps. Loading magnitudes were selected in-line with other studies (Dreischarf et al., 2014; Newell et al., 2017; Finley et al., 2018).

3.3. Study Design

The objective of this work is to understand the combined influence of IVD parameters on predicted rotational stiffness. To achieve this, the study was split into three studies. In the first study the influence of individual properties on the IVD was explored, through this the properties which had a significant contribution to the IVD stiffness were identified. In the second study, the combined influence of these significant properties was investigated. In the final study, the independence/convolution of combined parameters was explored. As previously discussed, the parameters which are studied are those relating to the AF as these dictate the stiffness of the IVD. The parameters which are

TABLE 1 | Elements, constitutive models, and properties of the IVD.

	Element type	Material model	Material properties
NP	3D, 4-node fluid element	Hydrostatic fluid	Incompressible (Nachemson, 1960; Goel et al., 1995)
AF ground matrix	3D, 8-node, solid element	Hyperelastic Mooney-Rivlin	$C_{10} = 0.7$ (Natali and Meroi, 1990; Little et al., 2008)
			$C_{01} = 0.2$ (Natali and Meroi, 1990; Little et al., 2008)
Collagen fibers	Rebar tension-only	Linear elastic, tension only	$E = 500$ MPa* (Ueno and Liu, 1987)
			Volume fraction, $V_f = 0.25$ (Marchand and Ahmed, 1990)
			$\theta = 30°$ (Shirazi-Adl et al., 1986)

*The stiffness of the collagen fibers is proportional to $E \cdot V_f$. As such, the stiffness of the fibers will be controlled by varying E.

explored are fiber angle, fiber stiffness, ground matrix C_{10} and ground matrix C_{01}.

3.3.1. Study One: What Are the Individual Influences of IVD Parameters?

In the first study, parameters of the IVD were varied individually. A large range of IVD parameters are found in literature (Galante, 1967; Cassidy et al., 1989; Marchand and Ahmed, 1990; Ebara et al., 1996; Gu et al., 1999; Holzapfel et al., 2005; Zhu et al., 2008), thus to capture most cases, each parameters was varied over a range of ±50% (with nine cases across the range). For each case, the four loading scenarios were modeled, and the stiffness extracted, by fitting a linear trend to the moment-rotation curve. Each stiffness was normalized against the stiffness of the baseline IVD (i.e., the IVD with parameters presented in **Table 1**). The parameters which had a greater than 10% influence over the IVD stiffness were deemed significant.

3.3.2. Study Two: What Are the Combined Influences of IVD Parameters?

In the second study, the combined effect of IVD parameters was investigated. In this, parameters were varied together across a full range of their potential combinations. For example, if two parameters were deemed significant, then this would result in a total of $9^2 = 81$ simulations, likewise if four parameters were deemed significant, this would require $9^4 = 6561$ simulations. This is why the first stage sought to identify those parameters which were significant, thus reducing the total number of simulations required.

3.3.3. Study Three: Is the Combined Influence Independent or Convoluted?

Study three explored if the effect of changing one parameter is independent of changes in other parameters. By way of explanation, assume in the first parametric study that a change in parameter *A* results in a stiffness increase of 50% while a change in parameter *B* results in a stiffness increase of 20%. If the effects of there parameters are independent, then changing both *A* and *B* together would result in an overall stiffness change of 80% (i.e., $1.5 \times 1.2 = 1.8$). If the influence of parameters was convoluted (i.e., not independent), then the combined influence would be other than 80%. Understanding independence of parameters on the overall IVD stiffness is important because, if independent, the full effect of a parameter can be understood from the parametric study presented in study one. However, if parameters are convoluted, then the effect of one parameters is dependent on the other parameters and thus a broader awareness must be maintained when specifying parameters in a patient specific FE model.

In a more generalized form, let P_θ, P_k, $P_{C_{10}}$ be the percentage change in IVD stiffness caused by a change in fiber angle, fiber stiffness, and ground matrix C_{10}, respectively (i.e., results from study 1). Likewise, let $P_{\theta,k,C_{10}}$ be the percentage change in IVD stiffness from combined changes of fiber angle, fiber stiffness and ground matrix C_{10} (i.e., results from study 2). If these parameters are independent then:

$$P_{\theta,k,C_{10}} = (1 + P_\theta)(1 + P_k)(1 + P_{C_{10}}) - 1 \quad (1)$$

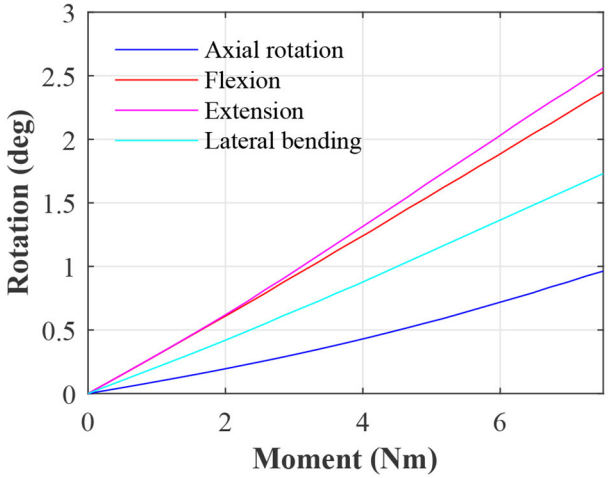

FIGURE 2 | Moment-rotation data for the IVD with default material properties.

In study three, the independence of parameters was tested by using Equation (1) to determine the expected combined effects of parameters from study 1, assuming independence. These were then compared to the effects predicted in study 2, and the coefficient of determination (R^2) was calculated.

4. RESULTS

4.1. Rotation Behavior of the Baseline IVD

To allow benchmarking against other studies, moment-rotations data for an IVD with the baseline parameters is presented in **Figure 2**.

4.2. Study One: What Are the Individual Influences of IVD Parameters?

Figure 3 shows the results of the first parametric study in which each parameter was varied by ±50%. For each case, stiffness was extracted by linear regression. To normalize stiffness values, the percentage change in stiffness compared to the baseline IVD is reported. To determine those parameters which have a significant effect on IVD stiffness, a threshold of ±10% was set (i.e., those parameters which when varied by ±50% caused a change in IVD stiffness of greater than ±10% where deemed significant). For the case of axial rotation, fiber angle and fiber stiffness were deemed significant. For the cases of flexion, extension and lateral bending, fiber angle, fiber stiffness and ground matrix C_{10} were deemed significant.

4.3. Study Two: What Are the Combined Influences of IVD Parameters?

Parameters deemed significant from study one, were progressed to study two, in which the combined influence of varying parameters were explored. **Figure 4** shows curves for the percentage change in stiffness, as a function of the significant parameter changes. For the axial rotation case (**Figure 4A**), this is represented by a single curve, while for the other cases

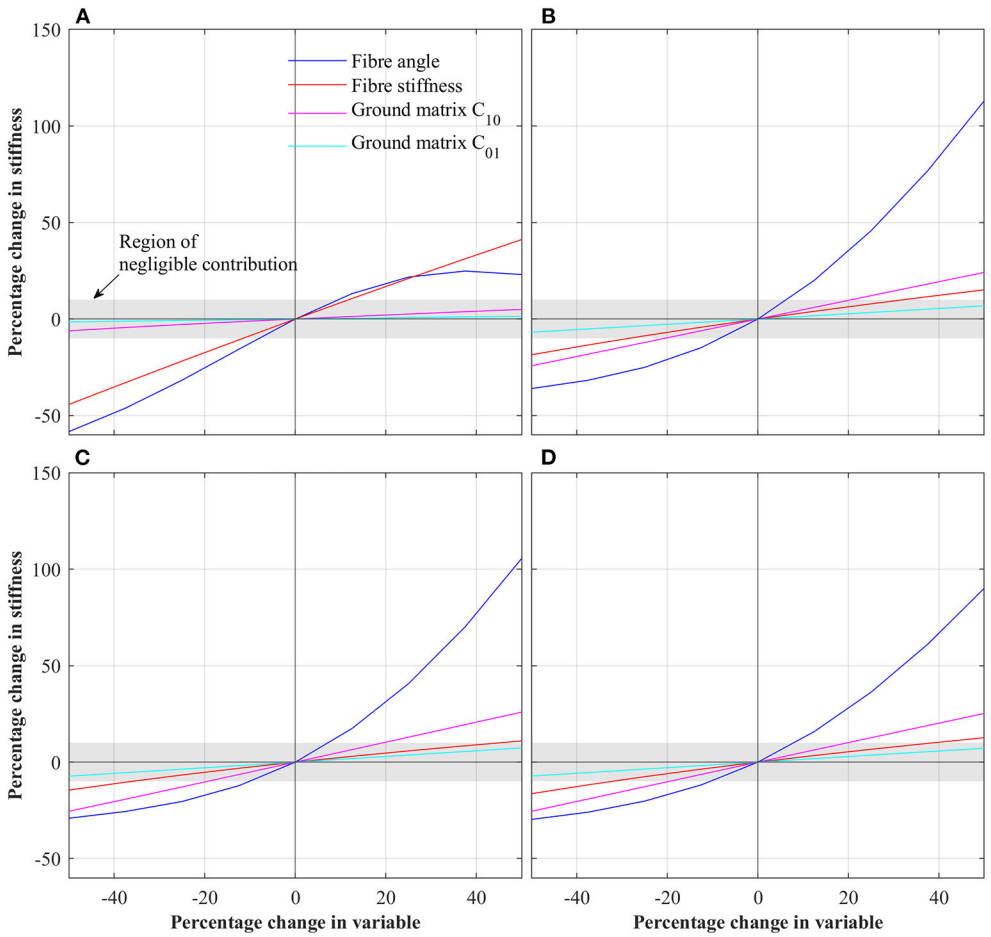

FIGURE 3 | Percentage change in IVD stiffness as a function of changing individual parameters for the different loading conditions. **(A)** Axial rotation. **(B)** Flexion. **(C)** Extension. **(D)** Lateral bending.

(**Figures 4B,C**) this is represented by a stack of curves. The results presented in **Figure 4** are semi-quantitative, for full quantitative data, contour plots of the same data is presented in the **Supplementary Material**.

4.4. Study Three: Is the Combined Influence Independent or Convoluted?

Figure 5 presents the results from study 3, which explored the independence of parameters effect of IVD stiffness. Each data point represents a single simulation from study 2, plotting the change in IVD stiffness measured in study two, against the predicted change in stiffness (assuming independence, using Equation 1). Independence is indicated by the locus of data points sitting on the dashed line. For readability, data points are labeled based upon the θ parameters, as this was observed to have the biggest influence on independence.

5. DISCUSSION

In this work, we used a previously validated FE model of an IVD to investigate the influence of biomechanical parameters on the overall stiffness of the IVD. Specifically, our study focused on parameters of the AF as these are the main source of variance in IVD models [it being well-accepted that for FE modeling of the young, healthy IVD, the NP can be modeled as an incompressible gel, Fagan et al., 2002a; Rohlmann et al., 2006; Little et al., 2008; Dong et al., 2013]. In the below discussion we explore how these parameters influence the overall stiffness of the IVD, in particular we identify which parameters are of greater significance, and we explore how the influence of these parameters combine. The focus here is to build a deeper understanding of how IVD parameters effect mechanical stiffness, with a focus toward patient specific models of the pediatric spine.

5.1. Rotation Behavior of Baseline IVD

The moment-rotation curves from the baseline IVD (see **Figure 2**) are in line with other studies in both terms of shape and magnitude. From numerical models, it is generally well-accepted that the IVD has a roughly linear moment-rotation response (Fagan et al., 2002b); this should not be confused with a functional spinal unit, which presents large non-linear behavior (Ayturk et al., 2010; Dreischarf et al., 2014). The magnitude of the moment-rotation response is in line with other studies (Dreischarf et al., 2014; Mills and Sarigul-Klijn, 2019). However,

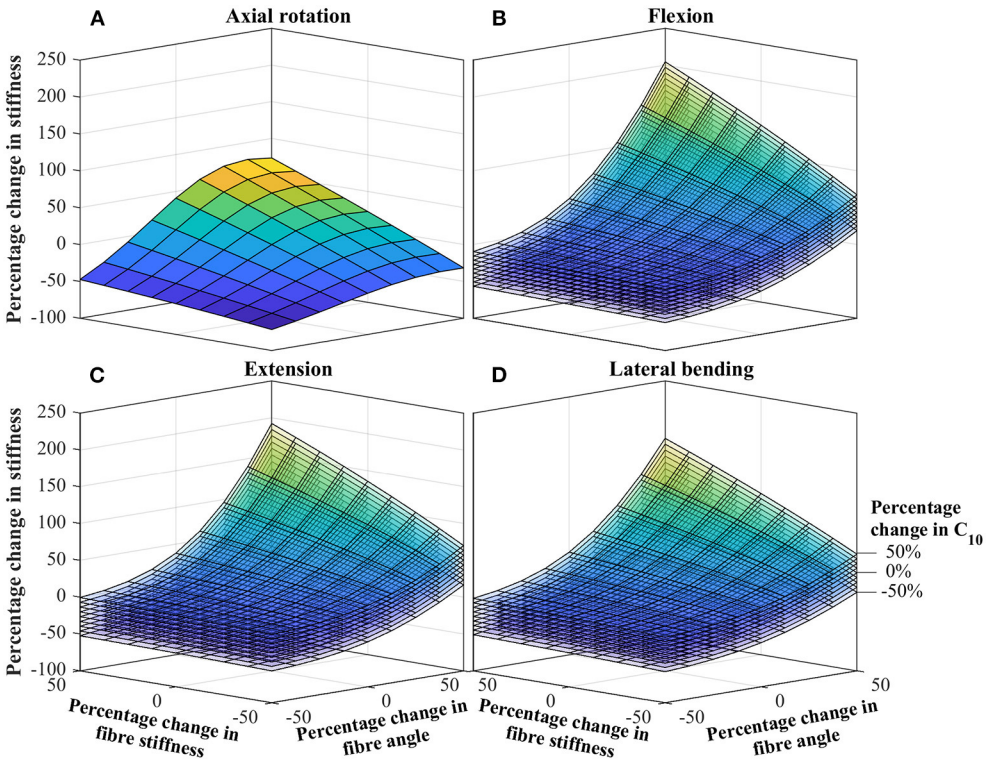

FIGURE 4 | Percentage change in IVD stiffness as a function of combined changing of significant parameters. **(A)** Axial rotation. **(B)** Flexion. **(C)** Extension. **(D)** Lateral bending. The stack of curves in **(B–D)** are for the percentage change in C_{10} as identified in **(D)**. Contour plots of the same data is presented in the **Supplementary Material**.

some numerical studies present IVDs with a noticeably lower stiffness (Fagan et al., 2002b), but this can be attributed to softer material properties. For example Fagan et al. (2002b) used an elastic modulus of 4 MPa for the AF ground matrix, which is significantly softer than the Mooney-Rivlin coefficients used in this study, which are approximately equivalent to an elastic modulus of 5.2 MPa for small deformation. For confirmation, the baseline IVD was simulated with the same AF ground matrix properties as in Fagan et al. which resulted in a similar stiffness.

5.2. What Are the Individual Influences of IVD Parameters?

Overwhelmingly, for all loading scenarios, fiber parameters dominate IVD stiffness (see **Figure 3**). These align with other studies on the influence of fiber properties within the IVD (Fagan et al., 2002b; Guerin and Elliott, 2007). Under axial rotation, the effect of fiber angle and fiber stiffness are much greater than that of the ground matrix C_{10} and C_{01}. Across the total variable range, the fiber angle and fiber stiffness had an absolute maximum effect of 44.25 and 58.33%, respectively. Conversely, the maximum absolute effect of C_{10} and C_{01} were 6.1 and 1.5%, respectively. Thus, it is concluded that during axial rotation, ground matrix stiffness parameters are of little importance.

The behavior under flexion, extension and lateral bending were similar, as these directions are all rotations about axes tangential to the transverse plane. As such, for simplicity, discussion here will focus on flexion, but the overall conclusions are transferable to extension and lateral bending. Under flexion, the fiber angle has the greatest impact, especially for positive increases in fiber angle, where a 50% in fiber angle resulted in a 113% increase in IVD stiffness. Conversely, for a −50% change in fiber angle, the IVD stiffness is reduce by 36%. Interestingly, the second most significant parameter is ground matrix C_{10}, with a maximum absolute effect of 24.2%, followed by the fiber stiffness with a maximum absolute effect of 18.5%. From these results, it is apparent that the most significant parameters affecting the IVD stiffness is the fiber angle (for flexion, extension, and lateral bending). Thus, in patient specific modeling, high-fidelity representation of the collagen fibers is imperative. Likewise, in efforts to calibrate a model to match experimental findings, fiber angle should be the first target.

For all loading conditions, the effect of the AF ground matrix C_{01} parameter was of negligible significance. In the first parametric study, the maximum effect of C_{01} was 1.5% for axial rotation, 6.8% for flexion, 7.3% for extension, and 7.2% for lateral bending. By way of explanation, the larger C_{10} term of the Mooney-Rivlin model dominates the lesser C_{01} term, such that changes in C_{01} have little impact on the overall stiffness of the ground matrix, and thus the overall IVD. Both experimental and modeling studies have shown the strains experienced in the AF are in the range of milli-strains (Shirazi-Adl et al., 1986; Disney et al., 2019; Tavana et al., 2020), whereas hyper-elastic models are

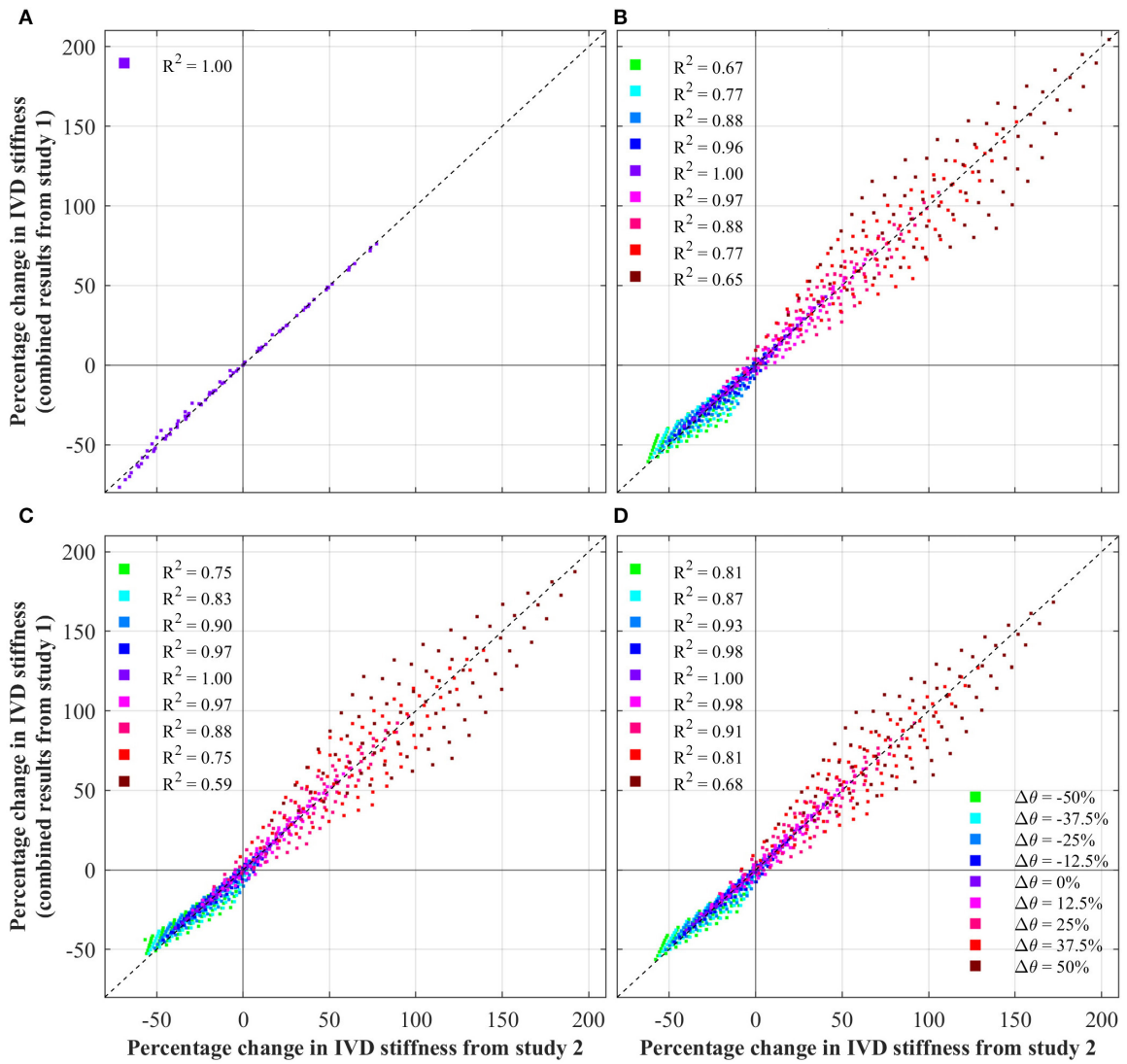

FIGURE 5 | Test of independence of IVD parameters, showing the change in IVD stiffness from the combined study (study 2) against that predicted by Equation (1). Note, in the case of axial rotation, ground matrix C_{10} was not a significant variable, and thus was not modified. For ease of interpretation, each data points is colored based upon its $\Delta\theta$. Additionally, the coefficient of determination (R^2) is shown for each θ, against the fit indicated by the dashed black line. **(A)** Axial rotation. **(B)** Flexion. **(C)** Extension. **(D)** Lateral bending.

relevant for larger strains. For example, considering the Mooney-Rivlin parameters used in this study, under uniaxial loading, the ground matrix behaves roughly linear for strains below 50%. Based upon this, we propose that during patient specific modeling (especially those focused on pseudo-static loading) the applicability of higher-order constitutive models of the AF ground matrix be considered.

5.3. What Are the Combined Influences of IVD Parameters?

Data from the combined influence study, **Figure 4**, demonstrates how the effect of individual parameters combine to give a much greater overall effect. Most noteworthy, a clear relationship is observed between the influence of fiber angle and fiber stiffness. For low fiber angles, the fiber stiffness appears to have little effect; conversely for large fiber angles, the fiber stiffness effect is dramatically magnified (and vice versa). The relationship is most apparent for flexion, extension and bending. For all cases, the influence of C_{10} appears uniform, having between a $\pm$25 and $\pm$35% on the overall stiffness, with little dependence of other parameters. This strengthens the earlier statements regarding the importance of high-fidelity fiber modeling, as a strong relation between the fiber angle and fiber stiffness is observed.

5.4. Study Three: Is the Combined Influence Independent or Convoluted?

As discussed above, an apparent relationship is observed between the effect of fiber angle and fiber stiffness. This

is explored in **Figure 5** which tests the independence of IVD parameters by plotting the changes in IVD stiffness from the combined parametric study (study 2) against the change in IVD stiffness predicted by Equation (1) (assuming independence). Under axial rotation it can be seen that changes in fiber angle and fiber stiffness have an independent effect on IVD stiffness. This is shown by data points sitting on the dashed line, and is further demonstrated by an R^2 of 1.00. This is important because it indicates that variances in one parameters don't impact the effect of the other parameter. Another way of understanding this, the relative effect of errors in one parameters will no magnify errors in another parameter.

However, under flexion, extension and later bending, a degree of dependence is observed between the various parameters, indicated by the locus of data points not sitting on the dashed line. This shows that there is a degree of convolution between the effect of different parameters on IVD stiffness. Interestingly, the degree of convolution is governed by the fiber angle. For a $\Delta\theta = 0\%$, the impact of different parameters follows Equation (1) (indicated by an R^2 of 1.00), however as the fiber angle increases or decreases, the convolution increases. This is particularly apparent for large fiber angles, where the convolution is greatest (indicated by an R^2 of 0.68). This reinforces the discussion from section 5.3, in which it was observed that increases in fiber angle, magnify the effect of changes in fiber stiffness.

Clearly, there is a convolution between fiber angle and fiber stiffness, which causes a magnified effect for flexion, extension and bending (especially for increases in fiber angle). This is relevant to patient specific modeling of the IVD as this demonstrates the independence/convolution of IVD parameters under different loadings. In the case of axial rotation, parameters of fiber angle and fiber stiffness are independent. This means that a complete understanding of the effect of these parameters, can be achieved by studying the results of the first parametric study (**Figure 3**). However, in the case of flexion, extension and bending, the effect of parameters are convoluted, which means that when considering the effects of various parameters, one must consider the convoluted behavior.

5.5. Inferences for Pediatric Patient Specific Modeling

Based upon these findings, we propose the following. (1) For patient specific models of the IVD, primary focus should be placed on accurate representation of fiber parameters. Specifically, for models focused on axial rotation both fiber angle and stiffness should be given equal attention, for other motions fiber angle be given greater attention. (2) Non-invasive interrogation of fiber angle for individual patients is a current challenge, thus new techniques need to be developed to incorporate these patient specific fiber parameters. Ultrasonography has been demonstrated as one technique for interrogating parameters such as lamellar number and thickness (both which affect fiber stiffness) (Langlais et al., 2019), this could be one avenue for further investigation. Further models such as the Michalek (2019) growth model could offer an avenue for integrating patient specific fiber angles. (3) The ground matrix parameters are of little significance for axial rotation, but are of secondary interest in for other motions. Currently, limited experimental data is available for ground matrix properties of pediatric IVDs, making this an area requiring further investigation.

For modeling of the pediatric IVD, our earlier literature search (section 2) concluded that fiber angles in the pediatric IVD likely match those of the adult. Thus, improved fidelity of fiber angle in patient specific models will improve the overall quality of predictions. Here, the (Michalek, 2019) growth model could offer potential and should be explored.

With respect to fiber stiffness, Galante (1967) demonstrated that patients of <26 years of age had reduced stiffness, up to a 33% reduction in fiber stiffness for patients of 10 years of age. This will be most significant during axial rotation, where a 33% reduction in fiber stiffness, would result in an approximate 28% reduction in IVD stiffness. For flexion, extension and lateral bending, this reduction would be −12, −9.1, and −10%, respectively. We propose that Galante (1967) can be used as a guide for patient specific fiber properties in pediatric models.

Considerations such as these are of increased significance when dealing with specific pediatric pathologies. Generally, little information is available on IVD parameters in such patients. The discussion above acts as further guidance to required areas of focus in such modeling. For example, in AIS, quantitative variation in the size and orientation of collagen fiber bundles has been observed in opposite sides of the AF (Roberts et al., 1993). Such changes would be expected to cause large variance in overall IVD behavior. Naturally, further investigation into IVD parameters in pediatric pathologies will aid in FE modeling of these pathologies.

5.6. Limitations

In any FE model of the IVD certain limitations are inherent and should be noted. First, this study used geometry from a single IVD, from which general conclusions were drawn. For this, it is argued that any effects of patient specific geometries can be extracted from medical imaging, thus focusing on a single, well-studied geometry will aid in translatability of results. Second, this study focused on a single constitutive model for all components, balancing model fidelity and complexity. For example, higher fidelity models can be considered which incorporate non-linear collagen fiber properties (Haut and Little, 1972; Sharabi et al., 2018), variable fiber distributions (Malandrino et al., 2013), visco-elastic effects (Castro and Alves, 2020), and osmotic effects (Cegoñino et al., 2014; Castro and Alves, 2020). While, these higher fidelity models would consider additional behaviors, they would also introduce additional parameters and more complexity. As this study is interested in comparing the relative contributions of individual IVD parameters, it becomes pertinent to focus on simpler constitutive models. Further, we argue that irrespective of the

constitutive model, the general findings in the parametric study are valid. Next, this study focused on an IVD in isolation. This has the advantage of only incorporate IVD behavior, but neglects the impact of the whole functional spinal unit. To account for this, the IAR method was used to embed realistic motions. Finally, the influence of NP hydrostatic pressure was not investigated in this study, but has been demonstrated the impact the mechanics and stiffness of the IVD, this should be considered in conjunction with the findings presented here.

6. CONCLUSION

This work has investigated the influence of various mechanical parameters on the stiffness behavior of the IVD under various loading conditions. Notably, while other studies have investigated the individual influence of individual parameters (Fagan et al., 2002b), this works has investigated the combined influence of parameters, demonstrating how these effects are convoluted, and can be magnified. These findings were contextualized with respect to the pediatric IVD, resulting in recommendations for patient specific models of the pediatric IVD and areas requiring further research. This work provides a valuable building block toward the development of such patient specific models.

DATA AVAILABILITY STATEMENT

The original contributions presented in the study are included in the article/**Supplementary Material**, further inquiries can be directed to the corresponding author/s.

AUTHOR CONTRIBUTIONS

JL developed the initial IVD model. EP conducted the parametric study, results analysis and wrote the manuscript. PP and JL reviewed the manuscript and provided valuable inputs. All authors contributed to the article and approved the submitted version.

ACKNOWLEDGMENTS

The authors gratefully acknowledge and thank the facilities and technical support provided by the High Performance Computing service at the Queensland University of Technology.

SUPPLEMENTARY MATERIAL

The Supplementary Material for this article can be found online at: https://www.frontiersin.org/articles/10.3389/fbioe.2021.632408/full#supplementary-material

REFERENCES

Aubin, C.-R., Clin, J., and Rawlinson, J. (2018). Biomechanical simulations of costo-vertebral and anterior vertebral body tethers for the fusionless treatment of pediatric scoliosis. *J. Orthopaed. Res.* 36, 254–264. doi: 10.1002/jor.23648

Ayturk, U. M., Garcia, J. J., and Puttlitz, C. M. (2010). The micromechanical role of the annulus fibrosus components under physiological loading of the lumbar spine. *J. Biomech. Eng.* 132:061007. doi: 10.1115/1.4001032

Bogduk, N. (2005). *Clinical Anatomy of the Lumbar Spine and Sacrum*. London: Elsevier; Churchill Livingstone.

Buckwalter, J. A. (1995). Spine update: aging and degeneration of the human intervertebral disc. *Spine* 20, 1307–1314. doi: 10.1097/00007632-199506000-00022

Cahill, P. J., Wang, W., Asghar, J., Booker, R., Betz, R. R., Ramsey, C., et al. (2012). The use of a transition rod may prevent proximal junctional kyphosis in the thoracic spine after scoliosis surgery: a finite element analysis. *Spine* 37, E687–E695. doi: 10.1097/BRS.0b013e318246d4f2

Cassidy, J. J., Hiltner, A., and Baer, E. (1989). Hierarchical structure of the intervertebral disc. *Connect. Tissue Res.* 23, 75–88. doi: 10.3109/03008208909103905

Castro, A. P., and Alves, J. L. (2020). Numerical implementation of an osmo-poro-visco-hyperelastic finite element solver: application to the intervertebral disc. *Comput. Methods Biomech. Biomed. Eng.* doi: 10.1080/10255842.2020.1839059. [Epub ahead of print].

Cegoñino, J., Moramarco, V., Calvo-Echenique, A., Pappalettere, C., and Pérez Del Palomar, A. (2014). A constitutive model for the annulus of human intervertebral disc: implications for developing a degeneration model and its influence on lumbar spine functioning. *J. Appl. Math.* 2014. doi: 10.1155/2014/658719

Cooper, R., Cardan, C., and Allen, R. (2001). Computer visualisation of the moving human lumbar spine. *Comput. Biol. Med.* 31, 451–469. doi: 10.1016/S0010-4825(01)00016-6

Cossette, J., Farfan, H., Robertson, G., and Wells, R. (1971). The instantaneous center of rotation of the third lumbar intervertebral joint. *J. Biomech.* 4, 149–153. doi: 10.1016/0021-9290(71)90025-X

Disney, C., Eckersley, A., McConnell, J., Geng, H., Bodey, A., Hoyland, J., et al. (2019). Synchrotron tomography of intervertebral disc deformation quantified by digital volume correlation reveals microstructural influence on strain patterns. *Acta Biomater.* 92, 290–304. doi: 10.1016/j.actbio.2019.05.021

Dong, L., Li, G., Mao, H., Marek, S., and Yang, K. H. (2013). Development and validation of a 10-year-old child ligamentous cervical spine finite element model. *Ann. Biomed. Eng.* 41, 2538–2552. doi: 10.1007/s10439-013-0858-7

Dreischarf, M., Zander, T., Shirazi-Adl, A., Puttlitz, C., Adam, C., Chen, C., et al. (2014). Comparison of eight published static finite element models of the intact lumbar spine: predictive power of models improves when combined together. *J. Biomech.* 47, 1757–1766. doi: 10.1016/j.jbiomech.2014.04.002

Ebara, S., Iatridis, J. C., Setton, L. A., Foster, R. J., Mow, V. C., and Weidenbaum, M. (1996). Tensile properties of nondegenerate human lumbar anulus fibrosus. *Spine* 21, 452–461. doi: 10.1097/00007632-199602150-00009

Fagan, M. J., Julian, S., and Mohsen, A. M. (2002a). Finite element analysis in spine research. *Proc. Instit. Mech. Eng.* 216, 281–298. doi: 10.1243/09544110260216568

Fagan, M. J., Julian, S., Siddall, D. J., and Mohsen, A. M. (2002b). Patient-specific spine models. part 1: finite element analysis of the lumbar intervertebral disc–A material sensitivity study. *Proc. Instit. Mech. Eng.* 216, 299–314. doi: 10.1243/09544110260216577

Finley, S. M., Brodke, D. S., Spina, N. T., DeDen, C. A., and Ellis, B. J. (2018). Febio finite element models of the human lumbar spine. *Comput. Methods Biomech. Biomed. Eng.* 21, 444–452. doi: 10.1080/10255842.2018.1478967

Galante, J. O. (1967). Tensile properties of the human lumbar annulus fibrosus. *Acta Orthopaed. Scand.* 38(Suppl 100), 1–91. doi: 10.3109/ort.1967.38.suppl-100.01

Goel, V. K., Monroe, B. T., Gilbertson, L. G., and Brinckmann, P. (1995). Interlaminar shear stresses and laminae separation in a disc: finite element analysis of the l3-l4 motion segment subjected to axial compressive loads. *Spine* 20, 689–698. doi: 10.1097/00007632-199503150-00010

Gu, W. Y., Mao, X. G., Foster, R. J., Weidenbaum, M., Mow, V. C., and Rawlins, B. A. (1999). The anisotropic hydraulic permeability of human lumbar anulus

fibrosus: Influence of age, degeneration, direction, and water content. *Spine* 24, 2449–2455. doi: 10.1097/00007632-199912010-00005

Guerin, H. L., and Elliott, D. M. (2007). Quantifying the contributions of structure to annulus fibrosus mechanical function using a nonlinear, anisotropic, hyperelastic model. *J. Orthopaed. Res*. 25, 508–516. doi: 10.1002/jor.20324

Haut, R. C., and Little, R. W. (1972). A constitutive equation for collagen fibres. *J. Biomech*. 5, 423–430. doi: 10.1016/0021-9290(72)90001-2

Hickey, D., and Hukins, D. (1980). X-ray diffraction studies of the arrangement of collagenous fibres in human fetal intervertebral disc. *J. Anat*. 131(Pt 1), 81–90.

Holzapfel, G. A., Schulze-Bauer, C. A. J., Feigl, G., and Regitnig, P. (2005). Single lamellar mechanics of the human lumbar anulus fibrosus. *Biomech. Model. Mechanobiol*. 3, 125–140. doi: 10.1007/s10237-004-0053-8

Iatridis, J. C., Setton, L. A., Weidenbaum, M., and Mow, V. C. (1997). The viscoelastic behavior of the non-degenerate human lumbar nucleus pulposus in shear. *J. Biomech*. 30, 1005–1013. doi: 10.1016/S0021-9290(97)00069-9

Iatridis, J. C., Weidenbaum, M., Setton, L. A., and Mow, V. C. (1996). Is the nucleus pulposus a solid or a fluid? Mechanical behaviors of the nucleus pulposus of the human intervertebral disc. *Spine* 21, 1174–1184. doi: 10.1097/00007632-199605150-00009

Langlais, T., Desprairies, P., Pietton, R., Rohan, P.-Y., Dubousset, J., Meakin, J. R., et al. (2019). Microstructural characterization of annulus fibrosus by ultrasonography: a feasibility study with an *in vivo* and *in vitro* approach. *Biomech. Model. Mechanobiol*. 18, 1979–1986. doi: 10.1007/s10237-019-01189-3

Lavecchia, C. E., Espino, D. M., Moerman, K. M., Tse, K. M., Robinson, D., Lee, P. V. S., et al. (2018). Lumbar model generator: a tool for the automated generation of a parametric scalable model of the lumbar spine. *J. R. Soc. Interface* 15:20170829. doi: 10.1098/rsif.2017.0829

Little, J., and Adam, C. (2015). Geometric sensitivity of patient-specific finite element models of the spine to variability in user-selected anatomical landmarks. *Comput. Methods Biomech. Biomed. Eng*. 18, 676–688. doi: 10.1080/10255842.2013.843673

Little, J., Pearcy, M., Tevelen, G., Evans, J., Pettet, G., and Adam, C. (2010). The mechanical response of the ovine lumbar anulus fibrosus to uniaxial, biaxial and shear loads. *J. Mech. Behav. Biomed. Mater*. 3, 146–157. doi: 10.1016/j.jmbbm.2009.09.002

Little, J. P., and Adam, C. (2011). Patient-specific computational biomechanics for simulating adolescent scoliosis surgery: predicted vs clinical correction for a preliminary series of six patients. *Int. J. Num. Methods Biomed. Eng*. 27, 347–356. doi: 10.1002/cnm.1422

Little, J. P., and Adam, C. J. (2012). *Patient-Specific Modeling of Scoliosis*. Berlin; Heidelberg: Springer.

Little, J. P., Pearcy, M. J., and Pettet, G. J. (2007). Parametric equations to represent the profile of the human intervertebral disc in the transverse plane. *Med. Biol. Eng. Comput*. 45, 939–945. doi: 10.1007/s11517-007-0242-6

Little, J. P., Visser, H. D., Pearcy, M. J., and Adam, C. J. (2008). Are coupled rotations in the lumbar spine largely due to the osseo-ligamentous anatomy?–A modeling study. *Comput. Methods Biomech. Biomed. Eng*. 11, 95–103. doi: 10.1080/10255840701552143

Malandrino, A., Noailly, J., and Lacroix, D. (2013). Regional annulus fibre orientations used as a tool for the calibration of lumbar intervertebral disc finite element models. *Comput. Methods Biomech. Biomed. Eng*. 16, 923–928. doi: 10.1080/10255842.2011.644539

Marchand, F., and Ahmed, A. M. (1990). Investigation of the laminate structure of lumbar disc anulus fibrosus. *Spine* 15, 402–410. doi: 10.1097/00007632-199005000-00011

Meir, A. R., Fairbank, J. C. T., Jones, D. A., McNally, D. S., and Urban, J. P. G. (2007). High pressures and asymmetrical stresses in the scoliotic disc in the absence of muscle loading. *Scoliosis* 2:4. doi: 10.1186/1748-7161-2-4

Michalek, A. J. (2019). A growth-based model for the prediction of fibre angle distribution in the intervertebral disc annulus fibrosus. *Biomech. Model. Mechanobiol*. 18, 1363–1369. doi: 10.1007/s10237-019-01150-4

Mills, M. J., and Sarigul-Klijn, N. (2019). Validation of an *in vivo* medical image-based young human lumbar spine finite element model. *J. Biomech. Eng*. 141:031003. doi: 10.1115/1.4042183

Nachemson, A. (1960). Lumbar intradiscal pressure: experimental studies on post-mortem material. *Acta Orthopaed. Scand*. 31(Suppl 43), 1–104. doi: 10.3109/ort.1960.31.suppl-43.01

Natali, A., and Meroi, E. (1990). Nonlinear analysis of intervertebral disk under dynamic load. *J. Biomech. Eng*. 112, 358–363. doi: 10.1115/1.2891196

Newell, N., Little, J., Christou, A., Adams, M., Adam, C., and Masouros, S. (2017). Biomechanics of the human intervertebral disc: a review of testing techniques and results. *J. Mech. Behav. Biomed. Mater*. 69, 420–434. doi: 10.1016/j.jmbbm.2017.01.037

Pearcy, M. J., and Bogduk, N. (1988). Instantaneous axes of rotation of the lumbar intervertebral joints. *Spine* 13, 1033–1041. doi: 10.1097/00007632-198809000-00011

Ponrartana, S., Fisher, C. L., Aggabao, P. C., Chavez, T. A., Broom, A. M., Wren, T. A. L., et al. (2016). Small vertebral cross-sectional area and tall intervertebral disc in adolescent idiopathic scoliosis. *Pediatr. Radiol*. 46, 1424–1429. doi: 10.1007/s00247-016-3633-8

Roberts, S., Menage, J., and Eisenstein, S. M. (1993). The cartilage end-plate and intervertebral disc in scoliosis: calcification and other sequelae. *J. Orthopaed. Res*. 11, 747–757. doi: 10.1002/jor.1100110517

Rohlmann, A., Zander, T., Schmidt, H., Wilke, H.-J., and Bergmann, G. (2006). Analysis of the influence of disc degeneration on the mechanical behaviour of a lumbar motion segment using the finite element method. *J. Biomech*. 39, 2484–2490. doi: 10.1016/j.jbiomech.2005.07.026

Sairyo, K., Goel, V. K., Masuda, A., Vishnubhotla, S., Faizan, A., Biyani, A., et al. (2006). Three-dimensional finite element analysis of the pediatric lumbar spine. Part I: pathomechanism of apophyseal bony ring fracture. *Eur. Spine J*. 15, 923–929. doi: 10.1007/s00586-005-1026-z

Schmidt, H., Heuer, F., Claes, L., and Wilke, H.-J. (2008). The relation between the instantaneous center of rotation and facet joint forces - a finite element analysis. *Clin. Biomech*. 23, 270–278. doi: 10.1016/j.clinbiomech.2007.10.001

Sharabi, M., Wade, K., and Haj-Ali, R. (2018). "Chapter 7: The mechanical role of collagen fibres in the intervertebral disc," in *Biomechanics of the Spine*, eds F. Galbusera and H. J. Wilke (London: Academic Press), 105–123. doi: 10.1016/B978-0-12-812851-0.00007-0

Shirazi-Adl, A., Ahmed, A., and Shrivastava, S. (1986). A finite element study of a lumbar motion segment subjected to pure sagittal plane moments. *J. Biomech*. 19, 331–350. doi: 10.1016/0021-9290(86)90009-6

Sivakamasundari, V., and Lufkin, T. (2012). Bridging the gap: understanding embryonic intervertebral disc development. *Cell Dev. Biol*. 1, 105–123. doi: 10.4172/2168-9296.1000103

Smit, T. H., Odgaard, A., and Schneider, E. (1997). Structure and function of vertebral trabecular bone. *Spine* 22, 2823–2833. doi: 10.1097/00007632-199712150-00005

Strickland, C. G., Aguiar, D. E., Nauman, E. A., and Talavage, T. M. (2011). Development of subject-specific geometric spine model through use of automated active contour segmentation and kinematic constraint-limited registration. *J. Digit. Imaging* 24, 926–942. doi: 10.1007/s10278-010-9336-z

Tavana, S., Clark, J., Prior, J., Baxan, N., Masouros, S., Newell, N., et al. (2020). Quantifying deformations and strains in human intervertebral discs using digital volume correlation combined with MRI (DVC-MRI). *J. Biomech*. 102:109604. doi: 10.1016/j.jbiomech.2020.109604

Taylor, J. (1975). Growth of human intervertebral discs and vertebral bodies. *J. Anat*. 120(Pt 1), 49–68.

Ueno, K., and Liu, Y. K. (1987). A three-dimenstional nonlinear finite element model of lumbar intervertebral joint in torsion. *J. Biomech. Eng*. 109, 200–209. doi: 10.1115/1.3138670

Urban, J. P., Roberts, S., and Ralphs, J. R. (2000). The nucleus of the intervertébral disc from development to degeneration. *Am. Zool*. 40, 53–61. doi: 10.1668/0003-1569(2000)040[0053:TNOTID]2.0.CO;2

Urban, J. P. G., and McMullin, J. F. (1988). Swelling pressure of the lumbar intervertebral discs. *Spine* 13, 179–187. doi: 10.1097/00007632-198802000-00009

Vergari, C., Ribes, G., MEnga, B. A., Adam, C., Miladi, L., Ilharreborde, B., et al. (2015). Evaluation of a patient-specific finite-element model to simulate conservative treatment in adolescent idiopathic scoliosis. *Spine Deformity* 3, 4–11. doi: 10.1016/j.jspd.2014.06.014

Walmsley, R. (1953). The development and growth of the intervertebral disc. *Edinburgh Med. J*. 60, 341–364.

Wilke, H.-J., Neef, P., Caimi, M., Hoogland, T., and Claes, L. E. (1999). New *in vivo* measurements of pressures in the intervertebral disc in daily life. *Spine* 24, 755–762. doi: 10.1097/00007632-199904150-00005

Wu, H.-C., and Yao, R.-F. (1976). Mechanical behavior of the human annulus fibrosus. *J. Biomech.* 9, 1–7. doi: 10.1016/0021-9290(76)90132-9

Zhu, D., Gu, G., Wu, W., Gong, H., Zhu, W., Jiang, T., et al. (2008). Micro-structure and mechanical properties of annulus fibrous of the l4-5 and l5-s1 intervertebral discs. *Clin. Biomech.* 23, S74–S82. doi: 10.1016/j.clinbiomech.2008.04.007

Conflict of Interest: The authors declare that the research was conducted in the absence of any commercial or financial relationships that could be construed as a potential conflict of interest.

frontiers in Bioengineering and Biotechnology

ORIGINAL RESEARCH
published: 10 March 2021
doi: 10.3389/fbioe.2021.643154

Patient-Specific Finite Element Models of Posterior Pedicle Screw Fixation: Effect of Screw's Size and Geometry

*Marco Sensale[1,2,3], Tanguy Vendeuvre[4,5], Christoph Schilling[6], Thomas Grupp[6,7], Michel Rochette[1] and Enrico Dall'Ara[2,3]**

[1] Ansys France, Lyon, France, [2] Department of Oncology and Metabolism, Mellanby Centre for Musculoskeletal Research, University of Sheffield, Sheffield, United Kingdom, [3] INSIGNEO Institute for in Silico Medicine, University of Sheffield, Sheffield, United Kingdom, [4] Spine and Neuromodulation Functional Unit, Poitiers University Hospital, Poitiers, France, [5] PRISMATICS Lab (Predictive Research in Spine/Neuromodulation Management and Thoracic Innovation/Cardiac Surgery), Poitiers University Hospital, Poitiers, France, [6] Aesculap AG, Research and Development, Tuttlingen, Germany, [7] Department of Orthopaedic Surgery, Physical Medicine and Rehabilitation, Ludwig Maximilians University of Munich, Munich, Germany

Pedicle screw fixation is extensively performed to treat spine injuries or diseases and it is common for thoracolumbar fractures. Post-operative complications may arise from this surgery leading to back pain or revisions. Finite element (FE) models could be used to predict the outcomes of surgeries but should be verified when both simplified and realistic designs of screws are used. The aim of this study was to generate patient-specific Computed Tomography (CT)-based FE models of human vertebrae with two pedicle screws, verify the models, and use them to evaluate the effect of the screws' size and geometry on the mechanical properties of the screws-vertebra structure. FE models of the lumbar vertebra implanted with two pedicle screws were created from anonymized CT-scans of three patients. Compressive loads were applied to the head of the screws. The mesh size was optimized for realistic and simplified geometry of the screws with a mesh refinement study. Finally, the optimal mesh size was used to evaluate the sensitivity of the model to changes in screw's size (diameter and length) and geometry (realistic or simplified). For both simplified and realistic models, element sizes of 0.6 mm in the screw and 1.0 mm in the bone allowed to obtain relative differences of approximately 5% or lower. Changes in screw's length resulted in 4–10% differences in maximum deflection, 1–6% differences in peak stress in the screws, 10–22% differences in mean strain in the bone around the screw; changes in screw's diameter resulted in 28–36% differences in maximum deflection, 6–27% differences in peak stress in the screws, and 30–47% differences in mean strain in the bone around the screw. The maximum deflection predicted with realistic or simplified screws correlated very well ($R^2 = 0.99$). The peak stress in screws with realistic or simplified design correlated well ($R^2 = 0.82$) but simplified models underestimated the peak stress. In conclusion, the results showed that the diameter of the screw has a major role on the mechanics of the screw-vertebral structure for each patient. Simplified screws can be used to estimate the mechanical properties of the implanted vertebrae, but the systematic underestimation of the peak stress should be considered when interpreting the results from the FE analyses.

Keywords: spine, spinal fractures, posterior fixation, finite element, sensitivity analysis

OPEN ACCESS

Edited by:
Alexandros E. Tsouknidas, University of Western Macedonia, Greece

Reviewed by:
Maria Angeles Perez Anson, University of Zaragoza, Spain
Wenfei Ni, Second Affiliated Hospital and Yuying Children's Hospital of Wenzhou Medical University, China

***Correspondence:**
Enrico Dall'Ara
e.dallara@sheffield.ac.uk

Specialty section:
This article was submitted to Biomechanics, a section of the journal Frontiers in Bioengineering and Biotechnology

Received: *17 December 2020*
Accepted: *18 February 2021*
Published: *10 March 2021*

Citation:
Sensale M, Vendeuvre T, Schilling C, Grupp T, Rochette M and Dall'Ara E (2021) Patient-Specific Finite Element Models of Posterior Pedicle Screw Fixation: Effect of Screw's Size and Geometry. Front. Bioeng. Biotechnol. 9:643154. doi: 10.3389/fbioe.2021.643154

INTRODUCTION

In the lumbar spine, pedicle screw fixation is the most widespread technique to achieve spinal fusion and stabilization (Verma et al., 2016). In 2008, approximately 415,000 spinal fusion surgeries were performed in the United States alone (Rajaee et al., 2012). The global pedicle screw system market has been predicted to increase of about 32% from 2018 to 2025 as reported by Fior Markets (Fior Markets, 2020). Pedicle screw fixation is the standard surgical procedure to treat different diseases of the spine, in particular, it is common for thoracolumbar fractures.

Despite the extensive use of pedicle screws in the current clinical practice, screw loosening and screw breakage are recurring mechanical complications of spinal fixation that can bring to a revision surgery in about 6% of cases (Prud'homme et al., 2015; Bredow et al., 2016). For this reason, surgery-related parameters should be optimized to improve the outcomes of this surgery. While surgeons decide the optimal size, insertion point and orientation of screws based on anatomical measurements on CT-images, finite element (FE) models are efficient tools to mechanically assess the stability of different configurations of the instrumented spine under different loading conditions. FE models of the vertebra should take into account different parameters related to the bone geometry, bone tissue heterogeneity, different boundary conditions, and before clinical applications they should be verified and validated [see for example (Assessing Credibility of Computational Modeling through Verification and Validation: Application to Medical Devices–ASME)]. Many studies assessed the optimal fixation to treat a burst fracture by simulating with FE models a system composed of three vertebrae and two intervertebral discs implanted with different configurations of rod and screws (e.g., monolateral vs. bilateral, short segment vs. long segment) (Li et al., 2014; Elmasry et al., 2017; Su et al., 2018; Wang et al., 2019). Other studies focused on the vertebra-screws interactions and proposed FE models validated with experimental measures: FE models were found to be good predictors of pull-out strength and stiffness obtained by experimental tests better than apparent density estimated from CT images (Abbeele et al., 2018; Chevalier et al., 2018; Widmer et al., 2020). The screw size and other insertion-related parameters have been tested with linear FE models (Qi et al., 2011; Newcomb et al., 2017), with non-linear FE models (material non-linearities, contact mechanics) (Chen et al., 2003; Bianco et al., 2017, 2019; Molinari et al., 2021), or assuming the bone as heterogeneous material with elastic properties driven by the local bone mineral density (BMD) (Matsukawa et al., 2016, 2020; Biswas et al., 2019; Molinari et al., 2021). In most cases a realistic screw geometry was used and only in a few studies the simplified geometry of the screw was modeled (Li et al., 2014; Su et al., 2018). The usage of simplified screws would enable the optimization and automation of the modeling procedure to evaluate vertebral and screws properties, if used in combination with morphing and reduced model order techniques (Campbell and Petrella, 2016). Although FE models of the instrumented spine are often proposed as tools for planning pedicle screw fixations to predict the optimal screw size and orientation for a given patient, little is known about the capability of predicting the biomechanical properties of the screw and of the vertebra if simplified or realistic screws are used. In particular, to the authors' knowledge, a comprehensive assessment of the effect of the mesh size and the sensitivity of the models to the screw size and geometry, in terms of stress in the screw, strain in the heterogeneous bone, and deflection of the screw within the bone, has not been reported in the literature yet. This gap in the literature makes it difficult to compare the outcomes from different studies and understanding the potential of the FE models in evaluating the biomechanics of the implanted vertebrae.

The aim of this study was to verify and evaluate the sensitivity of subject specific FE models of the vertebra with two pedicle screws for different sizes of the implant and in case of realistic and simplified geometry of the screw.

MATERIALS AND METHODS

Anonymized CT-scans of the thoracolumbar spine of three patients were collected. One vertebra per patient was segmented, converted to a FE model, virtually implanted with pedicle screws, and vertical loads were applied to the head of the screws, perpendicular to their axis. A mesh refinement study for realistic or simplified geometry of the screws was performed to choose the optimal mesh size that was used to evaluate the sensitivity of the model to changes in screw's size (diameter and length) and geometry (realistic or simplified). An overview of the study is presented in **Figure 1**.

Imaging and Image Processing

Three anonymized clinical pre-operative CT-scans of the thoracolumbar spine of three patients were analyzed. The scans were previously acquired at the University Hospital Centre (CHU) of Poitiers (France) and transferred only after anonymization (CHU86-RECH-R2020-02-01). These patients were treated with a posterior pedicle screw fixation for different reasons: two patients reported a vertebral fracture at L1 (Patients #1 and #3), one patient had osteoarthritis (Patients #2). The scanning parameters are reported in **Table 1**. In order to simplify the sensitivity study one vertebra with similar size was selected from each patient (L2, L3, and L4 for Patient #1, Patient #2, and Patient #3, respectively). The relative difference in the mean CT based BMD in the vertebral bodies was 21% between Patient #1 and Patient #2 and −24% between Patient #1 and Patient #3.

The pedicle widths and the distances between the approximated insertion points and the anterior wall of the vertebral body were measured in a cross-section corresponding to the approximated insertion points and including the longitudinal axes of the screws. From these measurements, and based on the advice of an experienced surgeon, it was concluded that the size of the vertebrae was ideal for the insertion of pedicle screws with diameter (D) equal to 6.5 mm and length (L) equal to 45 mm. The shape of the vertebrae was reconstructed by manual image segmentation of the CT cross-sections (3D Slicer, v4.10.1) (Fedorov et al., 2012). The resulting mask was smoothed with a Laplacian smoothing. The number of iterations was adjusted in

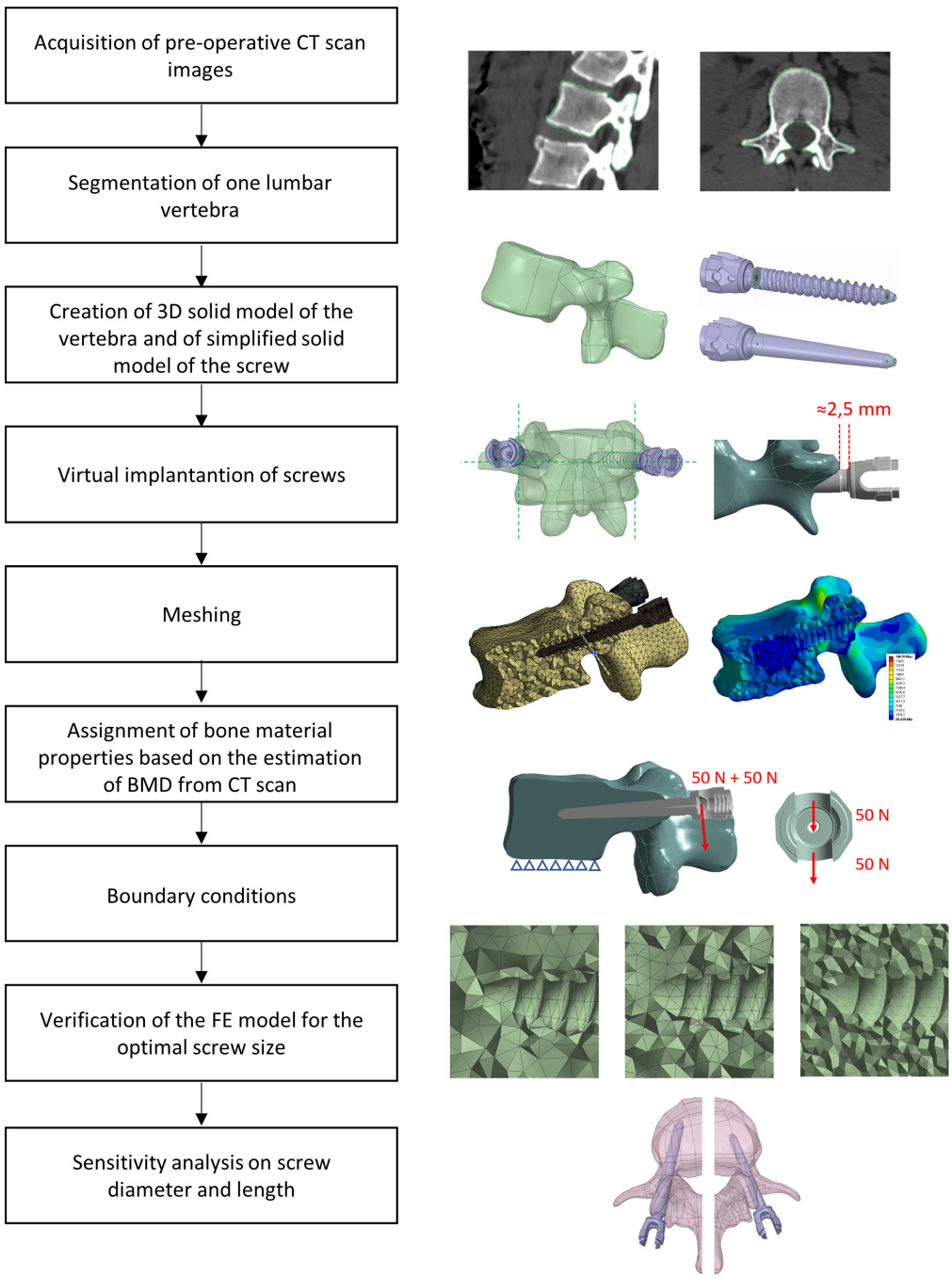

FIGURE 1 | Workflow used to generate, verify, and test the sensitivity of heterogeneous FE models of one vertebra implanted with two pedicle screws.

order to preserve the geometric features while avoiding shrinkage of the volume, which was verified by visual inspection of the overlapped CT images and mask.

Generation of the FE Model

The segmented vertebrae were exported as surface meshes (STL) and imported in the 3D modeling software Ansys® SpaceClaim Release 20.2 (Ansys Inc., Canonsburg, PA, United States). Through a reverse engineering process ("SkinSurface" command), a 3D solid model of each vertebra was reconstructed. The surface at the bottom of the model, representative of the inferior endplate, was used to apply the boundary conditions.

Afterward, the insertion of two pedicle screws (Aesculap® S4® Element MIS Monoaxial) was simulated. The realistic geometry of the implant was imported as STP file. Nine different sizes of pedicle screws available on the market were tested including D equal to 5.5, 6.5, or 7.5 mm and L equal to 45, 50, or 55 mm. Nine simplified screws with a smooth conic body without the

TABLE 1 | Parameters of acquisition of CT-scan images for the three patients.

Scanning parameters	Patient #1	Patient #2	Patient #3
Voltage (kV)	120	135	135
Current (mA)	181	200	273
Exposure (s)	1.38	0.5	0.5
In plane pixel size (mm^2)	0.98 × 0.98	0.88 × 0.88	0.68 × 0.68
Slice thickness (mm)	1.25	1.0	1.0
Model, manufacturer	Optima CT540, GE Healthcare, United States	Aquilion, Toshiba, JP	Aquilion, Toshiba, JP

thread were also generated to evaluate how the thread affected the loading distribution and deformation within the vertebra-screws construct. The solid model of the simplified screws was obtained from each of the nine realistic screws as following. The head of the screw until the end of the junction with the conic feature where the thread begins, and the last portion of the screw after the end of the thread were kept from the original realistic design. The two circular exposed sections were then connected with a conic surface (**Figure 2**).The realistic screws with the largest size ($D = 7.5$ mm, $L = 50$ mm) were virtually inserted at the pedicles by a Boolean subtraction. The insertion point was determined by following medical guidelines (Gertzbein and Robbins, 1990), which consist of finding the intersection point between a horizontal line passing through the transverse processes and a vertical line adjacent to the lateral border of the superior articular process. Screws were positioned parallel to the superior endplate, converging to the center of the vertebral body, keeping a distance of approximately 2.5 mm between the head of the screw and the superior articular processes (**Figure 1**). All other realistic and simplified screws were aligned to the position of the largest screws by registering their head, which were the same for every implant. Boolean subtraction from the original vertebra was applied for each pair of screws. In total eighteen models per vertebra were generated, nine with realistic geometries and nine with simplified geometries.

Each vertebra-screws construct was imported in Ansys® Mechanical Enterprise Release 20.2 (Ansys Inc., Canonsburg, PA, United States) for meshing. The vertebra and the screws were meshed separately with tetrahedral quadratic elements (T10). For the vertebra, a uniform meshing algorithm was used so that the CT-scan grid was sampled uniformly during the definition of material properties of the bone. The element size was defined based on a mesh convergence study (see section "Generation of the FE Model"). A bonded contact was considered at the interface between the screws and the vertebra.

Bone was modeled as isotropic and heterogeneous material with Young's modulus depending on the local BMD estimated from the CT images. In absence of an experimental densitometric calibration, the Hounsfield units were considered equal to BMD equivalent values (ρ_{QCT}), using a scale factor to convert the physical units to g/cm^3. This assumption was considered acceptable for the goal of this study, which is focused on the verification and sensitivity analysis of the models. From the BMD equivalent density, the apparent density (ρ_{App}) was obtained through Eq. 1 (Schileo et al., 2008):

$$\rho_{QCT} = \rho_{Ash} = \rho_{App} \times 0.6 \left(\frac{g}{cm^3}\right). \quad (1)$$

The Young's modulus was then calculated using the density-elasticity experimental equation specific for thoraco-lumbar vertebrae (Eq. 2) (Morgan et al., 2003):

$$E_{bone} = 4730\ \rho_{APP}^{1.56} \quad (2)$$

The Poisson's ratio of the bone was set to $\nu_{bone} = 0.3$ (Wirtz et al., 2000). The values of E_{bone} were calculated and assigned for each element by using the Bonemat software (Taddei et al., 2007). The screw was considered isotropic and homogeneous with Young's modulus and Poisson's ratio of Titanium: $E_{screw} = 102$ GPa, $\nu_{screw} = 0.36$ (Niinomi and Boehlert, 2015).

The model was loaded with a quasi-static uniformly distributed force of 200 N (100 N per screw) applied to the head of the screw in a direction perpendicular to the longitudinal axis of the screw and perpendicular to the superior endplate, toward the caudal direction (Chen et al., 2003; Biswas et al., 2019; **Figure 1**). The force was equally distributed between the two surfaces of the head of the screw that would interact with the rod (50 N on each surface) (**Figure 1**). This load configuration aimed to represent the load exercised by the upper chest on the most inferior vertebra of a short-segment pedicle screw construct and transmitted by a rod that would be tightened in a direction perpendicular to the screw axis as estimated in an *in-vivo* study (Rohlmann et al., 1997). However, it should be noted that the model has a linear behavior and that the results of simulations were interpreted relative to the optimal configuration, therefore the magnitude of the load is not critical. In addition, the nodes of the inferior endplate of the vertebral body were fixed in all three directions (Chen et al., 2003). ANSYS® Mechanical Enterprise Release 20.2 (Ansys Inc., Canonsburg, PA, United States) was used to solve the analysis. A workstation with processor model Intel(R) Xeon(R) CPU E5-2690 v3, 2.60 GHz was used. The analysis was run in parallel processing on 4 CPU Cores.

Mesh Refinement Study

For each patient, the model configuration corresponding to the optimal screw size ($D = 6.5$ mm, $L = 45$ mm) as advised by surgeons was tested for verification purposes. A mesh convergence study was conducted to estimate the optimal mesh size. The element size was changed separately in the bone and pedicle screws. Six maximum element sizes were tested for the screws between 0.4 and 1.2 mm while keeping the element size in the bone constant and equal to 1 mm. A maximum element size larger than 1.2 mm resulted in an inaccurate discretization of the circular cavity of the screw's body; the inferior boundary was considered at 0.4 mm based on the dimension of the smaller thread in the realistic screw (**Table 2**).

Moreover, maximum element sizes in the bone between 0.9 and 3 mm were tested for the finest mesh of the screw (0.4 mm) (**Table 3**). The lowest element size was to the voxel size of the CT-scan images of the three patients.

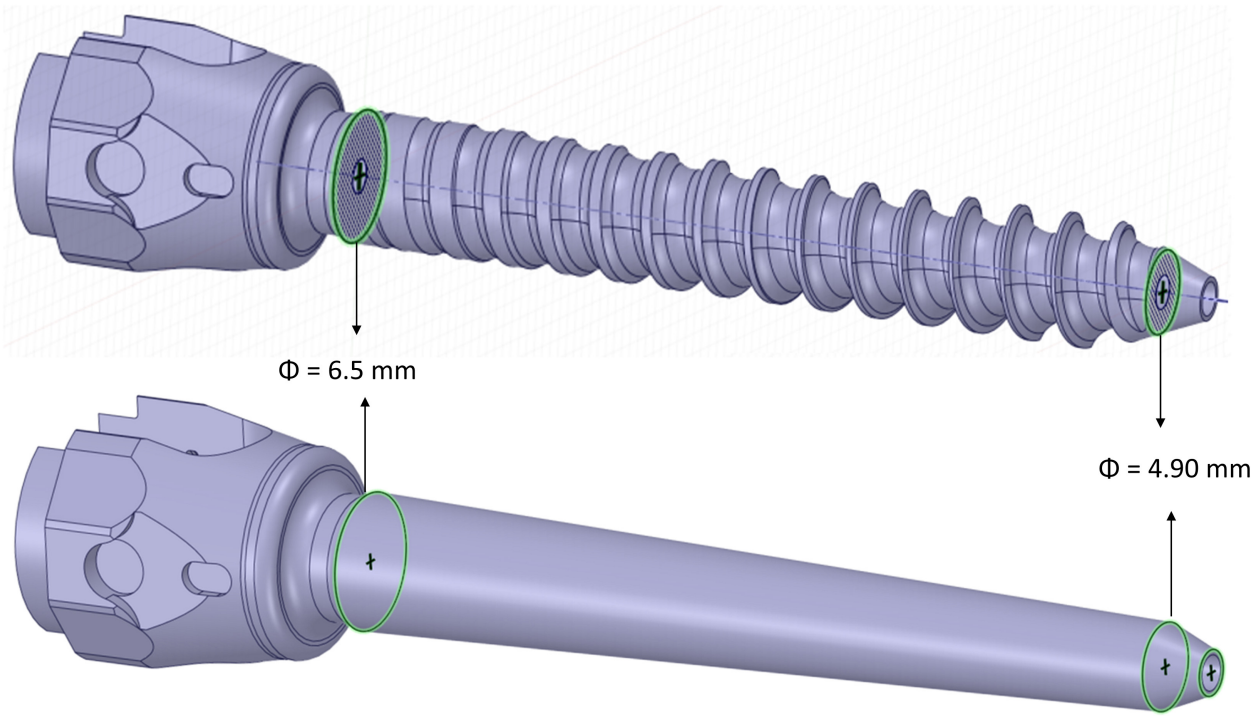

FIGURE 2 | 3D CAD models of simplified (bottom) and realistic (top) screws.

TABLE 2 | Number of Elements and Degrees of Freedom per screw, averaged over the three patients, for six element sizes tested for the screws (the maximum element size is reported), in models with simplified or realistic screws; Total CPU time (time * number of CPU Cores) to solve models with simplified or realistic screws.

E-size screws (mm)	E-size vertebra (mm)	#Elements per simplified screw	#DOF per simplified screw	#Elements per realistic screw	#DOF per realistic screw	Total CPU time (s) simplified screw	Total CPU time (s) realistic screw
1.2	1	11,489	1.2 E+05	14,340	1.5 E+05	384	560
1.0	1	16,867	1.7 E+05	20,340	2.1 E+05	468	584
0.8	1	28,909	2.8 E+05	33,893	3.3 E+05	508	608
0.6	1	61,918	5.7 E+05	68,439	6.5 E+05	548	592
0.5	1	105,509	9.5 E+05	112,882	1.0 E+06	556	624
0.4	1	199,297	1.8 E+06	210,545	1.9 E+06	676	760

TABLE 3 | Number of Elements and Degrees of Freedom in the vertebra, averaged over the three patients, for eight element sizes tested for the bone (the maximum element size is reported), in models with simplified or realistic screws; Total CPU time (time*number of CPU Cores) to solve models with simplified or realistic screws.

E-size vertebra (mm)	E-size screws (mm)	#Elements vertebra (simplified screw)	#DOF vertebra (simplified screw)	#Elements vertebra realistic screw	#DOF vertebra (realistic screw)	Total CPU time (s) (simplified screw)	Total CPU time (s) (realistic screw)
3.0	0.4	8,601	1.4 E+05	12,154	2.0 E+05	284	260
2.5	0.4	14,319	2.3 E+05	17,662	2.9 E+05	252	320
2.2	0.4	21,114	3.3 E+05	24,693	4.0 E+05	256	304
1.9	0.4	32,390	5.0 E+05	35,424	5.6 E+05	308	352
1.6	0.4	53,361	8.1 E+05	55,932	8.7 E+05	316	352
1.3	0.4	98,509	1.5 E+06	101,141	1.5 E+06	424	528
1.0	0.4	215,833	3.2 E+06	217,860	3.3 E+06	676	760
0.9	0.4	295,509	4.4 E+06	296,387	4.4 E+06	912	996

The computational time needed to solve the models with different element sizes is reported in **Tables 2**, **3**. As the models were run in parallel computing, the total CPU time is calculated as the CPU time times the number of CPU cores. It should be noted that due to the heterogeneous properties of bone, the value of Young's modulus in each element changes for different element sizes, making it impossible to uncouple the effect of mesh size from changes of material properties on the simulation outcomes.

Therefore, the outcomes of the mesh refinement study should be interpreted by considering both changes in element size and material properties in the bone tissue.

The following metrics were considered for the different mesh sizes:

- The maximum total deflection (d_{max}) of the head of the screw calculated as the magnitude of the displacement vector (nodal value).
- The peak Von Mises stress (σ_{VM}) in the screws (nodal value) for the finest mesh. For the coarser meshes the σ_{VM} was evaluated in the same coordinates, using the element shape functions to interpolate nodal values. Since the peak σ_{VM} in the screws always occurred in a node on the external surface, for coarser meshes the coordinates of that node could fall outside the screw. To avoid this issue the outputs of the models were compared in a point within the volume of the screw at a distance equal to 0.05 mm from the point with peak σ_{VM}.
- The peak Minimum Principal Strain (ε_{p3}) in the bone (nodal value) for the finest mesh. For the coarser meshes the ε_{p3} was evaluated in the same coordinates, using the element shape functions to interpolate nodal values. Some peaks were excluded from the analysis because their location was either close to the boundary conditions of the model, or in geometric sharp corners (for example close to the cuspid at the insertion point or close to the tip of screws), or in an area on the external surface of the vertebra potentially affected by segmentation problems (low values of Elastic modulus for the small elements of the finer mesh). In these cases, the next peak was considered.

Influence of Screw Size and Geometry on Mechanical Properties of Screws-Vertebra Structure

Once the optimal mesh size was chosen for the bone and the screws, the influence of the diameter and length of screws on the stability of the simulated structure, for both the realistic and simplified models, was evaluated. The diameter and length of the left and right screws were changed simultaneously. The effect of changing the size of the screws was estimated with respect to the structural and local parameters estimated for the optimal screw size ($D = 6.5$ mm; $L = 45$ mm). The following parameters were calculated for the three patients:

- The maximum total deflection (d_{max}) of the head of the screw calculated as the magnitude of the displacement vector (nodal value).
- The peak Von Mises stress (σ_{VM}) in the screws (nodal value). Some peaks were excluded from the analysis because their location was close to the sharp corner of the bone geometry generated by the Boolean subtraction at the screw insertion point. This happened only for Patient #1, for a screw diameter of 5.5 mm. In this case the next peak, at a distance higher than five element sizes from the sharp corner, was considered in the analysis.
- The mean Minimum Principal Strain (ε_{p3}) in the bone (nodal value). This value was calculated within a Region of Interest (ROI) defined at the screw-bone interface with a shape similar to the smooth conic body of simplified screws. The ROI was coaxial with the longitudinal axis of the screw and had a diameter equal to two times the diameter of the screw. Therefore, the dimensions of the ROI were scaled to each screw size. The same ROI was used for both simplified and realistic models.

For the patient characterized by the highest relative differences in σ_{VM} in the screws and ε_{p3} in the bone (Patient #2), the frequency plots for ε_{p3} for three screw sizes ($D = 7.5$ mm and $L = 50$ mm; $D = 6.5$ mm and $L = 45$ mm; $D = 5.5$ mm and $L = 40$ mm) were compared for models with simplified and realistic screw geometries.

Comparison Between Simplified and Realistic Screw Geometry

Linear regression analyses were performed between the predictions of d_{max} and σ_{VM} from the models with simplified and realistic screw geometry. The Slope, Intercept and coefficient of determination (R^2) were calculated for each linear regression.

RESULTS

Mesh Refinement Study

The percentage absolute change with respect to the finer mesh in d_{max} for both simplified and realistic screw models was lower than 0.1% (screw) and 0.5% (bone) for each tested element size (**Figures 3A,B**).

The percentage absolute change with respect to the finer mesh in peak σ_{VM} was higher for the realistic screw compared to the simplified one (**Figures 3C,D**). In particular, while for the simplified model a percentage relative difference lower than 5% was observed for each tested element size, for the realistic case an element size of 0.6 mm allowed to achieve relative differences of approximately 5% or below. The σ_{VM} distribution in the screws were similar for the models with different element size for both simplified and realistic screw geometry (**Figure 4**).

The peak ε_{p3} values occurred at the interface between the bone and the left screw for Patient #1 and #2, and at the interface between the bone and the right screw for Patient #3 (**Figure 5**). The absolute percentage relative differences in peak ε_{p3} were much higher than for the peak σ_{VM}. For both simplified and realistic models, element size of 1 mm in the bone led to absolute percentage relative difference of approximately 5% or below for the three patients (**Figures 3E,F**).

For the following analyses, an element size of 0.4 mm was chosen in the screws because the computational time was not significantly affected (**Tables 2**, **3**), and an element size of 1.0 mm was chosen in the bone.

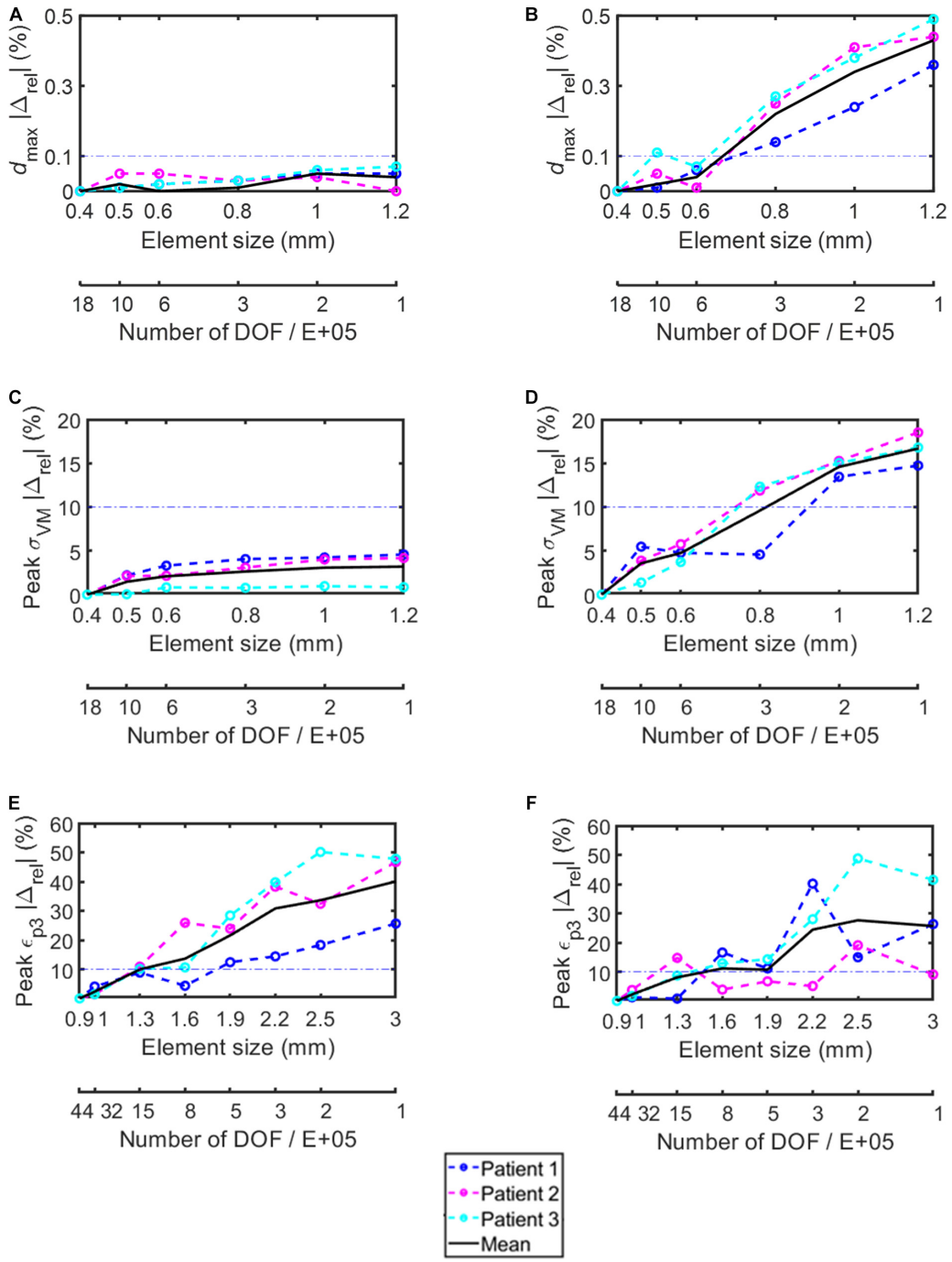

FIGURE 3 | Percentage absolute difference with respect to the finer mesh in the simplified screws **(A,C,E)** and in the realistic screws **(B,D,F)** for maximum total deflection **(A,B)**, peak von Mises stress in the screw **(C,D)**, and peak minimum principal strain in the bone **(E,F)**. Dashed lines represent results for each subject, continuous black lines represent averaged values, dash-dotted lines represent the chosen 10% difference chosen as threshold.

Effect of Size and Geometry of the Screw

The screw's diameter had a more significant influence on d_{max} than the screw's length in both simplified and realistic models, for both left and right screws (**Table 4**). Changes in length resulted in median values of percentage changes in d_{max} between 4 and 10%; whilst, changes in diameter resulted in median values of percentage changes in d_{max} between 28 and 36%. Similar changes were observed between right and left screws, for both simplified and realistic cases, and between simplified and realistic models, for both left and

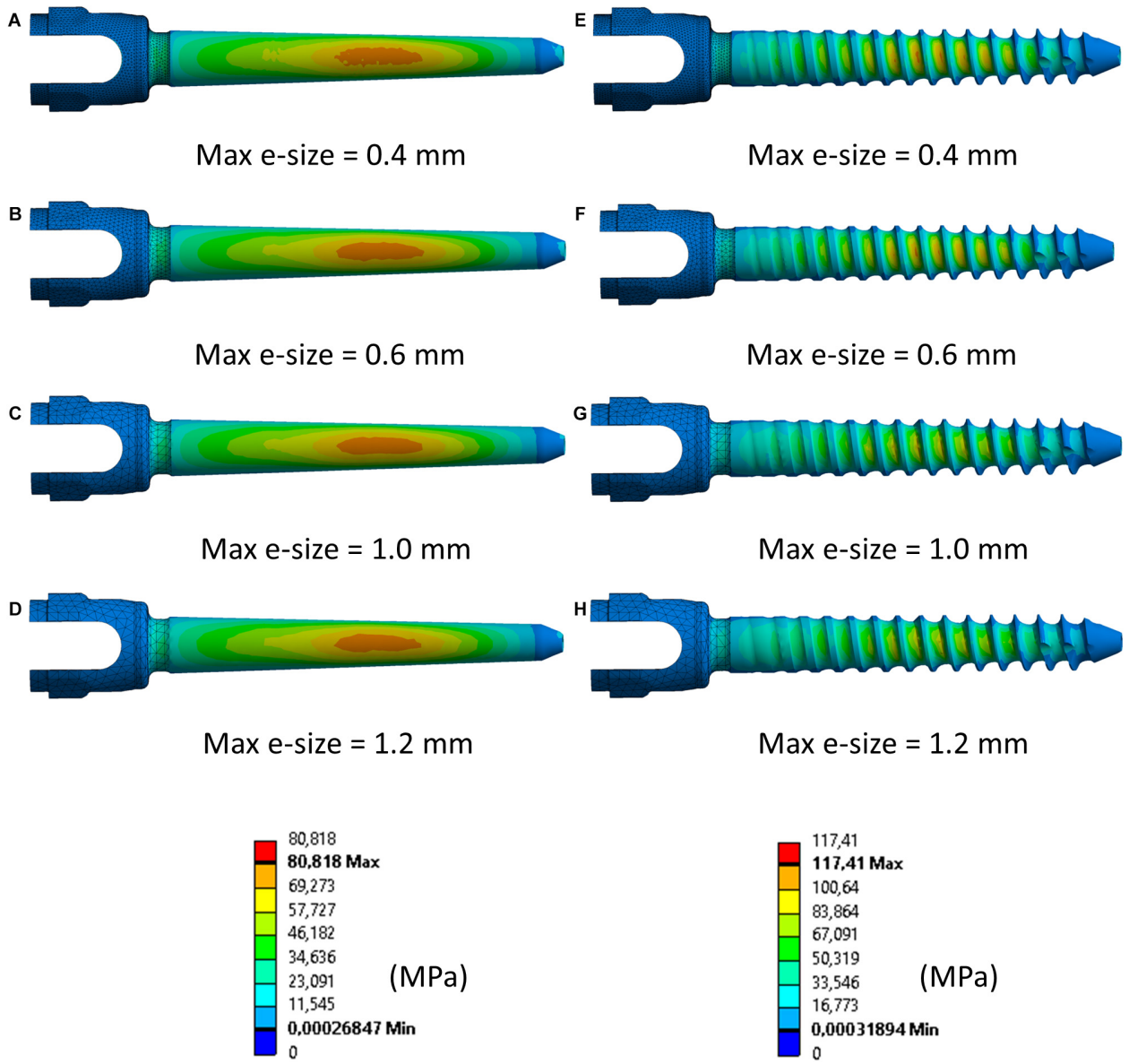

FIGURE 4 | Distribution of von Mises stress in simplified **(A–D)** and realistic **(E–H)** left screws (Patient #2) for four different element sizes. Compressed fibers side (caudal view). The mesh was hidden in the main body of the screw to better visualize the stress distribution.

right screws. Very similar trends were found for the three patients. As expected, for a fixed length, the d_{max} increased for lower diameters; for a fixed diameter, the d_{max} decreased for longer screws.

The diameter had higher impact on peak σ_{VM} than the length for both simplified and realistic models (**Table 5**). In fact, changes in length resulted in median values of percentage changes in peak σ_{VM} between 1 and 6%; instead, changes in diameter resulted in median values of percentage changes in peak σ_{VM} between 6 and 27%. For both simplified and realistic models, similar percentage differences and trends were found between right and left screws. However, an asymmetry was found for Patient #1 in the models with realistic screws with $D = 5.5$ mm: for the three values of L, percentage differences in peak σ_{VM} between 2 and 11% (left screws) and between 25 and 29% (right screws) were found. Since this patient had the largest pedicle among patients, models with screws with $D = 5.5$ mm were more sensitive to local changes in material properties. Generally, lower percentage differences in peak stress were found for the realistic screws compared to those obtained from simplified models. The percentage differences presented overall similar trends for the three patients. Also, the peak σ_{VM} in the screw was higher in realistic models compared to those with simplified screws. For a fixed length, the σ_{VM} increased for lower diameters; for a fixed diameter, the σ_{VM} decreased for longer screws. However, in some cases with realistic screws, this behavior was not observed probably due to differences in local

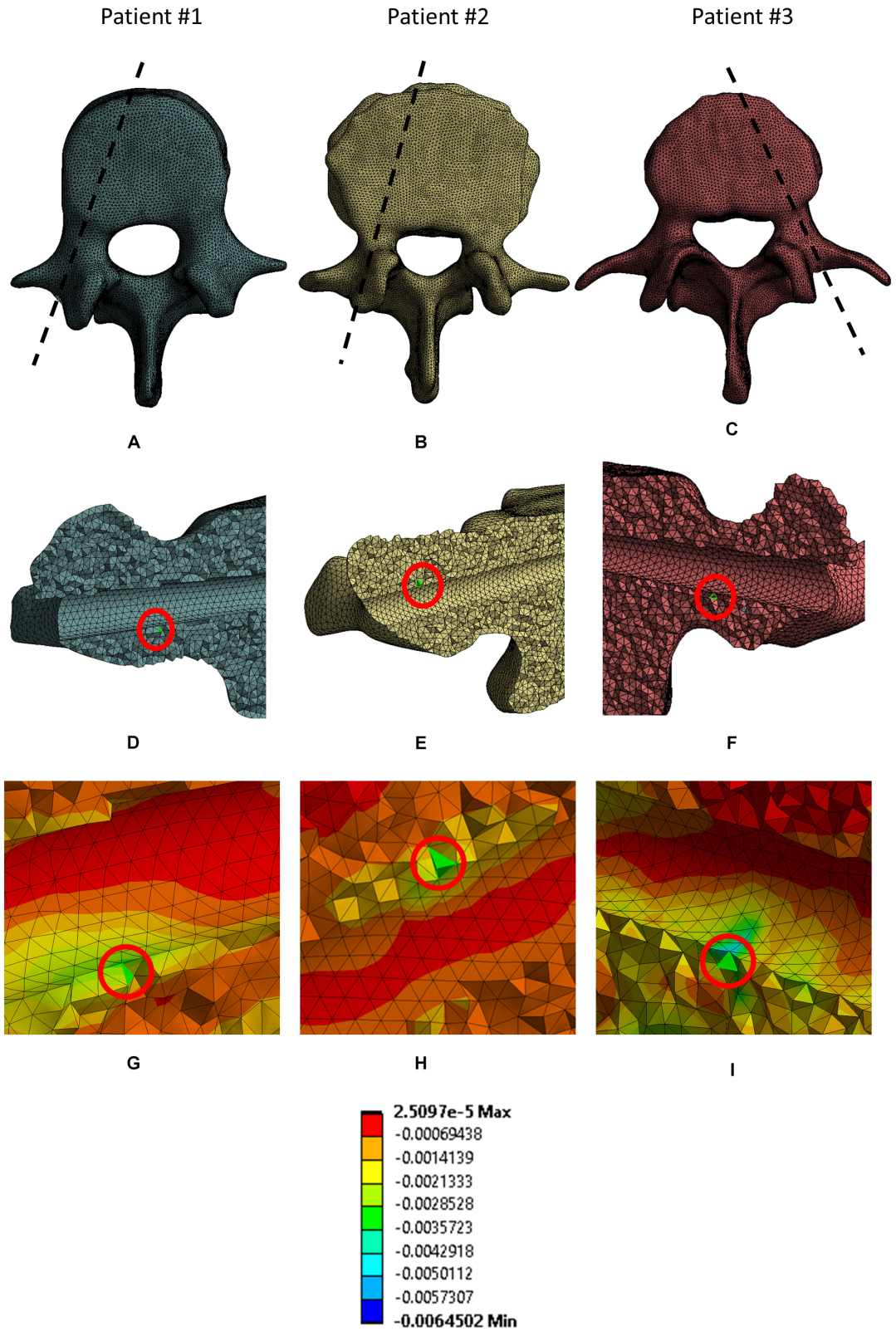

FIGURE 5 | Location of elements where peak ε_{p3} in the bone were. For each patient the following views are reported: the projection of the sagittal section corresponding to the location of the elements in a cranial view **(A–C)**; the location of the peak (red circle) in a sagittal section for each patient **(D–F)**; a magnified view of the mesh in the area corresponding to the selected peaks **(G–I)**.

TABLE 4 | Percentage difference in maximum total deflection of the head of the screw, for simplified and realistic models, reported as median value and minimum and maximum values with respect to the nominal condition ($D = 6.5$ mm and $L = 45$ mm) over the three patients.

Effect of screw size and shape: Δ_{rel} (%) in d_{max}

Model–side	Length	Diameter		
		7.5 mm	6.5 mm	5.5 mm
Simplified Left	40 mm	−10% (−9%, −10%)	4% (4%, −6%)	21% (18%, 24%)
	45 mm	−15% (−15%, −18%)	REF	18% (15%, 20%)
	50 mm	−19% (−19%, −23%)	−3% (−3%, −4%)	16% (13%, 17%)
Simplified Right	40 mm	−10% (−10%, −11%)	4% (4%, 5%)	20% (19%, 22%)
	45 mm	−16% (−15%, −17%)	REF	18% (17%, 19%)
	50 mm	−20% (−19%, −22%)	−3% (−2%, −3%)	16% (15%, 17%)
Realistic Left	40 mm	−8% (−8%, −9%)	5% (5%, 6%)	20% (18%, 23%)
	45 mm	−13% (−12%, 15%)	REF	17% (14%, 18%)
	50 mm	−16% (−15%, −18%)	−4% (−4%, −5%)	14% (11%, 14%)
Realistic Right	40 mm	−9% (−9%, −10%)	5% (4%, 6%)	21% (19%, 21%)
	45 mm	−13% (−13%, −14%)	REF	16% (15%, 17%)
	50 mm	−15% (−15%, −17%)	−4% (−3%, −4%)	13% (12%, 15%)

TABLE 5 | Percentage difference in peak Von Mises stress in the screws, for simplified and realistic models, reported with respect to the nominal condition ($D = 6.5$ mm and $L = 45$ mm) as median value and minimum and maximum values over the three patients.

Effect of screw size and shape: Δ_{rel} (%) of peak σ_{VM}

Model–side	Length	Diameter		
		7.5 mm	6.5 mm	5.5 mm
Simplified Left	40 mm	−10% (−8%, −13%)	1% (−4%, 4%)	15% (13%, 26%)
	45 mm	−13% (−10%, −13%)	REF	14% (2%, 19%)
	50 mm	−14% (−11%, −14%)	−1% (−1%, 0%)	9% (1%, 23%)
Simplified Right	40 mm	−12% (−9%, −14%)	0% (0%, 2%)	9% (6%, 37%)
	45 mm	−12% (−10%, −13%)	REF	10% (7%, 34%)
	50 mm	−14% (−14%, −16%)	−2% (−1%, −3%)	9% (5%, 35%)
Realistic Left	40 mm	−7% (−11%, 1%)	1% (−3%, 5%)	5% (−3%, 11%)
	45 mm	−7% (−10%, 1%)	REF	5% (0%, 7%)
	50 mm	−3% (−2%, −5%)	−4% (−2%, −4%)	3% (1%, 6%)
Realistic Right	40 mm	−4% (−9%, 0%)	3% (2%, 6%)	9% (5%, 27%)
	45 mm	−3% (−1%, −4%)	REF	5% (2%, 29%)
	50 mm	−3% (−3%, −6%)	−2% (−2%, −3%)	6% (4%, 25%)

mechanical properties of bone adjacent to screws among models with different screw sizes.

For both simplified and realistic models, the diameter affected the mean ε_{p3} more than the length (**Table 6** and **Figure 5**). In fact, changes in diameter resulted in median values of percentage changes in mean ε_{p3} between 30 and 47%, while changes in length resulted in median values of percentage changes in mean ε_{p3} between 10 and 22%. For both simplified and realistic models, similar percentage differences and trends were found between right and left screws. Generally, similar percentage differences in mean ε_{p3} were found for the models with realistic or simplified screws. Also, the mean ε_{p3} in simplified models were similar to those with realistic screws. The percentage differences presented overall similar trends for the three patients. For a fixed length, the mean ε_{p3} increased for lower diameters; for a fixed diameter, the mean ε_{p3} decreased for longer screws.

Comparison Between Simplified and Realistic Screw Geometry

If data were pooled for the different patients, sizes and sides, the d_{max} calculated for models with realistic or simplified screws correlated very well ($R^2 = 0.99$; Slope = 0.918, Intercept = 0.026 mm) (**Figure 6A**). A good correlation was also found between the peak σ_{VM} calculated from the realistic and simplified models ($R^2 = 0.82$) (**Figure 6B**). Nevertheless, the simplified models systematically underestimated the peak stress compared to the realistic ones (Slope = 1.2, Intercept ∼ 17 MPa).

The peak ε_{p3} was highly influenced by the combination of screw geometry (simplified vs. realistic) and the distribution of Young's modulus in the bone, whereas the distribution of values of ε_{p3} within a ROI around the screw was similar for simplified and realistic design of screws, with only a localized increase of strain for a few elements in the realistic screw models (**Figure 7**).

DISCUSSION

This study aimed to generate and verify a subject-specific CT-based FE model of the human vertebra implanted with two pedicle screws. The model was then used to evaluate the effect of the size and geometry of the pedicle screws on the mechanical properties of the screws-vertebra structure.

TABLE 6 | Percentage difference in mean Minimum principal strain in a ROI at the screw-vertebra interface, for simplified and realistic models, reported with respect to the nominal condition (D = 6.5 mm and L = 45 mm) as median value and minimum and maximum values over the three patients.

Effect of screw size and shape: Δ_{rel} (%) of mean ε_{p3}				
Model–side	**Length**	**Diameter**		
		7.5 mm	**6.5 mm**	**5.5 mm**
Simplified Left	40 mm	−11% (−10%, −14%)	8% (7%, 11%)	33% (22%, 37%)
	45 mm	−22% (−17%, −22%)	REF	25% (17%, 25%)
	50 mm	−26% (−25%, −31%)	−7% (−5%, −10%)	15% (10%, 18%)
Simplified Right	40 mm	−10% (−7%, −13%)	8% (7%, 12%)	31% (26%, 31%)
	45 mm	−19% (−18%, −19%)	REF	20% (18%, 23%)
	50 mm	−25% (−23%, −27%)	−6% (−4%, −8%)	12% (11%, 17%)
Realistic Left	40 mm	−11% (−7%, −11%)	9% (8%, 10%)	34% (26%, 34%)
	45 mm	−17% (−17%, −17%)	REF	24% (20%, 24%)
	50 mm	−24% (−22%, −25%)	−6% (−6%, −10%)	12% (10%, 18%)
Realistic Right	40 mm	−12% (−6%, −13%)	9% (4%, 11%)	30% (30%, 31%)
	45 mm	−17% (−17%, −18%)	REF	19% (18%, 21%)
	50 mm	−22% (−21%, −23%)	−7% (−7%, −10%)	8% (8%, 14%)

Element sizes of 0.6 mm in the screw and 1.0 mm in the bone were associated to a relative difference of approximately 5% for both simplified and realistic models. Similarly, Costa et al. (2019) reported that element size of 1 mm was required for CT-based subject specific heterogeneous FE models of healthy non-instrumented vertebrae loaded in compression. Widmer et al. (2020) reported the results from a validation study for CT-based subject specific heterogeneous animal (bovine and porcine) vertebrae with realistic pedicle screws. They opted for smaller element sizes at the level of the screw cavity compared to the bone farer from the implant resulting in about 230,000 tetrahedral elements in the bone and 10,000 shell elements in the screw; however, no mesh refinement study was reported. Bianco et al. (2019) compared the fixation strength of realistic pedicle screws with different dimensions, bone engagement and entry point preparation under axial and non-axial forces, and chose an element size in the bone of approximately 0.3 mm around the screw thread and 1 mm in regions farer from the implant obtaining differences in results under 8% with respect to the finest mesh. It should be noted that little details are usually reported in the literature about the choice of the mesh size in models to simulate the biomechanics of vertebrae implanted with pedicle screws. This is critical as "verification" is one of the important steps to give credibility to the models for the assessment of the efficacy of medical devices (ASME, 2020).

As expected, in this study percentage relative differences in peak σ_{VM} were higher in the realistic screws compared to the simplified ones. In fact, for the realistic screws different element sizes result in a more or a less accurate discretization of the thread features, which is not modeled in the simplified screw. It should be noted that the presence of the thread resulted in a 22–29% higher peak σ_{VM} in realistic models compared to simplified ones for the baseline configuration ($D = 6.5$ mm, $L = 45$ mm). This was due to the fact that areas of concentration of stress occurred close to the thread, which may play a larger role compared to the diameter of the screw. However, the σ_{VM} distribution over the screws was similar among the different mesh sizes for both realistic and simplified models, showing that the stress pattern is not much influenced by the element size.

The diameter of the screw had higher impact on the maximum displacement, on the peak σ_{VM} in the screws and on the mean ε_{p3} in the bone than the length of the screw. This shows that

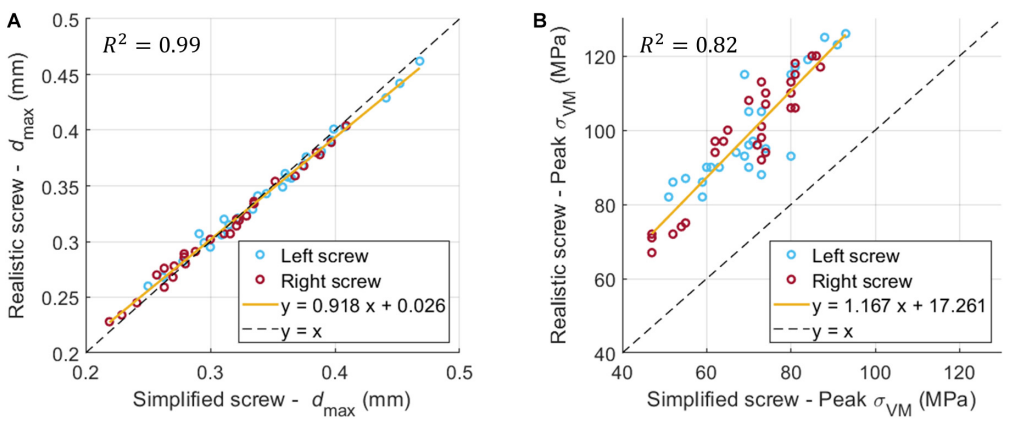

FIGURE 6 | Linear correlation between d_{max} **(A)** and σ_{VM} **(B)** for the realistic and simplified models (data pooled for the three patients, two sides, nine sizes).

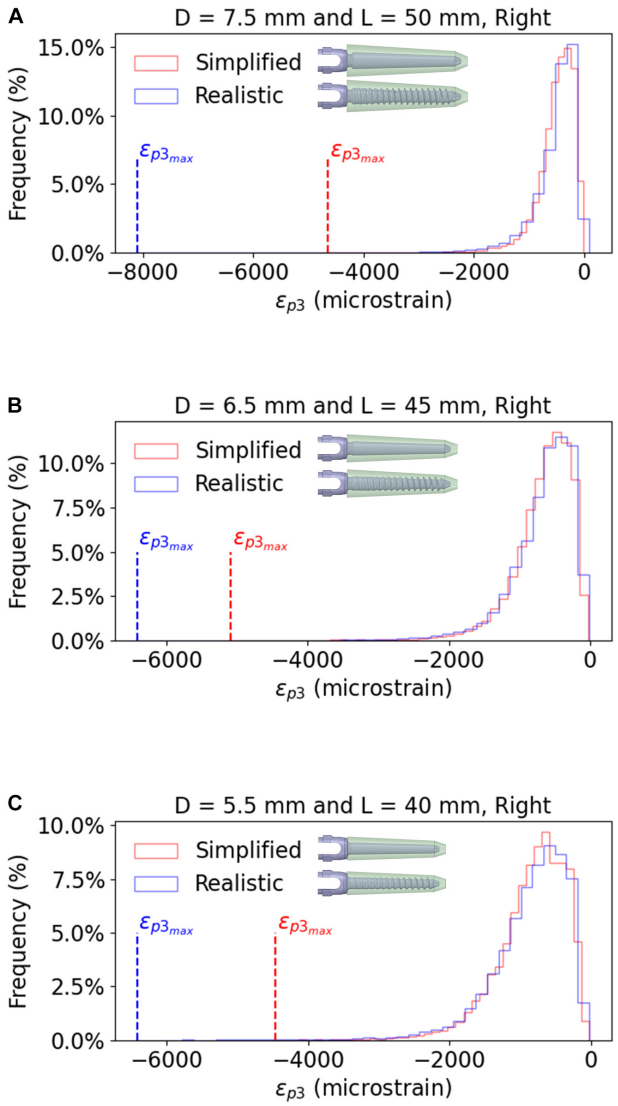

FIGURE 7 | Frequency plots for the values of ε_{p3} within a bone ROI around the right screw, for realistic and simplified models. The data are reported for the largest screw size **(A)**, the optimal screw size **(B)** and the smallest screw size **(C)**, evaluated for Patient #2. Similar trends were observed for the other patients and the left screws.

for mono-cortical screws the anchorage in the pedicle, which mainly consists of cortical bone, is more important compared to the anchorage within the vertebral body, which is mainly composed of trabecular bone. Therefore, finding the compromise between the largest diameter of the screws by avoiding iatrogenic fractures is crucial to provide a good anchorage on the cortical bone, which results in lower micromotions at the screw-vertebra interface and better distribution of stress, thus preventing post-operative complications. Our results are in line with most experimental and numerical studies in the literature, that showed the predominant effect of the diameter of the screws compared to their length (Zindrick et al., 1986; Chen et al., 2003; Cho et al., 2010; Matsukawa et al., 2016, 2020; Bianco et al., 2019; Biswas et al., 2019). Matsukawa et al. (2016) evaluated the effect of different screw sizes on fixation with a cortical bone trajectory, where screws are inserted pointing laterally in the transverse plane during superior screw angulation in the sagittal plane, and anchor only on cortical bone in the pedicle without the contribution of trabecular bone in the vertebral body (Santoni et al., 2009), by using an FE model including bone heterogeneities and realistic screw design. They found that some mechanical properties of the vertebra-screws construct were not significantly affected by increasing the diameter of screws. Even if our results for the impact of the diameter of the realistic screw seem to disagree with those by Matsukawa et al. (2016), this should be taken with caution as these differences may be due to different modeling techniques and different mechanical metrics used to evaluate the effect of the size of the screw. Matsukawa et al. (2020) investigated the effect of screw size on fixation in osteoporotic vertebrae by FE analysis. Their results showed that by increasing the diameter and the length of screws, the pullout strength and vertebral fixation strength increased; they also showed that the screw diameter had a more important effect than screw length on the vertebral fixation strength, similarly to the results of the present study. However, the modeling approach and boundary conditions of the two studies are substantially different so both outcomes are complementary.

Overall, the predictions of the simplified models correlated well with the predictions from the realistic ones, especially for the global structural properties (d_{max}). This finding suggests that geometrical differences between the two designs of screws and local differences of material properties around the screw between the two models do not influence the overall stiffness of the model. Inzana et al. (2016) modeled a homogeneous cylindrical block of trabecular or cortical bone and compared a simplified cylindrical screw with a bonded interface and a realistic threaded screw with frictional contact with a pseudo-threaded screw with calibrated contact conditions. They found that the simplified model underestimated (70% difference, averaged value extracted from **Figure 4** in that study) the displacement of the screw head with respect to the realistic case. They have also reported a similar overestimation of the global stiffness from the analysis of a model for the fixation of a proximal humerus fracture. In this study, it was found that the maximum deflection of the screw head was slightly higher in the simplified case, but a bonded interface was considered for both simplified and realistic models. The different results could be due to differences in material models, interfaces, geometries and applications between the two studies. Moreover, in this study the simplified models underestimated the peak σ_{VM}, due to the lack of stress raisers considered in the realistic design. These differences could also be amplified by local heterogeneity in the Elastic modulus of bone elements. In fact, the distribution of Young's modulus in the bone had a strong influence on the peak ε_{p3}, whereas the distribution of strain around the screw-bone interface was similar for simplified and realistic models. This finding highlights the importance of the choice of modeling the screw's geometry realistically or to use a simplified model depending on the application.

There are some limitations in this study. First, it is important to note that before this computational model can be used in the clinical setting, additional to the verification and sensitivity analysis of the model, a direct validation of this approach should be made with respect to measurements from *ex vivo* experiments. This study is the first step in the identification of the best approach to optimize the virtual assessment of pedicle fixation by accounting for realistic vertebral geometry and density distributions and by modeling the screw with a realistic or simplified geometry. Validation of the model against advanced time-lapsed mechanical testing, micro-CT imaging and digital volume correlation approaches (Dall'Ara et al., 2017) to measure the strain distribution in the bone tissue will follow in future studies. The screw-bone interface was modeled as perfect bonding. While this choice may lead to less realistic stress and strain patterns in the screw and in the bone, it simplifies the comparison between the models with realistic and simplified screws. Moreover, only the most inferior vertebra of a short-segment pedicle screw construct was modeled, excluding from the analysis the other features of the implanted spine unit. This choice was considered acceptable for this study that focused on vertical loads perpendicular to the axis of the screws. Nevertheless, in order to evaluate the effect of the screw size in physiological conditions, more complex geometry should be modeled. The insertion points of pedicle screws, as well as the orientation of the screw axes in the sagittal and transverse planes are important factors that influence the stress distribution on the screws and the bone. These two parameters should be considered in future parametric studies.

Finally, the effect of the size of the screw has been evaluated with nine discrete configurations instead of analyzing the possible range of parameters continuously with statistical methods. While this choice was driven by the configurations of screw size available in the market, a more general approach could have highlighted optimal combinations of diameter and length for the specific patients. In fact, the simplified design of the screw would allow to implement more easily a parametric model, and mesh morphing techniques could be applied to update the nodal positions to accommodate shape variations (Biancolini, 2017). This approach combined with reduced order modeling techniques could be used to accelerate the workflow and test several combinations of geometrical properties of the screw for a population of patients and to expand to non-linear analyses.

In conclusion, this study highlights the influence of size and geometry of screws on the biomechanics of a vertebra with two pedicle screws. In particular, the diameter of the screw should be optimized for each patient as it has a large impact on the stress in the screw. Moreover, modeling the screw with simplified geometry systematically underestimate the peak stress and should therefore be accounted for when interpreting the results from the FE analyses.

DATA AVAILABILITY STATEMENT

The raw data supporting the conclusions of this article will be made available by the authors by contacting the corresponding author. Results and example of the models are available at: https://bit.ly/37JflPc.

AUTHOR CONTRIBUTIONS

MS, TV, MR, and ED: research design. TV, CS, and TG: acquisition of data. MS and ED: analysis and interpretation of data. All authors drafted the manuscript and revised it critically, reviewed and agreed upon the final version of the manuscript.

FUNDING

This project was partially funded by the European Union's Horizon 2020 Research and Innovation Programme under the Marie Skłodowska-Curie grant agreement Spinner No. 766012, and by the Engineering and Physical Sciences Research Council (EPSRC) Frontier Multisim Grant (EP/K03877X/1 and EP/S032940/1).

ACKNOWLEDGMENTS

We gratefully acknowledge Dr. Abdollah Yassine Moufid for the help with the acquisition of data.

REFERENCES

Abbeele, M. V., den Valiadis, J.-M., Lima, L. V. P. C., Khalifé, P., Rouch, P., and Skalli, W. (2018). Contribution to FE modeling for intraoperative pedicle screw strength prediction. *Comput. Methods Biomech. Biomed. Eng.* 21, 13–21. doi: 10.1080/10255842.2017.1414200

ASME (2020). *Assessing Credibility of Computational Modeling through Verification and Validation: Application to Medical Devices – ASME*. Available online at: https://www.asme.org/codes-standards/find-codes-standards/v-v-40-assessing-credibility-computational-modeling-verification-validation-application-medical-devices (accessed October 26, 2020).

Bianco, R.-J., Arnoux, P.-J., Mac-Thiong, J.-M., and Aubin, C.-E. (2019). Thoracic pedicle screw fixation under axial and perpendicular loadings: a comprehensive numerical analysis. *Clin. Biomech.* 68, 190–196. doi: 10.1016/j.clinbiomech.2019.06.010

Bianco, R.-J., Arnoux, P.-J., Wagnac, E., Mac-Thiong, J.-M., and Aubin, C. -É (2017). Minimizing pedicle screw pullout risks: a detailed biomechanical analysis of screw design and placement. *Clin. Spine Surg.* 30, E226–E232. doi: 10.1097/BSD.0000000000000151

Biancolini, M. E. (2017). "RBF mesh morphing," in *Fast Radial Basis Functions for Engineering Applications*, ed. M. E. Biancolini (Cham: Springer International Publishing), 93–117. doi: 10.1007/978-3-319-75011-8_6

Biswas, J. K., Sahu, T. P., Rana, M., Roy, S., Karmakar, S. K., Majumder, S., et al. (2019). Design factors of lumbar pedicle screws under bending load: a finite element analysis. *Biocybern. Biomed. Eng.* 39, 52–62. doi: 10.1016/j.bbe.2018.10.003

Bredow, J., Boese, C. K., Werner, C. M. L., Siewe, J., Löhrer, L., Zarghooni, K., et al. (2016). Predictive validity of preoperative CT scans and the risk of pedicle screw loosening in spinal surgery. *Arch. Orthop. Trauma Surg.* 136, 1063–1067. doi: 10.1007/s00402-016-2487-8

Campbell, J. Q., and Petrella, A. J. (2016). Automated finite element modeling of the lumbar spine: using a statistical shape model to generate a virtual population of models. *J. Biomech.* 49, 2593–2599. doi: 10.1016/j.jbiomech.2016.05.013

Chen, S.-I., Lin, R.-M., and Chang, C.-H. (2003). Biomechanical investigation of pedicle screw–vertebrae complex: a finite element approach using bonded and contact interface conditions. *Med. Eng. Phys.* 25, 275–282. doi: 10.1016/S1350-4533(02)00219-9

Chevalier, Y., Matsuura, M., Krüger, S., Fleege, C., Rickert, M., Rauschmann, M., et al. (2018). Micro-CT and micro-FE analysis of pedicle screw fixation under different loading conditions. *J. Biomech.* 70, 204–211. doi: 10.1016/j.jbiomech.2017.12.023

Cho, W., Cho, S. K., and Wu, C. (2010). The biomechanics of pedicle screw-based instrumentation. *J. Bone Joint Surg. Br.* 92, 1061–1065. doi: 10.1302/0301-620X.92B8.24237

Costa, M. C., Eltes, P., Lazary, A., Varga, P. P., Viceconti, M., and Dall'Ara, E. (2019). Biomechanical assessment of vertebrae with lytic metastases with subject-specific finite element models. *J. Mech. Behav. Biomed. Mater.* 98, 268–290. doi: 10.1016/j.jmbbm.2019.06.027

Dall'Ara, E., Peña-Fernández, M., Palanca, M., Giorgi, M., Cristofolini, L., and Tozzi, G. (2017). Precision of digital volume correlation approaches for strain analysis in bone imaged with micro-computed tomography at different dimensional levels. *Front. Mater.* 4:31. doi: 10.3389/fmats.2017.00031

Elmasry, S., Asfour, S., and Travascio, F. (2017). Effectiveness of pedicle screw inclusion at the fracture level in short-segment fixation constructs for the treatment of thoracolumbar burst fractures: a computational biomechanics analysis. *Comput. Methods Biomech. Biomed. Engin.* 20, 1412–1420. doi: 10.1080/10255842.2017.1366995

Fedorov, A., Beichel, R., Kalpathy-Cramer, J., Finet, J., Fillion-Robin, J.-C., Pujol, S., et al. (2012). 3D Slicer as an image computing platform for the Quantitative Imaging Network. *Magn. Reson. Imaging* 30, 1323–1341. doi: 10.1016/j.mri.2012.05.001

Fior Markets (2020). *Global Pedicle Screw System Market by Product, Surgery Type, Indication, Application, Region, Industry Analysis, Size, Share, Growth, Trends, and Forecast 2018 to 2025 – Fior Markets*. Available online at: https://www.fiormarkets.com/report/global-pedicle-screw-system-market-by-product-polyaxial-375967.html (accessed October 26, 2020).

Gertzbein, S. D., and Robbins, S. E. (1990). Accuracy of pedicular screw placement in vivo. *Spine* 15, 11–14.

Li, C., Zhou, Y., Wang, H., Liu, J., and Xiang, L. (2014). Treatment of unstable thoracolumbar fractures through short segment pedicle screw fixation techniques using pedicle fixation at the level of the fracture: a finite element analysis. *PLoS One* 9:e99156. doi: 10.1371/journal.pone.0099156

Matsukawa, K., Yato, Y., and Imabayashi, H. (2020). Impact of screw diameter and length on pedicle screw fixation strength in osteoporotic vertebrae: a finite element analysis. *Asian Spine J.* doi: 10.31616/asj.2020.0353 [Epub ahead of print].

Matsukawa, K., Yato, Y., Imabayashi, H., Hosogane, N., Abe, Y., Asazuma, T., et al. (2016). Biomechanical evaluation of fixation strength among different sizes of pedicle screws using the cortical bone trajectory: what is the ideal screw size for optimal fixation? *Acta Neurochir. (Wien)* 158, 465–471. doi: 10.1007/s00701-016-2705-8

Molinari, L., Falcinelli, C., Gizzi, A., and Di Martino, A. (2021). Effect of pedicle screw angles on the fracture risk of the human vertebra: a patient-specific computational model. *J. Mech. Behav. Biomed. Mater.* 116:104359. doi: 10.1016/j.jmbbm.2021.104359

Morgan, E. F., Bayraktar, H. H., and Keaveny, T. M. (2003). Trabecular bone modulus–density relationships depend on anatomic site. *J. Biomech.* 36, 897–904. doi: 10.1016/S0021-9290(03)00071-X

Newcomb, A. G. U. S., Baek, S., Kelly, B. P., and Crawford, N. R. (2017). Effect of screw position on load transfer in lumbar pedicle screws: a non-idealized finite element analysis. *Comput. Methods Biomech. Biomed. Engin.* 20, 182–192. doi: 10.1080/10255842.2016.1209187

Niinomi, M., and Boehlert, C. J. (2015). "Titanium alloys for biomedical applications," in *Advances in Metallic Biomaterials: Tissues, Materials and Biological Reactions*. Springer Series in Biomaterials Science and Engineering, eds M. Niinomi, T. Narushima, and M. Nakai (Berlin: Springer), 179–213. doi: 10.1007/978-3-662-46836-4_8

Prud'homme, M., Barrios, C., Rouch, P., Charles, Y. P., Steib, J.-P., and Skalli, W. (2015). Clinical outcomes and complications after pedicle-anchored dynamic or hybrid lumbar Spine stabilization: a systematic literature review. *J. Spinal Disord. Tech.* 28, E439–E448. doi: 10.1097/BSD.0000000000000092

Qi, W., Yan, Y., Zhang, Y., Lei, W., Wang, P., and Hou, J. (2011). Study of stress distribution in pedicle screws along a continuum of diameters: a three−dimensional finite element analysis. *Orthop. Surg.* 3, 57–63. doi: 10.1111/j.1757-7861.2010.00112.x

Rajaee, S. S., Bae, H. W., Kanim, L. E. A., and Delamarter, R. B. (2012). Spinal fusion in the United States: analysis of trends from 1998 to 2008. *Spine* 37, 67–76. doi: 10.1097/BRS.0b013e31820ccfb

Rohlmann, A., Bergmann, G., and Graichen, F. (1997). Loads on an internal spinal fixation device during walking. *J. Biomech.* 30, 41–47. doi: 10.1016/S0021-9290(96)00103-0

Santoni, B. G., Hynes, R. A., McGilvray, K. C., Rodriguez-Canessa, G., Lyons, A. S., Henson, M. A. W., et al. (2009). Cortical bone trajectory for lumbar pedicle screws. *Spine J.* 9, 366–373. doi: 10.1016/j.spinee.2008.07.008

Schileo, E., Dall'Ara, E., Taddei, F., Malandrino, A., Schotkamp, T., Baleani, M., et al. (2008). An accurate estimation of bone density improves the accuracy of subject-specific finite element models. *J. Biomech.* 41, 2483–2491. doi: 10.1016/j.jbiomech.2008.05.017

Su, Y., Wang, X., Ren, D., Liu, Y., Liu, S., and Wang, P. (2018). A finite element study on posterior short segment fixation combined with unilateral fixation using pedicle screws for stable thoracolumbar fracture. *Medicine (Baltimore)* 97:e12046. doi: 10.1097/MD.0000000000012046

Taddei, F., Schileo, E., Helgason, B., Cristofolini, L., and Viceconti, M. (2007). The material mapping strategy influences the accuracy of CT-based finite element models of bones: an evaluation against experimental measurements. *Med. Eng. Phys.* 29, 973–979. doi: 10.1016/j.medengphy.2006.10.014

Verma, K., Boniello, A., and Rihn, J. (2016). Emerging techniques for posterior fixation of the lumbar Spine. *J. Am. Acad. Orthop. Surg.* 24, 357–364. doi: 10.5435/JAAOS-D-14-00378

Wang, W., Pei, B., Pei, Y., Shi, Z., Kong, C., Wu, X., et al. (2019). Biomechanical effects of posterior pedicle fixation techniques on the adjacent segment for the treatment of thoracolumbar burst fractures: a biomechanical analysis. *Comput. Methods Biomech. Biomed. Engin.* 22, 1083–1092. doi: 10.1080/10255842.2019.1631286

Widmer, J., Fasser, M.-R., Croci, E., Spirig, J., Snedeker, J. G., and Farshad, M. (2020). Individualized prediction of pedicle screw fixation strength with a finite element model. *Comput. Methods Biomech. Biomed. Engin.* 23, 155–167. doi: 10.1080/10255842.2019.1709173

Wirtz, D. C., Schiffers, N., Pandorf, T., Radermacher, K., Weichert, D., and Forst, R. (2000). Critical evaluation of known bone material properties to realize anisotropic FE-simulation of the proximal femur. *J. Biomech.* 33, 1325–1330. doi: 10.1016/S0021-9290(00)00069-5

Zindrick, M. R., Wiltse, L. L., Widell, E. H., Thomas, J. C., Holland, W. R., Field, B. T., et al. (1986). A biomechanical study of intrapeduncular screw fixation in the lumbosacral spine. *Clin. Orthop. Relat. Res.* 203, 99–112.

Conflict of Interest: MS and MR were employed by company Ansys (France). CS and TG were employed by company Aesculap (Germany).

The remaining authors declare that the research was conducted in the absence of any commercial or financial relationships that could be construed as a potential conflict of interest.

frontiers in Bioengineering and Biotechnology

ORIGINAL RESEARCH
published: 19 May 2021
doi: 10.3389/fbioe.2021.661837

Maintaining Bone Health in the Lumbar Spine: Routine Activities Alone Are Not Enough

Clément D. Favier[1*†], *Alison H. McGregor*[2†] *and Andrew T. M. Phillips*[1*†]

[1] Structural Biomechanics, Department of Civil and Environmental Engineering, Imperial College London, London, United Kingdom, [2] Musculoskeletal Lab, Department of Surgery and Cancer, Imperial College London, London, United Kingdom

OPEN ACCESS

Edited by:
Enrico Dall'Ara,
The University of Sheffield,
United Kingdom

Reviewed by:
Ginu Unnikrishnan,
Intelligent Automation, United States
Ridha Hambli,
Polytech Orléans, France
Jan S. Kirschke,
Technical University of Munich,
Germany

***Correspondence:**
Clément D. Favier
clement.favier13@imperial.ac.uk
Andrew T. M. Phillips
andrew.phillips@imperial.ac.uk

†ORCID:
Clément D. Favier
orcid.org/0000-0003-2354-461X
Alison H. McGregor
orcid.org/0000-0003-4672-332X
Andrew T. M. Phillips
orcid.org/0000-0001-6618-0145

Specialty section:
This article was submitted to Biomechanics, a section of the journal Frontiers in Bioengineering and Biotechnology

Received: 31 January 2021
Accepted: 14 April 2021
Published: 19 May 2021

Citation:
Favier CD, McGregor AH and Phillips ATM (2021) Maintaining Bone Health in the Lumbar Spine: Routine Activities Alone Are Not Enough. Front. Bioeng. Biotechnol. 9:661837. doi: 10.3389/fbioe.2021.661837

Public health organisations typically recommend a minimum amount of moderate intensity activities such as walking or cycling for two and a half hours a week, combined with some more demanding physical activity on at least 2 days a week to maintain a healthy musculoskeletal condition. For populations at risk of bone loss in the lumbar spine, these guidelines are particularly relevant. However, an understanding of how these different activities are influential in maintaining vertebral bone health is lacking. A predictive structural finite element modelling approach using a strain-driven algorithm was developed to study mechanical stimulus and bone adaptation in the lumbar spine under various physiological loading conditions. These loading conditions were obtained with a previously developed full-body musculoskeletal model for a range of daily living activities representative of a healthy lifestyle. Activities of interest for the simulations include moderate intensity activities involving limited spine movements in all directions such as, walking, stair ascent and descent, sitting down and standing up, and more demanding activities with large spine movements during reaching and lifting tasks. For a combination of moderate and more demanding activities, the finite element model predicted a trabecular and cortical bone architecture representative of a healthy vertebra. When more demanding activities were removed from the simulations, areas at risk of bone degradation were observed at all lumbar levels in the anterior part of the vertebral body, the transverse processes and the spinous process. Moderate intensity activities alone were found to be insufficient in providing a mechanical stimulus to prevent bone degradation. More demanding physical activities are essential to maintain bone health in the lumbar spine.

Keywords: lumbar vertebra, bone adaptation, structural finite element analysis, predictive modelling, strain-driven optimisation, sedentary behaviour

1. INTRODUCTION

Bone health relates to its capacity to resist the loads applied to it. It is widely accepted that bone adapts its structure, effectively the thickness of the cortex and the orientation and size of the trabeculae, to withstand the mechanical loads it is subjected to. Bone apposition occurs when the structure is over stimulated, while bone resorption is observed when bone is under stimulated. This process is called bone remodelling, and was theorised by Frost (1987, 2003) as the Mechanostat

principle. Following this principle, sedentary behaviours and low physical activity levels may be considered as a cause of osteoporosis (Lau and Guo, 2011), and exercise is usually recommended for the management of this condition (Nelson et al., 2007; Sinaki et al., 2010; Rossini et al., 2016; Benedetti et al., 2018). Public health organisations typically recommend a combination of daily moderate intensity activities and regular more demanding physical activities to maintain musculoskeletal health (Davies et al., 2019). While these guidelines are generally promoted for an aging population, they are also pertinent for a younger population who may be sedentary due to home confinement as a consequence of the current COVID-19 pandemic (Narici et al., 2020). Moderate intensity activities usually refer to walking or cycling for a minimum of 20 min everyday. More demanding physical activities such as heavy gardening, carrying heavy shopping or resistance exercise, involving the major muscle groups, should be practised at least twice a week. To maintain a healthy musculoskeletal system, lifting, and carrying activities recruiting the erector spinae and the abdominal muscles are deemed to be of importance. It is intuitive to understand how activities recruiting specific muscle groups will help maintaining muscular health. However, this is less obvious with skeletal health and an understanding of how these activities can be influential in maintaining lumbar spine bone health is lacking.

Finite element modelling is a computational method that can be used to predict bone architecture under particular loading conditions if coupled with an optimisation algorithm. Applied to the lumbar spine, this modelling approach can provide the necessary information to understand which activities stimulate particular regions of lumbar vertebrae, essential for maintaining lumbar spine bone health. Detailed models of the complete lumbar spine have been developed with accurate geometry derived from CT images (Little et al., 2008; Ayturk and Puttlitz, 2011; Park et al., 2013), although these do not propose any prediction of bone remodelling to its mechanical loading environment. Many finite element models with varying levels of complexity have been developed to study bone remodelling. A common phenomenological approach consists in adapting bone toward a homeostatic state of strain, strain energy, or stress (Tsubota et al., 2003; Adachi et al., 2010; Homminga et al., 2012; Badilatti et al., 2015; van Rijsbergen et al., 2018). Other models use a mechanistic approach combining mechanical and metabolic factors in the adaptation algorithm (Huiskes et al., 2000; Taylor et al., 2004). Modelling of interstitial fluid flow has also been investigated (Tsubota et al., 2009; Hambli and Kourta, 2015; Tiwari et al., 2018). However, few of these predictive models consider a representation of the lumbar vertebrae using a realistic geometry. Macroscale continuum models developed by Homminga et al. (2012) and van Rijsbergen et al. (2018) both predict bone remodelling of the lumbar spine in an altered mechanical environment using isotropic bone material properties and a strain energy density driven optimisation. Although this approach allows for the study of bone stiffness adaptation, isotropic material properties in a continuum model cannot capture the directionality of trabeculae. Microscale continuum models developed by Tsubota et al. (2003) and Badilatti et al. (2015) are able to capture the remodelling of individual trabeculae in an entire vertebra under a particular loading condition. However, the model developed by Badilatti et al. (2015) is based on high resolution μCT images which are ethically complicated to obtain on healthy volunteers due to radiation exposure and long acquisition times. Tsubota et al. (2003) limited their study to a simplified geometry by creating an axisymmetric model based on a cross-sectional photograph of a vertebral body available in the literature (Mosekilde, 1990). Both studies applied simplified loading on the vertebral bodies of their models, which is not representative of the range of recommended physical activities. Despite the simplified loading conditions these models were still computationally demanding due to the number of continuum elements needed to represent bone at microscale.

To avoid these limitations and understand the influence of mechanical loading from a range of physical activities on the vertebral architecture, a modelling framework originally developed for the femur (Phillips, 2012; Phillips et al., 2015) and pelvis (Zaharie and Phillips, 2018, 2019) has been adapted to study the five lumbar vertebrae. It combines a subject-specific musculoskeletal model which provides realistic loading conditions with predictive structural finite element modelling based on the same subject for increased consistency. The structural finite element approach is a computationally efficient alternative to microscale continuum modelling of bones (Pothuaud et al., 2004; van Lenthe et al., 2006; Phillips, 2012; Zaharie and Phillips, 2019). It uses idealised elements (shells and trusses) to model the structure of the bone, allowing modelling of the vertebrae at mesoscale, where structural finite elements can be larger than the individual trabeculae but still capture the trajectories of the trabeculae and the overall bone architecture.

2. MATERIALS AND METHODS

For each of the five lumbar vertebrae, the mesoscale structural model is obtained through iterative adaptation of a base finite element model subject to a loading envelope derived from musculoskeletal simulations of a range of physical activities representative of a healthy lifestyle. **Figure 1** illustrates the modelling framework.

2.1. Musculoskeletal Modelling

The load cases applied to the finite element model were obtained with a previously validated subject-specific musculoskeletal model of the lumbar spine and lower limbs (Favier et al., 2021). This musculoskeletal model is based on full-body high-resolution MRI scans of a healthy volunteer (26 yo, 175 *cm*, 67.8 *kg*) with no history of spine pathologies. It was developed in OpenSim 3.3 (Delp et al., 2007) and is available to download at https://simtk.org/projects/llsm/. Full-body motion capture data were collected with the same healthy volunteer for eighteen activities following a previously developed protocol (Favier et al., 2021). The study was granted ethical approval by the NHS Health Research Authority (REC reference: 17/HRA/0465) and the Imperial College Research Ethics Committee (ICREC reference: 17IC3811), and the volunteer gave written informed consent. Recorded activities include six static positions of the

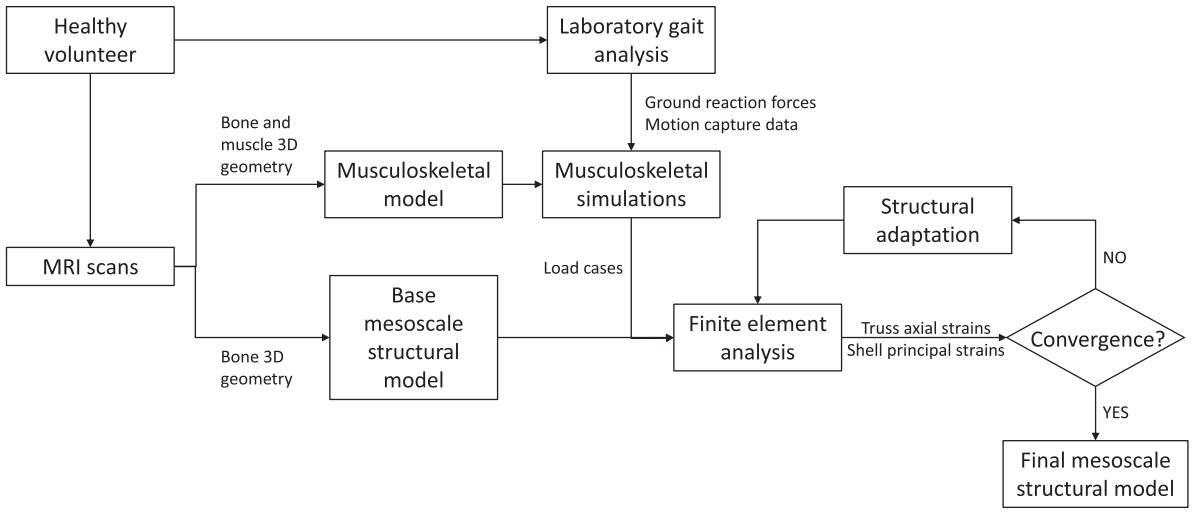

FIGURE 1 | Modelling framework.

spine (flexion at 20°, extension at 15°, lateral bending at 20° on both sides and axial rotation at 15° on both sides), five activities related to locomotion (level walking, stair ascent, stair descent, sit-to-stand, and stand-to-sit) and seven more demanding activities involving spine movements while sitting (maximum flexion, twisting, and lifting a box from floor to table (from both sides)) and standing (maximum flexion, lifting a box from floor to chest, twisting, and lifting a box from floor to floor (on both sides)). Musculoskeletal simulations were performed in OpenSim 3.3. An inverse kinematics approach was used to obtain joint angles for each of the recorded activities. Muscle forces were estimated using static optimisation where the sum of muscle activations squared was minimised for each frame of the kinematics. Joint reaction forces were also calculated at each lumbar joint using the JointReaction analysis tool available in OpenSim (Steele et al., 2012).

2.2. Finite Element Modelling

2.2.1. Structural Finite Element Base Model

Base models of the five lumbar vertebrae were created from the MRI scans of the same healthy volunteer recruited to develop the musculoskeletal model (Favier et al., 2021). These base structural models were generated using the same approach as described in Phillips (2012), Phillips et al. (2015), and Zaharie and Phillips (2018) and summarized here. The bone geometries were segmented in Mimics (Mimics Research 19.0, Materialise NV, Leuven, Belgium), reconstructed and exported as STL files following the protocol described in Favier et al. (2021). The STL files were then imported in 3-matic (3-matic Research 11.0, Materialise NV, Leuven, Belgium) where the coordinate systems of the vertebrae were adjusted to match the joint definitions used in the musculoskeletal model. The 3-matic meshing tools were used to create volumetric meshes of the vertebrae composed of four-noded tetrahedral elements with a 3 *mm* average edge length. These volumetric meshes were adapted to create structural meshes (**Figure 2A**) using MATLAB (The MathWorks, Inc., USA). Cortical bone was modelled with three-noded linear triangular shell elements defined by the nodes and element faces of the tetrahedral elements located on the external surface of the volumetric mesh. These shell elements were arbitrarily assigned an initial thickness of 0.1 *mm* in the base models. The internal nodes were used to create a network of two-noded truss elements representative of trabecular bone. Each node was linked to its closest sixteen neighbours. These truss elements were arbitrarily assigned an initial radius of 0.1 *mm* in the base models. The average element length of 3 *mm* and minimum nodal connectivity of 16 are considered to provide a sufficient mesh refinement and range of element directionalities to enable specific trabecular trajectories to develop during bone adaptation (Villette, 2016). All shell and truss elements were assigned linear isotropic material properties representative of bone material at the tissue level, with a Young's modulus of 18.0 *GPa* and a Poisson's ratio of 0.3 (Turner et al., 1999).

2.2.2. Loading Conditions

Loading conditions include joint reaction forces and muscle forces estimated with the musculoskeletal model, as well as inertial loads experienced during movements.

2.2.2.1. Joint Reaction Forces

For each lumbar vertebra, joint reaction forces calculated at the superior and inferior joint centres in OpenSim were transferred to the vertebral endplate areas with constructs called "load applicators" (**Figure 2A**). These applicators spread the point load calculated with the musculoskeletal model over the corresponding bone surface, performing a similar role to the intervertebral discs. The load applicators are composed of four layers of six-noded linear continuum wedge elements. To build

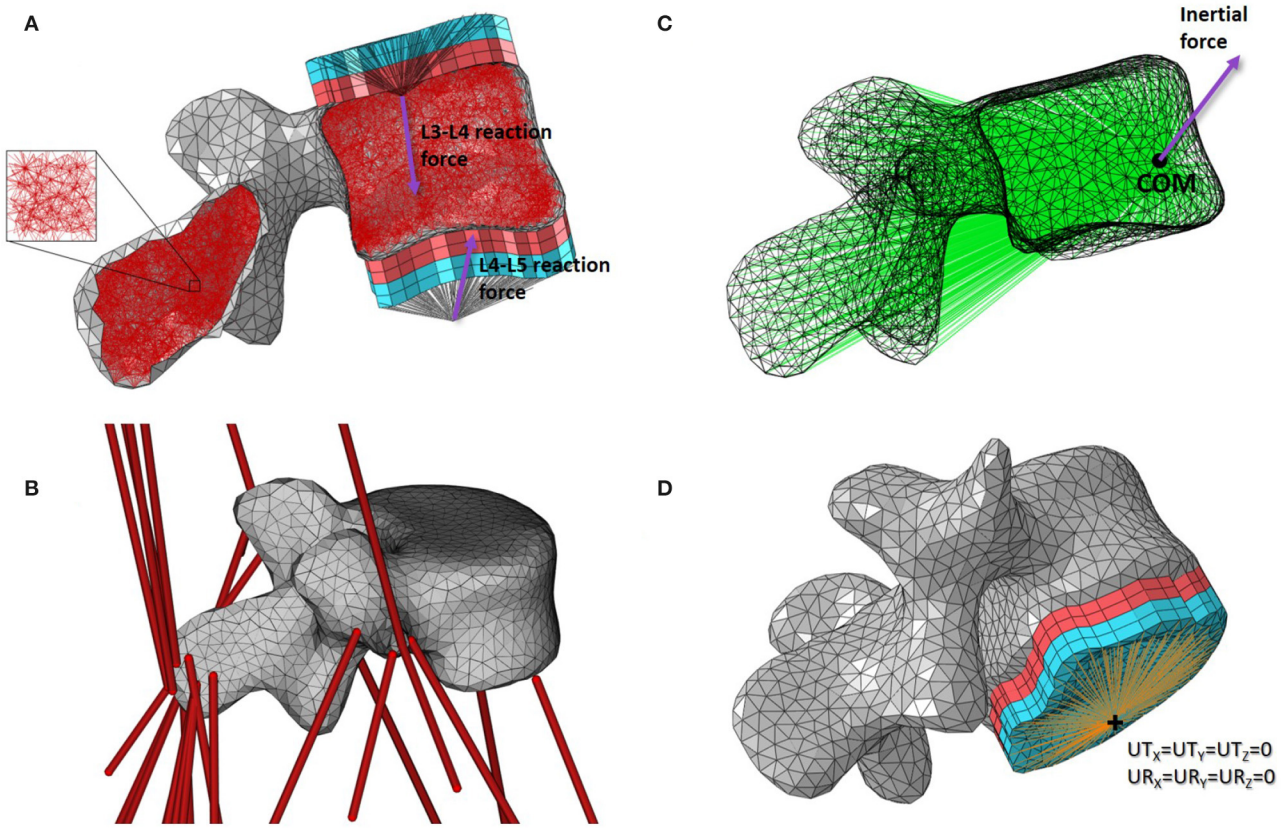

FIGURE 2 | Base mesoscale structural model of L4. **(A)** Side cut with load applicators. **(B)** 3D view with musculotendon actuators from the musculoskeletal model. **(C)** Side view with inertial load applicator. **(D)** 3D view with boundary condition. Cortical shell elements are shown in grey and trabecular truss elements in dark red. Wedge elements of the softer layers of the load applicators are shown in light red while the stiffer layers elements are in light blue. Truss elements connecting the nodes on the external layers of the load applicators to the joint centres where the joint reaction force is applied are shown in black. Truss elements of the inertia applicator connecting the nodes of the cortical elements to the centre of mass (COM) of the lumbar segment where the inertial force is applied are shown in green. Beam elements connecting the nodes on the external layer of the load applicator to the duplicate node at the joint centre for the boundary condition are shown in orange.

each layer, surface nodes corresponding to the vertebral endplates were projected four times with a distance of 2 *mm* outward and orthogonally to the average endplate plane. Nodes of the vertebral endplate areas are shared between the load applicator and the cortical shell elements, reducing significantly the CPU time during the finite element analysis. Material properties of these applicators are adopted from the work of Phillips et al. (2015). The two layers closest to the bone were assigned linear elastic material properties of a soft material similar to cartilage (E = 10 *MPa*; ν = 0.49). The two external layers were assigned linear elastic material properties of a stiffer material similar to bone (E = 18 *GPa*; ν = 0.3). In the musculoskeletal model, intervertebral joints are modelled with three rotational degrees of freedom which only allow the transfer of forces. Since no moments are transferred through these idealised joints, truss elements were used to connect the joint centres as defined in the musculoskeletal model with the external nodes of the load applicators. These trusses were assigned a 2.5 mm^2 circular cross sectional area and linear elastic material properties similar to bone (E = 18 *GPa*; ν = 0.3).

2.2.2.2. Muscle Forces

The attachment site coordinates and fibre direction of the OpenSim musculotendon actuators acting on each lumbar vertebra (**Figure 2B**) were extracted from the musculoskeletal model at each time frame with a dedicated plug-in developed by Modenese (van Arkel et al., 2013). A MATLAB script was then used to locate the surface nodes closest to the attachment sites in the finite element model. Muscle forces were applied as point loads, with the magnitude and direction of the force vector corresponding to the muscle force estimated from the musculoskeletal simulations.

2.2.2.3. Inertial Loads

To apply the inertial load of the lumbar segment to the vertebra, a construct called an "inertia applicator" based on the same concept as the load applicator was used. Spreading the inertial load over the volume of the vertebra is computationally demanding (Villette, 2016). Every cortical node of the vertebra was therefore connected to a node located at the centre of mass of the lumbar segment with soft truss elements (**Figure 2C**). These

trusses have a circular cross sectional area of 2.5 mm^2 and were assigned linear elastic material properties with a low stiffness (E = 5 *MPa*; $\nu = 0.3$) to avoid stiffening of the model. The "body kinematics" tool available in OpenSim 3.3 was used to determine the position and velocity of the vertebra in the global coordinate system at each timeframe. The direction and magnitude of the inertial load were calculated based on these positions and velocities, and the mass of the lumbar segment defined in the musculoskeletal model. The inertial load was applied at the node located at the centre of mass of the lumbar segment.

2.2.3. Boundary Conditions

The loading applied to the finite element model of the vertebra was obtained with the musculoskeletal model. At each time step, musculoskeletal simulations were solved for equilibrium of each segment. If all loads are applied, the vertebra should be at equilibrium in the finite element analysis, and no boundary condition should be needed. However, the musculoskeletal model represents bones as rigid bodies while the finite element model allows bones to deform, which compromises the equilibrium condition found in the musculoskeletal simulations. To ensure numerical stability of the finite element model, soft boundary conditions were applied using a similar approach as the load applicators. At the inferior joint, beam elements connecting the external nodes of the inferior endplate applicator with a coincident node at the joint centre were added (**Figure 2D**). This coincident node was constrained in all six degrees of freedom. The beam elements were assigned a circular cross section of 2.5 mm^2, a Young's modulus of 1 *GPa* and a Poisson's ratio of 0.3. These relatively soft material properties compared to the load applicator properties prevent stiffening of the vertebra's structure induced by the boundary condition.

2.3. Bone Adaptation Algorithm

The bone adaptation algorithm used in this study was developed in the Structural Biomechanics Group at Imperial College London (Phillips, 2012; Phillips et al., 2015). With the structural mesoscale finite element approach, all truss and shell elements representing bone are assigned the same linear isotropic material properties. Shell thickness and truss cross-sectional area (arbitrarily assigned in the base models) are then optimised in the simulation of bone adaptation. The algorithm follows the Mechanostat hypothesis (Frost, 1987, 2003), optimising bone toward a target strain in an iterative process. This process is implemented with a combination of MATLAB and Python (Python Software Foundation, Beaverton, OR, USA) scripts, and successive finite element models are run using the Abaqus/Standard solver (Dassault Systèmes, Vélizy-Villacoublay, France).

At each iteration i, bone is subjected to a loading envelope of n load cases representing a combination of different activities. The maximum absolute strain for each element j is extracted and compared to the target strain. Equation (1) defines the maximum absolute strain in truss elements.

$$\left|\epsilon_{i,j}\right|_{max} = max\left(\left|\epsilon_{11,j,\lambda}\right|\right) \quad (1)$$

where $\epsilon_{11,j,\lambda}$ is the axial strain in element j for the load case λ, with $\lambda = 1, ..., n$.

Equation (2) defines the maximum absolute strain in shell elements.

$$\left|\epsilon_{i,j}\right|_{max} = max\left(\left|\epsilon^{b}_{max,j,\lambda}\right|, \left|\epsilon^{b}_{min,j,\lambda}\right|, \left|\epsilon^{t}_{max,j,\lambda}\right|, \left|\epsilon^{t}_{min,j,\lambda}\right|\right) \quad (2)$$

where $\epsilon^{b}_{max,j,\lambda}$, $\epsilon^{b}_{min,j,\lambda}$, $\epsilon^{t}_{max,j,\lambda}$, $\epsilon^{t}_{min,j,\lambda}$ are the maximum and minimum principal strains in the bottom and top surfaces of the shell element j for the load case λ, with $\lambda = 1, ..., n$.

The strain ranges associated with the Mechanostat (Frost, 1987, 2003) are given in Equation (3). The target strain was given a value of $\epsilon_t = 1250\ \mu\epsilon$ (Aamodt et al., 1997; Phillips, 2012).

$$\phi_{i,j} = \begin{cases} 1, \text{ for } 0\mu\epsilon \leq \left|\epsilon_{i,j}\right|_{max} \leq 250\mu\epsilon & \text{(Dead zone)} \\ 1, \text{ for } 250\mu\epsilon < \left|\epsilon_{i,j}\right|_{max} < 1000\mu\epsilon & \text{(Bone resorption)} \\ 0, \text{ for } 1000\mu\epsilon \leq \left|\epsilon_{i,j}\right|_{max} \leq 1500\mu\epsilon & \text{(Lazy zone)} \\ 1, \text{ for } \left|\epsilon_{i,j}\right|_{max} > 1500\mu\epsilon & \text{(Bone deposition)} \end{cases} \quad (3)$$

One aspect of the adaptation algorithm that should be highlighted is the presence of a dead zone where bone is taken to resorp completely. In the base model, a randomised network of truss elements was created, resulting in a number of trusses in excess of that required. Trusses that are not needed to bear the load applied to the bone will fall in this dead zone.

For iteration $i + 1$, the cross-sectional area of each truss element and the thickness of each shell element are adjusted using Equations (4) and (5), respectively. Adaptation of trabecular bone was given preference compared to adaptation of cortical bone at each iteration in order to avoid oscillation of the shell element thicknesses in the initial iterations.

$$A_{i+1,j} = \begin{cases} A_{i,j}\frac{\left|\epsilon_{i,j}\right|_{max}}{\epsilon_t} & \text{if } \phi_{i,j} = 1 \\ A_{i,j} & \text{if } \phi_{i,j} \neq 1 \end{cases} \quad (4)$$

where $A_{i,j}$ is the cross section area of truss element j.

$$T_{i+1,j} = \begin{cases} \frac{T_{i,j}}{2}\left(1 + \frac{\left|\epsilon_{i,j}\right|_{max}}{\epsilon_t}\right) & \text{if } \phi_{i,j} = 1 \\ T_{i,j} & \text{if } \phi_{i,j} \neq 1 \end{cases} \quad (5)$$

where $T_{i,j}$ is the thickness of shell element j.

To increase computational efficiency, shell thicknesses were discretised linearly into 256 categories. The thickness of cortical bone varies between 0.2 and 0.9 *mm* in the vertebral body (Ritzel et al., 1997; Edwards et al., 2001). The thickness range of the shell elements was set between 0.1 and 2.0 *mm* to account for potential inter-subject variability. The same approach was used for the truss cross-sectional areas which were linearly discretised into 255 categories. The radius range of the truss elements was set between 0.1 and 2.0 *mm*, which characterises trabecular bone at a mesoscale level (Nagele et al., 2004; Phillips et al., 2015). An extra category with a radius of 1 μm was added and allocated to elements in the dead zone. With such a small radius, the contribution of these elements is negligible while the numerical stability of the model is maintained. Elements in the dead zone were also allowed to regrow and be reassigned to one of the 255 categories if appropriate at a later iteration.

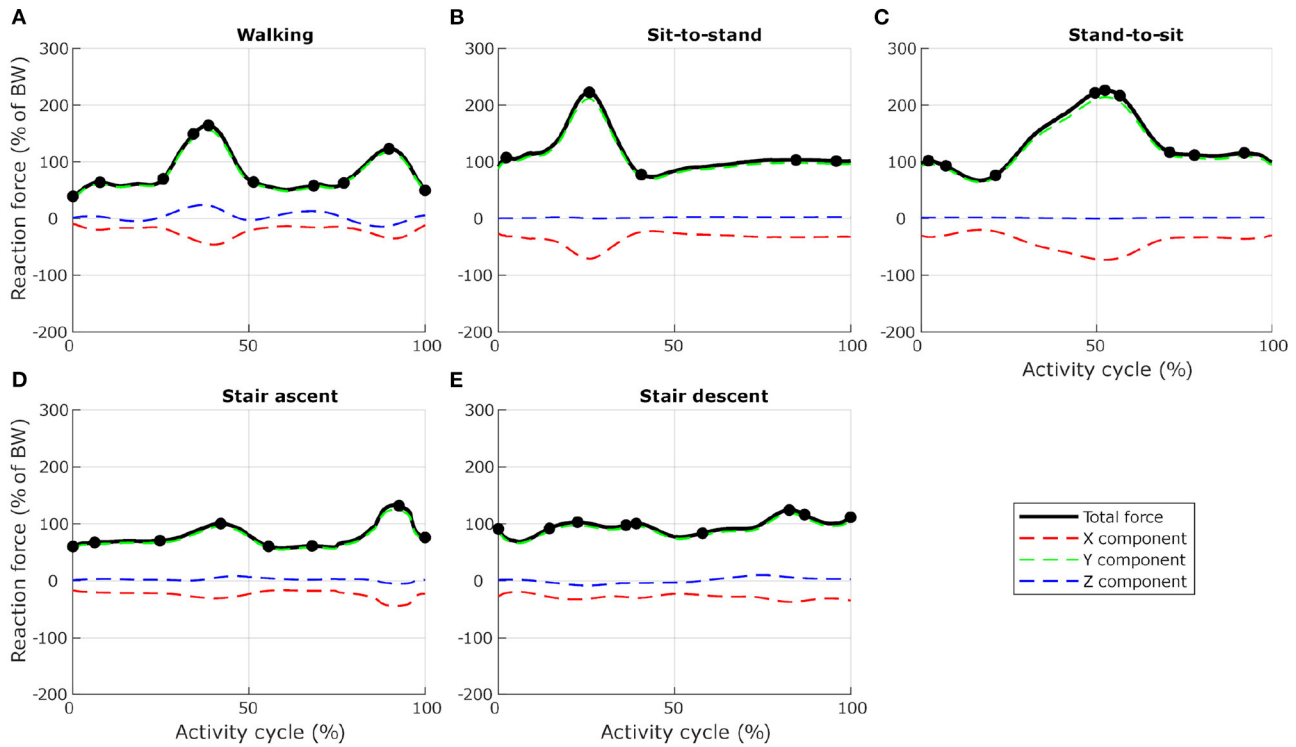

FIGURE 3 | Selection of load cases for L4, for five activities related to locomotion (**(A)** level walking, **(B)** standing up from a chair, **(C)** sitting down on a chair, **(D)** walking up the stairs, and **(E)** walking down the stairs). Total reaction force at L4–L5 joint derived from the musculoskeletal model and normalised to body weight (BW) are shown as black lines. Dots indicate the frames selected for the finite element analysis. Red, green, and blue dashed lines show X, Y, and Z components of the reaction force expressed in the vertebra coordinate system.

2.4. Loading Scenarios

Two loading scenarios were investigated in this study. A healthy scenario composed of all eighteen activities previously mentioned was investigated first. This scenario is representative of a healthy lifestyle. Adapting the base model of each lumbar vertebra to this set of load cases is expected to provide converged models with a trabecular and cortical architecture similar to that observed in healthy vertebrae. A second scenario representative of a more sedentary lifestyle was also investigated. For this scenario, the converged healthy models obtained previously were adapted to the same set of load cases where the seven more demanding activities involving lifting tasks and large combined movements of the spine toward the limits of the range of motion in the three anatomical planes were removed.

To ensure computational efficiency for each lumbar vertebra model, subsets of load cases were selected from the 12 dynamic activities based on the reaction force calculated at the inferior idealised joint in the musculoskeletal model. For each activity, the full set of frames was first subsampled at 10 *Hz* (every 10 frames) to reduce the number of frames for the simulations. Any peak value was also added to the subset. This initial subset was then optimised by removing frames until a 1% difference between the integrated load for the initial subset of frames and the integrated load for the final subset of frames was reached. At each selected frame, the corresponding muscle forces, joint reaction forces and inertia forces were applied in consecutive steps in the finite element model. **Figures 3**, **4** show the selected load cases from the dynamic activities for L4 with this method. For the static activities, a single frame was selected in the middle of each activity to obtain six additional load cases. The reaction force at L4–L5 joint for these load cases is shown in **Table 1** for reference. Load cases for the other vertebrae are available in the **Supplementary Material**.

2.5. Adapted Bone Architecture Analysis

The structural finite element approach used in this study allows a direct visual observation of the cortical and trabecular bone architecture. *In-vivo* observations of vertebral architecture are not abundant in the literature for healthy young subjects, as most studies focus on elderly and pathological populations. After adaptation to the healthy scenario, the structural architecture of the L4 model was compared to a description of the vertebra's internal architecture made by Gallois and Japiot (1925). Trabecular anisotropy in the lumbar vertebrae was characterised using coloured lines at each node. Every truss element was expressed as a normalised vector of X, Y, and Z components in the vertebra's coordinate system. These element vectors were then weighted based on the cross-sectional area of the elements. For each node, connected weighted element vectors were summed to create a node vector. The norm of

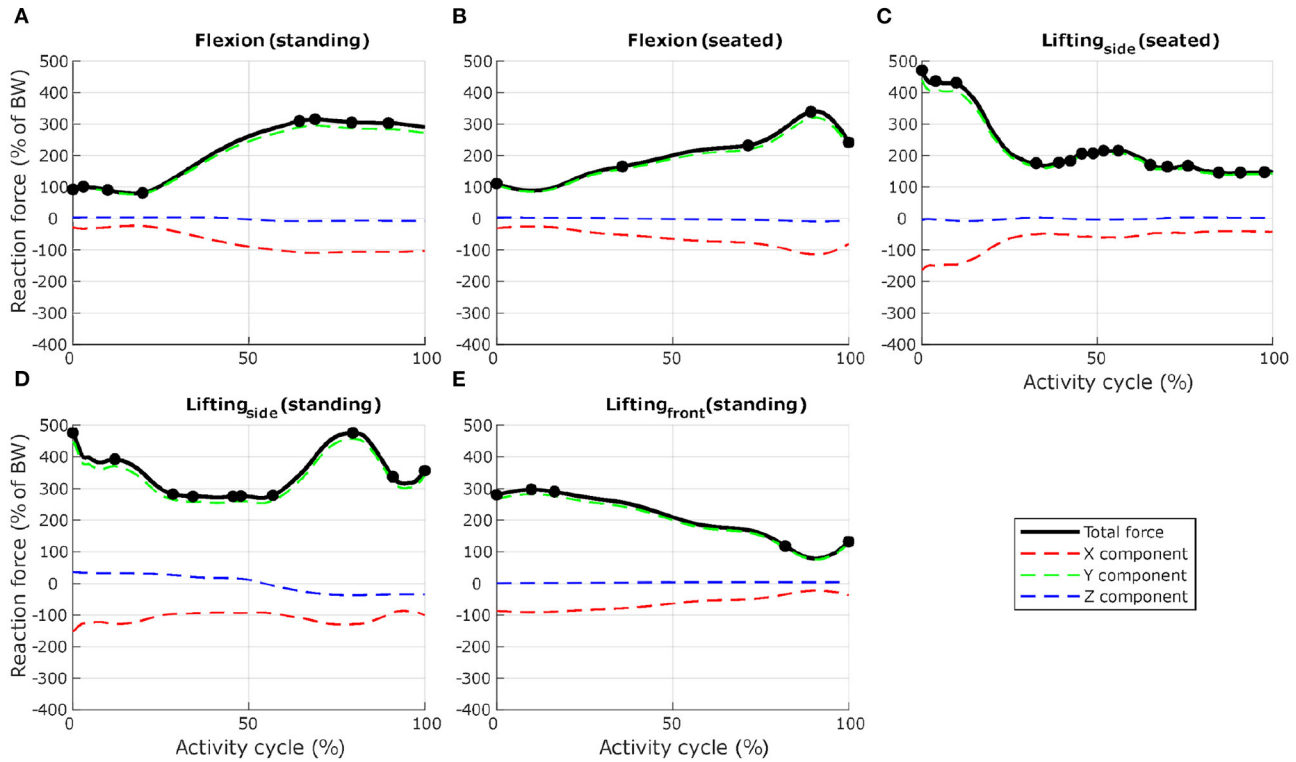

FIGURE 4 | Selection of load cases for L4, for seven activities involving spine movements (**(A)** forward flexion from upright standing to maximum flexion, **(B)** forward flexion from upright sitting, **(C)** in a seated position, twisting and lifting a box from the floor, from the right side to a table in front, **(D)** in a standing position, twisting and lifting a box from the floor, from the left side to the right side, and **(E)** in a standing position, lifting a box from the floor in front to the chest). Total reaction force at L4–L5 joint derived from the musculoskeletal model and normalised to body weight (BW) are shown as black lines. Dots indicate the frames selected for the finite element analysis. Load cases obtained with activities **(C,D)** were mirrored through the sagittal plane to obtain loading on the other side. Red, green, and blue dashed lines show X, Y, and Z components of the reaction force expressed in the vertebra coordinate system.

this node vector was used to scale the length of the line at each node. Components of the normalised node vector were used as RGB values for the line's colour, with X, Y, and Z components corresponding to red, green, and blue, respectively. With this method, if elements linking to a node are oriented along the X axis (respectively Y or Z) only, a red (respectively green or blue) line will be produced at this node. Similarly, if elements linking to a node are oriented at $\pm 45^{\circ}$ in the XY plane (respectively XZ plane or YZ plane), a yellow (respectively magenta or cyan) line will be produced at this node as a combination of red and green light. A white dot indicates a node without elements in the size range being looked at connected to it. A difference is made between the trusses with a radius larger than 0.1 *mm* referred to as the "primary structure," and the trusses with a radius of 0.1 *mm* referred to as the "secondary structure." The trabecular trusses of the primary structure resist the major loads experienced by the vertebra while the secondary structure is believed to give a base stiffness to the bone.

Cortical thickness and trabecular architecture of the five lumbar vertebrae adapted were also analysed in the healthy and the sedentary scenarios. To understand the influence of the different activities, each finite element (cortical shell or trabecular truss) was colour-coded in the adapted models based on the load case which resulted in the absolute maximum strain value (as defined in Equations 1 and 2). This allows a direct visualisation of the activities most beneficial to maintaining bone health, and gives an understanding of which areas of the lumbar vertebrae are stimulated by a given activity.

3. RESULTS

3.1. Healthy Scenario

On average, the structural finite element models converged in 25 iterations for the healthy scenario. The relative density, calculated as the ratio between the volume of all bone elements (cortical and trabecular) and the total volume of the vertebra, is 20.27% on average for the five adapted lumbar vertebrae. This value is within the range reported by Eriksen et al. (2002) (19.0%, SD 8.5%) and Muller (2004) (17.9%, SD 6.7%). 16.97% of the initial truss elements representing trabecular bone in the base models ended in the dead zone after adaptation to 115.2 load cases on average. The remaining truss elements have an average connectivity of 17.20 (SD 4.16). Characteristics of the converged models can be found in **Table 2**.

TABLE 1 | Reaction force at L4–L5 joint derived from the musculoskeletal model and used for the finite element analysis for six static positions of the spine.

	X component (% of BW)	Y component (% of BW)	Z component (% of BW)	Total reaction force (% of BW)
Flexion 20°	−60.5	174.8	3.5	185.0
Extension 15°	−74.5	190.1	4.2	204.2
Lateral bending 20° (right)	−45.8	127.3	13.2	135.9
Lateral bending 20° (left)	−45.4	129.0	−3.9	136.8
Axial rotation 15° (right)	−43.2	118.4	−2.2	126.0
Axial rotation 15° (left)	−29.1	90.2	5.3	94.9

Forces are normalised to body weight (BW).

TABLE 2 | Characteristics of the converged mesoscale structural finite element models after adaptation to the healthy and sedentary scenarios.

			L1	L2	L3	L4	L5	Average
	Cortical elements		2,964	3,390	3,620	3,600	3,712	3457.2
	Trabecular elements (initial mesh)		89,042	101,805	115,063	115,988	130,460	110471.6
	Vertebra volume (mm^3)		54,400	59,320	69,630	70,094	78,820	66,453
Healthy scenario	Load cases		114	115	118	116	113	115.2
	Iterations to convergence		25	23	30	20	27	25
	Trabecular elements (converged model)		79,826	86,905	93,452	98,558	96,483	91044.8
	Trabecular connectivity							
		Mean (SD)	18.20 (3.96)	17.45 (4.23)	16.77 (4.30)	17.21 (3.96)	16.38 (4.36)	17.20 (4.16)
		Minimum	1	1	1	1	1	1
		Maximum	49	45	53	46	31	44.8
	Trabecular volume (mm^3)		9,185	7,948	7,828	9,010	10,050	8,804
	Cortical volume (mm^3)		6,026	4,608	3,875	4,877	2,249	4,327
	Relative density (% of bone volume over total volume)		27.96	21.17	16.81	19.81	15.60	20.27
	Dead elements (% of initial trabecular elements)		10.35	14.64	18.78	15.03	26.04	16.97
Sedentary scenario	Load cases		51	48	51	51	52	50.6
	Iterations to convergence		24	38	56	39	44	40.2
	Trabecular elements (converged model)		49,535	57,404	38,233	63,703	61,477	54070.4
	Trabecular connectivity							
		Mean (SD)	14.70 (4.64)	13.36 (4.53)	10.75 (4.39)	12.78 (4.36)	13.88 (4.67)	13.10 (4.52)
		Minimum	1	1	1	1	1	1
		Maximum	28	37	26	36	28	31
	Trabecular volume (mm^3)		3,074	3,246	2,468	3,765	4,729	3,456
	Cortical volume (mm^3)		1,549	1,628	1,666	3,476	1,719	2,008
	Relative density (% of bone volume over total volume)		8.50	8.22	5.94	10.33	8.18	8.23
	Dead elements (% of initial trabecular elements)		37.95	33.95	59.09	35.36	36.28	40.53

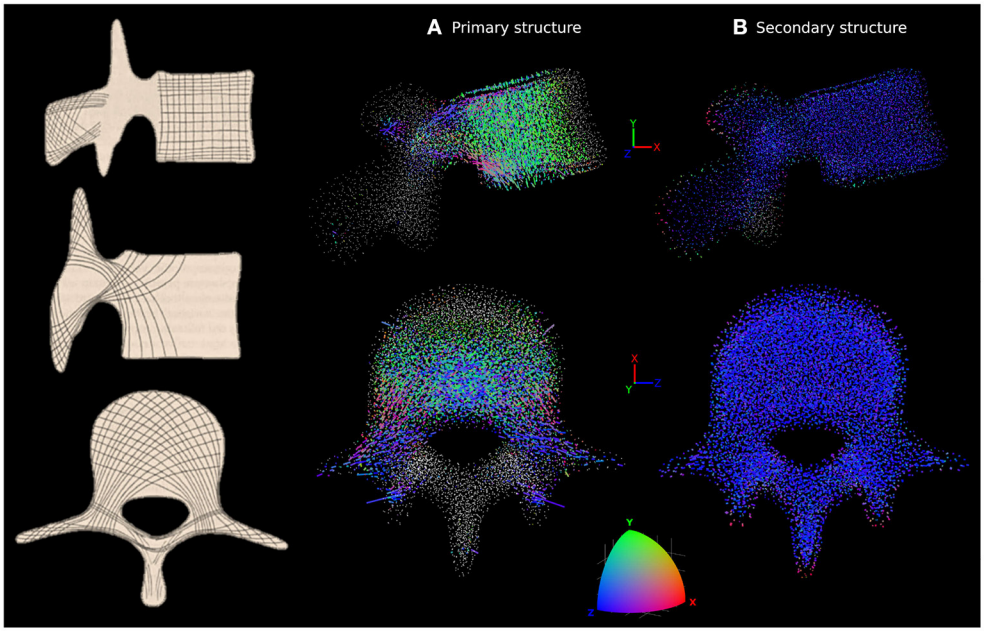

FIGURE 5 | Characterisation of anisotropy in the trabecular bone of L4 adapted to the healthy scenario. *In-vivo* observations by Gallois and Japiot (1925) are shown on the left. **(A)** Shows the orientation of the trabecular trusses of the primary structure (with a radius larger than 0.1 *mm*). **(B)** Shows the orientation of the trabecular trusses of the secondary structure (with a radius of 0.1 *mm*). For **(A,B)**, side view (top row) and top view (bottom row) are shown. Lines are attached to each trabecular node, with colour and length varying respectively with the orientations and radii of the truss elements connected to that particular node. The colour scale at the bottom shows how the colour of the lines should be interpreted. Orientation along the X, Y, or Z axes are in red, green, or blue, respectively. Any orientation that is not colinear with these axes shows as a combination of red, green and blue. A white dot indicates a node without elements in the size range being looked at connected to it.

Converged structural finite element models of the five lumbar vertebrae adapted to the healthy scenario are available in the **Supplementary Material**.

The adapted trabecular trajectories were studied with the coloured lines method for anisotropy characterisation. **Figure 5** shows the line plot for L4 compared to *in-vivo* observations by Gallois and Japiot (1925) on the left. **Figure 5A** focuses on trabecular truss elements with a radius larger than 0.1 *mm* forming the primary structure, while **Figure 5B** shows only the secondary structure composed of elements with a radius of 0.1 *mm*. The primary structure compares favourably with observations made by Gallois and Japiot (1925). There is a clear orientation along the Y axis for the trabeculae in the vertebral body as green is the dominant colour. This group of trabeculae runs perpendicular to the endplates and resists vertical compression. Blue is the dominant colour in the transverse processes and the vertebral arch, indicating that most trabeculae run medio-laterally in these parts of the vertebra, resisting tension in the transverse processes. Elements running diagonally across the vertebral body and the pedicles, finishing in the transverse and superior articular processes can also be identified in pink, purple, and grey. For the elements of the secondary structure, the lines are predominantly blue, indicating a principal orientation of the smaller truss elements along the Z axis. Line plots and MATLAB figure files for the five lumbar vertebrae are available in the **Supplementary Material**.

3.2. Sedentary Scenario

The average number of load cases over the five lumbar vertebrae was 50.6 for the eleven activities of the sedentary scenario. The structural finite element models converged in 40.2 iterations on average with a relative bone density of 8.23%, a mean connectivity of 13.10 (SD 4.52) and 40.53% of the trabecular elements in the dead zone (**Table 2**). Relative density is 58.39% lower than in the healthy scenario. This shows that moderate intensity activities alone are insufficient in providing a mechanical stimulus to prevent a decrease of bone density in the lumbar spine.

Looking at the cortical thickness in the converged models, a reduced range of activity results in a thinner cortex (**Figure 6**). In the healthy scenario the thicker shell elements are found in the posterior part of the vertebral body, the pedicles, and the transverse processes (**Figure 6A**), as these structures have to resist increased muscle forces due to movement of the lumbar spine about the medio-lateral axis during flexion extension activities and about the antero-posterior axis during lateral bending activities. In the sedentary scenario, the thickness of the cortex in these parts of the vertebrae reduces considerably, especially in L1, L2, and L3 (**Figure 6B**). Detailed views of the cortical thickness after adaptation to the healthy and to the sedentary scenarios can be found in the **Supplementary Material** for the five lumbar vertebrae.

Figures 7B, **8B** respectively show mid-sagittal and through-processes transverse slices of the five lumbar vertebrae adapted to the sedentary scenario, highlighting the areas at risk of trabecular

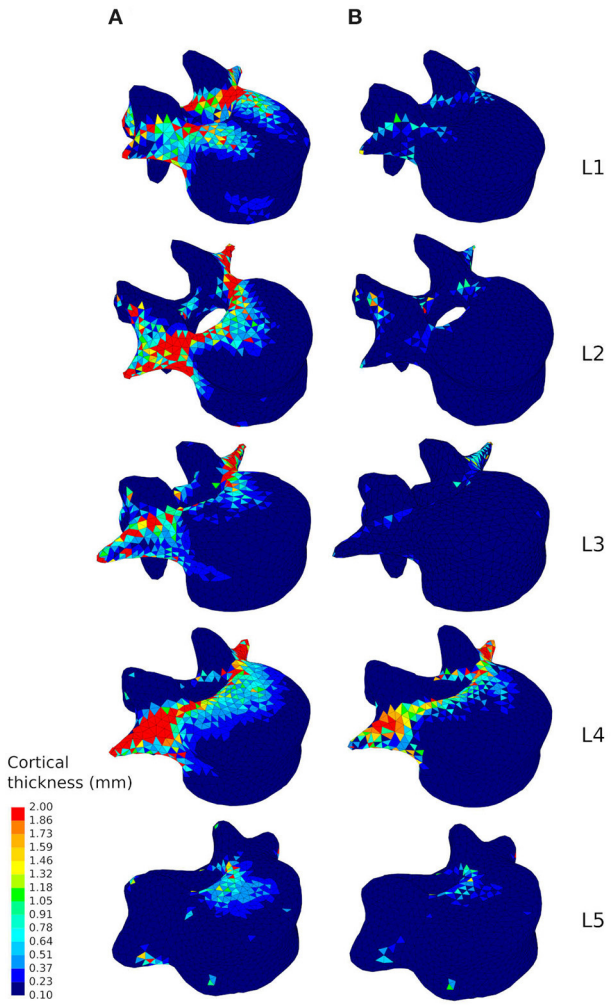

FIGURE 6 | Cortical thickness of the converged mesoscale structural models of the lumbar vertebrae ranging from 0.1 to 2.0 *mm* adapted to the healthy scenario **(A)** and the sedentary scenario **(B)**.

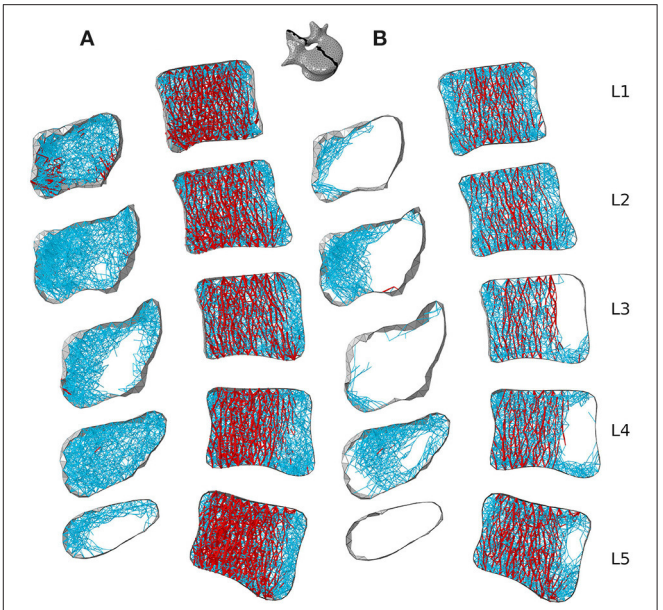

FIGURE 7 | 3 *mm* mid-sagittal (XY plane) slices for the converged models adapted to the healthy scenario **(A)** and the sedentary scenario **(B)**. Cortical shell elements are shown in grey. Thicker truss elements representing the primary structure are shown in red. Trabecular truss elements representing the secondary structure (with a radius of 0.1 *mm*) are shown in blue. Truss elements in the dead zone (with a radius of 1 μm) are not shown for clarity.

bone resorption when demanding activities involving spine movements are not performed, in comparison to the healthy scenario (**Figures 7A**, **8A**). The trabecular bone secondary structure present in the spinous and transverse processes tends to degrade when the vertebrae are subjected to a reduced range of activity (**Figures 7B**, **8B**). L3, L4, and L5 also show this trend in the frontal part of the vertebral body (**Figure 7B**). For all lumbar vertebrae, the larger trabeculae of the primary structure resisting vertical compression are clustered in the center of the vertebral body (**Figure 8B**). Apart for L2 and L4 where some of the broader structure remains, the primary structure is missing in the transverse processes for the sedentary scenario (**Figure 8B**). Detailed slices in the three anatomical planes showing the structure of the five lumbar vertebrae after adaptation to the healthy and to the sedentary scenarios can be found in the **Supplementary Material**.

3.3. Influence of Activities

Figure 9 shows how cortical regions of the lumbar vertebrae are influenced by the performed activities. In the healthy scenario (**Figure 9A**), the most influential activities for cortical adaptation are lifting tasks involving twisting movements of the spine. Lifting a box in the sagittal plane from the floor to the chest while standing has reduced influence on the cortical adaptation. In the sedentary scenario (**Figure 9B**), the most influential activities are walking, sit-to-stand, stair ascent and spine extension, while stair descent, spine flexion, lateral bending, and axial rotation have reduced influence.

Figures 10, **11** show how trabecular regions of the lumbar vertebrae are influenced by the performed activities in the healthy and sedentary scenarios, respectively. For both scenarios, the primary and secondary structures are influenced by the same activities. Similarly to cortical bone, lifting tasks involving twisting movements of the spine have the most influence on trabecular adaptation in the healthy scenario for truss elements of the primary (**Figures 10A,C**) and secondary (**Figures 10B,D**) structures. In the sedentary scenario, the most influential activities on the primary (**Figures 11A,C**) and secondary (**Figures 11B,D**) trabecular structures are sit-to-stand, stair ascent, and spine extension.

In the healthy scenario, sagittal slices of the primary (**Figure 10A**) and secondary (**Figure 10B**) trabecular structures also show that lifting activities performed in a standing position influence predominantly the posterior part of the vertebral body in L1 and L5 and the anterior part of the vertebral

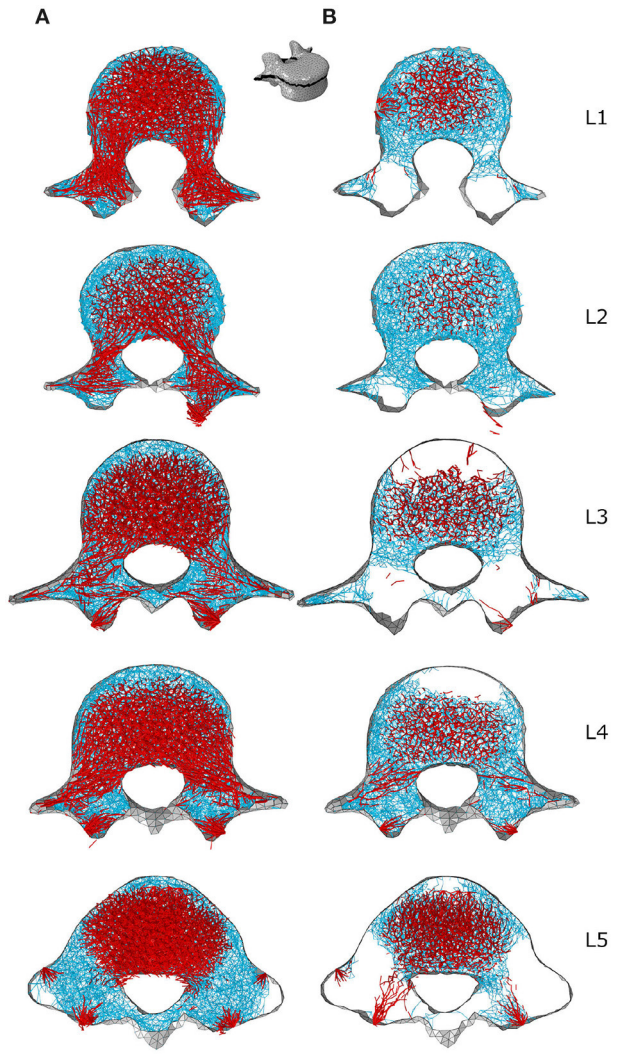

FIGURE 8 | Through-processes transverse (XZ plane) slices for the converged models adapted to the healthy scenario **(A)** and the sedentary scenario **(B)**. In the background, cortical shell elements are shown in grey. Thicker truss elements representing the primary structure located between the superior endplate and the through-processes transverse slice are shown in red. Trabecular truss elements representing the secondary structure (with a radius of 0.1 *mm*) are shown in blue for a 3 *mm* slice. Truss elements in the dead zone (with a radius of 1 μm) are not shown for clarity.

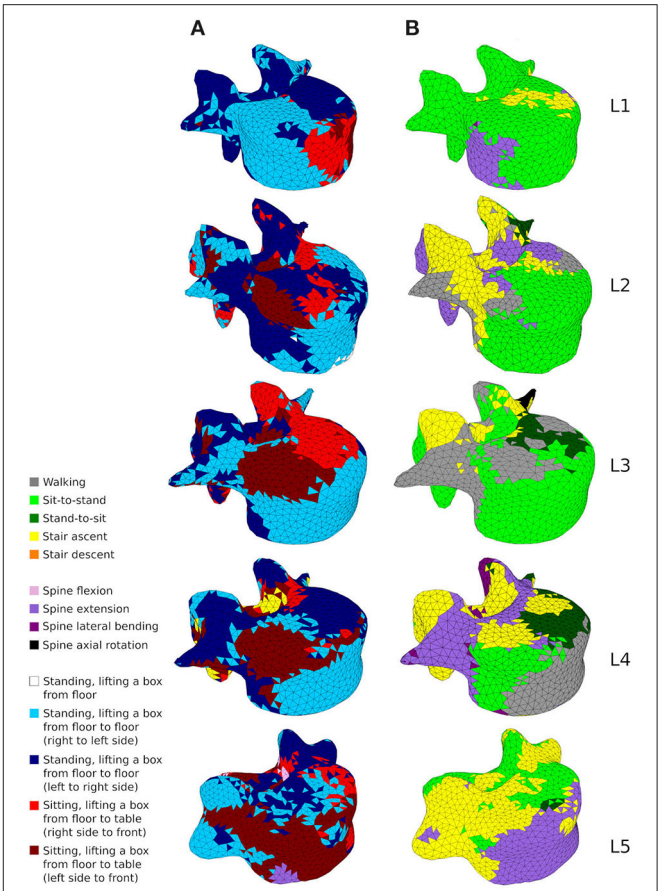

FIGURE 9 | A map showing which activity gives rise to the highest absolute maximum principal strain for the adaptation of the cortical shell elements in the healthy scenario **(A)** and the sedentary scenario **(B)**.

body in L2, L3, and L4, while lifting activities performed in a sitting position stimulate the other part of the vertebral bodies. It is also important to note that even in the sedentary scenario where walking might be expected to be one of the more onerous physical activities, it has reduced influence on the trabecular adaptation of the primary (**Figures 11A,C**) and secondary (**Figures 11B,D**) structures.

4. DISCUSSION

Combining physiological loading representative of a healthy lifestyle with the bone structural adaptation algorithm produces cortical and trabecular finite element structures of the lumbar vertebrae which compare favourably with *in-vivo* observations. Bone relative density found in the models (**Table 2**) is within the range reported by Eriksen et al. (2002) and Muller (2004). Cortical thickness in the anterior and posterior walls of the vertebral body (**Figure 6A**) are in agreement with the range reported by Ritzel et al. (1997) (0.1–0.4 *mm*). In the pedicles, the models show a thicker cortex on the inferior and superior regions, similar to the observations made by Maillot and Wolfram-Gabel (1993). Trajectories of the trabecular elements observed in the models (**Figure 5**) compare favourably with the observations made by Gallois and Japiot (1925). These comparisons provide an initial positive assessment of the modelling framework.

In addition to producing models of the lumbar vertebrae adapted to a large number of load cases, the modelling approach allows for visualisation of the structural architecture of the vertebrae. The line plots in **Figure 5** highlight the dominant trabecular trajectory at each node of the converged finite element model for the L4 vertebra. For the healthy scenario, it confirms that the predicted primary structure of the trabecular bone

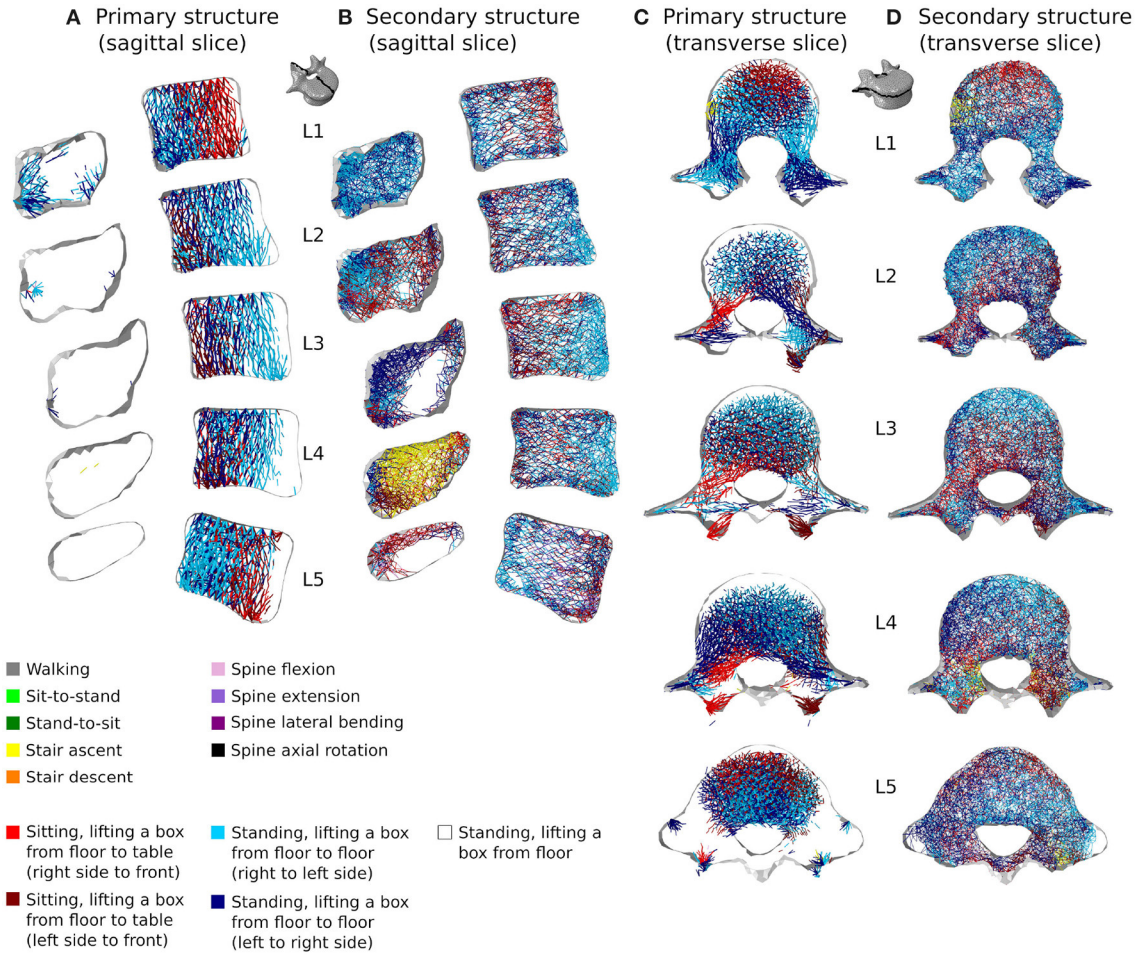

FIGURE 10 | 3 *mm* mid-sagittal (XY plane) and through-processes transverse (XZ plane) slices of the converged models in the healthy scenario, showing a map of which activity gives rise to the highest absolute maximum axial strain for the adaptation of the trabecular truss elements of the primary **(A,C)** and secondary **(B,D)** structures. Cortical shell elements are shown in light grey.

follows trajectories comparable to the observations of Gallois and Japiot (1925). It also shows that the secondary structure of the trabecular bone (trabecular trusses with a radius of 0.1 *mm*) are mostly aligned medio-laterally throughout the vertebra. The modelling framework also produces a mapping of the vertebrae (**Figures 9–11**) showing which of the performed activities are the most influential in the adaptation of the structural finite elements. This is a useful approach for understanding which activities are the most beneficial to bone formation in specific regions of the vertebrae. This could be used to inform physical training or rehabilitation treatment based on specific movements and activities. While this modelling framework uses hundreds of load cases to adaptatively produce mesoscale structural models of lumbar vertebrae, its computation cost remains low compared to other mechanical adaptation approaches used in the field. With a total of 119,588 elements, the L4 model converged in 20 iterations for the 116 load cases of the healthy scenario, with each iteration taking around 15 min (finite element analysis and structural adaptation) on a personal workstation (Intel Xeon E5-2630 v2 2.60 *GHz*, 12 CPUs, RAM 64 *GB*). This is computationally efficient compared to the classic microscale continuum modelling approach. For example, in their μCT derived model of L2, Badilatti et al. (2015) used 365 million elements and required 8 hours per iteration on a supercomputer with 1,024 CPUs to adapt the bone to three simplified load cases without any muscle forces. Despite the numerous advantages of the mesoscale structural models, some limitations inherent to the combined modelling approach and to the structural adaptation modelling choices remain and should be acknowledged.

Physiological loading and boundary conditions are essential to provide a realistic mechanical environment for finite element simulations (Bitsakos et al., 2005; Phillips et al., 2007; Speirs et al., 2007; Phillips, 2009). The combined multiscale modelling approach relies on a detailed musculoskeletal model with identical geometry to provide this mechanical environment (Favier et al., 2021). However, assumptions made for the musculoskeletal model will impact the finite element results (Wagner et al., 2010; Cronskaer et al., 2013; Zhu et al.,

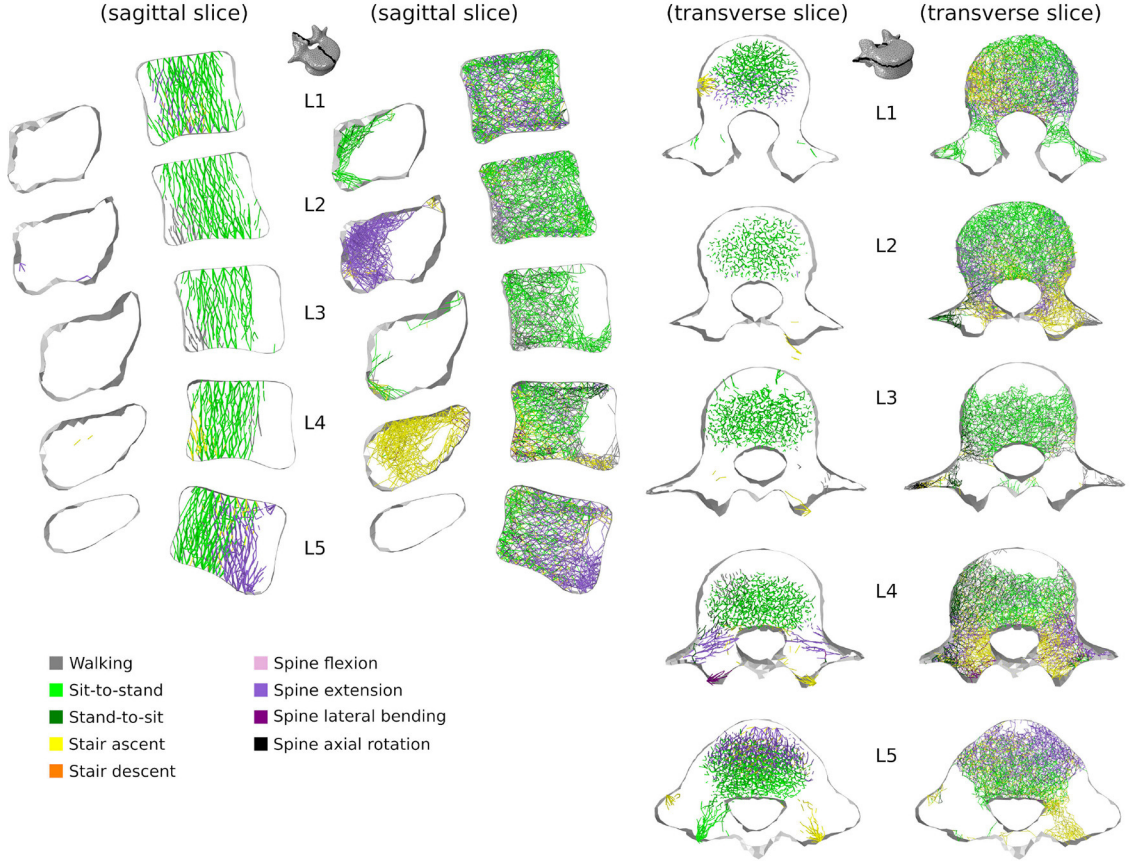

FIGURE 11 | 3 *mm* mid-sagittal (XY plane) and through-processes transverse (XZ plane) slices of the converged models in the sedentary scenario, showing a map of which activity gives rise to the highest absolute maximum axial strain for the adaptation of the trabecular truss elements of the primary **(A,C)** and secondary **(B,D)** structures. Cortical shell elements are shown in light grey.

2013). The idealised representation of intervertebral joints in the musculoskeletal model requires the development of load applicators in the finite element model to spread the reaction force calculated at the joint centre. In particular, the three degree of freedom joint neglects translations permitted by the intervertebral disc, ligaments, and facet joints. While it is possible to improve musculoskeletal models with ligaments (Damm et al., 2019) and a better intervertebral disc representation (Wang et al., 2020), future work will implement the ligaments, discs, and facet joints in a finite element model of multiple spinal units. This is expected to reduce the impact of idealised musculoskeletal joints on the vertebra of interest.

The converged mesoscale structural models show discontinuities in the cortex, with shell thickness varying significantly from one element to the next in some locations. This phenomenon could be addressed in future work to provide a smoother and more realistic thickness variation across the vertebral cortex. The trabecular density in the model is also impacted by the choice of element for the trabeculae. While it has been shown that truss elements ensure a physiological macroscale behaviour of bone (Villette and Phillips, 2015, 2018), local architecture may be improved through using a beam element based bone adaptation with an alternative approach to generating the initial network (Phillips, 2019). Another limitation of the current method is that it does not allow nodes from the initial mesh to realign for better supporting the loading envelope, and future work will focus on allowing structural elements of the trabecular bone to reorient during adaptation. It is also important to note that given the mesoscale nature of the model with radii of up to 2 *mm* being allowed during adaptation, truss element radii in the converged models were expected to exceed the range reported by Rho et al. (1998) and Keaveny et al. (2002) (25–150 μm). However, over 97% of the trabecular elements are within the reported physiological range, with maximum radii of 368 μm found in L5. In all cases, secondary structure elements represent more than 80% of the total number of trabecular elements. Refining the trabecular size categories in the adaptation algorithm and reducing the average length of the structural elements may improve the match between converged models and *in-vivo* observations. An additional limitation, characteristic of the strain-driven adaptation approach, is the choice of values for the target strain, lazy zone, and dead zone in

the optimisation algorithm. These values are in agreement with previous studies (Aamodt et al., 1997; Phillips, 2012; Zaharie and Phillips, 2018) and provide reasonable results, but are likely to change depending on age, sex, pathological conditions, and even regions of the skeletal system.

Despite the limitations associated with the current modelling approach, trends can be observed in bone adaptation to different scenarios. In a scenario of around a hundred load cases representing 18 activities typical of a healthy lifestyle, lifting activities involving bending and rotation of the spine were found to be the most influential in stimulating bone (**Figures 9A**, **10**). In a sedentary scenario where the loading conditions were altered to remove any demanding activities involving large spine movements, the remaining trabecular structure is mainly stimulated by sit-to-stand, stair ascent and spine extension activities (**Figure 11**). The resulting bone architecture (**Figures 7B**, **8B**) is similar to observations made on osteoporotic vertebrae (Jayasinghe et al., 1994). In this scenario, trabeculae tend to disappear completely in the anterior part of the vertebral body and the processes. This can be seen as an extreme degradation of bone and would imply that sedentary behaviours can rapidly lead to bone being unable to support occasional higher loads. However, it should be noted that the current study only predicts a final adapted state, with certain activities removed completely, as opposed to being reduced in daily frequency. For the sedentary scenario, a large amount of trabecular elements fall in the dead zone (**Table 2**). This is due to the adaptation not including a physiological bone remodelling rate and future developments should consider implementing a remodelling rate between 1,000 and 250 $\mu\epsilon$ to obtain a more gradual bone resorption. The results obtained with the current approach should therefore be viewed as a prediction of the regions at risk of bone resorption with sedentary behaviour. Future work comparing the structural architecture obtained in this scenario to vertebra specimens of sedentary or osteoporotic patient populations would provide further validation of the modelling framework and assist in quantifying the extent of this overestimation.

Moderate intensity activities alone are insufficient in providing a mechanical stimulus to prevent bone degradation. This supports the recommendations from the clinical field that an active lifestyle incorporating a wide range of activities is essential to maintain bone health in the lumbar spine. While other physiological factors may influence bone remodelling, activities involving large spine movements in the three anatomical planes and lifting tasks should be performed when possible to maintain lumbar vertebrae bone health. This is particularly relevant for populations subject to physical deconditioning and osteoporosis associated with a sedentary lifestyle (Lau and Guo, 2011), ageing (Guadalupe-Grau et al., 2009; Gomez-Cabello et al., 2012), or chronic low back pain (Weiner et al., 2003; Bjoernsdottir et al., 2012), who carry out these more onerous activities with reduced frequency and may be at risk of bone structural degradation.

DATA AVAILABILITY STATEMENT

The original contributions presented in the study are included in the article/**Supplementary Material**, further inquiries can be directed to the corresponding authors.

AUTHOR CONTRIBUTIONS

CF designed the study, developed the protocol for collecting motion capture and MRI data and acquired these data, carried out all modelling, and drafted the manuscript. AP and AM conceived of, designed and coordinated the study, and drafted the manuscript. All authors contributed to the article and approved the submitted version.

FUNDING

This work was supported by the Department of Civil and Environmental Engineering of Imperial College London.

ACKNOWLEDGMENTS

The authors want to thank Dr. Claire Villette and Dr. Dan Zaharie for sharing their knowledge and experience during this study.

SUPPLEMENTARY MATERIAL

The Supplementary Material for this article can be found online at: https://www.frontiersin.org/articles/10.3389/fbioe.2021.661837/full#supplementary-material

REFERENCES

Aamodt, A., Lund-Larsen, J., Eine, J., Andersen, E., Benum, P., and Husby, O. S. (1997). *In vivo* measurements show tensile axial strain in the proximal lateral aspect of the human femur. *J. Orthop. Res.* 15, 927–931. doi: 10.1002/jor.1100150620

Adachi, T., Kameo, Y., and Hojo, M. (2010). Trabecular bone remodelling simulation considering osteocytic response to fluid-induced shear stress. *Philos. Trans. R. Soc. A Math. Phys. Eng. Sci.* 368, 2669–2682. doi: 10.1098/rsta.2010.0073

Ayturk, U. M., and Puttlitz, C. M. (2011). Parametric convergence sensitivity and validation of a finite element model of the human lumbar spine. *Comput. Methods Biomech. Biomed. Eng.*14, 695–705. doi: 10.1080/10255842.2010.493517

Badilatti, S. D., Christen, P., Levchuk, A., Marangalou, J. H., van Rietbergen, B., Parkinson, I., et al. (2015). Large-scale microstructural simulation of load-adaptive bone remodeling in whole human vertebrae. *Biomech. Model. Mechanobiol.* 15, 83–95. doi: 10.1007/s10237-015-0715-8

Benedetti, M. G., Furlini, G., Zati, A., and Mauro, G. L. (2018). The effectiveness of physical exercise on bone density in osteoporotic patients. *BioMed Res. Int.* 2018:4840531. doi: 10.1155/2018/4840531

Bitsakos, C., Kerner, J., Fisher, I., and Amis, A. A. (2005). The effect of muscle loading on the simulation of bone remodelling in the proximal femur. *J. Biomech.* 38, 133–139. doi: 10.1016/j.jbiomech.2004.03.005

Bjoernsdottir, S., Jonsson, S., and Valdimarsdottir, U. (2012). Functional limitations and physical symptoms of individuals with chronic pain. *Scand. J. Rheumatol.* 42, 59–70. doi: 10.3109/03009742.2012.697916

Cronskaer, M., Rasmussen, J., and Tinnsten, M. (2013). Combined finite element and multibody musculoskeletal investigation of a fractured clavicle with reconstruction plate. *Comput. Methods Biomech. Biomed. Eng.* 18, 740–748. doi: 10.1080/10255842.2013.845175

Damm, N., Rockenfeller, R., and Gruber, K. (2019). Lumbar spinal ligament characteristics extracted from stepwise reduction experiments allow for preciser modeling than literature data. *Biomech. Model. Mechanobiol.* 19, 893–910. doi: 10.1007/s10237-019-01259-6

Davies, S. C., Atherton, F., McBride, M., and Calderwood, C. (2019). *UK Chief Medical Officers' Physical Activity Guidelines*. London: Department of Health. Gov.UK. Available online at: https://assets.publishing.service.gov.uk/government/uploads/system/uploads/attachment_data/file/832868/uk-chief-medical-officers-physical-activity-guidelines.pdf

Delp, S. L., Anderson, F. C., Arnold, A. S., Loan, P., Habib, A., John, C. T., et al. (2007). Opensim: open-source software to create and analyze dynamic simulations of movement. *IEEE Trans. Biomed. Eng.* 54, 1940–1950. doi: 10.1109/TBME.2007.901024

Edwards, W. T., Zheng, Y., Ferrara, L. A., and Yuan, H. A. (2001). Structural features and thickness of the vertebral cortex in the thoracolumbar spine. *Spine* 26, 218–225. doi: 10.1097/00007632-200101150-00019

Eriksen, E., Melsen, F., Sod, E., Barton, I., and Chines, A. (2002). Effects of long-term risedronate on bone quality and bone turnover in women with postmenopausal osteoporosis. *Bone* 31, 620–625. doi: 10.1016/S8756-3282(02)00869-4

Favier, C. D., Finnegan, M. E., Quest, R. A., Honeyfield, L., McGregor, A. H., and Phillips, A. T. M. (2021). An open-source musculoskeletal model of the lumbar spine and lower limbs: a validation for movements of the lumbar spine. *Comput. Methods Biomech. Biomed. Eng.* 1–16. doi: 10.1080/10255842.2021.1886284

Frost, H. M. (1987). Bone mass and the mechanostat: a proposal. *Anat. Rec.* 219, 1–9. doi: 10.1002/ar.1092190104

Frost, H. M. (2003). Bone's mechanostat: a 2003 update. *Anat. Rec.* 275A, 1081–1101. doi: 10.1002/ar.a.10119

Gallois, M., and Japiot, M. (1925). Architecture interieure des vertebres. *Rev. Chirurg.* 63, 687–708.

Gomez-Cabello, A., Ara, I., Gonzalez-Aguero, A., Casajus, J., and Vicente-Rodriguez, G. (2012). Effects of training on bone mass in older adults. *Sports Med.* 42, 301–325. doi: 10.2165/11597670-000000000-00000

Guadalupe-Grau, A., Fuentes, T., Guerra, B., and Calbet, J. A. (2009). Exercise and bone mass in adults. *Sports Med.* 39, 439–468. doi: 10.2165/00007256-200939060-00002

Hambli, R., and Kourta, A. (2015). A theory for internal bone remodeling based on interstitial fluid velocity stimulus function. *Appl. Math. Model.* 39, 3525–3534. doi: 10.1016/j.apm.2014.11.050

Homminga, J., Aquarius, R., Bulsink, V. E., Jansen, C. T., and Verdonschot, N. (2012). Can vertebral density changes be explained by intervertebral disc degeneration? *Med. Eng. Phys.* 34, 453–458. doi: 10.1016/j.medengphy.2011.08.003

Huiskes, R., Ruimerman, R., van Lenthe, G. H., and Janssen, J. D. (2000). Effects of mechanical forces on maintenance and adaptation of form in trabecular bone. *Nature* 405, 704–706. doi: 10.1038/35015116

Jayasinghe, J., Jones, S., and Boyde, A. (1994). Three-dimensional photographic study of cancellous bone in human fourth lumbar vertebral bodies. *Anat. Embryol.* 189, 259–274. doi: 10.1007/BF00239013

Keaveny, T. M., Morgan, E. F., and Yeh, O. C. (2002). "Chapter 8: Bone mechanics," in *Standard Handbook of Biomedical Engineering and Design*, ed M. Kutz (New York, NY: McGraw-Hill Professional), 1–24.

Lau, R. Y., and Guo, X. (2011). A review on current osteoporosis research: with special focus on disuse bone loss. *J. Osteop.* 2011:293808. doi: 10.4061/2011/293808

Little, J. P., Visser, H. D., Pearcy, M. J., and Adam, C. J. (2008). Are coupled rotations in the lumbar spine largely due to the osseo-ligamentous anatomy?-a modeling study. *Comput. Methods Biomech. Biomed. Eng.* 11, 95–103. doi: 10.1080/10255840701552143

Maillot, C., and Wolfram-Gabel, R. (1993). Pedicles of lumbar vertebrae. *Surg. Radiol. Anat.* 15, 295–300. doi: 10.1007/BF01627881

Mosekilde, L. (1990). "Age-related loss of vertebral trabecular bone mass and structure-biomechanical consequences," in *Biomechanics of Diarthrodial Joints*, eds V. C. Mow and A. Ratcliffe (New York, NY: Springer-Verlag), 83–96. doi: 10.1007/978-1-4612-3450-0_4

Muller, R. (2004). Long-term prediction of three-dimensional bone architecture in simulations of pre-, peri- and post-menopausal microstructural bone remodeling. *Osteop. Int.* 16, S25–S35. doi: 10.1007/s00198-004-1701-7

Nagele, E., Kuhn, V., Vogt, H., Link, T. M., Muller, R., Lochmuller, E. M., et al. (2004). Technical considerations for microstructural analysis of human trabecular bone from specimens excised from various skeletal sites. *Calc. Tissue Int.* 75, 15–22. doi: 10.1007/s00223-004-0151-8

Narici, M., Vito, G. D., Franchi, M., Paoli, A., Moro, T., Marcolin, G., et al. (2020). Impact of sedentarism due to the COVID-19 home confinement on neuromuscular, cardiovascular and metabolic health: Physiological and pathophysiological implications and recommendations for physical and nutritional countermeasures. *Eur. J. Sport Sci.* 1–22. doi: 10.1080/17461391.2020.1761076

Nelson, M. E., Rejeski, W. J., Blair, S. N., Duncan, P. W., Judge, J. O., King, A. C., et al. (2007). Physical activity and public health in older adults: recommendation from the American college of sports medicine and the American heart association. *Med. Sci. Sports Exerc.* 39, 1435–1445. doi: 10.1249/mss.0b013e3180616aa2

Park, W. M., Kim, K., and Kim, Y. H. (2013). Effects of degenerated intervertebral discs on intersegmental rotations, intradiscal pressures, and facet joint forces of the whole lumbar spine. *Comput. Biol. Med.* 43, 1234–1240. doi: 10.1016/j.compbiomed.2013.06.011

Phillips, A. T. M. (2009). The femur as a musculo-skeletal construct: a free boundary condition modelling approach. *Med. Eng. Phys.* 31, 673–680. doi: 10.1016/j.medengphy.2008.12.008

Phillips, A. T. M. (2012). Structural optimisation: biomechanics of the femur. *Proc. Instit. Civil Eng.* 165, 147–154. doi: 10.1680/eacm.10.00032

Phillips, A. T. M. (2019). "Modelling trabecular bone as a voronoi network," in *Bone Research Society Annual Meeting, 5th Joint Meeting with the British Orthopaedic Research Society* (Cardiff).

Phillips, A. T. M., Pankaj, P., Howie, C., Usmani, A., and Simpson, A. (2007). Finite element modelling of the pelvis: inclusion of muscular and ligamentous boundary conditions. *Med. Eng. Phys.* 29, 739–748. doi: 10.1016/j.medengphy.2006.08.010

Phillips, A. T. M., Villette, C. C., and Modenese, L. (2015). Femoral bone mesoscale structural architecture prediction using musculoskeletal and finite element modelling. *Int. Biomech.* 2, 43–61. doi: 10.1080/23335432.2015.1017609

Pothuaud, L., Rietbergen, B. V., Charlot, C., Ozhinsky, E., and Majumdar, S. (2004). A new computational efficient approach for trabecular bone analysis using beam models generated with skeletonized graph technique. *Comput. Methods Biomech. Biomed. Eng.* 7, 205–213. doi: 10.1080/10255840412331285943

Rho, J.-Y., Kuhn-Spearing, L., and Zioupos, P. (1998). Mechanical properties and the hierarchical structure of bone. *Med. Eng. Phys.* 20, 92–102. doi: 10.1016/S1350-4533(98)00007-1

Ritzel, H., Amling, M., Posl, M., Hahn, M., and Delling, G. (1997). The thickness of human vertebral cortical bone and its changes in aging and osteoporosis: a histomorphometric analysis of the complete spinal column from thirty-seven autopsy specimens. *J. Bone Miner. Res.* 12, 89–95. doi: 10.1359/jbmr.1997.12.1.89

Rossini, M., Adami, S., Bertoldo, F., Diacinti, D., Gatti, D., Giannini, S., et al. (2016). Guidelines for the diagnosis, prevention and management of osteoporosis. *Reumatismo* 68:1. doi: 10.4081/reumatismo.2016.870

Sinaki, M., Pfeifer, M., Preisinger, E., Itoi, E., Rizzoli, R., Boonen, S., et al. (2010). The role of exercise in the treatment of osteoporosis. *Curr. Osteop. Rep.* 8, 138–144. doi: 10.1007/s11914-010-0019-y

Speirs, A. D., Heller, M. O., Duda, G. N., and Taylor, W. R. (2007). Physiologically based boundary conditions in finite element modelling. *J. Biomech.* 40, 2318–2323. doi: 10.1016/j.jbiomech.2006.10.038

Steele, K. M., DeMers, M. S., Schwartz, M. H., and Delp, S. L. (2012). Compressive tibiofemoral force during crouch gait. *Gait Posture* 35, 556–560. doi: 10.1016/j.gaitpost.2011.11.023

Taylor, D., Casolari, E., and Bignardi, C. (2004). Predicting stress fractures using a probabilistic model of damage, repair and adaptation. *J. Orthop. Res.* 22, 487–494. doi: 10.1016/j.orthres.2003.08.022

Tiwari, A. K., Kumar, R., Tripathi, D., and Badhyal, S. (2018). *In silico* modeling of bone adaptation to rest-inserted loading: strain energy density versus

fluid flow as stimulus. *J. Theor. Biol.* 446, 110–127. doi: 10.1016/j.jtbi.2018.03.009

Tsubota, K., Adachi, T., and Tomita, Y. (2003). Effects of a fixation screw on trabecular structural changes in a vertebral body predicted by remodeling simulation. *Ann. Biomed. Eng.* 31, 733–740. doi: 10.1114/1.1574028

Tsubota, K., Suzuki, Y., Yamada, T., Hojo, M., Makinouchi, A., and Adachi, T. (2009). Computer simulation of trabecular remodeling in human proximal femur using large-scale voxel FE models: approach to understanding Wolff's law. *J. Biomech.* 42, 1088–1094. doi: 10.1016/j.jbiomech.2009.02.030

Turner, C. H., Rho, J., Takano, Y., Tsui, T. Y., and Pharr, G. M. (1999). The elastic properties of trabecular and cortical bone tissues are similar: results from two microscopic measurement techniques. *J. Biomech.* 32, 437–441. doi: 10.1016/S0021-9290(98)00177-8

van Arkel, R. J., Modenese, L., Phillips, A., and Jeffers, J. R. (2013). Hip abduction can prevent posterior edge loading of hip replacements. *J. Orthop. Res.* 31, 1172–1179. doi: 10.1002/jor.22364

van Lenthe, G., Stauber, M., and Muller, R. (2006). Specimen-specific beam models for fast and accurate prediction of human trabecular bone mechanical properties. *Bone* 39, 1182–1189. doi: 10.1016/j.bone.2006.06.033

van Rijsbergen, M., van Rietbergen, B., Barthelemy, V., Eltes, P., Lazáry, Á., Lacroix, D., et al. (2018). Comparison of patient-specific computational models vs. clinical follow-up, for adjacent segment disc degeneration and bone remodelling after spinal fusion. *PLoS ONE* 13:e0200899. doi: 10.1371/journal.pone.0200899

Villette, C. C. (2016). *Structural meso and microscale finite element based approaches for the prediction of bone architecture and fracture* (Ph.D. thesis). Imperial College London, London, United Kingdom.

Villette, C. C., and Phillips, A. T. M. (2015). Informing phenomenological structural bone remodelling with a mechanistic poroelastic model. *Biomech. Model. Mechanobiol.* 15, 69–82. doi: 10.1007/s10237-015-0735-4

Villette, C. C., and Phillips, A. T. M. (2018). Rate and age-dependent damage elasticity formulation for efficient hip fracture simulations. *Med. Eng. Phys.* 61, 1–12. doi: 10.1016/j.medengphy.2018.07.016

Wagner, D. W., Divringi, K., Ozcan, C., Grujicic, M., Pandurangan, B., and Grujicic, A. (2010). Combined musculoskeletal dynamics/structural finite element analysis of femur physiological loads during walking. *Multidisc. Model. Mater. Struct.* 6, 417–437. doi: 10.1108/15736101011095118

Wang, W., Wang, D., Groote, F. D., Scheys, L., and Jonkers, I. (2020). Implementation of physiological functional spinal units in a rigid-body model of the thoracolumbar spine. *J. Biomech.* 98:109437. doi: 10.1016/j.jbiomech.2019.109437

Weiner, D. K., Haggerty, C. L., Kritchevsky, S. B., Harris, T., Simonsick, E. M., Nevitt, M., et al. (2003). How does low back pain impact physical function in independent, well-functioning older adults? Evidence from the health ABC cohort and implications for the future. *Pain Med.* 4, 311–320. doi: 10.1111/j.1526-4637.2003.03042.x

Zaharie, D. T., and Phillips, A. T. M. (2018). Pelvic construct prediction of trabecular and cortical bone structural architecture. *J. Biomech. Eng.* 140:091001. doi: 10.1115/1.4039894

Zaharie, D. T., and Phillips, A. T. M. (2019). A comparative study of continuum and structural modelling approaches to simulate bone adaptation in the pelvic construct. *Appl. Sci.* 9:3320. doi: 10.3390/app9163320

Zhu, R., Zander, T., Dreischarf, M., Duda, G. N., Rohlmann, A., and Schmidt, H. (2013). Considerations when loading spinal finite element models with predicted muscle forces from inverse static analyses. *J. Biomech.* 46, 1376–1378. doi: 10.1016/j.jbiomech.2013.03.003

Conflict of Interest: The authors declare that the research was conducted in the absence of any commercial or financial relationships that could be construed as a potential conflict of interest.

frontiers in Bioengineering and Biotechnology

ORIGINAL RESEARCH
published: 26 May 2021
doi: 10.3389/fbioe.2021.669321

Biomechanical Effects of a Cross Connector in Sacral Fractures – A Finite Element Analysis

Meike Gierig[1†], Fangrui Liu[1†], Lukas Weiser[2], Wolfgang Lehmann[2], Peter Wriggers[1], Michele Marino[3] and Dominik Saul[2,4*†]*

[1] Institute of Continuum Mechanics, Leibniz University Hannover, Hanover, Germany, [2] Department of Trauma, Orthopedics and Reconstructive Surgery, Georg-August-University of Göttingen, Göttingen, Germany, [3] Department of Civil Engineering and Computer Science, University of Rome Tor Vergata, Rome, Italy, [4] Kogod Center on Aging and Division of Endocrinology, Mayo Clinic, Rochester, MN, United States

OPEN ACCESS

Edited by:
Enrico Dall'Ara,
The University of Sheffield,
United Kingdom

Reviewed by:
Peter Endre Eltes,
In Silico Biomechanics Laboratory,
National Center for Spinal Disorders,
Hungary
Tomaso Villa,
Politecnico di Milano, Italy

***Correspondence:**
Meike Gierig
gierig@ikm.uni-hannover.de
Dominik Saul
Dominik.Saul@med.uni-goettingen.de

[†] These authors have contributed equally to this work

Specialty section:
This article was submitted to Biomechanics, a section of the journal Frontiers in Bioengineering and Biotechnology

Received: 18 February 2021
Accepted: 30 April 2021
Published: 26 May 2021

Citation:
Gierig M, Liu F, Weiser L, Lehmann W, Wriggers P, Marino M and Saul D (2021) Biomechanical Effects of a Cross Connector in Sacral Fractures – A Finite Element Analysis. Front. Bioeng. Biotechnol. 9:669321. doi: 10.3389/fbioe.2021.669321

Background: Spinopelvic fractures and approaches of operative stabilization have been a source of controversial discussion. Biomechanical data support the benefit of a spinopelvic stabilization and minimally invasive procedures help to reduce the dissatisfying complication rate. The role of a cross connector within spinopelvic devices remains inconclusive. We aimed to analyze the effect of a cross connector in a finite element model (FE model).

Study Design: A FE model of the L1-L5 spine segment with pelvis and a spinopelvic stabilization was reconstructed from patient-specific CT images. The biomechanical relevance of a cross connector in a Denis zone I (AO: 61-B2) sacrum fracture was assessed in the FE model by applying bending and twisting forces with and without a cross connector. Biomechanical outcomes from the numerical model were investigated also considering uncertainties in material properties and levels of osseointegration.

Results: The designed FE model showed comparable values in range-of-motion (ROM) and stresses with reference to the literature. The superiority of the spinopelvic stabilization (L5/Os ilium) ± cross connector compared to a non-operative procedure was confirmed in all analyzed loading conditions by reduced ROM and principal stresses in the disk L5/S1, vertebral body L5 and the fracture area. By considering the combination of all loading cases, the presence of a cross connector reduced the maximum stresses in the fracture area of around 10%. This difference has been statistically validated ($p < 0.0001$).

Conclusion: The implementation of a spinopelvic stabilization (L5/Os ilium) in sacrum fractures sustained the fracture and led to enhanced biomechanical properties compared to a non-reductive procedure. While the additional cross connector did not alter the resulting ROM in L4/L5 or L5/sacrum, the reduction of the maximum stresses in the fracture area was significant.

Keywords: spinopelvic fracture, sacrum fracture, spinopelvic stabilization, finite element analysis, cross connector

INTRODUCTION

Representing the anatomical connection between the spine and pelvis, the sacrum acts as a biomechanical keystone. Anteriorly directed axial forces from the spinal column, the body weight (downward directed) and resistance to the ground (upward directed) act on the sacrum and its ligamentous fixation (Rizkalla et al., 2019). But the constant force transmission to the lower extremities makes the sacrum a highly stressed bone, with clearly defined weak points along the sacral foramina, notably prone to fragility fractures (Pascal-Moussellard et al., 2016; Borgström et al., 2020). Sacrum fractures lead to a severe pattern of injury which is highly unstable and associated with sacral nerve root injury, severe bleeding and soft tissue damage (Williams and Quinnan, 2016). The treatment of these injuries always has been a root of controversial discussion. Both the decision on whether to operate and on the way of stabilization have been diversely debated (Williams and Quinnan, 2016; Guerado et al., 2018). Loss of reduction in 26% and a malunion rate of 44% clarify that with a single iliosacral screw alone, the vertically unstable pelvis is not sufficiently treated (Keating et al., 1999).

Focusing on complex sacrum fractures, two entities need to be discerned, the osteoporotic fragility fracture and the high-energy fracture in the young. Since the fragility fractures of the pelvis have been extensively described by Rommens et al. (2015), they are getting more into the focus of trauma surgeons in developed countries due to the demographic transformation (Borgström et al., 2020). The osteoporotic sacral insufficiency fracture is reported with an incidence of 1–5% (Tsiridis et al., 2006). In this special multimorbid collective, surgical intervention must be narrowed down to the outright essential.

Apart from that, the complex traumatic sacrum fracture beside the rare entity of spinopelvic discontinuation in severe trauma patients depict utterly different fracture patterns. The traumatic central sacrum fractures are a condition that can be stated generally rare with an incidence of 2 per 100, 000 (Beckmann and Chinapuvvula, 2017), while within pelvic trauma patients, the unstable sacral fracture has an incidence of 17–30% (Jazini et al., 2017a). Regarding the operative treatment, complex fractures cannot adequately be reduced by only iliosacral screws but need vertical support and the neutralization of shearing forces (Guerado et al., 2018). In the mostly young patient with proper bone, the early mobilization and load/weight bearing are main factors to aim at in the operative therapy, while in the osteoporotic patient the immediate mobilization is crucial for the long-term outcome (Williams and Quinnan, 2016; Pulley et al., 2018).

The surgical technique that is mostly favored in complex spinopelvic injuries is the spinopelvic fixation from L4/5 to the ilium or the spinopelvic fixation from L4/5 to the ilium with a cross connector (CC). In terms of H-fractures of the sacrum, the CC is thought to stabilize the fracture components and prevent further discontinuation from the spine to the pelvis. After a posterior or anteroposterior stabilization, a rapid fusion of the bone and short postoperative immobilization of the patient are intended in order to avoid immobilization-induced complications (Wagner et al., 2015). This leads to a delicate balance between the stability of the construct and potentially occurring material fatigue (Melkerson, 2003).

While the biomechanically favorable impact of the lumbopelvic stabilization has been proven, the addition of a CC has not been biomechanically assessed to date. Nonetheless, there is reliable data that bilateral stabilization is necessary to immobilize the sacroiliac joint (Jazini et al., 2017a; Lindsey et al., 2018). In theory, after proximal L5 fixation, shearing and rotating forces could be addressed by cross connectors (Guerado et al., 2018). Thus, in lumbopelvic instrumentation, the addition of a cross-connecting device was mentioned by Bellabara et al. to "further stabilize . . . [the] hemipelvis" (Bellabarba et al., 2006). Similarly, a new minimally invasive approach that was introduced by the Hannover group used percutaneous L3 and L4 as well as iliac screws with long rods, connected with a 5.5 mm crossing rod in order to reach a "high construct rigidity" in lumbosacral fractures (Decker et al., 2019). The biomechanical proof of that rigidity remains to be elucidated.

If the surgeon decides to add a CC to his spinopelvic construct, he has to consider two facts. First, that there is no biomechanical approval of this concept. Second, the raised level of infection rate after the utilization of a CC with a reported rate of postoperative infection and healing disturbances around 16-38% due to the larger incision (Bellabarba et al., 2006; Schildhauer et al., 2006; König et al., 2012). There has been a long-lasting debate on the reasons of infection after spinopelvic- and cross-connector-application in spinal surgery, even after minimally invasive approaches have been widely established (Bellabarba et al., 2006; Williams and Quinnan, 2016; Barcellos et al., 2017; Jazini et al., 2017b; Decker et al., 2019). This is due to the preparative extent for an insertion of a cross connector, as it is challenging to insert it in a minimally invasive way. In cases of spinal decompression, the extensive approach is done either way, but otherwise the lumbopelvic construct can also be introduced in a minimally invasive approach without cross connectors. The price of additional stabilization comes with the danger of revision surgery, which especially in the elderly population can be a life-threatening term.

To determine the value of a CC in the clinical setting, we first created a finite element model out of patients' CT scans (before and after spinopelvic stabilization) and validated its anatomical and biomechanical properties. The patient suffered from a Denis zone I (AO: 61-B2) sacrum fracture. Second, we assessed the effect of the spinopelvic stabilization system on the lumbopelvic area consisting of the vertebra L5, the disc L5/S1, the device itself and the fracture area. The statistical significance of numerical evidence was evaluated by addressing uncertainties in material properties and different levels of osseointegration.

Finally, we validated the impact of an additional CC on this spinopelvic stabilization. We sought to elucidate whether a CC was able to additionally reduce the appearing forces in the sacral fracture area and prevent further dissociation.

MATERIALS AND METHODS

General Features and Subjects

Finite element models (FE models) were based on computed tomography (CT) images, built from patients from the University Medical Center Goettingen, Germany. CT scans that covered the whole pelvis and L1-L5 were selected for construction of the FE model. The geometries of sacrum and both iliac bones were defined from a patient (preoperatively without device, postoperatively with device including a CC in a nondisplaced sagittal sacrum fracture) who was a 66-year-old man (**Figures 1A,B**).

To simulate the preoperative spinal movement, all parts of the device have been removed. In analogy, the simulations without CC were conducted on the same geometrical model removing the CC. To easier visualize the models and since the device is implanted in L5, L1-L3 have been cut out and just L4-L5 and the pelvis were considered as bony structures in the numerical model.

The models were generated modeling the intervertebral disks (IVD) with annulus, nucleus and endplates, according to Spina and El Bojairami (El Bojairami et al., 2020; Spina et al., 2020). The ligamentous stabilization was considered taking primary ligament groups into account, which are the interspinous ligament (ISL), anterior sacroiliac ligament (ASL), long posterior sacroiliac ligament (LPSL), short posterior sacroiliac ligament (SPSL), supraspinous ligament (SS), sacrotuberal ligament (ST), iliolumbal ligament (ILL), anterior longitudinal ligament (ALL), interosseous sacroiliac ligament (ISIL), ligamentum flavum (LF), posterior longitudinal ligament (PLL), sacrospinal ligament (SL), and sacrotuberal ligament (TL).

The three models (without device; with device but without CC; with device and CC) were simulated applying three different loading conditions: flexion, right lateral bending, and left axial rotation.

The outcome parameters were range-of-motion (ROM) and maximum stresses. Depending on the area and the quantity of interest, the analyzed stress measures were von Mises stresses and maximum principal stresses (absolute values, Abs), with the latter being the maximum or minimum principal stresses depending on which absolute value is higher. The areas-of-interest were the disk L5/S1, the vertebral body L5, the fixation device and the fracture area. The overall effect of the CC on the disk L5/S1, L5, the fixation device, and the fracture zone was statistically evaluated in different bone qualities.

Volumes Reconstruction and Surfaces

Computerized tomography images consisted of 0.35 × 0.35 mm resolution and 0.5 mm slide thickness. The images were segmented using a combination of thresholding and manual techniques in MeVisLab 3.0.2 (MeVis Medical Solutions AG, Bremen, Germany) to create the bony geometries. 3D, triangular surface meshes of sacrum, ilium and spinal vertebrae (L4-pelvis)

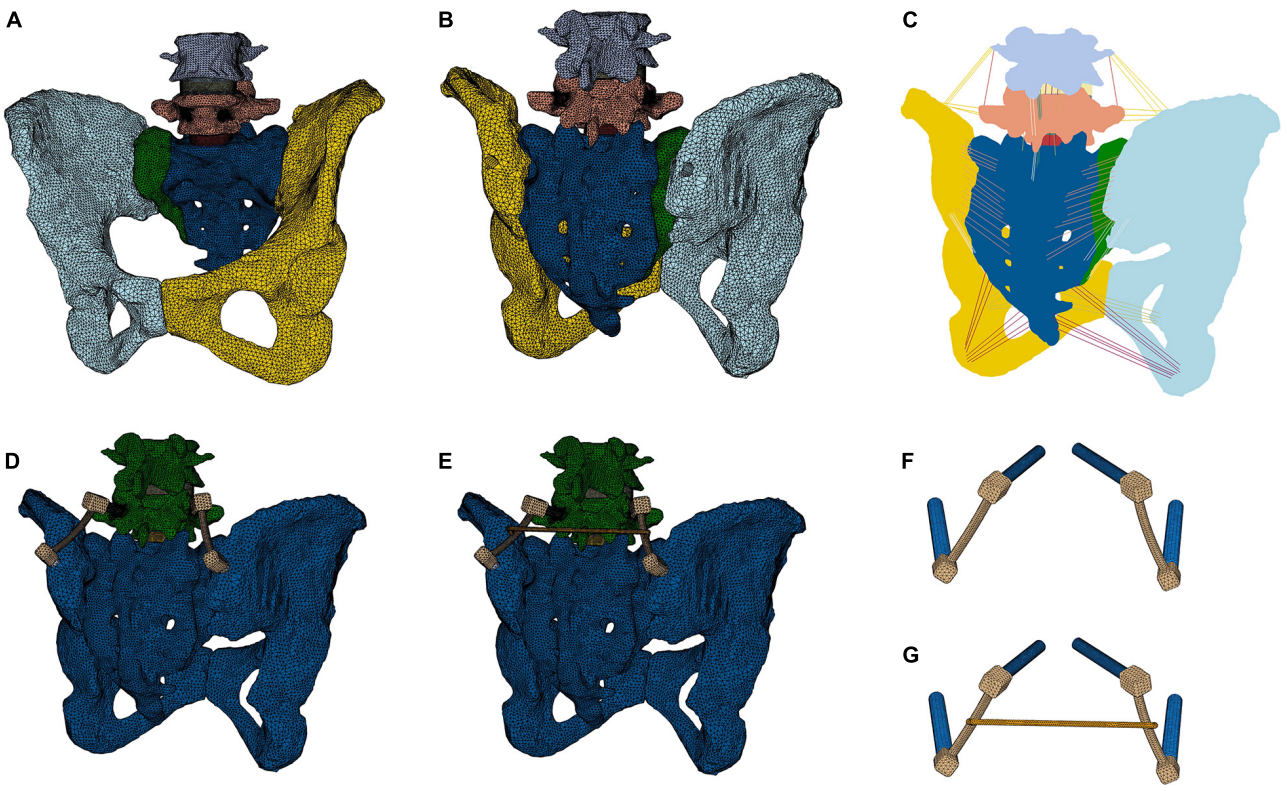

FIGURE 1 | Creation of a finite element model of the lumbopelvic area. The view from anterior **(A)** and posterior **(B,C)** and all ligamentous connections are demonstrated **(C)**. A lumbopelvic stabilization device from L5 to the Os ilium without **(D,F)** and with a cross connector **(E,G)** was modeled.

were exported. Since soft tissue can hardly be detected in CT images, the geometries of the intervertebral disks (IVD) were created in Autodesk Inventor 2016, based on the surface geometries and spatial positions of the lumbar bodies as well as considering lumbar anatomy in general. The meshes were then generated in Hypermesh 2019 (Altair Engineering, Troy, MI, United States) using triangular elements.

The facet joints between the vertebrae were considered as face-to-face contact with Coulomb friction and a friction coefficient of 0.1. The intervertebral disks were tied to the vertebra. The geometries and spatial positions of IVD and spatial positions of ligaments were approved by the clinical authors (DS, LW, and WL).

The surfaces of the fixation device and the screws were created in Hypermesh taking the dimensions from the device presented in section "Device." The screws were tied to the device. Screws have been inserted in the bones by creating holes in the initial geometry (initially reconstructed as intact from CT images) via standard Boolean operations implemented in Hypermesh. The screw thread was not geometrically modeled. For the simulations with the CC, the CC was tied to the device.

Meshing

The geometries of the bony structures, IVD and fixation device were spatially discretized by means of Lagrange tetrahedral elements with a linear interpolation of the displacement field in a standard Galerkin finite element formulation. All ligament groups (ISL, ASL, LPSL, SPSL, SS, ST, ILL, ALL, ISIL, LF, PLL, SL, and TL) were represented with two-noded truss elements (**Figure 1C** and **Table 1**). All meshing operations were performed in Hypermesh.

To distinguish between cortical and trabecular bone, the mesh of the bony structure was divided into a 1.5 mm thick outer domain for cortical and an interior for trabecular bone structure according to Yamamoto et al. (1989) and Lindsey et al. (2018). To consider different osseointegration levels, a 1.5 mm thick bone layer around the screws with separate material properties was defined.

Overall, each numerical model has been discretized with around 1.062.062 elements, of which 902.944 for the bony structures, 84.965 for the IVD, 73.997 for the fixation devices and 156 for the ligaments. Accordingly, the total number of degrees of freedom of each model is around 1.115.556.

Material Properties

The model and material properties were set based on previously published literature (Yamamoto et al., 1989; Lindsey et al., 2018). Linear elastic isotropic constitutive models were assigned to both cortical and trabecular bone. The annulus, nucleus, and endplates of IVDs are also modeled as isotropic in agreement with Shin et al. (2007, 2018) and El Bojairami et al. (2020). An isotropic modeling approach is chosen for the fibrosus annulus in the IVD, instead of an anisotropic one, because the directionality of fibers has been shown to have a limited influence on the mechanism of load transfer between vertebrae (Mengoni et al., 2016). The ligaments were modeled as non-linear spring elements using displacement-force load curves derived from the literature (Rohlmann et al., 2006b; Ayturk and Puttlitz, 2011; Finley et al., 2018).

The reference values of parameters employed in numerical simulations (if not differently specified) are listed in **Table 1**. In order to analyze the robustness of numerical results with uncertainties in parameters' values (i.e., uncertainties due to patient-specific material properties), we have also performed a campaign of numerical simulations by varying each parameter as reported in **Table 2**. In the parametric analysis, a single parameter was varied in each simulation and fifteen simulations were performed for each case study.

Model Validation

The range of motion obtained in numerical simulations was compared with the one reported in previously published experimental and numerical studies (Yamamoto et al., 1989; Tullberg et al., 1998; Ivanov et al., 2009; Jahng et al., 2013; Dreischarf et al., 2014; Kyaw et al., 2014; Lindsey et al., 2015; Nagamoto et al., 2015; Coombs et al., 2017; Jaramillo and Garcia, 2017; Kibsgård et al., 2017; Joukar et al., 2018; Mahato et al., 2019; **Supplementary Figures 1, 4**).

Biomechanical Assessment of Boundary and Loading Conditions

For all models, couples of 10 Nm were applied to produce flexion (in the sagittal plane), right lateral bending (in the frontal plane) and left axial rotation (in the transverse plane) (Yamamoto et al., 1989; Lindsey et al., 2015). The loads were applied using a master node at the middle of the top surface of L4. For realistic mechanical analyses, the force given by the body mass of thorax and head (300 N) – according to Danielson (Danielson et al., 1998) and Sterba (Sterba et al., 2018) – has been incorporated distributing the compressive load on the upper L4 surface in reference normal direction. Zero displacement boundary conditions were introduced in the joint between pelvis and femur. All models were analyzed in Abaqus (Dassault Systèmes, Vélizy-Villacoublay, France) and results were processed in Microsoft Excel (Microsoft Corporation, Redmond, WA, United States).

Three repair strategies have been compared: (1) without fixation, (2) fixation without CC, (3) fixation with CC. Within each of these situations, three loading conditions have been mathematically assessed: (1) anteroposterior bending, (2) lateral bending, and (3) torsion.

Lumbopelvic Stabilization

The simulated operative procedure was a lumbopelvic stabilization from L5 to the ilium with a pedicle screw on each side of L5 and one screw on each side to the ilium (IS screws), connected with a long rod on each side. These two long rods were connected with CC or not connected to each other (**Figures 1D,E**). The procedure was simulated according to Kim and Benzel (Benzel, 1999; Kim, 2006). Briefly, a pedicle screw was inserted at the dorsal facet of the mammillary process through the isthmus of the pedicle into the vertebral body without penetrating the spinal canal. A second screw was implanted from

TABLE 1 | Material parameter values employed in numerical simulations.

Part	Young's modulus (MPa)				Poisson's ratio	References	Element type
L4, L5, S1, Pelvis							
Cortical bone			10,000		0.3	(Panjabi et al., 1992; Rohlmann et al., 2006b; Rohlmann et al., 2006a; Zhang et al., 2009; Becker et al., 2020)	C3D6
Trabecular bone			100		0.2		C3D4
Intervertebral disc							
Endplate			100		0.4	(Zhong et al., 2006; Kurutz and Oroszváry, 2010)	C3D4
Annulus			4.2		0.45	(Zhang et al., 2009)	C3D4
Nucleus			4		0.49	(Lavaste et al., 1992)	C3D4
Ligaments (E_{lig})	<2.5%	2.5-5%	5%-10%	>10% strain		(Goel et al., 1993)	
ISL	200	285	525	510	0.3		T3D2
ASL	39	55	103	100	0.3		T3D2
LPSL	29	40	75	73	0.3		T3D2
SPSL	13	18	33	34	0.3		T3D2
SS	26	37	68	66	0.3		T3D2
ST	17	24	45	44	0.3		T3D2
ILL	40	57	105	102	0.3		T3D2
ALL		7.8 (<12% strain)		20(>12% strain)	T3D2		T3D2
ISIL		10 (<14% strain)		11.6(>14% strain)	T3D2		T3D2
LF		15 (<6.2% strain)		20 (>6.2% strain)	T3D2		T3D2
PLL		10 (<11% strain)		20 (>11% strain)	T3D2		T3D2
SL		8 (<20% strain)		15 (>20% strain)	T3D2		T3D2
TL		10 (<18% strain)		58.7 (>18% strain)	T3D2		T3D2
Implant							
Screws		105,000			0.36		C3D4
Device		210,000			0.29		C3D4
Connector		102,500			0.36		C3D4

TABLE 2 | Material properties uncertainties employed for the parametric analysis.

	Min (MPa)	Middle (MPa)	Max (MPa)	References
Cortical bone	5000	10000	12000	Panjabi et al., 1992; Rohlmann et al., 2006a,b; Zhang et al., 2009; Yang et al., 2016; Becker et al., 2020
Endplate	24	100	1000	Benzel, 1999; Jaramillo and Garcia, 2017; Mahato et al., 2019
Nucleus	1	4	10	Lavaste et al., 1992; Chen et al., 2008; Zhang et al., 2009
Annulus	2	4.2	6	Lavaste et al., 1992; Chen et al., 2008; Zhang et al., 2009
Ligaments	0.9 E_{lig}	E_{lig}	1.1 E_{lig}	

the posterior iliac crest, directing ventral and caudal toward the anterior inferior iliac spine. On each side, a long rod was used to connect these two screws (Aebi et al., 2007). All simulated surgeries were approved by the clinical authors (DS, LW and WL) and applied as in the postoperatively performed CT scans.

Device

The device model is constructed as an approximation of a device delivered by DePuySynthes (Warsaw, Indiana, United States). It consists of two L5 pedicle screws (titanium alloy), two iliac screws (titanium alloy), a rod with cross-link clamps (titanium, stainless steel) and a cross connector (titanium). The dimensions of the model are presented in **Supplementary Figure 5**. The screws are simplified as cylinders.

Levels of Osseointegration

Nine diverse levels of osseointegration of the devices have been taken into consideration according to Panjabi et al. (1992), Rohlmann et al. (2006a,b), and Zhang et al. (2009) from low integration (case 1), where the interface between the screws and the bone is equal to cancellous bone (100 MPa), to intermediate integration (cases 2 to 8), where the interface stiffness is in between cancellous and cortical bone (i.e., between 100 MPa and 10.000 MPa), and complete integration (case 9), where the interface is equal to cortical bone (10.000 MPa). For each

level of osseointegration, the values of the material constants of the screw-bone interface are listed in **Table 3**. If not explicitly specified, a level of osseointegration equal to 10.000 MPa (cortical bone) has been employed in the numerical simulation.

Range of Motion

Assessing the resulting range of motion (ROM) after spinopelvic stabilization was thought to deliver information on the impact of the cross connector on spinal mobility. For this purpose, on the middle top of L4 (a), L5 (b) and the sacrum (c), three distinctive measuring (Lagrangian) material points were identified. The angles that were produced by the vector $\underset{(ab)}{\longrightarrow}$ before and after the simulation depicted the range of motion from L4 to L5. The angle produced by the vector $\underset{(bc)}{\longrightarrow}$ before and after the simulation depicted the range of motion from L5 to the sacrum (**Figures 2A,B**). In analogy to Hammer and Klima, the sacroiliac joint motion was assessed and compared to the values presented in the literature (**Supplementary Figure 4**; Hammer and Klima, 2019).

Fracture Model

To examine the effect of the CC on the sacrum fracture itself, a fracture pattern was created in the sacrum, deduced from the most common sacrum fracture (**Figures 2K,L**). The fracture was simulated by a separation of the elements in the FE mesh along the prescribed pattern. A face-to-face contact with Coulomb friction and a friction coefficient of 0.2 was implemented between the two bony surfaces. In what follows, when referring to the fracture area, the separation surface at the fracture is meant. To assess the effect of the fixation procedure on the fracture area, the interfragmentary movement (IFM) is analyzed. In analogy to Carrera, four points at the fracture side were selected and the displacements due to the applied moments between initially superimposed points were calculated (Carrera et al., 2016; **Figure 7**).

Data Analysis

The resulting maximum stresses for each repair strategy (without fixation, fixation without CC, fixation with CC), for all three loading conditions (Flexion, lateral bending and torsion) and for the nine levels of osseointegration (*min* with interface stiffness comparable to cancellous bone, *average* with stiffness between cancellous and cortical bone and *max* with stiffness comparable to cortical bone) were calculated using post-processing routines in Abaqus (Dassault Systèmes, Vélizy-Villacoublay, France).

Statistical Analyses

Statistical analysis was performed using a two-way analysis of variants (ANOVA)/Mixed Model with post-hoc *t*-test and a Tukey correction for multiple hypothesis testing according to the recommendations of Lakens (Lakens, 2013) with GraphPad Prism version 9.00 (GraphPad Software, Inc.). In the violin plots, the mean, 25th as well as 75th percentile are displayed.

RESULTS

Effect of the Fixation Procedure on the Ranges of Motion

The ROM were compared for the L4/L5 movement (**Figures 2B–D**, vector $\underset{(ab)}{\longrightarrow}$), the L5/S1 movement (**Figures 2E–G** vector $\underset{(bc)}{\longrightarrow}$), and the sacroiliac joint movement (**Figures 2H–J** vector $\underset{(SI)}{\longrightarrow}$).

The addition of a fixation device led to a substantial decrease in ROM in the movement from L5 to the sacrum (**Figures 2E,F**). Similarly, decreased ROM can be seen in the sacroiliac joint (**Figures 2H–J**). The addition of a CC (**Figures 2D,G,J**) compared to the situation without the CC (**Figures 2C,F,I**), did not change the residual ROM substantially. The addition of a fixation did not result in a substantial change in ROM from L4 to L5 (**Figures 2B,C,D**).

Model Validation: ROM

We compared the range of motions (ROMs) of our finite element model for each movement with the ones reported on the basis of experimental or numerical studies by Yamamoto et al. (1989); Hungerford et al. (2004), Ivanov et al. (2009); Dreischarf et al. (2014), Kyaw et al. (2014); Lindsey et al. (2015), Nagamoto et al. (2015); Coombs et al. (2017), Hu et al. (2017); Jaramillo and Garcia (2017), Kibsgård et al. (2017); Cross et al. (2018), Joukar et al. (2018), and Mahato et al. (2019) (ROM for L4/L5 and L5/S1: **Supplementary Figure 1**; ROM for SI: **Supplementary Figure 4**). In the L4/L5 movement (vector $\underset{(ab)}{\longrightarrow}$), and L5/S1 movement (vector $\underset{(bc)}{\longrightarrow}$), our model was in excellent agreement with the literature for flexion and lateral bending, while showed slightly higher values for axial rotation (**Supplementary Figure 1**). Considering that the present work addresses a single case study of a diseased patient, the developed finite element model shows biomechanical performance in general agreement with literature data.

Effect of the Fixation Procedure on the Stresses in the Intervertebral Disc L5/S1

The consequences of the fixational device on the intervertebral disc were firstly evaluated. Since nucleus pulposus and annulus fibrosus showed similar values and tendencies, we decided to

TABLE 3 | Variations of the Young's modulus (MPa) and Poisson's ratio of the interface between the screws and the bone for the osseointegration analysis.

Cases	1	2	3	4	5	6	7	8	9
Young's modulus (MPa)	100	250	500	750	1000	2500	5000	7500	10000
Poisson's ratio	0.2	0.21	0.23	0.24	0.25	0.26	0.28	0.29	0.3

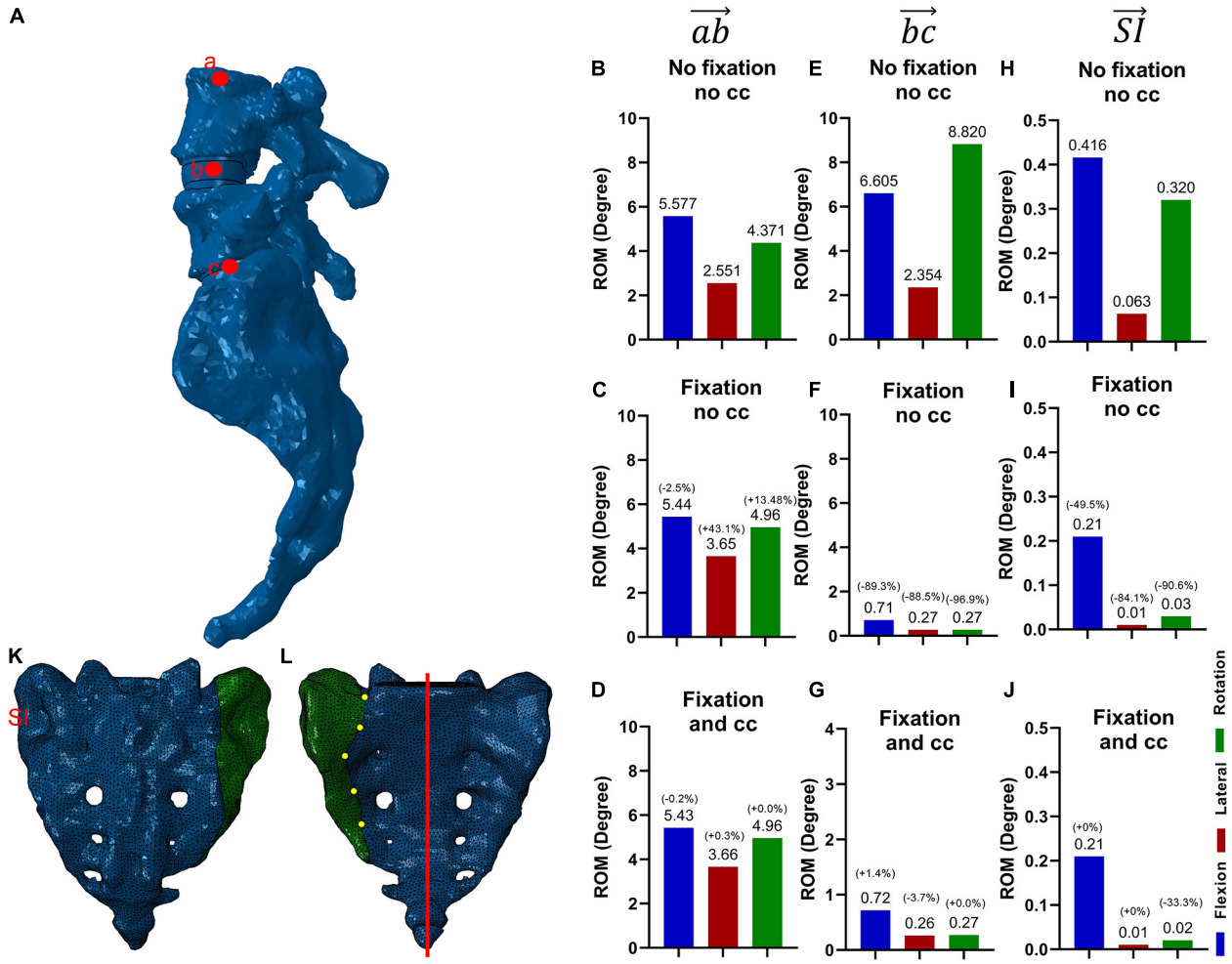

FIGURE 2 | Lumbopelvic axis and three measuring points for range of motion (ROM) **(A)** and corresponding motion (for all three conditions and vector $\underset{(ab)}{\longrightarrow}$ **B–D**, vector $\underset{(bc)}{\longrightarrow}$ **E–G**, $\underset{(SI)}{\longrightarrow}$ **H–J**) and addition of a central vertical sacral fracture (Denis zone I, K, L). The range of motion was assessed along the vector $\underset{(ab)}{\longrightarrow}$ for the motion from L4 to L5 without fixation **(B)**, with fixation without **(C)** and with **(D)** the cross connector, whereas the motion from L5 to the sacrum is labeled by the vector $\underset{(bc)}{\longrightarrow}$, again measured without fixation **(E)**, with fixation without **(F)** and with **(G)** the cross connector. The SI ROM is measured by the vector $\underset{(SI)}{\longrightarrow}$, and depicted in **H–J**. A central transalar sacrum fracture, Denis classification zone I (identified by yellow dots), was created to simulate the most common central sacrum fracture type **(K,L)** (Denis et al., 1988). The red line in L depicts the cut surface for **Figures 6D–F**.

just show the nucleus pulposus. Without fixation, the maximum principal stress was the highest in flexion, followed by rotation and lateral bending (**Figure 3A,D**). After adding a fixation device, the maximum principal stresses were reduced for all loading conditions, and there were no large differences with and without the use of a cross connector (**Figures 3B,C,E,F**).

Effect of the Fixation Procedure on the Stresses in the Fifth Vertebra (L5)

Next, the effects of a lumbopelvic stabilization on the fifth vertebra were assessed in terms of principal stresses (**Figure 4**). A fixation reduced the maximal principal stresses in flexion and axial rotation by more than 30% and in lateral bending by 28.6%. There were only marginal differences with and without the use of a cross connector (**Figures 4B,C,E,F**).

Effect of the Fixation Procedure on the Stresses in the Device

To guarantee a functional L5/Ilium stabilization and intact cross connector, the maximum "von Mises" stresses on the device were evaluated. In **Figure 5**, the stresses in the device were assessed with and without the cross connector. The maximum stress was similar in all loading cases and the addition of a cross connector did not lead to substantial lowering of the maximum "von Mises" stresses (**Figures 5A–D**). Material failure is one reason for post-surgery complications. Thus, the strength of the device is analyzed to ensure the resistance of the device by comparing the stresses in the screws with values reported by Amaritsakul and Shin (Amaritsakul et al., 2014; Shin et al., 2018). In these articles, the strength of pedicle screws (titanium alloy) of multiple shapes and dimensions were compared. Stresses

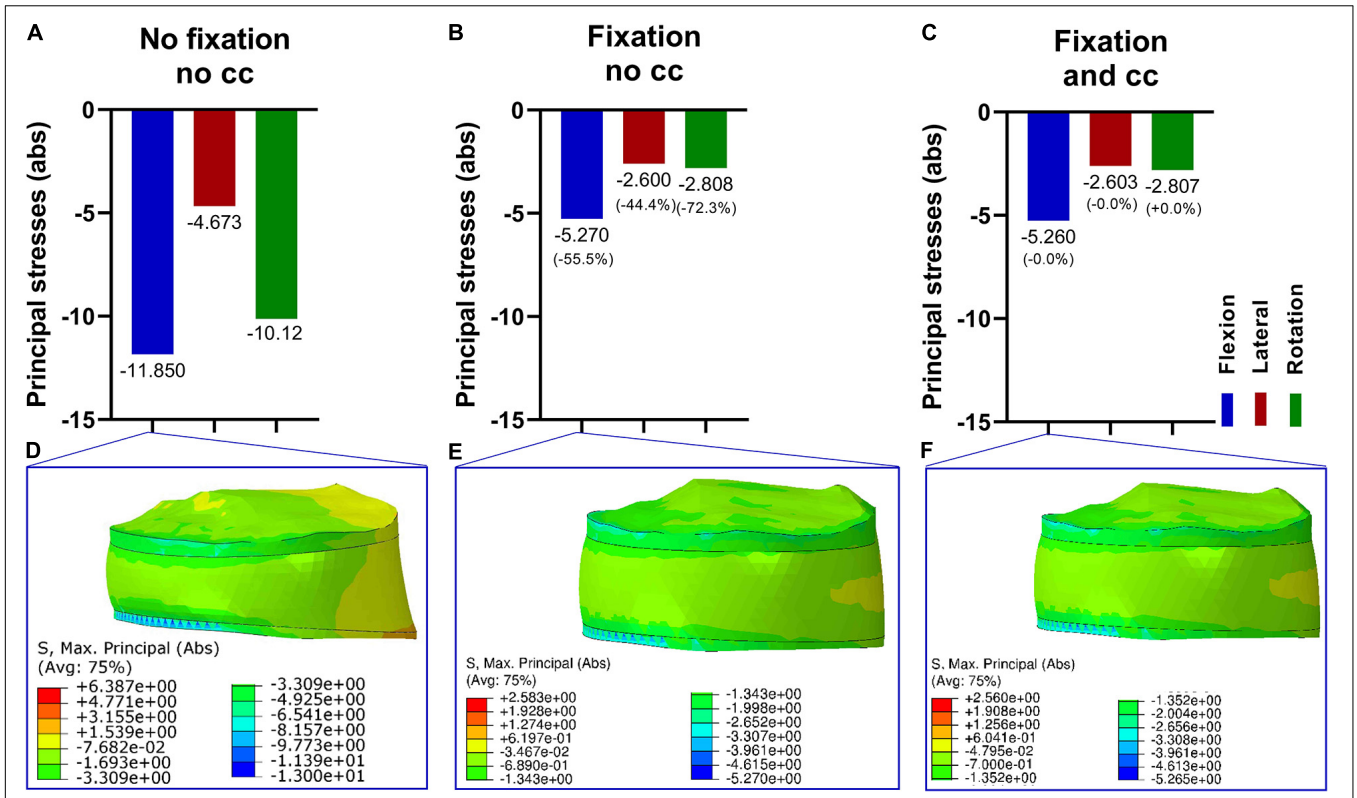

FIGURE 3 | Maximum principal stresses (absolute values) in the intervertebral disk L5/S1 (nucleus pulposus part) in three loading conditions **(A–C)** and corresponding stress distribution exemplarily depicted in the F/E situation **(D–F)**. Without fixation **(A,D)**, the resulting principal stresses were higher compared to the fixation procedure **(B,C,E,F)**. Upon fixation without cross connector **(B,E)** and with cross connector **(C,F)**, the differences appeared to be marginal.

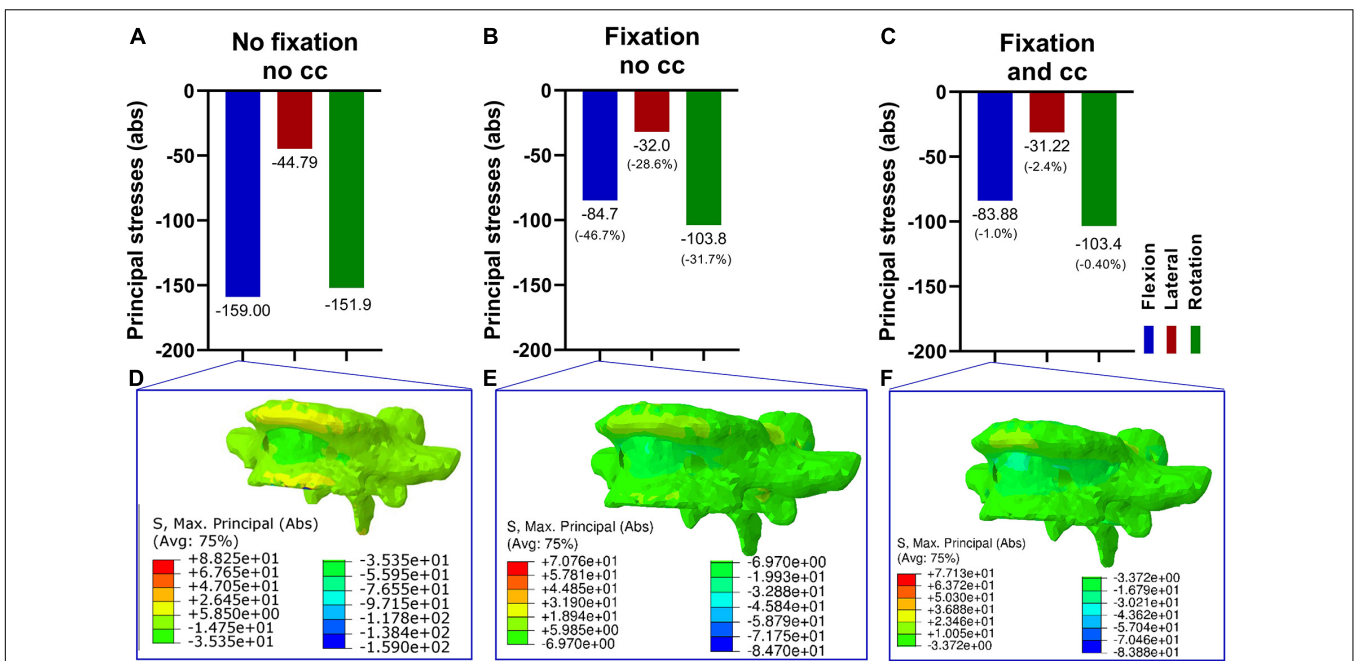

FIGURE 4 | Maximum principal stresses (absolute values) in the fifth vertebra in three loading conditions **(A–C)** and corresponding stress distribution exemplarily depicted in the F/E situation **(D–F)**. Without fixation **(A,D)**, the resulting principal stresses in F/E and rotation were higher compared to the fixation procedure **(B,C,E,F)**. Upon fixation without cross connector **(B,E)** and with cross connector **(C,F)**, the differences appeared to be marginal.

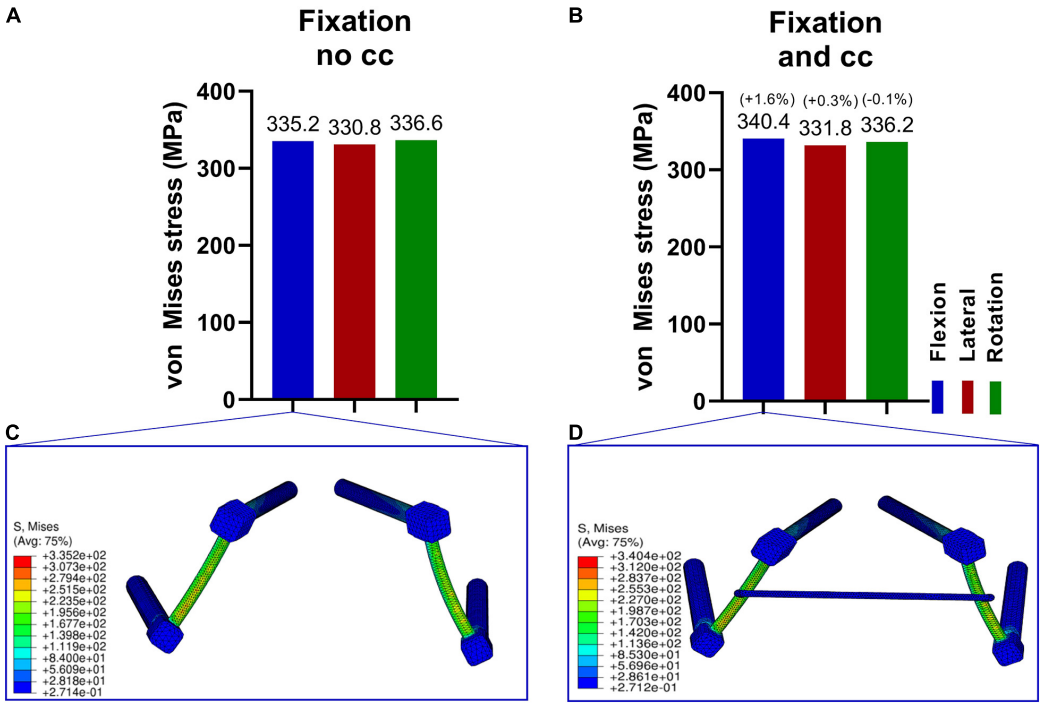

FIGURE 5 | Maximum von Mises stresses in the fixation device in three loading conditions **(A,B)** and corresponding stress distribution exemplarily depicted in the F/E situation **(C,D)**. The stresses in the fixation without cross connector **(A,C)** and with cross connector **(B,D)** are similar for all loading cases.

in the herein simulated screws (**Supplementary Figure 5B**) is in all loading cases much lower than the failure values reported by Amaritsakul (>500 MPa and in the range 1000–3000 MPa for several types of screws) and in the range of the values reported by Shin, that is around 100 MPa (Amaritsakul et al., 2014; Shin et al., 2018). The maximum stresses in the device occurs in the rods. The presented values are in a range in which no failure of such materials is to be expected.

Effect of the Fixation Procedure on the Fracture Area

The simulated fracture area was analyzed in terms of the maximum principal stresses and interfragmentary movements (IFM) in all conditions. While the fixation alone reduced the stresses under lateral bending and torsion substantially, the stresses increased in flexion. The addition of a cross connector reduced the stresses in the fracture area for all loading cases (**Figures 6A–F**).

In addition to the stress analyses, the interfragmentary movement (IFM) was analyzed according to Carrera et al. (2016). The corresponding displacements are presented in **Figure 7**. The fracture is significantly stabilized by a fixation. In contrast, the effect of the cross-connector is not that evident for the IFM. Overall, the effect of the cross-connector seems to be beneficial in terms of fracture area stress, while the interfragmentary movement is not reduced using a CC.

Statistical Analysis of Osseointegration Levels

To assess if the obtained differences were attributable to the cross connector, inter-case variability was introduced on the level of osseointegration. This might be relevant since osseointegration affects the way loads are transferred through the device. For this purpose, nine different levels of osseointegration (from low = 100 MPa/low bone quality/spongious bone to high = 10.000 MPa/high bone quality/spongious bone, **Table 3**), have been assessed according to Becker et al. (2020).

A two-way analysis of variance (ANOVA) was conducted to estimate whether differences between the two conditions (with and without cross connector [CC]) were effective or apparent. If so, a post-hoc *t*-test was performed to quantify these differences. The analysis addresses the axial rotation case.

The addition of a cross connector did not increase the resulting stress in the disk L5/S1 (**Figure 8A** $p = 0.2721$), and differences in L5 and the fixational device were not significant as well (**Figure 8B** $p = 0.0566$ and **Figure 8C**, $p = 0.4957$, respectively). On the other hand, in the fracture area, the cross connector reduced the occurring principal stresses significantly, with a difference on mean values corresponding to around a 10% variation (**Figure 8D**, $p < 0.0001$, $\delta = 3.392$).

Statistical Analysis of Material Properties Uncertainties

In order to investigate if the afore-traced comparison between different fixation procedures were robust also with respect to

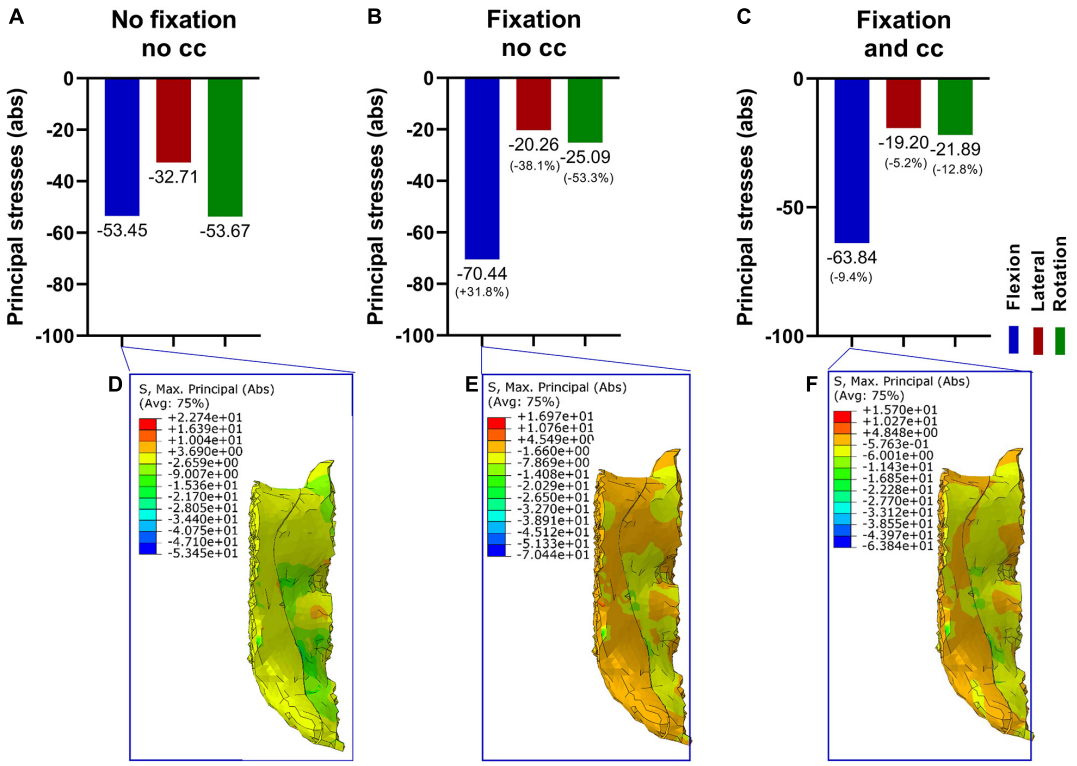

FIGURE 6 | Maximum principal stresses (absolute values) in the fracture area **(A–C)** and corresponding stress distribution exemplarily depicted in the flexion situation **(D–E)**. The fixation alone reduced the maximum stresses in lateral bending and rotation **(A,B,E)**, and a cross connector further reduced the occurring maximum stresses in all loading cases **(C,F)**.

uncertainties in material properties, additional finite element analyses were conducted for the axial rotation case by varying material properties within the ranges reported in **Table 2**. Therefore, an ANOVA test was performed on the biomechanical outcomes obtained with and without the cross connector.

Firstly, the effect on the stabilization obtained by the fixation procedure was assessed in terms of range of motion. Results (**Supplementary Figure 2**) indicate that, although the addressed variation of material properties might change the ROM up to 30%, the comparison of ROM between the case without CC and with CC is unaffected.

Moreover, stresses in the IVD L5/S1, L5, fracture and fixation are investigated. Results (**Supplementary Figure 3**) indicate that, despite the wide variations of model parameters, the stress comparison between the case without and with CC is not affected by such variations in the L5/S1 disk (**Supplementary Figure 3A**, $p = 0.2806$). However, the differences with and without the CC were small, but significant in L5 and the fixation device (L5: **Supplementary Figure 3B**, $p < 0.0001$, $\delta = 0.446$, fixation: **Supplementary Figure 3C**, $p = 0.0024$, $\delta = 0.473$). Comparable to the results from different osseointegration levels, contrasting different material properties likewise showed a significant difference in the fracture area with and without the CC, with about 10% difference on mean values (**Supplementary Figure 3D**, $p < 0.0001$, $\delta = 2.727$).

DISCUSSION

The unstable sacrum fracture needs operative reduction and biomechanical stability in order to heal properly. The naturally high complication and infection rate after operative procedures in this anatomical location demands smallest possible incisions yet providing most stability (Bellabarba et al., 2006).

Surgery of the lower spine and pelvis faces the difficulty of disparate patient cohorts: The young patient with proper bone parameters and the osteoporotic patient suffering a fragility fracture. Absolute stability of the surgical treatment is paramount in both. The more complex a sacrum fracture (or spinopelvic dissociation) gets, the more elaborate the fixation needs to be. Beginning with simple percutaneous iliosacral screws for uncomplicated sacrum fractures, the H-shaped sacrum fracture requires sophisticated spinopelvic stabilization with pedicle screws in L4 or L4 and L5 and a sacral-alar-iliac fixation, both of which are connected with a vertical rod. With such a bilateral construct, the applying vertical forces are adequately addressed (Jazini et al., 2017a). The armamentarium of spinal surgery also contains the possibility of adding a cross connector to these bilateral rods.

We created a finite element model to verify the stabilizing effect of a spinopelvic device (two 7.0 mm L5 screws, two 9.00 mm iliac screws) and assess the accessory effect of a CC in this anatomical area. Therefore, three load cases, compression with

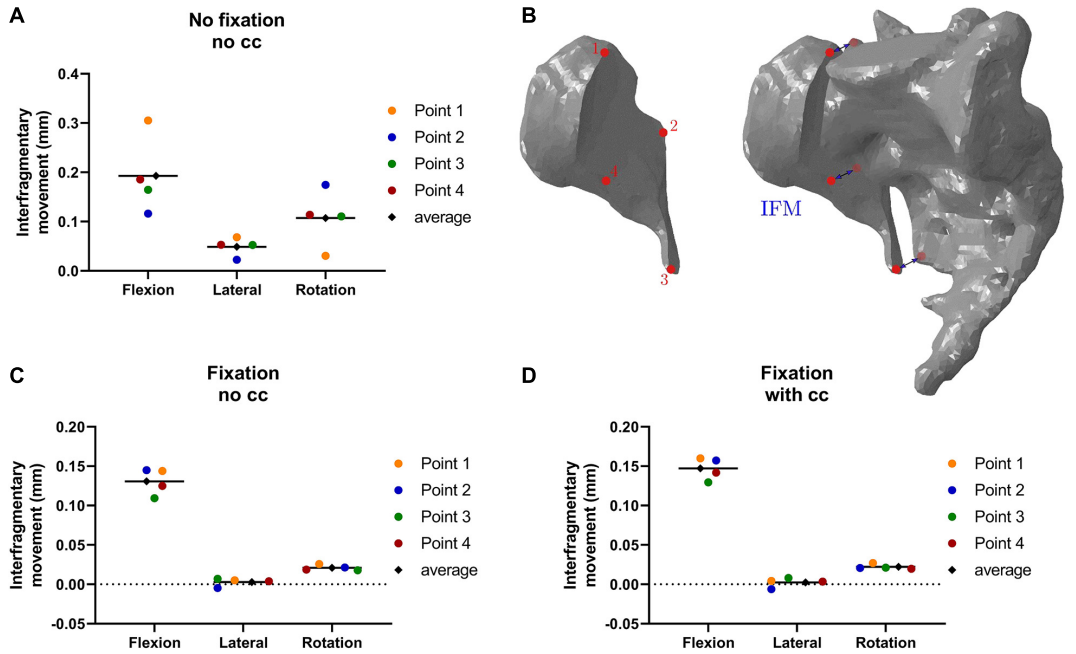

FIGURE 7 | Interfragmentary movement (IFM) in the fracture area in different conditions: Without fixation and cross connector **(A)**, with fixation and no cross connector **(C)** and with fixation and cross connector **(D)**, the points of measurement are depicted in **(B)**. In flexion, the interfragmentary movement is highest in all points and all conditions **(A–D)**. The fixation alone reduced the occurring interfragmentary movement substantially **(C)**, while an additional cross connector led to almost identical values **(D)**.

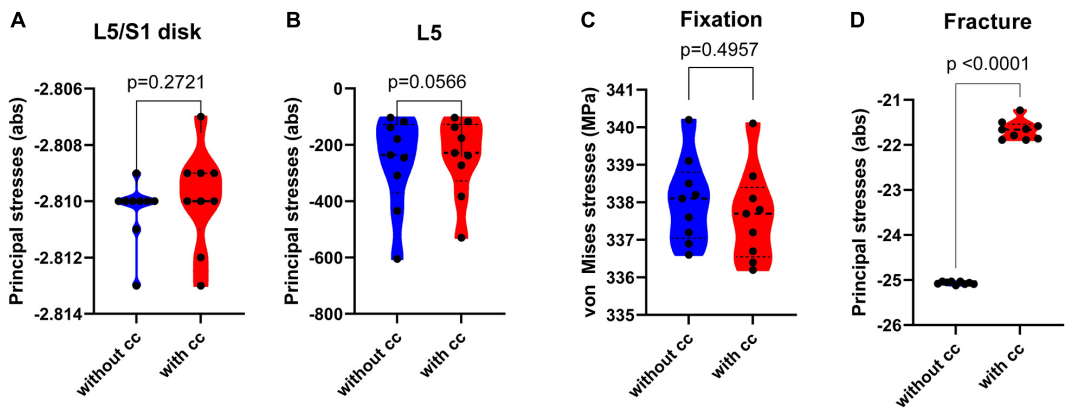

FIGURE 8 | Violin plots depicting the maximum principal stresses (absolute values) in the disk L5/S1 **(A)**, fifth lumbar vertebrae **(B)** and fracture area **(D)** and the von Mises stresses in the fixation device **(C)** in MPa, statistically validated in different variations of osseointegration (100 MPa to 10.000 MPa) for the axial rotation case. In the disk area L5/S1, the resulting effect of a cross connector was not significant [$F(1,8) = 1.391$, $p = 0.2721$, SS = 8.89*10^-7, $\delta = 0.0004$, subplot A]. In the lumbar vertebra L5 [$F(1,8) = 4.955$, $p = 0.0566$, SS = 1842, $\delta = 20.23$, subplot B] and fixational device [$F(1,8) = 100$, $p < 0.0001$, SS = 0.68, post-hoc t-test $t(16) = 0.6971$, $p = 0.4957$, $\delta = 0.39$, subplot C], the effect of a cross connector was not significant. In the fracture area, the resulting principal stresses (subplot D) were significantly lower after the addition of a cross connector [$F(1,8) = 2066$, $p < 0.0001$, SS = 51.78, post-hoc t-test $t(16) = 46.28$, $p < 0.0001$, $\delta = 3.392$] (Mean, 25th and 75th percentile).

flexion, with right lateral bending and with left axial rotation, were investigated for three lumbar models (without fixation, with fixation without CC, with fixation with CC).

The ROM in the IVD L5-S1 and the SI joint are significantly reduced (49.5–96.9%) when a fixation is used. In contrast, the reduction of the ROM in the IVD L4-L5 is not that evident. The ROM in lateral bending even shows a contrary trend and increases due to the use of a fixation. The differences in the ROM of the IVD L4-L5 to the ROM in IVD L5-S1 and the SI joint are due to the position of the device. Since the pedicle screws are fixated in the L5, only the lower spinal part is stabilized. In all three locations, the additional use of a CC could not or only marginally further reduce the ROM. Only the ROM in the SI joint in axial rotation was further reduced by 33.3 % compared to the

ROM using a fixation without CC which corresponds to another 3 % reduction compared to the original ROM without fixation.

Plenty of biomechanical studies for the analysis of spinal movement are available, out of which a few in particular analyzed the effect of a cross connector. In a biomechanical evaluation of zone 2 sacral fractures (as opposed to the zone 1 fracture considered in this study), the effect of a lumbopelvic fixation was analyzed in fifteen frozen cadaveric specimens by Jazini et al. (2017a). A transverse cross-connector, in combination with an anterior plate increased the pelvic ring stability especially in axial rotation and not in lateral flexion, but just if there was a "small-gap fracture model." Likewise, the addition of a cross connector did not add to the principal stresses in lateral bending in our study in the L5/S1 disk. Even for zone 1 fractures like we demonstrated, the fracture zone had to suffer from significantly less maximum stress, in particular in axial rotation, when a cross connector was implemented. The developed finite element model shows a good comparability to the biomechanical assessment from Jazini et al. (2017a) expanding their findings to zone 1 fractures.

Similarly, (Denis) type 2 fractures were assessed by Acklin et al. in 16 pelves. The authors compared different fixation techniques and a "double plating" method reduced the axial stiffness significantly compared to sole SI screws or a monolateral triangular stabilization (Acklin et al., 2018). Similar to a "double plating," the present study showed that the cross connector enhanced axial stiffness especially in the fracture area, while they do not refer to lateral bending or flexion.

Korovessis et al. (2001) applied one or two pedicle screw-rod constructs onto a polymethylmethacrylate block system in order to analyze differences in ROM due to the addition of rod-rod cross-links. The authors found a small, but measurable reduction in flexion and extension, but none in lateral bending. The whole construct was assessed, while we saw only minor differences in lateral bending after the addition of a cross connector. We saw the same nonsignificant differences in lateral bending within our construct.

Serhan and Slivka used a corporectomy model with polyethylene blocks to simulate the biomechanical properties of the lumbar spine. They found that regarding torsional stiffness, the implementation of one transverse connector enhanced stability by 45% (Melkerson, 2003). In the present FE model, the reduction of axial rotation was small when a cross connector was added after the usual stabilizing device in L5/S1, but substantial in the fracture area. Since the fracture itself needs stabilization for healing purposes, this area is of particular interest.

Decker et al. introduced a new minimally invasive stabilization technique for lumbosacral fractures, which yielded persuasive results in 10 patients using a L3/L4 and iliac screw with long rods, connected with a cross connector delivering "high construct rigidity," which we sought to verify with finite element analysis (Decker et al., 2019).

Lumbar fixation methods have often been assessed biomechanically. In a study on ten calf lumbar spines, one-level (L3-L4) and two-level (L2–L4) fixations with and without a transfixator were compared. For one-level constructs, the ROM was reduced in flexion and axial rotation, but not extension and lateral bending. We could not see additional effects of the transverse connector in L5/Ilium in flexion and lateral bending as well. In their study, and for two-level constructs, the ROM in flexion, extension and lateral bending was just slightly reduced, whereas axial rotation was dramatically reduced (Lim et al., 1996). Again, in our FE model, the effects on axial rotation were marginal, while the construct itself was more stable (in the sense of lower principal stresses) after a cross connector was added. In addition, the fracture area itself was stabilized substantially by a cross connector in both lateral flexion and axial rotation in our study.

Since cross-links can be designed differently, the diameter has been demonstrated to directly influence the stability of the construct: Comparing different cross-link brands regarding torsional motion and stiffness in L3-L4 stabilization, Dick et al. (1997) found no statistically significant differences for one or two cross-links in all movements (axial, flexion-extension, and lateral-flexion), but torsional loading, where every cross-link provided significantly more stiffness with an increase of 44% for one cross-link and a proportional effect of the cross-sectional area of the cross-link to the magnitude of increase in torsional stiffness (Dick et al., 1997). We used a transverse connector of 3.5 mm external diameter (9.62 mm^2), which lower compared to the four devices tested by Dick et al. Compared to their largest cross-link (50.27 mm^2 cross-sectional area), the one we used was clearly smaller and might be the reason for the moderate effect of our measurements with the cross connector on the axial stiffness, especially in L5/S1 and axial rotation. Within flexion-extension stiffness, Dick et al. could not find significant differences after the addition of a cross connector within their construct, which is in agreement with our findings.

Similar results have been published by Carson et al., combining experimental (instrumented spine segments) with finite element methods. The beneficial effect of a transfixated longitudinal spinal construct has been demonstrated for a one-level fixation. Axial and lateral loading were stabilized by a transfixation of bi-level constructs reducing the stress on internal components of force and moment (Carson et al., 1990). The construct itself has been stabilized by a cross connector in our study as well. In accordance to the study by Carson, this effect was most prominent in axial rotation.

Partially contrary to that, and especially in a long stabilizational device, in a biomechanical fresh-frozen cadaveric study, thoracal stabilizational devices after pedicle subtraction osteotomy (PSO) from T4-T10 were assessed, and one transverse connector had no additional stabilizing effect on flexion/extension, lateral bending or axial rotation (ROM) (Lehman et al., 2015). A PSO leads to substantial loss of integrity in a spinal segment, which is why it cannot be directly compared to a fracture model. Interestingly, these authors could see no stabilizing effect of an additional transverse connector, which we could detect in the fracture area for lateral bending and rotational stress.

The finite element model developed in this study indicates more stability in the fracture area with a transverse connector, especially in rotational movements and when variations of osseointegration are implemented. This could provide the basis for a faster healing of the bony area, but needs prospective clinical validation.

In addition, for more conclusive considerations, the finite element model shall be improved, for instance, by considering a longer spine segment, by improving material modeling approaches (i.e., considering an anisotropic behavior for the annulus fibrosus in the IVD and/or for bony structures), or by considering different fracture patterns. Finally, a validation on several case studies, possibly including a patient-specific assessment of material properties, should be conducted in the future.

CONCLUSION

By means of a computational study based on the finite element method, the results of the present work suggest that the cross connector did not ameliorate the range of motion in L4/L5 or L5/sacrum.

A fixation (with or without cross connector) reduced the occurring stresses in the disk L5/S1, vertebral body L5 and the fracture area. Moreover, considering the combination of all loading cases, the presence of a cross connector reduced the maximum stress in the fracture area of around 10%. This difference has been statistically evaluated by considering uncertainties in material properties and different levels of osseointegration (different qualities of the interface bone) in the axial rotation case (significant reduction of maximum stress in the fracture area, $p < 0.0001$).

DATA AVAILABILITY STATEMENT

The raw data supporting the conclusions of this article will be made available by the authors, without undue reservation.

AUTHOR CONTRIBUTIONS

DS, WL, MM, and MG designed the study. MM, MG, and FL performed all experimental procedures. DS, MM, MG, and FL carried out the data analysis. DS, MG, and MM wrote the manuscript. WL, LW, and PW critically revised it for important intellectual content. All authors have approved the final version of the article.

FUNDING

DS was funded by the Deutsche Forschungsgemeinschaft (DFG, German Research Foundation) – 413501650. MG, MM, and PW acknowledge the Masterplan SMART BIOTECS (Ministry of Science and Culture of Lower Saxony, Germany). MM was also funded by the Ministry of Education, University and Research (Italy) in the 2017 Rita Levi Montalcini Program for Young Researchers.

ACKNOWLEDGMENTS

The authors thank Lennart Viezens for his technical support.

SUPPLEMENTARY MATERIAL

The Supplementary Material for this article can be found online at: https://www.frontiersin.org/articles/10.3389/fbioe.2021.669321/full#supplementary-material

Supplementary Figure 1 | Validation of the FE model. The L4/L5 segment showed comparable flexion and lateral bending ranges of motion compared to the literature **(A,B)**, while the axial rotation appeared higher **(C)**. The same occurs for the L5/S1 segment **(D–F)**.

Supplementary Figure 2 | Effect of variation of parameters on ROM in axial rotation. The L4/L5 **(A)** segment showed comparable ROM when the material parameters were varied (L4/L5 ROM: with*without CC $F(1,14) = 1.000$, $p = 0.3343$, SS = 1.333*10ˆ-5, $\delta = 0.001$). The L5/S1 segment **(B)** similarly depicted a comparable ROM in the groups without and with CC (L5: with*without CC $F(1,14) = 3.027$, $p = 0.1038$, SS = 5.333 *10ˆ-5$\delta = 0.003$) (Mean, 25th and 75th percentile).

Supplementary Figure 3 | Effect of parameters on principal stresses (absolute values) for L5/S1 disk, L5 and fracture area and von Mises stresses for the fixation device in MPa (axial rotation). **(A)** In L5/S1, the variation of parameters did not significantly affect the maximum stresses in without and with cc groups (L5 disk stress: with*without CC $F(1,14) = 1.260$, $p = 0.2806$, SS = 5.333*10ˆ-5, $\delta = 0.0027$. In L5 **(B)**, the changes of parameters led to a marginal, but statistically relevant difference between the "without cc" and "with cc" group (L5: with*without CC $F(1,14) = 73.94$, $p < 0.0001$, SS = 1.408, post-hoc t-test $t(14) = 8.599$, $p < 0.0001$, $\delta = 0.4333$). In the fixation device **(C)**, the differences similarly appeared to be marginal, but significant (Fixation stress: with*without CC $F(1,14) = 13,72$, $p = 0.0024$, SS = 1,680, post-hoc t-test $t(14)3.704$, $p = 0.0024$, $\delta = 0.473$). In the fracture area **(D)**, the differences between the group with and without the CC appeared to be significant (Fracture stress: with*without CC Fracture stress: with*without CC $F(1,14) = 194.5$, $p < 0.0001$, SS = 61.06, post-hoc t-test $t(14) = 13.95$, $p < 0.0001$, $\delta = 2.853$) (Mean, 25th and 75th percentile).

Supplementary Figure 4 | Validation of the FE model in the sacroiliac joint (SI). The SI segment showed comparable flexion **(A)**, lateral bending **(B)**, and axial rotation **(C)** ranges of motion compared to the literature.

Supplementary Figure 5 | Structural parameters of the spinopelvic device. The L5 pedicle screw has a diameter of 7 mm, the iliac screw of 9 mm, with a length of 45 and 90mm, respectively. The cross connector has a length of 96.50 mm and diameter of 3.50 mm. The cylindrical cross connector is connected to the two screws with cross link clamps **(A)**. In addition, the maximum von Mises stresses in lateral bending with CC within the screws is shown **(B)**.

REFERENCES

Acklin, Y. P., Zderic, I., Richards, R. G., Schmitz, P., Gueorguiev, B., and Grechenig, S. (2018). Biomechanical investigation of four different fixation techniques in sacrum Denis type II fracture with low bone mineral density. *J Orthop Res* 36, 1624–1629. doi: 10.1002/jor.23798

Aebi, M., Arlet, V., and Webb, J. K. (2007). AO Spine Manual (2 Volumes) / Videos on DVD-ROM included: Vol. 1: Principles and Techniques, *1st Edn.* Vol. 2: Clinical Applications. Davos: AO Publishing.

Amaritsakul, Y., Chao, C.-K., and Lin, J. (2014). Biomechanical evaluation of bending strength of spinal pedicle screws, including cylindrical, conical, dual core and double dual core designs using numerical simulations and mechanical tests. *Med Eng Phys* 36, 1218–1223. doi: 10.1016/j.medengphy.2014.06.014

Ayturk, U. M., and Puttlitz, C. M. (2011). Parametric convergence sensitivity and validation of a finite element model of the human lumbar spine. *Comput Methods Biomech Biomed Engin* 14, 695–705. doi: 10.1080/10255842.2010.493517

Barcellos, A. L. L., Da Rocha, V. M., and Guimarães, J. A. M. (2017). Current concepts in spondylopelvic dissociation. *Injury* 48 Suppl 6, S5–S11. doi: 10.1016/S0020-1383(17)30789-1

Becker, Y. N., Motsch, N., Hausmann, J., and Breuer, U. P. (2020). Hybrid composite pedicle screw - finite element modelling with parametric optimization. *Informatics in Medicine Unlocked* 18, 100290. doi: 10.1016/j.imu.2020.100290

Beckmann, N. M., and Chinapuvvula, N. R. (2017). Sacral fractures: classification and management. *Emerg Radiol* 24, 605–617. doi: 10.1007/s10140-017-1533-3

Bellabarba, C., Schildhauer, T. A., Vaccaro, A. R., and Chapman, J. R. (2006). Complications associated with surgical stabilization of high-grade sacral fracture dislocations with spino-pelvic instability. *Spine (Phila Pa 1976)* 31, S80–S88. doi: 10.1097/01.brs.0000217949.31762.be

Benzel, E. C. ed (1999). *Spine surgery: Techniques, complication avoidance, and management*. New York, NY: Elsevier Churchill Livingstone.

Borgström, F., Karlsson, L., Ortsäter, G., Norton, N., Halbout, P., Cooper, C., et al. (2020). Fragility fractures in Europe: burden, management and opportunities. *Arch Osteoporos* 15, 59. doi: 10.1007/s11657-020-0706-y

Carrera, I., Gelber, P. E., Chary, G., González-Ballester, M. A., Monllau, J. C., and Noailly, J. (2016). Fixation of a split fracture of the lateral tibial plateau with a locking screw plate instead of cannulated screws would allow early weight bearing: a computational exploration. *Int Orthop* 40, 2163–2169. doi: 10.1007/s00264-015-3106-y

Carson, W. L., Duffield, R. C., Arendt, M., Ridgely, B. J., and Gaines, R. W. (1990). Internal forces and moments in transpedicular spine instrumentation. The effect of pedicle screw angle and transfixation–the 4R-4bar linkage concept. *Spine (Phila Pa 1976)* 15, 893–901. doi: 10.1097/00007632-199009000-00011

Chen, S.-H., Tai, C.-L., Lin, C.-Y., Hsieh, P.-H., and Chen, W.-P. (2008). Biomechanical comparison of a new stand-alone anterior lumbar interbody fusion cage with established fixation techniques - a three-dimensional finite element analysis. *BMC Musculoskelet Disord* 9:88. doi: 10.1186/1471-2474-9-88

Coombs, D. J., Rullkoetter, P. J., and Laz, P. J. (2017). Efficient probabilistic finite element analysis of a lumbar motion segment. *J Biomech* 61, 65–74. doi: 10.1016/j.jbiomech.2017.07.002

Cross, W. W., Berven, S. H., Slater, N., Lehrman, J. N., Newcomb, A. G. U. S., and Kelly, B. P. (2018). In Vitro Biomechanical Evaluation of a Novel. *Minimally Invasive, Sacroiliac Joint Fixation Device. Int J Spine Surg* 12, 587–594. doi: 10.14444/5072

Danielson, B. I., Willén, J., Gaulitz, A., Niklason, T., and Hansson, T. H. (1998). Axial loading of the spine during CT and MR in patients with suspected lumbar spinal stenosis. *Acta Radiol* 39, 604–611. doi: 10.3109/02841859809175484

Decker, S., Herden, J., Krettek, C., and Müller, C. W. (2019). A new minimally invasive U-shaped lumbopelvic stabilization technique. *Eur J Orthop Surg Traumatol* 29, 1223–1230. doi: 10.1007/s00590-019-02421-7

Denis, F., Davis, S., and Comfort, T. (1988). Sacral fractures: an important problem. Retrospective analysis of 236 cases. *Clin Orthop Relat Res* 227, 67–81.

Dick, J. C., Zdeblick, T. A., Bartel, B. D., and Kunz, D. N. (1997). Mechanical evaluation of cross-link designs in rigid pedicle screw systems. *Spine (Phila Pa 1976)* 22, 370–375. doi: 10.1097/00007632-199702150-00003

Dreischarf, M., Zander, T., Shirazi-Adl, A., Puttlitz, C. M., Adam, C. J., Chen, C. S., et al. (2014). Comparison of eight published static finite element models of the intact lumbar spine: predictive power of models improves when combined together. *J Biomech* 47, 1757–1766. doi: 10.1016/j.jbiomech.2014.04.002

El Bojairami, I., El-Monajjed, K., and Driscoll, M. (2020). Development and validation of a timely and representative finite element human spine model for biomechanical simulations. *Sci Rep* 10, 21519. doi: 10.1038/s41598-020-77469-1

Finley, S. M., Brodke, D. S., Spina, N. T., DeDen, C. A., and Ellis, B. J. (2018). FEBio finite element models of the human lumbar spine. *Comput Methods Biomech Biomed Engin* 21, 444–452. doi: 10.1080/10255842.2018.1478967

Goel, V. K., Kong, W., Han, J. S., Weinstein, J. N., and Gilbertson, L. G. (1993). A combined finite element and optimization investigation of lumbar spine mechanics with and without muscles. *Spine (Phila Pa 1976)* 18, 1531–1541.

Guerado, E., Cervan, A. M., Cano, J. R., and Giannoudis, P. V. (2018). Spinopelvic injuries. *Facts and controversies. Injury* 49, 449–456. doi: 10.1016/j.injury.2018.03.001

Hammer, N., and Klima, S. (2019). In-silico pelvis and sacroiliac joint motion-A review on published research using numerical analyses. *Clin Biomech (Bristol, Avon)* 61, 95–104. doi: 10.1016/j.clinbiomech.2018.12.005

Hu, P., Wu, T., Wang, H.-Z., Qi, X.-Z., Yao, J., Cheng, X.-D., et al. (2017). Influence of Different Boundary Conditions in Finite Element Analysis on Pelvic Biomechanical Load Transmission. *Orthop Surg* 9, 115–122. doi: 10.1111/os.12315

Hungerford, B., Gilleard, W., and Lee, D. (2004). Altered patterns of pelvic bone motion determined in subjects with posterior pelvic pain using skin markers. *Clin Biomech (Bristol, Avon)* 19, 456–464. doi: 10.1016/j.clinbiomech.2004.02.004

Ivanov, A. A., Kiapour, A., Ebraheim, N. A., and Goel, V. (2009). Lumbar fusion leads to increases in angular motion and stress across sacroiliac joint: a finite element study. *Spine (Phila Pa 1976)* 34, E162–E169. doi: 10.1097/BRS.0b013e3181978ea3

Jahng, T.-A., Kim, Y. E., and Moon, K. Y. (2013). Comparison of the biomechanical effect of pedicle-based dynamic stabilization: a study using finite element analysis. *Spine J* 13, 85–94. doi: 10.1016/j.spinee.2012.11.014

Jaramillo, H. E., and Garcia, J. J. (2017). Elastic Constants Influence On The L4-L5-S1 Annuli Fibrosus Behavior. *A Probabilistic Finite Element Analysis. Acta of Bioengineering and Biomechanics*. 19, 1–25. doi: 10.5277/ABB-00949-2017-02

Jazini, E., Klocke, N., Tannous, O., Johal, H. S., Hao, J., Salloum, K., et al. (2017a). Does Lumbopelvic Fixation Add Stability? A Cadaveric Biomechanical Analysis of an Unstable Pelvic Fracture Model. *J Orthop Trauma* 31, 37–46. doi: 10.1097/BOT.0000000000000703

Jazini, E., Weir, T., Nwodim, E., Tannous, O., Saifi, C., Caffes, N., et al. (2017b). Outcomes of lumbopelvic fixation in the treatment of complex sacral fractures using minimally invasive surgical techniques. *Spine J* 17, 1238–1246. doi: 10.1016/j.spinee.2017.04.032

Joukar, A., Shah, A., Kiapour, A., Vosoughi, A. S., Duhon, B., Agarwal, A. K., et al. (2018). Sex Specific Sacroiliac Joint Biomechanics During Standing Upright: A Finite Element Study. *Spine (Phila Pa 1976)* 43, E1053–E1060. doi: 10.1097/BRS.0000000000002623

Keating, J. F., Werier, J., Blachut, P., Broekhuyse, H., Meek, R. N., and O'Brien, P. J. (1999). Early fixation of the vertically unstable pelvis: the role of iliosacral screw fixation of the posterior lesion. *J Orthop Trauma* 13, 107–113. doi: 10.1097/00005131-199902000-00007

Kibsgård, T. J., Röhrl, S. M., Røise, O., Sturesson, B., and Stuge, B. (2017). Movement of the sacroiliac joint during the Active Straight Leg Raise test in patients with long-lasting severe sacroiliac joint pain. *Clin Biomech (Bristol, Avon)* 47, 40–45. doi: 10.1016/j.clinbiomech.2017.05.014

Kim, D. H. (2006). *Surgical anatomy & techniques to the spine*. Philadelphia, PA: Saunders Elsevier.

König, M. A., Jehan, S., Boszczyk, A. A., and Boszczyk, B. M. (2012). Surgical management of U-shaped sacral fractures: a systematic review of current treatment strategies. *Eur Spine J* 21, 829–836. doi: 10.1007/s00586-011-2125-7

Korovessis, P., Baikousis, A., Deligianni, D., Mysirlis, Y., and Soucacos, P. (2001). Effectiveness of transfixation and length of instrumentation on titanium and stainless steel transpedicular spine implants. *Journal of Spinal Disorders* 14, 109–117. doi: 10.1097/00002517-200104000-00004

Kurutz, M., and Oroszváry, L. (2010). Finite element analysis of weightbath hydrotraction treatment of degenerated lumbar spine segments in elastic phase. *J Biomech* 43, 433–441. doi: 10.1016/j.jbiomech.2009.10.004

Kyaw, T. A., Wang, Z., Sakakibara, T., Yoshikawa, T., Inaba, T., and Kasai, Y. (2014). Biomechanical effects of pedicle screw fixation on adjacent segments. *Eur J Orthop Surg Traumatol* 24 (Suppl. 1), S283–S287. doi: 10.1007/s00590-014-1416-1

Lakens, D. (2013). Calculating and reporting effect sizes to facilitate cumulative science: a practical primer for t-tests and ANOVAs. *Front Psychol* 4:863. doi: 10.3389/fpsyg.2013.00863

Lavaste, F., Skalli, W., Robin, S., Roy-Camille, R., and Mazel, C. (1992). Three-dimensional geometrical and mechanical modelling of the lumbar spine. *J Biomech* 25, 1153–1164. doi: 10.1016/0021-9290(92)90071-8

Lehman, R. A., Kang, D. G., Wagner, S. C., Paik, H., Cardoso, M. J., Bernstock, J. D., et al. (2015). Biomechanical stability of transverse connectors in the

setting of a thoracic pedicle subtraction osteotomy. *Spine J* 15, 1629–1635. doi: 10.1016/j.spinee.2015.03.010

Lim, T. H., Eck, J. C., An, H. S., Hong, J. H., Ahn, J. Y., and You, J. W. (1996). Biomechanics of transfixation in pedicle screw instrumentation. *Spine (Phila Pa 1976)* 21, 2224–2229. doi: 10.1097/00007632-199610010-00009

Lindsey, D. P., Kiapour, A., Yerby, S. A., and Goel, V. K. (2015). Sacroiliac Joint Fusion Minimally Affects Adjacent Lumbar Segment Motion: A Finite Element Study. *Int J Spine Surg* 9, 64. doi: 10.14444/2064

Lindsey, D. P., Parrish, R., Gundanna, M., Leasure, J., Yerby, S. A., and Kondrashov, D. (2018). Biomechanics of unilateral and bilateral sacroiliac joint stabilization: laboratory investigation. *J Neurosurg Spine* 28, 326–332. doi: 10.3171/2017.7.SPINE17499

Mahato, N. K., Dhason, R., and Ram, D. R. (2019). Quantifying Range of Motion and Stress Patterns at the Transitional Lumbosacral Junction: Pilot Study Using a Computational Model for Load-Bearing at Accessory L5-S1 Articulation. *Int J Spine Surg* 13, 17–23. doi: 10.14444/6002

Melkerson, M. N. (2003). "Spinal implants: are we evaluating them appropriately?," in *Proceedings of the Symposium on Spinal Implants: Are We Evaluating Them Appropriately? held in Dallas*, (West Conshohocken, PA: ASTM International).

Mengoni, M., Vasiljeva, K., Jones, A. C., Tarsuslugil, S. M., and Wilcox, R. K. (2016). Subject-specific multi-validation of a finite element model of ovine cervical functional spinal units. *J Biomech* 49, 259–266. doi: 10.1016/j.jbiomech.2015.12.005

Nagamoto, Y., Iwasaki, M., Sakaura, H., Sugiura, T., Fujimori, T., Matsuo, Y., et al. (2015). Sacroiliac joint motion in patients with degenerative lumbar spine disorders. *J Neurosurg Spine* 23, 209–216. doi: 10.3171/2014.12.SPINE14590

Panjabi, M. M., Goel, V., Oxland, T., Takata, K., Duranceau, J., Krag, M., et al. (1992). Human lumbar vertebrae. *Quantitative three-dimensional anatomy. Spine (Phila Pa 1976)* 17, 299–306. doi: 10.1097/00007632-199203000-00010

Pascal-Moussellard, H., Hirsch, C., and Bonaccorsi, R. (2016). Osteosynthesis in sacral fracture and lumbosacral dislocation. *Orthop Traumatol Surg Res* 102, S45–S57. doi: 10.1016/j.otsr.2015.12.002

Pulley, B. R., Cotman, S. B., and Fowler, T. T. (2018). Surgical Fixation of Geriatric Sacral U-Type Insufficiency Fractures: A Retrospective Analysis. *J Orthop Trauma* 32, 617–622. doi: 10.1097/BOT.0000000000001308

Rizkalla, J. M., Lines, T., and Nimmons, S. (2019). Classifications in Brief: The Denis Classification of Sacral Fractures. *Clin Orthop Relat Res* 477, 2178–2181. doi: 10.1097/CORR.0000000000000861

Rohlmann, A., Bauer, L., Zander, T., Bergmann, G., and Wilke, H.-J. (2006a). Determination of trunk muscle forces for flexion and extension by using a validated finite element model of the lumbar spine and measured in vivo data. *J Biomech* 39, 981–989. doi: 10.1016/j.jbiomech.2005.02.019

Rohlmann, A., Zander, T., Schmidt, H., Wilke, H.-J., and Bergmann, G. (2006b). Analysis of the influence of disc degeneration on the mechanical behaviour of a lumbar motion segment using the finite element method. *J Biomech* 39, 2484–2490. doi: 10.1016/j.jbiomech.2005.07.026

Rommens, P. M., Dietz, S.-O., Ossendorf, C., Pairon, P., Wagner, D., and Hofmann, A. (2015). Fragility fractures of the pelvis: should they be fixed? *Acta Chir Orthop Traumatol Cech* 82, 101–112.

Schildhauer, T. A., Bellabarba, C., Nork, S. E., Barei, D. P., Routt, M. L. C., and Chapman, J. R. (2006). Decompression and lumbopelvic fixation for sacral fracture-dislocations with spino-pelvic dissociation. *J Orthop Trauma* 20, 447–457. doi: 10.1097/00005131-200608000-00001

Shin, D. S., Lee, K., and Kim, D. (2007). Biomechanical study of lumbar spine with dynamic stabilization device using finite element method. *Computer-Aided Design* 39, 559–567. doi: 10.1016/j.cad.2007.03.005

Shin, J. K., Lim, B.-Y., Goh, T. S., Son, S. M., Kim, H.-S., Lee, J. S., et al. (2018). Effect of the screw type (S2-alar-iliac and iliac), screw length, and screw head angle on the risk of screw and adjacent bone failures after a spinopelvic fixation technique: A finite element analysis. *PLoS One* 13:e0201801. doi: 10.1371/journal.pone.0201801

Spina, N. T., Moreno, G. S., Brodke, D. S., Finley, S. M., and Ellis, B. J. (2020). Biomechanical effects of laminectomies in the human lumbar spine: a finite element study. *Spine J.* 21, 150–159. doi: 10.1016/j.spinee.2020.07.016

Sterba, M., Arnoux, P.-J., Labelle, H., Warner, W. C., and Aubin, C. -É (2018). Biomechanical analysis of spino-pelvic postural configurations in spondylolysis subjected to various sport-related dynamic loading conditions. *Eur Spine J* 27, 2044–2052. doi: 10.1007/s00586-018-5667-0

Tsiridis, E., Upadhyay, N., and Giannoudis, P. V. (2006). Sacral insufficiency fractures: current concepts of management. *Osteoporos Int* 17, 1716–1725. doi: 10.1007/s00198-006-0175-1

Tullberg, T., Blomberg, S., Branth, B., and Johnsson, R. (1998). Manipulation does not alter the position of the sacroiliac joint. A roentgen stereophotogrammetric analysis. *Spine (Phila Pa 1976)* 23, 1124–8;discussion1129. doi: 10.1097/00007632-199805150-00010

Wagner, D., Ossendorf, C., Gruszka, D., Hofmann, A., and Rommens, P. M. (2015). Fragility fractures of the sacrum: how to identify and when to treat surgically? *Eur J Trauma Emerg Surg* 41, 349–362. doi: 10.1007/s00068-015-0530-z

Williams, S. K., and Quinnan, S. M. (2016). Percutaneous Lumbopelvic Fixation for Reduction and Stabilization of Sacral Fractures With Spinopelvic Dissociation Patterns. *J Orthop Trauma* 30, e318–e324. doi: 10.1097/BOT.0000000000000559

Yamamoto, I., Panjabi, M. M., Crisco, T., and Oxland, T. (1989). Three-dimensional movements of the whole lumbar spine and lumbosacral joint. *Spine (Phila Pa 1976)* 14, 1256–1260. doi: 10.1097/00007632-198911000-00020

Yang, P., Zhang, Y., Ding, H.-W., Liu, J., Ye, L.-Q., Xiao, J., et al. (2016). Pedicle screw fixation with kyphoplasty decreases the fracture risk of the treated and adjacent non-treated vertebral bodies: a finite element analysis. *J Huazhong Univ Sci Technolog Med Sci* 36, 887–894. doi: 10.1007/s11596-016-1680-x

Zhang, Q. H., Zhou, Y. L., Petit, D., and Teo, E. C. (2009). Evaluation of load transfer characteristics of a dynamic stabilization device on disc loading under compression. *Med Eng Phys* 31, 533–538. doi: 10.1016/j.medengphy.2008.09.011

Zhong, Z.-C., Wei, S.-H., Wang, J.-P., Feng, C.-K., Chen, C.-S., and Yu, C. (2006). Finite element analysis of the lumbar spine with a new cage using a topology optimization method. *Med Eng Phys* 28, 90–98. doi: 10.1016/j.medengphy.2005.03.007

Conflict of Interest: The authors declare that the research was conducted in the absence of any commercial or financial relationships that could be construed as a potential conflict of interest.

frontiers in Bioengineering and Biotechnology

ORIGINAL RESEARCH
published: 28 May 2021
doi: 10.3389/fbioe.2021.661469

Experimental and Computational Comparison of Intervertebral Disc Bulge for Specimen-Specific Model Evaluation Based on Imaging

Marlène Mengoni, Fernando Y. Zapata-Cornelio, Vithanage N. Wijayathunga and Ruth K. Wilcox*

School of Mechanical Engineering, Institute of Medical and Biological Engineering, University of Leeds, Leeds, United Kingdom

Finite element modelling of the spinal unit is a promising preclinical tool to assess the biomechanical outcome of emerging interventions. Currently, most models are calibrated and validated against range of motion and rarely directly against soft-tissue deformation. The aim of this contribution was to develop an *in vitro* methodology to measure disc bulge and assess the ability of different specimen-specific modelling approaches to predict disc bulge. Bovine bone-disc-bone sections (N = 6) were prepared with 40 glass markers on the intervertebral disc surface. These were initially magnetic resonance (MR)-imaged and then sequentially imaged using peripheral-qCT under axial compression of 1 mm increments. Specimen-specific finite-element models were developed from the CT data, using three different methods to represent the nucleus pulposus geometry with and without complementary use of the MR images. Both calibrated specimen-specific and averaged compressive material properties for the disc tissues were investigated. A successful methodology was developed to quantify the disc bulge *in vitro*, enabling observation of surface displacement on qCT. From the finite element model results, no clear advantage was found in using geometrical information from the MR images in terms of the models' ability to predict stiffness or disc bulge for bovine intervertebral disc.

Keywords: intervertebral disc, bulge, modelling, reverse engineering, MRI

OPEN ACCESS

Edited by:
Hendrik Schmidt, Charité – Medical University of Berlin, Germany

Reviewed by:
Alessandro Borghi, University College London, United Kingdom
André P. G. Castro, Universidade de Lisboa, Portugal

****Correspondence:***
Marlène Mengoni
m.mengoni@leeds.ac.uk

Specialty section:
This article was submitted to Biomechanics, a section of the journal Frontiers in Bioengineering and Biotechnology

Received: *30 January 2021*
Accepted: *27 April 2021*
Published: *28 May 2021*

Citation:
Mengoni M, Zapata-Cornelio FY, Wijayathunga VN and Wilcox RK (2021) Experimental and Computational Comparison of Intervertebral Disc Bulge for Specimen-Specific Model Evaluation Based on Imaging. Front. Bioeng. Biotechnol. 9:661469. doi: 10.3389/fbioe.2021.661469

INTRODUCTION

Globally, back pain causes more disability than any other condition (James et al., 2018). While the specific causes are often unclear, changes to the structure and morphology of the intervertebral disc (IVD) are frequently implicated (de Schepper et al., 2010; Brinjikji et al., 2015). The development of new surgical interventions for the IVD have been hampered by the limitations in current preclinical testing methods. In particular, *in vitro* testing is challenging due to the hydrated nature of the tissues and natural variation that occurs between samples (Vadalà et al., 2015; Sikora et al., 2018). *In silico* finite element (FE) models are a promising preclinical testing tool, capable of targeting specific situations, organ/tissue behaviour, and accounting for population variation (Schmidt et al., 2007; Mengoni et al., 2016). In particular, there is potential for FE analysis to be used to examine nucleus

augmentation or replacement where design variables, such as the biomaterial properties or device size, and patient variables such as the properties of the surrounding tissues can be parametrically altered and evaluated. The credibility of such models depends, among other things, on the correct description of the mechanical properties for a specific context of use and on relevant validation (Jones and Wilcox, 2008).

Both calibration and validation of *in silico* models of the spine have been commonly undertaken using averaged data from *in vitro* experiments, including range of motion and load-displacement behaviour as well as IVD pressure (e.g., Schmidt et al., 2006, 2007; Ayturk and Puttlitz, 2011; Adam et al., 2015; Brummund et al., 2017). Since there often exists large specimen-to-specimen variation in the measured values, this approach does not allow direct validation or calibration of an individual specimen behaviour.

Comparisons between specimen-specific models and corresponding *in vitro* experimental tests of the same specimen have been undertaken in a limited number of studies, using global measures of behaviour such as stiffness or range of motion (e.g., Maquer et al., 2015; Sikora et al., 2018; Stadelmann et al., 2018). A number of methods of measuring localised deformation or strain have been applied to the disc, such as laser scanning (Heuer et al., 2007; Fewster et al., 2020), potentiometer based surface tracking (Brinckmann and Horst, 1985; Brinckmann and Grootenboer, 1991), stereo digital image correlation (Spera et al., 2011), and magnetic resonance (MR) imaging (O'Connell et al., 2007, 2011; Showalter et al., 2016; Tavana et al., 2020). However, these methods of measuring local tissue displacement have not yet been applied to validate specimen-specific *in silico* models. Local tissue displacement such as disc bulge can be a good measure to evaluate the capacity of a model to replicate the biomechanics of the disc directly, rather than of the disc and the motion segment geometry analysed through global measures. Disc bulge is also an indirect measure of the capacity of the annulus to sustain the nucleus compression.

Specimen-specific FE models are often constructed from computed tomography (CT) or MR image data. The use of high-resolution CT image data is considered to be the gold standard for the development of computational models of hard tissues due to the feasibility of generating image-based material parameters and the reliability of the image data (Jones and Wilcox, 2008). However, a CT protocol optimised for hard tissues will not be able to effectively provide information on IVD soft tissue structures. Magnetic resonance imaging can allow different soft tissue structures to be differentiated, although limitations of resolution in 3D scans, coupled with sensitivities to tissue condition and orientation (Wijayathunga et al., 2019), make the use of MR data more challenging for model generation.

Since both CT and MR data can be acquired in preclinical studies, there is potential to use both modalities to combine the advantages of each. When testing tissue *ex vivo* for preclinical assessment of therapies, it is not clear which geometrical information from both modalities affects the accuracy of FE models of the IVD for information of interest such as stiffness or bulge. Therefore, the main aims of this study were:

1. To develop a methodology to quantify the local surface deformations of the IVD *in vitro* ("disc bulge") in such a way that direct comparisons could be made with FE model predictions.
2. To assess the ability of a simple specimen-specific finite element (FE) methodology to predict the disc bulge, using different approaches to represent the internal geometry of the IVD.

MATERIALS AND METHODS

Bovine caudal IVDs were used in this study due to the similarities to human discs (Beckstein et al., 2008) and the lack of facet joints; this tissue is also often used in preclinical assessment of intervertebral disc repair (e.g., Chan et al., 2010; Miles et al., 2016; Hom et al., 2019; among other groups). The tissue was obtained from food-chain animals for which no ethical approval was required. In the experimental arm of the study, the IVDs were imaged using MRI before being sequentially loaded and imaged under CT. In the computational arm, FE models were generated from the initial image data. Experimental load-displacement values were used to calibrate the compressibility of the disc tissues, whilst the disc surface bulge, measured experimentally at 40 points, was used for point-wise comparison of the predicted disc displacement. The experimental and computational arms of this study are described in detail below and summarised in **Figure 1**.

Specimen Preparation, Imaging, and Mechanical Testing

The bovine tissue was sourced from a local abattoir and frozen at −80°C prior to use. Six osteodiscs (half vertebra-disc-half vertebra sections) were extracted from coccygeal levels 1–4 of two tails by making parallel cuts through adjacent vertebrae, leaving approximately 15 mm of bone on each side of the IVD (Sikora et al., 2018). The specimens were potted into polymethyl methacrylate (PMMA) endcaps (**Figure 2A**). CT- and MR-compatible large markers (PinPoint® Multi-Modality Fiducial Marker, Oncology Imaging Systems Ltd., United Kingdom) were embedded into the surface of the endcaps. Additionally, forty glass fiducial markers (∼1 mm diameter) were attached to the surface of each disc using petroleum jelly where required. These were arranged along eight locations on craniocaudal lines spaced at 45-degree intervals (**Figure 2B**), and with five glass markers per line.

Each potted osteodisc was placed between parallel Delrin fixtures in a rig that facilitated consistent positioning and alignment relative to the global axes on a 3T MR platform (MAGNETOM® Verio, Siemens Healthineers, Erlangen, Germany). The specimens were imaged using a T2-weighted turbo spin-echo sequence with 0.3 × 0.3 mm in-plane resolution and slice thickness of 1 mm.

The specimens were transferred to a CT-compatible compression rig (**Figure 3A**) fabricated in-house (Sikora, 2013). The rig enabled the specimens to be manually compressed via a screw-driven piston with transverse displacements and

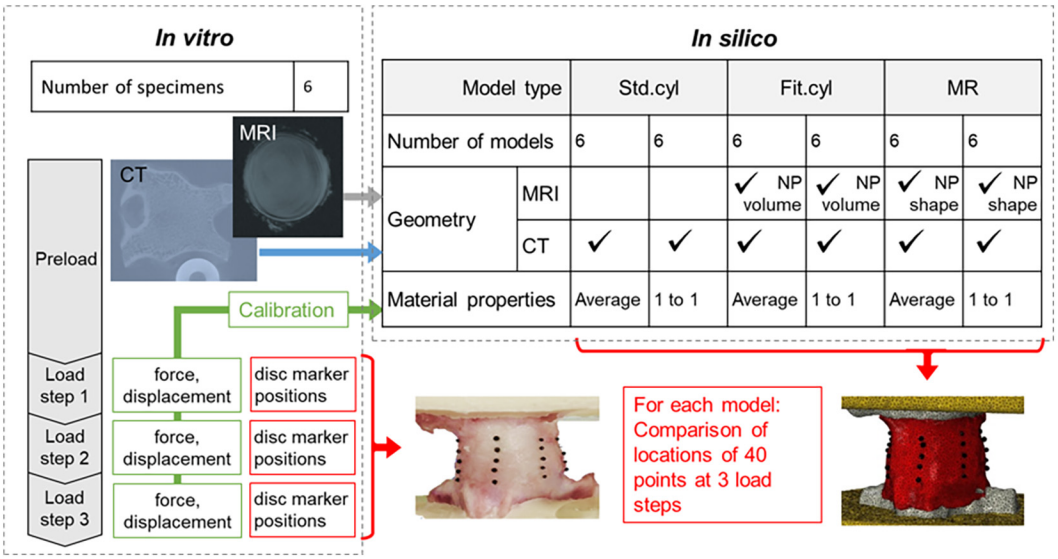

FIGURE 1 | Overview of the experimental *in vitro* and computational *in silico* arms of the study.

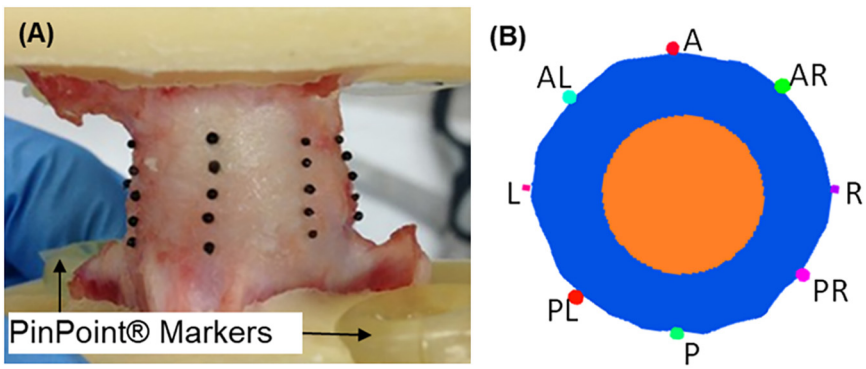

FIGURE 2 | (A) Osteodisc prepared for mechanical testing, with glass fiducial markers, CT- and MR-compatible PinPoint© markers, and PMMA endcaps. **(B)** Transverse plane slice through the intervertebral disc showing segmentation of the annulus fibrosus (blue), nucleus pulpous (orange) and fiducial glass beads, with classification of the eight zones of the disc (A, anterior; P, posterior; L, left; R, right).

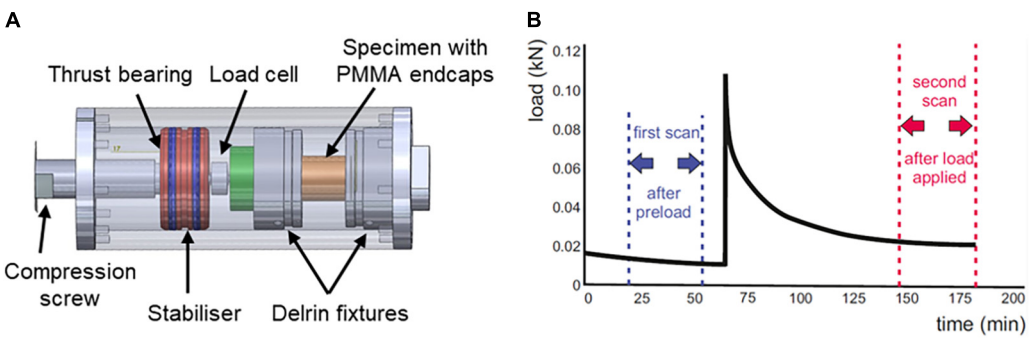

FIGURE 3 | (A) The CT-compatible compression rig. **(B)** Illustration of the timing of the CT image acquisition, showing the first "preloaded" scan and second scan following load step 1.

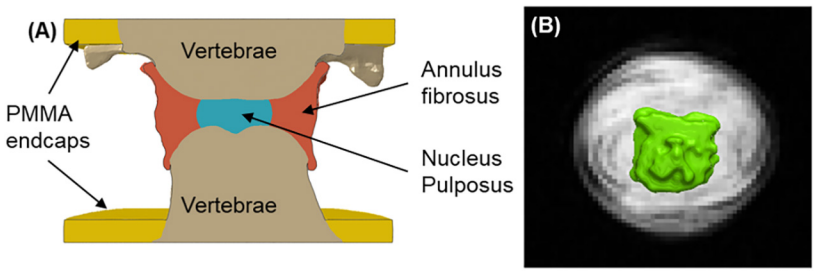

FIGURE 4 | (A) Longitudinal section through an FE model of one specimen (std. cyl. model). **(B)** Volume rendering (in green) of an MRI-segmented nucleus pulposus, with an axial slice through the centre of the disc, showing defined annulus fibrosus lamellar structure.

rotations constrained; the applied load was measured using a universal load cell (SLC31/01000, RDP Electronics Ltd., United Kingdom).

Each specimen was then axially compressed and imaged in a high-resolution peripheral-qCT scanner (XtremeCT, Scanco Medical, Switzerland) at an isotropic resolution of 82 μm (60 kVp and 900 μA), under a constant displacement. The specimen was placed between parallel platens and an initial pre-load of 50 N was applied to maintain alignment prior to the first scan. This was followed by four sequential axial compression displacement steps of approximately 1 mm each with a hold period of 90 min after each step prior to the subsequent CT scan to allow the specimen to relax (**Figure 3B**). This displacement increment was selected following pilot studies to enable the disc marker lateral displacements to be measurable at the image resolution. The exact applied displacement for each step was measured from the image data during image processing. The manual rotation of the screw to apply the displacement was performed very slowly (>30 s) to keep the strain-rate low.

Image Processing and *in vitro* Bulge Calculation

Computed tomography images were imported into Simpleware ScanIP (v 7.0, Synopsys, United States) after their greyscale-values had been rescaled to enable the use of previously calibrated bone properties (Zapata-Cornelio et al., 2017). The rescaled CT images at each compression step were rigidly registered to the CT images of specimens in their initial preloaded state ("preloaded CT images"), using the most caudal vertebrae as reference. Coordinates for all glass markers on the registered images were automatically calculated, using image processing and recognition (Python v2.7 with OpenCV v3.0). This automatic method was validated by manually extracting the marker positions on the CT images for one specimen.

Intervertebral disc bulge at each marker was calculated as the displacement of the marker centroid in the transverse plane, between the deformed and the initial stage.

Magnetic resonance images were resampled to the same resolution as the CT images, and rigidly registered to the preloaded CT images, using the PinPoint® markers as references.

Finite Element Modelling

The preloaded CT images were segmented in Simpleware ScanIP to separate bone, intervertebral disc, individual glass markers, and cement endcaps (**Figure 4A**), using automatic thresholding and manual operations for the outer surface of the annulus fibrosus (AF). The segmented markers were used to identify the closest node on the disc surface and were not subsequently included in the FE analysis. The registered MR images were segmented to isolate the nucleus pulposus (NP) and compute its volume (**Figure 4B**).

Given that accurate distinction of different soft tissue structures using image contrast was difficult on the CT scan, the NP and AF were separated as below to create three nucleus model types:

1. A cylindrical NP, centred within the AF in the transverse plane, with dimensions in such a way that NP:AF diameter ratio was 0.5 (Mengoni et al., 2017) (**std. cyl. model**);
2. A cylindrical NP, centred within the AF in the transverse plane, with dimensions so that the volume of the NP matched that measured on the MR image of the specimen (**fit. cyl. model**);
3. The NP geometry directly derived from the segmented MR image (**MR model**).

All specimens were modelled in a specimen-specific approach, with non-linear quasi-static FE analysis run in parallel using Abaqus CAE 2017 (Simulia, Dassault Systèmes).

The 18 models (six specimens each with three nucleus model types) were meshed with linear tetrahedral elements with size between 0.5 and 1.0 mm following previous mesh convergence studies (Jones and Wilcox, 2007; Luxmoore, 2013, see data associated with this paper for mesh size comparison). This led to an average of 1.15 million elements per model (range 0.9–1.6 million), 620 thousand of which represented the IVD (range 400–850 thousand). Boundary conditions were applied to simulate the experimental setup: the inferior face of the lower endcap was clamped while the superior face of the upper endcap was constrained in translation and rotation in the transverse plane. An axial compressive displacement was applied to the upper endcap, the magnitude of which was matched to the displacement measured in successive CT scans. The constitutive model and parameters used for the AF have

TABLE 1 | Material parameters.

Linear elastic materials					
	E (MPa)		***v* (–)**		
Bone	Linear dependency with greyscale, ranging from 3.6 MPa to 842 MPa (median 386.8 MPa)		0.3		Zapata-Cornelio et al., 2017
PMMA Cement	1035		0.3		Tarsuslugil et al., 2014
Hyperelastic materials					
	K (MPa)	C_{10} (MPa)	k_1 (MPa)	k_2 (–)	
Annulus (G.O.H. model)	Calibrated for load	0.25	1.43	1.63	Mengoni et al., 2017
		K (MPa)	C_{10} (MPa)	C_{01} (MPa)	
Nucleus (Mooney-Rivlin model)		Calibrated for load	0.07	0.02	Adam et al., 2015

been validated for a compression up to 30% (Sikora et al., 2018). As it is not known if it is valid for the displacement obtained in the fourth experimental step which yield over 50% compression, only the first three experimental compression steps were modelled.

The material parameters are summarised in **Table 1**. Bone was modelled as a linear elastic material, with element-by-element elastic modulus scaled using the underlying greyscale value of the CT image data, and Poisson's ratio of 0.3. In order to use a greyscale-based equation for the bone modulus (Zapata-Cornelio et al., 2017), the images underlying the high-resolution segmentation were down-sampled to an isotropic resolution of 0.5 mm. The greyscale-based model requires first a normalisation of the greyscale to 0–255. A linear mapping between the greyscale and the element elasticity modulus is then applied, with a mapping coefficient previously validated for bovine tails (Zapata-Cornelio et al., 2017). The cement endcaps were assigned an elastic modulus of 2.45 GPa, and Poisson's ratio of 0.3 (Tarsuslugil et al., 2014). The annulus fibrosus was modelled using a Holzapfel exponential model (Gasser et al., 2006), with an oblique/counter-oblique fibre orientation at 20° to the transverse plane and fibre properties previously validated for a similar axial loading setup (Mengoni et al., 2017; Sikora et al., 2018). The nucleus pulposus was modelled as a Mooney-Rivlin material (Adam et al., 2015).

For each model, NP and AF compressibility values were calibrated in order to replicate the experimental peak axial load achieved at each displacement step (**1-to-1 calibration**), producing different values of tissues compressibility for each model. The cost function of the optimisation was the RMS difference between the experimental and computational loads for each displacement step, optimised using a Trust Region Reflective method with opti4Abq (Mengoni, 2021). The calibration process was considered successful when the cost function was below 10% of the maximum experimental load, with initial conditions using the compressibility of water (1/2,200 MPa^{-1}) for both AF and NP. Only the compressibility values were calibrated because they have been shown to have the largest effect on the outcome of this type of models (Mengoni et al., 2017). As a comparison, FE models were also run where the compressibility of the disc tissues was set to the average value across all six specimens of the 1-to-1 calibrations within each nucleus model type (**average compressibility** models). Here the same value of tissue compressibility was applied to all specimens within each nucleus model type.

Data Analysis

The data associated with this study (CT and MR images, key anatomical measurements, FE models, and results of calibration) is openly available on the University of Leeds data repository (Mengoni and Wilcox, 2019).

All statistical analysis was performed using R v.3.5.0 (R Foundation for Statistical Computing) and statistical significance was set at $p < 0.05$.

Experimental Data

The applied displacement was measured from the micro-CT scan, measuring the distance between the inner surfaces of the PMMA endcaps.

To compare bulge values across samples and marker locations at each step, the *in vitro* bulge at each marker was normalised with respect to the applied displacement at each step. The normalisation was required as each specimen had a slightly different applied displacement. The normalised bulge was compared between the eight marker locations with a Welch-corrected ANOVA test after assessing normality with a Shapiro test and heteroscedasticity with a Levene test. Where a statistically significant difference was found, a post-hoc analysis was performed using a pairwise *t*-test with pooled SD and Bonferroni correction.

Computing Equivalent Poisson's Ratio

Compressibility values obtained by the optimisation algorithm were transformed into equivalent Poisson's ratio, assuming a linear-equivalent material model for both the annulus fibrosus and the nucleus pulposus (for which the shear modulus $G = 2C_{10}$; Timoshenko and Goodier, 1970):

$$\nu = \frac{3K - 4C_{10}}{6K + 4C_{10}}$$

Where K is the bulk modulus value obtained from the optimisation of compressibility, $C_{10} = 0.07\ MPa$ for the nucleus pulposus (**Table 1**) and $C_{10} = 1.92\ MPa$ for the annulus fibrosus

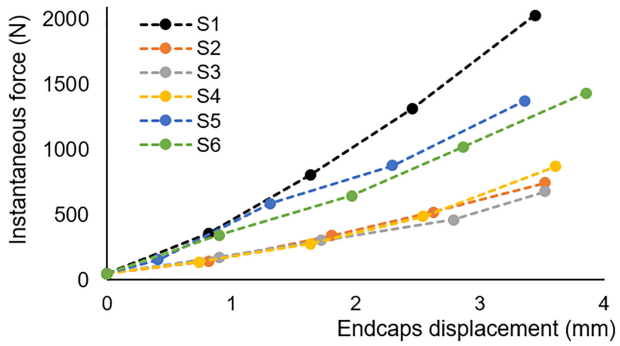

FIGURE 5 | *In vitro* load-displacement for all specimens, extracted from 2 spines (samples S1, S5, and S6 come from one spine; samples S2–4 come from the other spine); the load is the peak load measured, the displacement is as measured on CT scans with a resolution of 82 μm.

(value from a linear fit at small strain of the stress/strain data obtained from the Holzapfel model and parameters as in **Table 1**). Such a Poisson's ratio is provided as an easily interpretable parameter for comparison rather than a material parameter used in a model.

Comparison of Experimental and Computational Data

The computational axial load required for each displacement step was compared to the experimental equivalent using concordance correlation coefficients for each model type (three types of nucleus models and either one-to-one calibration or average compressibility). The concordance correlation coefficient is a measure of the agreement between values measured by two methods (Lin, 1989), hence of the ability of the *in silico* models to reproduce *in vitro* data.

As well as comparing bulge values between marker locations similarly to the experimental data analysis, the bulge was compared between *in vitro* and *in silico* values for each model type using a concordance correlation coefficient. Markers for which experimental displacement was in the lower tenth percentile were not included in this analysis to avoid comparisons with the smallest experimental displacements, which are likely to be more error-prone.

RESULTS

Experimental Specimens Mechanical Testing

The NP volume computed from the MR images ranged from 7 to 17% of the disc volume, with equivalent NP diameters between 26 and 41% of the corresponding AF average diameters. These volumes were consistently smaller than the standard cylindrical NP used in the std. cyl. FE models, which assumed an NP:AF diameter ratio of 50%.

The mechanical testing data showed a stiffening behaviour through the four loading steps (**Figure 5**). The applied displacement at each step across all samples was 0.89 ± 0.14 mm (mean ± st. dev.; measurement error of 82 μm); with a non-linear increase in force up to maximum of 2.0 kN.

The differences between the markers initial positions computed automatically and extracted manually were lower than 90 μm (i.e., about one pixel) in the transverse plane where bulge is computed. They were lower than 350 μm (i.e., about four pixels) in the axial direction whereas the axial distance between markers was about 800 μm.

The measured disc bulge across all steps and all markers was 0.24 ± 0.11 mm, 0.48 ± 0.22 mm, 0.67 ± 0.30 mm, and 0.84 ± 0.36 mm (mean ± st. dev. across all specimens and markers) for displacement steps 1–4, respectively (**Figure 6**). Generally, the anterior bulge was larger than the posterior bulge, with the differences being significant between some regions at each step (**Table 2**).

Calibration of *in silico* Material Parameters Using *in vitro* Load-Displacement Data

The calibration of compressibility values performed for each specimen led to a convergence of the RMS difference in the force for five specimens (and all nucleus model types), while for the final one it terminated due to convergence of the values of the parameters. For this specimen, the achieved RMS difference in force for all nucleus model types was between 10 and 15% of the load experimentally measured at displacement step 3.

The optimisation yielded equivalent Poisson's ratio values for the AF (mean ± std. dev.) of 0.494 ± 0.004 in the std. cyl models, and of 0.438 ± 0.08 for the other two nucleus model types (no significant differences between these two types). Equivalent Poisson's ratios for the NP were 0.493 ± 0.003 in the std. cyl models, and 0.482 ± 0.01 for the other two nucleus model types.

Following one-to-one calibration, the concordance correlation coefficients for loads at all time steps for all specimens were above 0.988 for all nucleus model types; while a reduction was observed for each of them in the average compressibility models (see **Table 3** and **Figure 7**).

Comparison of *in vitro* and *in silico* Values of Disc Bulge

No differences were seen between nucleus model types in the ability to model bulge values (**Table 3**). Across all specimens, all model types and all marker locations, about 36% of bulge data had a difference between *in vitro* measurements and *in silico* measurements lower than the image resolution (82 μm). The remaining cases were evenly split between those where the *in silico* values were smaller than the *in vitro* values and those where they were higher, as shown in **Figure 8** for the 1-to-1 calibration models (similar results are found for the average calibration model, data available at Mengoni and Wilcox, 2019). For all models, no significant differences were observed for the computational bulge values between marker locations, at any of the displacement steps.

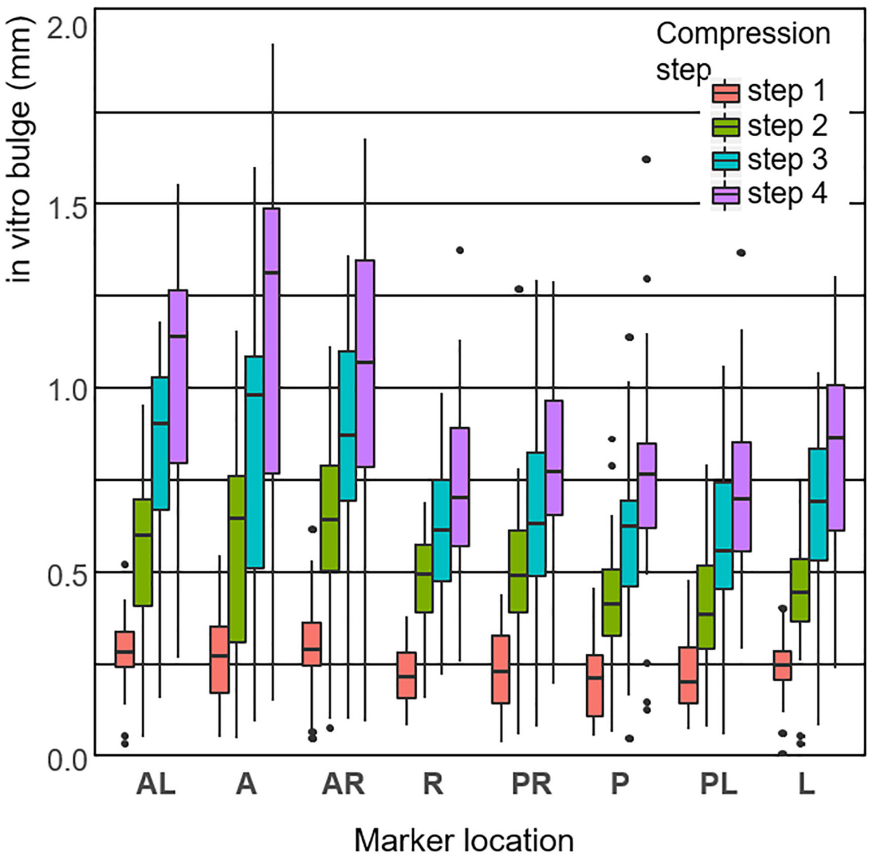

FIGURE 6 | Box-plot distribution of the *in vitro* surface disc bulge, measured by marker location (defined in **Figure 2**) and load step.

DISCUSSION

The present work successfully developed a methodology to quantify the IVD bulge *in vitro*, enabling observation of lateral surface displacement of the IVD on CT images under axial load. The pre-loaded CT images and MRI data were used to create specimen-specific image-based FE models of the IVD, and then used to analyse the effect of different approaches to combining geometrical information from MR images with the CT data. While a systematic methodology was developed to replicate the behaviour of the discs just after loading, no clear advantage of using MR geometrical data was seen in this bovine tissue study. The FE models were designed to analyse the variability between samples tested in the lab, the direct-controlled approach used in this study (direct comparison of data measured *in vitro* with data computed *in silico* on the same specimen, and controlled loading scenario) provided confidence that the methodology can capture the variation between samples rather than a generic behaviour. However, it was not meant to model clinical scenarios, nor did it indicate validity in other loading scenarios or for different outputs of interest. Key discussion points presented are with respect to the intended context of use and should not be extrapolated to other contexts. In particular, the FE modelling framework presented is not able to replicate any information related to time-dependent behaviour, changing level of hydration, or local interaction between different tissue types.

TABLE 2 | Region pairs at which a significant difference in *in vitro* bulge is observed (A, anterior; P, posterior; L, left; R, right), comparison made for the bulge normalised with respect to the applied displacement (numbers indicate the compression steps at which the difference occurs).

Surface regions	L	PL	P	PR	R
AL		3, 4	3, 4		4
A	4	3, 4	3, 4	4	4
AR		2, 3, 4	1, 2, 3, 4		4

Experimental Characterisation of IVD Bulge

A number of methods of measuring disc bulge *in vitro* have been developed previously but have not yet been employed to make direct comparisons with specimen-specific FE models. The use of a high-resolution qCT in this study facilitated the capture of precision 3D morphology and provided the advantage of enabling the assignment of greyscale-dependent material properties to the hard tissues in the FE models. It was shown previously that capturing the bone behaviour in

TABLE 3 | Concordance coefficients (CCC with 95% confidence interval in brackets) across all specimens and all displacements steps of *in silico* load and markers bulge (disregarding markers within the lowest 10 percentile of experimental bulge).

	Load		Bulge	
Model type	**1-to-1 calibration**	**Average compressibility**	**1-to-1 calibration**	**Average compressibility**
Std. cyl. model	0.992 (0.985–0.998)	0.972 (0.910–0.979)	0.681 (0.485–0.735)	0.591 (0.385–0.721)
Fit. cyl. model	0.988 (0.964–0.996)	0.886 (0.820–0.972)	0.682 (0.429–0.791)	0.576 (0.424–0.672)
MR model	0.995 (0.961–0.999)	0.972 (0.831–0.989)	0.663 (0.406–0.813)	0.599 (0.524–0.636)

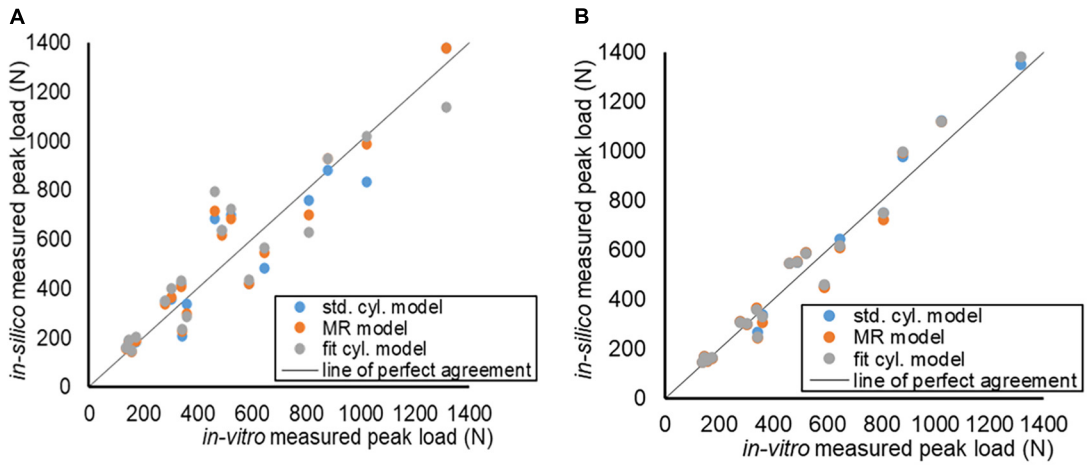

FIGURE 7 | Agreement of the *in vitro* and *in silico* load measurements, for each specimen and each model type. **(A)** Models using 1-to-1 calibration of the compressibility value. **(B)** Models using the average compressibility value.

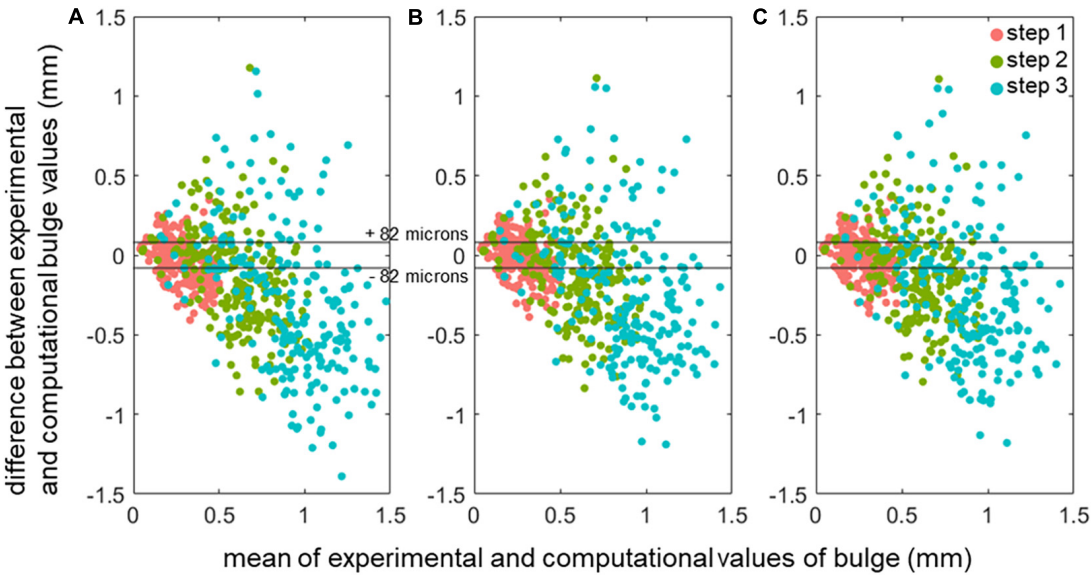

FIGURE 8 | Comparison of the *in silico* predicted displacements of the disc marker points versus the measured *in vitro* values, shown as mean-difference plots for the three different model types with the 1-to-1 calibration. **(A)** std. cyl. models **(B)** fit. cyl. models **(C)** MR models. The image resolution band is shown with horizontal lines.

static models of osteodiscs is important to replicate the apparent stiffness of the specimen (Sikora et al., 2018). Although MRI is able to provide more information on the internal structural deformations, the 3D resolution and spatial accuracy would not have been sufficient for this study. Instead, fiducial markers were used on the external disc surface, which enabled a

one-to-one comparison with corresponding nodal displacements on the FE model. This approach had the advantage in requiring no additional processing steps or assumptions to be made, meaning that the measurement error was due to the image resolution alone. Combined with an initial CT for greyscale-dependent properties of the bone, similar outcomes could be obtained by using 3D surface imaging rather than CT to compute the displacement of the fiducial markers, reducing the exposure of the tissue to repeated radiation and likely enabling shorter scanning times. Using an imaging method with shorter scanning times would enable measuring the bulge at several time points during relaxation, similarly to Heuer et al., 2007.

Regardless of the measurement method used, there are some limitations to the approach employed because of the time-dependent behaviour of the IVD tissue. In this study, the relaxed tissue was imaged, requiring the specimen to be held for 90 min prior to imaging in each step. The change in bulge during relaxation could not be estimated with the method used. While it has been shown in the canine thoracolumbar spine (Cassidy et al., 1990) that the bulge recovers at low compression levels (5% compression), it is less the case at slightly higher compression (∼15% compression), and there are no experimental data available at the higher compression levels applied in this work.

From the measurements made, the anterior region of the disc was seen to bulge more than the posterior. Similar results were obtained for human tissue under neutral axial compression, with larger radial displacements in the anterior than in the posterior regions on sagittal MRI slices (O'Connell et al., 2011). While this study used healthy bovine discs, the methodology employed could be applied to human discs, for example to examine the effects of different pathologies or herniation risks. In particular, the experimental and imaging framework developed here allows to capture some of the asymmetry in bulge which can also be observed clinically (Fardon et al., 2014). The MR imaging protocol used was optimised for human (cadaveric) spine imaging (Wijayathunga et al., 2019) and as such the framework is directly translatable to cadaveric tissue.

In silico Agreement of *in vitro* Measurements – Load

In this work, compressibility values used for the finite element models were calibrated to minimise the force difference between the force recorded upon loading and the force required in a static FE model of the IVD. Previous work on similar *in vitro* and *in silico* models had shown that compressibility was a major factor influencing stiffness outputs (Mengoni et al., 2017). The converged equivalent Poisson's ratios in this study were in the same range as found otherwise in the literature for IVD FE models that do not employ a multi-phasic representation of the disc (e.g., Marini and Ferguson, 2014; Adam et al., 2015; Casaroli et al., 2017), with almost incompressible materials. However, there was a significant difference in the outcome for the nucleus compressibility depending on how its volume was modelled: models with a large, standardised, nucleus required the use of a less compressible material model than a smaller sized nucleus, for which the size was based on MR image evaluation. Therefore, when using simple material models of the nucleus, the compressibility value should be chosen consistently with the manner in which the NP geometry is modelled.

The initial force was used for model calibration as it represents a more physiological value than the force recorded after a long relaxation without control of hydration level (on average 10 times lower). The reduction in the experimental force during relaxation is both due to the tissue relaxation itself and the change in hydration. The tissue compression leads to a reduction in water content, due to the fluid leaking out through the disc surface, which reduces the compressibility of the tissue. The exposure to air in itself has been observed to reduce the stiffness (Wilke et al., 1998). While not reported in this work, performing the same calibration for relaxed load values generated equivalent Poisson's ratios which are not physically relevant (values average of 0.2 for the nucleus, and the annulus requiring an auxetic behaviour; data available at Mengoni and Wilcox, 2019). The bulge values were on the contrary measured experimentally only in a relaxed position. This discrepancy constitutes the main limitation of this study as the methodology does not allow to measure the instantaneous bulge or the change in bulge during relaxation. This method was based on the assumption that the disc bulge does not recover significantly during relaxation, with previous work on canine spine demonstrating reduced bulge recovery with compression levels of 15% and higher (Cassidy et al., 1990). For human tissue, the change in bulge during creep experiments has been observed as being negligeable with respect to most measurement resolution methods (Heuer et al., 2007).

With relatively simple material models for all tissues and testing conditions, the agreement between *in silico* and *in vitro* load magnitudes were better than previous studies (Maquer et al., 2015; Mengoni et al., 2017), irrespective of the way the NP geometry was represented and whether 1-to-1 calibration was performed, or average values were used. The main difference in the current work probably is due to the attention and effort taken with regard to the dissection of the soft tissues surrounding the IVD. In the present study, all soft tissues were carefully removed to leave a bare IVD surface only, enabling the outer surface of the disc to be easily and accurately segmented from CT images. Previous studies, where excess soft tissue had been retained, have had to use an artificial method to identify the outer disc surface (Sikora et al., 2018). This had a major effect on the ability to build FE models from micro-CT scans and indicated that being able to reconstruct the overall volume of the IVD is a major factor in being able to model accurately load data in compression. The tissue preparation effort here was well paid off by the improved agreement of the models.

While validation work would be required to know if the average compressibility values can be used on other specimens, the fact that the agreement was substantial both for 1-to-1 calibration and average values increased confidence on the

validity of the average values for other specimens. Therefore, it may not be necessary to derive material properties through specimen-specific calibration, providing appropriate average values were already available.

It was found that, for bovine tissues models, using geometry information for the NP derived from MR images did not improve the ability of the models to predict load behaviour; this is likely due to the relatively arbitrary definition of tissue separation, even from MR data. Using MR sequences to define the outer AF boundary, or to give information about material properties, for example from T2 mapping, ρ_H-weighted or DTI sequences (Reutlinger et al., 2014; Stadelmann et al., 2018; Chetoui et al., 2019), would possibly be better ways to add value from MR data, especially for degenerated discs or when time-dependency behaviour is of interest, for which the level of tissue hydration is important.

In addition, for two of the model types, the agreement between the *in silico* and *in vitro* load data did not vary greatly between cases where the material compressibility values were derived for each specimen separately and cases where average values were used. There was only an improvement in using direct calibration of each specimen, as opposed to average values, in the case where the NP was represented as a cylinder centred in the disc and with volume derived from MR data (fit. cyl. models).

In silico Agreement of *in vitro* Measurements – Bulge

Including geometry information derived from MR images into the modelling methodology, whether only through evaluation of the nucleus volume or also by including its shape, did not produce significant differences in the accuracy of the *in silico* surface bulge of the IVD under compression. In particular, none of the nucleus model types were able to capture the differences between anterior and posterior bulge. It should be noted that the bovine disc is highly circular and thus that models in this study assumed a circular nucleus (except for the MR-models). This would not translate to the human intervertebral disc, and this conclusion may not apply in clinical scenarios. However, developing modelling methodologies valid for the bovine disc had interest in itself as the bovine spine is often used as a preclinical *in vitro* model for evaluating disc repairs. This work showed that simple *in silico* models of such preclinical evaluation are likely accurate enough to be used as complement to *in vitro* evaluation.

When evaluating the predicted disc bulge using the pointwise comparison of 40 locations on the disc surface, the level of agreement was only slightly improved when using models with a 1-to-1 calibration of compressibility properties versus those assigned an average value, and remained relatively poor for all nucleus geometry types. Accounting for the difference in lamellar strength and fibre orientation in the radial direction of the IVD (Elliott and Setton, 2000; Holzapfel et al., 2005) might enhance the ability to predict bulge. Differentiating the inner and outer annulus, with a core nucleus shape derived from MR and a more elliptical inner annulus, could also be used to the same aim. However, the large scatter seen in the mean-difference plot, without any clear locational trends, suggested these potential model improvements would not fully account for the current disparities. Errors in bulge may also be caused by the *in vitro* values being computed from images in a relaxed position while the *in silico* models were calibrated against peak force values.

Relatively simple constitutive models were used in this work and do not account for any fluid-flow effect of the tissues composing the IVD. This approach has shown to be valid when the purpose of the *in silico* models is to replicate global properties of osteodiscs or functional units, such as apparent stiffness (e.g., Mengoni et al., 2017; Sikora et al., 2018), facet joint contact (e.g., Ayturk and Puttlitz, 2011; Mengoni et al., 2016) or range of motions (e.g., Ayturk and Puttlitz, 2011; Sharabi et al., 2019). The present work showed that this modelling approach has some capacity to replicate more localised values such as disc bulge but the methodology was limited, including by the image acquisition time which required to measure bulge values after relaxation while the modelling interest was at peak load. It should be noted that changes in bulge under constant applied displacement are likely to be low, and only a single time-point was captured for each applied displacement. Therefore, the capacity to assess viscoelastic material models using the approach presented here is somewhat limited. Nevertheless, other material models could be partially assessed using the load relaxation data provided with this paper.

Despite the limitations of the current modelling method for predicting regional disc bulge, the combined *in vitro* and *in silico* methods presented in this study did provide an improved route for the evaluation of future modelling approaches, including those incorporating time-dependent material properties.

Conclusion

The experimental arm of this study presented a new methodology for examining 3D IVD bulge under axial load. The methodology allows direct 1-to-1 comparison of disc surface displacement with corresponding FE models and has the potential to be used to examine the effects of tissue degeneration or different modes of loading.

On the computational aspects, this study suggests that, in order to obtain substantial agreement on load magnitude, significant care should be taken on reconstructing the external geometry of the IVD. The results from the different approaches to modelling the NP indicate that the use of an MRI-derived NP boundary does not improve capacity to capture bulge in a bovine model calibrated for load.

DATA AVAILABILITY STATEMENT

The datasets presented in this study can be found in online repositories. The names of the repository/repositories and accession number(s) can be found below: University of Leeds data repository: https://doi.org/10.5518/586.

ETHICS STATEMENT

Ethical review and approval was not required for the animal study because this study uses animal tissue obtained from the food chain.

AUTHOR CONTRIBUTIONS

MM contributed to the design and conception of the work, data acquisition, analysis, and interpretation. FZ-C contributed to the design of the work, data acquisition, and analysis. VW contributed to the design of the work, data acquisition, and interpretation. RW contributed to the design and conception of the work, data analysis, and interpretation. All authors contributed to the drafting and critically reviewing the manuscript.

FUNDING

This work was funded by the European Research Council under Grant StG-2012-306615, Engineering and Physical Sciences Research Council under grant EP/K020757/1, and National Institute for Health Research (NIHR) Leeds Musculoskeletal Biomedical Research Centre.

REFERENCES

Adam, C., Rouch, P., and Skalli, W. (2015). Inter-lamellar shear resistance confers compressive stiffness in the intervertebral disc: an image-based modelling study on the bovine caudal disc. *J. Biomech.* 48, 4303–4308. doi: 10.1016/j.jbiomech.2015.10.041

Ayturk, U. M., and Puttlitz, C. M. (2011). Parametric convergence sensitivity and validation of a finite element model of the human lumbar spine. *Comput. Methods Biomech. Biomed. Eng.* 14, 695–705. doi: 10.1080/10255842.2010.493517

Beckstein, J. C., Sen, S., Schaer, T. P., Vresilovic, E. J., and Elliott, D. M. (2008). Comparison of animal discs used in disc research to human lumbar disc: axial compression mechanics and glycosaminoglycan content. *Spine (Phila Pa 1976).* 33, E166–E173.

Brinckmann, P., and Grootenboer, H. (1991). Change of disc height, radial disc bulge, and intradiscal pressure from discectomy. an in vitro investigation on human lumbar discs. *Spine* 16, 641–646. doi: 10.1097/00007632-199106000-00008

Brinckmann, P., and Horst, M. (1985). The influence of vertebral body fracture, intradiscal injection, and partial discectomy on the radial bulge and height of human lumbar discs. *Spine* 10, 138–145. doi: 10.1097/00007632-198503000-00005

Brinjikji, W., Diehn, F. E., Jarvik, J. G., Carr, C. M., Kallmes, D. F., Murad, M. H., et al. (2015). MRI findings of disc degeneration are more prevalent in adults with low back pain than in asymptomatic controls: a systematic review and meta-analysis. *American J. Neuroradiol.* 36, 2394–2399. doi: 10.3174/ajnr.a4498

Brummund, M., Brailovski, V., Petit, Y., Facchinello, Y., and Mac-Thiong, J. M. (2017). Impact of spinal rod stiffness on porcine lumbar biomechanics: finite element model validation and parametric study. *Proc. Instit. Mech. Eng.Part H J. Eng. Med.* 231, 1071–1080. doi: 10.1177/0954411917732596

Casaroli, G., Galbusera, F., Jonas, R., Schlager, B., Wilke, H.-J., and Villa, T. (2017). A novel finite element model of the ovine lumbar intervertebral disc with anisotropic hyperelastic material properties. *PLoS One* 12:e0177088. doi: 10.1371/journal.pone.0177088

Cassidy, J., Hiltner, A., and Baer, E. (1990). The response of the hierarchical structure of the intervertebral disc to uniaxial compression. *J. Mater. Sci. Mater. Med.* 1, 69–80. doi: 10.1007/bf00839071

Chan, S. C. W., Gantenbein-Ritter, B., Leung, V. Y. L., Chan, D., Cheung, K. M. C., and Ito, K. (2010). Cryopreserved intervertebral disc with injected bone marrow-derived stromal cells: a feasibility study using organ culture. *Spine J.* 10, 486–496. doi: 10.1016/j.spinee.2009.12.019

Chetoui, M. A., Boiron, O., Ghiss, M., Dogui, A., and Deplano, V. (2019). Assessment of intervertebral disc degeneration-related properties using finite element models based on ρH-weighted MRI data. *Biomech. Model. Mechanobiol.* 18, 17–28. doi: 10.1007/s10237-018-1064-1

de Schepper, E. I., Damen, J., van Meurs, J. B., Ginai, A. Z., Popham, M., Hofman, A., et al. (2010). The association between lumbar disc degeneration and low back pain: the influence of age, gender, and individual radiographic features. *Spine (Phila Pa 1976)* 35, 531–536. doi: 10.1097/brs.0b013e3181aa5b33

Elliott, D. M., and Setton, L. A. (2000). Anisotropic and inhomogeneous tensile behavior of the human anulus fibrosus: experimental measurement and material model predictions. *J. Biomech. Eng.* 123, 256–263. doi: 10.1115/1.1374202

Fardon, D. F., Williams, A. L., Dohring, E. J., Murtagh, F. R., Gabriel Rothman, S. L., and Sze, G. K. (2014). Lumbar disc nomenclature: version 2.0: Recommendations of the combined task forces of the North American Spine Society, the American Society of Spine Radiology and the American Society of Neuroradiology. *Spine J.* 14, 2525–2545.

Fewster, K. M., Haider, S., Gooyers, C. E., Callaghan, J., and Wong, A. (2020). A computerised system for measurement of the radial displacement of the intervertebral disc using a laser scanning device. *Comput. Methods Biomech. Biomed. Eng. Imaging Vis.* 8, 287–293. doi: 10.1080/21681163.2019.1674189

Gasser, T. C., Ogden, R. W., and Holzapfel, G. A. (2006). Hyperelastic modelling of arterial layers with distributed collagen fibre orientations. *J. R. Soc. Interface* 3, 15–35. doi: 10.1098/rsif.2005.0073

Heuer, F., Schmitt, H., Schmidt, H., Claes, L., and Wilke, H.-J. (2007). Creep associated changes in intervertebral disc bulging obtained with a laser scanning device. *Clin. Biomech.* 22, 737–744. doi: 10.1016/j.clinbiomech.2007.04.010

Holzapfel, G. A., Schulze-Bauer, C. A. J., Feigl, G., and Regitnig, P. (2005). Single lamellar mechanics of the human lumbar anulus fibrosus. *Biomech. Model. Mechanobiol.* 3, 125–140. doi: 10.1007/s10237-004-0053-8

Hom, W. W., Tschopp, M., Lin, H. A., Nasser, P., Laudier, D. M., Hecht, A. C., et al. (2019). Composite biomaterial repair strategy to restore biomechanical function and reduce herniation risk in an ex vivo large animal model of intervertebral disc herniation with varying injury severity. *PLoS One* 14:e0217357. doi: 10.1371/journal.pone.0217357

James, S. L., Abate, D., Abate, K. H., Abay, S. M., Abbafati, C., Abbastabar, H., et al. (2018). Global, regional, and national incidence, prevalence, and years lived with disability for 354 diseases and injuries for 195 countries and territories, 1990–2017: a systematic analysis for the Global Burden of Disease Study 2017. *Lancet* 392, 1789–1858.

Jones, A. C., and Wilcox, R. K. (2007). Assessment of factors influencing finite element vertebral model predictions. *J. Biomech. Eng.* 129, 898–903. doi: 10.1115/1.2800791

Jones, A. C., and Wilcox, R. K. (2008). Finite element analysis of the spine: towards a framework of verification, validation and sensitivity analysis. *Med. Eng. Phys.* 30, 1287–1304. doi: 10.1016/j.medengphy.2008.09.006

Lin, L. I.-K. (1989). A concordance correlation coefficient to evaluate reproducibility. *Biometrics* 45, 255–268. doi: 10.2307/2532051

Luxmoore, B. (2013). *Computational Simulation of the Intervertebral Disc.* PhD Thesis. Leeds: University of Leeds.

Maquer, G., Schwiedrzik, J., Huber, G., Morlock, M. M., and Zysset, P. K. (2015). Compressive strength of elderly vertebrae is reduced by disc degeneration and additional flexion. *J. Mech. Behav. Biomed. Mater.* 42, 54–66. doi: 10.1016/j.jmbbm.2014.10.016

Marini, G., and Ferguson, S. J. (2014). Modelling the influence of heterogeneous annulus material property distribution on intervertebral disk mechanics. *Ann. Biomed. Eng.* 42, 1760–1772. doi: 10.1007/s10439-014-1025-5

Mengoni, M. (2021). Using inverse finite element analysis to identify spinal tissue behaviour in situ. *Elsevier Methods* 185, 105–109. doi: 10.1016/j.ymeth.2020.02.004

Mengoni, M., Kayode, O., Sikora, S. N. F., Zapata-Cornelio, F. Y., Gregory, D. E., and Wilcox, R. K. (2017). Annulus fibrosus functional extrafibrillar and fibrous mechanical behaviour: experimental and computational characterisation. *R. Soc. Open Sci.* 4:170807. doi: 10.1098/rsos.170807

Mengoni, M., Vasiljeva, K., Jones, A. C., Tarsuslugil, S. M., and Wilcox, R. K. (2016). Subject-specific multi-validation of a Finite Element model of ovine cervical functional spinal units. *J. Biomech.* 49, 259–266. doi: 10.1016/j.jbiomech.2015.12.005

Mengoni, M., and Wilcox, R. K. (2019). *Bovine Intervertebral Disc Bulge Characterisation [Dataset]*. Leeds: University of Leeds. doi: 10.5518/586

Miles, D. E., Mitchell, E. A., Kapur, N., Beales, P. A., and Wilcox, R. K. (2016). Peptide:glycosaminoglycan hybrid hydrogels as an injectable intervention for spinal disc degeneration. *J. Mater. Chem. B* 4, 3225–3231. doi: 10.1039/c6tb00121a

O'Connell, G. D., Johannessen, W., Vresilovic, E. J., and Elliott, D. M. (2007). Human internal disc strains in axial compression measured noninvasively using magnetic resonance imaging. *Spine (Phila Pa 1976)* 32, 2860–2868. doi: 10.1097/brs.0b013e31815b75fb

O'Connell, G. D., Vresilovic, E. J., and Elliott, D. M. (2011). Human intervertebral disc internal strain in compression: the effect of disc region, loading position, and degeneration. *J. Orthop. Res.* 29, 547–555. doi: 10.1002/jor.21232

Reutlinger, C., Bürki, A., Brandejsky, V., Ebert, L., and Büchler, P. (2014). Specimen specific parameter identification of ovine lumbar intervertebral discs: on the influence of fibre-matrix and fibre-fibre shear interactions. *J. Mech. Behav. Biomed. Mater.* 30, 279–289. doi: 10.1016/j.jmbbm.2013.11.019

Schmidt, H., Heuer, F., Drumm, J., Klezl, Z., Claes, L., and Wilke, H.-J. (2007). Application of a calibration method provides more realistic results for a finite element model of a lumbar spinal segment. *Clin. Biomech.* 22, 377–384. doi: 10.1016/j.clinbiomech.2006.11.008

Schmidt, H., Heuer, F., Simon, U., Kettler, A., Rohlmann, A., Claes, L., et al. (2006). Application of a new calibration method for a three-dimensional finite element model of a human lumbar annulus fibrosus. *Clin. Biomech.* 21, 337–344. doi: 10.1016/j.clinbiomech.2005.12.001

Sharabi, M., Levi-Sasson, A., Wolfson, R., Wade, K. R., Galbusera, F., Benayahu, D., et al. (2019). The mechanical role of the radial fiber network within the annulus fibrosus of the lumbar intervertebral disc: a finite elements study. *J. Biomech. Eng.* 141:021006.

Showalter, B. L., De Lucca, J. F., Peloquin, J. M., Cortes, D. H., Yoder, J. H., Jacobs, N. T., et al. (2016). Novel human intervertebral disc strain template to quantify regional three-dimensional strains in a population and compare to internal strains predicted by a finite element model. *J. Orthop. Res.* 34, 1264−1273.

Sikora, S. N. F. (2013). *Experimental and Computational Study of the Behaviour of Trabecular Bone-Cement Interfaces*. Ph.D. Thesis. Leeds: University of Leeds.

Sikora, S. N. F., Miles, D. E., Tarsuslugil, S. M., Mengoni, M., and Wilcox, R. K. (2018). Examination of an in vitro methodology to evaluate the biomechanical performance of nucleus augmentation in axial compression. *Proc. Instit. Mech. Eng. Part H J. Eng. Med.* 232, 230–240. doi: 10.1177/0954411917752027

Spera, D., Genovese, K., and Voloshin, A. (2011). Application of stereo−digital image correlation to full−field 3−D deformation measurement of intervertebral disc. *Strain* 47, e572–e587.

Stadelmann, M. A., Maquer, G., Voumard, B., Grant, A., Hackney, D. B., Vermathen, P., et al. (2018). Integrating MRI-based geometry, composition and fiber architecture in a finite element model of the human intervertebral disc. *J. Mech. Behav. Biomed. Mater.* 85, 37–42. doi: 10.1016/j.jmbbm.2018.05.005

Tarsuslugil, S. M., O'Hara, R. M., Dunne, N. J., Buchanan, F. J., Orr, J. F., Barton, D. C., et al. (2014). Experimental and computational approach investigating burst fracture augmentation using PMMA and calcium phosphate cements. *Ann. Biomed. Eng.* 42, 751–762. doi: 10.1007/s10439-013-0959-3

Tavana, S., Clark, J. N., Prior, J., Baxan, N., Masouros, S. D., Newell, N., et al. (2020). Quantifying deformations and strains in human intervertebral discs using Digital Volume Correlation combined with MRI (DVC-MRI). *J. Biomech.* 102:109604. doi: 10.1016/j.jbiomech.2020.109604

Timoshenko, S., and Goodier, J. (1970). *Theory of Elasticity*, 3rd Edn. New York, NY: McGraw-Hill.

Vadalà, G., Russo, F., Pattappa, G., Peroglio, M., Stadelmann, V. A., Roughley, P., et al. (2015). A nucleotomy model with intact annulus fibrosus to test intervertebral disc regeneration strategies. *Tissue Eng. Part C Methods* 21, 1117–1124. doi: 10.1089/ten.tec.2015.0086

Wijayathunga, V. N., Tanner, S., Ridgway, J., and Wilcox, R. K. (2019). An in vitro study of the intervertebral disc structure using 3T magnetic resonance imaging. *Spine (Phila Pa 1976)* 44, 793–800. doi: 10.1097/brs.0000000000002958

Wilke, H. J., Jungkunz, B., Wenger, K., and Claes, L. E. (1998). Spinal segment range of motion as a function of *in vitro* test conditions: effects of exposure period, accumulated cycles, angular-deformation rate, and moisture condition. *Anat. Rec.* 251, 15–19. doi: 10.1002/(SICI)1097-0185(199805)251:1<15::AID-AR4>3.0.CO;2-D

Zapata-Cornelio, F. Y., Day, G. A., Coe, R. H., Sikora, S. N. F., Wijayathunga, V. N., Tarsuslugil, S. M., et al. (2017). Methodology to produce specimen-specific models of vertebrae: application to different species. *Ann. Biomed. Eng.* 45, 2451–2460. doi: 10.1007/s10439-017-1883-8

Conflict of Interest: The authors declare that the research was conducted in the absence of any commercial or financial relationships that could be construed as a potential conflict of interest.

frontiers in Bioengineering and Biotechnology

ORIGINAL RESEARCH
published: 01 April 2021
doi: 10.3389/fbioe.2021.646079

Biomechanical Investigation Between Rigid and Semirigid Posterolateral Fixation During Daily Activities: Geometrically Parametric Poroelastic Finite Element Analyses

*Mohammad Nikkhoo[1†], Meng-Ling Lu[2,3†], Wen-Chien Chen[2,4], Chen-Ju Fu[2,5], Chi-Chien Niu[2,6], Yang-Hua Lin[7] and Chih-Hsiu Cheng[2,7]**

[1] Department of Biomedical Engineering, Science and Research Branch, Islamic Azad University, Tehran, Iran, [2] Bone and Joint Research Center, Chang Gung Memorial Hospital, Taoyuan, Taiwan, [3] Department of Orthopedic Surgery, Chang Gung Memorial Hospital, Kaohsiung, Taiwan, [4] Department of Orthopedic Surgery, Chang Gung Memorial Hospital, Taoyuan, Taiwan, [5] Division of Emergency and Critical Care Radiology, Chang Gung Memorial Hospital, Taoyuan, Taiwan, [6] Department of Orthopedic Surgery, Chang Gung Memorial Hospital, Taoyuan, Taiwan, [7] School of Physical Therapy and Graduate Institute of Rehabilitation Science, College of Medicine, Chang Gung University, Taoyuan, Taiwan

While spinal fusion using rigid rods remains the gold standard treatment modality for various lumbar degenerative conditions, its adverse effects, including accelerated adjacent segment disease (ASD), are well known. In order to better understand the performance of semirigid constructs using polyetheretherketone (PEEK) in fixation surgeries, the objective of this study was to analyze the biomechanical performance of PEEK versus Ti rods using a geometrically patient-specific poroelastic finite element (FE) analyses. Ten subject-specific preoperative models were developed, and the validity of the models was evaluated with previous studies. Furthermore, FE models of those lumbar spines were regenerated based on postoperation images for posterolateral fixation at the L4–L5 level. Biomechanical responses for instrumented and adjacent intervertebral discs (IVDs) were analyzed and compared subjected to static and cyclic loading. The preoperative model results were well comparable with previous FE studies. The PEEK construct demonstrated a slightly increased range of motion (ROM) at the instrumented level, but decreased ROM at adjacent levels, as compared with the Ti. However, no significant changes were detected during axial rotation. During cyclic loading, disc height loss, fluid loss, axial stress, and collagen fiber strain in the adjacent IVDs were higher for the Ti construct when compared with the intact and PEEK models. Increased ROM, experienced stress in AF, and fiber strain at adjacent levels were observed for the Ti rod group compared with the intact and PEEK rod group, which can indicate the risk of ASD for rigid fixation. Similar to the aforementioned pattern, disc height loss and fluid loss were significantly higher at adjacent levels in the Ti rod group

OPEN ACCESS

Edited by:
Fabio Galbusera,
Galeazzi Orthopedic Institute (IRCCS), Italy

Reviewed by:
Maxim Bashkuev,
Charité – Medical University of Berlin, Germany
André P. G. Castro,
Universidade de Lisboa, Portugal

***Correspondence:**
Chih-Hsiu Cheng
chcheng@mail.cgu.edu.tw

[†] These authors have contributed equally to this work

Specialty section:
This article was submitted to Biomechanics, a section of the journal Frontiers in Bioengineering and Biotechnology

Received: 24 December 2020
Accepted: 02 March 2021
Published: 01 April 2021

Citation:
Nikkhoo M, Lu M-L, Chen W-C, Fu C-J, Niu C-C, Lin Y-H and Cheng C-H (2021) Biomechanical Investigation Between Rigid and Semirigid Posterolateral Fixation During Daily Activities: Geometrically Parametric Poroelastic Finite Element Analyses. Front. Bioeng. Biotechnol. 9:646079. doi: 10.3389/fbioe.2021.646079

after cycling loading which alter the fluid–solid interaction of the adjacent IVDs. This phenomenon debilitates the damping quality, which results in disc disability in absorbing stress. Such finding may suggest the advantage of using a semirigid fixation system to decrease the chance of ASD.

Keywords: personalized modeling, finite element analysis, poroelastic, PEEK, titanium, spinal biomechanics, posterolateral fixation

INTRODUCTION

Degenerative lumbar diseases such as the spinal stenosis, lumbar instability, degenerative spondylolisthesis, and spondylolytic spondylolisthesis can cause clinical symptoms such as the low back pain (Serhan et al., 2011). Posterolateral fusion (PLF) and posterior lumbar interbody fusion (PLIF) techniques using rigid rods [i.e., pure titanium (Ti), Ti alloy, or cobalt-chrome (CoCr) rods] have been widely used in the treatment of degenerative lumbar disease (Schwab et al., 1995; De Iure et al., 2012; Campbell et al., 2017). However, the persistence of symptoms and the progression of degenerative disease were reported in some cases after PLF/PLIF, which is recognized as adjacent segment disease (ASD) (Rahm and Hall, 1996; Wang et al., 2017).

To minimize the incidence of ASD, several dynamic systems such as artificial discs and dynamic stabilization implants have therefore been introduced (Beatty, 2018) which can preserve intervertebral disc (IVD) motion and unload the stress on adjacent levels (Huang et al., 2016). However, the indications of these treatments are limited and they are not applicable to patients who still require fusion surgery. Subsequently, semirigid rods using polyetheretherketone (PEEK) were successfully used in fixation surgeries and good outcomes were reported (Highsmith et al., 2007). Nonetheless, some conflicting outcomes have also been reported in the literature when comparing PEEK rods against rigid ones after spinal fixation (Ormond et al., 2016).

While different clinical and biomechanical experimental studies were performed to evaluate the applicability of PEEK semirigid rods for non-fusion surgeries (Chou et al., 2015; Huang et al., 2016; Li et al., 2016; Selim et al., 2018), finite element (FE) modeling can be utilized, in parallel, as a practical tool for non-invasive investigations. Abundant FE studies have investigated the effect of different diseases/disorders (Schmidt et al., 2007b; Bashkuev et al., 2018; Ozkal et al., 2020) and relevant treatment modalities and techniques (Nikitovic et al., 2017; Rijsbergen et al., 2018; Zhang et al., 2018a; Heo et al., 2020) in lumbar spine. However, most of the available spinal FE models in the literature are limited to a single geometry which can cause uncertainty in the results and affect the reliability of FE model prediction for clinical application (Laville et al., 2009; Nikkhoo et al., 2019, 2020; Liu et al., 2020; Ozkal et al., 2020). Therefore, a workflow including procedural generation of patient-specific geometry for FE simulations can enhance our understanding of treatment results for adopting clinical approaches.

Choosing a proper formulation and assigning mechanical properties are essential to simulate the complex behavior of the spine. IVDs have a hydrostatic function by bearing and distributing mechanical loads, storing energy, and restraining excessive motion in the spine. Since IVD is a non-homogeneous, well hydrated, and porous composite structure, various mathematical models (e.g., linear elastic, hyperelastic, viscoelastic, and poroelastic) were developed to simulate the biomechanics of the spine (Schmidt et al., 2013; Dreischarf et al., 2014). The intricate fluid–solid interactions in IVD, as a highly hydrated soft tissue, can be simulated by the poroelastic theory (Simon, 1992), and numerous studies used biphasic or multiphasic poroelastic FE models (Argoubi and Shirazi-Adl, 1996; Iatridis et al., 2003; Schmidt et al., 2010; Schroeder et al., 2010; Castro et al., 2014; Barthelemy et al., 2016; Castro and Alves, 2020) to mimic its time-dependent response. Hence, studying the biomechanical response of the spine during daily activities and assessment of the effect of damping characteristics (shock absorption mechanism) under cyclic loading could be beneficial when the objective is to investigate the spine biomechanics for spinal surgeries.

There remains a gap of knowledge in the detailed performance of semirigid constructs in spinal fixation surgeries to consider both the variation of anatomical geometries and the time-dependent response of the spine. Hence, the objective of this study was to comparatively analyze the biomechanical performance of PEEK versus Ti rods subjected to static and cyclic loading during daily activities using geometrically patient-specific poroelastic FE analyses.

MATERIALS AND METHODS

Patient-Specific Poroelastic FE Modeling

The geometries of the lumbosacral spine (L1–S1) were generated from lateral and anterior–posterior (AP) radiographs of 10 patients (age: 61.4 ± 8.1 years, BMI: 25.1 ± 1.7 kg/m^2, six females and four males) using a previously developed algorithm (Nikkhoo et al., 2020) (**Figure 1**). All patients presented with lumbar spine instability including single degenerative spondylolisthesis and spondylolytic spondylolisthesis in the lumbar region and underwent minimally invasive surgical procedures. All relevant clinical data were obtained from the data registry at Chang Gung Memorial Hospital, and a signed informed consent was acquired from all the participants prior to their enrolment in the clinical protocol, which was approved by the university research ethics committee.

Based on a previously validated FE model of the IVD (Nikkhoo et al., 2013a,b), a non-linear poroelastic FE model of the lumbosacral spine (L1–S1) was developed for 10 patients in relation to their preoperative (preop) geometries (**Figure 1**). Each FE model consists of six vertebrae (i.e., posterior bony elements

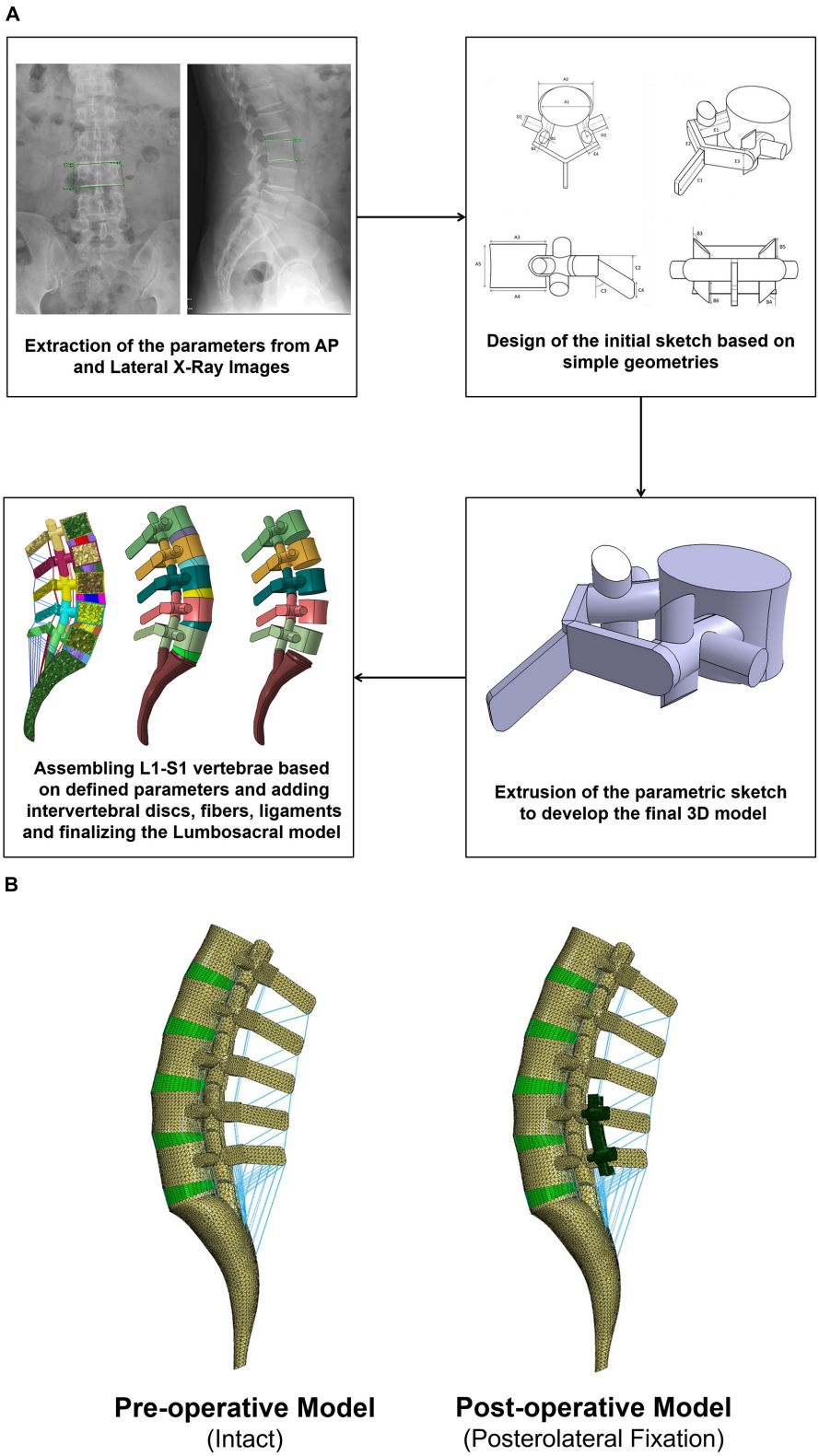

FIGURE 1 | (A) Procedure of personalized poroelastic finite element (FE) modeling of the lumbosacral spine and **(B)** preoperative (intact) and postoperative (posterolateral fixation) FE models.

and vertebral bodies including cancellous and cortical bones), five IVDs and 10 endplates (i.e., L1–L2, L2–L3, L3–L4, L4–L5, L5–S1), and seven ligaments [i.e., anterior longitudinal ligament (ALL), posterior longitudinal ligament (PLL), ligamentum flavum (LF), transverse ligament (TL), capsular ligament (CL), interspinous ligament (ISL), and supraspinous ligament (SSL)], as well as five pairs of facet joints. The IVDs were represented by a reinforced composite material including the annulus fibrosus (AF), ground substance, nucleus pulposus (NP), and AF collagen fibers.

The non-linear drained solid phase of the AF and NP was simulated based on the Mooney–Rivlin hyperelastic theory in alignment with the literature (Schmidt et al., 2007a; El-Rich et al., 2009) (**Table 1**). Poroelasticity was considered for vertebral bodies, endplates, and IVDs in the FE model. Permeability values were considered dependent on void ratio (**Table 1**) (Argoubi and Shirazi-Adl, 1996; Ferguson et al., 2004) as follows:

$$k = k_0 \left[\frac{e(1+e_0)}{e_0(1+e)}\right]^2 exp\left[M\left(\frac{1+e}{1+e_0}-1\right)\right] \quad (1)$$

Where k_0 is the initial permeability and e is defined as follows:

$$e = \frac{\emptyset_f}{1-\emptyset_f} \quad (2)$$

Where $\emptyset_f$ is the porosity of the tissue which varies with tissue deformation. The six concentric reinforced fiber layers with an orientation of $\pm 35°$ within a distance of 1 mm were embedded in the AF ground substance (Naserkhaki et al., 2016). A constant boundary pore pressure of 0.25 MPa was imposed on all external surfaces of the IVDs to mimic the swelling phenomenon (Schmidt et al., 2010; Galbusera et al., 2011a). Ligaments were modeled using non-linear truss elements which could be activated only in tension (**Figure 2**) (Shirazi-Adl et al., 1986a; Pintar et al., 1992). The ligaments were attached at fixed points in a primary standard anatomy-based geometrical lumbosacral spine model, and their length could be updated according to the measured parameters of the bony parts for different individuals.

The mechanical properties of the other tissues were adopted based on previous studies (Shirazi-Adl et al., 1986b; Goto et al., 2003; Schmidt et al., 2007a) (**Table 1**). To simulate the articulation of the facet joints, a surface-to-surface contact rule for both tangential and normal directions was applied to model within a gap length of 0.5 mm (Naserkhaki et al., 2016; Naserkhaki and El-Rich, 2017). The meshing sensitivity analyses were performed, and the FE models were evaluated using a total of 186,325 elements for all the models.

The validity of the IVD time-dependent response was previously validated based on the achieved results from a motion

TABLE 1 | Mechanical properties of the patient-specific poroelastic finite element model.

Spinal component	Material behavior	Mechanical properties	References
Cortical bone	Linear poroelastic	E = 12,000 MPa, ν = 0.3, $k_0 = 1 \times 10^{-20}$ (m^4/N s), e = 0.02	Argoubi and Shirazi-Adl, 1996; Goto et al., 2003; Ferguson et al., 2004; Schmidt et al., 2010; Galbusera et al., 2011b; Park et al., 2013
Cancellous bone	Linear poroelastic	E = 200 MPa, ν = 0.25, $k_0 = 1 \times 10^{-13}$ (m^4/N s), e = 0.4	Argoubi and Shirazi-Adl, 1996; Ferguson et al., 2004; Schmidt et al., 2007a, 2010; Galbusera et al., 2011b; Shih et al., 2013
Endplate	Linear poroelastic	E = 5 MPa, ν = 0.1, $k_0 = 7.5 \times 10^{-15}$ (m^4/N s), e = 4	Argoubi and Shirazi-Adl, 1996; Goto et al., 2003; Ferguson et al., 2004; Schmidt et al., 2007a, 2010; Galbusera et al., 2011b
Annulus fibrosus ground	Incompressible poro-hyperelastic (Mooney–Rivilin)	C10 = 0.18, C01 = 0.045, $k_0 = 3 \times 10^{-16}$ (m^4/N s), e = 2.33	Argoubi and Shirazi-Adl, 1996; Ferguson et al., 2004; El-Rich et al., 2009; Schmidt et al., 2010; Galbusera et al., 2011b
Nucleus pulposus	Incompressible poro-hyperelastic (Mooney–Rivilin)	C10 = 0.12, C01 = 0.030, $k_0 = 7.5 \times 10^{-16}$ (m^4/N s), e = 4	Argoubi and Shirazi-Adl, 1996; Ferguson et al., 2004; Schmidt et al., 2007a, 2010; Galbusera et al., 2011b
Collagen fibers	Non-linear elastic	Stiffness increasing from the inner to the outer layer	Shirazi-Adl et al., 1986b; Schmidt et al., 2006
ALL, PLL, LF, ISL, SSL, ITL, CL	Non-linear elastic	Non-linear curves in **Figure 2**	Shirazi-Adl et al., 1986a; Pintar et al., 1992
Pedicle screws	Elastic	E = 110,000 MPa, ν = 0.3	Zhang et al., 2018b
Rigid rod (Ti)	Elastic	E = 110,000 MPa, ν = 0.3	Zhang et al., 2018b
Semirigid rod (PEEK)	Elastic	E = 3,500 MPa, ν = 0.3	Zhang et al., 2018b

ALL, anterior longitudinal ligament; PLL, posterior longitudinal ligament; LF, ligamentum flavum; ISL, interspinous ligament; SSL, supraspinous ligament; ITL, intertransverse ligament; CL, capsular ligament.

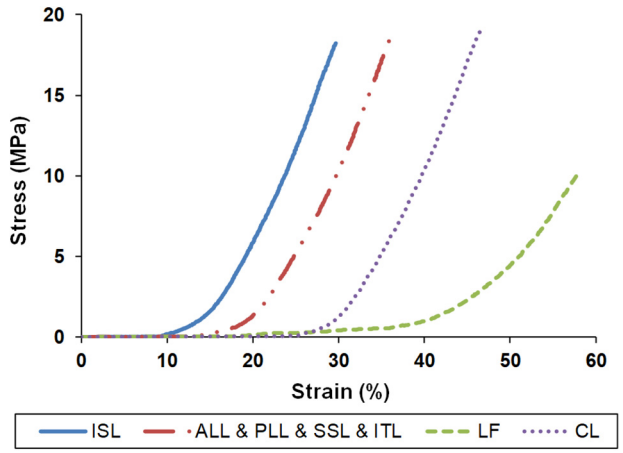

FIGURE 2 | Stress–strain properties of the ligaments for finite element modeling. ISL, interspinous ligament; ALL, anterior longitudinal ligament; PLL, posterior longitudinal ligament; SSL, supraspinous ligament; ITL, intertransverse ligament; LF, ligamentum flavum; CL, capsular ligament.

segment subjected to short-term creep, long-term creep, and a daily cycle (Nikkhoo et al., 2013a; Ghobadiha et al., 2019). To evaluate the validity of the preop lumbar spine FE models, a combined loading scenario (i.e., the combination of the compressive forces and bending moments; **Table 2**) (Dreischarf et al., 2011, 2014) was applied to the models and the results of range of motion (ROM), intradiscal pressure (IDP), and facet joint forces (FJF) were compared with previous numerical studies from eight well-established FE models of the lumbar spine (Dreischarf et al., 2014). To apply the physiological compression loads, the follower load technique (Patwardhan et al., 1999; Shirazi-Adl and Parnianpour, 2000; Dreischarf et al., 2014) was used as described in **Table 2**. The rotational moments were applied to the superior surface of L1, and Dirichlet boundary conditions were considered at the sacral region to inhibit any displacement/rotation in all degrees of freedom.

Patient-Specific Posterolateral Fixation FE Modeling

Biomechanical investigation between rigid and semirigid posterolateral fixation during daily activities was selected as the application for this validated parametric poroelastic model. For this purpose, postoperative (postop) FE models of the same patients were regenerated and developed based on postop images. Posterolateral fixation surgery at the L4–L5 level was mimicked in the FE models by simulating a wide laminectomy and removing the PLL and LF while preserving the IVD and spinous process. A posterior bilateral pedicle screw fixation construct was then implemented based on measurements from the postop images. The screws and rods were considered as linear elastic based on reported data in the literature (Zhang et al., 2018b) (**Table 1**). Tie contact condition was used to constrain equal translational and rotational motions for attached surfaces between the vertebrae, screws, and rods for mimicking the permanent fusion. For each patient, the simulations were performed using corresponding materials for Ti and PEEK (**Table 1**) with the relevant postop model (**Figure 1B**). Following an 8-h preconditioning resting period under the constant compressive load of 200 N (Galbusera et al., 2011a), a 16-h cyclic compressive loading of 500–1,000 N (40 and 20 min, respectively) was applied to the postop FE models. The cyclic axial compressive loading was simulated by the follower load technique (Patwardhan et al., 1999; Shirazi-Adl and Parnianpour, 2000; Dreischarf et al., 2014) using connector elements. Different rotational movements (i.e., flexion, extension, right and left lateral bending, and right and left axial rotation) were superimposed using 10 N m moment before and after cyclic loading (i.e., points 1 and 2 in **Figure 3**) to model the rotational motions in the morning and evening. The rotational moments were linearly applied and removed in 10 s (i.e., 5 s for loading and 5 s for unloading), and only one motion was evaluated in each diurnal loading simulation. The rotational moments were applied to the superior surface of L1, and Dirichlet boundary conditions were considered at the sacral region. Biomechanical responses including motion patterns, IVD height loss, fluid loss, experienced stress in AF, and collagen fiber strain were analyzed before and after cyclic loading under the same loading and boundary conditions.

Statistical Analyses on the Results of Different FE Models

The simulation results of the motion patterns (i.e., ROM), disc height loss, fluid loss, experienced stress in AF, and collagen fiber strain were all compared among the rigid and semirigid models. As the data were not normally distributed, the non-parametric Friedman with Nemenyi *post hoc* tests were conducted to determine the differences of the calculated results. The p values less than 0.05 were considered as significant statistical differences.

RESULTS

The numerical precisions for the FE models were verified using mesh sensitivity analyses. The intersegmental ROMs for the preop models were consistent with previous numerical data from the literature (**Figure 4**). Besides, the calculated IDP (**Figure 5**) and FJF (**Figure 6**) fell within a comparable range to previous studies in different directions.

Compared with preop FE models, the ROMs at the instrumented level were significantly decreased for both Ti (averagely decreased to 4.01° in flexion, 2.62° in extension, 2.45° in lateral bending, and 1.18° in axial rotation) and PEEK (averagely decreased to 2.95° in flexion, 1.87° in extension, 1.92° in lateral bending, and 1.06° in axial rotation) fixation systems (**Figure 7A**). However, the calculated ROMs at the instrumented level were higher for the PEEK construct in flexion, extension, and lateral bending (**Figure 7A**). The ROMs at the adjacent levels were significantly increased for Ti rods compared with the intact models in flexion, extension, and lateral bending (**Figures 7B,C**). Nonetheless, no significant changes were detected between the ROM of the adjacent IVDs for the intact and PEEK construct FE models (**Figures 7B,C**).

TABLE 2 | Combined loading conditions for simulation of lumbar spine in different movements.

Direction	Compressive load* (N)	Moment (N m)	References
Flexion	1,175	7.5	Rohlmann et al., 2009; Dreischarf et al., 2014
Extension	500	7.5	Rohlmann et al., 2009; Dreischarf et al., 2014
Lateral bending	700	7.8	Dreischarf et al., 2012, 2014
Axial rotation	720	5.5	Dreischarf et al., 2011, 2014

**The follower load technique (Patwardhan et al., 1999; Shirazi-Adl and Parnianpour, 2000; Dreischarf et al., 2014) was used to simulate the compressive loading.*

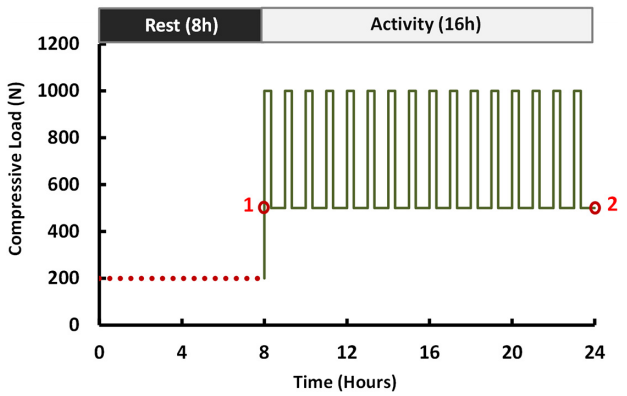

FIGURE 3 | Loading scenario of the compressive force (flexion, extension, lateral bending, and axial rotation moments of 10 N m were applied at points 1 and 2).

During cyclic loading, the disc height averagely decreased by 6.58, 6.13, and 5.79% at L3–L4, L4–L5, and L5–S1, respectively, in the intact FE models. In postop models, increased disc height loss and fluid loss in adjacent levels were observed for Ti fixation system models compared with the intact ones (**Figure 8**). Moreover, disc height loss and fluid loss in the adjacent IVDs were significantly higher for the Ti construct when compared with the PEEK models (**Figure 8**). The axial stress and collagen fiber strain in AF significantly increased in adjacent levels for posterolateral fixation models (**Figures 9**, **10**) in flexion and extension. However, the axial stress and collagen fiber strain in adjacent IVDs were higher for the Ti construct when compared with the PEEK models (**Figures 9**, **10**). The variations of the increased stress and fiber strain in adjacent levels were minimal and not significant for lateral bending and axial rotation, respectively, after applying the cyclic loading (**Figures 9**, **10**).

DISCUSSION

The rigid instrumented PLF and PLIF have been the gold standard treatment techniques for spinal stenosis, disc degeneration, and spondylolisthesis. Conversely, numerous studies have demonstrated unwanted side effects of the rigid PLF/PLIF, including pseudarthrosis, loss of motion, back pain, and ASD (Rahm and Hall, 1996; Wang et al., 2017). It was reported that using an interbody device can enhance the postop biomechanical stability and increase the fusion rate (Lidar et al., 2005; Aygün et al., 2014; Lee et al., 2014; Campbell et al., 2017). However, implanting the interbody device may increase the segmental rigidity which could result in increasing the mechanical stress to the adjacent segments (Chiang et al., 2006; Sudo et al., 2006). A less rigid stabilization system can theoretically preserve part of rotational motion in instrumented level and unload the extra exposed stress on adjacent levels (Lee et al., 2014; Huang et al., 2016). Therefore, a quantitative study to analyze the biomechanical behavior of the lumbar spine in response to PLF surgery using rigid versus semirigid rods may be beneficial for clinicians. Spinal fixation construct is the most essential part of the fusion approach, and the current study therefore aimed to investigate the fixation itself. For this purpose, the posterolateral fixation was utilized for simulating the postop models with Ti and PEEK rods, and the bone graft fusion between the transverse processes was neglected, which is a common simplification in the literature (Goto et al., 2003; Gornet et al., 2011; Jin et al., 2012; Jahng et al., 2013).

The current study employed a geometrically patient-specific poroelastic FE modeling technique to evaluate the intersegmental motions and load sharing of the lumbar spine by developing pre- and postop simulations. The time-dependent responses of the FE model subjected to cyclic loading were investigated in this study by considering the poroelastic theory for vertebra, IVDs, and endplates which was mostly ignored in previous relevant studies (Jin et al., 2012; Jahng et al., 2013; Guo et al., 2019). Considering a time-dependent model by calculating the interactions of disc solid structures and interstitial fluid can determine IVD endurance to cyclic loadings (Galbusera et al., 2011b; Castro et al., 2018). Therefore, this study provided the calculated disc height loss, fluid loss, altered stress, and strain in the AF region which can better quantify the effect of rigid and semirigid posterolateral fixation surgery on biomechanical response of the lumbar spine.

Moreover, we used a parametric subject-specific FE model which can be regenerated for different patients based on simple lateral and AP X-ray images. Hence, we repeated the simulations for 10 patients (in total, 30 pre- and postop FE models) to consider interanatomical variability to investigate the influence of posterolateral fixation surgery using rigid and semirigid rods. Repeating the calculations for different patients and considering the influences of the geometry (anatomical parameters such as vertebra dimensions, disc height, lordosis angle, etc.) can better evaluate if the observed differences in the results for rigid versus semirigid posterolateral fixation systems are significant or not. Previous FE models in the literature are constrained to unique geometry, typically based on one subject. The intrinsic geometric

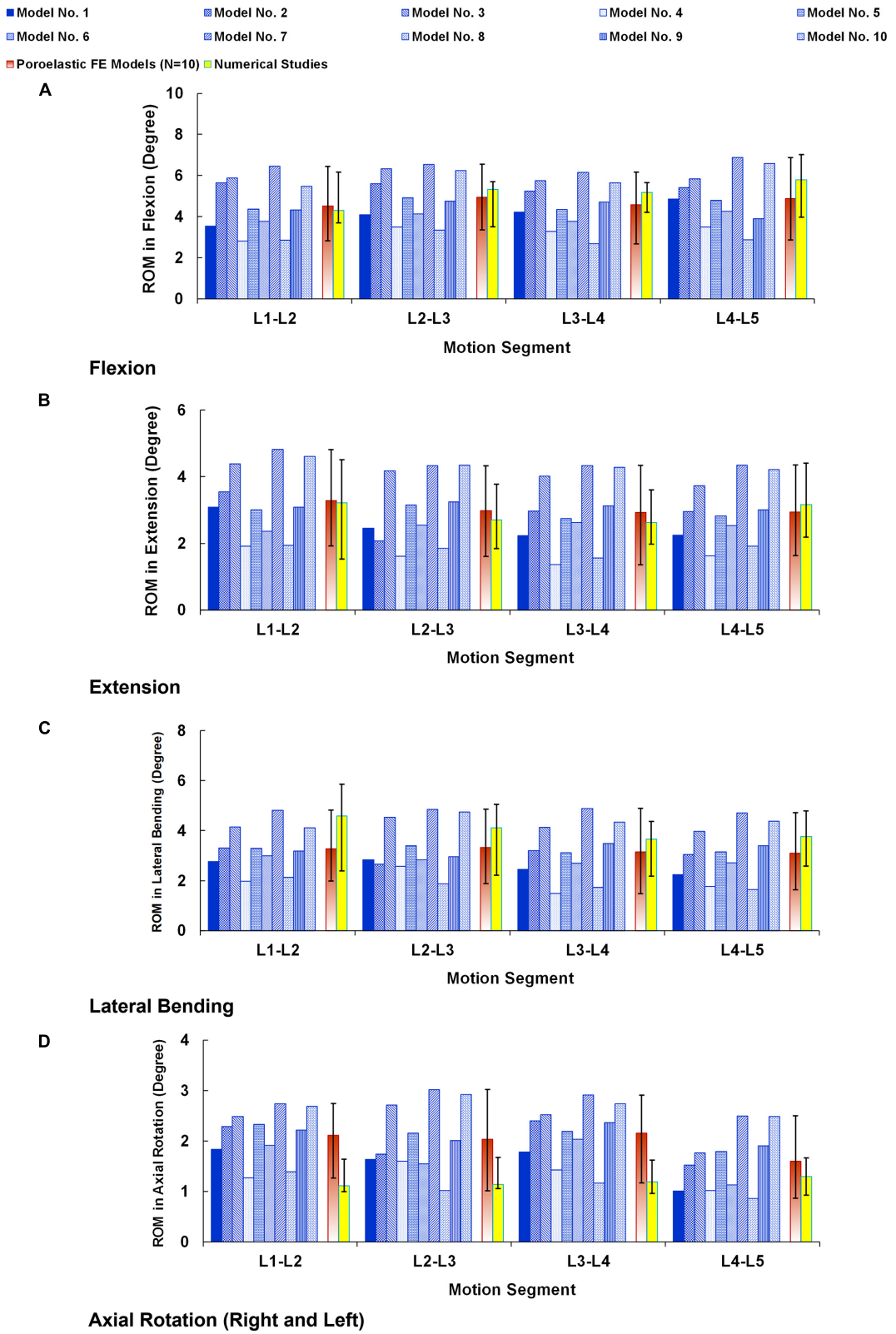

FIGURE 4 | Intersegmental range of motions (ROMs) for preoperative FE models compared with the numerical studies (Dreischarf et al., 2014) in **(A)** flexion, **(B)** extension, **(C)** lateral bending, and **(D)** axial rotation. The reported ROMs in lateral bending and axial rotation are the average in the left and right directions. The error bars indicate the ranges of the results.

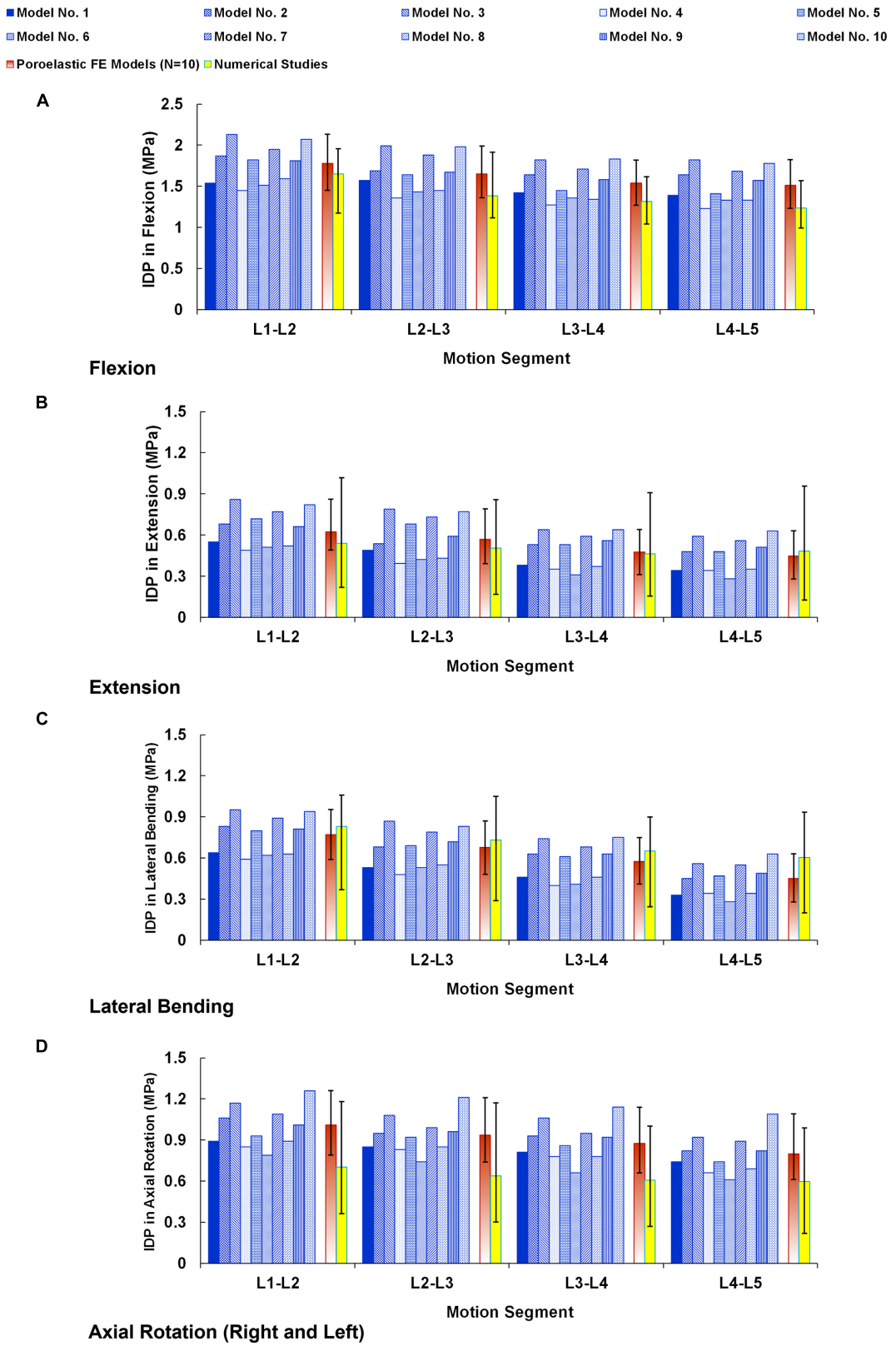

FIGURE 5 | Intradiscal pressure (IDP) for preoperative FE models compared with the numerical studies (Dreischarf et al., 2014) in **(A)** flexion, **(B)** extension, **(C)** lateral bending, and **(D)** axial rotation. The reported IDPs in lateral bending and axial rotation are the average in the left and right directions. The error bars indicate the ranges of the results.

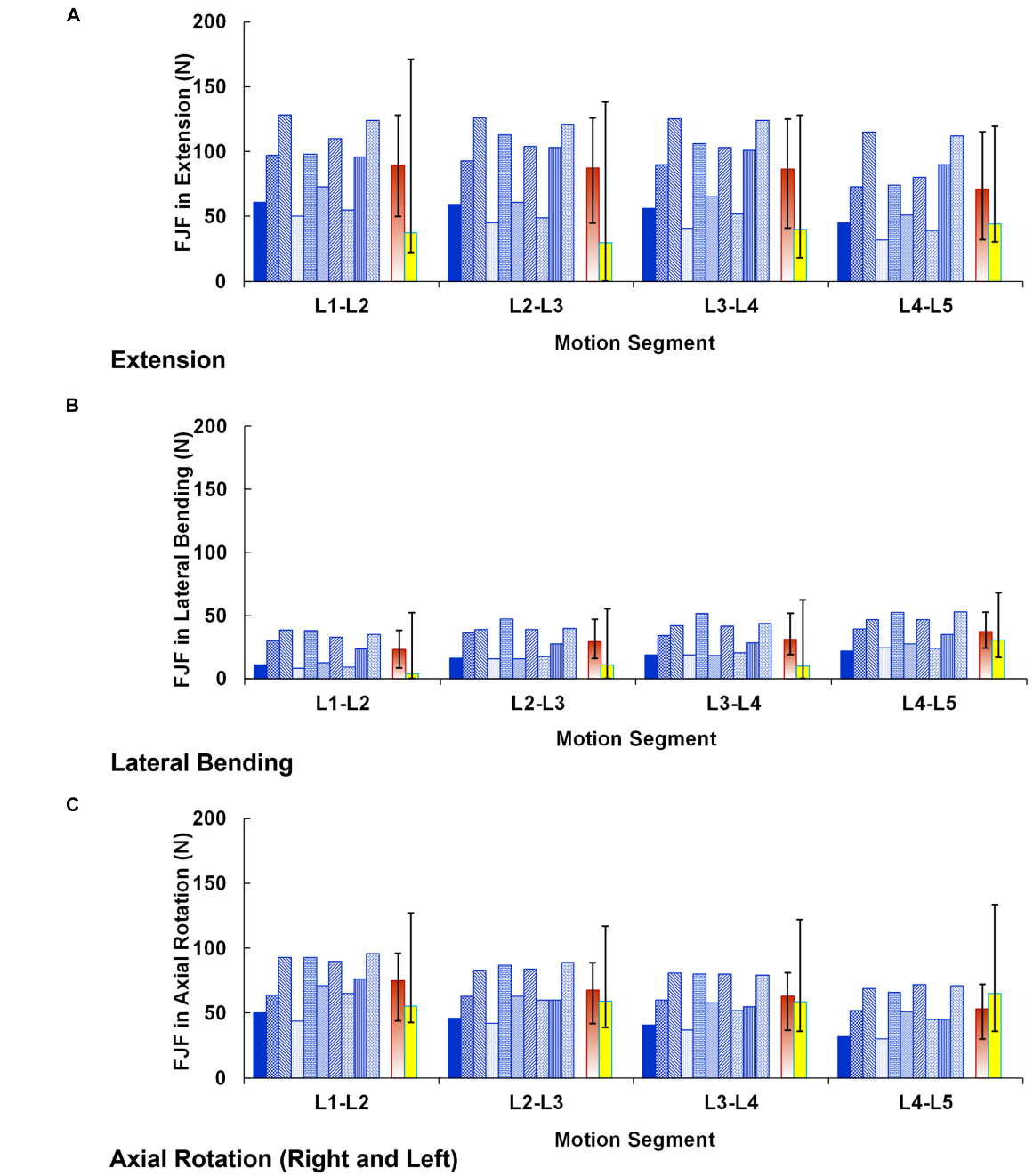

FIGURE 6 | Facet joint forces (FJF) for preoperative FE models compared with the numerical studies (Dreischarf et al., 2014) in **(A)** extension, **(B)** lateral bending, and **(C)** axial rotation. The reported FJFs in lateral bending and axial rotation are the average in the left and right directions. The error bars indicate the ranges of the results.

differences among patients may cause indecision in the results and decrease the reliability of the FE model prediction. This study provided a validated parametric poroelastic FE model to evaluate the results for different patients and provide more accurate clinical outcome. Although the clinical applicability of this FE modeling technique was previously confirmed, the attained results from these 10 preop poroelastic models (i.e., ROM, IDP, and FJF) were generally in alignment with previous

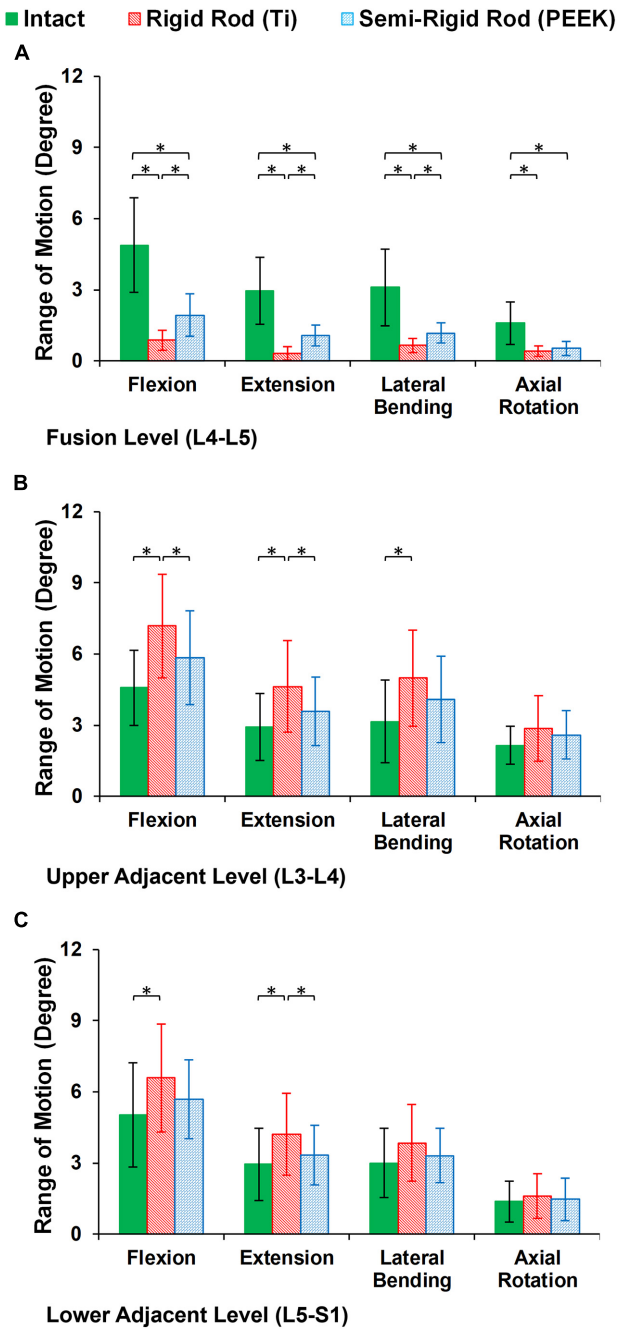

FIGURE 7 | Intersegmental range of motions (ROMs) for postoperative FE models in the **(A)** instrumented level (L4–L5), **(B)** upper adjacent level (L3–L4), and **(C)** lower adjacent level (L5–S1). The error bars indicate the standard deviations, and "*" shows that p values < 0.05.

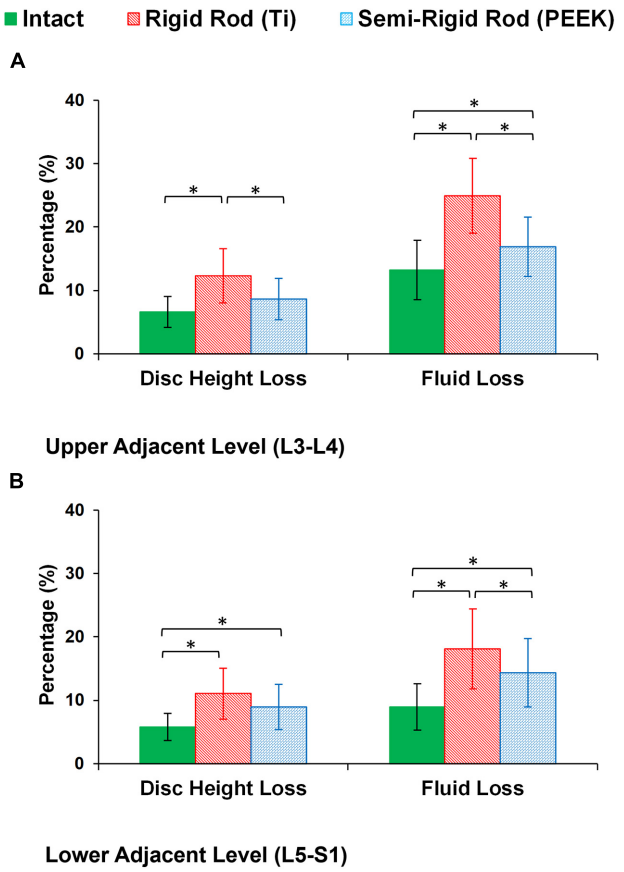

FIGURE 8 | Percentage of disc height loss and fluid loss for postoperative FE models in the **(A)** upper adjacent level (L3–L4) and **(B)** lower adjacent level (L5–S1). The error bars indicate the standard deviations, and "*" shows that p values < 0.05.

published studies (Dreischarf et al., 2014) confirming the validity of these models. The mechanical responses achieved by different models (**Figures 4–6**) confirm the important influences of the geometry and curvature of the lumbar spine.

The postop simulations showed that the average ROM significantly decreased for both Ti and PEEK rod constructs at the instrumented level (L4–L5) in all directions. As expected, the ROM in the instrumented level was significantly higher in the PEEK models compared with Ti ones based on its structural flexibility. Increased ROMs at adjacent levels (L3–L4 and L5–S1) were observed for the Ti rod group compared with the intact and PEEK rod group which may indicate the risk of disc degeneration in adjacent levels for rigid fixation. Minor alterations in adjacent level ROM were observed in lateral bending, and the differences in axial rotation were not significant. Similar to the aforementioned pattern, disc height loss and fluid loss were significantly higher at adjacent levels in the Ti rod group after 16 h of cycling loading during daily activities, which alter the fluid–solid interaction of the adjacent IVDs.

Disc height loss is an important clinical indicator for disc degeneration. The loss of disc height across all levels of the preop FE models was approximately uniform but was altered in the postop models. The rigidity of the Ti rod system in the L4–L5 level subsequently increased the load sharing through the adjacent levels revealing a significant increase in disc height loss and fluid loss. Previous clinical studies reported IVD height loss in adjacent levels for 30–95% of the patients who had fusion

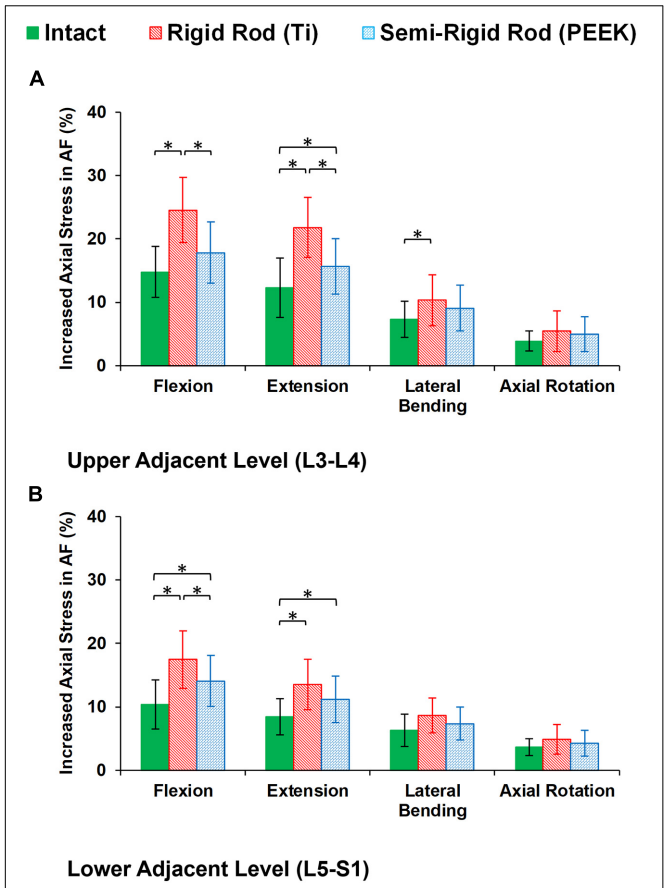

FIGURE 9 | Increased axial stress in annulus fibrosus (AF) for postoperative FE models in the **(A)** upper adjacent level (L3–L4) and **(B)** lower adjacent level (L5–S1) in different directions. The reported results in lateral bending and axial rotation are the average in left and right directions. The error bars indicate the standard deviations, and "*" shows that p values < 0.05.

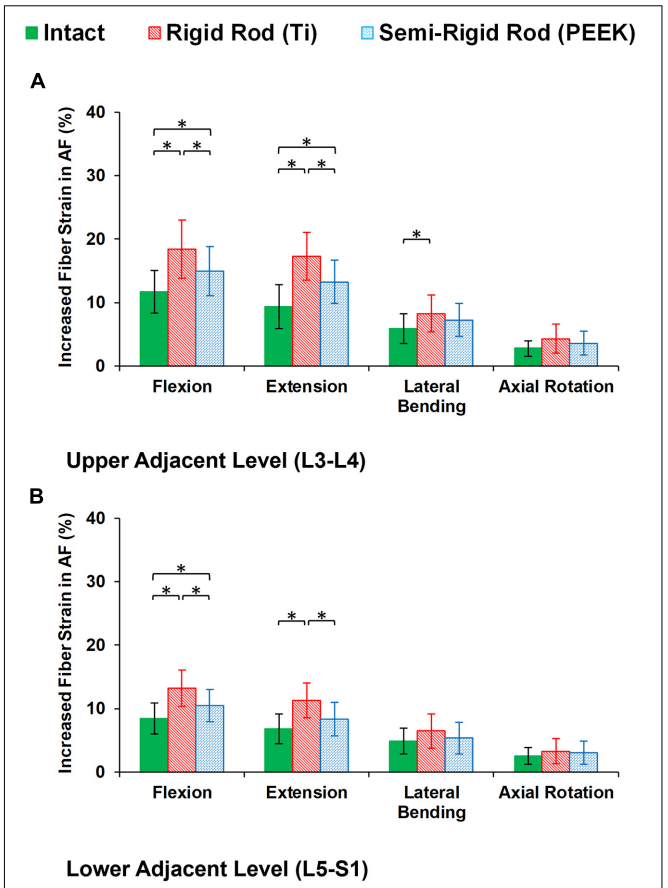

FIGURE 10 | Increased fiber strain in annulus fibrosus (AF) for postoperative FE models in the **(A)** upper adjacent level (L3–L4) and **(B)** lower adjacent level (L5–S1) in different directions. The reported results in lateral bending and axial rotation are the average in the left and right directions. The error bars indicate the standard deviations, and "*" shows that p values < 0.05.

surgery utilizing Ti rods (Miyakoshi et al., 2000; Ishihara et al., 2001). Consistent with previous clinical (Huang et al., 2016) and *in vitro* (Turner et al., 2010; Gornet et al., 2011; Chou et al., 2015) studies, the PEEK construct preserved part of the ROM at the fused level and reduced the abnormal compensatory load sharing at the adjacent levels. Similar patterns were observed regarding fluid loss in adjacent IVDs in postop FE models. Fluid loss debilitates the damping quality, which results in disc disability in absorbing tress. Such finding may suggest the advantage of using a semirigid fixation system to decrease the chance of ASD. The achieved standard deviations in the reported results show considerable ranges for the altered mechanical responses after surgery in different patients, which highlights the importance of interanatomical variability in clinical evaluations.

The findings of this study also confirmed that stress and fiber strain in the AF region were significantly increased in adjacent levels for the fused model in sagittal plane movements (i.e., flexion and extension). Besides, the increased stress and strain were significantly higher in rigid Ti fixation compared with the semirigid PEEK rod. The PEEK rod system transfers more of the compressive load from the posterior column to the anterior side. This demonstrates the ability to change the stress distribution and improve the conditions similar to the intact lumbar spine. After repetitive cyclic loading, greater fluid loss and disc height loss were observed in the rigid construct, which results in decreasing the effect of fluid phase in overall bulk strength that may lead to more experienced stress and strain in the solid phase. The ROM, fluid flow, and load sharing results are in general agreement with those presented in previous studies (Gornet et al., 2011; Chou et al., 2015; Huang et al., 2016) confirming the potential advantages of PEEK over Ti fixation.

Few simplifications were assumed for this study. First, the geometry of the patient-specific FE models was constructed based on simplified structures on X-ray images, and the same material properties were used for all different individuals in this study. In addition, more simplifications were considered regarding the poroelastic FE modeling of the IVD compared with some previous works in the literature (Castro et al., 2014; Barthelemy et al., 2016; Rijsbergen et al., 2018; Castro and Alves, 2020). As discussed in detail in a previous work (Nikkhoo et al., 2020),

this parametric patient-specific FE modeling technique can accurately predict the biomechanical response of the lumbar spine in association with various surgical interventions and has the potential to be used in clinical evaluations. As we focused on clinical functionality of this modeling technique, the variation in mechanical properties for different patients was neglected, although it remains a potential framework for our future works. Second, we used the osseoligamentous FE models for this study and the effect of active muscle forces was ignored. Since the objective of this study was to evaluate the effect of posterolateral fixation surgery using rigid and semirigid rods on lumbar spine biomechanics, we applied the common follower load technique (Patwardhan et al., 1999; Shirazi-Adl and Parnianpour, 2000) to account for compressive loading regime for both static and simulated daily activities. Nevertheless, although the current osseoligamentous FE model compensates for the global response for this study, enhancing the model by inserting muscle force effects may improve the model assumptions, especially if we can extract the patient-specific muscle forces *via* dynamic algorithms. Third, we considered the fully saturated porous media in FE model calculations which is a simplification for the patients' IVDs which may be denatured or degenerated. When we calculate the fluid flow and consequently investigate disc height changes and fluid loss, it is important to have accurate data for initial void ratio and fluid saturation rate. This was an unavoidable limitation in this study, and we assumed constant conditions (i.e., similar void ratios based on **Table 1** and fully saturated porous media) for all patients. On the other hand, we mimicked the posterolateral fixation surgery in the L4–L5 level and its IVD was intact in the simulations. To check the influence of mild and moderate degeneration in L4–L5 IVD, extra calculations were performed for three models using altered material properties (Galbusera et al., 2011a), and no significant changes were observed for the variations of the stress and strain patterns in adjacent levels. As we compared the three scenarios for each patient, the achieved results can be reliable for an overall comparison and this limitation may be tolerated.

CONCLUSION

This study presents a validated geometrically patient-specific poroelastic FE modeling technique, which has the potential to be utilized for clinical applications to analyze lumbar spine biomechanics. This FE model was applied to investigate the effect of posterolateral fixation surgery on the biomechanics of the adjacent levels, and rigid (Ti) versus semirigid (PEEK) rod fixation systems were compared. The results indicated that increased ROM, experienced stress in AF, and fiber strain at adjacent levels were observed for the Ti rod compared with the intact and PEEK rod, which may progress the risk of disc degeneration in adjacent levels for rigid fixation. Similarly, disc height loss and fluid loss were significantly higher at adjacent levels in the Ti rod group after daily cycling loading which alter the fluid–solid interaction of the discs and can be an important clinical indicator for degeneration. In summary, this study confirms the differences in the poroelastic characteristics of adjacent discs for semirigid (PEEK) and rigid (Ti) constructs and reveals the advantage of PEEK for decreasing the risk of ASD.

DATA AVAILABILITY STATEMENT

The raw data supporting the conclusions of this article will be made available by the authors, without undue reservation.

ETHICS STATEMENT

Written informed consent was obtained from the individual(s) for the publication of any potentially identifiable images or data included in this article.

AUTHOR CONTRIBUTIONS

All authors listed above have made substantial contributions to the conception and design of the study, analysis and interpretation of data, preparing the manuscript, and also attest to the validity and legitimacy of the data and its interpretation, and approved it for publication.

FUNDING

The authors thank the Chang Gung Memorial Hospital Research Program (CRRPG3H0062 and CMRPD1J0152), the Healthy Aging Research Center, Chang Gung University, Taiwan (EMRPD1L0411), and the Ministry of Science and Technology of the Republic of China (107-2221-E-182-018-MY3 to C-HC) for scientific funding and support.

ACKNOWLEDGMENTS

The authors appreciate Mrs. Zahra Khoz's help during this study.

REFERENCES

Argoubi, M., and Shirazi-Adl, A. (1996). Poroelastic creep response analysis of a lumbar motion segment in compression. *J. Biomech.* 29, 1331–1339. doi: 10.1016/0021-9290(96)00035-8

Aygün, H., Çakar, A., Hüseyinoğlu, N., Hüseyinoğlu, U., and Çelik, R. (2014). Clinical and radiological comparison of posterolateral fusion and posterior interbody fusion techniques for multilevel lumbar spinal stabilization in manual workers. *Asian Spine J.* 8:571. doi: 10.4184/asj.2014.8.5.571

Barthelemy, V. M. P., van Rijsbergen, M. M., Wilson, W., Huyghe, J. M., van Rietbergen, B., and Ito, K. (2016). A computational spinal motion segment model incorporating a matrix composition-based model of the intervertebral disc. *J. Mech. Behav. Biomed. Mater.* 54, 194–204. doi: 10.1016/j.jmbbm.2015.09.028

Bashkuev, M., Reitmaier, S., and Schmidt, H. (2018). Effect of disc degeneration on the mechanical behavior of the human lumbar spine: a probabilistic finite element study. *Spine J.* 18, 1910–1920. doi: 10.1016/j.spinee.2018.05.046

Beatty, S. (2018). We need to talk about lumbar total disc replacement. *Int. J. Spine Surg.* 12, 201–240. doi: 10.14444/5029

Campbell, R. C., Mobbs, R. J., Lu, V. M., Xu, J., Rao, P. J., and Phan, K. (2017). Posterolateral fusion versus interbody fusion for degenerative spondylolisthesis: systematic review and meta-analysis. *Glob. Spine J.* 7, 482–490. doi: 10.1177/2192568217701103

Castro, A. P. G., and Alves, J. L. (2020). Numerical implementation of an osmo-poro-visco-hyperelastic finite element solver: application to the intervertebral disc. *Comput. Methods Biomech. Biomed. Eng.* (in press):1–13. doi: 10.1080/10255842.2020.1839059

Castro, A. P. G., Wilson, W., Huyghe, J. M., Ito, K., and Alves, J. L. (2014). Intervertebral disc creep behavior assessment through an open source finite element solver. *J. Biomech.* 47, 297–301. doi: 10.1016/j.jbiomech.2013.10.014

Castro, A. P. G., Yao, J., Battisti, T., and Lacroix, D. (2018). Poroelastic modeling of highly hydrated collagen hydrogels: experimental results vs. numerical simulation with custom and commercial finite element solvers. *Front. Bioeng. Biotechnol.* 6:142. doi: 10.3389/fbioe.2018.00142

Chiang, M.-F., Zhong, Z.-C., Chen, C.-S., Cheng, C.-K., and Shih, S.-L. (2006). Biomechanical comparison of instrumented posterior lumbar interbody fusion with one or two cages by finite element analysis. *Spine* 31, E682–E689. doi: 10.1097/01.brs.0000232714.72699.8e

Chou, W.-K., Chien, A., and Wang, J.-L. (2015). Biomechanical analysis between PEEK and titanium screw-rods spinal construct subjected to fatigue loading. *J. Spin. Disord. Techn.* 28, E121–E125. doi: 10.1097/bsd.0000000000000176

De Iure, F., Bosco, G., Cappuccio, M., Paderni, S., and Amendola, L. (2012). Posterior lumbar fusion by peek rods in degenerative spine: preliminary report on 30 cases. *Eur. Spine J.* 21(Suppl. 1), S50–S54. doi: 10.1007/s00586-012-2219-x

Dreischarf, M., Rohlmann, A., Bergmann, G., and Zander, T. (2011). Optimised loads for the simulation of axial rotation in the lumbar spine. *J. Biomech.* 44, 2323–2327. doi: 10.1016/j.jbiomech.2011.05.040

Dreischarf, M., Rohlmann, A., Bergmann, G., and Zander, T. (2012). Optimised in vitro applicable loads for the simulation of lateral bending in the lumbar spine. *Med. Eng. Phys.* 34, 777–780. doi: 10.1016/j.medengphy.2012.04.002

Dreischarf, M., Zander, T., Shirazi-Adl, A., Puttlitz, C. M., Adam, C. J., Chen, C. S., et al. (2014). Comparison of eight published static finite element models of the intact lumbar spine: predictive power of models improves when combined together. *J. Biomech.* 47, 1757–1766. doi: 10.1016/j.jbiomech.2014.04.002

El-Rich, M., Arnoux, P. J., Wagnac, E., Brunet, C., and Aubin, C. E. (2009). Finite element investigation of the loading rate effect on the spinal load-sharing changes under impact conditions. *J. Biomech.* 42, 1252–1262. doi: 10.1016/j.jbiomech.2009.03.036

Ferguson, S. J., Ito, K., and Nolte, L.-P. (2004). Fluid flow and convective transport of solutes within the intervertebral disc. *J. Biomech.* 37, 213–221. doi: 10.1016/s0021-9290(03)00250-1

Galbusera, F., Schmidt, H., Neidlinger-Wilke, C., and Wilke, H.-J. (2011a). The effect of degenerative morphological changes of the intervertebral disc on the lumbar spine biomechanics: a poroelastic finite element investigation. *Comput. Methods Biomech. Biomed. Eng.* 14, 729–739. doi: 10.1080/10255842.2010.493522

Galbusera, F., Schmidt, H., Noailly, J., Malandrino, A., Lacroix, D., Wilke, H.-J., et al. (2011b). Comparison of four methods to simulate swelling in poroelastic finite element models of intervertebral discs. *J. Mech. Behav. Biomed. Mater.* 4, 1234–1241. doi: 10.1016/j.jmbbm.2011.04.008

Ghobadiha, E., Nikkhoo, M., and Naserkhaki, S. (2019). Poroelastic finite element modeling of a lumbar spine motion segment and validation in different motions for clinical studies. *Iran. J. Orthopaed. Surg.* 17, 142–152.

Gornet, M. F., Chan, F. W., Coleman, J. C., Murrell, B., Nockels, R. P., Taylor, B. A., et al. (2011). Biomechanical assessment of a PEEK rod system for semi-rigid fixation of lumbar fusion constructs. *J. Biomech. Eng.* 133:081009. doi: 10.1115/1.4004862

Goto, K., Tajima, N., Chosa, E., Totoribe, K., Kubo, S., Kuroki, H., et al. (2003). Effects of lumbar spinal fusion on the other lumbar intervertebral levels (three-dimensional finite element analysis). *J. Orthop. Sci.* 8, 577–584. doi: 10.1007/s00776-003-0675-1

Guo, T.-M., Lu, J., Xing, Y.-L., Liu, G.-X., Zhu, H.-Y., Yang, L., et al. (2019). A 3-dimensional finite element analysis of adjacent segment disk degeneration induced by transforaminal lumbar interbody fusion after pedicle screw fixation. *World Neurosurg.* 124, e51–e57. doi: 10.1016/j.wneu.2018.11.195

Heo, M., Yun, J., Park, S. H., Choi, Y. S., Lee, S. S., and Park, S. (2020). Design of a lumbar interspinous fixation device for minimally invasive surgery and spine motion stabilization. *J. Med. Biol. Eng.* 40, 1–10. doi: 10.1007/s40846-019-00485-8

Highsmith, J. M., Tumialán, L. M., and Rodts, G. E. (2007). Flexible rods and the case for dynamic stabilization. *Neurosurg. Focus* 22, 1–5. doi: 10.3171/foc.2007.22.1.11

Huang, W., Chang, Z., Song, R., Zhou, K., and Yu, X. (2016). Non-fusion procedure using PEEK rod systems for lumbar degenerative diseases: clinical experience with a 2-year follow-up. *BMC Musculosk. Disord.* 17:53. doi: 10.1186/s12891-016-0913-2

Iatridis, J. C., Laible, J. P., and Krag, M. H. (2003). Influence of fixed charge density magnitude and distribution on the intervertebral disc: applications of a Poroelastic and Chemical Electric (PEACE) model. *J. Biomech. Eng.* 125, 12–24. doi: 10.1115/1.1537190

Ishihara, H., Osada, R., Kanamori, M., Kawaguchi, Y., Ohmori, K., Kimura, T., et al. (2001). Minimum 10-Year follow-up study of anterior lumbar interbody fusion for isthmic spondylolisthesis. *J. Spin. Disord.* 14, 91–99. doi: 10.1097/00002517-200104000-00001

Jahng, T.-A., Kim, Y. E., and Moon, K. Y. (2013). Comparison of the biomechanical effect of pedicle-based dynamic stabilization: a study using finite element analysis. *Spine J.* 13, 85–94. doi: 10.1016/j.spinee.2012.11.014

Jin, Y. J., Kim, Y. E., Seo, J. H., Choi, H. W., and Jahng, T.-A. (2012). Effects of rod stiffness and fusion mass on the adjacent segments after floating mono-segmental fusion: a study using finite element analysis. *Eur. Spine J.* 22, 1066–1077. doi: 10.1007/s00586-012-2611-6

Laville, A., Laporte, S., and Skalli, W. (2009). Parametric and subject-specific finite element modelling of the lower cervical spine. Influence of geometrical parameters on the motion patterns. *J. Biomech.* 42, 1409–1415. doi: 10.1016/j.jbiomech.2009.04.007

Lee, J. C., Kim, Y., Soh, J.-W., and Shin, B.-J. (2014). Risk factors of adjacent segment disease requiring surgery after lumbar spinal fusion. *Spine* 39, E339–E345. doi: 10.1097/brs.0000000000000164

Li, C., Liu, L., Shi, J.-Y., Yan, K.-Z., Shen, W.-Z., and Yang, Z.-R. (2016). Clinical and biomechanical researches of polyetheretherketone (PEEK) rods for semi-rigid lumbar fusion: a systematic review. *Neurosurg. Rev.* 41, 375–389. doi: 10.1007/s10143-016-0763-2

Lidar, Z., Beaumont, A., Lifshutz, J., and Maiman, D. J. (2005). Clinical and radiological relationship between posterior lumbar interbody fusion and posterolateral lumbar fusion. *Surg. Neurol.* 64, 303–308. doi: 10.1016/j.surneu.2005.03.025

Liu, M. Y., Tsai, T. T., Chen, L. H., Liang, W. H., Lai, P. L., and Tai, C. L. (2020). Biomechanical comparison of lumbar motion unit stability following posterior instrumentation with facet spacers and facet screws. *J. Med. Biol. Eng.* 40, 220–229. doi: 10.1007/s40846-019-00501-x

Miyakoshi, N., Abe, E., Shimada, Y., Okuyama, K., Suzuki, T., and Sato, K. (2000). Outcome of One-level posterior lumbar interbody fusion for spondylolisthesis and postoperative intervertebral disc degeneration adjacent to the fusion. *Spine* 25, 1837–1842. doi: 10.1097/00007632-200007150-00016

Naserkhaki, S., and El-Rich, M. (2017). Sensitivity of lumbar spine response to follower load and flexion moment: finite element study. *Comput. Methods Biomech. Biomed. Engin.* 20, 550–557. doi: 10.1080/10255842.2016.1257707

Naserkhaki, S., Jaremko, J. L., Adeeb, S., and El-Rich, M. (2016). On the load-sharing along the ligamentous lumbosacral spine in flexed and extended postures: finite element study. *J. Biomech.* 49, 974–982. doi: 10.1016/j.jbiomech.2015.09.050

Nikitovic, D., Más, Y., Gracia, L., Ibarz, E., Gabarre, S., Peña, D., et al. (2017). Finite element simulation and clinical follow-up of lumbar spine biomechanics with dynamic fixations. *PLoS One* 12:e0188328. doi: 10.1371/journal.pone.0188328

Nikkhoo, M., Cheng, C. H., Wang, J. L., Khoz, Z., El-Rich, M., Hebela, N., et al. (2019). Development and validation of a geometrically personalized finite element model of the lower ligamentous cervical spine for clinical applications. *Comput. Biol. Med.* 109, 22–32. doi: 10.1016/j.compbiomed.2019.04.010

Nikkhoo, M., Haghpanahi, M., Parnianpour, M., and Wang, J.-L. (2013a). Dynamic responses of intervertebral disc during static creep and dynamic cyclic loading:

a parametric poroelastic finite element analysis. *Biomed. Eng. Appl. Basis Commun.* 25:1350013.

Nikkhoo, M., Hsu, Y.-C., Haghpanahi, M., Parnianpour, M., and Wang, J.-L. (2013b). A meta-model analysis of a finite element simulation for defining poroelastic properties of intervertebral discs. *Proc. Instit. Mech. Eng. Part H* 227, 672–682.

Nikkhoo, M., Khoz, Z., Cheng, C.-H., Niu, C.-C., El-Rich, M., and Khalaf, K. (2020). Development of a novel geometrically-parametric patient-specific finite element model to investigate the effects of the lumbar lordosis angle on fusion surgery. *J. Biomech.* 102:109722. doi: 10.1016/j.jbiomech.2020.109722

Ormond, D. R., Albert, L. Jr., and Das, K. (2016). Polyetheretherketone (PEEK) rods in lumbar spine degenerative disease: a case series. *Clin. Spine Surg.* 29, E371–E375. doi: 10.1097/BSD.0b013e318277cb9b

Ozkal, F. M., Cakir, F., and Sensoz, E. (2020). Schematization of cannulated screw fixations in femoral neck fractures using genetic algorithm and finite element method. *J. Med. Biol. Eng.* 40, 673–687. doi: 10.1007/s40846-020-00528-5

Park, W. M., Kim, K., and Kim, Y. H. (2013). Effects of degenerated intervertebral discs on intersegmental rotations, intradiscal pressures, and facet joint forces of the whole lumbar spine. *Comput. Biol. Med.* 43, 1234–1240. doi: 10.1016/j.compbiomed.2013.06.011

Patwardhan, A. G., Havey, R. M., Meade, K. P., Lee, B., and Dunlap, B. (1999). A follower load increases the load-carrying capacity of the lumbar spine in compression. *Spine* 24, 1003–1009. doi: 10.1097/00007632-199905150-00014

Pintar, F. A., Yoganandan, N., Myers, T., Elhagediab, A., and Sances, A. (1992). Biomechanical properties of human lumbar spine ligaments. *J. Biomech.* 25, 1351–1356. doi: 10.1016/0021-9290(92)90290-h

Rahm, M. D., and Hall, B. B. (1996). Adjacent-segment degeneration after lumbar fusion with instrumentation: a retrospective study. *J. Spinal Disord.* 9, 392–400.

Rijsbergen, M. V., Rietbergen, B. V., Barthelemy, V., Eltes, P., Lazáry, Á, Lacroix, D., et al. (2018). Comparison of patient-specific computational models vs. clinical follow-up, for adjacent segment disc degeneration and bone remodelling after spinal fusion. *PLoS One* 13:e0200899. doi: 10.1371/journal.pone.0200899

Rohlmann, A., Zander, T., Rao, M., and Bergmann, G. (2009). Realistic loading conditions for upper body bending. *J. Biomech.* 42, 884–890. doi: 10.1016/j.jbiomech.2009.01.017

Schmidt, H., Galbusera, F., Rohlmann, A., and Shirazi-Adl, A. (2013). What have we learned from finite element model studies of lumbar intervertebral discs in the past four decades? *J. Biomech.* 46, 2342–2355. doi: 10.1016/j.jbiomech.2013.07.014

Schmidt, H., Heuer, F., Simon, U., Kettler, A., Rohlmann, A., Claes, L., et al. (2006). Application of a new calibration method for a three-dimensional finite element model of a human lumbar annulus fibrosus. *Clin. Biomech.* 21, 337–344. doi: 10.1016/j.clinbiomech.2005.12.001

Schmidt, H., Kettler, A., Heuer, F., Simon, U., Claes, L., and Wilke, H. J. (2007a). Intradiscal pressure, shear strain, and fiber strain in the intervertebral disc under combined loading. *Spine* 32, 748–755. doi: 10.1097/01.brs.0000259059.90430.c2

Schmidt, H., Kettler, A., Rohlmann, A., Claes, L., and Wilke, H. J. (2007b). The risk of disc prolapses with complex loading in different degrees of disc degeneration - a finite element analysis. *Clin. Biomech.* 22, 988–998. doi: 10.1016/j.clinbiomech.2007.07.008

Schmidt, H., Shirazi-Adl, A., Galbusera, F., and Wilke, H. J. (2010). Response analysis of the lumbar spine during regular daily activities–a finite element analysis. *J. Biomech.* 43, 1849–1856. doi: 10.1016/j.jbiomech.2010.03.035

Schroeder, Y., Huyghe, J. M., van Donkelaar, C. C., and Ito, K. (2010). A biochemical/biophysical 3D FE intervertebral disc model. *Biomech. Model. Mechanobiol.* 9, 641–650. doi: 10.1007/s10237-010-0203-0

Schwab, F. J., Nazarian, D. G., Mahmud, F., and Michelsen, C. B. (1995). Effects of spinal instrumentation on fusion of the lumbosacral spine. *Spine* 20, 2023–2028. doi: 10.1097/00007632-199509150-00014

Selim, A., Mercer, S., and Tang, F. (2018). Polyetheretherketone (PEEK) rods for lumbar fusion: a systematic review and meta-analysis. *Intern. J. Spine Surg.* 12, 190–200. doi: 10.14444/5027

Serhan, H., Mhatre, D., Defossez, H., and Bono, C. M. (2011). Motion-preserving technologies for degenerative lumbar spine: the past, present, and future horizons. *SAS J.* 5, 75–89. doi: 10.1016/j.esas.2011.05.001

Shih, S. L., Liu, C. L., Huang, L. Y., Huang, C. H., and Chen, C. S. (2013). Effects of cord pretension and stiffness of the Dynesys system spacer on the biomechanics of spinal decompression- a finite element study. *BMC Musculoskelet. Disord.* 14:191. doi: 10.1186/1471-2474-14-191

Shirazi-Adl, A., Ahmed, A. M., and Shrivastava, S. C. (1986a). A finite element study of a lumbar motion segment subjected to pure sagittal plane moments. *J. Biomech.* 19, 331–350. doi: 10.1016/0021-9290(86)90009-6

Shirazi-Adl, A., Ahmed, A. M., and Shrivastava, S. C. (1986b). Mechanical response of a lumbar motion segment in axial torque alone and combined with compression. *Spine* 11, 914–927.

Shirazi-Adl, A., and Parnianpour, M. (2000). Load-bearing and stress analysis of the human spine under a novel wrapping compression loading. *Clin. Biomech.* 15, 718–725. doi: 10.1016/s0268-0033(00)00045-0

Simon, B. R. (1992). Multiphase poroelastic finite element models for soft tissue structures. *Appl. Mech. Rev.* 45, 191–218. doi: 10.1115/1.3121397

Sudo, H., Oda, I., Abumi, K., Ito, M., Kotani, Y., and Minami, A. (2006). Biomechanical study on the effect of five different lumbar reconstruction techniques on adjacent-level intradiscal pressure and lamina strain. *J. Neurosurg.* 5, 150–155. doi: 10.3171/spi.2006.5.2.150

Turner, J. L., Paller, D. J., and Murrell, C. B. (2010). The mechanical effect of commercially pure titanium and polyetheretherketone rods on spinal implants at the operative and adjacent levels. *Spine* 35, E1076–E1082. doi: 10.1097/BRS.0b013e3181df1b85

Wang, H., Ma, L., Yang, D., Wang, T., Liu, S., Yang, S., et al. (2017). Incidence and risk factors of adjacent segment disease following posterior decompression and instrumented fusion for degenerative lumbar disorders. *Medicine* 96:e6032. doi: 10.1097/MD.0000000000006032

Zhang, Z., Fogel, G. R., Liao, Z., Sun, Y., and Liu, W. (2018a). Biomechanical analysis of lumbar interbody fusion cages with various lordotic angles: a finite element study. *Comput. Methods Biomech. Biomed. Engin.* 21, 247–254. doi: 10.1080/10255842.2018.1442443

Zhang, Z., Li, H., Fogel, G. R., Liao, Z., Li, Y., and Liu, W. (2018b). Biomechanical analysis of porous additive manufactured cages for lateral lumbar interbody fusion: a finite element analysis. *World Neurosurg.* 111, e581–e591. doi: 10.1016/j.wneu.2017.12.127

Conflict of Interest: The authors declare that the research was conducted in the absence of any commercial or financial relationships that could be construed as a potential conflict of interest.

frontiers in Bioengineering and Biotechnology

ORIGINAL RESEARCH
published: 07 June 2021
doi: 10.3389/fbioe.2021.685799

A Robust Multiscale and Multiphasic Structure-Based Modeling Framework for the Intervertebral Disc

*Minhao Zhou[1], Shiyin Lim[1] and Grace D. O'Connell[1,2]**

[1] Berkeley Biomechanics Laboratory, Department of Mechanical Engineering, University of California, Berkeley, Berkeley, CA, United States, [2] Department of Orthopaedic Surgery, University of California, San Francisco, San Francisco, CA, United States

A comprehensive understanding of multiscale and multiphasic intervertebral disc mechanics is crucial for designing advanced tissue engineered structures aiming to recapitulate native tissue behavior. The bovine caudal disc is a commonly used human disc analog due to its availability, large disc height and area, and similarities in biochemical and mechanical properties to the human disc. Because of challenges in directly measuring subtissue-level mechanics, such as *in situ* fiber mechanics, finite element models have been widely employed in spinal biomechanics research. However, many previous models use homogenization theory and describe each model element as a homogenized combination of fibers and the extrafibrillar matrix while ignoring the role of water content or osmotic behavior. Thus, these models are limited in their ability in investigating subtissue-level mechanics and stress-bearing mechanisms through fluid pressure. The objective of this study was to develop and validate a structure-based bovine caudal disc model, and to evaluate multiscale and multiphasic intervertebral disc mechanics under different loading conditions and with degeneration. The structure-based model was developed based on native disc structure, where fibers and matrix in the annulus fibrosus were described as distinct materials occupying separate volumes. Model parameters were directly obtained from experimental studies without calibration. Under the multiscale validation framework, the model was validated across the joint-, tissue-, and subtissue-levels. Our model accurately predicted multiscale disc responses for 15 of 16 cases, emphasizing the accuracy of the model, as well as the effectiveness and robustness of the multiscale structure-based modeling-validation framework. The model also demonstrated the rim as a weak link for disc failure, highlighting the importance of keeping the cartilage endplate intact when evaluating disc failure mechanisms *in vitro*. Importantly, results from this study elucidated important fluid-based load-bearing mechanisms and fiber-matrix interactions that are important for understanding disease progression

OPEN ACCESS

Edited by:
Luca Cristofolini, University of Bologna, Italy

Reviewed by:
André P. G. Castro, Universidade de Lisboa, Portugal
Diane Wagner, Indiana University, Purdue University Indianapolis, United States

***Correspondence:**
Grace D. O'Connell
g.oconnell@berkeley.edu

Specialty section:
This article was submitted to Biomechanics, a section of the journal Frontiers in Bioengineering and Biotechnology

Received: *25 March 2021*
Accepted: *10 May 2021*
Published: *07 June 2021*

Citation:
Zhou M, Lim S and O'Connell GD (2021) A Robust Multiscale and Multiphasic Structure-Based Modeling Framework for the Intervertebral Disc. Front. Bioeng. Biotechnol. 9:685799. doi: 10.3389/fbioe.2021.685799

and regeneration in intervertebral discs. In conclusion, the methods presented in this study can be used in conjunction with experimental work to simultaneously investigate disc joint-, tissue-, and subtissue-level mechanics with degeneration, disease, and injury.

Keywords: finite element modeling, multiscale modeling, multiphasic modeling, structure-based modeling, structure-function relationship, bovine caudal disc, intervertebral disc degeneration

INTRODUCTION

Mechanical dysfunction of the intervertebral disc can lead to reduced mobility and debilitating pain (Adams and Roughley, 2006). Disc prolapse and herniation mostly occur in the posterolateral region, where stresses, strains, and intradiscal pressure in the annulus fibrosus (AF) are higher (Shah et al., 1978; Adams and Hutton, 1985; Steffen et al., 1998; O'Connell et al., 2007b; O'Connell et al., 2011; Wilke et al., 2016; Liu et al., 2017). The posterolateral region has also been linked to increasing bulging and protrusion of the nucleus pulposus under fatigue, with some discs experiencing full herniations (Wilke et al., 2016). Previous researchers have tracked progression of disc failure from bulging to herniation (Adams et al., 2000; Vernon-Roberts et al., 2007), but further investigation is limited due to experimental challenges in directly assessing *in situ* mechanics (e.g., fiber mechanics), which result in large variations in reported *in situ* fiber mechanics data. For example, earlier *in vitro* joint-level studies reported AF fiber strains that varied from ∼0.3 to 20% under axial compression, which may cause contradicting predictions regarding the likelihood of disc failure under physiological conditions (Shah et al., 1978; Stokes, 1987; Heuer et al., 2008a,b, 2012; Wang et al., 2009; Spera et al., 2011). Thus, despite recent advancements in experimental techniques, *in situ* fiber mechanics at the joint level remain poorly understood.

Human intervertebral disc cadaveric tissues are the benchmark for spine biomechanics research, but limited tissue availability and challenges in controlling for important variables, such as sex, age, and level of degeneration, can impact study designs (e.g., sample size) and confound results (Iatridis et al., 2005; Alini et al., 2008; Michalek and Iatridis, 2012; Costi et al., 2020). For these reasons, many researchers have resorted to large animal models, including ovine, porcine, and bovine, to investigate intervertebral disc biomechanics (Alini et al., 2008). Particularly, bovine caudal discs are more accessible than human discs, easier to handle than discs from smaller animals (e.g., rat and mouse discs), and have biochemical and mechanical properties similar to human discs (Demers et al., 2004; Beckstein et al., 2008; Showalter et al., 2012; Bezci et al., 2019). Furthermore, previous work demonstrated the effectiveness of using bovine discs to study the effect of injuries and degeneration by effectively inducing injuries (e.g., needle punctures) and degeneration (e.g., enzyme digestion) in the tissues *in vitro* (Korecki et al., 2008a; Roberts et al., 2008; Michalek and Iatridis, 2012). Despite improvements in availability, accessibility, consistency, and ease of manipulation, experimental limitations still prevent assessment of intradiscal deformations and stress distributions between disc components with injuries or degeneration. Instead, *in vitro* studies primarily assess joint-level bulk mechanics, compositional changes, or biological response (Oshima et al., 1993; Korecki et al., 2008a,b; Roberts et al., 2008; Walter et al., 2011; Michalek and Iatridis, 2012; Bezci et al., 2015, 2020a,b; Bezci and O'Connell, 2018). The growing wealth of data that can be obtained from the bovine caudal discs makes it an ideal animal model to develop a validated and comprehensive computational tool to assess *in situ* mechanics. Additionally, because of lower inter-specimen variability, bovine disc models can be more effectively and reliably validated with experimental data than human disc models.

Finite element models (FEM) have been used to complement experimental studies, providing a powerful tool for predicting hard-to-measure, three-dimensional mechanical and biochemical responses (Zhou et al., 2020c). Since the 1970s, FEMs have advanced the field of spinal biomechanics significantly by providing insights into disc joint-level mechanics and tissue-level stress and strain distributions (Shirazi-Adl et al., 1984; Shirazi-Adl, 1992; Galbusera et al., 2011a,b; Schmidt et al., 2013). However, many joint-level FEMs describe disc components as single-phasic elastic or hyperelastic materials and thus do not account for water content (Kurowski and Kubo, 1986; Kim et al., 1991; Rohlmann et al., 2006; Schmidt et al., 2007b), which is a primary constituent in all biological tissues and plays an important role in the tissue's load-bearing capability (Ateshian et al., 1994). More recent models have accounted for tissue water content by describing disc components as poroelastic materials, which significantly advanced the field by enabling investigations into the stress-bearing role of the interstitial tissue water content, as well as tissue's time-dependent behavior (Natarajan et al., 2006; Wilson et al., 2007; Galbusera et al., 2011a,b; Barthelemy et al., 2016; van Rijsbergen et al., 2018; Castro and Alves, 2020). However, these models have limited capability in describing the osmotic response, which has been shown to alter mechanical behavior and change with degeneration (Ishihara et al., 1996; Wognum et al., 2006; Wuertz et al., 2007).

In addition to the limitations in accounting for tissue's fluid content and osmotic response, most FEMs are developed based on homogenization theory, where every model element includes a homogenized description of tissue subcomponents (e.g., fibers and extrafibrillar matrix) and, thus, does not accurately represent the heterogeneous AF native architecture, where fibers and extrafibrillar matrix are distinct materials that occupy separate volumes. As a result, these models are not capable of directly investigating subtissue-level mechanics (e.g., *in situ* fiber or interfibrillar stress and strain distributions; Yin and Elliott, 2005). To address some of these issues, we

previously developed and validated a structure-based FEM of the AF that replicated its native tissue architecture, with fiber bundles modeled as a separate material from the extrafibrillar matrix (Zhou et al., 2020a). In this approach, model parameters directly represented tissue mechanical (e.g., modulus, Poisson's ratio, etc.) or biochemical properties (e.g., proteoglycan content, referential hydraulic permeability, etc.). To account for tissue water content and osmotic behavior, triphasic mixture theory was employed to describe the swelling capacity of the extrafibrillar matrix (Lai et al., 1991; Ateshian et al., 2004). Our model was able to robustly and accurately predict multilamellar AF mechanics under various loading configurations and testing boundary conditions, including uniaxial tension, biaxial tension, and simple shear (Zhou et al., 2020a). More recently, by incorporating a structure-based fiber engagement analysis, we were also able to apply this model to explain the relationship between specimen geometry and AF tensile mechanics that was originally observed by Adams and Green (1993) and Zhou et al. (2020b).

The objective of this study was to expand our structure-based multiscale modeling-validation approach to study joint-level mechanics of the intervertebral disc under both healthy and degenerated conditions. Degeneration has been shown to alter subtissue-level fiber mechanics, which plays an important role in stress distributions, damage accumulation, and bulk tissue failure (Werbner et al., 2019). Understanding mechanisms of stress distribution within the disc and its subcomponents can help develop robust designs for tissue repair or replacement implants, such as tissue engineered discs. Therefore, we (1) developed and validated a joint-level FEM that was capable of investigating the multiscale and multiphasic structure-function relationship in bovine caudal discs, and (2) used the validated FEM to investigate the effect of loading condition and degeneration on multiscale disc mechanics at joint, tissue, and subtissue scales.

MATERIALS AND METHODS

Model Development

FEMs were developed to represent a bone-disc-bone motion segment from the bovine tail (**Figure 1A**). Neighboring tissues (e.g., facet joints, ligaments, etc.) were not included in the model to minimize confounding effects and to more closely represent motion segment specimens prepared for experimental testing. Model geometry was created in Solidworks (2020) and finite element meshes were generated using ABAQUS and ANSA pre-processor (Abaqus 6.14; ANSA 15.2.0). Mesh size was determined based on results from our previous mesh convergence study (Zhou et al., 2020b). PreView was used to define boundary and

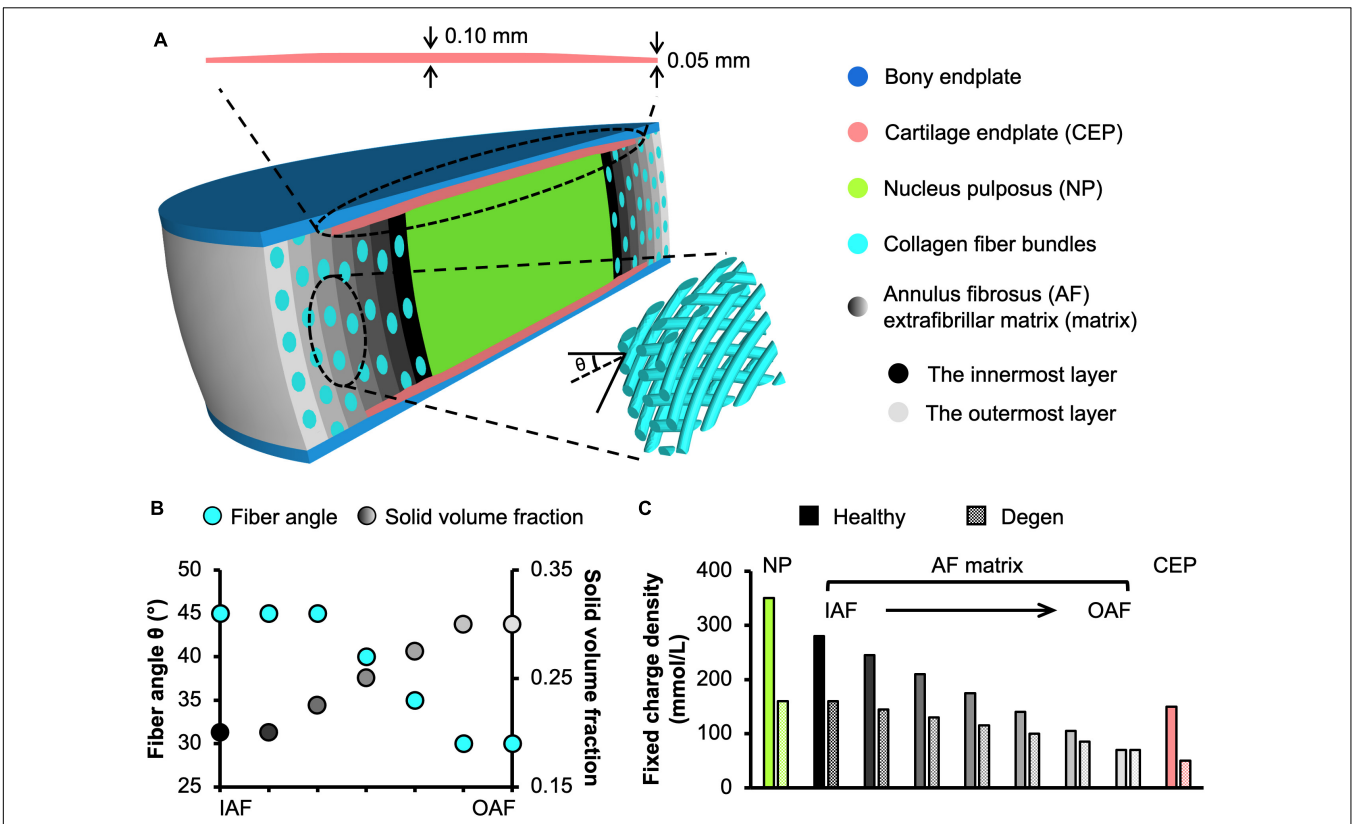

FIGURE 1 | (A) Schematic of the multiscale, structure-based bovine caudal disc motion segment model. The extrafibrillar matrix and collagen fibers of the annulus fibrosus (AF) were modeled as distinct materials occupying separate volumes. Insets present the cartilage endplate geometry (top) and the angle-ply fiber structure (bottom right). **(B)** AF fiber angle and solid volume fraction from the inner AF (IAF) to the outer AF (OAF). **(C)** Fixed charge density distribution in healthy and degenerated (Degen) disc models.

loading conditions and the fully developed models were solved by FEBio (PreView 2.1; FEBio 2.8.5; Maas et al., 2012). Due to limited computational resources, the current available solver was only able to process a maximum of ∼200 million non-zero entries in the stiffness matrix. Thus, models created in this study were scaled down at 1:5 scale.

To ensure that this scaling and the resulting changes in the number of AF lamellae modeled did not affect model predictions, preliminary work was performed to determine the effect of scaling ratio between 1:4 and 1:6 on model-predicted compressive and torsional mechanics. Compressive stress-strain behavior and normalized torsional stiffness-rotation response from the 1:4, 1:5, and 1:6 scale models were consistent (**Supplementary Figure 1**), suggesting that scaling and number of AF lamellae modeled did not affect model predictions when the model included enough AF lamellae. Thus, bovine caudal disc motion segment models were developed at 1:5 scale for computational efficiency (∼2.1 million elements). Finite element meshes of the model were shown in **Supplementary Figure 2**.

Model geometry was determined based on data reported in the literature. At full scale, the radius and height of bovine caudal discs are 14.20 ± 0.85 mm and 6.90 ± 0.35 mm, respectively, assuming a circular cross section in the transverse plane (O'Connell et al., 2007a). Thus, the 1:5 scaled model radius and height (not including both bony endplates) were created at 2.85 and 1.40 mm, respectively (**Figure 1A**). The nucleus pulposus (NP) was assumed to have the same circular cross section in the transverse plane, but with a ∼50% smaller radius (1.45 mm; **Figure 1A**; O'Connell et al., 2007a). The AF was created using our previously reported structure-based modeling approach, where the tissue was described as a fiber-reinforced angle-ply composite containing distinct materials for fiber bundles and the extrafibrillar matrix (**Figure 1A**; Zhou et al., 2020a). Due to limited computational resources, the native bovine AF structural features, including lamellar thickness, fiber radius, and interfibrillar spacing, were preserved during scaling to reduce the total number of elements needed. This scaling approach, which has been widely applied and validated for human disc models (Shirazi-Adl et al., 1984; Goel et al., 1995a; Galbusera et al., 2011a,b), maintained fiber volume fraction and preserved mesh quality for model convergence and model predictions (Zhou et al., 2020b). As such, seven concentric AF layers were created (lamellar thickness = 0.2 mm; Adam et al., 2015). Fiber bundles were uniformly distributed, full-length cylinders welded to the surrounding matrix (Goel et al., 1995a; Michalek et al., 2009; Schollum et al., 2010). Due to the lack of bovine caudal disc anatomy data in the literature, fiber bundle geometry from the human AF was used, based on the similar collagen networks reported between human and bovine discs (Yu et al., 2002, 2007). Specifically, the fiber bundle radius was 0.06 mm, and interfibrillar spacing within each lamella was 0.22 mm (Marchand and Ahmed, 1990). Fiber angles were oriented at ± 45° to the transverse plane in the inner AF and decreased along the radial direction to ± 30° in the outer AF (**Figure 1A**–bottom inset; **Figure 1B**–turquoise circles; Matcher et al., 2004). Cartilage endplates (CEP) covered the superior and inferior ends of the NP and the inner-middle AF (**Figure 1A**–cartilage endplate); spatial variation in CEP thickness was included based on data in the literature (**Figure 1A**–top inset; Berg-Johansen et al., 2018). Bony endplates were modeled to cover the superior and inferior ends of the disc (**Figure 1A**–bony endplate). All interfaces were defined as welded interfaces (Adam et al., 2015).

Triphasic mixture theory was employed to account for tissue water content and osmotic response (Lai et al., 1991; Ateshian et al., 2004). The Holmes-Mow description was employed to model the strain-dependent tissue permeability (k) of the NP, AF, and CEP (Eq. 1), where J was the determinant of the deformation gradient tensor (F), k_0 represented hydraulic permeability in the reference configuration, φ_0 represented tissue solid volume fraction, and M represented the exponential strain-dependence coefficient. Tissue fluid phase model parameters were determined based on reported values for bovine tissues when available (**Table 1**–Fluid phase). AF solid volume fraction (i.e., 100% minus water content as a percentage) varied linearly along the radial direction, increasing from 0.2 in the inner AF to 0.3 in the outer AF (**Table 1** and **Figure 1B**–grayscale circles). Fixed charge density represented proteoglycan content in the NP, CEP, and AF extrafibrillar matrix, allowing for osmotic swelling. Radial variation in fixed charge density was determined based on our recent work that provided high-spatial-resolution measurements of bovine caudal disc biochemical composition (**Figure 1C**–solid bars; Bezci et al., 2019). The collagen fiber bundles were assumed to have no swelling capability (i.e., zero fixed charge density). Free diffusivity (D_0)

TABLE 1 | Triphasic material properties of the bovine caudal disc tissues.

NP			AF		CEP
			Matrix	Fibers	
Fluidphase	φ_0	0.2[a]	See **Figure 1B**[a]		0.4[c,*]
	$k_0 \times 10^{-16}$ (m^4/Ns)	5.5[b]	64[b]	64[b]	5.6[c,*]
	M	1.92[c,*]	4.8[c,*]	4.8[c,*]	3.79[c,*]
Solid phase	E (MPa)	0.4[b]	0.74[b]	0.74[b]	0.31[g]
	ν	0.24[d]	0.16[c,*]	0.16[c,*]	0.18[c,*]
	β	0.95[c,*]	3.3[c,*]	3.3[c,*]	0.29[c,*]
	E_{lin}: (MPa)	N.A.	N.A.	600[e]	N.A.
	γ	N.A.	N.A.	5.95[f,*]	N.A.
	λ_0	N.A.	N.A.	1.05[e]	N.A.

NP, nucleus pulposus; AF, annulus fibrosus; CEP, cartilage endplate; φ_0, solid volume fraction; k_0, referential hydraulic permeability; M, exponential strain-dependence coefficient for permeability; E, Young's modulus; ν, Poisson's ratio; β, exponential stiffening coefficient of the Holmes–Mow model; E_{lin}, collagen fiber bundle linear-region modulus; γ, collagen fiber bundle toe-region power-law exponent; λ_0, collagen fiber bundle toe- to linear-region transitional stretch.

**The parameter was determined based on experimental studies using matching human intervertebral disc tissues due to the lack of corresponding data obtained from bovine caudal disc tissues.*

[a] *Beckstein et al. (2008).*

[b] *Périé et al. (2005).*

[c] *Cortes et al. (2014).*

[d] *Farrell and Riches (2013).*

[e] *Fratzl et al. (1998), Gentleman et al. (2003), van der Rijt et al. (2006), and Shen et al. (2008).*

[f] *Zhou et al. (2020a).*

[g] *Wu et al. (2015).*

and within-tissue diffusivity (D) of Na^+ and Cl^- were set based on data reported in Gu et al. (2004); 100% ion solubility was assumed ($D_{0,\ Na^+} = 0.00116 mm^2/s$; $D_{0,\ Cl^-} = 0.00161 mm^2/s$; $D_{Na^+} = 0.00044 mm^2/s$; $D_{Cl^-} = 0.00069\ mm^2/s$). The solution osmotic coefficient (0.927) was determined based on a linear interpolation of data reported in Robinson and Stokes (1949) and Partanen et al. (2017).

$$k(J) = k_0 \left(\frac{J-\varphi_0}{1-\varphi_0}\right)^2 e^{\frac{1}{2}M(J^2-1)} \tag{1}$$

To describe NP, CEP, and AF extrafibrillar matrix mechanics, a compressible hyperelastic Holmes-Mow material description was used (Eqs 2–4; Cortes et al., 2014). Particularly, I_1 and I_2 represented the first and second invariants of the right Cauchy-Green deformation tensor, $\boldsymbol{C}(\boldsymbol{C} = \boldsymbol{F}^T\boldsymbol{F})$, E represented Young's modulus, ν represented Poisson's ratio, and β represented the exponential stiffening coefficient. AF collagen fibers were modeled using the same compressible hyperelastic Holmes-Mow ground matrix but reinforced with a power-linear fiber description to account for AF non-linearity and anisotropy (Eq. 5). γ represented the power-law exponent in the toe region, E_{lin} represented the fiber modulus in the fiber linear region, and λ_0 represented the transition stretch between the toe and linear regions (Holzapfel and Ogden, 2017). B was a function of γ, $E_{lin.}$, and λ_0 ($B = \frac{E_{lin}}{2}(\frac{(\lambda_0^2-1)}{2(\gamma-1)} + \lambda_0^2)$. Solid phase parameters were determined based on bovine experimental studies when available (**Table 1**–solid phase), and collagen fiber properties were determined based on type I collagen uniaxial tensile test experimental data (**Table 1**–solid phase: E_{lin}, γ, and λ_0). For all material properties, data from healthy human discs was used when bovine properties were not available, due to similarities in tissue properties (**Table 1**–"*").

$$W(I_1, I_2, J) = \frac{1}{2}c\left(e^Q - 1\right) \tag{2}$$

$$Q = \frac{\beta(1+\nu)(1-2\nu)}{E(1-\nu)}\left[\left(\frac{E}{1+\nu} - \frac{E\,\nu}{(1+\nu)(1-2\nu)}\right)(I_1-3) + \frac{E\,\nu}{(1+\nu)(1-2\nu)}(I_2-3) - \left(\frac{E}{1+\nu} + \frac{E\,\nu}{(1+\nu)(1-2\nu)}\right) lnJ^2\right] \tag{3}$$

$$c = \frac{E(1-\nu)}{2\beta(1+\nu)(1-2\nu)} \tag{4}$$

$$\lambda_n = \begin{cases} 0 & \lambda_n < 1 \\ \frac{E_{lin}}{4\gamma(\gamma-1)}(\lambda_0^2-1)^{2-\gamma}(\lambda_n-1)^{\gamma} & 1 \le \lambda_n \le \lambda_0 \\ E_{lin}(\lambda_n-\lambda_0) + B(\lambda_n^2-\lambda_0^2) + \frac{E_{lin}}{4\gamma(\gamma-1)}(\lambda_0^2-1)^{2-\gamma}(\lambda_n-1)^{\gamma} & \lambda_n > \lambda_0 \end{cases} \tag{5}$$

Bony endplates were modeled as a compressible hyperelastic material using the Neo-Hookean description (Eq. 6). I_1, I_2, J were defined as above. $E_{\text{bony endplates}}$ and $\nu_{\text{bony endplates}}$ represented the Young's modulus (12,000 MPa) and Poisson's ratio (0.3) of the bony endplates, which were determined based on reported data in the literature (Choi et al., 1990; Goel et al., 1995b; Dreischarf et al., 2014).

$$W_{bony\ endplates}(I_1, I_2, J) = \frac{E_{bony\ endplates}}{4(1+\nu_{bony\ endplates})}(I_1-3) - \frac{E_{bony\ endplates}}{2(1+\nu_{bony\ endplates})}lnJ + \frac{E_{bony\ endplates}\ \nu_{bony\ endplates}}{(1+\nu_{bony\ endplates})(1-2\nu_{bony\ endplates})}(lnJ)^2 \tag{6}$$

Multiscale Model Validation

Model robustness and accuracy (i.e., predictive power) were evaluated by simulating a range of loading modalities tested in experiments. All models were simulated using steady-state analyses and the model output were evaluated at equilibrium. Model-predicted properties were compared to experimental measurements at the joint, tissue, and subtissue levels.

Joint-Level Validation

At the joint level, resting intradiscal pressure, compressive mechanics, and torsional mechanics were evaluated for the motion segment model described in Section "Model Development." Resting intradiscal pressure was defined as the average NP pressure after swelling and was compared to *in vivo* and *in vitro* intradiscal pressure data (Urban and McMullin, 1988; Ishihara et al., 1996; Sato et al., 1999; Wilke et al., 1999; Nguyen et al., 2008). Both human intervertebral disc and bovine caudal disc intradiscal pressure data were included for validation, because previous studies have shown similar results between the two species (Oshima et al., 1993; Ishihara et al., 1996; Alini et al., 2008).

Disc compressive and torsional mechanics were evaluated by applying loading protocols described in corresponding experimental studies (Beckstein et al., 2008; Showalter et al., 2012). After swelling (triphasic) in 0.15 M phosphate-buffered saline, compressive mechanics were evaluated by applying a 0.5 MPa axial compression. Boundary conditions at the top and bottom bony endplates were defined to represent boundary conditions reported in Beckstein et al. (2008). The normalized compressive stiffness was calculated as the slope of the model-predicted compressive load-displacement curve in the linear region, which was then normalized by the model geometry (i.e., cross-sectional area and height; Beckstein et al., 2008). Torsional mechanics were evaluated by applying a 0.5 MPa axial compressive preload immediately followed by a 10° axial rotation. Boundary conditions at the top and bottom bony endplates were defined to represent boundary conditions reported in Showalter et al. (2012). Normalized torsional stiffness was calculated by normalizing the slope of the torque-rotation curve between 7.5° and 10° by the model polar moment of inertia (Showalter et al., 2012; Bezci et al., 2018). The model was considered valid for predicting disc intradiscal pressure and stiffness when model-predicted values were within one standard deviation of reported mean values.

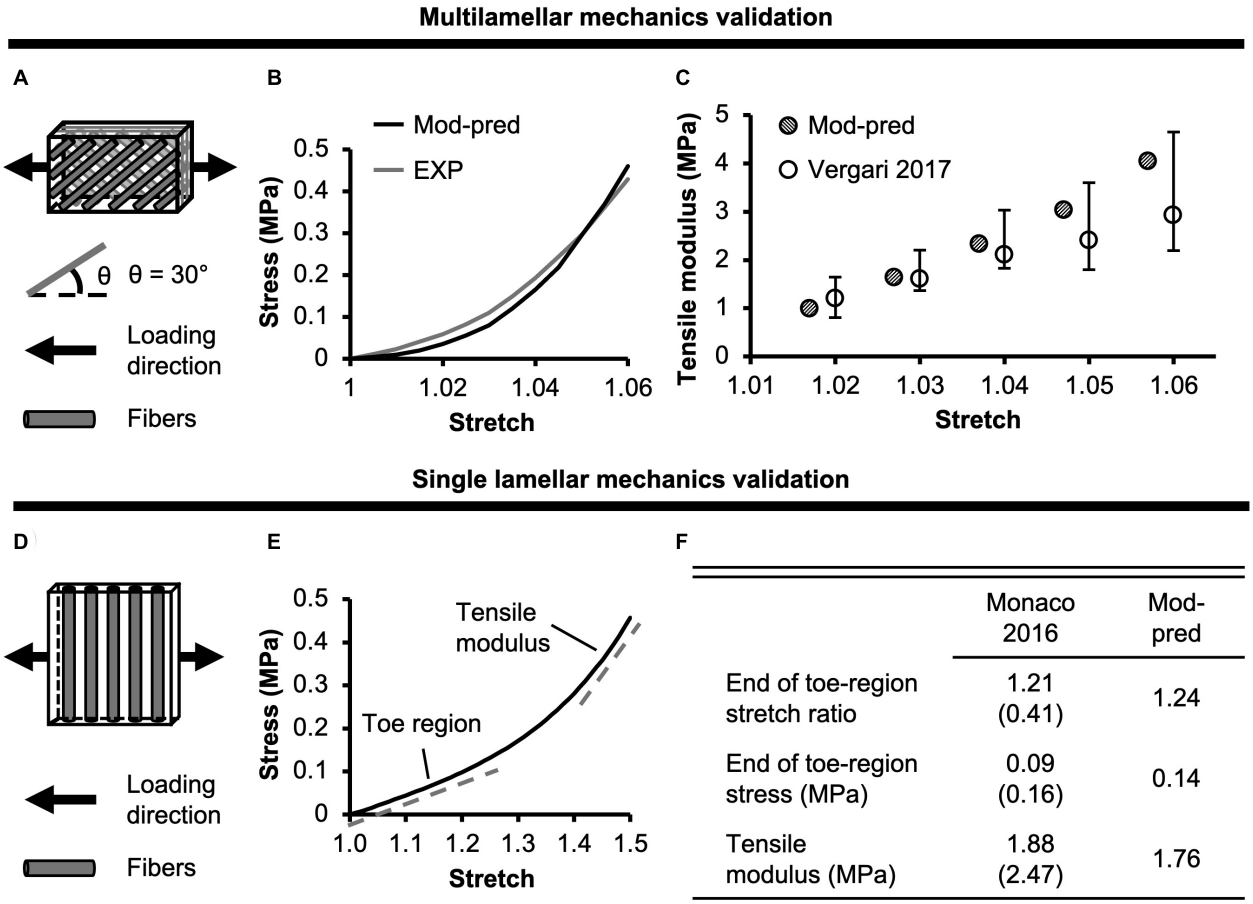

	Monaco 2016	Mod-pred
End of toe-region stretch ratio	1.21 (0.41)	1.24
End of toe-region stress (MPa)	0.09 (0.16)	0.14
Tensile modulus (MPa)	1.88 (2.47)	1.76

FIGURE 2 | (A) Model validation schematic for multilamellar mechanics of bovine annulus fibrosus (AF). Model geometry and loading conditions were determined based on protocols reported in Vergari et al. (2017). **(B)** Model-predicted (Mod-pred) bovine AF multilamellar stress-stretch response compared to representative experimental (EXP) data from Vergari et al. (2017). **(C)** Model-predicted tensile modulus at five specified stretch ratios compared to experimental data from Vergari et al. (2017). **(D)** Model validation for single lamellar mechanics of bovine AF. Model geometry and loading conditions were determined based on protocols reported in Monaco et al. (2016). **(E)** Model-predicted bovine single lamellar stress-stretch response. **(F)** Model-predicted bovine AF single lamellar tensile mechanical properties compared to experimental data [mean (standard deviation)] from Monaco et al. (2016).

To assess the influence of including water content and osmotic response on predicted mechanical behavior, a 1:5 hyperelastic disc model, which is more commonly used in FEMs of the intervertebral disc, was created. In the model, all disc components were modeled using hyperelastic material descriptions, and its compressive stiffness was evaluated by applying a 0.5 MPa axial compression and calculating the slope of the linear region of the stress-strain curve.

Tissue-Level Validation

At the tissue level, both model-predicted AF mechanical properties and swelling properties were evaluated for model validation. A structure-based FEM was created for bovine multilamellar AF tissue specimens to simulate uniaxial tensile tests performed by Vergari and coworkers (**Figure 2A**; Vergari et al., 2017). After swelling (triphasic) in 0.15 M phosphate-buffered saline, a 1.1 uniaxial tensile stretch was applied along the circumferential direction (**Figure 2A**). Boundary conditions were defined to represent no slipping between the grips and the multilamellar tissue sample surface, as reported in Vergari et al. (2017). Tensile modulus was calculated as the slope of the stress-stretch curve at stretch ratios between 1.02 and 1.06 in 0.01 increments, as reported in the literature (Vergari et al., 2017). Tissue explant models of the NP and inner-middle AF were created to evaluate model-predicted swelling behavior in 0.15 M phosphate-buffered saline. Swelling ratios were calculated as the difference between post- and pre-swelling weight divided by the tissue pre-swelling weight and compared to data reported in Bezci et al. (2019). If model-predicted mechanical and swelling properties were within one standard deviation of reported mean values, the model was considered valid for predicting the respective behavior.

Subtissue-Level Validation

At the subtissue level, model-predicted AF mechanics were evaluated for model validation. A structure-based model was created for bovine single lamellar AF specimens to simulate uniaxial tensile tests performed by Monaco and coworkers

(**Figure 2D**; Monaco et al., 2016). After swelling (triphasic) in 0.15 M phosphate-buffered saline, a 1.5 uniaxial tensile stretch was applied to the specimen transverse to the fiber direction (**Figure 2D**). Boundary conditions were defined to effectively replicate the flexible rake system applied in Monaco et al. (2016). Model-predicted uniaxial tensile mechanics were only assessed transverse to the fiber direction, because to the best of the authors' knowledge, no studies have evaluated bovine single lamellar AF mechanics along the fiber direction analogous to Holzapfel and coworkers' work using the human AF (Holzapfel et al., 2005). Tensile modulus was calculated as the slope of the stress-stretch curve in the linear region. The model-predicted mechanical properties, including modulus and the stress and strain at the end of the toe-region, were compared to experimental data (Monaco et al., 2016). The model was considered valid for predicting subtissue-level mechanics if the model-predicted mechanical properties were within one standard deviation of reported mean values.

Effect of Loading Condition on Multiscale Bovine Caudal Disc Mechanics

After validation, three loading conditions were applied to the motion segment model described in Section "Model Development" to evaluate the effect of loading condition on multiscale bovine caudal disc mechanics. All three cases were loaded in two steps. First, swelling in 0.15 M phosphate-buffered saline was simulated. Then, one of the three loading conditions was assessed, including Case *A*: 0.5 MPa axial compression, **Case *B***: 10° axial rotation, and **Case *C***: 0.5 MPa axial precompression followed by 10° axial rotation. For **Case *A***, axial compression was simulated between 0–1.0 MPa, but only data from 0.5 MPa axial compression was presented, as it corresponded to experimental data reported in the papers that we compared and validated our model to (Beckstein et al., 2008; Showalter et al., 2012; Bezci et al., 2018). Additionally, the 0.5 MPa axial compression more closely mimicked the compressive stress observed in low-intensity daily activities (e.g., relaxed standing and sitting, walking, etc.; Wilke et al., 1999). For **Cases *B*** and ***C***, disc height was not allowed to change during rotation. Model boundary conditions were defined as in Section "Multiscale Model Validation," while **Cases *B*** and ***C*** shared identical boundary conditions. All models were simulated using steady-state analyses with the output evaluated at equilibrium. The effect of loading condition was evaluated at the joint, tissue and subtissue levels, as follows:

Joint-Level Mechanics

Average solid stress (i.e., stress absorbed by tissue solid matrix) and fluid pressure (i.e., stress absorbed by the tissue interstitial fluid) of the entire bovine caudal disc, including the NP, AF, and CEP, were evaluated for all three cases. The relative contribution of solid stress was evaluated as the solid stress divided by the total stress, which was calculated as the sum of solid stress and fluid pressure based on triphasic mixture theory (Lai et al., 1991). Similarly, the relative contribution of fluid pressure was calculated by normalizing the fluid pressure by the total stress.

Tissue-Level Mechanics

NP, AF, and CEP *in situ* swelling ratios were evaluated post-swelling. After the applied mechanical loading, average solid stress, strain, and fluid pressure in the NP, AF, and CEP were evaluated for all three cases. For each disc component, the relative contribution of the solid stress and fluid pressure to the total stress was evaluated. The total stress was calculated as the sum of the component's solid stress and fluid pressure. Disc bulging of the inner and outer AF was assessed under 0.5 MPa axial compression (**Case *A***) and was calculated by dividing the respective change in mid-disc-height radius with loading by the post-swelling disc radius (reported as a percentage value).

Subtissue-Level Mechanics

Average fiber stretch was evaluated within each AF lamellae after swelling and after loading. Swelling-induced fiber stretch was calculated as the post-swelling fiber length divided by the initial fiber length. Post-loading fiber stretch was calculated as the post-mechanical loading fiber length divided by the post-swelling fiber length. Average solid stress in the fibers and extrafibrillar matrix was evaluated post-loading. The relative solid stress contribution of collagen fibers and extrafibrillar matrix to the overall AF solid stress, which was calculated as the sum of fiber and matrix solid stress, was also assessed. Additionally, post-loading fiber solid stress profiles along the fiber length from the inferior to the superior end of the disc were evaluated in both the inner- and outermost AF lamellae.

Effect of Degeneration on Multiscale Bovine Caudal Disc Mechanics

The effect of degeneration on multiscale disc mechanics was investigated under the three loading conditions evaluated in Section "Effect of Loading Condition on Multiscale Bovine Caudal Disc Mechanics." Degeneration was achieved by reducing tissue proteoglycan content, which was simulated by reducing the fixed charge density in the NP, AF, and CEP (Adams and Roughley, 2006). Bovines are commonly slaughtered between 18 and 24 months and do not experience spontaneous degeneration within that timespan (Alini et al., 2008). Therefore, fixed charge density distribution for the degenerated disc was determined based on trends observed in degenerated human discs (**Figure 1C**–checkered bars; Urban and Maroudas, 1979; Beckstein et al., 2008; Bezci et al., 2019), as well as data reported from *ex vivo* degeneration models in relevant bioreactor studies (Castro et al., 2014; Paul et al., 2018). All model-predicted properties discussed and evaluated in Section "Effect of Loading Condition on Multiscale Bovine Caudal Disc Mechanics" were evaluated with degeneration. Additionally, model-predicted resting intradiscal pressure, normalized compressive stiffness, and normalized torsional stiffness were also calculated for the degenerated disc model and compared to available experimental data for a more rigorous model validation (Urban and McMullin, 1988; Sato et al., 1999; Showalter et al., 2012; Bezci et al., 2018). All models were simulated using steady-state analyses with the output evaluated at equilibrium.

RESULTS

Multiscale Model Validation

Joint-Level Validation

Model-predicted intradiscal pressure value for the healthy disc was 0.17 MPa, which was within the range of reported experimental values (<0.90× standard deviation from reported mean values; **Figure 3A**–black diagonal bar vs. white bars enclosed by black lines).

Model-predicted compressive stress-strain response was non-linear for healthy disc models developed using hyperelastic and triphasic mixture theory material descriptions, agreeing well with experimental observations (**Figure 3B**–solid lines). However, the hyperelastic disc model predicted a stiffer joint-level response than the triphasic model, which accounted for water content and osmotic behavior (Healthy). For the hyperelastic model, predicted normalized compressive stiffness was 12.52 MPa and did not agree with any available datasets (>1.2× standard deviations from reported means). Employing the triphasic material description resulted in a normalized compressive stiffness of 8.12 MPa, agreeing well with Beckstein et al. (2008) and two of three datasets collected, but not published, by Newell et al. (2020) (moduli calculated at a more relevant loading range than the previously published data, see **Supplementary Figure 3**). Model-predicted compressive stiffness was within 0.8 standard deviation of the reported mean for the three agreed datasets (**Figure 3C**–black diagonal bar vs. Beckstein et al., 2008 and Newell et al., 2020). However, our model was not able to accurately predict the compressive stiffness reported by the remaining dataset collected for Newell et al. (2020), which represents data from the authors' own laboratory (18.74 ± 3.35 MPa, **Supplementary Figure 3**–Berkeley). The model-predicted compressive stiffness was >3.0 × standard deviations from the reported mean of this single dataset since the experimental data from our laboratory was higher than values reported by other institutes (**Figure 3C**–black diagonal bar vs. Newell et al., 2020).

A pseudo-linear torque-rotation response was observed for the healthy disc (**Figure 3D**–solid line). Model-predicted normalized torsional stiffness was 36 kPa/°, matching well with reported values (<0.75× standard deviation from the reported mean values; **Figure 3E**–black diagonal vs. white bars).

Tissue- and Subtissue-Level Validation

For multilamellar AF specimens, model-predicted stress-stretch response under uniaxial tension was non-linear, agreeing well with the literature (**Figure 2B**). Model-predicted tensile modulus agreed with the literature but tended to be on the higher end of reported values, particularly as stretch increased (**Figure 2C**). For single lamellar AF specimens, model-predicted stress-stretch response under uniaxial tension was also non-linear, agreeing well with the literature (**Figure 2E**). Model-predicted mechanical properties for the toe and linear regions were well within one standard deviation of the reported mean (<0.35× standard deviation from the reported mean; **Figure 2F**). Based on our model predictions, *ex situ* swelling ratio was 1.10 for the healthy NP tissue and 0.76 for the inner-middle AF, which were both within one standard deviation of the reported means (<0.88× standard deviation; **Figure 4A**).

Effect of Loading Condition on Multiscale Bovine Caudal Disc Mechanics

Joint-Level Mechanics

Fluid pressure contributed significantly to the disc's overall load-bearing capacity, especially for loading conditions that incorporated axial compression. In healthy disc models, the average solid stress and average fluid pressure were both approximately 0.2 MPa under axial compression, resulting in relatively equal contribution to the total stress in the disc (**Figure 5**–**Case *A***). Lower solid stress (0.11 MPa) and fluid pressure (0.13 MPa) were observed under axial rotation, but the relative contribution of solid stress and fluid pressure remained almost identical (**Figure 5**–**Case *B*** vs. ***A***). Compared to **Case *A***, the combined loading more than doubled the solid stress to 0.43 MPa but did not change the fluid pressure (0.24 MPa). Thus, the resulting relative contribution of the solid stress increased to 64% of the total stress (**Figure 5**–**Case *C*** vs. ***A***).

Tissue-Level Mechanics

Different applied boundary and loading conditions resulted in heterogeneous solid stress, fluid pressure, and strain distributions throughout the disc (**Figure 6**). Large solid stresses were observed in the outer AF, especially in **Cases *A*** and ***C*** (**Figure 6A**–"*"). Compared to **Case *A***, the rotation-only loading condition resulted in lower solid stresses in all disc components (**Figure 6A**–**Case *B*** vs. ***A***), where the solid stress in the NP, CEP, and AF decreased by more than 80, 67, and 42% (**Figure 7A**–**Case *B*** vs. ***A***). Under combined loading, a two-fold increase in AF and CEP average solid stress was observed (**Figure 7A**–**Case *C*** vs. ***A***: black and pink solid bars). However, the addition of rotation to axial compression did not change the NP solid stress (**Figure 7A**–**Case *C*** vs. ***A***: green solid bar).

In situ swelling ratios for the NP, AF, and CEP were 0.25, 0.13, and 0.03, respectively (**Figure 4B**–Healthy; **Figure 4C**–black solid bars). Under axial compression, average fluid pressure was 0.14 MPa in the AF, which was ∼70% lower than that in the NP (0.47 MPa) and ∼60% lower than that in the CEP (0.36 MPa; **Figure 7B**–**Case *A***: solid bars). Fluid pressure under the torsion-only loading was generally lower than that under the compression-only loading. Particularly, compared to **Case *A***, NP and AF fluid pressure were both ∼40% lower while CEP fluid pressure was ∼60% lower (**Figure 7B**–**Case *B*** vs. ***A***). Interestingly, compared to the compression-only loading condition, combining axial compression with rotation did not have a significant effect on the fluid pressure in any disc components (**Figure 7B**–**Case *C*** vs. ***A***).

As expected, the relative fluid pressure to the total stress was significant and tissue-specific. Across all three loading conditions, fluid pressure accounted for more than 85% of the total stress in the NP and more than 70% of the total stress in the CEP (**Figure 8**–NP). The relative contribution of fluid pressure was

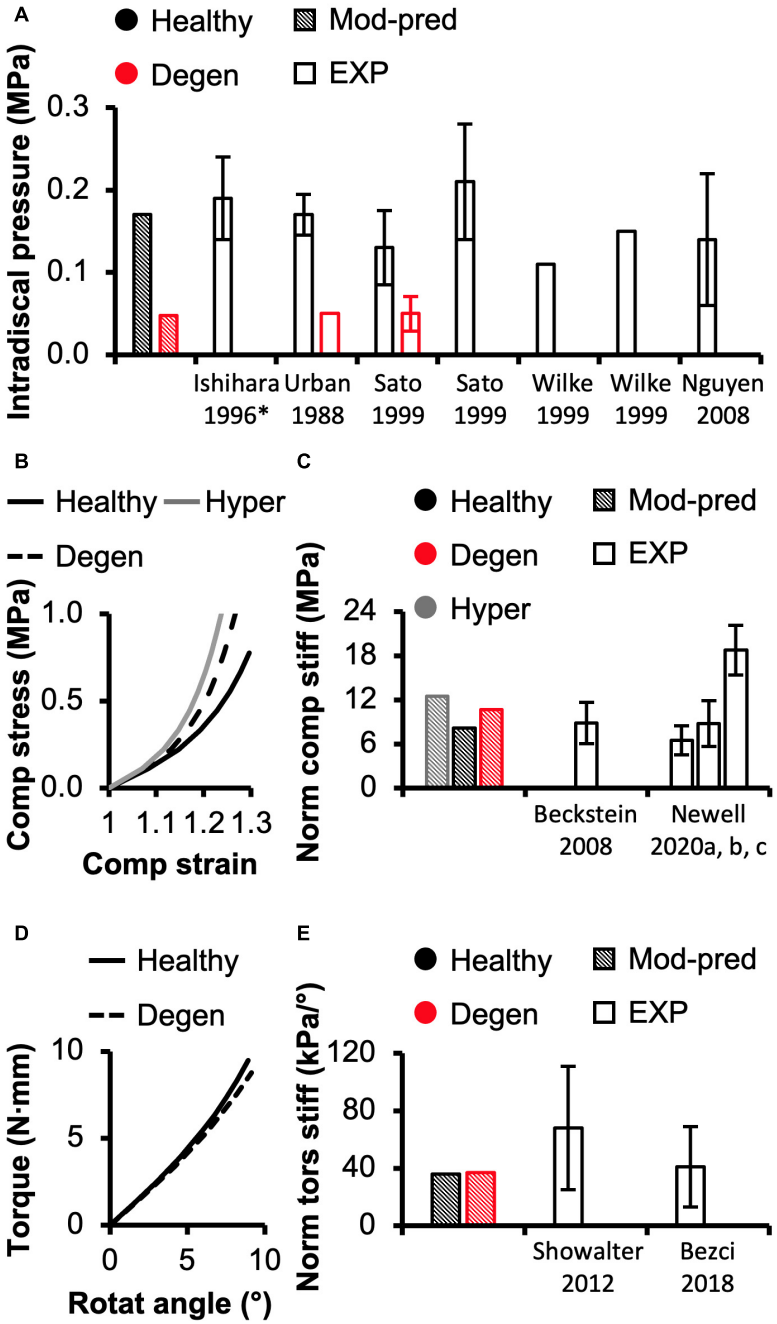

FIGURE 3 | (A) Model-predicted (Mod-pred) resting intradiscal pressure in healthy and degenerated (Degen) disc models compared to experimental (EXP) values. Data reported by Ishihara et al. (1996) (noted by *) were obtained from bovine caudal discs while data reported by the other listed studies were obtained from human intervertebral discs, which have shown to share comparable intradiscal pressure values. Variations were not reported in Wilke et al. (1999). **(B)** Representative model-predicted compressive (Comp) stress-strain response of hyperelastic (Hyper), healthy, and degenerated disc models under axial compression. **(C)** Model-predicted normalized (Norm) compressive stiffness (stiff) compared to EXP values. **(D)** Representative model-predicted torsional (tors) response of healthy and degenerated discs when evaluated for torsional mechanics. **(E)** Model-predicted normalized torsional stiffness compared to EXP values.

smaller in the AF, but nevertheless accounted for 20–36% of the total AF stress (**Figure 8**–AF). Compared to the compression-only loading condition, the torsion-only loading resulted in a slight increase in the relative fluid pressure in the NP (**Figure 8**–**Case *B*** vs. ***A***). However, the combined loading did not alter the relative solid stress or fluid pressure contribution in the NP but resulted in a ∼25% larger solid stress contribution in the AF (**Figure 8**–**Case *C*** vs. ***A***). The relative solid and fluid contribution in the CEP was not affected by applied loading conditions (**Figure 8**–CEP).

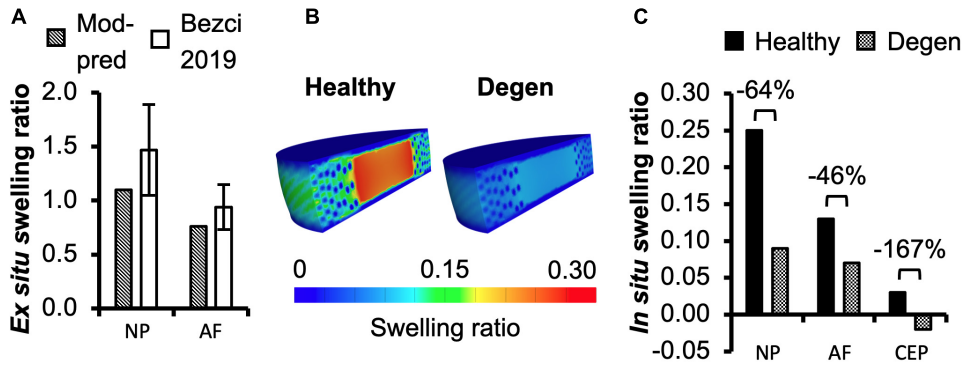

FIGURE 4 | (A) Model-predicted (Mod-pred) *ex situ* swelling ratios of the nucleus pulposus (NP) and the inner-middle annulus fibrosus (AF) compared to experimental (EXP) data reported by Bezci et al. (2019). **(B,C)** Model-predicted *in situ* swelling ratios of the NP, AF, and cartilage endplate (CEP) in healthy and degenerated (Degen) disc models. Relative changes in *in situ* swelling ratio with degeneration are labeled above corresponding neighboring bars.

Large strains were observed at the AF-NP-CEP interface (i.e., the rim) and in the outer AF (**Figure 6C**–"^"). Under axial compression, NP and AF strains were comparable (0.16 and 0.13, respectively) and were approximately twofold greater than strains in the CEP (0.07; **Figure 7C**–**Case *A***). Under axial rotation, strains in the NP decreased by ∼75%; however, AF and CEP strains increased by ∼20% (**Figure 7C**–**Case *B*** vs. ***A***). Compression combined with rotation increased AF strains by 80% from 0.13 to 0.24 and increased CEP strains by more than 200% from 0.07 to 0.18. However, the combined loading did not greatly alter NP strains (∼5% change; **Figure 7C**–**Case *C*** vs. ***A***).

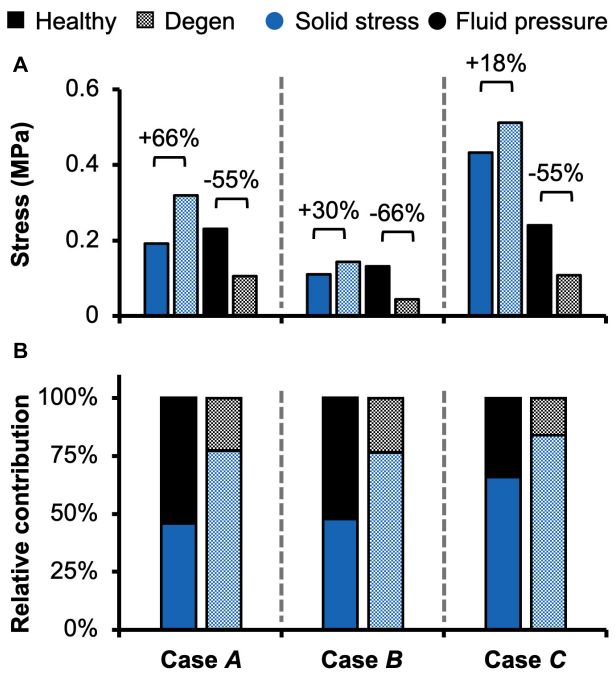

FIGURE 5 | Model-predicted **(A)** solid stress and fluid pressure, as well as **(B)** their relative contribution to the total stress taken by the disc in healthy and degenerated (Degen) models for Cases *A*, *B*, and *C*. Relative changes in solid stress or fluid pressure with degeneration are labeled above corresponding neighboring bars.

Assessment of AF radial displacement at the mid-disc height under axial compression showed outward bulging for both the inner and outer AF after swelling (**Figure 9A**). In the outer AF, the relative outward bulging increased with applied load, reaching ∼1.8% under 0.5 MPa axial compression (**Figure 9B**–black solid circles). In the inner AF, the relative bulging reached a maximum of ∼0.4% under 0.2 MPa of compression but then decreased with additional applied compressive load (**Figure 9B**–red solid circles).

Subtissue-Level Mechanics

The triphasic swelling step applied to all model cases prior to the applied mechanical loading resulted in an average swelling-induced fiber stretch of 1.05 in the inner AF and 1.02 in the outer AF. After applying 0.5 MPa of axial compression, the post-loading fiber stretch was ∼1.05 and was relatively consistent throughout the AF (**Figure 10A**–black solid circles). The magnitude of fiber stretch under the torsion-only loading was comparable, but there was a linear increase in fiber stretch from the innermost AF layer (1.04) to the outermost layer (1.07; **Figure 10A**–blue solid circles). Under the combined loading, the fiber stretch was nearly twofold greater than that under the single-axis loading conditions and was ∼1.10 through the AF (**Figure 10A**–red solid circles).

Average fiber solid stress was relatively consistent throughout the AF under axial compression, ranging from 0.22 MPa in the inner AF to 0.29 MPa in the outer AF (**Figure 10B**–black solid circles). Under the rotation-only loading, fiber stress in the inner AF was 60% lower than the compression-only condition; however, large changes in fiber solid stress were not observed in the outer AF (**Figure 10B**–blue vs. black solid circles). Under the combined loading, fiber stress increased linearly from 0.37 MPa in the inner AF to 0.80 MPa in the outer AF. Compared to **Case *A***, the fiber stress was increased by 70% in the inner AF and by 300% in the outer AF (**Figure 10B**–red vs. black solid circles). The solid stress of AF extrafibrillar matrix, as well as its observed trends with loading condition were both comparable to that of

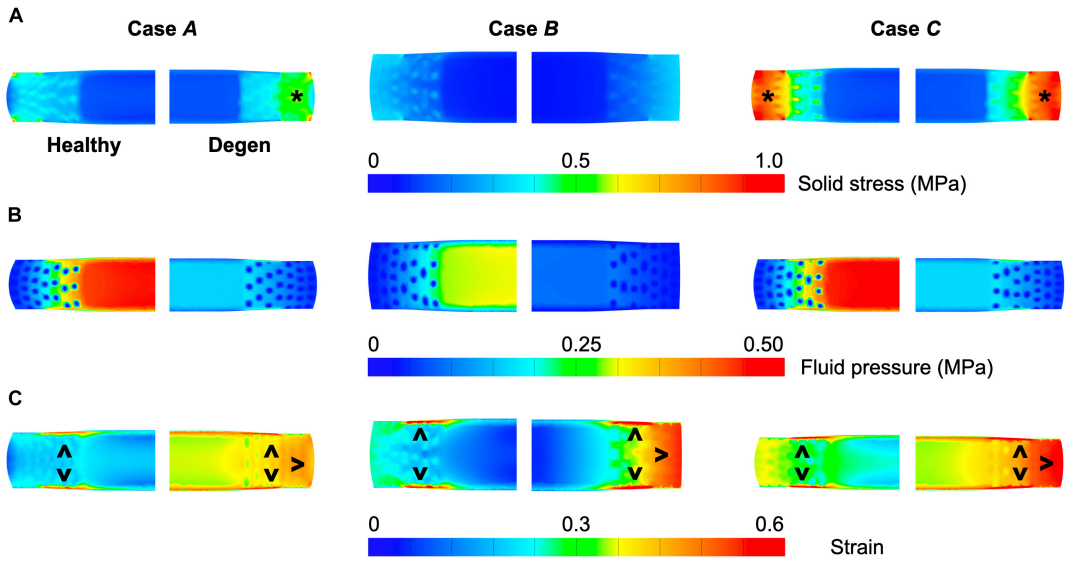

FIGURE 6 | Representative post-loading disc mid-frontal (or coronal) plane **(A)** solid stress, **(B)** fluid pressure, and **(C)** strain distributions in healthy and degenerated (Degen) disc models. Black asterisks highlight stress concentrations. Black triangles point at strain concentrations.

the fibers. Thus, across all three loading conditions, AF collagen fibers and extrafibrillar matrix contributed equally to the overall AF solid stress (**Supplementary Figure 4**).

Fiber solid stress profiles were tracked along the fiber length between the inferior and superior bony endplates. In all cases, fiber solid stress distributions were symmetric about the mid-transverse plane, due to disc symmetry (**Figure 11**). For **Cases *A*** and ***C***, peak fiber solid stresses in the outer AF were observed right below the bony endplates, and peak fiber solid stresses in the inner AF were observed at the mid-disc height (**Figure 11**–**Cases *A*** and ***C***: solid lines). By contrast, fiber stress was relatively consistent along the fiber length in both the inner and outer AF for **Case *B*** (**Figure 11**–**Case *B***: solid lines). The combined loading amplified the fiber stress difference between the inner- and outermost lamellae, which shared comparable fiber stresses under the compression- or rotation-only loading conditions (**Figure 11**–solid black vs. gray lines).

Effect of Degeneration on Multiscale Bovine Caudal Disc Mechanics

Joint-Level Mechanics

Resting intradiscal pressure decreased by ∼70% with degeneration (0.048 MPa) and was within the range of reported values (<0.10× standard deviation from the reported mean values; **Figure 3A**–red bars). Normalized compressive stiffness increased by ∼30% with degeneration (10.67 MPa; **Figures 3B,C**). Normalized torsional stiffness was approximately 37 kPa/°, which was not affected by degeneration (**Figures 3D,E**).

With degeneration, stresses were redistributed with the tissue solid component taking on more of the overall total stress (**Figure 5**–Degen vs. Healthy). Across the three loading conditions, degeneration increased solid stress by 18–66%, depending on the disc components, and the greatest relative increase with degeneration was observed in the compression-only loading condition (**Figure 5A**–checkered vs. solid bars). Fluid pressure decreased by ∼60% for all three loading conditions. Thus, the resulting relative contribution of solid stress increased from 45–65% in the healthy discs to 75–85% in the degenerated discs (**Figure 5B**–checkered vs. solid bars).

Tissue-Level Mechanics

As expected, degeneration reduced tissue swelling capability (**Figures 4B,C**–checkered vs. solid bars). The NP *in situ* swelling ratio reduced by >60%, decreasing from 0.25 to 0.09 with degeneration. Similarly, *in situ* AF swelling ratio decreased by ∼45% from 0.13 to 0.07 with degeneration. Interestingly, the CEP *in situ* swelling ratio became negative (−0.02) in the degenerated disc, indicating a loss of tissue volume after swelling (**Figures 4B,C**). The decrease in swelling capacity resulted in a 40–90% decrease in fluid pressure, depending on the tissue types and applied loading conditions. Particularly, large degeneration-induced fluid pressure decreases were mostly observed in the NP and CEP (**Figure 7B**–checkered vs. solids bars).

Similar to joint-level observations, degeneration redistributed stress in each disc component by decreasing the relative contribution of fluid pressure and increasing the relative contribution of solid stress (**Figure 8**–Degen vs. Healthy). The greatest stress redistribution was observed in the CEP, where the relative fluid pressure contribution decreased from ∼70–80% in the healthy discs to ∼20–50% in the degenerate discs. Noticeably, in **Case *B***, the CEP relative fluid pressure contribution reduced by more than 75% from 83% in the healthy disc to 20% in the degenerate disc (**Figure 8**–CEP: checkered vs. solid bars). In the NP, the decrease in fluid contribution was relatively consistent for all three loading conditions. Particularly, degeneration reduced NP fluid contribution by ∼20–30%, decreasing from ∼85–95%

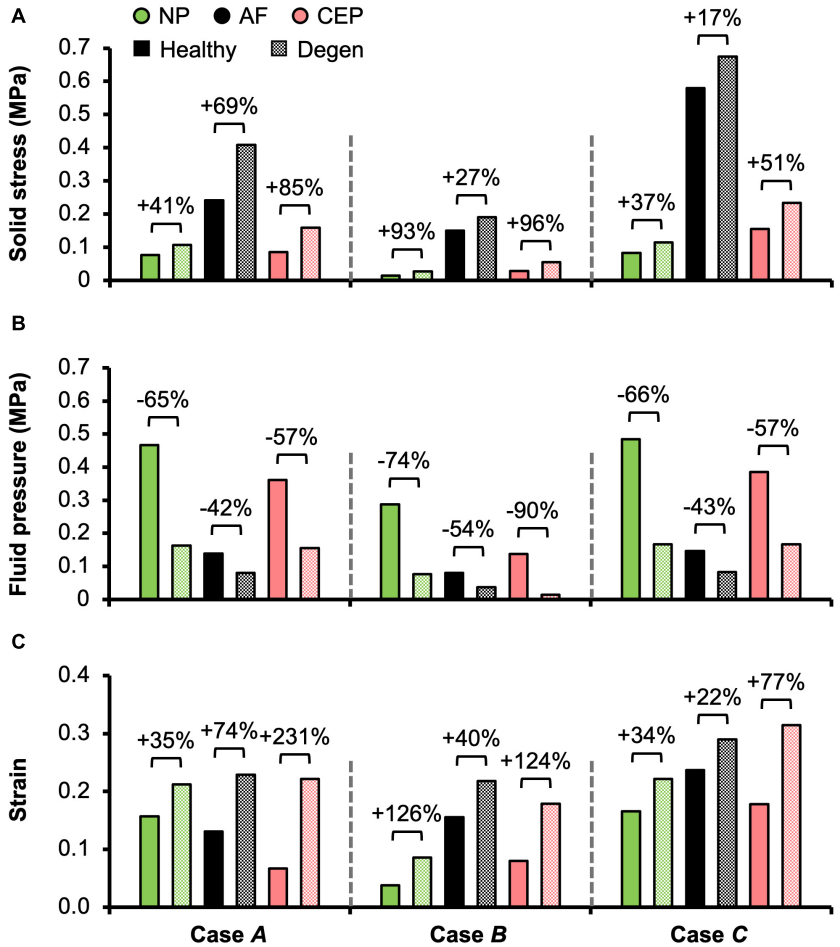

FIGURE 7 | Model-predicted post-loading average **(A)** solid stress, **(B)** fluid pressure, and **(C)** strain in the nucleus pulposus (NP), annulus fibrosus (AF), and cartilage endplate (CEP) in healthy and degenerated (Degen) disc models. Relative changes in NP, AF, and CEP solid stress, strain, or fluid pressure with degeneration are labeled above corresponding neighboring bars.

in the healthy discs to ∼60–75% with degeneration (**Figure 8**–NP: checkered vs. solid bars). In the AF, the relative fluid pressure contribution decreased by ∼50% with degeneration, ranging from 11 to 17% in the degenerated discs compared to 20–36% in the healthy discs (**Figure 8**–AF: checkered vs. solid bars). Degeneration also increased the average strain in each disc components by ∼20–240%, with the largest increase observed in the CEP. Similar to the healthy disc, peak strains were observed at the AF-NP-CEP interface (i.e., the rim) and in the outer AF (**Figure 6C**–"^").

The outer AF was still expected to bulge outward with the level of degeneration simulated in this study. Relative outward bulging for the outer AF at 0.5 MPa axial compression was ∼1%, which was ∼45% smaller than that in the degenerated disc (**Figure 9**–checkered vs. solid black circles). While the inner AF appeared to bulge outward slightly, calculating the relative change in radial displacement between the post-swelling and post-loading configuration showed that the inner AF moved inward toward the NP by 0.3% (**Figure 9A**–Degen; **Figure 9B**–checkered black circles). Although the inner AF moved toward the NP, collapse of the inner AF into the NP, which has been reported for more severely degenerated discs (Adams and Roughley, 2006), was not observed in our model.

Subtissue-Level Mechanics

Degeneration increased the average post-loading fiber stretch throughout the AF and had a greater impact on the inner AF than the outer AF (**Figure 10A**–checkered vs. solid black circles). For **Case *A*,** average fiber stretch decreased linearly from 1.10 in the inner AF to 1.07 in the outer AF (**Figure 10A**–checkered black circles), representing a 90% increase in fiber stretch in the inner AF and a 50% increase in the outer AF with degeneration (**Figure 10A**–inset: black circles). For **Case *B***, the average fiber stretch was ∼1.08 and was relatively consistent throughout the AF (**Figure 10A**–checkered blue circles), where degeneration increased inner AF fiber stretch by more than 70% and increased outer AF fiber stretch by ∼20% (**Figure 10A**–inset: blue circles). Under the combined loading condition, average fiber stretch exceeded the 1.10 threshold in all AF lamellae, decreasing from 1.14 in the inner AF to 1.11 in the outer

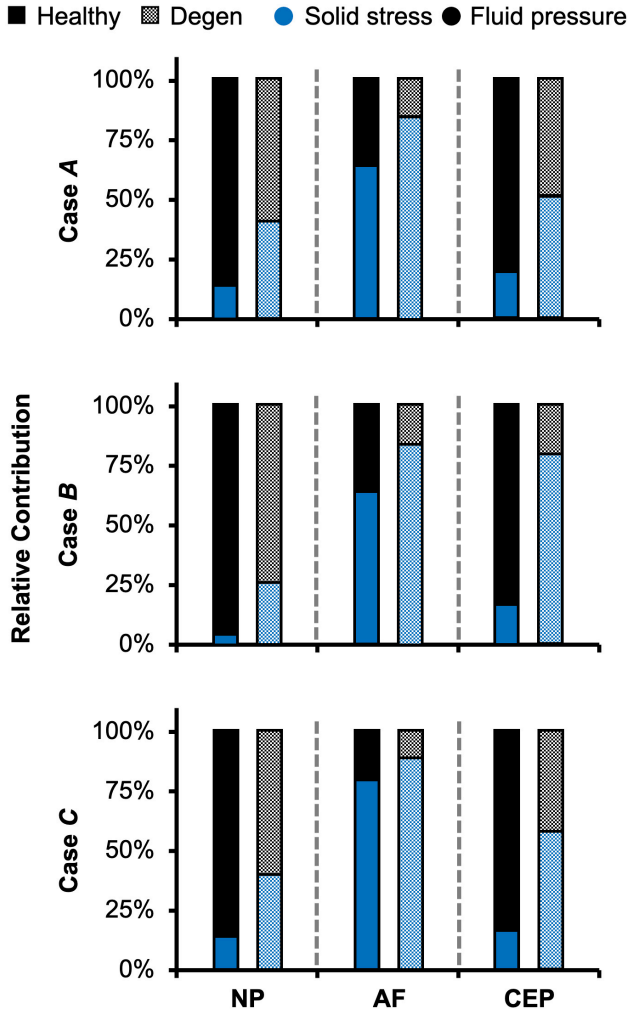

FIGURE 8 | Model-predicted relative contribution of solid stress and fluid pressure in the nucleus pulposus (NP), annulus fibrosus (AF), and cartilage endplate (CEP) in healthy and degenerated (Degen) disc models for Cases *A*, *B*, and *C* after the applied mechanical loading.

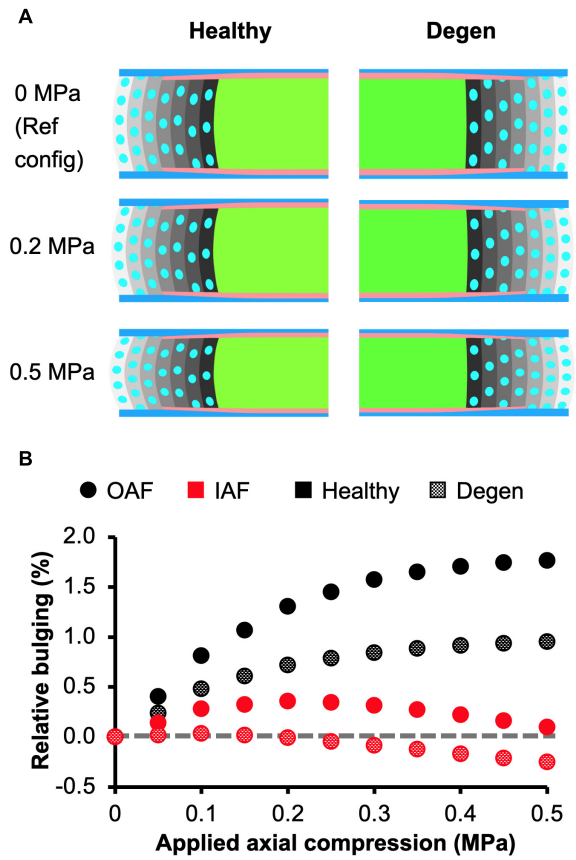

FIGURE 9 | (A) Disc mid-frontal (or coronal) cross sections demonstrating the relative annulus fibrosus (AF) bulging in healthy and degenerated (Degen) disc models under axial compression. The relative AF bulging was calculated using the post-swelling 0 MPa configuration as the reference configuration (Ref config). **(B)** Relative bulging in the inner and outer AF in healthy and degenerated disc models. Positive and negative relative bulging suggest outward and inward AF bulging compared to the reference configuration, respectively. The gray horizontal dashed line represents the relative disc bulging threshold, below which the AF was predicted to bulge inward compared to the reference configuration.

AF (**Figure 10A**–checkered red circles). However, although the inner AF fiber stretch increased by ∼50% with degeneration, the outer AF fiber stretch was not affected (**Figure 10A**–inset: red circles).

The overall increase in fiber stretch with degeneration did not result in a similar increase in fiber or extrafibrillar matrix solid stress. Under the compression-only loading, solid stress in the fibers increased by more than 40% in the inner AF and by ∼85% in the outer AF (**Figure 10B**–inset). However, the increases in both fiber and matrix solid stresses were smaller and not as consistent for **Cases *B*** and ***C*** (**Figure 10B**). Degeneration did not alter the AF fiber/matrix solid stress contribution (**Supplementary Figure 4B**), nor the pattern of stress distribution along the fiber length, but did increase the stress magnitude, with the largest increase observed for the compression-only loading (**Figure 11**–dashed vs. solid lines).

DISCUSSION

This study developed and validated a multiscale and multiphasic structure-based finite element model of the bovine caudal disc motion segment. During development and validation, model parameters were determined based on tissue- or subtissue-level experimental data reported in the literature, as opposed to being calibrated to joint-level mechanics prior to validation. The model validation results highlight the model accuracy and robustness, as well as the advantages of employing the proposed multiscale, structure-based modeling-validation framework. After validation, the model was used to investigate the effect of loading condition and degeneration on solid stress, fluid pressure, and strain distributions at joint, tissue and subtissue scales. While only three loading conditions and one level of degeneration were assessed, results from this study

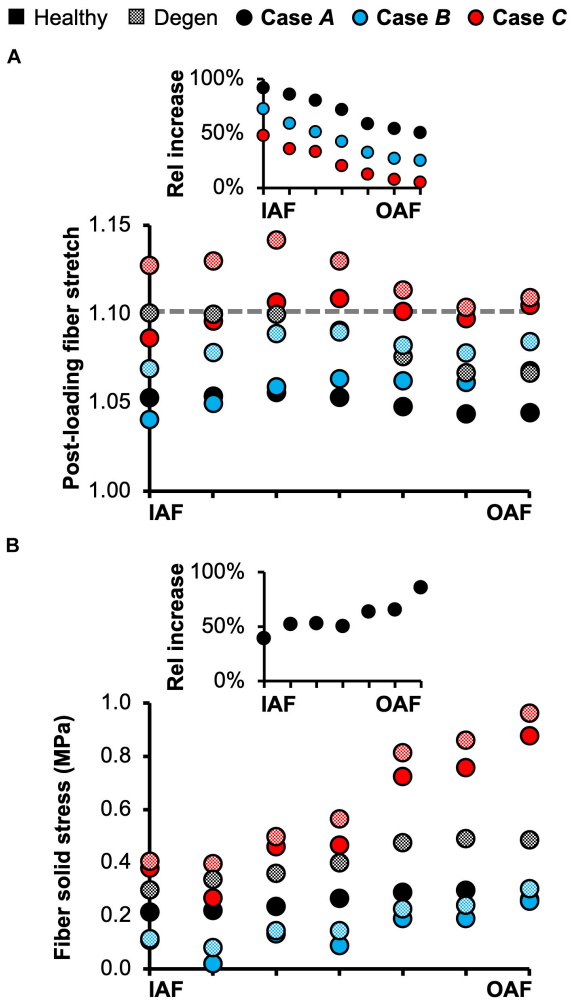

FIGURE 10 | (A) Model-predicted average annulus fibrosus (AF) post-loading fiber stretch along the disc radial direction from the inner AF (IAF) to outer AF (OAF) in healthy and degenerated (Degen) disc models. The gray horizontal dashed line highlights the fiber stretch threshold, above which the fibers have a more significant chance of failure based on previous experimental observations. The threshold value was determined based on data reported by Skaggs et al. (1994) and Isaacs et al. (2014). The inset presents the relative (Rel) percentage change in average fiber stretch with degeneration along the disc radial direction. **(B)** Model-predicted post-loading average AF solid stress along the disc radial direction from the IAF to OAF. The inset presents the relative increase in fiber solid stress with degeneration for Case *A*.

demonstrate the model's capability in investigating the shifts in disc load bearing or stress distribution mechanisms that can act to induce degenerative remodeling or damage accumulation.

Validation is critical for overall model performance, including accuracy and robustness. Most intervertebral disc models are only validated with respect to global disc measurements, such as axial displacement or intradiscal pressure. This limited validation approach can contribute to inaccurate model predictions, especially at tissue and subtissue scales, where model validation is not usually performed (Shirazi-Adl et al., 1984; Kim et al., 1991; Schmidt et al., 2007b; Galbusera et al., 2011a). Some studies calibrated model parameters, especially those associated with the AF, through optimization algorithms in order for the model predictions to fit experimental datasets measured in tests conducted under specific loading modalities (e.g., axial compression, flexion; Schmidt et al., 2006, 2007a; Malandrino et al., 2013); however, this framework requires models to be recalibrated for each new loading modality or disc geometry. The current study expanded upon our previously reported multiscale validation framework by performing model validation at joint, tissue, and subtissue levels (Zhou et al., 2020a; **Figures 3**, **4**). A total of 16 validation cases were assessed and model-predicted properties agreed well with all but one dataset. Differences in joint stiffness between the outstanding dataset, which originate from our previous work, and our model predictions, are likely caused by the non-ideal machine compliance during experimental data collection (Newell et al., 2020). Importantly, model parameters were directly obtained from tissue- or subtissue-level experimental data and no adjustments were made to match tissue- or joint-level behavior. These results demonstrated the model's predictive power and the effectiveness of the multiscale validation framework.

The structure-based modeling approach may improve clinical relevance and expand potential use for finite element models of the disc joint. At the tissue level, modeling discrete AF lamellae allowed for reproduction of radial variations in AF biochemical composition (i.e., proteoglycan content and water content). Describing variations in localized proteoglycan content is important for simulating and replicating morphological changes observed with degeneration, including the decrease in disc height, increased outward radial bulging, and inward bulging of the inner AF in severely degenerated discs (Yang and O'Connell, 2019). At the subtissue level, modeling collagen fiber bundles allowed us to explicitly evaluate fiber stress and strain distributions, rather than relying on indirect assessment, such as vector summation to evaluate fiber strain (Schmidt et al., 2007b). The separate fiber bundles generated more realistic predictions of *in situ* fiber mechanics and allowed for direct investigations into fiber-matrix interactions. For example, our findings demonstrate that a ∼50% decrease in proteoglycans caused a 40–90% increase in fiber stress when the disc was loaded under axial compression (**Figure 10B**–checkered vs. solid black circles). It should be noted that this study only assessed the moderate to severe degeneration level. Thus, additional work is needed to determine whether a decrease in only NP proteoglycan content, as observed in early degeneration, would result in similar increases in fiber stress.

Attributed to the structure-based modeling approach, the majority of our model parameters can be directly linked to tissue mechanical (e.g., modulus, Poisson's ratio, etc.) or biochemical properties (e.g., water content, proteoglycan content, etc.; **Table 1**). Model parameters with physical significance help address concerns regarding overparameterization, which is a common issue associated with homogeneous finite element models, where model parameter calibration relies heavily on optimization algorithms (Yin and Elliott, 2005; Eskandari et al., 2019). Taken together, explicitly modeled disc structures with physically relevant model parameters benefit further investigations into disc joint behavior with degeneration, disease,

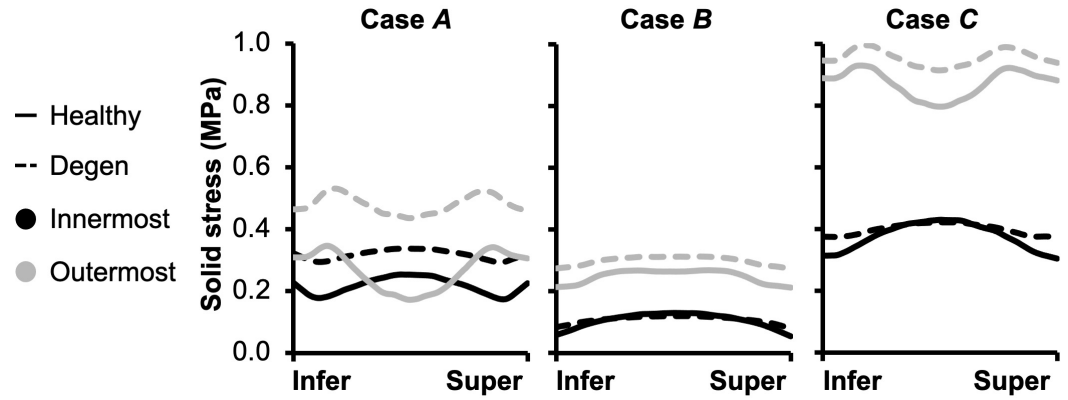

FIGURE 11 | Model-predicted post-loading annulus fibrosus (AF) fiber solid stress profiles along the fiber length from the inferior (Infer) to the superior (Super) bony endplates. The stress distributions were evaluated for the inner- and outermost AF layers in both healthy and degenerated (Degen) discs.

or injury. For example, collagen fiber diameter and stiffness can be readily modified based on structural and mechanical changes noted with degeneration, or diseases such as diabetes (Adams and Roughley, 2006; Li et al., 2013; Svensson et al., 2018). Furthermore, the model can be easily modified to evaluate advanced tissue engineering designs (e.g., angle-ply disc replacements) before conducting costly and time-intensive *in vivo* studies in large animal models (Martin et al., 2014), or to help track time-dependent changes during bioreactor organ cultures (Frauchiger et al., 2018; Pfannkuche et al., 2020).

The importance of accounting for tissue water content and osmotic response was elucidated by assessing the relative stress contribution from tissue solid matrix and interstitial fluid (**Figures 5–8**). The contribution of fluid pressure plays a pivotal role in the disc's load-bearing capacity (Adams and Roughley, 2006), but to the best of the authors' knowledge, it has not been quantified. Inclusion of triphasic material properties allows for direct measurements of fluid pressure. Based on our model predictions for healthy discs, fluid pressure accounted for 35–55% of the total stress (**Figure 5**). More specifically, the fluid pressure contribution in the NP was greater than 85% (**Figure 8**), agreeing with previous findings for the healthy articular cartilage, which has a comparable fixed charge density and water content as healthy NP tissues (Maroudas et al., 1969; Armstrong and Mow, 1982; Lüssea et al., 2000; Shapiro et al., 2002). Degeneration reduced tissue swelling capacity, altering the disc's load-bearing mechanism by shifting more stress to the tissue solid matrix (**Figures 5**, **8**). This shift in stress-bearing was particularly noticeable under axial compression, where the decrease in fluid pressure (i.e., 0.13 MPa) was balanced by an equivalent increase in solid stress (**Figure 5A–Case *A***). Despite the decrease in relative fluid pressure contribution with degeneration, fluid pressure still accounted for up to 25% of the total stress and contributed to more than 60% of NP stress (**Figures 5**, **8**–checkered bars).

Models that do not incorporate tissue swelling describe stress as being entirely absorbed by the solid matrix (single-phasic hyperelastic material description), which likely contributed to overestimations in AF fiber stretch. For example, a previous model that employed single-phasic material descriptions for the disc predicted a fiber stretch of ∼1.12 under the rotation-only loading, even with the inclusion of posterior functional spinal structures (Schmidt et al., 2007b). However, experimental data on AF single lamellar tensile mechanics reported AF fiber bundle failure stretch as 1.14 ± 0.04 (Skaggs et al., 1994; Isaacs et al., 2014). Thus, such a model would suggest a relatively high likelihood of disc failure, contradicting to *in vitro* studies that showed low risk of disc failure under axial rotation (Berger-Roscher et al., 2017). The single-phasic material description may also help explain the overestimated compressive stiffness predicted by our hyperelastic model, as omission of water content and osmotic response led to higher AF solid matrix stress and larger fiber deformations that stiffened the disc joint (**Figures 3B,C**). Thus, our proposed model can potentially provide valuable insights into cell mechanobiology studies, as more accurate predictions of solid matrix stress and stretch data are required in order to apply physiological loading to cells or tissues *in vitro* (Martin et al., 2014).

The predictive power of our model was further demonstrated by evaluating the multiscale disc mechanics under different loading conditions and degeneration. Single-axis loading conditions (i.e., compression-only or rotation-only) resulted in a fiber solid stress <0.3 MPa and fiber stretch between 1.03 and 1.07 for the healthy disc model, which was comparable to *in situ* subfailure fiber stretch data obtained from photogrammetry-based studies (1.07–1.11; Heuer et al., 2008a,b; Heuer et al., 2012). Taken together, our model predictions for fiber stretch and stress suggest low risks of failure under the single-axis loading conditions, especially under axial rotation, as the average AF fiber stretch did not exceed 1.10 even with degeneration, which agrees well with recent six-degree of freedom testing results (Berger-Roscher et al., 2017). In contrast, multi-axis loading increased the likelihood of damage accumulation and disc failure as axial rotation combined with compression increased the average fiber stretch to 1.10 and almost tripled the average fiber stress in the outer AF from 0.3 to 0.9 MPa, which is much closer

to the 1.0 MPa threshold reported in the literature (Skaggs et al., 1994; Holzapfel et al., 2005; Isaacs et al., 2014).

Degeneration increased the fiber stretch and fiber solid stress under all three simulated loading conditions, especially under the compression-only loading (**Figure 10**–**Case *A*** insets and **Figure 11**). Interestingly, under the combined loading, the average AF fiber stretch exceeded the 1.10 threshold for failure or significant damage accumulation (range: 1.11–1.14) but the average fiber solid stress still remained below 1.0 MPa. Taken together, these findings suggest that disc failures, especially those initiated in the AF (e.g., clefts, tears, etc.) may be strain-driven rather than stress-driven, agreeing with our previous tissue-level study (Werbner et al., 2017). Six degree of freedom testing machines provide the best approach for elucidating disc failure mechanisms *in vitro* (Costi et al., 2020). However, their high cost and complexity have limited their use. This model may provide a high-throughput approach to better understand the role of complex loading on damage accumulation and ultimate tissue failure (e.g., disc herniation).

Disc failure, especially those induced *in vitro*, have been commonly shown to occur through endplate fracture or annulus prolapse (Adams and Hutton, 1985; Wilke et al., 2016; Berger-Roscher et al., 2017). Across the three loading conditions evaluated, strain concentrations and peak fiber stresses were observed near the NP-AF-CEP interface and at the outer AF, especially in the degenerated disc (**Figure 7C**–"^"; **Figure 11**–gray solid lines). With degeneration, the CEP exhibited a volume loss post-swelling, likely caused by the compression from surrounding tissues due to differences in swelling capacities (**Figure 4C**). These results further highlight the NP-AF-CEP interface (i.e., the rim) as a weak link for disc failure. It should be noted that the flatter interface modeled between the CEP and the NP/AF was more representative of discs found in ovine, porcine, and human rather than bovine, which has a more concave CEP-NP-AF interface. Thus, it is within our expectations that our model-predicted peak stress and strain locations match well with *in vitro* failure locations observed in human and ovine discs (Adams and Hutton, 1985; Wilke et al., 2016; Berger-Roscher et al., 2017).

Although this study presents a strong validation and a robust modeling-validation framework, it is not without limitations. First, disc degeneration was simulated by only reducing tissue fixed charge density (i.e., proteoglycan content), without including any degeneration-related structural changes, such as AF lesions and decreased disc height. The omission of these structural or morphological changes might explain model predictions that contradicted previous experimental observations. For example, it has been widely accepted that degeneration results in higher disc flexibility in axial rotation, which was not predicted by our model within the simulated axial rotation range (Mimura et al., 1994; Galbusera et al., 2014). Additionally, previous experimental studies showed that annular bulging increases with degeneration and injury (Heuer et al., 2008b; Zou et al., 2009). While our model accurately predicted relative AF bulging in healthy discs (O'Connell et al., 2007b), it predicted that AF bulging decreased with degeneration (**Figure 9**–Degen vs. Healthy). Secondly, flexion/extension and lateral bending, which are important physiological loading modalities that have been shown to initiate disc failure at the CEP, were not assessed (Berger-Roscher et al., 2017). Ongoing and future work will include applying this multiscale, structure-based modeling-validation framework to human intervertebral discs to evaluate the risk of disc failure with early to moderate, or even more severe degenerative changes in tissue composition.

This study used a multiscale, structure-based modeling-validation framework to examine multiscale bovine caudal disc mechanics, including but not limited to fluid pressure, solid stress, and fiber stretch and strain. The model accurately predicted variations in disc mechanics under various loading conditions and with degeneration. Importantly, results from this study elucidated important load-bearing mechanisms and fiber-matrix interactions that are important for understanding disease progression and regeneration in intervertebral discs. In conclusion, the methods presented in this study can be used in conjunction with experimental work to simultaneously investigate disc joint-, tissue-, and subtissue-level mechanics with degeneration, disease, and injury.

DATA AVAILABILITY STATEMENT

The raw data supporting the conclusions of this article will be made available by the authors, without undue reservation.

AUTHOR CONTRIBUTIONS

MZ: conceptualization, methodology, software, validation, investigation, data collection and analysis, writing, review and editing, visualization, and project administration. SL: validation, investigation, writing, review and editing, and visualization. GDO: supervision, writing, review and editing, project administration, and funding acquisition. All authors contributed to the article and approved the submitted version.

FUNDING

The work was supported by the National Science Foundation (CAREER BMMB: 1751212).

ACKNOWLEDGMENTS

The authors thank Nicolas Newell from Imperial College London for his valuable advice. The authors also thank both Timothy P. Holsgrove from University of Exeter and Nicolas Newell for providing the permission to use the raw data collected for Newell et al. (2020).

SUPPLEMENTARY MATERIAL

The Supplementary Material for this article can be found online at: https://www.frontiersin.org/articles/10.3389/fbioe.2021.685799/full#supplementary-material

REFERENCES

Adam, C., Rouch, P., and Skalli, W. (2015). Inter-lamellar shear resistance confers compressive stiffness in the intervertebral disc: an image-based modelling study on the bovine caudal disc. *J. Biomech.* 48, 4303–4308. doi: 10.1016/j.jbiomech.2015.10.041

Adams, M. A., and Green, T. P. (1993). Tensile properties of the annulus fibrosus. *Eur. Spine J.* 2, 203–208. doi: 10.1007/bf00299447

Adams, M. A., and Hutton, W. C. (1985). Gradual disc prolapse. *Spine* 10, 524–531. doi: 10.1097/00007632-198507000-00006

Adams, M. A., and Roughley, P. J. (2006). What is intervertebral disc degeneration, and what causes it? *Spine* 31, 2151–2161. doi: 10.1097/01.brs.0000231761.73859.2c

Adams, M. A., Freeman, B. J., Morrison, H. P., Nelson, I. W., and Dolan, P. (2000). Mechanical initiation of intervertebral disc degeneration. *Spine* 25, 1625–1636. doi: 10.1097/00007632-200007010-00005

Alini, M., Eisenstein, S. M., Ito, K., Little, C., Kettler, A. A., Masuda, K., et al. (2008). Are animal models useful for studying human disc disorders/degeneration? *Eur. Spine J.* 17, 2–19. doi: 10.1007/s00586-007-0414-y

Armstrong, C. G., and Mow, V. C. (1982). Variations in the intrinsic mechanical properties of human articular cartilage with age, degeneration, and water content. *J. Bone Joint Surg. Am.* 64, 88–94. doi: 10.2106/00004623-198264010-00013

Ateshian, G. A., Chahine, N. O., Basalo, I. M., and Hung, C. T. (2004). The correspondence between equilibrium biphasic and triphasic material properties in mixture models of articular cartilage. *J. Biomech.* 37, 391–400. doi: 10.1016/s0021-9290(03)00252-5

Ateshian, G. A., Lai, W. M., Zhu, W. B., and Mow, V. C. (1994). An asymptotic solution for the contact of two biphasic cartilage layers. *J. Biomech.* 27, 1347–1360. doi: 10.1016/0021-9290(94)90044-2

Barthelemy, V. M. P., Van Rijsbergen, M. M., Wilson, W., Huyghe, J. M., Van Rietbergen, B., and Ito, K. (2016). A computational spinal motion segment model incorporating a matrix composition-based model of the intervertebral disc. *J. Mech. Behav. Biomed. Mater.* 54, 194–204. doi: 10.1016/j.jmbbm.2015.09.028

Beckstein, J. C., Sen, S., Schaer, T. P., Vresilovic, E. J., and Elliott, D. M. (2008). Comparison of animal discs used in disc research to human lumbar disc: axial compression mechanics and glycosaminoglycan content. *Spine* 33, E166–E173.

Berger-Roscher, N., Casaroli, G., Rasche, V., Villa, T., Galbusera, F., and Wilke, H. J. (2017). Influence of complex loading conditions on intervertebral disc failure. *Spine* 42, E78–E85.

Berg-Johansen, B., Han, M., Fields, A. J., Liebenberg, E. C., Lim, B. J., Larson, P. E., et al. (2018). Cartilage endplate thickness variation measured by ultrashort echo-time MRI is associated with adjacent disc degeneration. *Spine* 43, E592–E600.

Bezci, S. E., Klineberg, E. O., and O'Connell, G. D. (2018). Effects of axial compression and rotation angle on torsional mechanical properties of bovine caudal discs.ÂăJ. Mech. Behav. Biomed. Mater.Âă77, 353–359. doi: 10.1016/j.jmbbm.2017.09.022

Bezci, S. E., and O'Connell, G. D. (2018). Osmotic pressure alters time-dependent recovery behavior of the intervertebral disc. *Spine* 43, E334–E340.

Bezci, S. E., Lim, S., and O'Connell, G. D. (2020a). Nonlinear stress-dependent recovery behavior of the intervertebral disc. *J. Mech. Behav. Biomed. Mater.* 110:103881. doi: 10.1016/j.jmbbm.2020.103881

Bezci, S. E., Nandy, A., and O'Connell, G. D. (2015). Effect of hydration on healthy intervertebral disk mechanical stiffness. *J. Biomech. Eng.* 137:101007.

Bezci, S. E., Torres, K., Carraro, C., Chiavacci, D., Werbner, B., Lim, S., et al. (2020b). Transient swelling behavior of the bovine caudal disc. *J. Mech. Behav. Biomed. Mater.* 112:104089. doi: 10.1016/j.jmbbm.2020.104089

Bezci, S. E., Werbner, B., Zhou, M., Malollari, K. G., Dorlhiac, G., Carraro, C., et al. (2019). Radial variation in biochemical composition of the bovine caudal intervertebral disc. *JOR Spine* 2:e1065.

Castro, A. P. G., and Alves, J. L. (2020). Numerical implementation of an osmo-poro-visco-hyperelastic finite element solver: application to the intervertebral disc. *Comput. Methods Biomech. Biomed. Eng.* 28, 1–13. doi: 10.1080/10255842.2020.1839059

Castro, A. P. G., Paul, C. P. L., Detiger, S. E. L., Smit, T. H., Van Royen, B. J., Pimenta Claro, J. C., et al. (2014). Long-term creep behavior of the intervertebral disk: comparison between bioreactor data and numerical results. *Front. Bioeng. Biotechnol.* 2:56.

Choi, K., Kuhn, J. L., Ciarelli, M. J., and Goldstein, S. A. (1990). The elastic moduli of human subchondral, trabecular, and cortical bone tissue and the size-dependency of cortical bone modulus. *J. Biomech.* 23, 1103–1113. doi: 10.1016/0021-9290(90)90003-l

Cortes, D. H., Jacobs, N. T., DeLucca, J. F., and Elliott, D. M. (2014). Elastic, permeability and swelling properties of human intervertebral disc tissues: a benchmark for tissue engineering. *J. Biomech.* 47, 2088–2094. doi: 10.1016/j.jbiomech.2013.12.021

Costi, J. J., Ledet, E. H., and O'Connell, G. D. (2020). Spine biomechanical testing methodologies: the controversy of consensus vs scientific evidence. *JOR Spine* 4:e1138.

Demers, C. N., Antoniou, J., and Mwale, F. (2004). Value and limitations of using the bovine tail as a model for the human lumbar spine. *Spine* 29, 2793–2799. doi: 10.1097/01.brs.0000147744.74215.b0

Dreischarf, M., Zander, T., Shirazi-Adl, A., Puttlitz, C. M., Adam, C. J., Chen, C. S., et al. (2014). Comparison of eight published static finite element models of the intact lumbar spine: predictive power of models improves when combined together. *J. Biomech.* 47, 1757–1766. doi: 10.1016/j.jbiomech.2014.04.002

Eskandari, M., Nordgren, T. M., and O'Connell, G. D. (2019). Mechanics of pulmonary airways: linking structure to function through constitutive modeling, biochemistry, and histology. *Acta Biomaterialia* 97, 513–523. doi: 10.1016/j.actbio.2019.07.020

Farrell, M. D., and Riches, P. E. (2013). On the poisson's ratio of the nucleus pulposus. *J. Biomech. Eng.* 135, 104501–104504.

Fratzl, P., Misof, K., Zizak, I., Rapp, G., Amenitsch, H., and Bernstorff, S. (1998). Fibrillar structure and mechanical properties of collagen. *J. Struct. Biol.* 122, 119–122. doi: 10.1006/jsbi.1998.3966

Frauchiger, D. A., Chan, S. C., Benneker, L. M., and Gantenbein, B. (2018). Intervertebral disc damage models in organ culture: a comparison of annulus fibrosus cross-incision versus punch model under complex loading. *Eur. Spine J.* 27, 1785–1797. doi: 10.1007/s00586-018-5638-5

Galbusera, F., Schmidt, H., Neidlinger-Wilke, C., Gottschalk, A., and Wilke, H. J. (2011a). The mechanical response of the lumbar spine to different combinations of disc degenerative changes investigated using randomized poroelastic finite element models. *Eur. Spine J.* 20, 563–571. doi: 10.1007/s00586-010-1586-4

Galbusera, F., Schmidt, H., Neidlinger-Wilke, C., and Wilke, H. J. (2011b). The effect of degenerative morphological changes of the intervertebral disc on the lumbar spine biomechanics: a poroelastic finite element investigation. *Comput. Methods Biomech. Biomed. Eng.* 14, 729–739. doi: 10.1080/10255842.2010.493522

Galbusera, F., Van Rijsbergen, M., Ito, K., Huyghe, J. M., Brayda-Bruno, M., and Wilke, H. J. (2014). Ageing and degenerative changes of the intervertebral disc and their impact on spinal flexibility. *Eur. Spine J.* 23, 324–332.

Gentleman, E., Lay, A. N., Dickerson, D. A., Nauman, E. A., Livesay, G. A., and Dee, K. C. (2003). Mechanical characterization of collagen fibers and scaffolds for tissue engineering. *Biomaterials* 24, 3805–3813. doi: 10.1016/s0142-9612(03)00206-0

Goel, V. K., Monroe, B. T., Gilbertson, L. G., and Brinckmann, P. (1995a). Interlaminar shear stresses and laminae separation in a disc: finite element analysis of the L3-L4 motion segment subjected to axial compressive loads. *Spine* 20, 689–698. doi: 10.1097/00007632-199503150-00010

Goel, V. K., Ramirez, S. A., Kong, W., and Gilbertson, L. G. (1995b). Cancellous bone Young's modulus variation within the vertebral body of a ligamentous lumbar spine—application of bone adaptive remodeling concepts. *J. Biomed. Eng.* 117, 266–271. doi: 10.1115/1.2794180

Gu, W. Y., Yao, H., Vega, A. L., and Flagler, D. (2004). Diffusivity of ions in agarose gels and intervertebral disc: effect of porosity.ÂăAnn. Biomed. Eng.Âă32, 1710–1717. doi: 10.1007/s10439-004-7823-4

Heuer, F., Schmidt, H., and Wilke, H. J. (2008a). Stepwise reduction of functional spinal structures increase disc bulge and surface strains. *J. Biomech.* 41, 1953–1960. doi: 10.1016/j.jbiomech.2008.03.023

Heuer, F., Schmidt, H., and Wilke, H. J. (2008b). The relation between intervertebral disc bulging and annular fiber associated strains for simple and complex loading. *J. Biomech.* 41, 1086–1094. doi: 10.1016/j.jbiomech.2007.11.019

Heuer, F., Schmidt, H., Käfer, W., Graf, N., and Wilke, H. J. (2012). Posterior motion preserving implants evaluated by means of intervertebral disc bulging and annular fiber strains. *Clin. Biomech.* 27, 218–225. doi: 10.1016/j.clinbiomech.2011.09.004

Holzapfel, G. A., and Ogden, R. W. (2017). *Biomechanics: Trends in Modeling and Simulation*, Vol. 316. Berlin: Springer.

Holzapfel, G. A., Schulze-Bauer, C. A. J., Feigl, G., and Regitnig, P. (2005). Single lamellar mechanics of the human lumbar anulus fibrosus. *Biomech. Model. Mechanobiol.* 3, 125–140. doi: 10.1007/s10237-004-0053-8

Iatridis, J. C., MacLean, J. J., and Ryan, D. A. (2005). Mechanical damage to the intervertebral disc annulus fibrosus subjected to tensile loading. *J. Biomech.* 38, 557–565. doi: 10.1016/j.jbiomech.2004.03.038

Isaacs, J. L., Vresilovic, E., Sarkar, S., and Marcolongo, M. (2014). Role of biomolecules on annulus fibrosus micromechanics: effect of enzymatic digestion on elastic and failure properties. *J. Mech. Behav. Biomed. Mater.* 40, 75–84. doi: 10.1016/j.jmbbm.2014.08.012

Ishihara, H., McNally, D. S., Urban, J. P., and Hall, A. C. (1996). Effects of hydrostatic pressure on matrix synthesis in different regions of the intervertebral disk. *J. Appl. Physiol.* 80, 839–846. doi: 10.1152/jappl.1996.80.3.839

Kim, Y. E., Goel, V. K., Weinstein, J. N., and Lim, T. H. (1991). Effect of disc degeneration at one level on the adjacent level in axial mode. *Spine* 16, 331–335. doi: 10.1097/00007632-199103000-00013

Korecki, C. L., Costi, J. J., and Iatridis, J. C. (2008a). Needle puncture injury affects intervertebral disc mechanics and biology in an organ culture model. *Spine* 33, 235–241. doi: 10.1097/brs.0b013e3181624504

Korecki, C. L., MacLean, J. J., and Iatridis, J. C. (2008b). Dynamic compression effects on intervertebral disc mechanics and biology. *Spine* 33, 1403–1409. doi: 10.1097/brs.0b013e318175cae7

Kurowski, P., and Kubo, A. I. Z. O. H. (1986). The relationship of degeneration of the intervertebral disc to mechanical loading conditions on lumbar vertebrae. *Spine* 11, 726–731. doi: 10.1097/00007632-198609000-00012

Lai, W. M., Hou, J. S., and Mow, V. C. (1991). A triphasic theory for the swelling and deformation behaviors of articular cartilage. *J. Biomech. Eng.* 113, 245–258. doi: 10.1115/1.2894880

Li, Y., Fessel, G., Georgiadis, M., and Snedeker, J. G. (2013). Advanced glycation end-products diminish tendon collagen fiber sliding. *Matrix Biol.* 32, 169–177. doi: 10.1016/j.matbio.2013.01.003

Liu, Q., Yang, X. P., Li, K., Yang, T., Ye, J. D., and Zhang, C. Q. (2017). Internal strains of anulus fibrosus in the intervertebral disc under axial compression load. *Biomed. Res.* 8, 3483–3486.

Lüssea, S., Claassen, H., Gehrke, T., Hassenpflug, J., Schünke, M., Heller, M., et al. (2000). Evaluation of water content by spatially resolved transverse relaxation times of human articular cartilage. *Magn. Reson. Imaging* 18, 423–430. doi: 10.1016/s0730-725x(99)00144-7

Maas, S. A., Ellis, B. J., Ateshian, G. A., and Weiss, J. A. (2012). FEBio: finite elements for biomechanics. *J. Biomech. Eng.* 134:011005.

Malandrino, A., Noailly, J., and Lacroix, D. (2013). Regional annulus fibre orientations used as a tool for the calibration of lumbar intervertebral disc finite element models. *Comput. Methods Biomech. Biomed. Eng.* 16, 923–928. doi: 10.1080/10255842.2011.644539

Marchand, F. R., and Ahmed, A. M. (1990). Investigation of the laminate structure of lumbar disc anulus fibrosus. *Spine* 15, 402–410. doi: 10.1097/00007632-199005000-00011

Maroudas, A., Muir, H., and Wingham, J. (1969). The correlation of fixed negative charge with glycosaminoglycan content of human articular cartilage. *Biochimica et Biophysica Acta* 177, 492–500. doi: 10.1016/0304-4165(69)90311-0

Martin, J. T., Milby, A. H., Chiaro, J. A., Kim, D. H., Hebela, N. M., Smith, L. J., et al. (2014). Translation of an engineered nanofibrous disc-like angle-ply structure for intervertebral disc replacement in a small animal model. *Acta Biomater.* 10, 2473–2481. doi: 10.1016/j.actbio.2014.02.024

Matcher, S. J., Winlove, C. P., and Gangnus, S. V. (2004). The collagen structure of bovine intervertebral disc studied using polarization-sensitive optical coherence tomography. *Phys. Med. Biol.* 49, 1295–1306. doi: 10.1088/0031-9155/49/7/016

Michalek, A. J., and Iatridis, J. C. (2012). Height and torsional stiffness are most sensitive to annular injury in large animal intervertebral discs. *Spine J.* 12, 425–432. doi: 10.1016/j.spinee.2012.04.001

Michalek, A. J., Buckley, M. R., Bonassar, L. J., Cohen, I., and Iatridis, J. C. (2009). Measurement of local strains in intervertebral disc anulus fibrosus tissue under dynamic shear: contributions of matrix fiber orientation and elastin content. *J. Biomech.* 42, 2279–2285. doi: 10.1016/j.jbiomech.2009.06.047

Mimura, M., Panjabi, M. M., Oxland, T. R., Crisco, J. J., Yamamoto, I., and Vasavada, A. (1994). Disc degeneration affects the multidirectional flexibility of the lumbar spine. *Spine* 19, 1371–1380. doi: 10.1097/00007632-199406000-00011

Monaco, L. A., DeWitte-Orr, S. J., and Gregory, D. E. (2016). A comparison between porcine, ovine, and bovine intervertebral disc anatomy and single lamella annulus fibrosus tensile properties. *J. Morphol.* 277, 244–251. doi: 10.1002/jmor.20492

Natarajan, R. N., Williams, J. R., and Andersson, G. B. (2006). Modeling changes in intervertebral disc mechanics with degeneration. *J. Bone Joint Surg. Am.* 88(Suppl._2), 36–40. doi: 10.2106/jbjs.f.00002

Newell, N., Rivera Tapia, D., Rahman, T., Lim, S., O'Connell, G. D., and Holsgrove, T. P. (2020). Influence of testing environment and loading rate on intervertebral disc compressive mechanics: an assessment of repeatability at three different laboratories. *JOR Spine* 3:e21110.

Nguyen, A. M., Johannessen, W., Yoder, J. H., Wheaton, A. J., Vresilovic, E. J., Borthakur, A., et al. (2008). Noninvasive quantification of human nucleus pulposus pressure with use of T1ρ-weighted magnetic resonance imaging. *J. Bone Joint Surg. Am.* 90, 796–802. doi: 10.2106/jbjs.g.00667

O'Connell, G. D., Johannessen, W., Vresilovic, E. J., and Elliott, D. M. (2007a). Human internal disc strains in axial compression measured noninvasively using magnetic resonance imaging. *Spine* 32, 2860–2868. doi: 10.1097/brs.0b013e31815b75fb

O'Connell, G. D., Vresilovic, E. J., and Elliott, D. M. (2007b). Comparison of animals used in disc research to human lumbar disc geometry. *Spine* 32, 328–333. doi: 10.1097/01.brs.0000253961.40910.c1

O'Connell, G. D., Vresilovic, E. J., and Elliott, D. M. (2011). Human intervertebral disc internal strain in compression: the effect of disc region, loading position, and degeneration. *J. Orthop. Res.* 29, 547–555. doi: 10.1002/jor.21232

Oshima, H., Ishihara, H., Urban, J. P. G., and Tsuji, H. (1993). The use of coccygeal discs to study intervertebral disc metabolism. *J. Orthop. Res.* 11, 332–338. doi: 10.1002/jor.1100110304

Partanen, J. I., Partanen, L. J., and Vahteristo, K. P. (2017). Traceable thermodynamic quantities for dilute aqueous sodium chloride solutions at temperatures from (0 to 80) C. Part 1. activity coefficient, osmotic coefficient, and the quantities associated with the partial molar enthalpy. *J. Chem. Eng. Data* 62, 2617–2632. doi: 10.1021/acs.jced.7b00091

Paul, C. P., Emanuel, K. S., Kingma, I., Van Der Veen, A. J., Holewijn, R. M., Vergroesen, P. P. A., et al. (2018). Changes in intervertebral disk mechanical behavior during early degeneration. *J. Biomech. Eng.* 140:091008.

Périé, D., Korda, D., and Iatridis, J. C. (2005). Confined compression experiments on bovine nucleus pulposus and annulus fibrosus: sensitivity of the experiment in the determination of compressive modulus and hydraulic permeability. *J. Biomech.* 38, 2164–2171. doi: 10.1016/j.jbiomech.2004.10.002

Pfannkuche, J. J., Guo, W., Cui, S., Ma, J., Lang, G., Peroglio, M., et al. (2020). Intervertebral disc organ culture for the investigation of disc pathology and regeneration–benefits, limitations, and future directions of bioreactors. *Connect. Tissue Res.* 61, 304–321. doi: 10.1080/03008207.2019.1665652

Roberts, S., Menage, J., Sivan, S., and Urban, J. P. (2008). Bovine explant model of degeneration of the intervertebral disc. *BMC Musculoskelet. Disord.* 9:24.

Robinson, R. A., and Stokes, R. H. (1949). Tables of osmotic and activity coefficients of electrolytes in aqueous solution at 25 C. *Trans. Faraday Soc.* 45, 612–624. doi: 10.1039/tf9494500612

Rohlmann, A., Zander, T., Schmidt, H., Wilke, H. J., and Bergmann, G. (2006). Analysis of the influence of disc degeneration on the mechanical behaviour of a lumbar motion segment using the finite element method. *J. Biomech.* 39, 2484–2490. doi: 10.1016/j.jbiomech.2005.07.026

Sato, K., Kikuchi, S., and Yonezawa, T. (1999). In vivo intradiscal pressure measurement in healthy individuals and in patients with ongoing back problems. *Spine* 24, 2468–2474. doi: 10.1097/00007632-199912010-00008

Schmidt, H., Galbusera, F., Rohlmann, A., and Shirazi-Adl, S. A. (2013). What have we learned from finite element model studies of lumbar intervertebral discs in the past four decades? *J. Biomech.* 46, 2342–2355. doi: 10.1016/j.jbiomech.2013.07.014

Schmidt, H., Heuer, F., Drumm, J., Klezl, Z., Claes, L., and Wilke, H. J. (2007a). Application of a calibration method provides more realistic results for a finite element model of a lumbar spinal segment. *Clin. Biomech.* 22, 377–384. doi: 10.1016/j.clinbiomech.2006.11.008

Schmidt, H., Heuer, F., Simon, U., Kettler, A., Rohlmann, A., Claes, L., et al. (2006). Application of a new calibration method for a three-dimensional finite element model of a human lumbar annulus fibrosus. *Clin. Biomech.* 21, 337–344. doi: 10.1016/j.clinbiomech.2005.12.001

Schmidt, H., Kettler, A., Heuer, F., Simon, U., Claes, L., and Wilke, H. J. (2007b). Intradiscal pressure, shear strain, and fiber strain in the intervertebral disc under combined loading. *Spine* 32, 748–755. doi: 10.1097/01.brs.0000259059.90430.c2

Schollum, M. L., Robertson, P. A., and Broom, N. D. (2010). How age influences unravelling morphology of annular lamellae–a study of interfibre cohesivity in the lumbar disc. *J. Anat.* 216, 310–319. doi: 10.1111/j.1469-7580.2009.01197.x

Shah, J. S., Hampson, W. G., and Jayson, M. I. (1978). The distribution of surface strain in the cadaveric lumbar spine. *J. Bone Joint Surg. Br.* 60, 246–251. doi: 10.1302/0301-620x.60b2.659474

Shapiro, E. M., Borthakur, A., Gougoutas, A., and Reddy, R. (2002). 23Na MRI accurately measures fixed charge density in articular cartilage. *Magn. Reson. Med.* 47, 284–291. doi: 10.1002/mrm.10054

Shen, Z. L., Dodge, M. R., Kahn, H., Ballarini, R., and Eppell, S. J. (2008). Stress-strain experiments on individual collagen fibrils. *Biophys. J.* 95, 3956–3963. doi: 10.1529/biophysj.107.124602

Shirazi-Adl, A. (1992). Finite-element simulation of changes in the fluid content of human lumbar discs. mechanical and clinical implications. *Spine* 17, 206–212. doi: 10.1097/00007632-199202000-00015

Shirazi-Adl, S. A., Shrivastava, S. C., and Ahmed, A. M. (1984). Stress analysis of the lumbar disc-body unit in compression. a three-dimensional nonlinear finite element study. *Spine* 9, 120–134. doi: 10.1097/00007632-198403000-00003

Showalter, B. L., Beckstein, J. C., Martin, J. T., Beattie, E. E., Orías, A. A. E., Schaer, T. P., et al. (2012). Comparison of animal discs used in disc research to human lumbar disc: torsion mechanics and collagen content. *Spine* 37, E900–E907.

Skaggs, D. L., Weidenbaum, M., Iatridis, J. C., Ratcliffe, A., and Mow, V. C. (1994). Regional variation in tensile properties and biochemical composition of the human lumbar anulus fibrosus. *Spine* 19, 1310–1319. doi: 10.1097/00007632-199406000-00002

Spera, D., Genovese, K., and Voloshin, A. (2011). Application of stereo-digital image correlation to full-field 3-D deformation measurement of intervertebral disc. *Strain* 47, e572–e587.

Steffen, T., Baramki, H. G., Rubin, R., Antoniou, J., and Aebi, M. (1998). Lumbar intradiscal pressure measured in the anterior and posterolateral annular regions during asymmetrical loading. *Clin. Biomech.* 13, 495–505. doi: 10.1016/s0268-0033(98)00039-4

Stokes, I. A. (1987). Surface strain on human intervertebral discs. *J. Orthop. Res.* 5, 348–355. doi: 10.1002/jor.1100050306

Svensson, R. B., Smith, S. T., Moyer, P. J., and Magnusson, S. P. (2018). Effects of maturation and advanced glycation on tensile mechanics of collagen fibrils from rat tail and Achilles tendons. *Acta Biomaterialia* 70, 270–280. doi: 10.1016/j.actbio.2018.02.005

Urban, J. P. G., and Maroudas, A. (1979). The measurement of fixed charged density in the intervertebral disc. *Biochimica et Biophysica Acta* 586, 166–178. doi: 10.1016/0304-4165(79)90415-x

Urban, J. P., and McMullin, J. F. (1988). Swelling pressure of the lumbar intervertebral discs: influence of age, spinal level, composition, and degeneration. *Spine* 13, 179–187. doi: 10.1097/00007632-198802000-00009

van der Rijt, J. A., Van Der Werf, K. O., Bennink, M. L., Dijkstra, P. J., and Feijen, J. (2006). Micromechanical testing of individual collagen fibrils. *Macromol. Biosci.* 6, 697–702. doi: 10.1002/mabi.200600063

van Rijsbergen, M., van Rietbergen, B., Barthelemy, V., Eltes, P., Lazáry, Á, Lacroix, D., et al. (2018). Comparison of patient-specific computational models vs. clinical follow-up, for adjacent segment disc degeneration and bone remodelling after spinal fusion. *PloS One* 13:e0200899. doi: 10.1371/journal.pone.0200899

Vergari, C., Chan, D., Clarke, A., Mansfield, J. C., Meakin, J. R., and Winlove, P. C. (2017). Bovine and degenerated human annulus fibrosus: a microstructural and micromechanical comparison. *Biomech. Model. Mechanobiol.* 16, 1475–1484. doi: 10.1007/s10237-017-0900-z

Vernon-Roberts, B., Moore, R. J., and Fraser, R. D. (2007). The natural history of age-related disc degeneration: the pathology and sequelae of tears. *Spine* 32, 2797–2804. doi: 10.1097/brs.0b013e31815b64d2

Walter, B. A., Korecki, C. L., Purmessur, D., Roughley, P. J., Michalek, A. J., and Iatridis, J. C. (2011). Complex loading affects intervertebral disc mechanics and biology. *Osteoarthr. Cartil.* 19, 1011–1018. doi: 10.1016/j.joca.2011.04.005

Wang, S., Xia, Q., Passias, P., Wood, K., and Li, G. (2009). Measurement of geometric deformation of lumbar intervertebral discs under in-vivo weightbearing condition. *J. Biomech.* 42, 705–711. doi: 10.1016/j.jbiomech.2009.01.004

Werbner, B., Spack, K., and O'Connell, G. D. (2019). Bovine annulus fibrosus hydration affects rate-dependent failure mechanics in tension. *J. Biomech.* 89, 34–39. doi: 10.1016/j.jbiomech.2019.04.008

Werbner, B., Zhou, M., and O'Connell, G. D. (2017). A novel method for repeatable failure testing of annulus fibrosus. *J. Biomech. Eng.* 139:111001.

Wilke, H. J., Kienle, A., Maile, S., Rasche, V., and Berger-Roscher, N. (2016). A new dynamic six degrees of freedom disc-loading simulator allows to provoke disc damage and herniation. *Eur. Spine J.* 25, 1363–1372. doi: 10.1007/s00586-016-4416-5

Wilke, H. J., Neef, P., Caimi, M., Hoogland, T., and Claes, L. E. (1999). New in vivo measurements of pressures in the intervertebral disc in daily life. *Spine* 24, 755–762. doi: 10.1097/00007632-199904150-00005

Wilson, W., Huyghe, J. M., and Van Donkelaar, C. C. (2007). Depth-dependent compressive equilibrium properties of articular cartilage explained by its composition. *Biomech. Model. Mechanobiol.* 6, 43–53. doi: 10.1007/s10237-006-0044-z

Wognum, S., Huyghe, J. M., and Baaijens, F. P. (2006). Influence of osmotic pressure changes on the opening of existing cracks in 2 intervertebral disc models. *Spine* 31, 1783–1788. doi: 10.1097/01.brs.0000227267.42924.bb

Wu, Y., Cisewski, S. E., Sachs, B. L., Pellegrini, V. D., Kern, M. J., Slate, E. H., et al. (2015). The region-dependent biomechanical and biochemical properties of bovine cartilaginous endplate. *J. Biomech.* 48, 3185–3191. doi: 10.1016/j.jbiomech.2015.07.005

Wuertz, K., Urban, J. P. G., Klasen, J., Ignatius, A., Wilke, H. J., Claes, L., et al. (2007). Influence of extracellular osmolarity and mechanical stimulation on gene expression of intervertebral disc cells. *J. Orthop. Res.* 25, 1513–1522. doi: 10.1002/jor.20436

Yang, B., and O'Connell, G. D. (2019). Intervertebral disc swelling maintains strain homeostasis throughout the annulus fibrosus: a finite element analysis of healthy and degenerated discs. *Acta Biomaterialia* 100, 61–74. doi: 10.1016/j.actbio.2019.09.035

Yin, L., and Elliott, D. M. (2005). A homogenization model of the annulus fibrosus. *J. Biomech.* 38, 1674–1684. doi: 10.1016/j.jbiomech.2004.07.017

Yu, J., Peter, C., Roberts, S., and Urban, J. P. (2002). Elastic fibre organization in the intervertebral discs of the bovine tail. *J. Anat.* 201, 465–475. doi: 10.1046/j.1469-7580.2002.00111.x

Yu, J., Tirlapur, U., Fairbank, J., Handford, P., Roberts, S., Winlove, C. P., et al. (2007). Microfibrils, elastin fibres and collagen fibres in the human intervertebral disc and bovine tail disc. *J. Anat.* 210, 460–471. doi: 10.1111/j.1469-7580.2007.00707.x

Zhou, M., Bezci, S. E., and O'Connell, G. D. (2020a). Multiscale composite model of fiber-reinforced tissues with direct representation of sub-tissue properties. *Biomech. Model Mechanobiol.* 19, 745–759. doi: 10.1007/s10237-019-01246-x

Zhou, M., Werbner, B., and O'Connell, G. D. (2020b). Fiber engagement accounts for geometry-dependent annulus fibrosus mechanics: a multiscale, Structure-Based Finite Element Study. *J. Mech. Behav. Biomed. Mater.* 115:104292. doi: 10.1016/j.jmbbm.2020.104292

Zhou, M., Werbner, B., and O'Connell, G. D. (2020c). Historical review on combined experimental and computational approaches for investigating annulus fibrosus mechanics. *J. Biomech. Eng.* 142:030802.

Zou, J., Yang, H., Miyazaki, M., Morishita, Y., Wei, F., McGovern, S., et al. (2009). Dynamic bulging of intervertebral discs in the degenerative lumbar spine. *Spine* 34, 2545–2550. doi: 10.1097/brs.0b013e3181b32998

Conflict of Interest: The authors declare that the research was conducted in the absence of any commercial or financial relationships that could be construed as a potential conflict of interest.

frontiers in Bioengineering and Biotechnology

ORIGINAL RESEARCH
published: 09 June 2021
doi: 10.3389/fbioe.2021.676003

Quantitative MRI to Characterize the Nucleus Pulposus Morphological and Biomechanical Variation According to Sagittal Bending Load and Radial Fissure, an *ex vivo* Ovine Specimen Proof-of-Concept Study

Jean-Philippe Deneuville[1,2], Maksym Yushchenko[3], Tanguy Vendeuvre[1,2,4], Arnaud Germaneau[2], Maxime Billot[1], Manuel Roulaud[1], Mathieu Sarracanie[3], Najat Salameh[3] and Philippe Rigoard[1,2,4]*

[1] PRISMATICS Lab (Predictive Research in Spine/Neuromodulation Management and Thoracic Innovation/Cardiac Surgery), Poitiers University Hospital, Poitiers, France, [2] Institut Pprime UPR 3346, CNRS – Université de Poitiers – ISAE-ENSMA, Poitiers, France, [3] Department of Biomedical Engineering, Center for Adaptable MRI Technology (AMT Center), University of Basel, Allschwil, Switzerland, [4] Department of Spine, Neuromodulation and Rehabilitation, Poitiers University Hospital, Poitiers, France

OPEN ACCESS

Edited by:
Marwan El-Rich,
Khalifa University, United Arab Emirates

Reviewed by:
Maxim Bashkuev,
Charité Medical University of Berlin, Germany
Mohammad Nikkhoo,
Islamic Azad University, Iran

***Correspondence:**
Arnaud Germaneau
arnaud.germaneau@univ-poitiers.fr

Specialty section:
This article was submitted to Biomechanics, a section of the journal Frontiers in Bioengineering and Biotechnology

Received: 04 March 2021
Accepted: 18 May 2021
Published: 09 June 2021

Citation:
Deneuville J-P, Yushchenko M, Vendeuvre T, Germaneau A, Billot M, Roulaud M, Sarracanie M, Salameh N and Rigoard P (2021) Quantitative MRI to Characterize the Nucleus Pulposus Morphological and Biomechanical Variation According to Sagittal Bending Load and Radial Fissure, an ex vivo Ovine Specimen Proof-of-Concept Study. Front. Bioeng. Biotechnol. 9:676003. doi: 10.3389/fbioe.2021.676003

Background and context: Low back pain is a dramatic burden worldwide. Discography studies have shown that 39% of chronic low back pain patients suffer from discogenic pain due to a radial fissure of intervertebral disc. This can have major implications in clinical therapeutic choices. The use of discography is restricted because of its invasiveness and interest in it remains low as it represents a static condition of the disc morphology. Magnetic Resonance Imaging (MRI) appears to be less invasive but does not describe the biomechanical dynamic behavior of the fissure.

Purpose: We aimed to seek a quantitative MRI protocol combined with *ex vivo* sagittal loading to analyze the morphological and biomechanical changes of the intervertebral disc structure and stress distribution.

Study design: Proof of concept.

Methods: We designed a proof-of-concept ovine study including 3 different 3.0 T-MRI sequences (T_2-weighted, T_1 and T_2 mapping). We analyzed 3 different mechanical states (neutral, flexion and extension) on a fresh ovine spine specimen to characterize an intervertebral disc before and after puncturing the anterior part of the annulus fibrosus. We used a mark tracking method to calculate the bending angles and the axial displacements of the discal structures. In parallel, we created a finite element model to calculate the variation of the axial stress and the maximal intensity shear stress, extrapolated from our experimental boundary conditions.

Results: Thanks to an original combination of specific nuclear relaxation time quantifications (T_1, T_2) of the discal tissue, we characterized the nucleus movement/deformation into the fissure according to the synchronous mechanical load. This revealed a link between disc abnormality and spine segment range of motion capability. Our finite element model highlighted significant variations within the stress distribution between intact and damaged disc.

Conclusion: Quantitative MRI appears to provide a new opportunity to characterize intra-discal structural morphology, lesions and stress changes under the influence of mechanical load. This preliminary work could have substantial implications for non-invasive disc exploration and could help to validate novel therapies for disc treatment.

Keywords: intervertebral disc, nucleus biomechanics, quantitative MRI, low back pain, disc degeneration, radial fissure, mechanical diagnosis and therapy

INTRODUCTION

Low back pain is the leading cause of disability worldwide (Vos et al., 2016) and represents a dramatic economic burden for western countries (Maetzel and Li, 2002; Walker et al., 2003; Dagenais et al., 2008). Back pain is frequently associated with intervertebral disc degeneration, defined as "an aberrant, cell-mediated response to progressive structural failure" (Adams and Roughley, 2006). Several pathways can lead to disc degeneration (Adams and Dolan, 2012). One of them, starts from a centrifugal (from center to periphery) and radial fissure of the annulus which alters disc stress distribution (McNally et al., 1996) and creating a stress gradient between the posterior annulus and the nucleus pulposus (Stefanakis et al., 2014). These mechanical changes can modify the cellular activities leading to dysregulation of the TIMP/MMP expression (TIMP for Tissue Inhibitor of Metallo-Proteinase and MMP for Matrix Metallo-Proteinase) (Le Maitre et al., 2004, 2007). This, in turn, leads to the acceleration of the normal ageing nucleus dehydration (Antoniou et al., 1996). Such modifications can stimulate the nociceptors naturally present in the outer third of the annulus (García-Cosamalón et al., 2010) or those which proliferate alongside the fissure (Coppes et al., 1990, 1997; Lama et al., 2018). All of these phenomena define one structural substrate of discogenic backpain.

Aiming to reverse the pathological status of the disc, multiple treatment options are available, ranging from conservative management to interventional therapies. Robust concepts supporting physiotherapy and manual therapies base their intervention on the presence of a directional preference (McKenzie, 1981; McKenzie and May, 2003; Laslett et al., 2005), which implies a dynamic disc theory. From a clinical perspective, directional preference is a direction of movement alleviating patient pain, while the other directions have no effect or worsen the pain. When observed on a patient with back pain, this type of clinical sign is specific (94%) to discogenic pain (Laslett et al., 2005) and appears to function as an effective guide for treatment (May and Aina, 2012; May et al., 2018). In addition to disc surgery, which is limited to refractory patients, interventional therapies include chemonucleolysis using chymopapain (Javid et al., 1983) – historically the first intradiscal injected drug – collagenase, chondroitinase (Ishibashi et al., 2019), ozone (Paradiso and Alexandre, 2005), radiopaque gelled ethanol (Hashemi et al., 2020), and thermocoagulation (Freeman, 2006). Other novel intradiscal therapies, such as neurotrophic growth factor (Knezevic et al., 2017), platelet-rich plasma (Li et al., 2017) and stem cell (Meisel et al., 2019) appear promising but require further and large-scale validation. Treatment indication can be outlined by correlating a clinical phenotype to a specific morphological disc profile. However, this task becomes extremely challenging when a degenerative process occurs among pain-free and healthy subjects (Brinjikji et al., 2015).

As adequate treatment requires precise diagnostics and as the standard MRI fails, one has to fall back to discography. This procedure has historically been accepted as the reference standard imaging procedure for the diagnosis of discogenic pain. By injecting a contrast agent into the central nucleus, this procedure triggers a mechanical distension of the inner annulus, reproducing the concordant patient pain (Bogduk et al., 2013). By assessing the spreading of the contrast agent with an X-Ray or a CT-scan, the clinician can identify a centrifugal nucleus radial fissure. Discography studies have demonstrated that 39% of patients with chronic low back pain present discogenic pain associated with an annular radial fissure at the level of the injured disc (Manchikanti et al., 2018). The extent of the fissure can be graded using the Dallas classification (Sachs et al., 1987). Furthermore, patient pain has been shown to be proportional to the extent of the fissure toward the periphery (Vanharanta et al., 1987; Moneta et al., 1994). However, since discography is performed on patients in prone position, it enables the physician to analyze only a static aspect of the annular fissure. It provides no information about the potential mobility of the nucleus and the dynamic evolution of the fissure. Although this procedure has been modified to avoid any degenerative process (Bogduk, 2013; McCormick et al., 2019), some studies still show that discography could provide negative side-effects (Carragee et al., 2009). Because of these definitive disadvantages, its use has been restricted to a few highly specific conditions, and substantial efforts are being placed in the development of non-invasive markers (Aprill and Bogduk, 1992).

In recent years, Thompson et al. (2009) described the connection between positive discographies on more than 2400 discs and signal intensity alterations observed via Magnetic Resonance Imaging (MRI) on T_1- and T_2-weighted scans, corresponding to inflammation of the vertebral endplate, named "MODIC sign" (Modic et al., 1984). Such signs are associated with patient pain (Thompson et al., 2009) and translate as a non-traumatic way of diagnosing discogenic backpain. However, MODIC signs describe only the inflammatory state of the endplates, and not the morphology or the dynamic behavior of the disc itself. The Pfirrmann classification is another way to describe degenerative lumbar disc (Pfirrmann et al., 2001). This classification encompasses a multi-parameter description of the disc on T_2-weighted MR images (disc height, signal intensity, etc.) allowing a grading system of the degenerative process. Several studies validate the correlation between MRI findings and histochemical composition of the intervertebral disc (Tertti et al., 1991; Benneker et al., 2005). However, none of these parameters take into account the dynamic behavior of the disc. While MRI seemed less accurate than discography to detect radial fissure (Osti and Fraser, 1992), other works suggest that successful detection is possible via MRI (Yu et al., 1988; Saifuddin et al., 1998). A specific relationship was found between radial fissure and positive discography (Aprill and Bogduk, 1992) by delineating a high intensity zone (HIZ) in the annulus fibrosus (AF), as the latter appears hyperintense compared to the nucleus pulposus (NP) on T_2-weighted MR images. However, as HIZ is frequent among pain-free subjects, controversy exists and still persists (Khan et al., 2014).

Contrarily to qualitative T_1- and T_2-weighted MRI, where the signal intensity interpretation can be affected by several experimental factors, biased perception, or scanner variability, quantitative MRI provides an absolute, objective and lower-variability characterization of the imaged anatomical structures. In intervertebral discs, typically quantified parameters are the T_1, T_2, or $T_{1\rho}$ relaxation times, magnetization transfer (MT) ratio, and the apparent diffusion coefficient (ADC). These parameters can potentially be used as non-invasive biomarkers for different degeneration stages since they are related to the disc histochemical composition and condition, such as for example water, proteoglycan, or collagen content, matrix integrity, loading or aging (Tertti et al., 1991; Watanabe et al., 2007; Mwale et al., 2008; Menezes-Reis et al., 2015; Hwang et al., 2016; Galley et al., 2017; Paul et al., 2018; Enokida et al., 2020). In general, mapping the relaxation time constants provides the advantage of more accurate and reproducible differentiation between the disc tissues of NP and AF and reduced segmentation variability.

To our knowledge, there is no reference available in the literature regarding MRI capability of detecting annulus fissures and characterizing their biomechanical and morphological variations as a function of bending load. We hypothesized that we could non-invasively identify an annular radial fissure and analyze the dynamic behavior of the NP migration by using optimized T_1 and T_2 mapping protocols to assess and quantify the degree of disc fissuring, along with the degree of nucleus displacement/deformation through the fissure, depending on the spine position.

We present here the first results of an *ex vivo* study. Quantitative and anatomical MRI scans were performed on a loaded fresh lamb spine specimen under 3 different mechanical states (neutral, flexion, extension) in both intact and damaged conditions (anterior radial fissure for the purpose of this Proof-Of-Concept study). Our first objective was to assess whether our MRI protocol allows to detect and further characterize a radial fissure within the annulus. Our second objective was to determine the deformation/displacement fields induced in the nucleus pulposus based on the imposed bending angle of flexion/extension, in both intact and damaged conditions. Our third and last objective was to elaborate a simplified finite element model from the actual geometry and boundary conditions in order to study the contribution of the radial fissure onto the stress distribution in the nucleus.

MATERIALS AND METHODS

Specimen

We used a fresh lamb spine specimen, comprising 3 vertebrae (L1-L3) and 2 intervertebral discs (2 functional units) of the upper lumbar spine (lamb fillet). The specimen was kept at 4^{circ}C the night before the experiment. Two functional units were kept, such that a healthy control disc could be used at all times for comparison (e.g., in case of aberrant findings).

With the exception of ligamentous and articular capsule tissue, all soft tissue was otherwise removed. In the vertebral body of the 1st and 3rd vertebra, we inserted 2 MR compatible sticks of length L = 8 cm, and diameter Ø = 6 mm. We kept the specimen hydrated at all times by wrapping it inside saline soaked gauze (Wilke et al., 1998b).

An hour and a half prior to the experiment (Adams, 1995), to avoid over-hydration (McMillan et al., 1996), we creep-loaded the specimen using an axial compressive load of 60 N, resulting in stress of 0.03 MPa. The load was applied by an elastic compressive system, which we set on the transverse vertebral process of the 1st and 3rd vertebra. To simulate an apparent compressive load resulting from muscle activity and gravity (Callaghan et al., 1998), the compressive elastic system was maintained throughout the experiment (**Figure 1A**).

First, the specimen was imaged under several mechanical states with intact discs (see below). Secondly, we punctured the anterior part of the annulus using a lumbar puncture needle (18G – 1.2 mm diameter) to damage the disc. The resulting fissure represented 54% of the total height and 27% of the disc transversal diameter. We chose to damage the anterior part of the disc from its inherently easier access in comparison with the posterior part to have a perfectly reproducible lesion model. Besides, similar types of fissure have been documented using discography (Saifuddin et al., 1998) or cadaveric studies (Yu et al., 1988).

MRI Acquisitions

All images were acquired using a 3.0-Tesla imager (Siemens Healthineers, Erlangen, Germany). Room temperature was kept

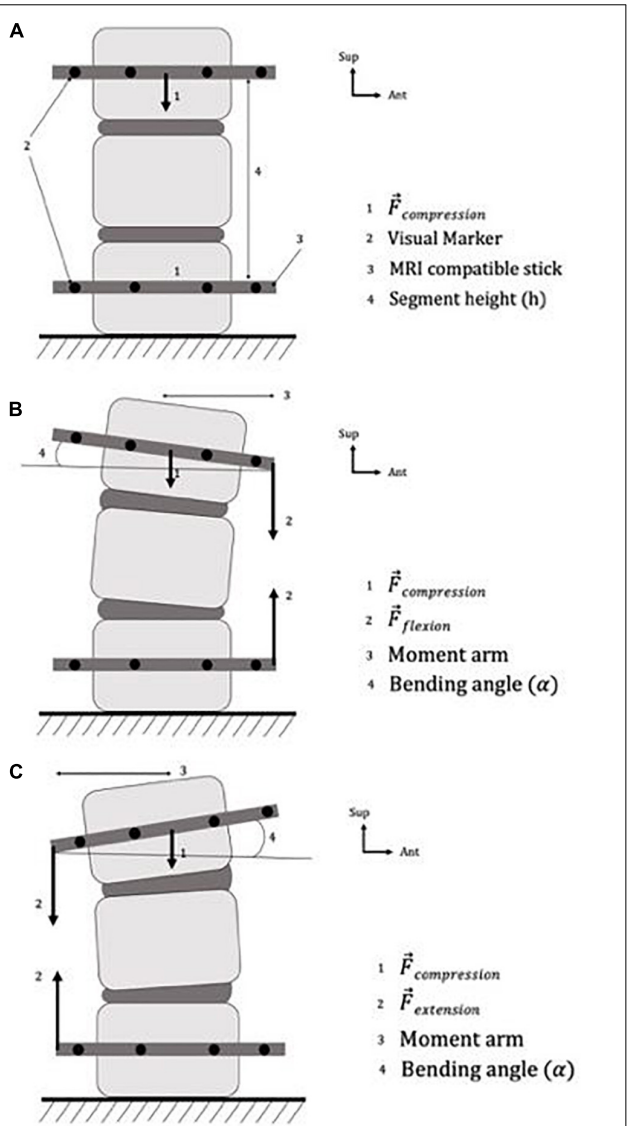

FIGURE 1 | Specimen preparation and boundary conditions of the specimen, in panels **(A)** neutral position, **(B)** flexion position, **(C)** extension position.

constant at 24°C during the entire examination, and three different MR sequences were performed:

(1) Anatomical images were acquired using a multi-slice 2D T_2-weighted Turbo Spin Echo (T_2-w TSE) sequence with fat suppression, number of averages NA = 10, echo time TE = 99 ms, repetition time TR = 3800 ms, and echo train length = 21. A total of 16 axial slices with resolution 0.31 0.31 1 mm^3, and in-plane field of view (FOV) of 84 100 mm^2 covering the disk and part of the adjacent vertebrae were obtained in 21 min 41 s.

(2) T_2 mapping was performed using a multi-echo Spin Echo sequence with TR = 4500 ms, and NA = 1. An echo train of 32 with first echo at 30 ms and echo spacing of 30 ms was used. A single transverse slice with in-plane resolution of 0.52 0.52 mm^2 (FOV = 84 99 mm^2) and slice thickness of 2 mm was acquired in 12 min.

(3) T_1 mapping was obtained from multiple Inversion Recovery (IR) Turbo-Spin-Echo sequences with TE/TR = 14/6000 ms, NA = 1, and inversion times of 30, 60, 130, 300, 600, 1300, 3000, 5800 ms. All 8 acquisitions were performed across a single transverse slice of resolution 0.52 0.52 mm^2, with corresponding FOV = 84 99 mm^2 and slice thickness of 2 mm, acquired in 18 min.

We used the same imaging protocol for each mechanical state of the specimen, resulting in a total of 18 scans. Axial slice orientation was chosen to provide a better visualization and a more appropriate modeling of the NP, the AF and its fissure within the disc with respect to the sagittal view.

Image Processing

Images were processed using in-house scripts and functions developed with MATLAB (MathWorks, Natick, MA, United States). T_1 and T_2 maps were obtained after normalizing the data and fitting them pixel-wise using either an exponential build-up (S_1) or decay (S_2) model:

$$S_1 = a \cdot (1 - 2 \cdot e^{t/T_1})$$

$$S_2 = b \cdot e^{-t/T_2}$$

With S_i the normalized signal intensity in arbitrary units, t the time obtained from the echo train or inversion times, and a/b constants of the fitting models. Relaxation times are tied to the magnetic properties of the different tissue species and are expected to vary significantly between the different disc compartments.

Mechanical Loading

We controlled the boundary conditions by fixing the lower vertebra and using rubber bands in different configurations depending on the various elastic systems targeted. The first rubber band applied axial compressive loading (as described above), and the second one applied bending loading (either in extension or in flexion). We used this elastic loading system to modify the position of the specimen in the sagittal plane: flexion was created by applying a bending load on the anterior part of the sticks (**Figure 1B**) and extension on the posterior part (**Figure 1C**). Our loading protocol is described in **Table 1**.

Measurements

We used a mark tracking system to calculate the bending angle and the axial displacement (**Figure 1A**). In particular, we placed visible marks on the sticks and on the vertebra specimens, and measured their respective positions relative to each other before and during each loading step (Germaneau et al., 2016).

We calculated the bending angle using the following process:

- We determined the baseline angle made by the upper MRI-compatible sticks and the horizontal one (α_0) from the specimen in neutral loading.

TABLE 1 | Mechanical states and the corresponding estimated boundary conditions of the specimen.

Step	Mechanical loading state	Axial compression (N)	Bending force (N)	Bending moment (N.m)
0	Neutral	0	0	0
1	Neutral (**Figure 1A**)	59.7	0	0
2	Flexion (**Figure 1B**)	59.7	81.1	2.1
3	Extension (**Figure 1C**)	59.7	80.9	2.8
Fissure				
4	Extension (**Figure 1C**)	59.7	80.5	2.8
5	Flexion (**Figure 1B**)	59.7	81.0	2.1
6	Neutral (**Figure 1A**)	59.7	0	0

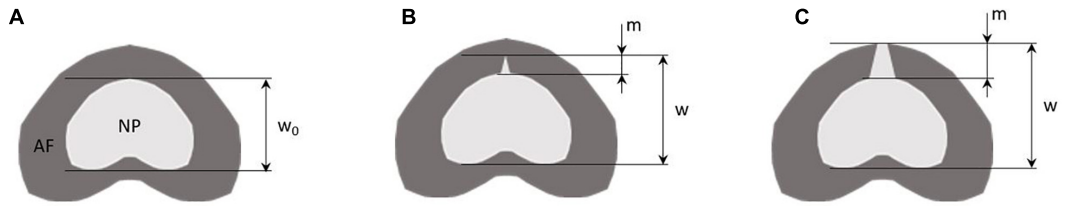

FIGURE 2 | Method to calculate the nucleus sagittal boundary displacement (w), the degree of nucleus pulposus (NP) migration (m) within the annulus fibrosus (AF), and the nucleus sagittal strain for each mechanical step. Panel **(A)** is the reference mechanical loading state, i.e., step 1, panel **(B)** is a mechanical state with partial migration of the annulus m < 50% of the total annulus thickness, panel **(C)** is a mechanical state at total migration of the annulus m > 50% of the total annulus thickness. Nucleus sagittal boundary displacement is calculated for each mechanical state by $w - w_0$. Nucleus sagittal strain is calculated for each mechanical state by $(w - w_0)/w_0$. Migration m is calculated from the proportion of nucleus displacement within the annulus.

- The same measurement was repeated with the bending loading, i.e., flexion or extension (α).
- We subtracted α_0 to α and obtained the corresponding bending angle. A negative value represents a flexion, and a positive value an extension.

We calculated the axial strain from the following process:

- In resting state, we determined the overall height of the vertebral specimen by measuring the distance between the two upper parts of the MRI-compatible sticks (h_0).
- The same measurement was repeated with mechanical loading (h).
- We computed the axial strain as the variation of h relative to the baseline value h_0 at resting state. A negative value represents a height reduction (i.e., a compression) and positive value a height increase.

We compared bending angles and strain values after each loading step. We evaluated the measurement uncertainty (from measurement repetition on known imposed values) at 0.1% for axial strain and 0.1° for angle variation (Germaneau et al., 2016).

Furthermore, we measured nucleus displacement and inferred its strain in the sagittal direction from the T_1 maps. Displacement on sagittal disk boundaries was calculated as the relative difference in distance between the nucleus boundaries at the reference mechanical state (step 1) and the studied state (e.g., step 3, **Figure 2**).

Total sagittal nucleus displacement was computed as the relative difference between the distances of the nucleus and spinal cord centroids at the reference state (step 1) and each studied step (e.g., step 4). To determine the position of each centroid, we segmented and isolated the nucleus pulposus and the spinal canal from the T_1 maps (**Figure 3**). The spinal cord is a fixed and identifiable structure that provides a good reference for the centroid tracking process. Nucleus displacement was obtained with an uncertainty of 0.05 mm.

We inferred the nucleus sagittal strain according to:

$$\varepsilon = (w - w0)/w0$$

where w0 is the distance between anterior and posterior nucleus boundaries at step 1 (**Figure 2A**, reference state), and w is the distance between anterior and posterior nucleus boundaries at the investigated steps (**Figures 2B,C**).

We further evaluated the degree of migration of the nucleus in the fissure during the different mechanical loading steps. This migration was calculated as the ratio between the displacement of the nucleus in the fissure, and the annulus thickness (**Figure 2**).

Finite Element Model

A finite element (FE) model was developed to perform a stress analysis from a simplified geometry extracted using MRI. Our aim was to use this specific FE model from the actual geometry and the actual boundary conditions in order to calculate the stress distribution in the nucleus and the contribution of the radial fissure. FE analysis was carried out using SolidWorks software (Dassault Systèmes Corporation, Waltham, MA, United States). The geometry of the model was defined using points extracted from the boundary of the annulus and nucleus segmented based on a threshold on the MR images acquired in the intact and fissured states (**Figure 4**). For this stress analysis, homogeneous

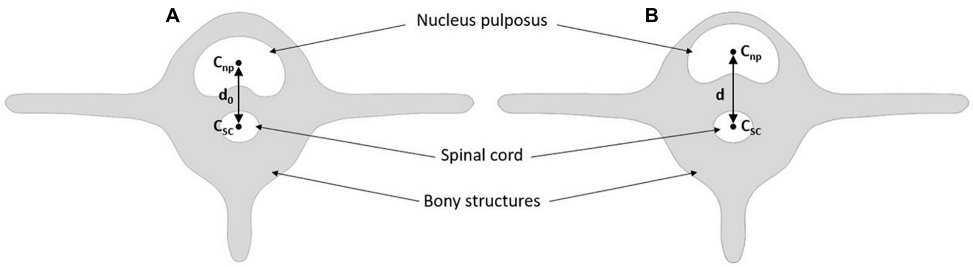

FIGURE 3 | Method to calculate global nucleus sagittal displacement. Panel **(A)** is the reference mechanical loading state, i.e., step 1. Panel **(B)** is the studied mechanical state, i.e., step 2 to 6 (**Table 1**). C_{np} is the centroid of the nucleus pulpous; C_{sc} is the centroid of the spinal cord; d_0 is the reference distance; d is the distance of the studied mechanical state.

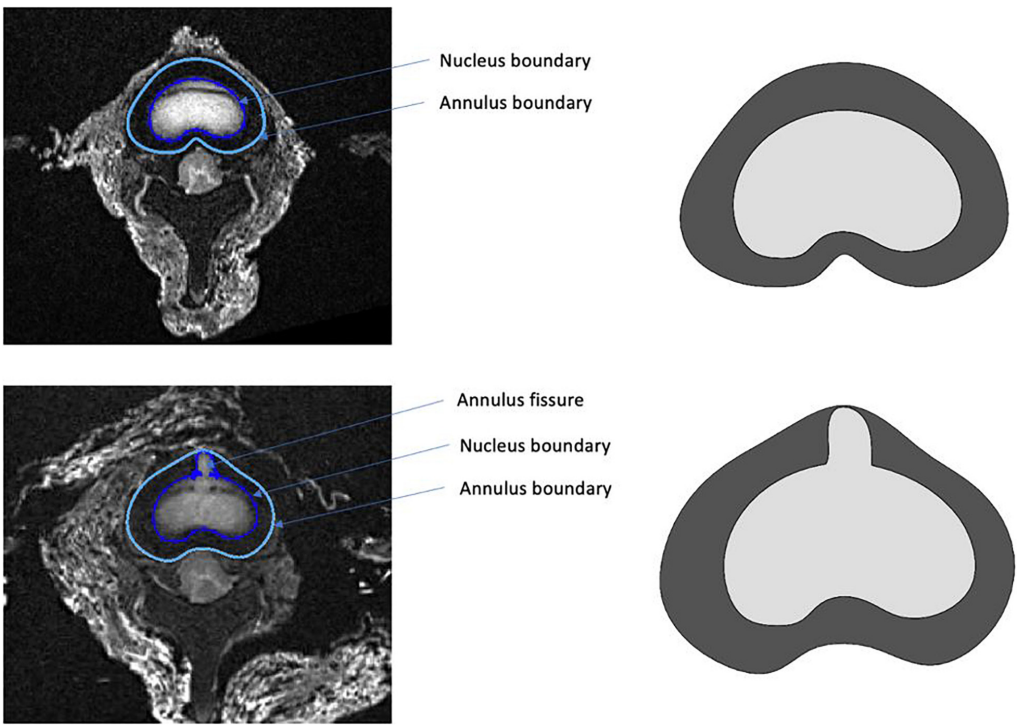

FIGURE 4 | Example of segmentation performed in the intact (top) and fissured (bottom) states, used as input for the finite element model.

behavior was considered to model materials (Shin et al., 2007), of which the properties are specified in **Table 2**.

The boundary conditions applied to the endplates of the FE model corresponded to the loading imposed during experiments to create bending moments. For that operation, moment was applied on the upper plate of the disk and displacement was considered null on the inferior plate. From there, axial stress and intensity of shear stress induced in the nucleus could be obtained.

RESULTS

MR Imaging Results

Examples of T_2-weighted images, T_1 and T_2 maps are presented in **Figures 5**, **6** for each mechanical state of the specimen, with or without radial fissure radial fissure, respectively. On **Figure 5**, the anterior fissure is clearly visible for each MRI sequence.

According to the Dallas classification (Sachs et al., 1987), the analyses of the T_2_w TSE, T_1 and T_2 maps reveals a fissure shape similar to a grade II discogram in neutral and extension positions, whereas it is similar to a grade I discogram in flexion position. T_1 and T_2 maps reveal tissue infiltration within the fissure in neutral and in extension positions based on the respective relaxation times measured in the different compartments. This infiltration is no longer visible in flexion position of the specimen, and the magnetic properties of the infiltrated tissue are similar to those of the annulus fibrosus ($T_1 > 800$ ms, $T_2 > 80$ ms). These maps confirm that the nucleus deformed in accordance with the loading direction in a greater extent when the annulus is fissured.

TABLE 2 | Young Modulus and Poisson ratio used for the finite element model of the disc.

	Young modulus (MPa)	Poisson ratio	Reference
Nucleus	1	0.499	Shin et al., 2007
Annulus	8.4	0.45	

Total Disc and Nucleus Mechanical Displacements and Strains

Axial strain, bending angle variation, nucleus boundary sagittal displacement, nucleus total sagittal displacement, and nucleus sagittal strain for each mechanical condition are summarized in **Table 3**. Steps 1 to 3 (**Table 1**) present our findings for the intact specimen at different mechanical states. Between steps 3 and 4, an experimental anterior fissure was performed at the annulus fibrosus site. Accordingly, steps 4 to 6 present the results for the damaged specimen.

Axial strain results show an increase with time when comparing two steps with the same mechanical state, e.g., steps 1 and 6. Specimen angle results also show an increase with time. There is a considerable change in nucleus behavior before and after fissuring the annulus. Displacement of the nuclear boundaries increases with extension after the fissuring (+2.8 mm), whereas posterior displacement decreases with flexion (−1.6 mm). The same behavior is visible for nucleus global displacement (+4.6 mm for extension and −2 mm for flexion). The strongest effect of the fissure is observed on the sagittal strain (+27% in extension and +2.5% in flexion). Both flexion and extension with an intact nucleus lead to nucleus compression (negative strain values of −5.6% and −6.1% respectively). In contrast, with a fissured annulus, only flexion leads to nucleus compression (−3.1%), whereas extension causes its stretching (+21.1%).

Stress Analysis

The maps of axial stress and intensity of maximal shear stress for intact and fissured specimen are shown in **Figures 7**, **8**, for both flexion and extension loading. For the intact specimen, we observed classical behavior with compressive and tensile components in accordance with bending loads. For the fissured specimen, we observed increased stress value in the vicinity of the fissure (around 0.2 MPa). The distribution of the intensity of maximal shear stress further exacerbates this difference by displaying increased values in front of the fissure (around 0.2 MPa), whereas maps were homogeneous in the intact disc.

DISCUSSION

Original Findings

Our first and secondary aims were to detect radial fissure of the annulus fibrosus using quantitative MRI, and to characterize the biomechanical behavior of the fissured and intact intervertebral disc, respectively. We defined an original protocol combining qualitative and axial quantitative MRI, computed segmentation, mark tracking analysis and FE modeling. This original approach enabled characterizing the morphology and the biomechanics of the radial fissure the nucleus pulposus according to sagittal bending load and the presence / absence of an anterior radial fissure.

By comparison, classical MRI approach assess either the grade of degeneration (Pfirrmann et al., 2001), the inflammatory status of the endplate (Modic et al., 1984), the presence of a high intensity zone in the annulus (Aprill and Bogduk, 1992) or the external geometry of the disc (Fardon et al., 2014). None of these parameters are a direct observation of a radial fissure. In addition, discography allow a morphologic characterization of the fissure but it is invasive (Carragee et al., 2009) and does not explore the dynamic nature of this fissure (Bogduk, 2013).

Data from this proof-of-concept study tend to confirm the dynamic nature of the nucleus pulposus under the influence of bending loads, i.e., deformation/displacement of the nucleus pulposus away from the direction of the load. A systematic review confirmed this behavior for healthy discs, but findings were conflicting regarding pathological discs (Kolber and Hanney, 2009). We can highlight that none of the papers included in this review used a protocol similar to ours.

Our specimen was prepared according to the guidelines for spinal cadaveric studies by controlling for hydration and axial creep load (Adams, 1995; Wilke et al., 1998b). Due to experimental limitations, the axial compressive load was lower than the recommended value (60 N versus 300 N in the guidelines) and was instead applied longer in order to reach the equivalent effect (90 min versus 30 min in the guidelines).

Adjunction of quantitative imaging improves the precision of disc morphometric characterization and enables experimenters to measure both nucleus displacement with good accuracy (0.1 voxel) and strain under various loading conditions (flexion-extension). By comparing the T_1 relaxation times of the tissues at the fissure level to those of the nucleus, it appears reasonable to claim that the nucleus moves toward/deformed into the fissure under bending load influence. Our study showed that T_1 and T_2 values are relevant parameters for automated segmentation of the different disc regions. This justifies future effort in developing fast quantitative acquisitions that will offer objective metrics for the analysis of the disc biomechanics. Indeed, and as indicated by the plethora of studies in the field, there is a clear need of establishing robust quality criteria for image analyses used in clinical research and clinical trials. This task is all the more difficult as conventional MR images display only shades of gray that are very dependent on the hardware (coil profile, field strength, field homogeneity) and the operator (sequence parameters, patient positioning, signal intensity thresholds for segmentation, etc.).

When comparing two steps within the same mechanical state, e.g., steps 2 and 5, an increase of axial strain and bending angle with time was expected. This corresponds to the creep load induced by compressive axial load. However, between step 1 (intact disc in neutral state) and step 6 (fissured disc in neutral state) the angle difference is + 4°, indicating that the specimen's position shifted from neutral toward extension even though the elastic bending system had been removed. This value is much

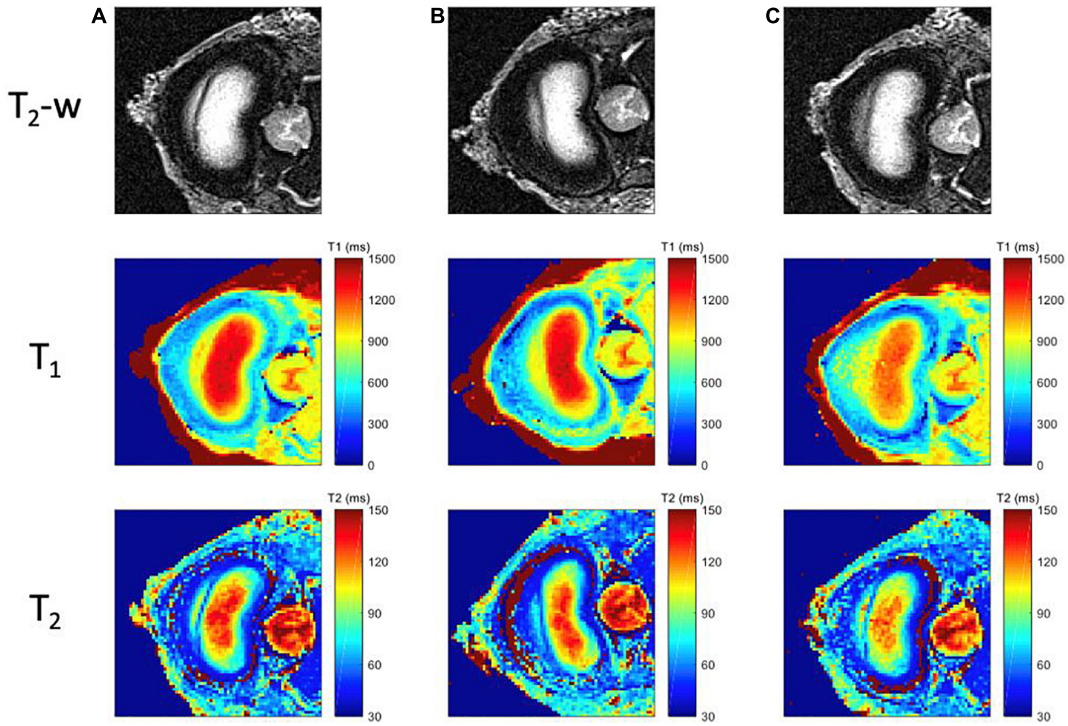

FIGURE 5 | MR images for each mechanical loading state of the intact specimen. First row corresponds to the T_2-weighted images; second row to the computed T_1 maps, with a scale ranging from 0 ms (blue) to 1500 ms (red); and third row to the T_2 maps, with a scale ranging from 20 ms (blue) to 150 ms (red); for three different positions **(A)** Neutral (step 1) **(B)** Flexion (step 2), **(C)** Extension (step 3).

TABLE 3 | Axial strain, angle variation, nucleus boundary sagittal displacement, nucleus global sagittal displacement, nucleus sagittal strain, migration of the nucleus in the annulus and cumulative time under axial compression for each mechanical loading step.

Step	Axial strain[1]	Specimen angle[2]	Angle variation[3]	Nucleus boundary sagittal displacement[4]	Nucleus global sagittal displacement[4]	Nucleus sagittal strain[1]	Migration of nucleus in the annulus[5]	Cumulative time under axial compression
1 (Neutral)	−4	4.7	–	–	–	–	–	Ih30
2 (Flexion)	−7.3	−8.8	−13.5	−2.2	−3.6	−5.6	0	3h
3 (Extension)	−8.3	10.4	5.7	2.2	−0.9	−6.1	0	4h30
Fissure								
4 (Extension)	−8.8	11.1	6.4	5.0	3.7	21.1	100	6h30
5 (Flexion)	−7.5	−8.9	−13.6	−0.6	−1.6	−3.1	21	8h30
6 (Neutral)	−4.6	8.7	4.0	4.5	1.5	20.8	100	10h

[1] *In percentage, negative value corresponds to a decrease of the height of the specimen.*
[2] *In degrees, negative value corresponds to a flexion angle, positive value to an extension one.*
[3] *In degrees, negative value corresponds to a flexion angle, positive value to an extension one. This angle corresponds to the actual specimen angle respective to the baseline's one (step 1 neutral).*
[4] *In millimeters, negative value corresponds to a posterior displacement, positive value to an anterior one.*
[5] *In percentage.*

greater than what we observed for the other two mechanical states (+ 0.7° for extension and − 0.1° for flexion). This observation, albeit not expected, could explain why MRI and mechanical results of step 6 (fissured disc in neutral state) are very close to those of step 4 (fissured disc in extension). This sizable increase of extension angle in step 6 could be a consequence of the manually performed anterior fissure and should be further explored in future studies.

Our results also revealed a link between disc abnormality and range of motion by using a non-invasive diagnostic method differing from interventional intra-discal procedures. While discography highlights the physical presence of a fissure within the annulus under fixed positional conditions, it remains impossible to observe the migration of the nucleus under postural influence (Walker et al., 2008). Using our non-invasive MRI approach, we observed and quantified the migration of the

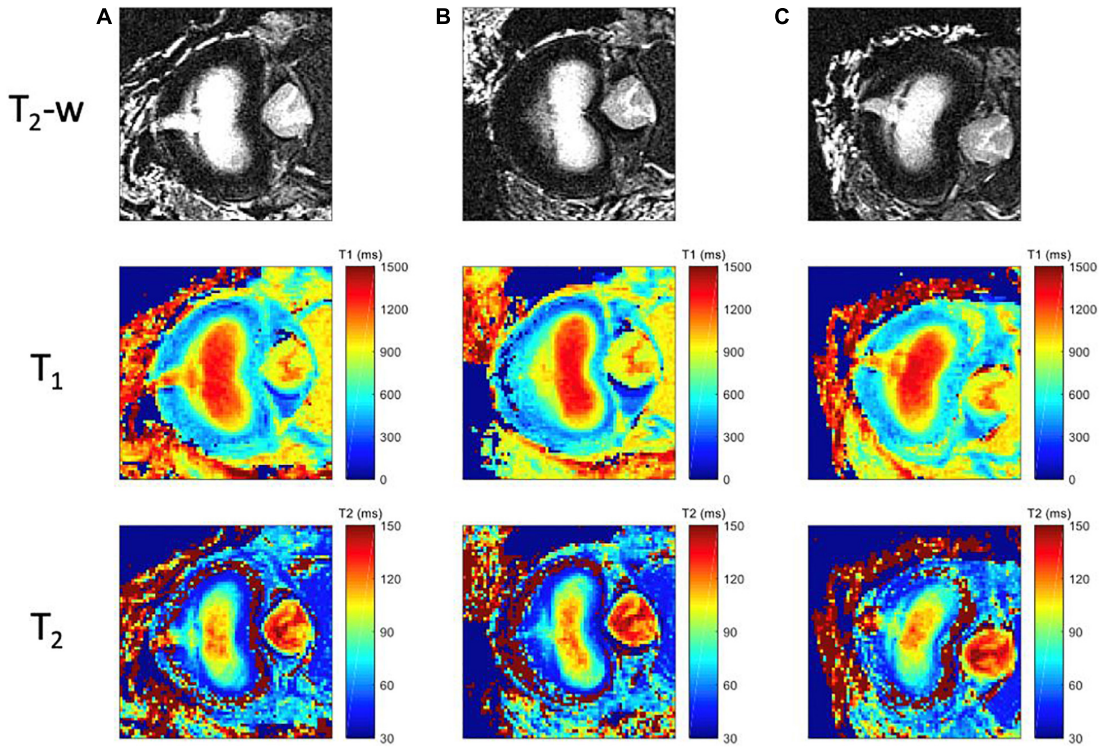

FIGURE 6 | MR images for each mechanical loading state of the specimen with radial tear. First row corresponds to the T_2-weighted images; the second row to T_1 maps, with a scale ranging from 0 ms (blue) to 1500 ms (red); and third row to the T_2 maps, with a scale ranging from 20 ms (blue) to 150 ms (red); for three different positions **(A)** Neutral (step 6), **(B)** Flexion (step 5), **(C)** Extension (step 4).

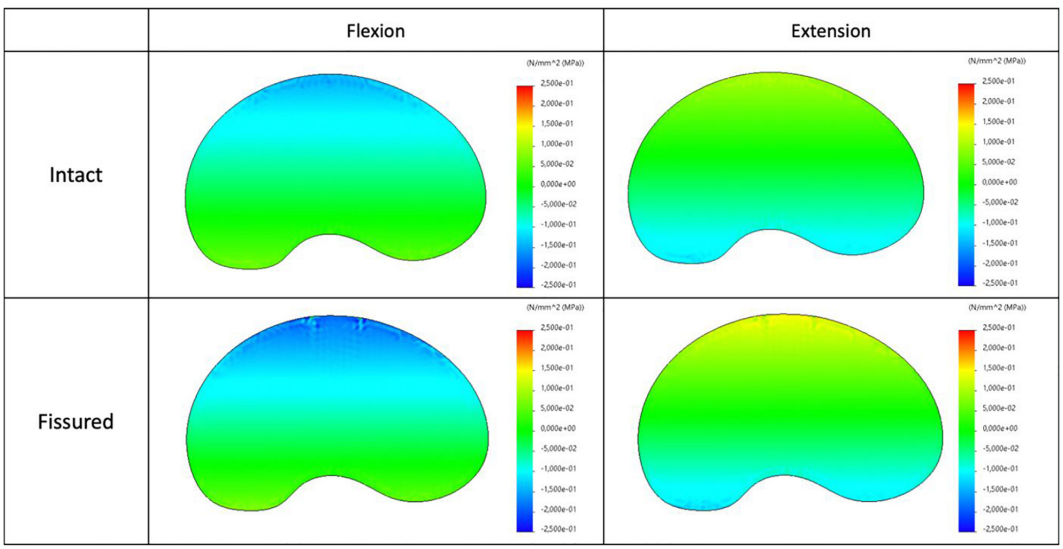

FIGURE 7 | Distribution of the axial stress map for intact (top) and fissured (bottom) disc with flexion (left) and extension (right) loading.

nucleus into the annulus from the quantitative maps, under conditions equivalent to the physiological loading (up to 5-6 degrees per level) usually observed for daily range of motion in humans (Alini et al., 2008). In this work, the artificial fissure induced considerable damage including the migration of the nucleus within the full thickness of the annulus (100% of migration). As a result, the nucleus strain increased with stretching in the sagittal direction inducing reduction of internal pressure. Yet, flexion partially restored not only the nucleus morphology with observed migration dropping from 100 to 21%,

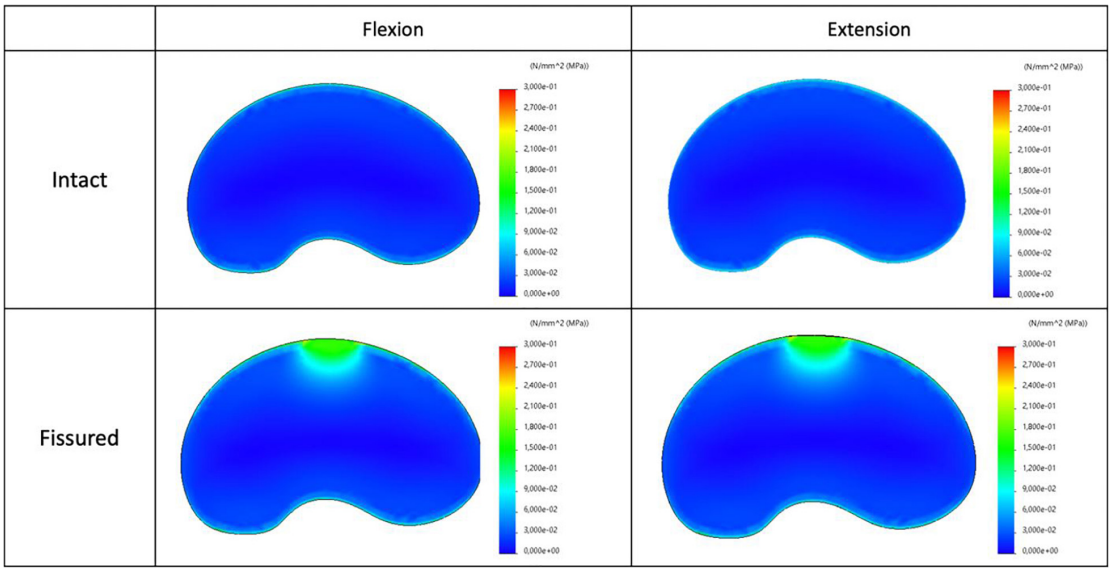

FIGURE 8 | Distribution of the intensity of maximal shear stress for intact (top) and fissured (bottom) disc with flexion (left) and extension (right) loading.

but also the internal pressure with a measured compression strain of 3.1% restoring internal pressure, and consequently physiological capabilities of the disc. These observations confirm the dynamic behavior changes of the fissure.

Ultimately, we used a simplified finite element model, based on geometry directly extracted from MRI data. This approach was enriched by the real boundary conditions quantified during the experiments. This dual approach enabled simultaneous measurement of stress and strain fields on the nucleus, thereby providing a complete biomechanical analysis of the normal and pathological disc. From a clinical point of view, the migration of the nucleus pulposus alongside the fissure could become a nociceptive trigger, leading patient pain. Furthermore, in this case, the singularity and its evolution observed from MRI maps can be linked to stress variation in the nucleus with an increasing of shear components.

Study Limitations

Despite being encouraging, our results suffer from several limitations. This study is a proof-of-concept study performed on only one disc. Repeating the protocol on multiple samples would allow us to assess the reproducibility of our method and to draw more robust conclusions from a statistical point of view. Another limitation could arise from the animal nature of our specimen and its difference with human discs. Indeed, quadrupedal station induces geometrical changes (O'Connell et al., 2007), variations in mechanical properties (Alini et al., 2008) and chemical composition of the disc (Zhang et al., 2014). Nonetheless, a recent review (Daly et al., 2016) concluded that ovine disc is a reasonable choice for preliminary biomechanical or injury model studies. Animal models are currently used in surgical, biomechanical (Casaroli et al., 2017) and histological studies (Schollum et al., 2008). Rather than species type, age and degeneration state of the specimen might actually have a stronger impact on the results since both of these parameters alter disc biomechanics (Adams et al., 1996). With age and degeneration, there is a decrease in the disc notochordal cell population. This triggers a reduction of proteoglycan secretion, leading in turn to a drop in nuclear hydration. Type II collagen is progressively replaced by type I collagen, leading to a more fibrous nucleus (Adams and Roughley, 2006). All of these processes impact the mechanical behavior of the nucleus according to motion and can affect the magnetic properties, such as T_1 and T_2. As our specimen comes from a young animal with no sign of degenerative disc, the results could not be generalized beyond these criteria. Another limitation comes from the type of fissure induced in our study. Our experimental setup ensured good access to the anterior part of the disc without damaging the specimen. Though rare, anterior fissures are encountered in discography (Saifuddin et al., 1998) or cadaveric studies (Yu et al., 1988). However, most of the fissures associated with discogenic backpain are either posterior or postero-lateral (Bogduk et al., 2013). Because of the different shape and thickness of the anterior annulus (Cassidy et al., 1989), results could be different with a posterior fissure. Ultimately, MRI examination time needs to be shortened to envision *in vivo* studies. Since ours was the first study of its kind, basic MR sequences were used in order to assess the feasibility of T_1 and T_2 maps as markers to investigate the disc biomechanics. As a consequence, repeating the current imaging protocol in the 3 different conditions leads to a 6-h examination. Such scan time did not have an impact on our specimen since it has been shown that no change in mechanical properties is observed after 20 h of testing (Wilke et al., 1998a), but faster acquisition schemes need to be implemented to allow a potential transfer to patients *in vivo*. We propose to implement strategies that enable simultaneous acquisitions of T_1 and T_2 (Ma et al., 2013) in future studies.

Concerning FE analysis, we used a simplified model to determine stress distribution according to imposed motion and the presence of a fracture in the annulus. Even if we used real geometry and boundary conditions read during experiments, our model had some limitations. As already performed for previous works from literature, we considered linear behaviors and isotropic properties (Shin et al., 2007; Zanjani-Pour et al., 2016). This approach was sufficient in the present work to analyze stress distribution. However, to validate the model, it would be necessary to identify the mechanical properties of tissues and to implement them in the model which could be validated from comparison of displacement and strain fields. Furthermore, we did not model the facet joints in accordance with the limited values of imposed moments (3 N.m). According to our experiments, facet joints were not activated for this magnitude of applied loads, however, they would have to be modeled for higher imposed moments.

Future directions would include replicating this study using a greater number of ovine discs, along with inducing different orientations for the radial fissure in order to better reflect clinical conditions, and applying additional movement directions, typically including the coronal and frontal plans. If results are consistent, our ambition would be to design the next phase of *ex vivo* studies using human cadaveric discs at different levels of degeneration and age, and thereby make it possible to transfer our MRI methods to *in vivo* clinical applications.

Future Clinical Implications

Once adapted to *in vivo* experimentations and combined with classical assessment tools (MRI, X-ray, etc.), such protocol would help clinicians to assess patients with discogenic pain and/or radicular pain due to disc herniation. Together with the directional preference concept (May and Aina, 2012; May et al., 2018), it would help to identify patients who could benefit from a physiotherapeutic mechanical treatment (McKenzie and May, 2003) from those who need surgery. We believe that this protocol would ease the clinical decision-making process, and hence optimize patient care as well as reduce health cost related to back pain.

CONCLUSION

In this Proof-of-Concept study, we demonstrated the possibility to characterize the morphological and biomechanical parameters of a radial fissure within an *ex vivo* ovine disc. To do so, we combined quantitative T_1 an T_2 mapping MRI, T_2-weighted MRI, computed segmentation, mark tracking analysis and finite element modeling.

Each MRI sequence allowed a clear and original visualization of the discal damage, i.e., radial fissure, non-invasively. The nucleus pulposus moved anteriorly with extension bending load and posteriorly with flexion bending load. After the anterior annulus was damaged, the nuclear displacement and strain increased for extension load and decreased for flexion load. The displacement and strain of the nucleus appeared to follow the direction of the fissure and the direction of the bending load.

This preliminary work, once validated on a larger scale, could have substantial applications for:

- radio-clinical non-invasive disc explorations and correlations with patient lumbar pain,
- dynamic characterization of the disc under physiological and pathological conditions.

DATA AVAILABILITY STATEMENT

The raw data supporting the conclusions of this article will be made available by the authors, without undue reservation.

AUTHOR CONTRIBUTIONS

J-PD, TV, and PR: conceptualization. AG, MY, MS, and NS: methodology. J-PD, AG, MY, MS, and NS: software and validation. MS and NS: resources. J-PD, AG, NS, and PR: writing—original draft preparation. J-PD, TV, AG, MB, MR, NS, and PR: writing—review and editing. AG, NS, and PR: supervision and project administration. NS, MS, and PR: funding acquisition. All authors have read and agreed to the published version of the manuscript.

REFERENCES

Adams, M. A. (1995). Spine Update: mechanical testing of the spine - an appraisal of methodology. results and conclusion. *Spine* 20, 2151–2156.

Adams, M. A., and Dolan, P. (2012). Intervertebral disc degeneration: evidence for two distinct phenotypes. *J. Anat.* 221, 497–506. doi: 10.1111/j.1469-7580.2012.01551.x

Adams, M. A., McNally, D. S., and Dolan, P. (1996). "Stress" distributions inside intervertebral discs. the effects of age and degeneration. *J. Bone Joint Surg. Br.* 78, 965–972. doi: 10.1302/0301-620x78b6.1287

Adams, M. A., and Roughley, P. J. (2006). What is intervertebral disc degeneration, and what causes it? *Spine* 31, 2151–2161. doi: 10.1097/01.brs.0000231761.73859.2c

Alini, M., Eisenstein, S. M., Ito, K., Little, C., Kettler, A. A., Masuda, K., et al. (2008). Are animal models useful for studying human disc disorders/degeneration? *Eur. Spine J.* 17, 2–19. doi: 10.1007/s00586-007-0414-y

Antoniou, J., Steffen, T., Nelson, F., Winterbottom, N., Hollander, A. P., Poole, R. A., et al. (1996). The human lumbar intervertebral disc: evidence for changes in the biosynthesis and denaturation of the extracellular matrix with growth, maturation, ageing, and degeneration. *J. Clin. Invest.* 98, 996–1003. doi: 10.1172/JCI118884

Aprill, C., and Bogduk, N. (1992). High-intensity zone: a diagnostic sign of painful lumbar disc on magnetic resonance imaging. *Br. J. Radiol.* 65, 361–369. doi: 10.1259/0007-1285-65-773-361

Benneker, L. M., Heini, P. F., Anderson, S. E., Alini, M., and Ito, K. (2005). Correlation of radiographic and MRI parameters to morphological and biochemical assessment of intervertebral disc degeneration. *Eur. Spine J.* 14, 27–35. doi: 10.1007/s00586-004-0759-4

Bogduk, N. (2013). *Practice Guidelines for Spinal Diagnostic and Treatment Procedures*, 2nd Edn. San Francisco, CA: International Spine Intervention Society.

Bogduk, N., Aprill, C., and Derby, R. (2013). Lumbar discogenic pain: state-of-the-art review: lumbar discogenic pain. *Pain Med.* 14, 813–836. doi: 10.1111/pme.12082

Brinjikji, W., Luetmer, P. H., Comstock, B., Bresnahan, B. W., Chen, L. E., Deyo, R. A., et al. (2015). Systematic literature review of imaging features of spinal

degeneration in asymptomatic populations. *Am. J. Neuroradiol.* 36, 811–816. doi: 10.3174/ajnr.A4173

Callaghan, J. P., Gunning, J. L., and McGill, S. M. (1998). The relationship between lumbar spine load and muscle activity during extensor exercises. *Phys. Ther.* 78, 8–18. doi: 10.1093/ptj/78.1.8

Carragee, E. J., Don, A. S., Hurwitz, E. L., Cuellar, J. M., Carrino, J., and Herzog, R. (2009). 2009 ISSLS prize winner: does discography cause accelerated progression of degeneration changes in the lumbar disc: a ten-year matched cohort study. *Spine* 34, 2338–2345. doi: 10.1097/BRS.0b013e3181ab5432

Casaroli, G., Galbusera, F., Jonas, R., Schlager, B., Wilke, H.-J., and Villa, T. (2017). A novel finite element model of the ovine lumbar intervertebral disc with anisotropic hyperelastic material properties. *PloS One* 12:e0177088. doi: 10.1371/journal.pone.0177088

Cassidy, J. J., Hiltner, A., and Baer, E. (1989). Hierarchical structure of the intervertebral disc. *Connect. Tissue Res.* 23, 75–88.

Coppes, M. H., Marani, E., Thomeer, R. T. W. M., and Groen, G. J. (1997). Innervation of "painful". Lumbar Discs. *Spine* 22, 2342–2349. doi: 10.1097/00007632-199710150-00005

Coppes, M. H., Marani, E., Thomeer, R. T. W. M., Oudega, M., and Groen, G. J. (1990). Innervation of annulus fibrosis in low back pain. *Lancet* 336, 189–190. doi: 10.1016/0140-6736(90)91723-n

Dagenais, S., Caro, J., and Haldeman, S. (2008). A systematic review of low back pain cost of illness studies in the United States and internationally. *Spine J.* 8, 8–20. doi: 10.1016/j.spinee.2007.10.005

Daly, C., Ghosh, P., Jenkin, G., Oehme, D., and Goldschlager, T. (2016). A review of animal models of intervertebral disc degeneration: pathophysiology, regeneration, and translation to the clinic. *BioMed. Res. Int.* 2016:5952165. doi: 10.1155/2016/5952165

Enokida, S., Tanishima, S., Tanida, A., Mihara, T., Takeda, C., Yamashita, E., et al. (2020). Evaluation of age-related changes in lumbar facet joints using T2 mapping. *J. Orthop. Sci.* 25, 46–51. doi: 10.1016/j.jos.2019.02.017 *y2019,

Fardon, D. F., Williams, A. L., Dohring, E. J., Murtagh, F. R., Gabriel Rothman, S. L., and Sze, G. K. (2014). Lumbar disc nomenclature: version 2.0. *Spine J.* 14, 2525–2545. doi: 10.1016/j.spinee.2014.04.022

Freeman, B. J. C. (2006). IDET: a critical appraisal of the evidence. *Eur. Spine J.* 15, 448–457. doi: 10.1007/s00586-006-0156-2

Galley, J., Maestretti, G., Koch, G., and Hoogewoud, H.-M. (2017). Real T1 relaxation time measurement and diurnal variation analysis of intervertebral discs in a healthy population of 50 volunteers. *Eur. J. Radiol.* 87, 13–19. doi: 10.1016/j.ejrad.2016.12.001

García-Cosamalón, J., Del Valle, M. E., Calavia, M. G., García-Suárez, O., López-Muñiz, A., Otero, J., et al. (2010). Intervertebral disc, sensory nerves and neurotrophins: who is who in discogenic pain: intervertebral disc, sensory nerves and neurotrophins. *J. Anat.* 217, 1–15. doi: 10.1111/j.1469-7580.2010.01227.x

Germaneau, A., Vendeuvre, T., Saget, M., Doumalin, P., Dupré, J. C., Brémand, F., et al. (2016). A novel approach for biomechanical spine analysis: mechanical response of vertebral bone augmentation by kyphoplasty to stabilise thoracolumbar burst fractures. *J. Mech. Behav. Biomed. Mater.* 59, 291–303. doi: 10.1016/j.jmbbm.2016.02.002

Hashemi, M., Dadkhah, P., Taheri, M., Katibeh, P., and Asadi, S. (2020). Effectiveness of intradiscal injection of radiopaque gelified ethanol (DiscoGel ®) *versus* percutaneous laser disc decompression in patients with chronic radicular low back pain. *Korean J. Pain* 33, 66–72. doi: 10.3344/kjp.2020.33.1.66

Hwang, D., Kim, S., Abeydeera, N. A., Statum, S., Masuda, K., Chung, C. B., et al. (2016). Quantitative magnetic resonance imaging of the lumbar intervertebral discs. *Quant. Imaging Med. Surg.* 6, 744–755. doi: 10.21037/qims.2016.12.09

Ishibashi, K., Iwai, H., and Koga, H. (2019). Chemonucleolysis with chondroitin sulfate ABC endolyase as a novel minimally invasive treatment for patients with lumbar intervertebral disc herniation. *J. Spine Surg.* 5, S115–S121. doi: 10.21037/jss.2019.04.24

Javid, M. J., Nordby, E. J., Ford, L. T., Hejna, W. J., Whisler, W. W., Burton, C., et al. (1983). Safety and efficacy of chymopapain (Chymodiactin) in herniated nucleus pulposus with sciatica. results of a randomized, double-blind study. *JAMA* 249, 2489–2494.

Khan, I., Hargunani, R., and Saifuddin, A. (2014). The lumbar high-intensity zone: 20 years on. *Clin. Radiol.* 69, 551–558. doi: 10.1016/j.crad.2013.12.012

Knezevic, N. N., Mandalia, S., Raasch, J., Knezevic, I., and Candido, K. D. (2017). Treatment of chronic low back pain – new approaches on the horizon. *J. Pain Res.* 10, 1111–1123. doi: 10.2147/JPR.S132769

Kolber, M. J., and Hanney, W. J. (2009). The dynamic disc model: a systematic review of the literature. *Phys. Ther. Rev.* 14, 181–189. doi: 10.1179/174328809X452827

Lama, P., Le Maitre, C. L., Harding, I. J., Dolan, P., and Adams, M. A. (2018). Nerves and blood vessels in degenerated intervertebral discs are confined to physically disrupted tissue. *J. Anat.* 233, 86–97. doi: 10.1111/joa.12817

Laslett, M., Öberg, B., Aprill, C. N., and McDonald, B. (2005). Centralization as a predictor of provocation discography results in chronic low back pain, and the influence of disability and distress on diagnostic power. *Spine J.* 5, 370–380. doi: 10.1016/j.spinee.2004.11.007

Le Maitre, C. L., Freemont, A. J., and Hoyland, J. A. (2004). Localization of degradative enzymes and their inhibitors in the degenerate human intervertebral disc. *J. Pathol.* 204, 47–54. doi: 10.1002/path.1608

Le Maitre, C. L., Pockert, A., Buttle, D. J., Freemont, A. J., and Hoyland, J. A. (2007). Matrix synthesis and degradation in human intervertebral disc degeneration. *Biochem. Soc. Trans.* 35, 652–655. doi: 10.1042/BST0350652

Li, P., Zhang, R., and Zhou, Q. (2017). Efficacy of platelet-rich plasma in retarding intervertebral disc degeneration: a meta-analysis of animal studies. *BioMed. Res. Int.* 2017:7919201. doi: 10.1155/2017/7919201

Ma, D., Gulani, V., Seiberlich, N., Liu, K., Sunshine, J. L., Duerk, J. L., et al. (2013). Magnetic resonance fingerprinting. *Nature* 495, 187–192. doi: 10.1038/nature11971

Maetzel, A., and Li, L. (2002). The economic burden of low back pain: a review of studies published between 1996 and 2001. *Best Pract. Res. Clin. Rheumatol.* 16, 23–30. doi: 10.1053/berh.2001.0204

Manchikanti, L., Soin, A., and Beyamin, R. (2018). An update of the systematic appraisal of theaccuracy and utility of discography in chronicspinal pain. *Pain Physician* 1, 91–110. doi: 10.36076/ppj.2018.2.91

May, S., and Aina, A. (2012). Centralization and directional preference: a systematic review. *Man. Ther.* 17, 497–506. doi: 10.1016/j.math.2012.05.003

May, S., Runge, N., and Aina, A. (2018). Centralization and directional preference: an updated systematic review with synthesis of previous evidence. *Musculoskelet. Sci. Pract.* 38, 53–62. doi: 10.1016/j.msksp.2018.09.006

McCormick, Z. L., Lehman, V. T., Plastaras, C. T., Walega, D. R., Huddleston, P., Moussallem, C., et al. (2019). Low-pressure lumbar provocation discography according to spine intervention society/international association for the study of pain standards does not cause acceleration of disc degeneration in patients with symptomatic low back pain: a 7-year matched cohort study. *Spine* 44, E1161–E1168. doi: 10.1097/BRS.0000000000003085

McKenzie, R. (1981). *The Lumbar Spine. First*. Wellington: Spinal Publication.

McKenzie, R., and May, S. (2003). *The Lumbar Spine: Mechanical Diagnosis and Therapy–Volume 1*. New Zealand, OC: Spinal Publications.

McMillan, D. W., Garbutt, G., and Adams, M. A. (1996). Effect of sustained loading on the water content of intervertebral discs: implications for disc metabolism. *Ann. Rheum. Dis.* 55, 880–887. doi: 10.1136/ard.55.12.880

McNally, D. S., Shackleford, I. M., Goodship, A. E., and Mulholland, R. C. (1996). In vivo stress measurement can predict pain on discography. *Spine* 21, 2580–2587.

Meisel, H.-J., Agarwal, N., Hsieh, P. C., Skelly, A., Park, J.-B., Brodke, D., et al. (2019). Cell therapy for treatment of intervertebral disc degeneration: a systematic review. *Global Spine J.* 9, 39S–52S. doi: 10.1177/2192568219829024

Menezes-Reis, R., Salmon, C. E. G., Carvalho, C. S., Bonugli, G. P., Chung, C. B., and Nogueira-Barbosa, M. H. (2015). T1rho and T2 mapping of the intervertebral disk: comparison of different methods of segmentation. *AJNR Am. J. Neuroradiol.* 36, 606–611. doi: 10.3174/ajnr.A4125

Modic, M. T., Pavlicek, W., Weinstein, M. A., Boumphrey, F., Ngo, F., Hardy, R., et al. (1984). Magnetic resonance imaging of intervertebral disk disease. clinical and pulse sequence considerations. *Radiology* 152, 103–111. doi: 10.1148/radiology.152.1.6729099

Moneta, G. B., Videman, T., Kaivanto, K., Aprill, C. N., Spivey, M., Vanharanta, H., et al. (1994). Reported pain during lumbar discography as a function of anular ruptures and disc degeneration: a re-analysis of 833 discograms. *Spine* 19, 1968–1974.

Mwale, F., Iatridis, J. C., and Antoniou, J. (2008). Quantitative MRI as a diagnostic tool of intervertebral disc matrix composition and integrity. *Eur. Spine J.* 17, 432–440. doi: 10.1007/s00586-008-0744-4

O'Connell, G. D., Vresilovic, E. J., and Elliott, D. M. (2007). Comparison of animals used in disc research to human lumbar disc geometry. *Spine* 32, 328–333. doi: 10.1097/01.brs.0000253961.40910.c1

Osti, O., and Fraser, R. (1992). MRI and discography of annular tears and intervertebral disc degeneration. a prospective clinical comparison. *J. Bone Joint Surg. Br.* 74, 431–435. doi: 10.1302/0301-620X.74B3.1587896

Paradiso, R., and Alexandre, A. (2005). The different outcomes of patients with disc herniation treated either by microdiscectomy, or by intradiscal ozone injection. *Acta Neurochir. Suppl.* 92, 139–142. doi: 10.1007/3-211-27458-8_30

Paul, C. P. L., Smit, T. H., de Graaf, M., Holewijn, R. M., Bisschop, A., van de Ven, P. M., et al. (2018). Quantitative MRI in early intervertebral disc degeneration: T1rho correlates better than T2 and ADC with biomechanics, histology and matrix content. *PloS One* 13:e0191442. doi: 10.1371/journal.pone.0191442

Pfirrmann, C. W. A., Metzdorf, A., Zanetti, M., Hodler, J., and Boos, N. (2001). Magnetic resonance classification of lumbar intervertebral disc degeneration. *Spine* 26, 1873–1878. doi: 10.1097/00007632-200109010-00011

Sachs, B. L., Vanharanta, H., Spivey, M. A., Guyer, R. D., Videman, T., Rashbaum, R. F., et al. (1987). Dallas discogram description - a new classification of CT/discography in low-back disorders. *Spine* 12, 287–294.

Saifuddin, A., Emanuel, R., White, J., Renton, P., Braithwaite, I., and Taylor, B. A. (1998). An analysis of radiating pain at lumbar discography. *Eur. Spine J.* 7, 358–362. doi: 10.1007/s005860050090

Schollum, M. L., Robertson, P. A., and Broom, N. D. (2008). ISSLS prize winner: microstructure and mechanical disruption of the lumbar disc annulus: part I: a microscopic investigation of the translamellar bridging network. *Spine* 33, 2702–2710. doi: 10.1097/BRS.0b013e31817bb92c

Shin, D. S., Lee, K., and Kim, D. (2007). Biomechanical study of lumbar spine with dynamic stabilization device using finite element method. *Comput.-Aided Des.* 39, 559–567. doi: 10.1016/j.cad.2007.03.005

Stefanakis, M., Luo, J., Pollintine, P., Dolan, P., and Adams, M. A. (2014). ISSLS Prize winner: mechanical influences in progressive intervertebral disc degeneration. *Spine* 39, 1365–1372. doi: 10.1097/BRS.0000000000000389

Tertti, M., Paajanen, H., Laato, M., Aho, H., Komu, M., and Kormano, M. (1991). Disc degeneration in magnetic resonance imaging. a comparative biochemical, histologic, and radiologic study in cadaver spines. *Spine* 16, 629–634. doi: 10.1097/00007632-199106000-00006

Thompson, K. J., Dagher, A. P., Eckel, T. S., Clark, M., and Reinig, J. W. (2009). Modic changes on MR images as studied with provocative diskography: clinical relevance—a retrospective study of 2457 disks. *Radiology* 250, 849–855. doi: 10.1148/radiol.2503080474

Vanharanta, H., Sachs, B. L., Spivey, M., Guyer, R. D., Hochschuler, H., Rashbaum, R. F., et al. (1987). The Relashionship of pain provocation to lumbar disc deterioration as seen by CT/Discography. *Spine* 12, 295–298.

Vos, T., Allen, C., Arora, M., Barber, R. M., Bhutta, Z. A., Brown, A., et al. (2016). Global, regional, and national incidence, prevalence, and years lived with disability for 310 diseases and injuries, 1990–2015: a systematic analysis for the Global Burden of Disease Study 2015. *Lancet* 388, 1545–1602. doi: 10.1016/S0140-6736(16)31678-6

Walker, B. F., Muller, R., and Grant, W. D. (2003). Low back pain in australian adults: the economic burden. *Asia Pac. J. Public Health* 15, 79–87. doi: 10.1177/101053950301500202

Walker, J., El Abd, O., Isaac, Z., and Muzin, S. (2008). Discography in practice: a clinical and historical review. *Curr. Rev. Musculoskelet. Med.* 1, 69–83. doi: 10.1007/s12178-007-9009-9

Watanabe, A., Benneker, L. M., Boesch, C., Watanabe, T., Obata, T., and Anderson, S. E. (2007). Classification of intervertebral disk degeneration with axial T2 mapping. *Am. J. Roentgenol.* 189, 936–942. doi: 10.2214/AJR.07.2142

Wilke, H.-J., Jungkunz, B., Wenger, K., and Claes, L. E. (1998a). Spinal segment range of motion as a function of in vitro test conditions: effects of exposure period, accumulated cycles, angular-deformation rate, and moisture condition. *Anat. Rec.* 251, 15–19.

Wilke, H.-J., Wenger, K., and Claes, L. (1998b). Testing criteria for spinal implants: recommendations for the standardization of in vitro stability testing of spinal implants. *Eur. Spine J.* 7, 148–154. doi: 10.1007/s005860050045

Yu, S. W., Sether, L. A., Ho, P. S., Wagner, M., and Haughton, V. M. (1988). Tears of the anulus fibrosus: correlation between MR and pathologic findings in cadavers. *AJNR Am. J. Neuroradiol.* 9, 367–370.

Zanjani-Pour, S., Winlove, C. P., Smith, C. W., and Meakin, J. R. (2016). Image driven subject-specific finite element models of spinal biomechanics. *J. Biomech.* 49, 919–925. doi: 10.1016/j.jbiomech.2016.02.025

Zhang, Y., Lenart, B. A., Lee, J. K., Chen, D., Shi, P., Ren, J., et al. (2014). Histological features of endplates of the mammalian spine: from mice to men. *Spine* 39, E312–E317. doi: 10.1097/BRS.0000000000000174

Conflict of Interest: The authors declare that the research was conducted in the absence of any commercial or financial relationships that could be construed as a potential conflict of interest.

frontiers in Bioengineering and Biotechnology

ORIGINAL RESEARCH
published: 10 June 2021
doi: 10.3389/fbioe.2021.661258

Load Distribution in the Lumbar Spine During Modeled Compression Depends on Lordosis

Andreas Müller[1,2,3]*, *Robert Rockenfeller*[4], *Nicolas Damm*[1], *Michael Kosterhon*[5], *Sven R. Kantelhardt*[5], *Ameet K. Aiyangar*[2,6] and *Karin Gruber*[1,3]

[1] Institute for Medical Engineering and Information Processing (MTI Mittelrhein), University Koblenz-Landau, Koblenz, Germany, [2] Mechanical Systems Engineering, Swiss Federal Laboratories for Materials Science and Technology (EMPA), Duebendorf, Switzerland, [3] Department of Mathematics and Natural Sciences, Institute of Sports Science, University Koblenz-Landau, Koblenz, Germany, [4] Department of Mathematics and Natural Sciences, Mathematical Institute, UniversityKoblenz-Landau, Koblenz, Germany, [5] Department of Neurosurgery, University Medical Centre, Johannes Gutenberg-University Mainz, Mainz, Germany, [6] Department of Orthopedic Surgery, University of Pittsburgh, Pittsburgh, PA, United States

Excessive or incorrect loading of lumbar spinal structures is commonly assumed as one of the factors to accelerate degenerative processes, which may lead to lower back pain. Accordingly, the mechanics of the spine under medical conditions, such as scoliosis or spondylolisthesis, is well-investigated. Treatments via both conventional therapy and surgical methods alike aim at restoring a "healthy" (or at least pain-free) load distribution. Yet, surprisingly little is known about the inter-subject variability of load bearings within a "healthy" lumbar spine. Hence, we utilized computer tomography data from 28 trauma-room patients, whose lumbar spines showed no visible sign of degeneration, to construct simplified multi-body simulation models. The subject-specific geometries, measured by the corresponding lumbar lordosis (LL) between the endplates of vertebra L1 and the sacrum, served as ceteris paribus condition in a standardized forward dynamic compression procedure. Further, the influence of stimulating muscles from the *M. multifidus* group was assessed. For the range of available LL from 28 to 66°, changes in compressive and shear forces, bending moments, as well as facet joint forces between adjacent vertebrae were calculated. While compressive forces tended to decrease with increasing LL, facet forces were tendentiously increasing. Shear forces decreased between more cranial vertebrae and increased between more caudal ones, while bending moments remained constant. Our results suggest that there exist significant, LL-dependent variations in the loading of "healthy" spinal structures, which should be considered when striving for individually appropriate therapeutic measures.

Keywords: biomechanics, forward dynamics, MBS model, musculo skeletal model, lumbar lordosis, curvature, Cobb angle

OPEN ACCESS

Edited by:
Marwan El-Rich,
Khalifa University,
United Arab Emirates

Reviewed by:
Navid Arjmand,
Sharif University of Technology, Iran
Luigi La Barbera,
Politecnico di Milano, Italy

***Correspondence:**
Andreas Müller
andreas.mueller@uni-koblenz.de

Specialty section:
This article was submitted to Biomechanics, a section of the journal Frontiers in Bioengineering and Biotechnology

Received: *30 January 2021*
Accepted: *19 April 2021*
Published: *10 June 2021*

Citation:
Müller A, Rockenfeller R, Damm N, Kosterhon M, Kantelhardt SR, Aiyangar AK and Gruber K (2021) Load Distribution in the Lumbar Spine During Modeled Compression Depends on Lordosis. Front. Bioeng. Biotechnol. 9:661258. doi: 10.3389/fbioe.2021.661258

1. INTRODUCTION

The spine constitutes a highly mobile skeletal structure with a wide inter-individual variation in the characteristics of its double-S shape. High mechanical stresses in daily life and sports may cause injuries that trigger long-term degenerative processes of the intervertebral disks (IVD) or the facet joints. The lumbar spine is particularly affected by degenerative phenomena because it carries the

whole weight of the body above the affected level (Hajihosseinali et al., 2015). Deviations in the double-S shape may alter internal load distributions and accelerate degenerative processes. These deviations are commonly quantified using the *Cobb method* (Cobb, 1948), which was originally introduced to describe degrees of scoliosis, i.e., deviations in the coronal plane (White and Panjabi, 1990, Chapter 3.1). Adapting the Cobb method to the sagittal plane, the *lumbar lordosis* (LL) can be defined as the sagittal Cobb angle between upper endplate of vertebra L1 and the endplate of the sacrum (SA). In contrast to scoliosis, quantitative investigations regarding the effects of deviations in the sagittal curvature on spinal load distributions are scarce, especially when distinguishing between thoracic kyphosis (Briggs et al., 2007; Bruno et al., 2012) and lumbar lordosis (Keller et al., 2005; Bruno et al., 2017). While the latter studies were principally able to show an effect of changes in lordosis on the load distribution within the lumbar spine, a depiction of quantitative dependencies is to date still missing.

Understanding the variability in loading of certain spinal structures can be beneficial in clinical contexts, e.g., for the classification of pathologies or planning of surgical interventions. It is assumed that degenerative alterations are a result of sagittal imbalance (Glassman et al., 2005), which can be measured, for example, by the sagittal vertical axis, i.e., the minimal distance between the C7 plumb-line and the posterior-superior vertebral corner of SA (Jackson and McManus, 1994), or the odontoid hip axis, i.e., the angle between the vertical line through the hip axis and a line from the hip axis to the dens of C2 (Le Huec et al., 2019). A further important characteristic constitutes the *spino-pelvic configuration*, usually represented by the three angular measurands pelvic incidence (PI), sacral slope (SS), and pelvic tilt (PT). It holds $PI = SS + PT$ and it is assumed that optimal sagittal balance corresponds to a small PI-to-LL difference (ΔPILL), particularly $|\Delta PILL| = |PI - LL| \leq 15^\circ$ (Rothenfluh et al., 2015). Higher discrepancy between these two parameters is thought to result in spinal diseases and malfunctions (Roussouly and Pinheiro-Franco, 2011; Senteler et al., 2014; Bassani et al., 2019). For example, hyperlordosis (large LL) is assumed to accelerate discopathies and facet joint degenerations, whereas hypolordosis (small LL) is connected with high compressive peak forces in the IVDs. These and similar plausibility statements frequently occur in the literature, however, mainly in absence of a corresponding quantification (cf. Shirazi-Adl et al., 2002; Keller et al., 2005; Meakin et al., 2009; Gezelbash et al., 2016; Jentzsch et al., 2017). Hence, the aim of this study was to conduct a quantitative investigation regarding the influence of varying LL on the load distribution within the lumbar spine using forward dynamic models.

2. MODEL AND METHODS

A total of 28 lumbar spinal models were constructed on the basis of *in vivo* computer tomography (CT) data from trauma-room patients with otherwise healthy spines (i.e., no signs of degeneration; 32.7 ± 14.5 years, where the age of two subjects was not known), provided anonymized by the University Medical Center in Mainz (**Figure 1A**). These images were taken in supine position, where the loading of spinal structures is significantly reduced compared to standing position (Wilke et al., 1999, Table 1). After semi-automatic segmentation, the resulting surfaces were loaded as rigid bodies into the MBS tool Simpack (Dassault Systèmes Deutschland GmbH, Munich, Germany), and oriented to upright (standing) position, under preservation of the subject-specific geometries, namely curvature, disk space, and facet joint gap. The whole lumbar spine was rigidly re-oriented from supine to upright without altering the relative, intersegmental orientations. "Upright" was defined such that the cranial endplate of the L3 vertebra was oriented parallel to the transversal plane (Rupp et al., 2015, Table 1), i.e., perpendicular to the line of action of the gravitational force. The individual L3 vertebral orientation with respect to the other vertebrae remained unchanged from the original supine state. This definition was maintained for all the models to ensure comparability. The model details described in the following had been previously validated against *in vitro* and *in vivo* data (Damm et al., 2019).

The six degrees-of-freedom, visco-elastic intervertebral body joints between two adjacent vertebrae, representing IVDs, were modeled by non-linear torque-angle and compressive force-deformation characteristics as well as linear shear force-deformation and damping (Damm et al., 2019, Figure 4, Equations 1 and 2). The center of mass of the sacrum was placed in the origin of a coordinate system, where positive z points upwards (cranial), positive y points frontal (anterior), and positive x points right (dexter). As compressive force was measured as the vertical (superior–inferior) part of the force in each reference frame, it could also be referred to as z-force. Accordingly, the (anterior–posterior) shear force is referred to as y-force and the flexion-extension moment around the transversal axis as x-torque. Facet joints were represented by one degree-of-freedom, linear visco-elastic force elements, oriented perpendicular to the regression plane between the (curved) surfaces of the adjacent superior and inferior articular facets. Forces were measured perpendicular to the regression plane between the superior and inferior articular facets, where negative (pulling) forces were not considered for these structures. In fact in some cases, particularly for the upper spinal levels, the facet force remained at 0 N, indicating the absence of compression, i.e., no facet surface contact due to the loading distribution. Instead, the capsule ligaments were compensating for the pulling force.

Next, subject-specific ligament and muscle insertion points on the bony surfaces were identified by anatomical landmarks (Schünke et al., 2015), checked and confirmed by the clinical co-authors (neuro-surgeons from the University Medical Center in Mainz), and connected by one-dimensional force elements (see **Figures 1B–D**). Ligaments were likewise modeled as visco-elastic passive elements, exhibiting a non-linear force-lengths characteristic and linear damping (Damm et al., 2019, Figure 5, Equations 6 and 7). With regard to muscle representation, *M. multifidus* and *M. psoas* major were modeled by point-to-point Hill-type active force elements (Rockenfeller and Günther, 2016, Appendix A). For both ligaments and muscles, pre-strain, and slack lengths, respectively, were scaled with the subject-specific geometries (Rockenfeller et al., 2020). Maximum muscle

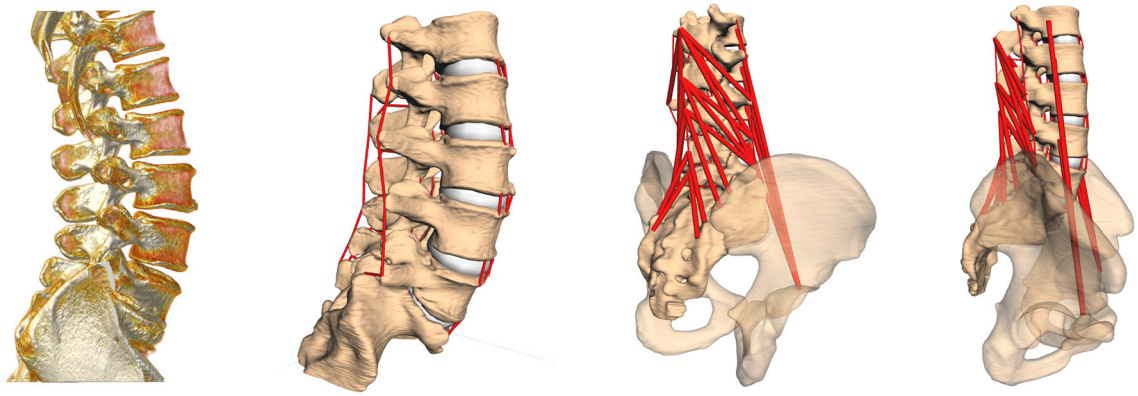

FIGURE 1 | (A) CT image of the lumbar spine, rotated to standing position. **(B)** Computer model based on the subject-specific CT geometries, including passive structures [intervertebral disks (IVDs), facet joints and ligaments]. **(C,D)** In a last step, active force elements, muscles, are inserted into the model according to individual landmarks. The pelvis serves as origin for the *M. psoas major* group.

forces were adapted from the literature (Christophy et al., 2012), with 21 N for strands from the *M. multifidus* and 80 N for strands from the *M. psoas major*.

To ensure maximum possible comparability between our forward dynamic loading simulations, boundary conditions for each spine were standardized as follows: First, the lumber spine was encastered at the sacrum level. Second, the anterior–posterior and medial-lateral translation of vertebra L1 was prohibited to avoid tilting, while the other degrees of freedom were not restricted. This restriction was supposed to represent multi-level stabilizing musculature, which was not implemented here, in order to emphasize the effect of changes in load distribution per change in LL. Third, a load of 500 N, representing the upper body weight (Nachemson, 1981, Table 1), was applied on the center of mass of the vertebral body L1 (see **Figure 2**). Fourth, a standardized forward dynamics simulation of a 2 s time horizon, ensured each spine to reach a final equilibrium state

Fourth, possible influence of muscle activity on spinal loading was investigated for only the *M. multifidus* group, which is known to have a stabilizing effect on the lumbar spine (Macintosh and Bogduk, 1986; Danneels et al., 2001; Ward et al., 2009). Therefore, a total of five different scenarios regarding muscle participation were conducted: (i) "no muscles," denoting the absence of any active or passive muscle force, (ii) "passive muscles ($u = 0$)," denoting the absence of any neural stimulation/excitation $0 \leq u \leq 1$ (cf. Rockenfeller and Günther, 2016), and (iii)–(v) "active muscles ($u = 0.1, 0.25$, or 0.5)," denoting the degree of stimulation of the *M. multifidus* group.

To assess the influence of the sagittal curvature on the simulation results, we defined the LL as a measure parameter to define the degree of lumbar lordosis (Vrtovec et al., 2009). Therefore, the cranial endplates of L1 and SA are virtually extended and their intersection angle in the sagittal plane is determined, cf. **Figure 2D**. From the available data, we obtained a mean LL of 44.0 ± 11.0° with a range between 28.0 and 66.3°, which corresponds well with literature data (Chernukha et al., 1998; Lafage et al., 2009). Smaller LL indicate hypolordotic spines (**Figure 2A**) and larger LL indicate hyperlordotic spines (**Figure 2C**). However, it should be noted that the LL alone does not necessarily constitute a unique measure, as different internal (L2–L5) curvatures may correspond to the same overall LL (Been and Kalichman, 2014, Figure 2). Therefore, we additionally compared the LL to the anatomic parameters that characterize the *sagittal balance*, namely PI, SS, and ΔPILL. The PI is the angle between the lines going from the midpoint of the line connecting the femur heads to the midpoint of the S1 endplate and the normal of the S1 endplate at this midpoint. The SS is the angle between the S1 endplate and the transversal plane (Lafage et al., 2009) (see again **Figure 2D**). The ΔPILL value is the difference between PI and LL. We obtained a PI of 46.3 ± 10.1° (mean ± standard deviation) with a range between 29.5 and 62.5°, a SS of 41.7 ± 7.6° with a range between 24.1 and 56.0°, and a ΔPILL of 2.3 ± 6.6° with a range between −11.2 and 16.0°. **Figure 3** shows the relation between LL and PI ($R^2 = 0.65$), LL and SS ($R^2 = 0.82$), as well as LL and ΔPILL ($R^2 = 0.18$) for our 28 samples. On average, an increase of one degree LL was associated with an increase of ∼0.74° in PI and 0.62° in SS, which well corresponds to literature data—cf. Roussouly et al. (2005, Tables 1, 2) and Naserkhaki et al. (2016, Figure 1). For ΔPILL, we found a decrease of 0.26° per degree LL, which has, to our knowledge, not yet been reported. As only a single hypolordotic spine exhibited a $|\Delta\text{PILL}| > 15°$, we did not perform ΔPILL-dependent analysis, as presented in Senteler et al. (2014), Rothenfluh et al. (2015).

The output quantities, which were assumed to depend on the LL, obtained from our standardized forward dynamic simulations, were (i) the changes in sagittal Cobb angles for all vertebrae between the start ($t = 0$ s, no loading) and the end ($t = 2$ s, loaded equilibrium) of the simulation, (ii) the compressive (z-)forces in the IVDs between two adjacent vertebrae, (iii)

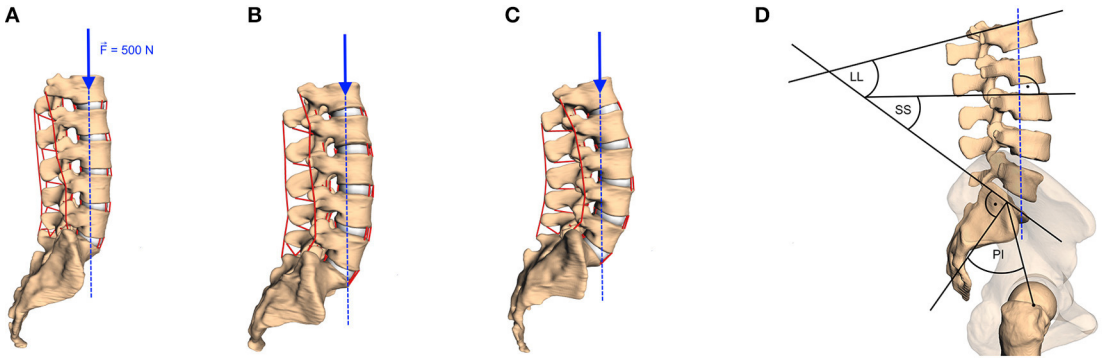

FIGURE 2 | Examples of lumbar spinal curvature: **(A)** hypolordotic (LL= 28°), **(B)** regular (LL= 49.2°), and **(C)** hyperlordotic (LL= 66.3°). The method of calculating the LL, the sacral slope (SS), and the pelvic incident (PI) is sketched in **(D)** and described in the text. A vertical force of 500 N (blue arrows with dashed line of action) was applied on the COM of the vertebral body of L1 in all models.

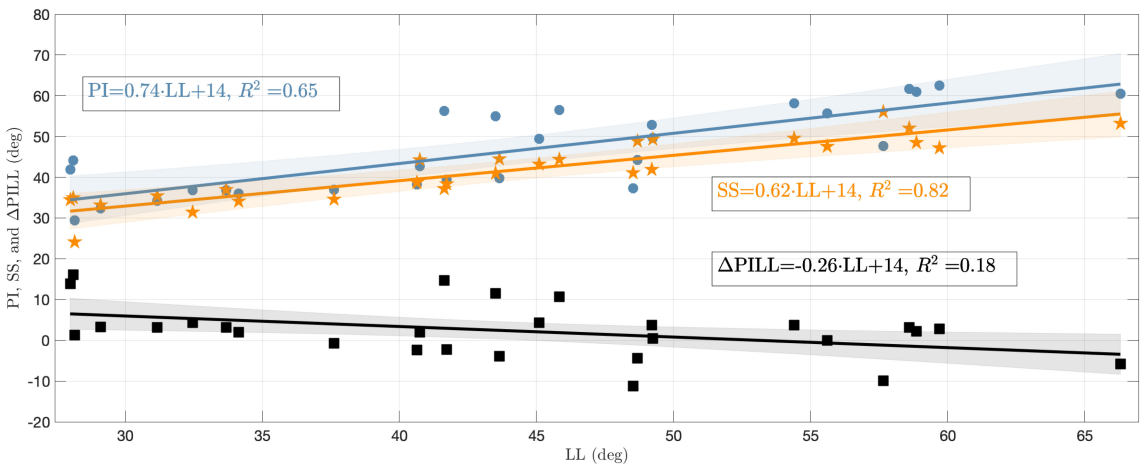

FIGURE 3 | PI, SS, and ΔPILL plotted against LL. The blue circles represent the PI, orange asterisks the SS, and black squares the ΔPILL for the 28 individual lumbar spines. Regressions lines (with confidence bands) are displayed in corresponding colors and their equations as well as coefficients of determination (R^2) are stated in the annotations.

the IVD shear (y-)forces, (iv) the IVD torques around the transversal (x-)axis, and (v) the facet joint forces. To assess the LL dependency of these quantities, a regression line for each vertebra (respectively level) and for each mode was calculated in a least-squares sense. A subsequent significance-of-correlation t-test was carried out, using the test statistic

$$T = \frac{r \cdot \sqrt{n-2}}{\sqrt{1-r^2}} ,$$

where $r = \mathrm{cor}(\mathrm{LL}, Y)$ denotes Pearson's correlation coefficient between LL and the observed quantity Y, and $n = 27$ (number of available spinal models minus one) the degrees of freedom (see Zar, 1972). The corresponding p-value was calculated as

$$p = 2 \cdot \left(1 - F_{t_n}(T)\right) ,$$

where F_{t_n} denotes the cumulative distribution function of the Student's t-distribution with n degrees of freedom. Small p-values indicate that the observed correlation is unlikely under the null hypothesis "$r = 0$," which should thus be rejected. All obtained correlations r along with the corresponding p-values are summarized in Table 1 (**Appendix A**). The resultant slopes s of the regression lines can be calculated by $s = r \cdot \sigma(Y)/\sigma(\mathrm{LL})$, with σ being the standard deviation operator. Uncertainty of the regression analysis is indicated by 95% confidence bands $f(\mathrm{LL}) \pm \omega(\mathrm{LL})$ around the regression line $f(\mathrm{LL})$, with

$$\omega(\mathrm{LL}) = t_{n-2,0.95} \cdot \sigma(Y) \cdot \sqrt{\frac{1}{n} + \frac{\left(\mathrm{LL} - \overline{\mathrm{LL}}\right)^2}{(n-1)^2 \cdot \sigma(LL)^2}} ,$$

where $t_{n-2,0.95}$ denotes the 95%-quantile of the t-distribution with $n-2$ degrees of freedom, and $\overline{\mathrm{LL}}$ the mean value of LL. Slopes for all modes and output quantities, together with their

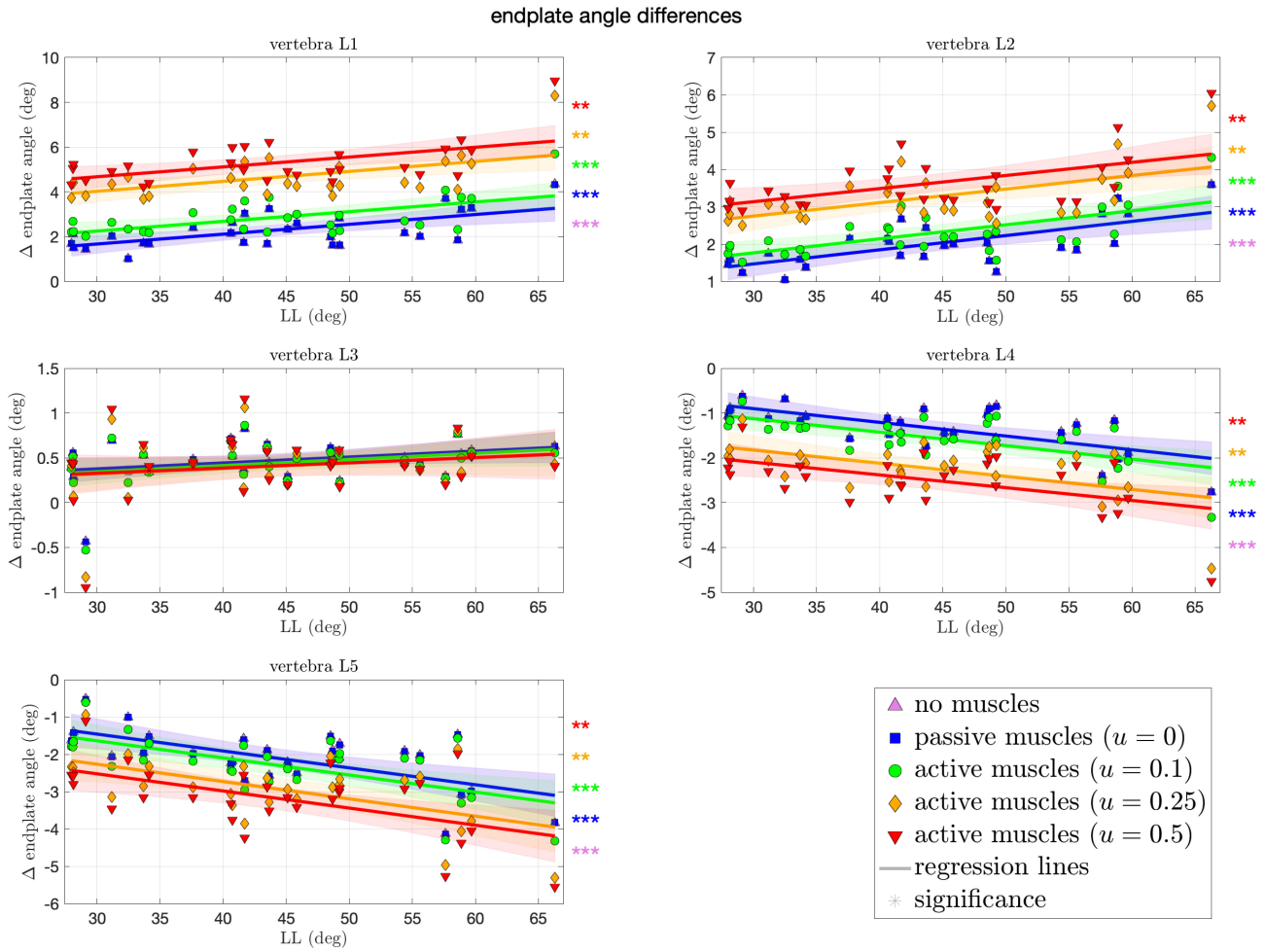

FIGURE 4 | Differences in Cobb angles during compression of all 28 vertebrae against LL. Colors and marker symbols of the data points and the corresponding regression lines consistently correspond to the modes: lilac up-pointing triangles for simulations without muscles involved; blue squares for passive muscles; as well as green circles, orange diamonds, and red down-pointing triangles for muscle stimulation of $u \in \{0.1, 0.25, 0.5\}$, respectively. Confidence bands of the regression are shown as pale areas of the corresponding color. The significance of the statistical test is indicated by alongside asterisks (** = significant with $0.001 \leq p < 0.05$, *** = highly significant with $p < 0.001$).

95% confidence intervals (CI), are listed in Table 2 (likewise **Appendix A**).

3. RESULTS

Orienting the spine upright from supine position, as well as applying loading and possibly muscle forces, changes the initial LL between start ($t = 0\,\mathrm{s}$) and end ($t = 2\,\mathrm{s}$) of the simulation. In **Figure 4**, these changes are quantified for each spinal level and each muscle stimulation protocol. Expectedly, for the mid vertebra L3, no significant changes in the Cobb angle were observed for any muscle stimulation. For the neighboring vertebrae L2 and L4, we observed a moderate, yet (highly) significant, increase, and decrease, respectively, of $\sim 1.5^\circ$ over the whole LL range, i.e., $\sim 0.03^\circ$ change per degree LL (see Table 2 in **Appendix A** for concrete values and CI). This trend is continued for the outer vertebrae L1 and L5, where a higher change of $\sim 2^\circ$ (0.045° per degree LL) increase for L1 and decrease for L5 is observed over the whole LL range. Notably, changes in scenarios with highly stimulated muscles were less significant than for passive or moderately stimulated muscles, indicating a stabilizing effect.

Figure 5 depicts the compressive force resulting at each level of each spinal model at the end of the simulation. These forces ranged from 446–746 N, both at the L5–SA level. For the upper levels L1–L2 and L2–L3, we observed no significant difference across all curvatures. The more caudal the level, the more significant the decrease in force for the cases of no muscles and passive muscles alike, up to $-2.8\,\mathrm{N}$ (CI: $[-4.6, -1]\,\mathrm{N}$) per degree LL at the L5–SA level for high muscle stimulation. In case of highly stimulated muscles, the most significant decrease in compressive force happens at the level L4–L5. Tendencies toward an increase in compressive force with LL were not found at all, although the most hyperlordotic spinal model yielded the highest

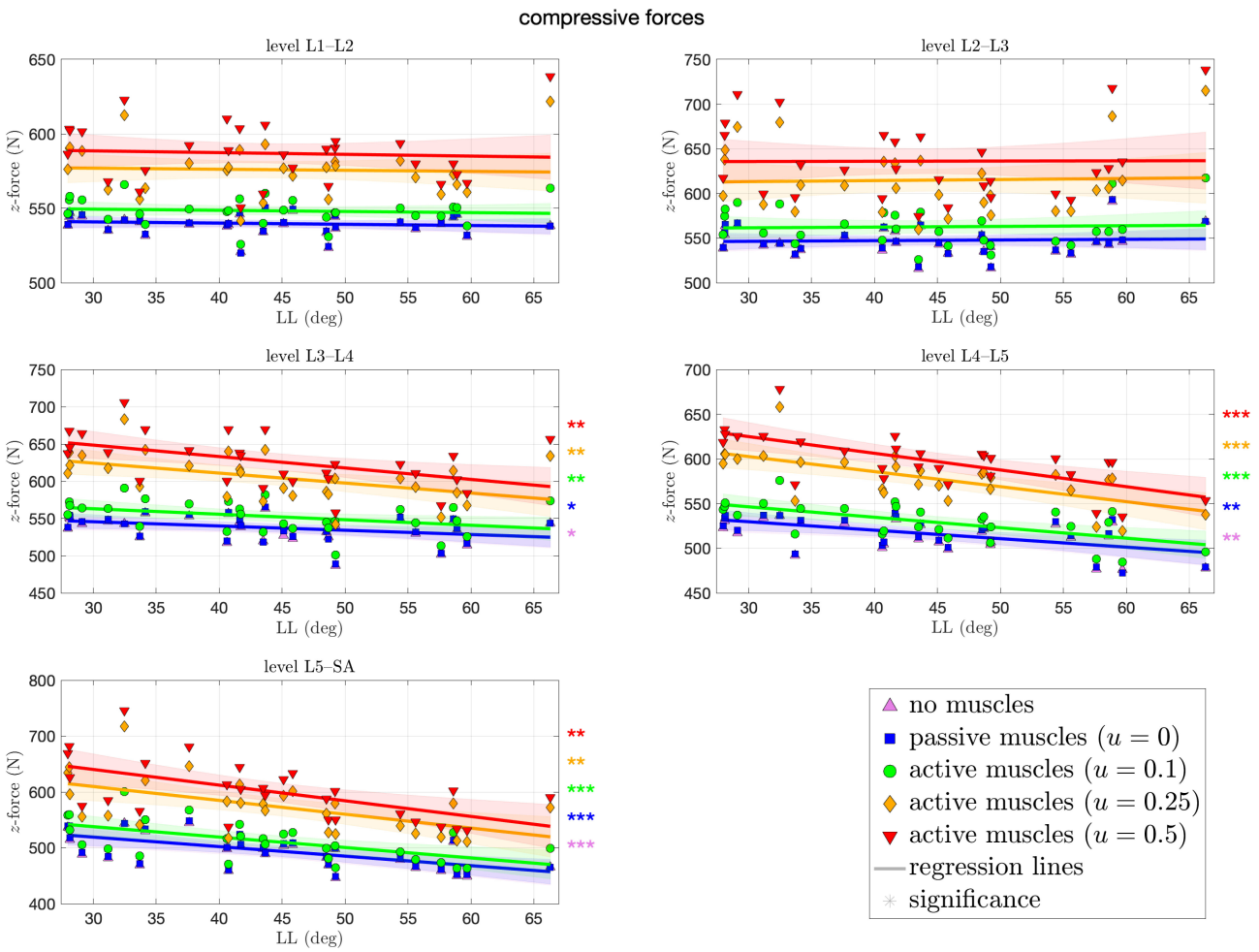

FIGURE 5 | Compressive (*z*-)force between each pair of adjacent vertebrae against lumbar lordosis (LL). Colors and marker symbols of the data points and the corresponding regression lines consistently correspond to the modes: lilac up-pointing triangles for simulations without muscles involved; blue squares for passive muscles; as well as green circles, orange diamonds, and red down-pointing triangles for muscle stimulation of $u \in \{0.1, 0.25, 0.5\}$, respectively. Confidence bands of the regression are shown as pale areas of the corresponding color. The significance of the statistical test is indicated by alongside asterisks (* = tendency with $0.05 \leq p \leq 0.1$, ** = significant with $0.001 \leq p < 0.05$, *** = highly significant with $p < 0.001$).

forces in the upper segments. Throughout all levels, an increase in muscle stimulation yielded absolute higher compressive forces.

Figure 6 depicts the shear forces resulting at each level of each spinal model at the end of the simulation. These forces ranged from −114 N (L1–L2) to 438 N (L5–SA). Contrary to the compressive force, shear forces (highly) significantly decreased (increased in posterior direction) with ∼1.6 N per degree LL at the L1–L2 level. The more caudal the level, the more of an increase in shear force, absolute and with LL, was observed, although significance is only given on the L5–SA level with up to 1.9 N (CI: [−0.14,4] N) per degree LL. Throughout all levels, an increase in muscle stimulation yielded higher anteriorly directed shear forces.

Figure 7 depicts the bending moments around the transversal axis at each level of each spinal model at the end of the simulation. Depending on the degree of muscle stimulation and level, bending moments lie mostly within the range of ±3 Nm, with negative values (indicating forward bending) occur predominantly on the L5–SA level. None of the correlation coefficients was significantly different from zero, i.e., there was no LL dependence. Except for the L4–L5 level, higher muscle stimulation was associated with higher absolute bending moments. Absolute moments around the transversal and longitudinal axes were not significantly different from zero.

Finally, **Figure 8** shows the forces within the sinister (left column of the figure) and dexter (right column) facet joint. On the first glance, we observe in each level and for each mode on each side a trend toward an increase of facet force with LL. This increase is, however, only significant for certain cases, predominantly for the lower levels and lower muscle stimulation, respectively, with an increase of as much as 1.6 N per degree LL at the L5–SA level. Especially on the L1–L2 and L3–L4 level, no significance was found at all. Throughout all levels, an increase in muscle stimulation yielded absolute higher facet forces.

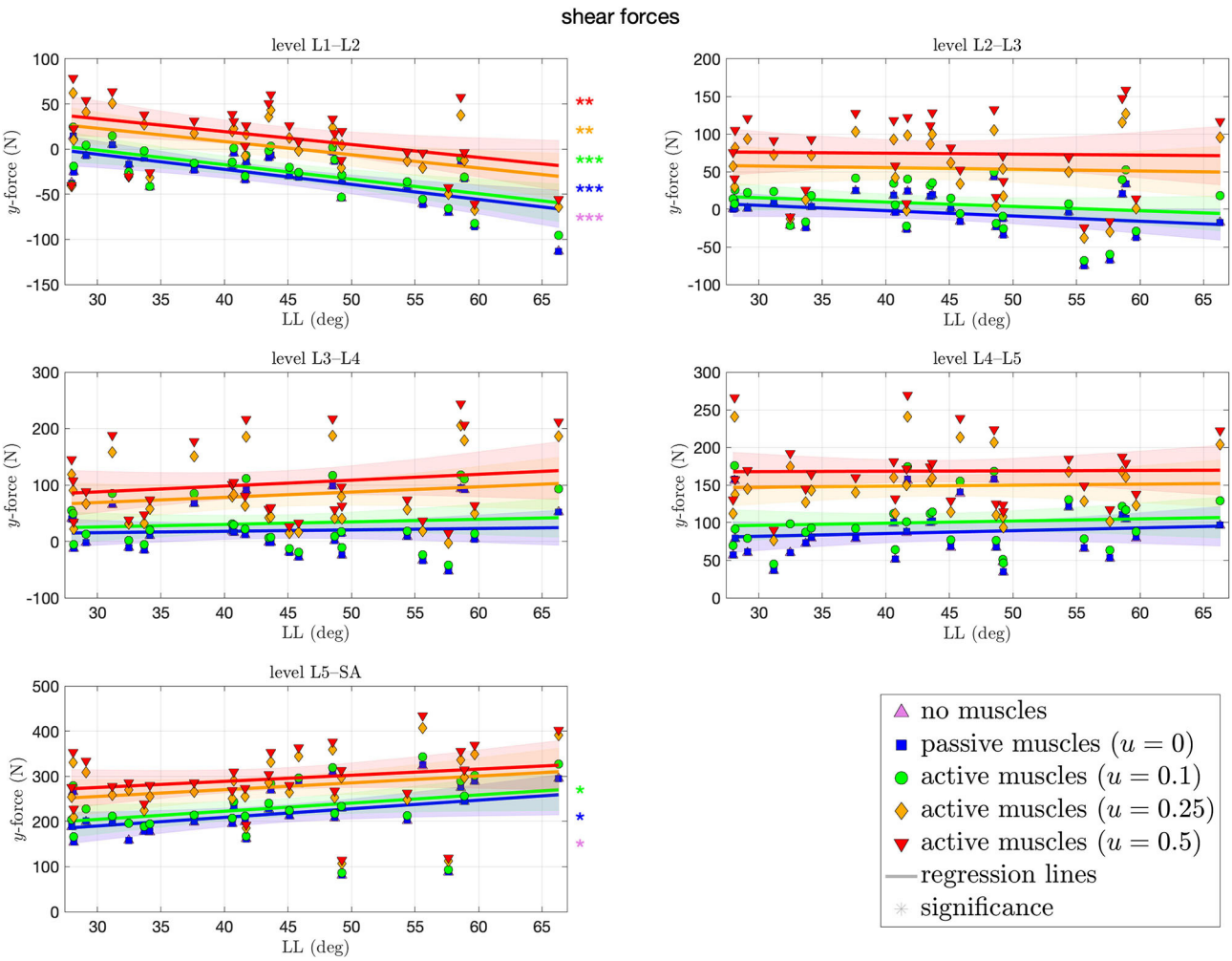

FIGURE 6 | Shear (*y*-)force between each pair of adjacent vertebrae against lumbar lordosis (LL). Colors and marker symbols of the data points and the corresponding regression lines consistently correspond to the modes: lilac up-pointing triangles for simulations without muscles involved; blue squares for passive muscles; as well as green circles, orange diamonds, and red down-pointing triangles for muscle stimulation of $u \in \{0.1, 0.25, 0.5\}$, respectively. Confidence bands of the regression are shown as pale areas of the corresponding color.

4. DISCUSSION

We have shown the effect of varying LL and varying stimulation of the *M. multifidus* on the load distribution within the lumbar spine during forward dynamic compression. Therefore, the CT data from 28 asymptomatic subjects in supine position were transferred into a priorly validated MBS model and underwent standardized loading conditions, representing upright standing. The range of observed LL in our study (28–66.3°) well coincides with prior observations of 28.8–72.9° (Wood et al., 1996, Table 1). Likewise, the changes in LL due to the transition between unloaded supine and loaded standing position consistently account for only a few degrees—cf. **Figure 4** (upper left), Wood et al. (1996), and Meakin et al. (2009). Contrary to existing literature on the influence of curvature on spinal loading (Briggs et al., 2007; Bruno et al., 2012, 2017; Galbusera et al., 2014; Naserkhaki et al., 2016), the novelty of our study lies in the formulation of quantitative statements regarding the LL-dependent load distribution during forward dynamic simulations, e.g., "Per one degree increase in LL, the compressive force within the IVD between L5 and SA decreases by 2.8 N (CI: $[-4.6, -1]$ N)." Of course, our absolute output values have to be treated with caution when comparing them directly to *in vivo* (or more elaborated *in silico*) situations. Yet, this study might serve as an impulse for subsequent quantitative corroborations of conjectured coherences. In the following, we consider clinical applications, depending on patient-specific lordosis, and address the role of muscles in the stabilization of the lumbar spine.

4.1. Clinical Implications of Varying LL

In clinical practice, physicians are mostly faced with hypolordosis (small LL) due to degenerative diseases, e.g., reduced height of the intervertebral disk space or flattening of vertebrae

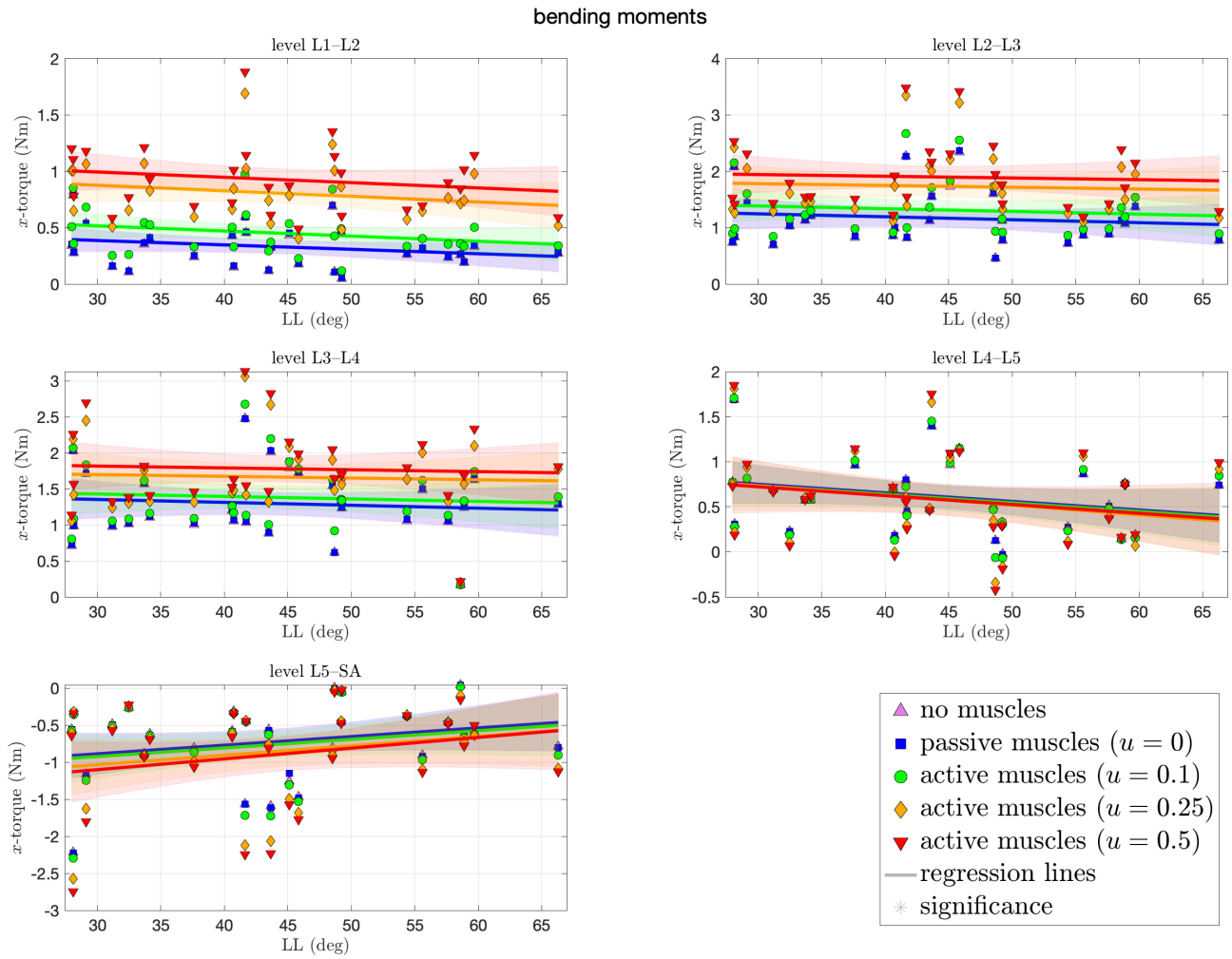

FIGURE 7 | Bending moments (x-torques) around the transversal axis between each pair of adjacent vertebrae against lumbar lordosis (LL). Colors and marker symbols of the data points and the corresponding regression lines consistently correspond to the modes: lilac up-pointing triangles for simulations without muscles involved; blue squares for passive muscles; as well as green circles, orange diamonds, and red down-pointing triangles for muscle stimulation of $u \in \{0.1, 0.25, 0.5\}$, respectively. Confidence bands of the regression are shown as pale areas of the corresponding color.

due to osteoporotic changes. LL is known to decrease with increasing age (Gelb et al., 1995). With lower LL, the gravity line is located anteriorly, away from its ideal position between the hip joints. As a consequence, compressive force on the intervertebral disks increases (see also our **Figure 5**), which may favor discopathies that result in further decrease of the LL. A recent meta-analysis of 13 studies with a total of 796 patients (Chun et al., 2017) found that patients with small LL tend to suffer more often from low back pain (independent of the underlying pathology). In a subgroup analysis of five studies, comparing individuals with disk herniation or severe degeneration with a healthy control group, it was further observed that this condition is more likely to occur in individuals with hypolordosis.

Contrary, in a hyperlordotic spine (high LL), the gravity line is located dorsally and thus close to the posterior spinal structures, such as the facet joints and spinous processes. This may favor diseases, such as posterior facets arthritis, Baastrup disease, and spondylolisthesis (Roussouly and Pinheiro-Franco, 2011). Accordingly, we observed in our model a tendency of increasing facet force with increasing LL (see **Figure 8**). These findings coincide with clinical investigations (Sahin et al., 2015), which found a significant correlation of high LL values with the degree of lumbar facet joint degeneration in CT scans of 723 patients.

Sagittal imbalance in general has been shown to correlate with clinical symptoms (Glassman et al., 2005; Senteler et al., 2014; Rothenfluh et al., 2015). Particularly, an anterior misalignment of C7, and thus of the thoracic weight, results in high compression mainly caused by compensatory muscular forces (Galbusera et al., 2013). This effect is less prominent, yet still identifiable, for backward misalignment (Bassani et al., 2019). Hence, careful evaluation of the individual LL and sagittal profile of patients is of utmost importance to avoid

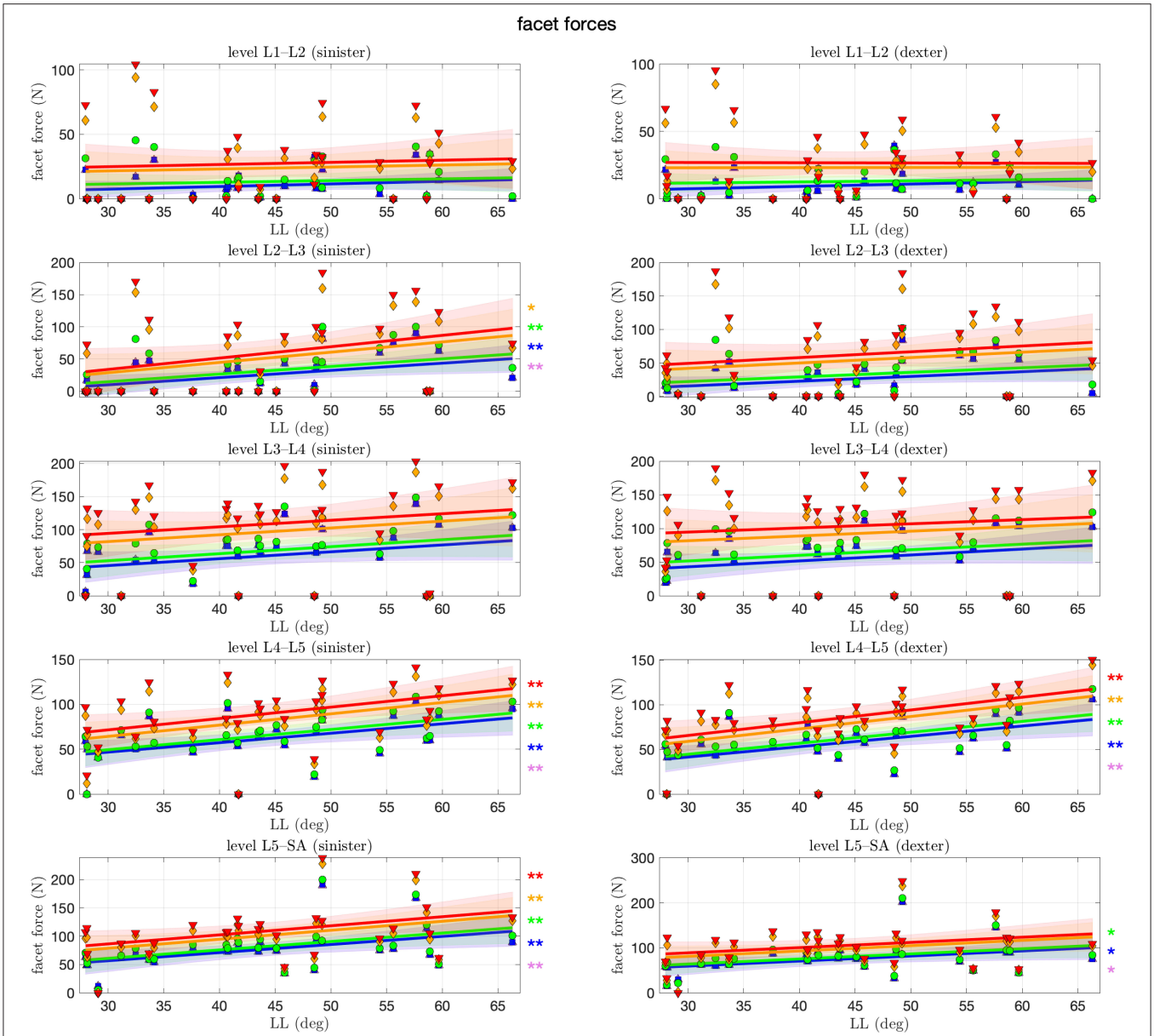

FIGURE 8 | Facet force between each pair of adjacent articular facets against lumbar lordosis (LL). Colors and marker symbols of the data points and the corresponding regression lines consistently correspond to the modes: lilac up-pointing triangles for simulations without muscles involved; blue squares for passive muscles; as well as green circles, orange diamonds, and red down-pointing triangles for muscle stimulation of $u \in \{0.1, 0.25, 0.5\}$, respectively. The significance of the statistical test is indicated by alongside asterisks (* = tendency with $0.05 \leq p \leq 0.1$, ** = significant with $0.001 \leq p < 0.05$).

acceleration of degenerative processes. Although lumbar posture can be influenced to a certain extent by muscle hypertrophy training (Scannell and McGill, 2003), in severe cases surgical correction might be required. In general, utilization of subject-specific lumbar spine models might have the ability to assist surgeons to correctly restore the individual balance. These models should be based on (supine) CT data and (standing) radiographs to allow precise measurements of anatomical parameters, such as PI, LL, and other (multi-level) Cobb angles.

4.2. The Role of *M. multifidus* in Stabilizing the Lumbar Spine

Lower back muscles, and especially the *M. multifidus*, play an important role in stabilizing the lumbar spine (Macintosh and Bogduk, 1986; Goel et al., 1993; Kaigle et al., 1995; Wilke et al., 1995; Panjabi, 1999; Danneels et al., 2001; Ward et al., 2009). For example, lower back pain patients were shown to have significantly smaller cross-sectional area of their *M. multifidus* (Danneels et al., 2000; Kamaz et al., 2007; Hides et al., 2008) and were less able to voluntarily contract the *M. multifidus*

in atrophic segments (Wallwork et al., 2009). This becomes particularly crucial for hypolordotic spines, where holding forces in posterior structures are required. As we have shown in **Figure 4**, LL increases with increasing muscle force, which is consistent to findings regarding the correlation of muscle volume and LL (Meakin and Aspden, 2012; Meakin et al., 2013).

As we introduced the varying stimulation of the *M. multifidus* as a second ceteris paribus condition in our model, the influence of varying muscle force on the load distribution could be assessed. In **Figures 5–8**, we observed an increase in compressive and shear forces as well as facet forces with increasing muscle stimulation. However, the significance of the LL dependence of these forces were smaller for higher stimulation values, consistent to observations regarding the application of follower load (Patwardhan et al., 1999). Hence, higher muscle forces seem to compensate for structural deficiencies, see again Scannell and McGill (2003). These findings underline the important interplay between LL and muscle forces (primarily of the *M. multifidus*) in the development of degenerative spinal diseases. Thus, future individualized therapy planning should benefit from careful consideration of the delicate equilibrium of individual curvature and muscle strength.

5. LIMITATIONS AND PERSPECTIVES

Several simplifying assumptions regarding our model approach might have an influence on the absolute values of angles, forces, and bending moments that were presented in **Figures 4–8**. First, our model only consists of pelvis, lumbar vertebrae, IVDs, ligaments, facet joints, and two muscle groups. Yet, geometries and muscle as well as ligament insertion points were extracted from subject-specific CT data. Second, the orientation of the spine with respect to a horizontal L3 endplate in general does not account for real-life variation. As no vertebra C7 was available for most spines, a more realistic balance with respect to the C7 plumb-line could not be performed. Third, as neither data about subject-specific weight or muscle cross-section area was available, loading and muscle forces had to be chosen generically.

For each of the mentioned limitations, it might be worth to conduct a sensitivity analysis regarding the LL dependence of the load distribution. Regarding additional structures and muscles, a quantitative assessment of LL-dependent stabilizing effects could lead to individual muscle hypertrophy training plans toward appropriate posture. Regarding the vertebral orientation, a systematic variation of spinal alignment, as a second independent variable besides LL, might yield configurations with particular high (or low) loading in certain structures that could be connected to lower back pain. Regarding the loading protocol, the herein investigated compression ought to be replaced by common movement tasks, e.g., flexion-extension, equipped with as much individualized information as available.

6. CONCLUSION

The load distribution and stabilizing effect of the *M. multifidus* for different LL were investigated by using simplified forward dynamic MBS models of the lumbar spine. Based on clinical CT data, 28 models with subject-specific geometries, including passive structures as well as two muscle groups, were constructed. To emphasize a possible dependence of load distribution on the LL, standardized orientation and loading conditions as well as generic parameters for passive and active structures were used. Resulting compressive and shear IVD forces, IVD bending moments, and facet forces were displayed and quantitatively connected to LL via the corresponding correlations. Tendentiously, IVD compressive forces in hypolordotic lumbar spines were higher than in hyperlordotic lumbar spines. In contrast, facet joint forces increased with increasing LL. Alterations in shear forces depended on the vertebral level and bending moments did not show any significant change at all. Simulations with higher stimulation of the *M. multifidus* resulted in less significant load distributions, which may be explained by the stabilizing effect of these muscles. The clinical relevance of our findings was discussed.

DATA AVAILABILITY STATEMENT

The data analyzed in this study is subject to the following licenses/restrictions: medical CT data of patients. Requests to access these datasets should be directed to andreas.mueller@uni-koblenz.de.

AUTHOR CONTRIBUTIONS

AM performed the model calculations, modified the MBS model, and drafted the scaffold of the manuscript. RR performed the statistical analysis and supervised the writing. ND developed the basic MBS model components, particularly the geometries on the basis of medical image data. MK and SK equally contributed to the identification of ligament and muscle insertion points as well as the discussion from a medical point of view. AA contributed to the biomechanical discussion and conducted a final review of the manuscript. KG helped in developing the model, provided the MBS graphics, and conducted a final review of the manuscript. All authors contributed to the article and approved the submitted version.

FUNDING

AM was supported by funding from Mechanical Systems Engineering Laboratory, EMPA-Swiss Federal Laboratories for Materials Science and Technology, Duebendorf, Switzerland.

SUPPLEMENTARY MATERIAL

The Supplementary Material for this article can be found online at: https://www.frontiersin.org/articles/10.3389/fbioe.2021.661258/full#supplementary-material

REFERENCES

Bassani, T., Casaroli, G., and Galbusera, F. (2019). Dependence of lumbar loads on spinopelvic sagittal alignment: an evaluation based on musculoskeletal modeling. *PLoS ONE* 14:e0207997. doi: 10.1371/journal.pone.0207997

Been, E., and Kalichman, L. (2014). Lumbar lordosis. *Spine J.* 14, 87–97. doi: 10.1016/j.spinee.2013.07.464

Briggs, A. M., van Dieën, J. H., Wrigley, T. V., Greig, A. M., Phillips, B., Lo, S. K., et al. (2007). Thoracic kyphosis affects spinal loads and trunk muscle force. *Phys. Ther.* 87, 595–607. doi: 10.2522/ptj.20060119

Bruno, A., Anderson, D., D'Agostino, J. M., and Bouxsein, M. (2012). The effect of thoracic kyphosis and sagittal plane alignment on vertebral compressive loading. *J. Bone Miner. Res.* 27, 2144–2151. doi: 10.1002/jbmr.1658

Bruno, A. G., Mokhtarzadeh, H., Allaire, B. T., Velie, K. R., de Paolis Kaluza, M. C., Anderson, D. E., et al. (2017). Incorporation of CT–based measurements of trunk anatomy into subject–specific musculoskeletal models of the spine influences vertebral loading predictions. *J. Orthopaed. Res.* 35, 2164–2173. doi: 10.1002/jor.23524

Chernukha, K. V., Daffner, R. H., and Reigel, D. H. (1998). Lumbar lordosis measurement. A new method versus Cobb technique. *Spine* 23, 74–79. doi: 10.1097/00007632-199801010-00016

Christophy, M., Faruk, S. N. A., Lotz, J. C., and O'Reilly, O. M. (2012). A musculoskeletal model for the lumbar spine. *Biomech. Model. Mechanobiol.* 11, 19–34. doi: 10.1007/s10237-011-0290-6

Chun, S. W., Lim, C. Y., Kim, K., Hwang, J., and Chung, S. G. (2017). The relationships between low back pain and lumbar lordosis: A systematic review and meta-analysis. *The Spine Journal* 17, 1180–1191. doi: 10.1016/j.spinee.2017.04.034

Cobb, J. R. (1948). Outline for the study of scoliosis. The American Academy of Orthopedic Surgeons Instructional Course Lectures, volume 5. Ann Arbor, MI: Edwards.

Damm, N., Rockenfeller, R., and Gruber, K. (2019). Lumbar spinal ligament characteristics extracted from stepwise reduction experiments allow for preciser modeling than literature data. *Biomechanics and Modeling in Mechanobiology* 19, 893–910. doi: 10.1007/s10237-019-01259-6

Danneels, L., Vanderstraeten, G., Cambier, D., Witvrouw, E., and de Cuyper, H. (2000). CT imaging of trunk muscles in chronic low back pain patients and healthy control subjects. *European Spine Journal* 9, 266–272. doi: 10.1007/s005860000190

Danneels, L., Vanderstraeten, G., Cambier, D., Witvrouw, E., Stevens, V., and de Cuyper, H. (2001). A functional subdivision of hip, abdominal, and back muscles during asymmetric lifting. *Spine* 26, 114–121. doi: 10.1097/00007632-200103150-00003

Galbusera, F., Brayda-Bruno, M., Costa, F., and H. J. Wilke (2014). Numerical evaluation of the correlation between the normal variation in the sagittal alignment of the lumbar spine and the spinal loads. *Journal of Orthopaedic Research* 32, 537–544. doi: 10.1002/jor.22569

Galbusera, F., H. J. Wilke, Brayda-Bruno, M., Costa, F., and Fornari, M. (2013). Influence of sagittal balance on spinal lumar loads: a numerical approach. *Clin. Biomech.* 28, 370–377. doi: 10.1016/j.clinbiomech.2013.02.006

Gelb, D. E., Lenke, L. G., Bridwell, K. H., Blanke, K., and McEnery, K. W. (1995). An analysis of sagittal spinal alignment in 100 asymptomatic middle and older aged volunteers. *Spine* 20, 1351–1358. doi: 10.1097/00007632-199520120-00005

Gezelbash, F., Shirazi-Adl, A., Arjmand, N., El-Ouaaid, Z., Plamondon, A., and Meakin, J. R. (2016). Effects of sex, age, body height and body weight on spinal loads: sensitivity analyses in a subject-specific trunk muscle musculoskeletal model. *J. Biomech.* 49, 3492–3501. doi: 10.1016/j.jbiomech.2016.09.026

Glassman, S. D., Bridwell, K., Dimar, J. R., Horton, W., Berven, S., and Schwab, F. (2005). The impact of positive sagittal balance in adult spinal deformity. *Spine* 30, 2024–2029. doi: 10.1097/01.brs.0000179086.30449.96

Goel, V. G., Kong, W., Han, J. S., Weinstein, J. N., and Gilbertson, L. G. (1993). A combined finite element and optimization investigation of lumbar spine mechanics with and without muscles. *Spine* 18, 1531–1541. doi: 10.1097/00007632-199318110-00019

Hajihosseinali, M., Arjmand, N., and Shirazi-Adl, A. (2015). Effect of body weight on spinal loads in various activities: a personalized biomechanical modeling approach. *J. Biomech.* 48, 276–282. doi: 10.1016/j.jbiomech.2014.11.033

Hides, J., Gilmore, C., Stanton, W., and Bohlscheid, E. (2008). Multifidus size and symmetry among chronic LBP and healthy asymptomatic subjects. *Manual Ther.* 13, 43–49. doi: 10.1016/j.math.2006.07.017

Jackson, R. P., and McManus, A. C. (1994). Radiographic analysis of sagittal plane alignment and balance in standing volunteers and patients with low back pain matched for age, sex, and size a prospective controlled clinical study. *Spine* 19, 1611–1618. doi: 10.1097/00007632-199407001-00010

Jentzsch, T., Geiger, J., König, M. A., and Werner, C. M. L. (2017). Hyperlordosis is associated with facet joint pathology at the lower lumar spine. *Clin. Spine Surg.* 30, 129–135. doi: 10.1097/BSD.0b013e3182aab266

Kaigle, A. M., Holm, S. H., and Hansson, T. H. (1995). Experimental instability in the lumbar spine. *Spine* 20, 421–430. doi: 10.1097/00007632-199502001-00004

Kamaz, M., Kireşi, D., Oğuz, H., Emlik, D., and Levendoğlu, F. (2007). CT measurement of trunk muscle areas in patients with chronic low back pain. *Diagn. Interv. Radiol.* 13, 144–148.

Keller, T. S., Colloca, C. J., Harrison, D. E., Harrison, D. D., and Janik, T. J. (2005). Influence of spine morphology on intervertebral disc loads and stresses in asymptomatic adults: Implications for the ideal spine. *Spine J.* 5, 297–309. doi: 10.1016/j.spinee.2004.10.050

Lafage, V., Schwab, F., Patel, A., Hawkinson, N., and Farcy, J. P. (2009). Pelvic tilt and truncal inclination: two key radiographic parameters in the setting of adults with spinal deformity. *Spine* 34, E599–E606. doi: 10.1097/BRS.0b013e3181aad219

Le Huec, J. C., Thompson, W., Mohsinaly, Y., Barrey, C., and Faundez, A. (2019). Sagittal balance of the spine. *Eur. Spine J.* 28, 1889–1905. doi: 10.1007/s00586-019-06083-1

Macintosh, J. E., and Bogduk, N. (1986). The biomechanics of the lumbar multifidus. *Clin. Biomech.* 1, 202–213. doi: 10.1016/0268-0033(86)90147-6

Meakin, J. R., and Aspden, R. M. (2012). Modelling the effect of variation in sagittal curvature on the force required to produce a follower load in the lumbar spine. *J. Mech. Med. Biol.* 12:1250013. doi: 10.1142/S0219519412004466

Meakin, J. R., Fulford, J., Seymour, R., Welsman, J. R., and Knapp, K. M. (2013). The relationship between sagittal curvature and extensor muscle volume in the lumbar spine. *J. Anat.* 222, 608–614. doi: 10.1111/joa.12047

Meakin, J. R., Gregory, J. S., Aspden, R. M., Smith, F. W., and Gilbert, F. J. (2009). The intrinsic shape of the human lumbar spine in the supine, standing and sitting postures: characterization using an active shape model. *J. Anat.* 215, 206–211. doi: 10.1111/j.1469-7580.2009.01102.x

Nachemson, A. L. (1981). Disc pressure measurements. *Spine* 6, 93–97. doi: 10.1097/00007632-198101000-00020

Naserkhaki, S., Jaremko, J. L., and El-Rich, M. (2016). Effects of inter-individual lumbar spine geometry variation on load-sharing: geometrically personalized finite element study. *J. Biomech.* 49, 2909–2917. doi: 10.1016/j.jbiomech.2016.06.032

Panjabi, M. M. (1999). The stabilizing system of the spine. Part I. Function, dysfunction, adaption, and enhancement. *J. Spinal Disord. Tech.* 5, 383–389. doi: 10.1097/00002517-199212000-00001

Patwardhan, A. G., Havey, R. M., Meade, K. P., Lee, B., and Dunlap, B. (1999). A follower load increases the load-carrying capacity of the lumbar spine in compression. *Spine* 24, 1003–1009. doi: 10.1097/00007632-199905150-00014

Rockenfeller, R., and Günther, M. (2016). Extracting low-velocity concentric and eccentric dynamic muscle properties from isometric contraction experiments. *Mathematical Biosciences* 278, 77–93. doi: 10.1016/j.mbs.2016.06.005

Rockenfeller, R., Müller, A., Damm, N., Kosterhon, M., Kantelhardt, S. R., Frank, R., et al. (2020). Muscle-driven and torque-driven centrodes during modeled flexion of individual lumbar spines are disparate. *Biomech. Model. Mechanobiol.* 20, 267–279. doi: 10.1007/s10237-020-01382-9

Rothenfluh, D. A., Mueller, D. A., Rothenfluh, E., and Min, K. (2015). Pelvic incidence-lumbar lordosis mismatch predisposes to adjacent segment disease after lumbar spinal fusion. *Eur. Spine J.* 24, 1251–1258. doi: 10.1007/s00586-014-3454-0

Roussouly, P., Gollogly, S., Berthonnaud, E., and Dimnet, J. (2005). Classification of the normal variation in the sagittal alignment of the human lumbar spine and pelvis in standing position. *Spine* 30, 346–353. doi: 10.1097/01.brs.0000152379.54463.65

Roussouly, P., and Pinheiro-Franco, J. L. (2011). Biomechanical analysis of the spino-pelvic organization and adaptation in pathology. *Eur. Spine J.* 20, S609–S618. doi: 10.1007/s00586-011-1928-x

Rupp, T. K., Ehlers, W., Karajan, N., Günther, M., and Schmitt, S. (2015). A forward dynamics simulation of human lumbar spine flexion predicting the load sharing of intervertebral discs, ligaments, and muscles. *Biomech. Model. Mechanobiol.* 14, 1081–1105. doi: 10.1007/s10237-015-0656-2

Sahin, M. S., Ergün, A., and Aslan, A. (2015). The relationship between osteoarthritis of the lumbar facet joints and lumbosacropelvic morphology. *Spine* 40, E1058–E1062. doi: 10.1097/BRS.0000000000001070

Scannell, J. P., and McGill, S. M. (2003). Lumbar posture-should it, and can it, be modified? A study of passive tissue stiffness and lumbar position during activities of daily living. *Phys. Ther.* 83, 907–917. doi: 10.1093/ptj/83.10.907

Schünke, M., Schulte, E., Schumacher, U., Voll, M., and Wesker, K. (2015). *Prometheus Lernatlas der Anatomie*. Stuttgart: Thieme.

Senteler, M., Weisse, B., Snedeker, J. G., and Rothenfluh, D. A. (2014). Pelvic incidence–lumbar lordosis mismatch results in increased segmental joint loads in the unfused and fused lumbar spine. *Eur. Spine J.* 23, 1384–1393. doi: 10.1007/s00586-013-3132-7

Shirazi-Adl, A., Sadouk, S., Parnianpour, M., Pop, D., and El-Rich, M. (2002). Muscle force evaluation and the role of posture in human lumbar spine under compression. *Eur. Spine J.* 11, 519–526. doi: 10.1007/s00586-002-0397-7

Vrtovec, T., Pernus, F., and Likar, B. (2009). A review of methods for quantitative evaluation of spinal curvature. *Eur. Spine J.* 18, 593–607. doi: 10.1007/s00586-009-0913-0

Wallwork, T. L., Stanton, W. R., Freke, M., and Hides, J. A. (2009). The effect of chronic low back pain on size and contraction of the lumbar multifidus muscle. *Manual Ther.* 14, 496–500. doi: 10.1016/j.math.2008.09.006

Ward, S. R., Tomiya, A., Regev, G. J., Thacker, B. E., Benzl, R. C., Kim, C. W., et al. (2009). Passive mechanical properties of the lumbar multifidus muscle support its role as a stabilizer. *J. Biomech.* 42, 1384–1389. doi: 10.1016/j.jbiomech.2008.09.042

White, A. A. III, and Panjabi, M. M. (1990). *Clinical Biomechanics of the Spine*, Vol. 2. Philadelphia, PA: JB Lippincott Company.

Wilke, H. J., Neef, P., Caimi, M., Hoogland, T., and Cleas, L. E. (1999). New *in vivo* measurements of pressures in the intervertebral discs in daily life. *Spine* 24, 755–762. doi: 10.1097/00007632-199904150-00005

Wilke, H. J., Wolf, S., Claes, L. E., Arand, M., and Wiesend, A. (1995). Stability increase of the lumbar spine with different muscle groups. A biomechanical *in vitro* study. *Spine* 20, 192–198. doi: 10.1097/00007632-199501150-00011

Wood, K. B., Kos, P., Schendel, M., and Persson, K. (1996). Effect of patient position on the sagittal-plane profile of the thoracolumbar spine. *J. Spinal Disord.* 9, 165–169. doi: 10.1097/00002517-199604000-00014

Zar, J. H. (1972). Significance testing of the Spearman rank correlation coefficient. *J. Am. Stat. Assoc.* 67, 578–580. doi: 10.1080/01621459.1972.10481251

Conflict of Interest: The authors declare that the research was conducted in the absence of any commercial or financial relationships that could be construed as a potential conflict of interest.

frontiers in Bioengineering and Biotechnology

ORIGINAL RESEARCH
published: 17 June 2021
doi: 10.3389/fbioe.2021.660013

Sensitivity of Intervertebral Disc Finite Element Models to Internal Geometric and Non-geometric Parameters

*Yuekang Du[1], Saman Tavana[1], Tamanna Rahman[1], Nicoleta Baxan[2], Ulrich N. Hansen[1] and Nicolas Newell[1]**

[1] Biomechanics Group, Department of Mechanical Engineering, Imperial College London, London, United Kingdom,
[2] Biological Imaging Centre, Central Biomedical Services, Imperial College London, London, United Kingdom

Finite element models are useful for investigating internal intervertebral disc (IVD) behaviours without using disruptive experimental techniques. Simplified geometries are commonly used to reduce computational time or because internal geometries cannot be acquired from CT scans. This study aimed to (1) investigate the effect of altered geometries both at endplates and the nucleus-anulus boundary on model response, and (2) to investigate model sensitivity to material and geometric inputs, and different modelling approaches (graduated or consistent fibre bundle angles and glued or cohesive inter-lamellar contact). Six models were developed from 9.4 T MRIs of bovine IVDs. Models had two variations of endplate geometry (a simple curved profile from the centre of the disc to the periphery, and precise geometry segmented from MRIs), and three variations of NP-AF boundary (linear, curved, and segmented). Models were subjected to axial compressive loading (to 0.86 mm at a strain rate of 0.1/s) and the effect on stiffness and strain distributions, and the sensitivity to modelling approaches was investigated. The model with the most complex geometry (segmented endplates, curved NP-AF boundary) was 3.1 times stiffer than the model with the simplest geometry (curved endplates, linear NP-AF boundary), although this difference may be exaggerated since segmenting the endplates in the complex geometry models resulted in a shorter average disc height. Peak strains were close to the endplates at locations of high curvature in the segmented endplate models which were not captured in the curved endplate models. Differences were also seen in sensitivity to material properties, graduated fibre angles, cohesive rather than glued inter-lamellar contact, and NP:AF ratios. These results show that FE modellers must take care to ensure geometries are realistic so that load is distributed and passes through IVDs accurately.

Keywords: intervertebral disc, finite element model, magnetic resonance imaging, cohesive elements, sensitivity

OPEN ACCESS

Edited by:
Grace D. O'Connell, University of California, Berkeley, United States

Reviewed by:
John Peloquin, University of Delaware, United States
Alicia R. Jackson, University of Miami, United States

****Correspondence:***
Nicolas Newell
n.newell09@imperial.ac.uk

Specialty section:
This article was submitted to Biomechanics, a section of the journal Frontiers in Bioengineering and Biotechnology

Received: *28 January 2021*
Accepted: *25 May 2021*
Published: *17 June 2021*

Citation:
Du Y, Tavana S, Rahman T, Baxan N, Hansen UN and Newell N (2021) Sensitivity of Intervertebral Disc Finite Element Models to Internal Geometric and Non-geometric Parameters. Front. Bioeng. Biotechnol. 9:660013. doi: 10.3389/fbioe.2021.660013

INTRODUCTION

Intervertebral discs (IVDs) lie between vertebra in the spine and act to distribute loading while allowing the spine to bend and flex (Bogduk, 2005; Adams and Roughley, 2006). The IVD consists of the anulus fibrosus (AF), nucleus pulposus (NP) and the endplates that enclose the NP and AF above and below. As the IVD degenerates, its height reduces (Adams et al., 1987), the relative ratio

of NP to AF cross-sectional area decreases (Adams et al., 1996), and the stiffness of individual components increases (Iatridis et al., 1998, 1999; O'Connell et al., 2009). Previously, these changes have been investigated using experimental techniques, however, it is challenging to measure stresses and strains within the IVD without disrupting it, and therefore, there has been an increasing trend towards the use of FE models for investigations of this kind.

Previous FE studies on human lumbar spines have explored the effect of altering geometric features of the IVD (Robin et al., 1994; Natarajan and Andersson, 1999; Noailly et al., 2007; Meijer et al., 2011; Niemeyer et al., 2012). All of these studies have found the disc height significantly affects the response of the IVD, and some have shown that NP position (Noailly et al., 2007), and endplate width and depth (Natarajan and Andersson, 1999; Meijer et al., 2011; Niemeyer et al., 2012) are important factors. Similarly, the nature of the contact between lamella in the AF in FE models has been shown to affect model response (Adam et al., 2015), and a method of using cohesive contact between lamella has been proposed by Mengoni et al. (2015). Recent FE studies on bovine (Mengoni et al., 2017), and human discs (Yang et al., 2019), have demonstrated the importance of the NP:AF ratio, few studies have investigated the effect of changes to the internal IVD geometry. This is likely due to the challenges associated with defining the boundary between the NP and AF. Recent advances in magnetic resonance imaging (MRI) allow accurate internal geometries to be identified (O'Connell et al., 2011; Tavana et al., 2020, 2021). In some cases, these geometries are substantially different to those that are used in current FE models, and the effect of these inaccuracies has not previously been investigated.

The aim of this study is to use high resolution MRI scans, and FE models to investigate the effect of altered geometries both at the boundary between the NP and the AF, and at the endplates on the response of the IVD. Specific aims include quantifying the effect of altered geometries on IVD;

(a) stiffness and strain distributions
(b) sensitivity to altered material properties
(c) sensitivity to graduated fibre bundle angles (increasing from outer to inner AF)
(d) sensitivity to modelling inter-lamellar behaviour with cohesive contact
(e) sensitivity to altered NP:AF ratio.

MATERIALS AND METHODS

For this study, a vertebral body—disc—vertebral body specimen was dissected from the most caudal disc of a fresh-frozen bovine tail acquired from a local butcher. Soft tissue was removed before being scanned on a 9.4 T MRI scanner (Bruker BioSpec, Ettlingen, Germany) equipped with a volume RF resonator [T_2-weighted RARE sequence, coronal plane, resolution = (90 × 90) μm^2, slice thickness = 800 μm, 17 min scan time], such that internal geometries could be acquired.

Experimental Data

Experimental data, against which the FE models could be compared was obtained from previous literature (Newell et al., 2017). During these experiments ten bovine IVDs were axially compressed to 15% strain at a range of strain rates and the force-displacement response of each sample was recorded. For comparison purposes only data from mid-range strain rates (0.1/s) were used in this study.

FE Model Development

Non-linear, implicit, axisymmetric FE models using Marc (v2017, MSC Software, California, United States) were developed based on measurements from the mid-coronal slice of the high-resolution MRI images (**Figure 1A**).

Geometry

Six FE models were developed, with two variations of endplate geometry (simple and segmented), and three variations of NP-AF boundary (linear, curved, and segmented) (**Figure 2**). Since the bovine tail disc is almost perfectly round all FE models were axisymmetric (Adam et al., 2015). The simple endplate geometries (Model 1.1, 1.2, and 1.3) had central and peripheral IVD heights measured from the mid-coronal MRI slice but a smooth curve between these two points. The segmented endplate geometries (Model 2.1, 2.2, and 2.3) were obtained from the mid-coronal MRI slice using Mimics (v16, Materialise, Leuven, Belgium) but also had central and peripheral IVD heights that matched those of the simple endplate geometry models. The linear NP-AF boundary models had a vertical, linear boundary between the NP and AF, while the curved NP-AF boundary models had a quadratically polynomial boundary. Both the linear, and curved NP-AF boundary models had a NP:AF ratio determined from measurements at the mid-height of the mid-coronal slice of the IVD. As with the endplates, the segmented NP-AF boundary was obtained from the mid-coronal MRI slice using Mimics.

The AF was modelled with rebar elements to represent the collagen fibre bundles, surrounded by non-linear solid quadrilateral elements to represent the AF ground matrix. For the models with segmented NP-AF boundary, each lamella layer was segmented, while the number of rebar layers for the linear and curved models was set to the number of layers that could be identified on the mid-coronal slice of the MRIs. The NP was modelled with non-linear solid triangular elements. For this study endplates and vertebral bodies were assumed to be rigid as the effect of the endplates, and VBs on the behaviour of bovine IVD FE models has been found to be negligible (<2.5% difference in the peak force; Newell et al., 2017). A convergence study was performed on each specimen to ensure that the mesh density was sufficient.

Material Properties

The properties of each material used in the models are shown in **Table 1**. The AF matrix and the NP were assigned non-linear hyperelastic material properties (Mooney-Rivlin). The strain energy function for this material model is shown in

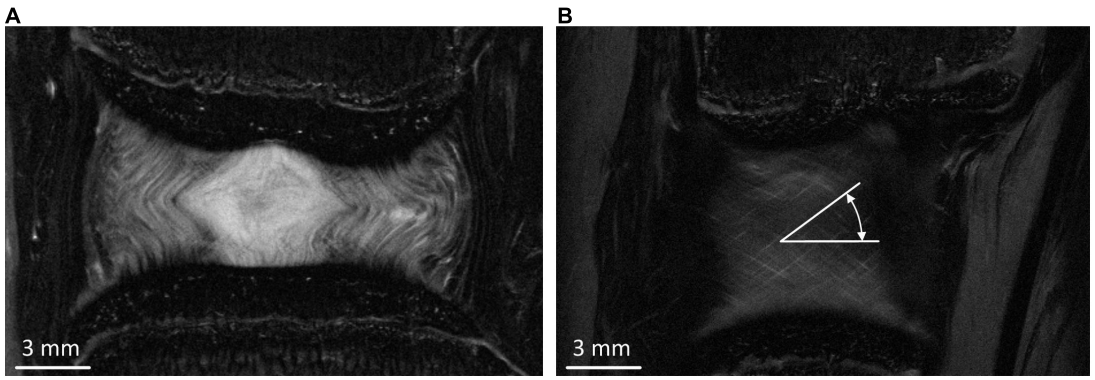

FIGURE 1 | (A) Middle coronal slice of the MRI of the bovine IVD. **(B)** Typical peripheral MRI slice from which fibre bundle angles were measured.

Eq. 1, where W is the strain-energy density function, I_1 and I_2 are strain invariants, and C_{10} and C_{01} are material constants (Mooney, 1940):

$$W = C_{10}\,(I_1-3) + C_{01}(I_2-3) \quad (1)$$

The AF fibre bundles were modelled using tension only rebar elements with a Young's modulus (YM) of 415 MPa which was obtained from the results of an optimisation study (Newell et al., 2017). The fibre bundles were aligned at ±30.45° to the transverse plane which was an average of six measurements taken from different coronal MRI slices at regular intervals from the inner to outer AF (**Figure 1B**). The cross-sectional area of each fibre bundle was set to be 3.212×10^{-2} mm^2, and spacing of the bundles was set to 4.35 bundles/mm (Marchand and Ahmed, 1990; Adam et al., 2015). The bulk modulus of the NP and AF ground matrix was set at 2,000 MPa to ensure near incompressibility.

Boundary Conditions

Replicating the experimental setup described by Newell et al. (2017), the inferior boundary of the IVD was fixed, and a displacement of 0.86 mm, which corresponded to a central disc axial strain of 15%, was applied to the superior boundary of the IVD. Since the models with segmented endplates had a shorter overall (or average) disc height (eventhough the central disc heights were kept the same), and the displacement of 0.86 mm was applied to all models, the models with segmented endplates were subjected to higher overall (or average) axial strains. Since the model was axisymmetric, nodes along the axis of symmetry were fixed in the radial direction.

Sensitivity Study

The influence of the AF C_{10}, AF C_{01}, fibre bundle YM, and fibre bundle angle values were investigated by varying their baseline value by ±20% and observing the effect on the peak force.

Graduated Fibre Bundle Angle

A number of previous FE studies have modelled fibre bundles with a constant orientation from outer to inner AF (Shirazi-Adl et al., 1986; Marchand and Ahmed, 1990; Natali and Meroi, 1990; Adam et al., 2015; Newell et al., 2017). However, in human IVDs fibre bundle angle has been reported to vary linearly from 28(outer) to 45(inner) in the radial direction relative to the transverse plane (Cassidy et al., 1989), and has been included in a number of other FE studies (Ayturk and Puttlitz, 2011; Schmidt et al., 2012). From the MRI scans, fibre bundle angles of 27.4° and 37.4° were measured at the outer most layer and inner most layer, respectively. In order to understand the effect of including a variation in fibre bundle angle, each layer of fibre bundles were assigned material properties individually in the model. The outer most layer was assigned 27.4° and the inner most layer was assigned 37.4°, while intermediate angles were varied linearly between these two angles.

Modelling Inter-lamellar Behaviour With Cohesive Contact

Interactions between lamellar in the AF were modelled using cohesive elements which allows the interfaces to be described by traction-separation laws. Normal cohesive stiffness (Knn = 1.18 MPa/mm), and tangential cohesive stiffness (Ktt and Kss = 1.31 MPa/mm) values were taken from Mengoni et al. (2015) who derived values using an optimisation algorithm and simulations of tension experiments where ovine AF samples were loaded radially. A stiffening factor in compression was assigned to ensure penetration between elements in adjacent lamellae was minimal. Preliminary investigations showed that a factor of 100,000 was sufficient to ensure that ±20% change resulted in a less than 2% change in peak force.

NP:AF Ratio

The NP:AF ratio was doubled (increasing the NP radius compared to the AF width but keeping the overall IVD width constant) in each of the models to investigate the effect of NP:AF ratio on the mechanics of the disc. Doubling the ratio ensured that there was a clear divergence from the baseline geometry while keeping within the physiological bounds of reported NP:AF ratios (O'Connell et al., 2007; Adam et al., 2015; Newell et al., 2017). In all baseline models the number of rebars/mm was defined based on measurements from Marchand and Ahmed (1990) (4.35 bundles/mm = 0.22 mm interbundle

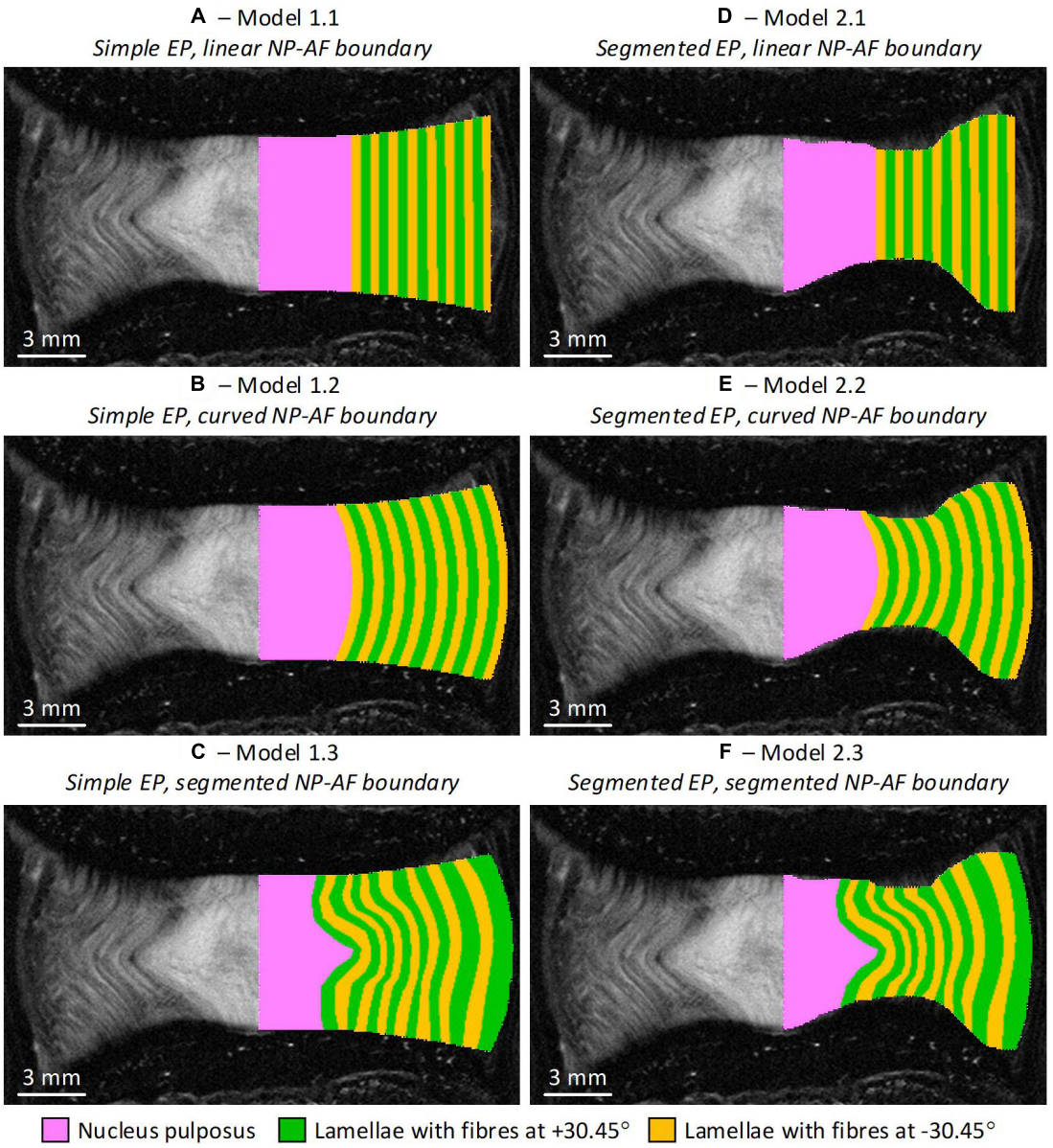

FIGURE 2 | Initial geometry of the six axisymmetric FE models overlaid on the MRI slice from which the geometries were obtained. Note the axis of symmetry in the models is along the mid-sagittal plane of the IVD. **(A)** Model 1.1—simple endplates, linear NP-AF boundary, **(B)** Model 1.2—simple endplates, curved NP-AF boundary, **(C)** Model 1.3—simple endplates, segmented NP-AF boundary, **(D)** Model 2.1—segmented endplates, linear NP-AF boundary, **(E)** Model 2.2—segmented endplates, curved NP-AF boundary, **(F)** Model 2.3—segmented endplates, segmented NP-AF boundary. Note the fibre bundle angles are relative to the transverse plane.

spacing) (**Figure 3A**). When increasing the NP:AF ratio care was taken to ensure that the total number of fibre bundles, was the same between the baseline, and adjusted NP:AF ratio models (**Figure 3**). This was achieved by calculating the difference between the circumference of each lamella of the baseline and the altered NP:AF ratio models using the horizontal distance from each lamella to the axisymmetric axis. The fibre bundle spacing was then adjusted to ensure each new model had the same fibre volume as the baseline models (**Figure 3**).

RESULTS

Taking measurements from the MRIs, the sample had a central disc height of 8.41 mm, sagittal plane width of 25.56 mm, a coronal plane width of 24.36 mm, and an area of 489.30 mm^2. A convergence study was performed on each specimen to ensure that the mesh density was sufficient. This involved subdividing the number of elements and comparing the peak force obtained using the original mesh with that obtained with the subdivided mesh. If peak forces were within 1%

TABLE 1 | Baseline material properties for components of each of the FE models.

Component	Material model	Material parameters (MPa)	References
Collagen fibre bundles	Linearly elastic	415	Newell et al., 2017
AF ground substance	Hyperelastic	C_{10} = 0.7, C_{01} = 0.2	Natali and Meroi, 1990
Nucleus pulposus	Hyperelastic	C_{10} = 0.07, C_{01} = 0.02	Adam et al., 2015

the original mesh was considered converged, otherwise further subdivisions were performed until consistent (within 1%) peak forces were found. This resulted in models having an average of 1,163 ± 469 elements.

Stiffness and Stress Distributions

The responses obtained from all the FE models were stiffer than the average experimental response reported by Newell et al. (2017; **Figure 4**). A trend was seen for the stiffness to increase as the complexity of the model geometry increased. All models with segmented endplates had a greater stiffness than those with simple endplates.

In all models the predominant direction of the minimum principal strain at maximum displacement was axial (**Figure 5**). Axial strains were compressive throughout the IVD in all models, and particularly high along the endplates. Peak axial strains were lowest in the models with segmented endplates, in comparison to the simple endplates (-0.22, -0.34, -0.42, -0.51, -0.64, and -1.00, for Models 1.1, 1.2, 1.3, 2.1, 2.2, and 2.3, respectively). Peak axial and radial strains were seen at locations of high endplate curvature, particularly at the mid-AF-endplate boundary of the segmented endplate models. High compressive axial strains were generally seen at the NP-AF boundary at mid-height in all models. In all models a band of high circumferential strains was seen close to the mid-height of the disc but this band veered away from mid-height in the models with segmented internal geometry (Models 1.3 and 2.3).

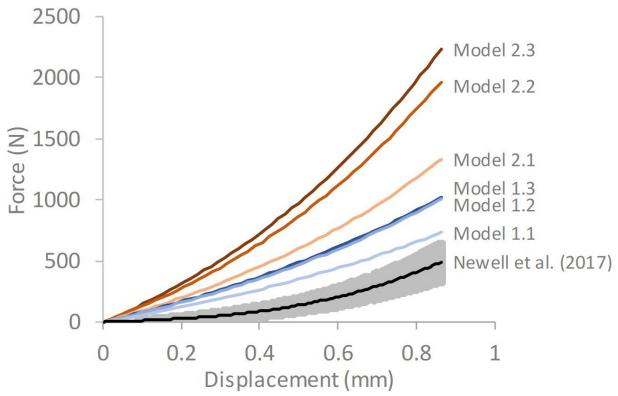

FIGURE 4 | Force-displacement response of each of the six models compared against average experimental response from Newell et al. (2017) The grey shaded region on the experimental data represents ± 1 standard deviation. Model 1.1—simple endplates, linear NP-AF boundary, Model 1.2—simple endplates, curved NP-AF boundary, Model 1.3—simple endplates, segmented NP-AF boundary, Model 2.1—segmented endplates, linear NP-AF boundary, Model 2.2—segmented endplates, curved NP-AF boundary, Model 2.3—segmented endplates, segmented NP-AF boundary.

Sensitivity to Altered Material Properties

The models were most sensitive to properties of the fibre bundles, particularly to fibre bundle angle (**Figure 6D**). The AF C_{01} Mooney constant had a greater effect than the AF C_{10} Mooney constant in all models (**Figures 6A,B**). Models with segmented endplates (2.1, 2.2, and 2.3), on average were less sensitive to changes in material properties in comparison to models with a simple endplate (Models 1.1, 1.2, and 1.3). Models 2.2 and 2.3 (segmented endplates with curved and segmented internal geometry, respectively) had similar sensitivities to all four material parameters, and both were less sensitive to the AF Mooney constants, and the fibre bundle angle, but more sensitive to the fibre bundle YM than Model 2.1 (segmented endplate, linear NP-AF boundary). Similarly, Models 1.2 and 1.3 (simple endplates with curved and segmented internal geometry, respectively) were less sensitive to the AF Mooney constants, and

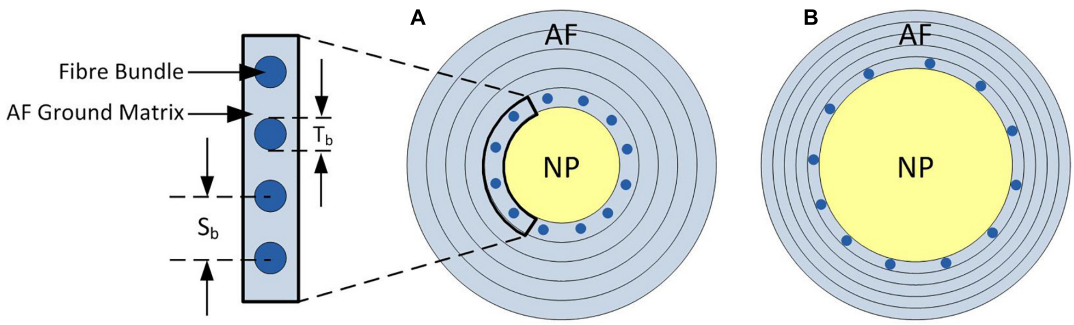

FIGURE 3 | Schematic of axial cross-section of the IVD demonstrating the change in fibre bundle spacing required to allow a fair comparison between models when adjusting the NP:AF ratio. **(A)** Shows a baseline NP:AF ratio with a cut out showing the fibre bundle thickness (Tb), and interbundle spacing (Sb), **(B)** shows an increased NP:AF ratio with larger interbundle spacing. Bundles are only shown in the inner most lamella in both schematics, with a total of 12 bundles shown in both **(A,B)**, although larger interbundle spacing in **(B)** resulting in the same fibre bundle volume as that shown in **(A)**. Note these schematics are not to scale.

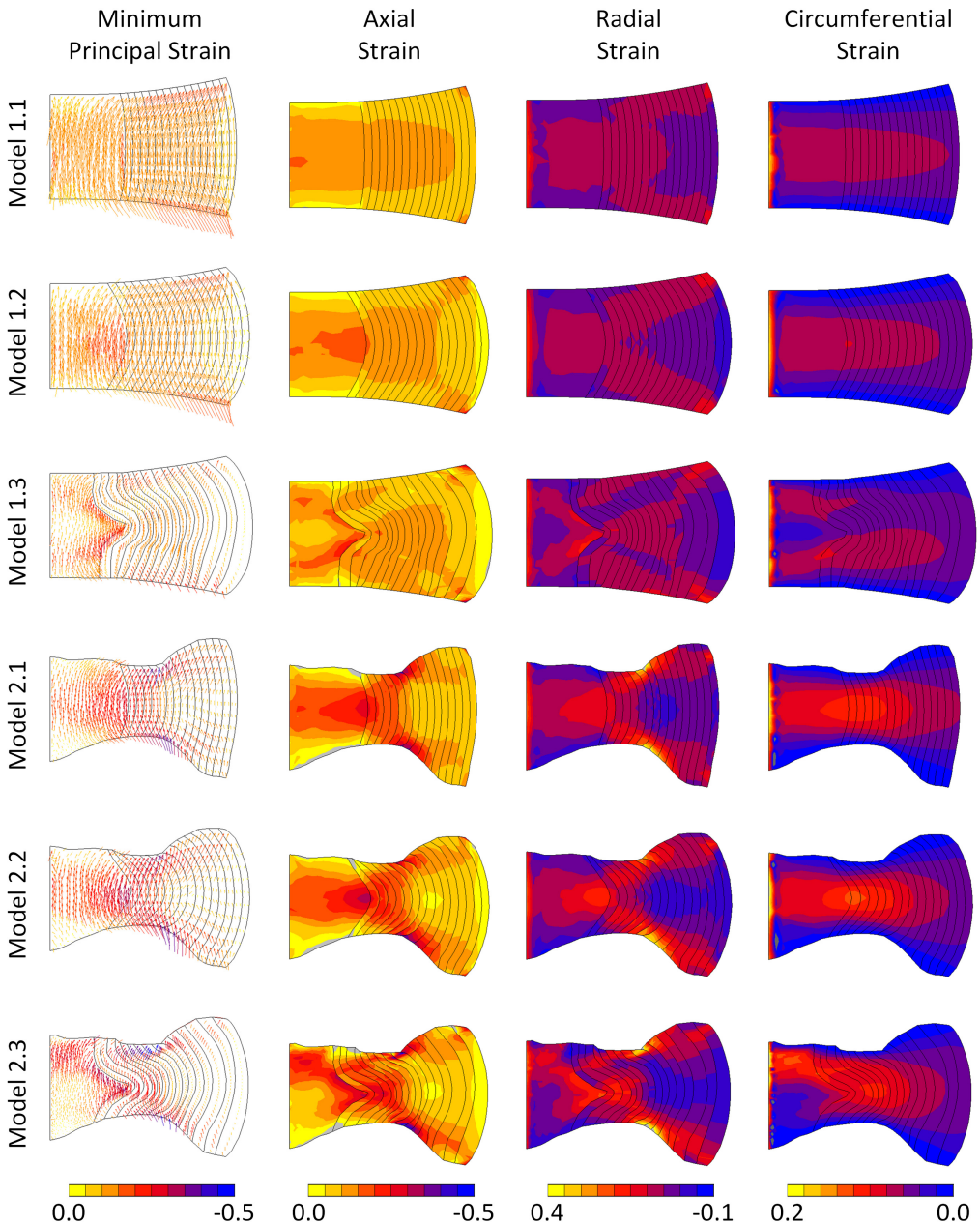

FIGURE 5 | Minimum principal, axial, radial, and circumferential strain distributions in each of the six models at maximum displacement. Vectors in the left column indicate minimum principal strain directions and the colours refer to magnitudes of the minimum principal strains.

the fibre bundle angle, but more sensitive to the fibre bundle YM than Model 1.1 (simple endplate, linear NP-AF boundary).

Effect of Graduated Fibre Bundle Angle

A comparison of the percentage change in peak force between the baseline and varied fibre bundle angle models is shown in **Figure 7A**. On average, varying the fibre bundle angle resulted in a 5.0 ± 2.8% decrease in peak force in all six models in comparison to the constant fibre bundle angle models. However, Models 2.2 and 2.3 (segmented endplates with curved and segmented internal geometry, respectively) were relatively insensitive to the variation in fibre bundle angle with a percentage change of 0.9 and 2.2%, respectively, compared to 5.9–11.6% for the other models.

Sensitivity to Modelling Inter-lamellar Behaviour With Cohesive Contact

A comparison of percentage change in peak force between the glued, and cohesive inter-lamellar contact models is shown in **Figure 6B**. Allowing cohesive contact caused a decrease in

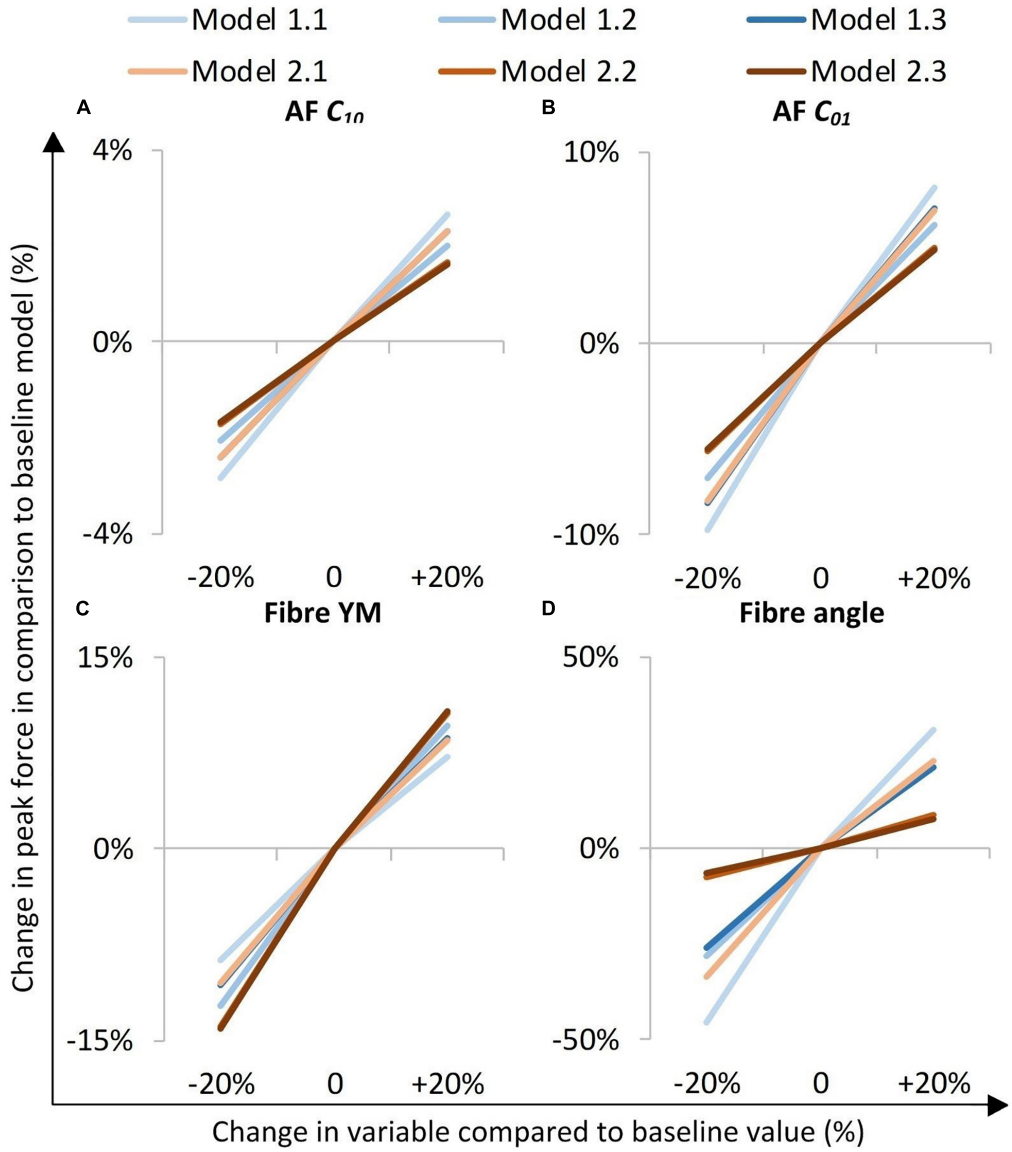

FIGURE 6 | Sensitivity study overview. The y-axis represents a percentage change in peak axial force from that obtained in the initial baseline run of each of the six models when a parameter was changed by ±20%. **(A,B)** are AF ground matrix material properties, **(C,D)** are AF fibre properties.

stiffness in comparison to the glued models for all six geometries. There were only small differences in the percentage reduction in peak force compared to the baseline models between models, with an average reduction of 32.2 ± 2.2%.

Sensitivity to Altered NP:AF Ratio

Increasing the NP:AF ratio resulted in a reduction in peak force in all models in comparison to the baseline runs. Models 1.1 and 2.1 (simple EP, linear NP-AF boundary and segmented EP, linear NP-AF boundary) saw the greatest reduction in peak force in comparison to the curved, and segmented internal geometry models with the same endplate geometry (1.2 and 1.3, and 2.2 and 2.3, respectively). Reductions in peak force were higher in the segmented endplate models, compared to the simple endplate models (13.3 ± 4.7% vs. 7.2 ± 2.3%, respectively).

DISCUSSION

FE modellers are required to find a balance between geometric accuracy and keeping computational complexity low. It is therefore common to simplify model geometry to increase the likelihood of convergence. In this study ultra-high field MRI was used to obtain accurate internal geometry of an intact IVD to evaluate its effect on the response of an IVD FE model.

The six models developed in this study all had geometry based on the same MR image of a bovine IVD, however, differences

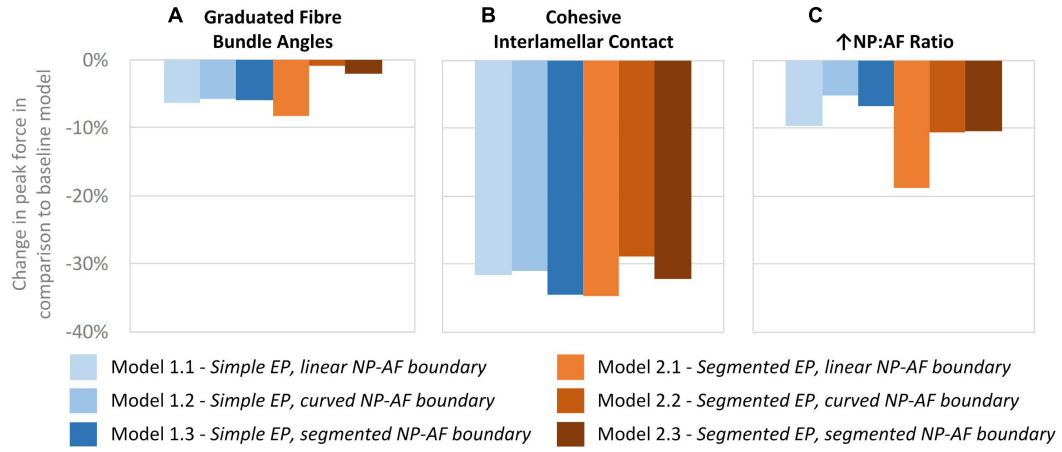

FIGURE 7 | Percentage changes in peak force compared to baseline models after **(A)** graduating the fibre bundle angles, **(B)** cohesive inter-lamellar contact, and **(C)** increasing the NP:AF ratio.

were seen in terms of the location of peak strain (**Figure 5**), and the overall stiffness of each model (**Figure 4**). Maximum strains were seen at locations of high curvature in the segmented endplate models, which could not be captured in the curved endplate models. An increase in model complexity resulted in increased model stiffness, with the average peak force doubling in the segment endplate models compared to the curved endplate models (919 ± 162 N and 1,845 ± 465 N, respectively), and the average peak force being 1.44, and 1.58 times larger than the linear NP-AF boundary model (Model 1.1—simple EP, linear NP-AF boundary and Model 2.1—segmented EP, linear NP-AF boundary) in the curved (Model 1.2—simple EP, curved NP-AF boundary and segmented EP, Model 2.3—curved NP-AF boundary) and segmented (Model 1.3—simple EP, segmented NP-AF boundary and Model 2.3—segmented EP, segmented NP-AF boundary) NP-AF boundary models, respectively. The high stiffnesses in the segmented endplate models was affected by the average height being 1.22 mm shorter than the curved endplate models (7.92 vs. 9.14 mm). Even though the central, and peripheral discs heights were the same in all models the change in average height meant that the overall applied strain was greater in the segmented endplate models compared to the simple endplate models. The differences in stiffness between the segmented and simple endplate models may have been smaller had the average, rather than just central and peripheral disc heights been kept consistent between the two approaches. Additionally, a linear or curved estimation of the NP-AF boundary created idealised strain distributions (**Figure 5**) that neglected the effects of non-uniform lamella geometries such as variations in width and curvatures.

The force-displacement response of Model 1.1 (simple endplates, linear NP-AF boundary) was closest to the experimental data obtained by Newell et al. (2017; **Figure 4**). This was expected since Model 1.1's geometry was the most similar to the models in that study in that the endplates were curved, the boundary between the NP and AF was linear, and the AF fibre YM used in this study (415 MPa) was obtained through the optimisation process described in Newell et al. (2017) that ensured a close match between experimental and numerical results. The slightly stiffer response of Model 1.1 compared the experimental data is likely due to the relatively lower NP-AF ratios, obtained from the MRIs, being used in this study (0.66:1 for Model 1.1) compared to 3.72:1 used in Newell et al. (2017). As shown in **Figure 7C**, increasing the NP-AF ratio decreases model stiffness, therefore had a lower NP-AF ratio been used by Newell et al. (2017), their optimised fibre stiffnesses may have been lower and therefore a closer match between experimental and numerical response may have been seen in this study.

An increase in deviation from the experimental data was seen with increasing geometric complexity (**Figure 4**). This is likely due to all models using the same material properties, including AF fibre YM properties that were obtained in an optimisation study (Newell et al., 2017) where model geometry was most similar to Model 1.1 (simple EP, linear NP-AF boundary) in this study. Using the same optimisation algorithm described in (Newell et al., 2017) the material properties (AF fibre YM and AF C_{10}) of all the models used in this study can also be optimised to obtain a close match between numerical and experimental response. This results in the optimised values shown in **Figure 8** where lower AF fibre YM and AF C_{10} values were seen in the more complex models. For researchers who wish to model IVDs with accurate internal geometries it is likely that less stiff material properties are required to obtain an overall response that can be validated against experimental data. For example, the optimised AF fibre YM and AF C_{10} values for Model 2.3 (segmented endplates, segmented NP-AF boundary) were 60.63 and 0.121 MPa, respectively, which is at the lower end of the range of values that have been used in previous FE studies [44–500 MPa for AF Fibre YM and 0.0146–0.7 MPa for the AF C_{10} value (Newell et al., 2019b)].

Irrespective of geometry, the models were most sensitive to the fibre YM, and the fibre angle (on average a 10.5 ± 1.8%, and 21.6 ± 12.0% change in peak force compared to the baseline runs when adjusted by 20% of the original fibre YM and fibre angle, respectively), and relatively insensitive to the AF ground

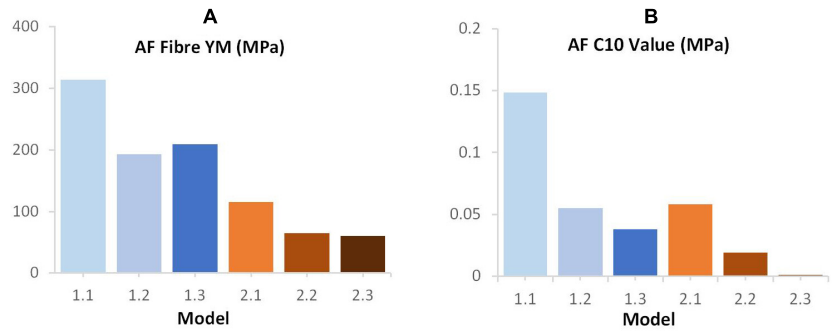

FIGURE 8 | Final **(A)** AF fibre YM **(B)** C_{10} values following optimisation of these parameters in order to achieve a good fit between the computational and experimental data reported by Newell et al. (2017).

matrix properties (C_{10} and C_{01} Mooney constants—**Figure 6**). Although care must be taken when comparing absolute values since the sensitivity study carried out here spanned a supra-physiologic range of force these findings are similar to those of Newell et al. (2017) in terms of Fibre YM who modelled bovine discs with a curved endplate, and linear NP-AF boundary (on average a 12.9% change in peak force). Interestingly, graduating the fibre bundle angles from inner to outer AF had a relatively small effect on the overall stiffness of the model with the average peak force of all models being 5.0 ± 2.8% lower compared to baseline runs, and the peak force being just 2.2% lower in the segmented endplate, segmented NP-AF boundary model (2.3). This suggests that future studies should focus on ensuring the accuracy of the average fibre bundle angle, rather than the accuracy of fibre bundle angles in individual lamella to ensure accurate load transfer through the IVD, particularly if a segmented NP-AF boundary and segmented endplates are used. However, previous FE studies have reported sensitivity to fibre angles in terms of IVD response to torsion (Yang and O'Connell, 2017), swelling (Yang and O'Connell, 2018, 2019a), and axial stiffness (Shirazi-Adl, 1989), with the general consensus being that anatomically relevant fibre angles are important for understanding the internal stress distributions through the disc. As demonstrated in this study, and in Stadelmann et al. (2018) it is possible to use high resolution MRI to obtain these angles non-invasively. There have been two recent FE studies investigating the effect of NP:AF ratio with Yang et al. (2019) finding a positive correlation between relative NP size and IVD stiffness, and Mengoni et al. (2017) finding a negative correlation. These differences could be due to modelling bovine rather than human discs, fibres at an orientation of ± 20 degrees compared to ± 43 degrees, or modelling 20 lamella layers compared to one in the Mengoni et al. (2017) and Yang et al. (2019) studies, respectively. In this study, doubling the NP:AF ratio (equivalent to on average, increasing the NP:Disc diameter from 0.38 ± 0.01 to 0.55 ± 0.01) reduced the peak force by 10.3 ± 4.7% supporting the findings of Mengoni et al. (2017) who saw a ∼32% decrease in peak force of bovine specimens at a similar axial displacement as the maximum in this study (0.86 mm—taken from **Figure 6** in Mengoni et al., 2017) when increasing the NP:Disc diameter from 0.4 to 0.6. Conversely, Yang et al. (2019) found a 23.8% increase in normalised stiffness of human IVDs under axial compression when increasing the NP:Disc diameter from 0.35 to 0.6. Depending on the method of modelling AF fibres, adjusting the NP:AF ratio can affect the total fibre volume, since IVD FE models are sensitive to fibre properties (**Figure 6C**) it is important to ensure that a change in total fibre volume does not affect conclusions made about altering the NP:AF ratio. In this study this was accounted for by ensuring the fibre volume was consistent before and after adjusting the NP:AF ratio.

A network of elastic fibres and collagen cross-bridges exist between lamellae in the AF which provides resistance to shearing strains (Yu et al., 2002; Pezowicz et al., 2006; Schollum et al., 2008). Most current IVD FE studies omit this inter-lamellar behaviour and either glue the boundary between lamellae (Dreischarf et al., 2014; Yang and O'Connell, 2019a,b; Yang et al., 2019), or use continuum models (Jacobs et al., 2014; Showalter et al., 2016; Newman et al., 2021). Adam et al. (2015) investigated allowing adjacent lamellae to slide freely across each other, however, experimental studies have shown that inter-lamella shearing strain is due to skewing, rather than sliding (Michalek et al., 2009; Vergari et al., 2016). A number of studies have included inter-lamellar interactions in models of several lamellar layers through the incorporation of elements or fibres in a zone between lamellar (Labus et al., 2014; Derrouiche et al., 2019; Kandil et al., 2019, 2020; Ghezelbash et al., 2021; Tamoud et al., 2021), however, the computational complexity of some of these approaches can render them impractical for modelling the whole disc (Ghezelbash et al., 2021). Mengoni et al. (2015) derived normal and tangential cohesive stiffness values that have been assigned to cohesive elements in this study to represent inter-lamellar interactions. To our knowledge this is the first time that these elements have been applied to a full IVD model and the technique proved to have potential to model the inter-lamellar behaviour more physiologically than glued contact between lamellae. Introducing this cohesive behaviour reduced the IVD stiffness (on average 32 ± 2% reduction in peak force compared to the glued baseline models – **Figure 7B**), which, as expected is lower than the 40% reduction shown by Adam et al. when allowing total free sliding between lamellae.

Bovine samples were modelled in this study because they are almost perfectly round (O'Connell et al., 2007; Adam et al., 2015) providing the opportunity to model axisymmetrically and thus reducing computational cost compared to full 3-D models. Beckstein et al. (2008) found the normalised stiffness of bovine IVDs to be within 12% of human IVDs suggesting similarities in mechanical properties, however, future studies to investigate how the findings in this study relate to human IVDs is required, particularly since the internal geometry of just one bovine IVD has been modelled here. Modelling one IVD was sufficient to investigate the effect of the different modelling techniques deployed in this study, however, a study on a larger population with various internal geometries, for example investigating how the internal geometry changes with degeneration and how that affects FE model behaviour would be of interest. Modelling axisymmetrically significantly reduces computational time but does not allow modes of loading other than axial compression. This meant that some geometric intricacies were simplified, and the NP was assumed to be perfectly in the centre of the IVD where in fact it was offset by approximately 1.26 mm from the centre of the disc when measured on a mid-transverse slice of the MRIs. Yang et al. (2019) found little difference in disc joint stiffness under flexion, extension, and lateral bending when changing the NP:Disc area ratio from 0.21 to 0.6, however the study did not investigate the effect of endplate and internal geometry complexity under these modes of loading.

In this study IVDs were loaded at an intermediate strain rate of 0.1/s. Previous studies have demonstrated an increase in stiffness with strain rate (Smeathers and Joanes, 1988; Yingling et al., 1997; Race et al., 2000; Kemper et al., 2007; Costi et al., 2008; Newell et al., 2017), and a recent study has demonstrated that the NP has little effect on the response of IVDs at high loading rates (Newell et al., 2019a), which differs from its function at low strain rates (Seroussi et al., 1989; Meakin and Hukins, 2000). It is therefore possible that FE models are less sensitive to geometric simplifications at higher strain rates, although further work would be required to confirm this. In this study IVDs were only subjected to pure axial compression. In order to comprehensively understand the effect of internal geometry on the outcomes of FE models, future studies should extend this analysis to investigate IVD response in combined loading and in flexion-extension, axial rotation, and lateral bending.

The complexity of the models used in this study were deliberately kept low to reduce the effects of confounding variables such as cartilage endplate properties, NP fluid phase (poroelasticity), NP swelling pressure, preload, vertebral bone properties, changes in the fibre volume fraction through the AF, and asymmetries in endplate shapes in planes other than the sagittal from which the geometry was segmented for Models 2.1—2.3 in this study. Additionally, the MRIs were obtained while the sample was well hydrated, and musculature had been removed. *In vivo*, internal geometries may change depending on posture and the time of the day and therefore the geometry used here represents the geometry at a single time point, and a single posture. Although outside the focus of this study, it is recommended that these factures, as well as those highlighted in this study are considered when developing more complex patient specific models of human discs that aim to replicate *in vivo* conditions.

CONCLUSION

Geometric simplifications in FE models of IVDs create idealised load transfer that may not be physiologic. These simplifications affect model response, particularly in terms of stiffness and strain distributions, sensitivity to average fibre angles, and sensitivity to modelling inter-lamellar contact. Therefore, defining more realistic internal and external geometry of the IVD can significantly affect IVD FE model response, and it is likely that a more realistic geometry leads to a more accurate strain distribution within the IVD. It is recommended that these geometric intricacies are incorporated into IVD FE models before material properties are optimised to develop a validated model. This is particularly important if the models are being used for clinical applications such as developing repair strategies that aim to replicate the mechanical behaviour of healthy discs.

DATA AVAILABILITY STATEMENT

The original contributions presented in the study are included in the article/supplementary material, further inquiries can be directed to the corresponding author/s.

AUTHOR CONTRIBUTIONS

YD, UH, and NN designed the study. NB, ST, and NN designed the sequences and obtained the MRI images. YD and TR developed and ran the FE models. YD, ST, and TR analysed the data and drafted the manuscript which was edited by NN, NB, and UH. All authors approved the manuscript before submission.

FUNDING

Part of this work was funded by an Imperial College Research Fellowship for NN and an EPSRC DTP CASE Conversion Studentship for TR (EP/R513052/1).

REFERENCES

Adam, C., Rouch, P., and Skalli, W. (2015). Inter-lamellar shear resistance confers compressive stiffness in the intervertebral disc: an image-based modelling study on the bovine caudal disc. *J. Biomech.* 48, 4303–4308.

Adams, M. A., and Roughley, P. J. (2006). What is intervertebral disc degeneration, and what causes it? *Spine (Phila Pa 1976)* 31, 2151–2161. doi: 10.1097/01.brs.0000231761.73859.2c

Adams, M. A., Dolan, P., and Hutton, W. C. (1987). Diurnal variations in the stresses on the lumbar spine. *Spine (Phila Pa 1976)* 12, 130–137.

Adams, M. A., McNally, D. S., and Dolan, P. (1996). "Stress" distributions inside intervertebral discs. The effects of age and degeneration. *J. Bone Joint Surg. Br.* 78, 965–972.

Ayturk, U. M., and Puttlitz, C. M. (2011). Parametric convergence sensitivity and validation of a finite element model of the human lumbar spine. *Comput. Methods Biomech. Biomed. Eng.* 14, 695–705. doi: 10.1080/10255842.2010.493517

Beckstein, J. C., Sen, S., Schaer, T. P., Vresilovic, E. J., and Elliott, D. M. (2008). Comparison of animal discs used in disc research to human lumbar disc: axial compression mechanics and glycosaminoglycan content. *Spine (Phila Pa 1976)* 33, E166–E173. doi: 10.1097/BRS.0b013e31824d911c

Bogduk, N. (2005). *Clinical Anatomy of the Lumbar Spine and Sacrum*, 4th Edn. London: Elsevier Health Sciences.

Cassidy, J. J., Hiltner, A., and Baer, E. (1989). Hierarchical structure of the intervertebral disc. *Connect. Tissue Res.* 23, 75–88. doi: 10.3109/03008208909103905

Costi, J. J., Stokes, I. A., Gardner-Morse, M. G., and Iatridis, J. C. (2008). Frequency-dependent behaviour of the intervertebral disc in response to each of six degree of freedom dynamic loading: solid phase and fluid phase contributions. *Spine (Phila Pa 1976)* 33, 1731–1738. doi: 10.1097/BRS.0b013e31817bb116

Derrouiche, A., Zaïri, F., and Zaïri, F. (2019). A chemo-mechanical model for osmo-inelastic effects in the annulus fibrosus. *Biomech. Model. Mechanobiol.* 18, 1773–1790. doi: 10.1007/s10237-019-01176-8

Dreischarf, M., Zander, T., Shirazi-Adl, A., Puttlitz, C., Adam, C., Chen, C., et al. (2014). Comparison of eight published static finite element models of the intact lumbar spine: predictive power of models improves when combined together. *J. Biomech.* 47, 1757–1766. doi: 10.1016/j.jbiomech.2014.04.002

Ghezelbash, F., Eskandari, A. H., Shirazi-Adl, A., Kazempour, M., Tavakoli, J., Baghani, M., et al. (2021). Modeling of human intervertebral disc annulus fibrosus with complex multi-fiber networks. *Acta Biomater.* 123, 208–221. doi: 10.1016/j.actbio.2020.12.062

Iatridis, J. C., Kumar, S., Foster, R. J., Weidenbaum, M., and Mow, V. (1999). Shear mechanical properties of human lumbar annulus fibrosus. *J. Orthop. Res.* 17, 732–737. doi: 10.1002/jor.1100170517

Iatridis, J. C., Setton, L. A., Foster, R. J., Rawlins, B. A., Weidenbaum, M., and Mow, V. C. (1998). Degeneration affects the anisotropic and nonlinear behaviors of human anulus fibrosus in compression. *J. Biomech.* 31, 535–544. doi: 10.1016/S0021-9290(98)00046-3

Jacobs, N. T., Cortes, D. H., Peloquin, J. M., Vresilovic, E., and Elliott, D. (2014). Validation and application of an intervertebral disc finite element model utilizing independently constructed tissue-level constitutive formulations that are nonlinear, anisotropic, and time-dependent. *J. Biomech.* 47, 2540–2546. doi: 10.1016/j.jbiomech.2014.06.008

Kandil, K., Zaïri, F. F., Derrouiche, A., and Messager, T. (2019). Interlamellar-induced time-dependent response of intervertebral disc annulus: a microstructure-based chemo-viscoelastic model. *Acta Biomater.* 100, 75–91. doi: 10.1016/j.actbio.2019.10.005

Kandil, K., Zaïri, F., Messager, T., and Zaïri, F. (2020). Interlamellar matrix governs human annulus fibrosus multiaxial behavior. *Sci. Rep.* 10:19292. doi: 10.1038/s41598-020-74107-8

Kemper, A. R., McNally, C., and Duma, S. M. (2007). The influence of strain rate on the compressive stiffness properties of human lumbar intervertebral discs. *Biomed. Sci. Instrum.* 43, 176–181.

Labus, K. M., Han, S. K., Hsieh, A. H., and Puttlitz, C. M. (2014). A computational model to describe the regional interlamellar shear of the annulus fibrosus. *J. Biomech. Eng.* 136:51009. doi: 10.1115/1.4027061

Marchand, F., and Ahmed, A. M. (1990). Investigation of the laminate structure of lumbar disc anulus fibrosus. *Spine (Phila Pa 1976)* 15, 402–410. doi: 10.1097/00007632-199005000-00011

Meakin, J. R. R., and Hukins, D. W. L. W. (2000). Effect of removing the nucleus pulposus on the deformation of the annulus fibrosus during compression of the intervertebral disc. *J. Biomech.* 33, 575–580. doi: 10.1016/S0021-9290(99)00215-8

Meijer, G. J. M., Homminga, J., Veldhuizen, A. G., and Verkerke, G. J. (2011). Influence of interpersonal geometrical variation on spinal motion segment stiffness. *Spine (Phila Pa 1976)* 36, 929–935. doi: 10.1097/BRS.0b013e3181fd7f7f

Mengoni, M., Kayode, O., Sikora, S. N. F., Zapata-Cornelio, F. Y., Gregory, D., and Wilcox, R. (2017). Annulus fibrosus functional extrafibrillar and fibrous mechanical behaviour: experimental and computational characterisation. *R. Soc. Open Sci.* 4:170807. doi: 10.1098/rsos.170807

Mengoni, M., Luxmoore, B. J., Wijayathunga, V. N., Jones, A., Broom, N., and Wilcox, R. (2015). Derivation of inter-lamellar behaviour of the intervertebral disc annulus. *J. Mech. Behav. Biomed. Mater.* 48, 164–172. doi: 10.1016/j.jmbbm.2015.03.028

Michalek, A. J., Buckley, M. R., Bonassar, L. J., Cohen, I., and Iatridis, J. (2009). Measurement of local strains in intervertebral disc anulus fibrosus tissue under dynamic shear: contributions of matrix fiber orientation and elastin content. *J. Biomech.* 42, 2279–2285. doi: 10.1016/j.jbiomech.2009.06.047

Mooney, M. (1940). A theory of large elastic deformation. *J. Appl. Phys.* 11, 582–592.

Natali, A., and Meroi, E. (1990). Nonlinear analysis of intervertebral disk under dynamic load. *J. Biomech. Eng.* 112, 358–363. doi: 10.1115/1.2891196

Natarajan, R. N., and Andersson, G. B. J. (1999). The influence of lumbar disc height and cross-sectional area on the mechanical rsponse of the disc to physiological loading. *Spine (Phila Pa 1976)* 24, 1873–1881.

Newell, N., Carpanen, D., Evans, J. H., Pearcy, M. J., and Masouros, S. D. (2019a). Mechanical function of the nucleus pulposus of the intervertebral disc under high rates of loading. *Spine (Phila Pa 1976)* 44, 1035–1041.

Newell, N., Carpanen, D., Grigoriadis, G., Little, J. P., and Masouros, S. D. (2019b). Material properties of human lumbar intervertebral discs across strain rates. *Spine J.* 19, 2013–2024.

Newell, N., Grigoriadis, G., Christou, A., Carpanen, D., and Masouros, S. (2017). Material properties of bovine intervertebral discs across strain rates. *J. Mech. Behav. Biomed. Mater.* 65, 824–830.

Newman, H. R., DeLucca, J. F., Peloquin, J. M., Vresilovic, E. J., and Elliott, D. M. (2021). Multiaxial validation of a finite element model of the intervertebral disc with multigenerational fibers to establish residual strain. *JOR Spine* e1145. doi: 10.1002/jsp2.1145

Niemeyer, F., Wilke, H. J., and Schmidt, H. (2012). Geometry strongly influences the response of numerical models of the lumbar spine-A probabilistic finite element analysis. *J. Biomech.* 45, 1414–1423. doi: 10.1016/j.jbiomech.2012.02.021

Noailly, J., Wilke, H.-J., Planell, J. A., and Lacroix, D. (2007). How does the geometry affect the internal biomechanics of a lumbar spine bi-segment finite element model? Consequences on the validation process. *J. Biomech.* 40, 2414–2425. doi: 10.1016/J.JBIOMECH.2006.11.021

O'Connell, G. D. G., Guerin, H. L. H., and Elliott, D. M. (2009). Theoretical and uniaxial experimental evaluation of human annulus fibrosus degeneration. *J. Biomech. Eng.* 131:111007. doi: 10.1115/1.3212104

O'Connell, G. D., Vresilovic, E. J., and Elliott, D. M. (2007). Comparison of animals used in disc research to human lumbar disc geometry. *Spine (Phila Pa 1976)* 32, 328–333. doi: 10.1097/01.brs.0000253961.40910.c1

O'Connell, G., Vresilovic, E., and Elliott, D. (2011). Human intervertebral disc internal strain in compression: the effect of disc region, loading position, and degeneration. *J. Orthop. Res.* 29, 547–555.

Pezowicz, C. A., Robertson, P. A., and Broom, N. D. (2006). The structural basis of interlamellar cohesion in the intervertebral disc wall. *J. Anat.* 208, 317–330. doi: 10.1111/j.1469-7580.2006.00536.x

Race, A., Broom, N. D., and Robertson, P. (2000). Effect of loading rate and hydration on the mechanical properties of the disc. *Spine (Phila Pa 1976)* 25, 662–669. doi: 10.1097/00007632-200003150-00003

Robin, S., Skalli, W., and Lavaste, E. (1994). Influence of geometrical factors on the behaviour of lumbar spine segments: a finite element analysis. *Eur. Spine J.* 3, 84–90.

Schmidt, H., Galbusera, F., Rohlmann, A., Zander, T., and Wilke, H. (2012). Effect of multilevel lumbar disc arthroplasty on spine kinematics and facet joint loads in flexion and extension: a finite element analysis. *Eur. Spine J.* 21, S663–S674. doi: 10.1007/s00586-010-1382-1

Schollum, M. L., Robertson, P. A., and Broom, N. D. (2008). ISSLS prize winner: microstructure and mechanical disruption of the lumbar disc annulus. *Spine (Phila Pa 1976)* 33, 2702–2710. doi: 10.1097/BRS.0b013e31817bb92c

Seroussi, R. E., Krag, M. H., Muller, D. L., and Pope, M. H. (1989). Internal deformations of intact and denucleated human lumbar discs subjected to

compression, flexion, and extension loads. *J. Orthop. Res.* 7, 122–131. doi: 10.1002/jor.1100070117

Shirazi-Adl, A. (1989). On the fibre composite material models of disc annulus – comparison of predicted stresses. *J. Biomech.* 22, 357–365.

Shirazi-Adl, A., Ahmed, A. M., and Shrivastava, S. C. (1986). A finite element study of a lumbar motion segment subjected to pure sagittal plane moments. *J. Biomech.* 19, 331–350. doi: 10.1016/0021-9290(86)90009-6

Showalter, B. L., DeLucca, J. F., Peloquin, J. M., Cortes, D. H., Yoder, J. H., Jacobs, N. T., et al. (2016). Novel human intervertebral disc strain template to quantify regional three-dimensional strains in a population and compare to internal strains predicted by a finite element model. *J. Orthop. Res.* 34, 1264–1273. doi: 10.1002/jor.23137

Smeathers, J. E., and Joanes, D. N. (1988). Dynamic compressive properties of human lumbar intervertebral joints: a comparison between fresh and thawed specimens. *J. Biomech.* 21, 425–433. doi: 10.1016/0021-9290(88)90148-0

Stadelmann, M. A., Maquer, G., Voumard, B., Grant, A., Hackney, D., Vermathen, P., et al. (2018). Integrating MRI-based geometry, composition and fiber architecture in a finite element model of the human intervertebral disc. *J. Mech. Behav. Biomed. Mater.* 85, 37–42. doi: 10.1016/j.jmbbm.2018.05.005

Tamoud, A., Zaïri, F., Mesbah, A., and Zaïri, F. (2021). A microstructure-based model for time-dependent mechanics of multi-layered soft tissues and its application to intervertebral disc annulus. *Meccanica* 56, 585–606. doi: 10.1007/s11012-020-01281-4

Tavana, S., Baxan, N., Masouros, S. D. D., Freedman, B. A., Hansen, U. N., and Newell, N. (2021). The effect of degeneration on internal strains and the mechanism of failure in human intervertebral discs analysed using Digital Volume Correlation (DVC) and Ultra-High Field MRI. *Front. Bioeng. Biotechnol.* 8:610907. doi: 10.3389/fbioe.2020.610907

Tavana, S., Clark, J. N. N., Prior, J., Baxan, N., Masouros, S. D., Newell, N., et al. (2020). Quantifying deformations and strains in human intervertebral discs using Digital Volume Correlation combined with MRI (DVC-MRI). *J. Biomech.* 102:109604. doi: 10.1016/j.jbiomech.2020.109604

Vergari, C., Mansfield, J., Meakin, J. R., and Winlove, P. C. (2016). Lamellar and fibre bundle mechanics of the annulus fibrosus in bovine intervertebral disc. *Acta Biomater.* 37, 14–20. doi: 10.1016/j.actbio.2016.04.002

Yang, B., and O'Connell, G. D. (2017). Effect of collagen fibre orientation on intervertebral disc torsion mechanics. *Biomech. Model. Mechanobiol.* 16, 2005–2015. doi: 10.1007/s10237-017-0934-2

Yang, B., and O'Connell, G. D. (2018). Swelling of fiber-reinforced soft tissues is affected by fiber orientation, fiber stiffness, and lamella structure. *J. Mech. Behav. Biomed. Mater.* 82, 320–328. doi: 10.1016/j.jmbbm.2018.03.039

Yang, B., and O'Connell, G. D. (2019a). GAG content, fiber stiffness, and fiber angle affect swelling-based residual stress in the intact annulus fibrosus. *Biomech. Model. Mechanobiol.* 18, 617–630. doi: 10.1007/s10237-018-1105-9

Yang, B., and O'Connell, G. D. (2019b). Intervertebral disc swelling maintains strain homeostasis throughout the annulus fibrosus: a finite element analysis of healthy and degenerated discs. *Acta Biomater.* 100, 61–74. doi: 10.1016/j.actbio.2019.09.035

Yang, B., Lu, Y., Um, C., and O'Connell, G. (2019). Relative nucleus pulposus area and position alters disc joint mechanics. *J. Biomech. Eng.* 141, 1–11. doi: 10.1115/1.4043029

Yingling, V. R., Callaghan, J. P., and McGill, S. M. (1997). Dynamic loading affects the mechanical properties and failure site of porcine spines. *Clin. Biomech.* 12, 301–305. doi: 10.1016/S0268-0033(97)00009-0

Yu, J., Peter, C., Roberts, S., and Urban, J. (2002). Elastic fibre organization in the intervertebral discs of the bovine tail. *J. Anat.* 201, 465–475.

Conflict of Interest: The authors declare that the research was conducted in the absence of any commercial or financial relationships that could be construed as a potential conflict of interest.

The handling editor declared a past co-authorship with one of the authors NN.

frontiers in Bioengineering and Biotechnology

ORIGINAL RESEARCH
published: 14 July 2021
doi: 10.3389/fbioe.2021.680769

Biomechanical Analysis of Cervical Artificial Disc Replacement Using Cervical Subtotal Discectomy Prosthesis

Jin Wo[1†], Zhenjing Lv[2†], Jing Wang[3†], Kui Shen[1], Haoran Zhu[1], Yang Liu[1], Yuen Huang[4], Guodong Sun[1,5*] and Zhizhong Li[1,5,6*]*

[1] Department of Orthopedics, First Affiliated Hospital, Jinan University, Guangzhou, China, [2] Department of Spine Orthopedics, Guangdong Hospital of Integrated Traditional Chinese and Western Medicine, Foshan, China, [3] Department of Neurosurgery, First Affiliated Hospital, Jinan University, Guangzhou, China, [4] Department of Rehabilitation, First Affiliated Hospital, Jinan University, Guangzhou, China, [5] Department of Orthopedics, Fifth Affiliated Hospital, Heyuan Shenhe People's Hospital, Jinan University, Heyuan, China, [6] Department of Orthopedics, Heyuan People's Hospital, Heyuan Affiliated Hospital of Jinan University, Heyuan, China

OPEN ACCESS

Edited by:
Hendrik Schmidt,
Charité Medical University of Berlin, Germany

Reviewed by:
André P. G. Castro,
Universidade de Lisboa, Portugal
Fangsen Cui,
Agency for Science, Technology and Research (A*STAR), Singapore

***Correspondence:**
Zhizhong Li
lizhizhongjd@163.com
Guodong Sun
sgd96@jnu.edu.cn
Yuen Huang
835010749@qq.com

[†] These authors have contributed equally to this is work

Specialty section:
This article was submitted to Biomechanics, a section of the journal Frontiers in Bioengineering and Biotechnology

Received: 15 March 2021
Accepted: 11 June 2021
Published: 14 July 2021

Citation:
Wo J, Lv Z, Wang J, Shen K, Zhu H, Liu Y, Huang Y, Sun G and Li Z (2021) Biomechanical Analysis of Cervical Artificial Disc Replacement Using Cervical Subtotal Discectomy Prosthesis. Front. Bioeng. Biotechnol. 9:680769. doi: 10.3389/fbioe.2021.680769

Background: Anterior cervical discectomy and fusion (ACDF) sacrifices segmental mobility, which can lead to the acceleration of adjacent segment degeneration. The challenge has promoted cervical artificial disc replacement (CADR) as a substitute for ACDF. However, CADR has revealed a series of new issues that are not found in ACDF, such as hypermobility, subsidence, and wear phenomenon. This study designed a cervical subtotal discectomy prosthesis (CSDP) consisting of a cervical disc prosthesis structure (CDP structure), cervical vertebra fixation structure (CVF structure), link structure, and locking screw, aiming to facilitate motion control and reduce subsidence. The aim of this study was to assess the biomechanics of the CSDP using finite element (FE) analysis, friction-wear test, and non-human primates implantation study.

Study Design: For the FE analysis, based on an intact FE C_2-C_7 spinal model, a CSDP was implanted at C_5-C_6 to establish the CSDP FE model and compare it with the Prestige LP prosthesis (Medtronic Sofamor Danek, Minneapolis, MN, United States). The range of motion (ROM), bone-implant interface stress, and facet joint force were calculated under flexion extension, lateral bending, and axial rotation. In addition, CSDP was elevated 1 mm to mimic an improper implantation technique to analyze the biomechanics of CSDP errors in the FE model. Moreover, the friction-wear test was conducted *in vitro* to research CSDP durability and observe surface wear morphology and total wear volume. Finally, the CSDP was implanted into non-human primates, and its properties were evaluated and verified by radiology.

Results: In the FE analysis, the ROM of the CSDP FE model was close to that of the intact FE model in the operative and adjacent segments. In the operative segment, the CSDP error FE model increased ROM in flexion extension, lateral bending, and axial rotation. The maximum stress in the CSDP FE model was similar to that of the intact FE model and was located in the peripheral cortical bone region. The facet joint force changes were minimal in extension, lateral bending, and axial rotation loads in CSDP. In

the friction-wear test, after the 150-W movement simulation, both the CVF-link-junction and the CDP-link-junction had slight wear. In the CSDP non-human primate implantation study, no subsidence, dislocation, or loosening was observed.

Conclusion: In the FE analysis, the biomechanical parameters of the CSDP FE model were relatively close to those of the intact FE model when compared with the Prestige LP FE model. In terms of CSDP error FE models, we demonstrated that the implantation position influences CSDP performance, such as ROM, bone-implant interface stress, and facet joint force. In addition, we performed a friction-wear test on the CSDP to prove its durability. Finally, CSDP studies with non-human primates have shown that the CSDP is effective.

Keywords: biomechanics, cervical artificial disc replacement, finite element analysis, prosthesis, range of segmental motion, stress, facet joint

INTRODUCTION

Anterior cervical discectomy and fusion (ACDF) has been successfully applied to obtain functional recovery in degenerative disc disease; however, the treatment requires fusing segments (Mo et al., 2015). Although clinical evidence is still not sufficient to verify that adjacent segment degeneration is caused by the fusion, it is widely recognized that the range of motion (ROM) at non-fused levels will increase inevitably when segmental motion is abolished by the fusion. The increased ROM was considered to be linked with intervertebral disc pressure and even non-fused segment degeneration (Hilibrand and Robbins, 2004; Dmitriev et al., 2005; Carrier et al., 2013). Additionally, a reoperation rate of 10% was caused by other ACDF complications, such as implantation site pain and implant-bone non-union (Zhong et al., 2016). These issues have facilitated the development of cervical artificial disc replacement (CADR) as a substitute method for ACDF.

As an alternative method, CADR preserves segmental mobility by maintaining adjacent intervertebral disc pressure and avoiding adjacent segment degeneration (Sasso et al., 2011; Pandey et al., 2017). To date, the U.S. Food and Drug Administration (FDA) has approved seven CADR devices (Nunley et al., 2018). Most of these devices have polymer-on-metal or metal-on-metal designs to form ball-in-socket sliding articulation (Gandhi et al., 2015). These prostheses have produced satisfactory testing results in clinical trials. However, they also have some problems, such as subsidence, dislocation, and wear phenomenon (Di Martino et al., 2015).

Among these issues, subsidence has been one of the most commonly reported problems, with an incidence of 3–10% (Anderson and Rouleau, 2004). Moreover, reduced bone mineral density caused by overpolishing the end plate and prosthesis design-related uneven stress distribution exacerbate subsidence (Anderson and Rouleau, 2004; Thaler et al., 2013). The wear phenomenon is a physical process caused by motion across a bearing surface. In prostheses, it is associated with the formation of particular wear debris, loss of joint height, and, ultimately, joint failure. More importantly, the particulate debris will induce inflammation mediated by various cytokines. This inflammatory response can lead to pain, osteolysis, and prosthetic loosening (Anderson and Rouleau, 2004; Matge et al., 2015). Additionally, previous research has suggested that the ball-in-socket sliding articulation may induce hypermobility at the surgical level, leading to increased stress on the operative segment and facet joints (Chang et al., 2007b; Kowalczyk et al., 2011; Lee et al., 2011). This stress may play an important role in "operative segment degeneration," which is one of the major factors that may compromise the long-term results of CADR (Rundell et al., 2008). Thus, the above-mentioned problems have become the focus of CADR improvements and need to be considered when developing new artificial cervical discs.

In this study, we have designed a cervical subtotal discectomy prosthesis (CSDP), consisting of the cervical disc prosthesis structure (CDP structure), cervical vertebra fixation structure (CVF structure), link structure, and locking screw. Artificial disc designs will behave mechanically different because of the distinctiveness of each implant design. These varying designs resulted in different biomechanical alterations in the cervical spine after arthroplasty. Therefore, the purpose of this research was to estimate biomechanical patterns of CSDP at the C_5-C_6 level of the cervical spine and to analyze the underlying mechanisms.

The finite element (FE) analysis, an ideal method for research on spine biomechanics, can predict cervical biomechanical responses to different cervical artificial discs (Faizan et al., 2012). Moreover, the FE analysis has unique advantages for measuring biomechanical parameters, such as bone-implant interface stress and implant internal structure stress, which are closely related to subsidence, dislocation, and wear of an implant (Lazaro et al., 2010).

In this experiment, we analyzed and compared biomechanics of the CSDP and Prestige LP prosthesis (Medtronic Sofamor Danek, Minneapolis, MN, United States) by the FE analysis. The main biomechanical parameters included ROM, bone-implant interface stress distribution, and facet joint force. In addition, CADR complications have also been attributed to iatrogenic circumstances, for example, improper positioning of the device (Bertagnoli et al., 2005). Therefore, we moved the CSDP up 1 mm to simulate improper positioning of

the device, and the biomechanics were measured by the FE analysis under the same conditions. Moreover, we conducted a friction-wear test *in vitro* to research CSDP durability and to understand the long-term mechanical influences of internal structure interaction. Finally, the CSDP was implanted into non-human primates, and its properties were evaluated and verified by radiology.

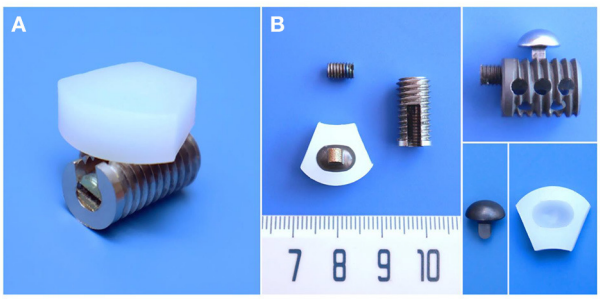

FIGURE 1 | Structural design and material specifications of cervical subtotal discectomy prosthesis (CSDP). **(A)** Oblique views of the assembled CSDP. **(B)** The CSDP consists of cervical disc prosthesis (CDP) structure, cervical vertebra fixation (CVF) structure, link structure, and locking screw. The link structure constitutes the ellipsoid-in-socket articulation with the CDP structure and is fixed on the CVF structure by the locking screw.

MATERIALS AND METHODS

Design Considerations and Material Specifications of CSDP

The CSDP itself consists of four primary components: CDP structure (ultrahigh molecular weight polyethylene, UHMWPE), CVF structure, link structure, and locking screw (titanium alloy). As an artificial cervical disc, the motion function of the CSDP depends on the articulation composed of the CDP structure and link structure. Different from ball-in-socket articulation-designed artificial discs, the CSDP has an ellipsoid-in-socket articulation design to limit hypermobility. In addition to constituting the articulation of CSDP, another function of the link structure is affixing the CDP structure to the CVF structure by locking screws. The CVF structure is cylindrical with screw threads on the surface. Similar to "hemiarthroplasty," CSDP fixation depends on the CVF structure in the vertebra; therefore, the CVF structure should be implanted first in CSDP surgery. Before CVF-structure implantation, the inferior vertebra at the operative level was grooved using curettage and a high-speed burr, and the groove was placed close to the upper end plate. Then, the CVF structure was screwed into the groove for early fixation. Moreover, several tunnels, similar to a cervical fusion cage, were reserved in the CVF structure to achieve fusion after long-term implantation (**Figure 1**).

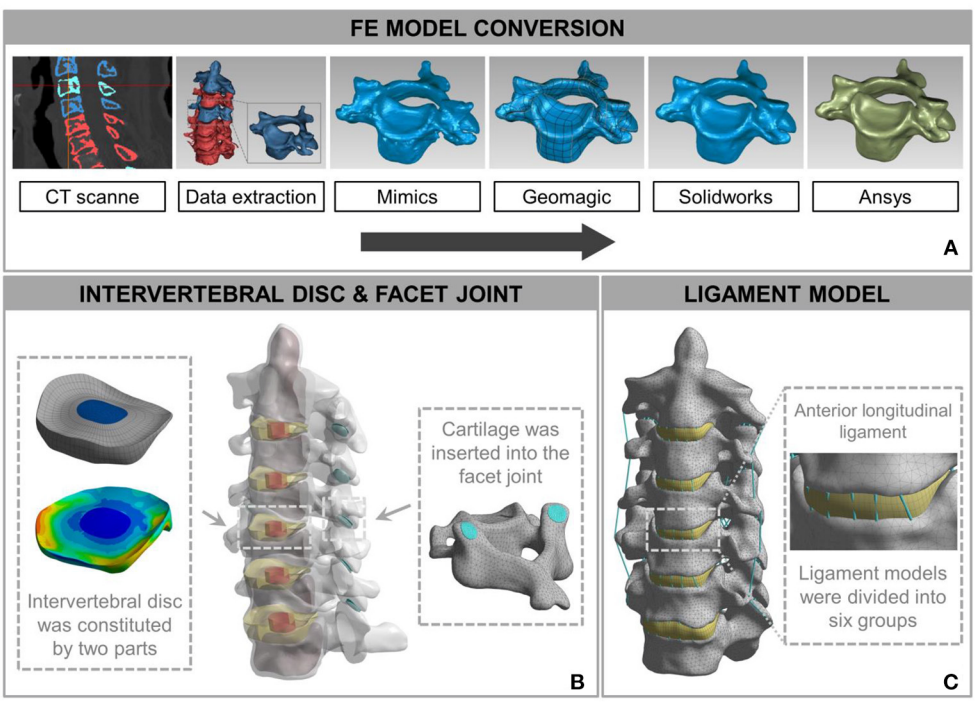

FIGURE 2 | Development and validation of intact finite element (FE) cervical spine model. **(A)** The conversion procedure for developing FE cervical vertebrae models included reconstructing a geometrical structure of vertebrae (Mimics 20.0), performing smooth operation (Geomagic 12), and supporting format conversion by computer-aided design (CAD) software (Solidworks 2015). Then, the output document was imported into FE software (Ansys Workbench 18.0) to build the cervical spine components. **(B)** A model consisting of a vertebra disc and an intervertebral disc was constructed by cartilage and intervertebral discs inserted into the facet joint and the intervertebral space. **(C)** The intact FE cervical spine model with ligament construction.

TABLE 1 | Material property and mesh type of the prostheses and cervical spine components.

Component	Young modulus (MPa)	Poisson ratio	Cross section area (mm^2)	Element type	References
Bone					
Cortical bone	12,000.0	0.29	–	Tetrahedron	Ng et al., 2004; Zhang et al., 2006; Lee et al., 2011
Cancellous bone	450.0	0.29	–	Tetrahedron	
Post bone	3,500.0	0.29	–	Tetrahedron	
End plate	500.0	0.40	–	Tetrahedron	
Cartilage	10.4	0.40	–	Hexahedron	
Nucleus	1.0	0.49	–	Hexahedron	
Annulus	3.4	0.40	–	Hexahedron	
Ligaments					
Anterior longitudinal	10.0	0.30	6.0	Link	Lee et al., 2011; Yu et al., 2016
Posterior longitudinal	10.0	0.30	5.0	Link	
Ligamentumflavum	1.5	0.30	5.0	Link	
Interspinous	1.5	0.30	10.0	Link	
Supraspinous	1.5	0.30	5.0	Link	
Capsular	10.0	0.30	46.0	Link	
Artificial disc					
Titanium alloy	110,000.0	0.30	–	Tetrahedron	Lee et al., 2011; Yu et al., 2016
UHMWPE	3,000.0	0.30	–	Tetrahedron	

Finite Element Biomechanical Analysis

Development of Intact FE Cervical Spine Model

The FE model of C_2-C_7 was developed based on CT images of a healthy subject (male, age 31 years, height 175 cm, weight 74 kg) without radiographic changes in cervical vertebrae or a history of cervical disc disease. The procedure for developing the intact C_2-C_7 FE cervical spine model is shown in **Figure 2**. Computed tomography scans of the subject were obtained at 0.5-mm intervals. Computed tomographic images re-established the three-dimensional structure of the vertebrae by image-processing software (Mimics 20.0, Materialise, Leuven, Belgium) and were then executed according to the smooth operation (Geomagic 12, Geomagic, Morrisville, NC, United States). After format conversion by computer-aided design (CAD) software (Solidworks 2015, Dassault, Vélizy-Villacoublay, France), the output was imported into FE software (Ansys Workbench 18.0, Ansys, Canonsburg, PA, United States) to construct cervical vertebrae (**Figure 2A**). The cartilages were imported into articular processes to constitute facet joints, and the frictional coefficient was set at 0.1. The intervertebral discs were divided into two parts: nucleus pulposus and annulus fibrosus. The FE model composed of the cervical vertebrae, facet joints, and intervertebral discs was built using the above process (**Figure 2B**). The ligament models contained the anterior longitudinal ligament, capsular ligament, posterior longitudinal ligament, interspinous ligament, supraspinous ligament, and ligamentum flavum, which were divided into six groups with geometrical linear contact elements utilizing tension.

The calculation time of the three meshes (mesh 1: 0.5 mm; mesh 2: 1 mm; and mesh 3: 1.5 mm) in the same configuration of the same computer were 98, 56, and 24 min. The differences between the tissues of mesh 1 and mesh 2 were <1%. Mesh 2 was considered to be a convergent mesh of intact FE cervical spine model. The numbers of nodes and elements in the intact FE cervical spine model were 446,263 and 226,402, respectively, which guaranteed the accuracy of calculations related to the mesh itself. The model and material properties were set based on previously published literature (Ng et al., 2004; Zhang et al., 2006; Lee et al., 2011; Yu et al., 2016). Material properties of the prostheses and the cervical spine components are presented in **Table 1**. Finally, we established an FE model of the intact C_2-C_7 spinal segment (**Figure 2C**).

For validation, the intact FE model was loaded in flexion extension, lateral bending, and axial rotation by imposing 1.5 Nm on C_2 with C_7 firmly fixed. For this purpose, on the middle top of C2–C7, six distinctive measuring material points were identified. The angles that were produced by the vector connected by adjacent points before and after the simulation depicted the ROM from C2 to C7. Under respective loading situations in light of prior experiments, ROM was compared with outcomes in the literature by Pelker et al. (1991), Panjabi et al. (2001), Kubo et al. (2003) and Ng et al. (2004) aiming to evaluate the validity of the intact FE model.

Development of CADR FE Model

The CSDP and Prestige LP were modeled using actual specimen sizes and material properties available in the literature (**Table 2**). The Prestige LP model consisted of two titanium end plates with the upside-down dome of the superior end plate articulating with the groove of the inferior end plate, and with the frictional coefficient set at 0.2. In order to simplify the CSDP model, three structures were constructed, namely, the CDP structure, CVF structure, and link structure. The CDP structure was made of UHMWPE, and the CVF structure and link structure were made

TABLE 2 | ROM validation of intact FE cervical spine model.

Segment	Flexion extension (ROM)		Lateral bending (ROM)		Axial rotation (ROM)	
	Intact FE model (°)	Range (°)	Intact FE model (°)	Range (°)	Intact FE model (°)	Range (°)
C_2/C_3	6.3	5.9–7.5	4.9	3.4–15.4	5.6	2.3–7.7
C_3/C_4	7.9	7.3–11.5	4.5	3.4–15.4	7.8	2.3–13.0
C_4/C_5	8.0	7.4–10.1	4.2	3.4–15.4	7.8	2.3–13.6
C_5/C_6	8.4	7.2–9.9	3.7	3.1–15.4	5.9	2.3–13.8
C_6/C_7	7.9	5.7–11.5	3.7	3.4–15.4	4.8	2.1–10.8

entirely of titanium alloy. The CVF structure and link structure were set to bond upon contact, replacing the function of the locking screw. Friction contact was also used for the ellipsoid-in-socket articulation of CSDP constituted by the CDP structure and link structure, and the frictional coefficient was set at 0.08 (**Figure 3A**).

The two models were implanted into the C_5-C_6 segment, where CADR is most frequently carried out. To imitate the Prestige LP insertion, the C_5-C_6 anterior longitudinal ligament, intervertebral disc, and end plate were removed. Then, the Prestige LP model was implanted at the C_5-C_6 segment in accordance with the clinical condition. During the CSDP insertion process, first, the CVF structure was inserted, and the cylindrical bone of the C_6 vertebra was removed. Following this procedure, the CDP structure was implanted, after which the anterior longitudinal ligaments, nucleus pulposus, annulus fibrosus, and 20% of the C_6 end plate were removed without removing the C_5 end plate. In addition, we moved the CSDP up by 1 mm to mimic an imprecise surgical insertion situation as a CSDP error FE model (**Figure 3B**). The bond upon contact condition was defined at the bone-implant interface.

By applying 1 Nm of flexion extension, lateral bending, and axial torsion combined with a 73.6 N compressive follower load on C_2, the intact FE, CSDP FE, Prestige LP FE, and CSDP error FE models will bend or rotate under load (Yu et al., 2016). Simultaneously, C_7 is fixed throughout the loading process. Range of motion, bone-implant interface stress distribution, and facet joint force analysis were carried out by quasistatic testing under the load conditions mentioned above to predict biomechanical patterns at the C_5-C_6 level of the cervical spine.

Friction-Wear Test

The friction-wear test detects wear on the two junctions of CSDP: the junction composed of the CVF structure and the link structure (CVF-link-junction) and the junction composed of the CDP structure and the link structure (CDP-link-junction). The experiment simulates the wear process of the two CSDP junctions after 150-W movements in simulated body fluid (SBF) and non-SBF environments, respectively. The contact stress on CVF-link-junction was 10 MPa and on CDP-link-junction was 5 MPa. The surface wear morphology and total wear volume were measured by the Multi-Function Tribometer (MFT-5000, Rtec, San Jose, CA, United States).

CSDP Implantation in Non-human Primates

Care and experimental procedures for non-human primates were approved by the Institutional Animal Care and Use Committee (IACUC). This study was conducted in compliance with relevant Chinese law and regulations on the management of laboratory animals promulgated by the State Science and Technology Commission. Eight male *Macaca fascicularis* (Huazhen Biotechnology, Guangzhou, China), 9.2–12.1 years and 9.5–10.2 kg, were fed in an indoor facility accredited by the Association for Assessment and Accreditation of Laboratory Animal Care International. The animals were housed in individual stainless-steel cages in a specific room where an environmental temperature of 21–25°C and a relative humidity range of 40–60% were maintained. Although individually housed, the animals were provided continuous auditory, visual, and olfactory contact with neighboring conspecifics. In addition to the standard non-human primate diet, water and fresh fruits were available *ad libitum*. Small amounts of primate treat and various cage-enrichment devices were supplied.

Prior to the surgery, each animal was sedated with ketamine (6 mg/kg) followed by endotracheal intubation and general anesthesia using 1.5% isoflurane. The neck area was shaved with razors and prepared with iodophor. The surgery was performed using an aseptic technique. The anterior approach to the cervical spine was adapted to the non-human primate model through a right-sided longitudinal incision (**Figure 4A**). Once the anterior cervical vertebral elements were exposed, the C_5-C_6 intervertebral disc was identified by x-ray, and a CSDP implantation surgery was performed. First, the C_6 vertebral body was grooved using curettage and a high-speed burr with the groove positioned close to the C_6 upper end plate. The CVF structure was then implanted at the C_6 groove. Second, the cartilage of the vertebral end plates was preserved, and the annulus and nucleus pulposus were removed. Finally, the CDP structure and link structure were implanted at C_5-C_6 and were fixed on the CVF structure by the lock screw (**Figure 4B**). The incision was sutured using layers, and the animals were returned to their home cages after recovery from anesthesia.

To prevent postoperative infection, the animals were treated with cefotaxime sodium (50 mg/kg IM, twice a day for 3 days). To alleviate acute postoperative pain, the animals were treated with rotundine (3 mg/kg IM, two times a day for 3 days). The observation was carried out using a CT scanner (Siemens,

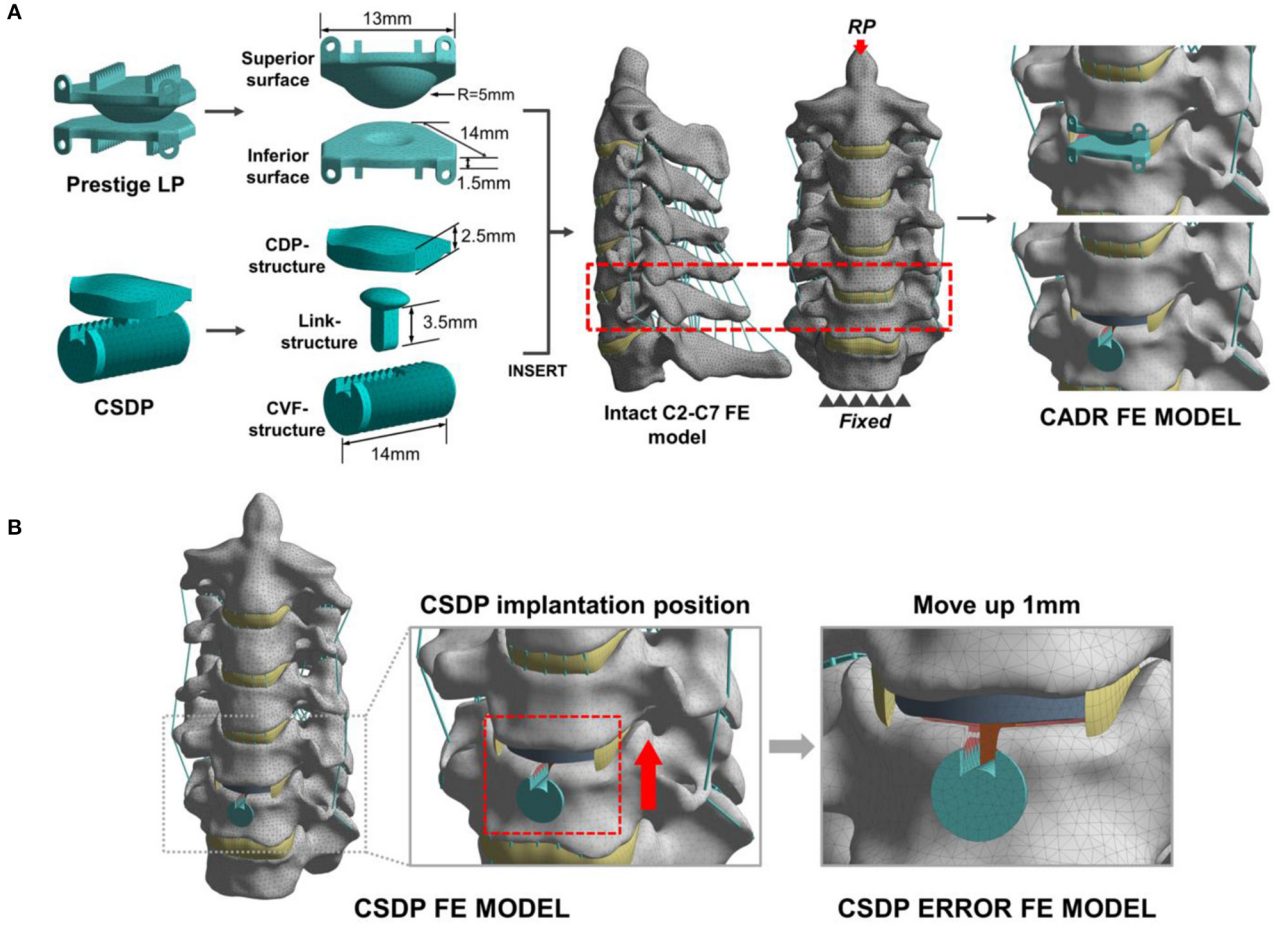

FIGURE 3 | Development and experimental conditions of the cervical artificial disc replacement (CADR) FE model. **(A)** The Prestige LP finite element (FE) model was composed of superior surface and inferior surface structures. The cervical subtotal discectomy prosthesis (CSDP) FE model was divided into three parts: cervical disc prosthesis (CDP) structure, cervical vertebra fixation (CVF) structure, and link structure. The Prestige LP and CSDP FE models were implanted at C_5-C_6. **(B)** The CSDP was moved up by 1 mm to simulate an imprecise surgical insertion situation as a CSDP error FE model.

Munich, Germany) and a 2.0 MRI scanner (Siemens, Munich, Germany) 1 month before surgery and 1 year after surgery.

RESULTS

Validation of Intact FE Cervical Spine Model

In the FE analysis, ROM outputs acquired from the intact FE model that we constructed were compared with data from previous experiments to estimate the validity of the model (Penning, 1978; Panjabi et al., 1986, 2001; Penning and Wilmink, 1987; Moroney et al., 1988; Mimura et al., 1989; Pelker et al., 1991; Holmes et al., 1994; Lai et al., 1994; Clausen et al., 1997; Kubo et al., 2003). Range of motion at each segment in the model was all in the range of results observed in previous experimental studies, although the segmental ROM for lateral bending was near the lower bound of the range given in previous experimental studies (**Figure 5** and **Table 2**). Based on these results, we demonstrated the validity of the intact FE cervical spine model.

Range of Motion of Intact FE Cervical Spine Model and CADR FE Models

Flexion–Extension Load

Under the follower load of 73.6 N and the flexion–extension load of 1 Nm, ROM in CSDP and Prestige LP FE models was 28.89° and 31.84°, respectively. Compared with 29.59° in the intact FE model, ROM was decreased by 2.37% in the CSDP FE model and increased by 7.6% in the Prestige LP FE model. Although ROM in flexion extension at the C_5-C_6 segment increased by 17.76% in the case of the Prestige LP FE model, the CSDP FE model showed a decrease of 6.57% when contrasted with the intact FE model. The ratio of C_5-C_6 and C_2-C_7 ROM was 18.21% for the CSDP model and 20.82% for the Prestige LP FE model.

Lateral Bending Load

As in the flexion–extension load, no significant differences were found in the intact segments between the intact FE model and the CADR model in the lateral bending load. However, ROM of the C_5-C_6 level was 21.4% higher

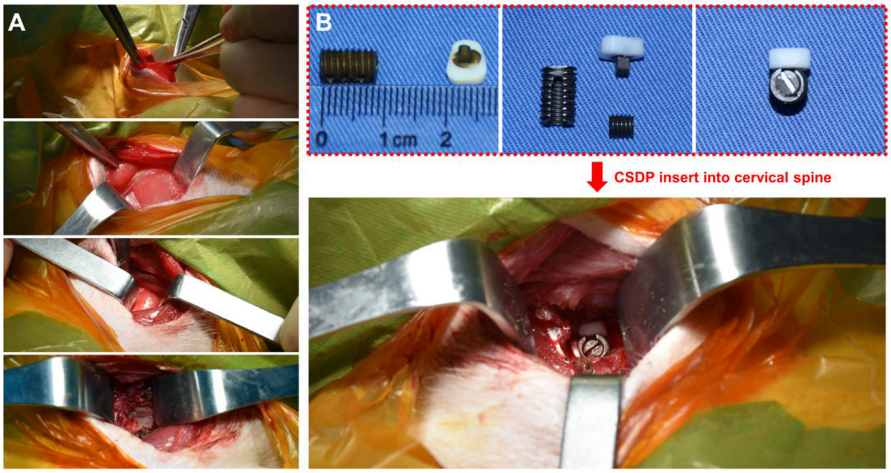

FIGURE 4 | Non-human primate cervical subtotal discectomy prosthesis (CSDP) implantation surgery. **(A)** After separating the skin, the platysma was cut with an electric knife. Then, the envelope fascia was sharply separated until the sternocleidomastoid muscle was seen. The sternocleidomastoid muscle was separated from the scapulohyoid muscle. Finally, the vertebral body was exposed by peeling off the longuscolli. **(B)** The size of the CSDP was modified based on the cervical spine anatomy of the non-human primates before implantation.

in the Prestige LP FE model and 0.6% lower in CSDP FE model compared with the intact FE model. The ratio of the C_5-C_6 ROM with respect to C_2-C_7 in the Prestige LP FE model and CSDP FE model was 22.52 and 19.96%, respectively.

Axial Rotation Load

Under axial rotation load, no significant differences were found in the intact segments between the intact FE and CADR models. Compared with 14.6° in the intact FE model, ROM in the Prestige LP FE model increased by 12.53% and decreased by 0.96% in the CSDP FE model. Range of motion at the C_5-C_6 level was 35.85% higher in the Prestige LP FE model and 5.03% lower in the CSDP FE model when compared with the intact FE model. The ratio of the C_5-C_6 ROM with respect to C_2-C_7 in the Prestige LP and CSDP FE models was 26.29 and 20.89%, respectively, and differed from the 21.78% in the intact FE model (**Figure 6**).

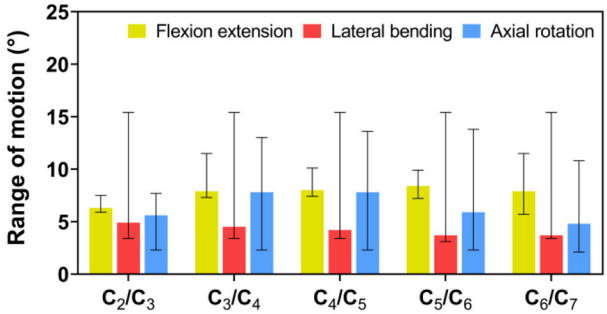

FIGURE 5 | Validation of intact finite element (FE) cervical spine model. Range of motion (ROM) outputs obtained from the intact FE model were compared with the literature data to assess the validity of the model. ROM at each segment in the intact FE model was entirely in the range of literature results.

Stress Analysis of Intact FE Cervical Spine Model and CADR FE Models

Von Mises Stress

The Von Mises stress on the bone-implant interface in CADR FE models in flexion, extension, lateral bending, and axial rotation is shown in **Figure 7A**. Maximum stress on the inferior surface in the intact, Prestige LP, and CSDP-CDP-structure FE models was higher than that on the superior surface of these models (**Figure 7B**). Stress was concentrated in the central region in the Prestige LP FE model, and the average stress was much higher than in the CSDP-CDP structure and intact FE models. The maximum stress in the Prestige LP FE model was 18.839 MPa, observed in axial rotation loading. In addition, maximum stress was 3.267 and 9.464 MPa in the intact and CSDP-CDP structure FE models, respectively. The stress distribution of the CSDP-CDP structure FE model showed a trend similar to that of the intact FE model, which was located in the peripheral region but had relatively higher stress than in the intact FE model.

For the CSDP-CVF structure, maximum stress observed in flexion loading was 11.351 MPa and was nearer to the location of the link structure, instead of the bottom; however, in flexion, the corresponding maximum stress was 18.174 MPa for the Prestige LP FE model (**Figure 8**).

Facet Joint Force

The outputs of facet joint forces are presented in **Figure 9**. Under the flexion load, the facet joint was in an extended position, and the pressure value was not measured. In extension loading, the facet joint force increased by 167.95% in the

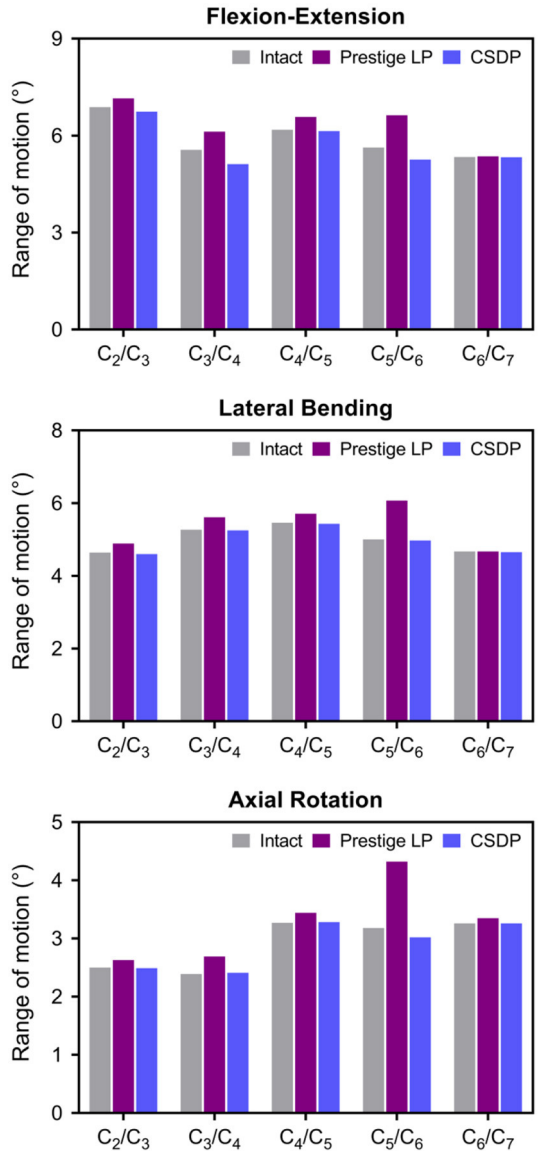

FIGURE 6 | Range of motion (ROM) of intact finite element (FE) cervical spine model and cervical artificial disc replacement (CADR) FE models. In three loads, no significant differences were found at the C_5-C_6 level and other segments between the intact FE and cervical subtotal discectomy prosthesis (CSDP) FE models. ROM at the C_5-C_6 level was higher in the Prestige LP FE model than in the intact and CSDP FE models.

Prestige LP relative to the intact FE model, while the value did not increase extremely in the CSDP FE model. The facet joints force in the lateral bending load within all CADR FE models was higher than in the intact FE model. The variation of lateral bending facet joint force in the Prestige LP and CSDP FE models was 295.13 and 2.86% of the intact value, respectively. Contrasted with the intact FE model in axial rotation, the maximum increase in facet force was 111.35% with the Prestige LP, whereas it was 0.47% with the CSDP FE model.

Biomechanical Analysis of CSDP Error FE Model

Range of Motion of CSDP Error FE Model

The results showed that ROM at C_2-C_7 increased by replacement with the CSDP error FE model, relative to the CSDP FE model. The CSDP error FE model had a significant influence on ROM in axial rotation but not in flexion extension and lateral bending. At the operative segment, with respect to the CSDP FE model, the CSDP error FE model produced a small increase of 21.67 and 16.5% ROM in flexion extension and lateral bending, respectively, while there was a 36.09% increase in axial rotation. Nevertheless, the Prestige LP FE model was more affected than the CSDP error FE model in ROM. When the CSDP error FE model was compared with the Prestige LP FE model, small decreases of 3.59, 4.84, and 5.11% were observed in flexion extension, lateral bending, and axial rotation, respectively (**Figure 10A**).

Von Mises Stress of CSDP Error FE Model

The Von Mises stress on the bone-implant interface of the CSDP error FE model was significantly greater than that in the CSDP FE model. Maximum stress was 9.464 MPa in the CSDP FE model, while in lateral bending it had a value of 13.057 MPa in the CSDP error FE model. Different from the CSDP FE model, the stress distribution of the CSDP error-CDP-structure FE model was observed in the CDP-structure central region and was significantly higher (**Figure 10B**). The stress sustained by the CSDP error-CVF-structure FE model was still found at the link structure, with the maximum being 16.631 MPa (**Figure 10C**).

Facet Joint Force of CSDP Error FE Model

The maximum stresses on facet joints in the CSDP error FE model were observed during axial rotation. Moreover, in the FE models of intact and CSDP, stress was also observed in axial rotation (**Figure 10D**). Although the CSDP error FE model produced higher facet-joint force than the CSDP did, the maximum facet joint force in the Prestige LP FE model was greater in all CADR FE models.

Friction-Wear Test

The results of CVF-link-junction and CDP-link-junction in the SBF and non-SBF environments after 150-W movement simulation are shown in **Figure 11**. In SBF, the CVF-link-junction and CDP-link-junction have slight wear. Especially in the CVF-link-junction, the total wear volume is much lower in SBF than in non-SBF. For the wear morphology cross-section observation of the CDP-link-junction, the wear depth was only approximately 5 μm in the SBF, which is lower than the 20 μm in the non-SBF.

Radiological Observation of CSDP in Non-human Primates

Figure 12 shows the CT and MRI scans 1 month before and 1 year after CSDP implantation in non-human primates. CT showed that after 1 year, CSDP subsidence, dislocation, and loosening were not observed. In addition, 1 year after CSDP implantation, the inside of the CVF structure was filled with

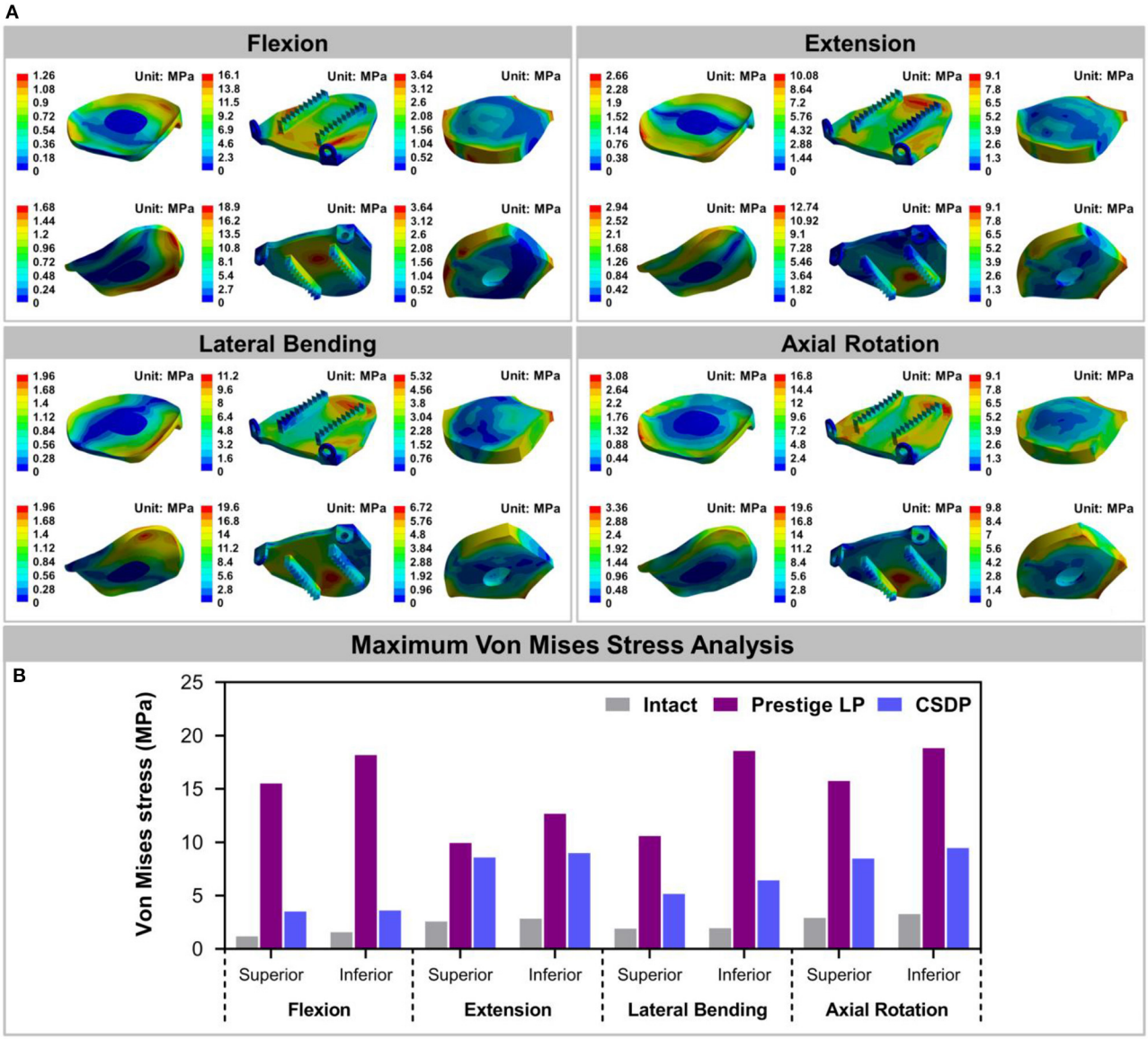

FIGURE 7 | Stress analysis of the intact finite element (FE) cervical spine model and cervical artificial disc replacement (CADR) FE models. **(A)** The Von Mises stress can be observed, including intact, Prestige LP, and cervical subtotal discectomy prosthesis–cervical disc prosthesis (CSDP-CDP) structure FE models in flexion, extension, lateral bending, and axial rotation loads. Stress of the Prestige LP FE model, distributed in the central region, was much higher than that of the CDP structure FE and intact FE models. Stress distribution of the CSDP-CDP structure FE model was similar to that of the intact FE model, located in the peripheral region. **(B)** Maximum Von Mises stress analysis of the intact, Prestige LP, and CSDP-CDP structure FE models.

the trabecular bone, and the CVF structure had undergone intravertebral fusion. Based on the MRI result, no spinal cord edema, degeneration of the adjacent intervertebral disc, or inflammation of the surrounding vertebral body was observed in the surgical segment.

DISCUSSION

Cervical artificial disc replacement aims to prevent adjacent segment degeneration by restoring intervertebral disc mobility in degenerative segmental motion. The Prestige LP prosthesis was chosen because of its current global popularity and because it is similar to most ball-in-socket sliding articulations used today (Choi et al., 2020). The Prestige LP is an open two-piece, semi-constrained design with metal-on-metal ball-in-socket articulation. The CSDP is an open four-piece, semi-constrained design with polymer-on-metal ellipsoid-in-socket articulation. Biomechanical studies have shown that ball-in-socket sliding articulation may not substantially control motion and may cause hypermobility at the surgical level (Kowalczyk et al., 2011).

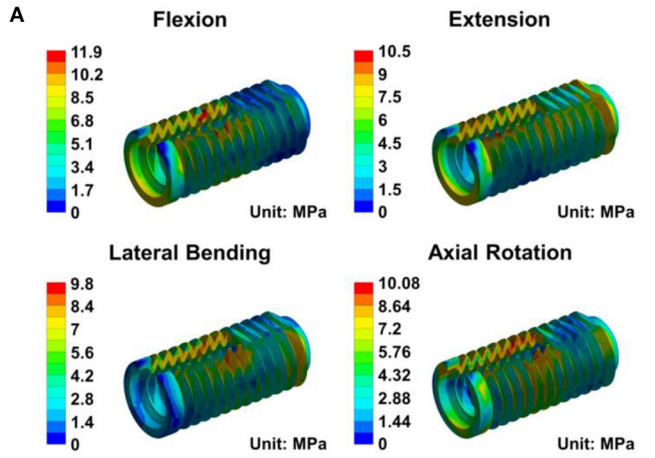

FIGURE 8 | Stress analysis of cervical subtotal discectomy prosthesis–cervical vertebra fixation (CSDP-CVF) structure. **(A)** Maximum stress for the CSDP-CVF structure finite element (FE) model, located nearby the link structure, instead of the bottom. **(B)** Maximum Von Mises stress analysis of CSDP-CVF structure FE models. Maximum stress in the CVF structure was less than that of the Prestige LP inferior surface in all loads.

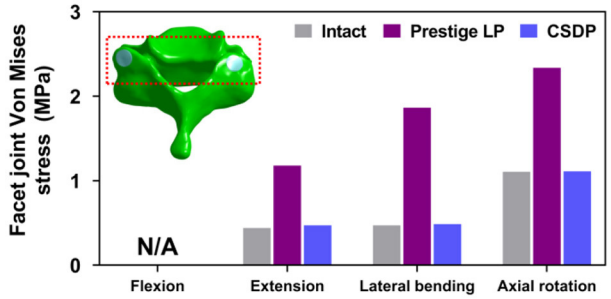

FIGURE 9 | Facet joint force analysis of the cervical subtotal discectomy prosthesis (CSDP) finite element (FE) model.

Hypermobility was a direct negative factor that increases strain in implanted segments and facet joints. Under the hypermobility condition, increasing the load through the capsular ligament during physiological situations and CADR sliding articulation configuration would alter the load transmit mode at the surgical segment. In this study, ROM distribution through C_2-C_7 segments in the CSDP FE model was almost similar to that in the intact FE model, whereas it had changed in the Prestige LP FE model. Although spinal motion in the implanted site was preserved in the Prestige LP FE model, ROM increased by 17–35% compared with the intact FE model, possibly because of a hypermobility condition. In previous studies, similar results have suggested that a significantly increased ROM at the operative segment was found after replacement with the Prestige model (Chang et al., 2007b). The coincidental result of this study and previous *in vivo* research confirmed this conclusion. As for the CSDP error FE model, C_5-C_6 ROM was significantly greater than that in the intact and CSDP FE models regardless of motion loads. However, the Prestige LP model generated a greater increase in C_5-C_6 ROM than the CSDP error FE model did in both groups.

Subsidence and dislocation are problems that may result from intrinsic design flaws of the devices. The subsidence tendency is associated with interfacial stress increases, leading to a high bone-implant interface stress situation (Lin et al., 2009). Therefore, bone-implant interface stress may dissipate evenly in prostheses rather than in concentrated areas (Anderson and Rouleau, 2004). The stress distribution of the Prestige LP model was uneven and mostly focused on central and posterior regions; the CSDP-CDP structure FE model was similar to the intact FE model located in the peripheral cortical bone region. Moreover, the maximum stress on the superior and inferior surfaces of the Prestige LP FE model was higher compared with the CSDP FE model. It is generally acknowledged that subsidence is most often caused by improper device design that affects end plate preparation and stress distribution; however, a decrease in bone quality can also lead to subsidence (Bertagnoli et al., 2005). Bone resection may affect the structural integrity of end plates, resulting in decreased end plate bone quality. Because of the structural design of the CSDP, the C_5 end plate could be saved and, therefore, decrease the risk of subsidence during operation.

The anchorage structure of the prosthesis also determines the propensity for subsidence. The potential of an artificial disc to generate interface resorption and subsequent subsidence depends on a variety of biomechanical factors that can be expressed in terms of relative movement between bone and implant at the interface (Weinans et al., 1993). Stress distribution on the surface of the anchorage structure may reflect trends in load transfer and relative movement. Similar to biomechanical disruption of the bone-implant interface of an acetabular cup in total hip replacement, micromotion can also be intensified with the displacement of the anchorage structure relative to vertebral bodies during repetitive loading. The results of stress analysis showed that the CSDP-CVF structure dissipated stress more

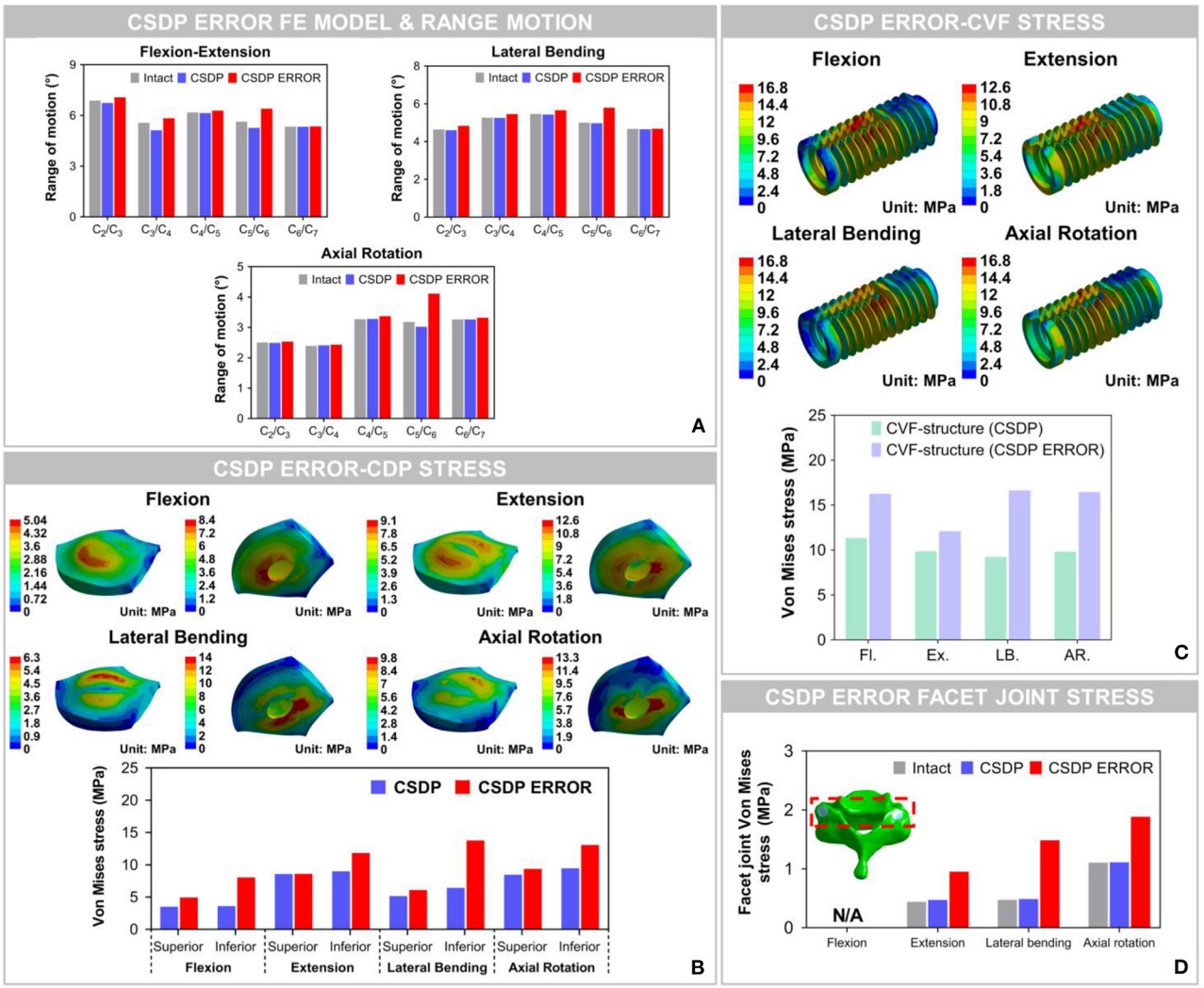

FIGURE 10 | Biomechanical analysis of the cervical subtotal discectomy prosthesis (CSDP) error finite element (FE) model. **(A)** The results illustrated that range of motion (ROM) increased at the C_5-C_6 level with CSDP error FE model replacement, and the CSDP error FE model had a greater effect on ROM in axial rotation than in flexion extension and lateral bending. **(B)** After the CSDP FE model was replaced with the CSDP error model, stress was concentrated in the central region of the CSDP error-CDP-structure FE model. **(C)** Stress sustained by the CSDP error-CVF-structure FE model was higher than that by the CSDP-CVF-structure FE model, yet still similar to that by the CSDP FE model. **(D)** Facet joint force within the CSDP error FE model was higher than that in the intact and CSDP FE models. Maximum facet joint force in the CSDP error FE model was observed during axial rotation.

evenly to provide physiological bonding at the bone-implant interface. With the Prestige LP FE model, high bone-implant interface stress occurred at the posterior flanges on the inferior surface, producing maximum stress at 18.839 MPa.

Device wear and deterioration can occur at any interface, most commonly at the bearing surfaces but also at the host-implant or implant-implant interfaces. Wear production varies, depending on the material used and mechanisms of biomechanical stress applied to the implant. The anchorage structure is indispensable in preventing the migration of the prosthesis; however, stress located in connection with various CSDP structures, especially at the junction of the link structure and CVF structure, is high. In the FE analysis, the maximum stress was observed at the CVF-link-junction. Although the link structure is attached to the CVF structure by a locking screw, it still allows micro-movements. It has been reported that high-stress distribution may increase the risk of wear (Lee et al., 2016). In addition, the movement of the CSDP depends on the joint CDP structure and link structure, which will also cause wear phenomena in the long term. Therefore, we carried out a friction-wear test on these joint structures. In the SBF environment, the surface wear morphology and wear volume of these joint structures illustrated that CSDP has a long-term life. Conversely, the FE analysis showed that the stress on joint interfaces increased in the CSDP error model. Although the stress in the CSDP error-CDP structure FE model was less than the corresponding yield

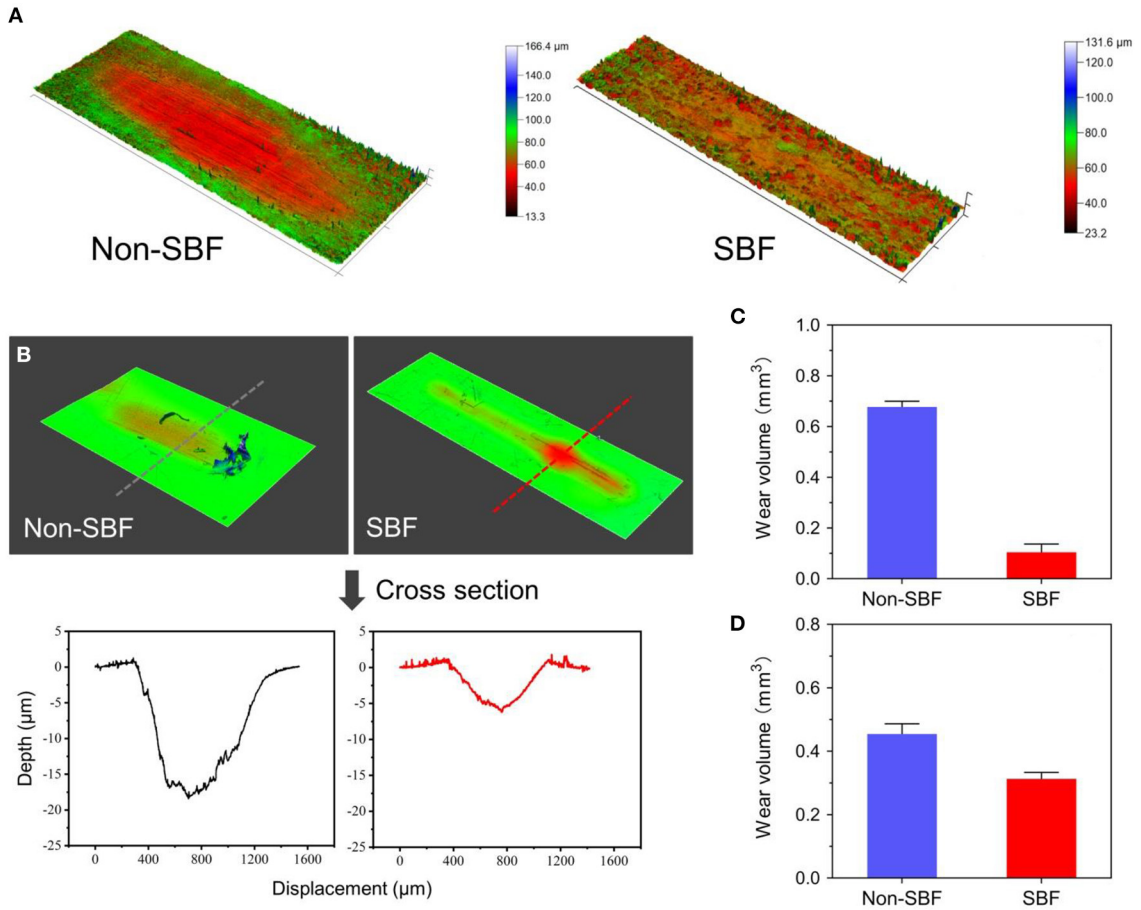

FIGURE 11 | Surface wear morphology observation and wear volume. **(A)** Surface wear morphology observation of cervical vertebra fixation (CVF) link junction; the color represents the degree of wear. **(B)** The wear morphology cross-section of cervical disc prosthesis (CDP) link junction. Total wear volume of the **(C)** CVF link junction and the **(D)** CDP link junction was quantified.

stress of UHMWPE (28 MPa), the stress distribution of the CSDP error-CDP structure, to some extent, increases the risk of wear, which may affect long-term follow-up results. It has been reported that high-stress distribution in the UHMWPE zone may increase the risk of wear inside the core (Lee et al., 2011, 2016). Therefore, the implantation technology of CSDP is vital, especially the implantation position, which can reduce the wear in the CSDP.

Increased force on facet joints after ADR has been cited as a reason for degenerative changes in implanted segments and poor clinical results; however, biomechanical or clinical evidence has not been clear (Huang et al., 2004; Anderson et al., 2008). In this study, the stress sustained by facet joints increased by 7.3% in the case of the CSDP FE model, and by 167.9 and 115.9% in the case of the Prestige LP and CSDP error models, respectively, demonstrating a remarkable stress increase in CADR segments. Chang et al. (2007a) reported that stress increased by 25.1% under an extension load in comparison with intact segments. Rundell et al. (2008) indicated that stiffness of implanted segments was reduced and ROM increased, while facet joint force varied from 7.7 to 95.3 N depending on the insertion location. In another study on "ball-and-socket" cervical disc prostheses, Rousseau et al. (2008) suggested that pressure on facet joints may increase from 15 to 86% by adjusting the center of rotation and that a posterior center of rotation with a large radius was most effective in lowering pressure. Ahn and DiAngelo used a computer simulation model to show that facet-joint force on implanted segments increased during extension from 38.1 to 691 N in normal segments (Ahn and DiAngelo, 2008). The results of this study indicated that increased pressure on facet joints after CADR might occur with all loads and in various forms and degrees, possibly because of intrinsic design flaws or improper positioning of devices. In conclusion, both CSDP error and Prestige LP FE models might change the force transfer path of motion segments in facet joints.

Similar to other *in vitro* experiments, biomechanical experiments still need to be verified by *in vivo* animal experiments, especially in large animals. The comparable kinematics of the lower cervical spine was one of the

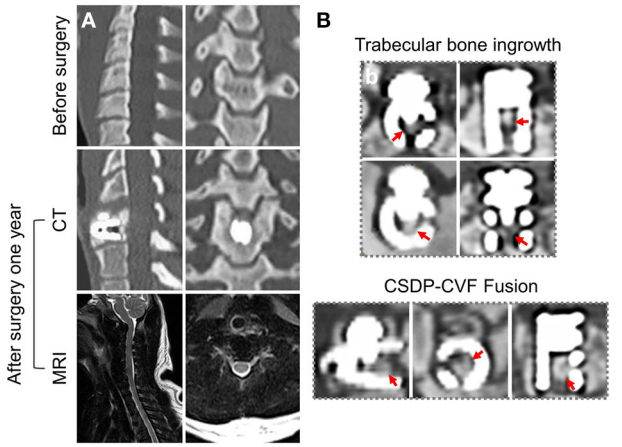

FIGURE 12 | Radiological observation of cervical subtotal discectomy prosthesis (CSDP) in non-human primates. **(A)** CT and MRI 1 month before and 1 year after CSDP implantation in non-human primates. **(B)** The trabecular bone grows into the interior of the cervical vertebra fixation (CVF) structure through the tunnel.

criteria used in selecting non-human primates as the animal model for CADR. The upright spine mechanical system of non-human primates is suitable for CADR research. It is absolutely a "worst-case" scenario with regard to evaluating the biomechanics and durability of a cervical prosthesis. Non-human primates are not braced or immobilized after surgery, and they rapidly ambulate and perform their natural gymnastics, trapeze utilization, and cage rocking within the first postoperative week. In this study, human-sized CSDP could not be used in the non-human primates at C_5-C_6. The disc space dimensions of non-human primates are more accommodating to the smaller human-sized prosthetic implants; therefore, we adapted the size of CSDP according to non-human primate cervical spine anatomy. CT radiographic assessment showed the CSDP remained very stable at the operative level. Based on CT radiographic analysis, there were no incidences of migration or subsidence. Furthermore, the CVF structure fusion phenomenon indicated that the CSDP shows biochemical stability because the implant of surface osseo-integration and vertebral fusion require a stable mechanical condition. There were no significant perioperative complications (i.e., no loosening, no osteolysis, and no translational instabilities).

In this experiment, we aimed to determine CSDP biomechanical patterns of the cervical spine to understand underlying biomechanics and how the CSDP load transfer pattern affected segmental motion. The research has some limitations. First, the FE analysis was computational, and certain assumptions were made during the study. The assumption of the bond upon contact condition for bone and implant is a limitation of this study. The bone-implant interface is much more complex, with relative motions and separations, such as that of CDP-structure bone. However, an appropriately validated model can still provide comparative results to guide orthopedic surgery. The implantation experiment using the CSDP in non-human primates also verified its biomechanical stability. Second, the experimental period of CSDP implantation in non-human primates was short. CADR complications often take a long time to appear. Third, the friction-wear test simplifies the experimental conditions, such as friction movement and loading conditions. Simplified friction movement and loading conditions may not completely reflect the actual wear process of CSDP in the body. Despite these limitations, this research still provides sufficient information to understand more about CSDP biomechanics.

CONCLUSION

This research has deepened the understanding of how the CSDP affects implant segmental motion as well as stress distribution in the bone-implant interface. Overall, it helps to understand the possible mechanism for the failures and how CSDP designs predispose to the problem. In the FE analysis, compared with those of the Prestige LP FE model, the biomechanical parameters of the CSDP FE model were relatively close to those of the intact FE cervical spine model. The CSDP error FE models proved that the performance of the CSDP, namely, ROM, bone-implant interface stress, and facet-joint force, is affected by the implantation position. In addition, we conducted friction-wear tests on the CSDP based on the results of the FE analysis to understand its degree of durability. Finally, the CSDP had satisfactory performance in non-human primate experiments.

DATA AVAILABILITY STATEMENT

The original contributions presented in the study are included in the article/supplementary material, further inquiries can be directed to the corresponding author/s.

ETHICS STATEMENT

The animal study was reviewed and approved by Huazhen Biotechnology, Guangzhou, China.

AUTHOR CONTRIBUTIONS

ZLi, GS, and YH designed the experiments. JWo, ZLv, and JWa performed the research. YL assisted with the FE models and data analysis. KS and HZ contributed to animal study design. JWo and JWa prepared the manuscript. ZLi and GS revised the manuscript. All authors contributed to the article and approved the submitted version.

FUNDING

This work was supported by the National Natural Science Foundation of China (No. 31970862), the Natural Science

Foundation of Guangdong Province (Nos. 2018A030313576, 2019A1515011335), the Science and Technology Program of Guangzhou (No. 201803010001), and the Medical Research Project of Foshan Municipal Health Bureau (No. 20210072).

ACKNOWLEDGMENTS

The authors wish to thank Shishu Huang for critical comments, and Ms. Charron of Yale University for revising and editing the manuscript.

REFERENCES

Ahn, H. S., and DiAngelo, D. J. (2008). A biomechanical study of artificial cervical discs using computer simulation. *Spine* 33, 883–892. doi: 10.1097/BRS.0b013e31816b1f5c

Anderson, P. A., and Rouleau, J. P. (2004). Intervertebral disc arthroplasty. *Spine* 29, 2779–2786. doi: 10.1097/01.brs.0000146460.11591.8a

Anderson, P. A., Sasso, R. C., and Riew, K. D. (2008). Comparison of adverse events between the Bryan artificial cervical disc and anterior cervical arthrodesis. *Spine* 33, 1305–1312. doi: 10.1097/BRS.0b013e31817329a1

Bertagnoli, R., Zigler, J., Karg, A., and Voigt, S. (2005). Complications and strategies for revision surgery in total disc replacement. *Orthop. Clin. N. Am.* 36, 389–395. doi: 10.1016/j.ocl.2005.03.003

Carrier, C. S., Bono, C. M., and Lebl, D. R. (2013). Evidence-based analysis of adjacent segment degeneration and disease after ACDF: a systematic review. *Spine J.* 13, 1370–1378. doi: 10.1016/j.spinee.2013.05.050

Chang, U. K., Kim, D. H., Lee, M. C., Willenberg, R., Kim, S. H., and Lim, J. (2007a). Changes in adjacent-level disc pressure and facet joint force after cervical arthroplasty compared with cervical discectomy and fusion. *J. Neurosurg. Spine* 7, 33–39. doi: 10.3171/SPI-07/07/033

Chang, U. K., Kim, D. H., Lee, M. C., Willenberg, R., Kim, S. H., and Lim, J. (2007b). Range of motion change after cervical arthroplasty with ProDisc-C and Prestige artificial discs compared with anterior cervical discectomy and fusion. *J Neurosurg. Spine* 7, 40–46. doi: 10.3171/SPI-07/07/040

Choi, H., Purushothaman, Y., Baisden, J., and Yoganandan, N. (2020). Unique biomechanical signatures of Bryan, Prodisc C, and Prestige LP cervical disc replacements: a finite element modelling study. *Eur. Spine J.* 29, 2631–2639. doi: 10.1007/s00586-019-06113-y

Clausen, J. D., Goel, V. K., Traynelis, V. C., and Scifert, J. (1997). Uncinate processes and Luschka joints influence the biomechanics of the cervical spine: quantification using a finite element model of the C5-C6 segment. *J. Orthop. Res.* 15, 342–347. doi: 10.1002/jor.1100150305

Di Martino, A., Papalia, R., Albo, E., Cortesi, L., Denaro, L., and Denaro, V. (2015). Cervical spine alignment in disc arthroplasty: should we change our perspective? *Eur. Spine J.* 24, S810–S825. doi: 10.1007/s00586-015-4258-6

Dmitriev, A. E., Cunningham, B. W., Hu, N., Sell, G., Vigna, F., and McAfee, P. C. (2005). Adjacent level intradiscal pressure and segmental kinematics following a cervical total disc arthroplasty: an *in vitro* human cadaveric model. *Spine* 30, 1165–1172. doi: 10.1097/01.brs.0000162441.23824.95

Faizan, A., Goel, V. K., Garfin, S. R., Bono, C. M., Serhan, H., Biyani, A., et al. (2012). Do design variations in the artificial disc influence cervical spine biomechanics? A finite element investigation. *Eur. Spine J.* 21, S653–S662. doi: 10.1007/s00586-009-1211-6

Gandhi, A. A., Kode, S., DeVries, N. A., Grosland, N. M., Smucker, J. D., and Fredericks, D. C. (2015). Biomechanical analysis of cervical disc replacement and fusion using single level, two level, and hybrid constructs. *Spine* 40, 1578–1585. doi: 10.1097/BRS.0000000000001044

Hilibrand, A. S., and Robbins, M. (2004). Adjacent segment degeneration and adjacent segment disease: the consequences of spinal fusion? *Spine J.* 4, 190S−194S. doi: 10.1016/j.spinee.2004.07.007

Holmes, A., Wang, C., Han, Z. H., and Dang, G. T. (1994). The range and nature of flexion extension motion in the cervical-spine. *Spine* 19, 2505–2510. doi: 10.1097/00007632-199411001-00003

Huang, R. C., Lim, M. R., Girardi, F. P., and Cammisa, F. P. (2004). The prevalence of contraindications to total disc replacement in a cohort of lumbar surgical patients. *Spine* 29, 2538–2541. doi: 10.1097/01.brs.0000144829.57885.20

Kowalczyk, I., Lazaro, B. C. R., Fink, M., Rabin, D., and Duggal, N. (2011). Analysis of *in vivo* kinematics of 3 different cervical devices: Bryan disc, ProDisc-C, and Prestige LP disc. *J. Neurosurg. Spine* 15, 630–635. doi: 10.3171/2011.8.SPINE11273

Kubo, S., Goel, V. K., Yang, S. J., and Tajima, N. (2003). Biomechanical evaluation of cervical double-door laminoplasty using hydroxyapatite spacer. *Spine* 28, 227–234. doi: 10.1097/01.BRS.0000042246.09816.20

Lai, H., Goto, S., Yamagata, M., Tamaki, T., Moriya, H., Takahashi, K., et al. (1994). Three-dimensional motion of the upper cervical spine in rheumatoid arthritis. *Spine* 19, 272–276. doi: 10.1097/00007632-199402000-00004

Lazaro, B. C. R., Yucesoy, K., Yuksel, K. Z., Kowalczyk, I., Rabin, D., Fink, M., et al. (2010). Effect of arthroplasty design on cervical spine kinematics: analysis of the Bryan Disc, ProDisc-C, and Synergy Disc. *Neurosurg. Focus* 28:E6. doi: 10.3171/2010.3.FOCUS1058

Lee, J. H., Park, W. M., Kim, Y. H., and Jahng, T. A. (2016). A biomechanical analysis of an artificial disc with a shock-absorbing core property by using whole-cervical spine finite element analysis. *Spine* 41, E893–E901. doi: 10.1097/BRS.0000000000001468

Lee, S. H., Im, Y. J., Kim, K. T., Kim, Y. H., Park, W. M., and Kim, K. (2011). Comparison of cervical spine biomechanics after fixed- and mobile-core artificial disc replacement: a finite element analysis. *Spine* 36, 700–708. doi: 10.1097/BRS.0b013e3181f5cb87

Lin, C. Y., Kang, H., Rouleau, J. P., Hollister, S. J., and La Marca, F. (2009). Stress analysis of the interface between cervical vertebrae end plates and the Bryan, Prestige LP, and ProDisc-C cervical disc prostheses an *in vivo* image-based finite element study. *Spine* 34, 1554–1560. doi: 10.1097/BRS.0b013e3181aa643b

Matge, G., Berthold, C., Gunness, V. R. N., Hana, A., and Hertel, F. (2015). Stabilization with the Dynamic Cervical Implant: a novel treatment approach following cervical discectomy and decompression. *J. Neurosurg. Spine* 22, 237–245. doi: 10.3171/2014.10.SPINE131089

Mimura, M., Moriya, H., Watanabe, T., Takahashi, K., Yamagata, M., and Tamaki, T. (1989). Three-dimensional motion analysis of the cervical spine with special reference to the axial rotation. *Spine* 14, 1135–1139. doi: 10.1097/00007632-198911000-00001

Mo, Z. J., Zhao, Y. B., Du, C. F., Sun, Y., Zhang, M., and Fan, Y. B. (2015). Does location of rotation center in artificial disc affect cervical biomechanics? *Spine* 40, E469–E475. doi: 10.1097/BRS.0000000000000818

Moroney, S. P., Schultz, A. B., Miller, J. A., and Andersson, G. B. (1988). Load-displacement properties of lower cervical spine motion segments. *J. Biomech.* 21, 769–779. doi: 10.1016/0021-9290(88)90285-0

Ng, H. W., Teo, E. C., and Zhang, Q. H. (2004). Biomechanical effects of C2-C7 intersegmental stability due to laminectomy with unilateral and bilateral facetectomy. *Spine* 29, 1737–1745. doi: 10.1097/01.BRS.0000134574.36487.EB

Nunley, P. D., Coric, D., Frank, K. A., and Stone, M. B. (2018). Cervical disc arthroplasty: current evidence and real-world application. *Neurosurgery* 83, 1087–1106. doi: 10.1093/neuros/nyx579

Pandey, P. K., Pawar, I., Gupta, J., and Verma, R. R. (2017). Comparison of outcomes of single-level anterior cervical discectomy with fusion and single-level artificial cervical disc replacement for single-level cervical degenerative disc disease. *Spine* 42, E41–E49. doi: 10.1097/BRS.0000000000001696

Panjabi, M. M., Crisco, J. J., Vasavada, A., Oda, T., Cholewicki, J., Nibu, K., et al. (2001). Mechanical properties of the human cervical spine as shown by three-dimensional load-displacement curves. *Spine* 26, 2692–2700. doi: 10.1097/00007632-200112150-00012

Panjabi, M. M., Summers, D. J., Pelker, R. R., Videman, T., Friedlaender, G. E., and Southwick, W. O. (1986). Three-dimensional load-displacement curves due to forces on the cervical spine. *J. Orthop. Res.* 4, 152–161. doi: 10.1002/jor.1100040203

Pelker, R. R., Duranceau, J. S., and Panjabi, M. M. (1991). Cervical spine stabilization. A three-dimensional, biomechanical evaluation of

rotational stability, strength, and failure mechanisms. *Spine* 16, 117–122. doi: 10.1097/00007632-199116020-00003

Penning, L. (1978). Normal movements of the cervical spine. *Am. J. Roentgenol.* 130, 317–326. doi: 10.2214/ajr.130.2.317

Penning, L., and Wilmink, J. T. (1987). Rotation of the cervical spine. A CT study in normal subjects. *Spine* 12, 732–738. doi: 10.1097/00007632-198710000-00003

Rousseau, M. A., Bonnet, X., and Skalli, W. (2008). Influence of the geometry of a ball-and-socket intervertebral prosthesis at the cervical spine - a finite element study. *Spine* 33, E10–E14. doi: 10.1097/BRS.0b013e31815e62ea

Rundell, S. A., Auerbach, J. D., Balderston, R. A., and Kurtz, S. M. (2008). Total Disc replacement positioning affects facet contact forces and vertebral body strains. *Spine* 33, 2510–2517. doi: 10.1097/BRS.0b013e318186b258

Sasso, R. C., Anderson, P. A., Riew, K. D., and Heller, J. G. (2011). Results of cervical arthroplasty compared with anterior discectomy and fusion: four-year clinical outcomes in a prospective, randomized controlled trial. *J. Bone Joint Surg.* 93, 1684–1692. doi: 10.2106/JBJS.J.00476

Thaler, M., Hartmann, S., Gstottner, M., Lechner, R., Gabl, M., and Bach, C. (2013). Footprint mismatch in total cervical disc arthroplasty. *Eur. Spine J.* 22, 759–765. doi: 10.1007/s00586-012-2594-3

Weinans, H., Huiskes, R., and Grootenboer, H. J. (1993). Quantitative analysis of bone reactions to relative motions at implant-bone interfaces. *J. Biomech.* 26, 1271–1281. doi: 10.1016/0021-9290(93)90351-E

Yu, C. C., Liu, P., Huang, D. G., Jiang, Y. H., Feng, H., and Hao, D. J. (2016). A new cervical artificial disc prosthesis based on physiological curvature of end plate: a finite element analysis. *Spine J.* 16, 1384–1391. doi: 10.1016/j.spinee.2016.06.019

Zhang, Q. H., Teo, E. C., Ng, H. W., and Lee, V. S. (2006). Finite element analysis of moment-rotation relationships for human cervical spine. *J. Biomech.* 39, 189–193. doi: 10.1016/j.jbiomech.2004.10.029

Zhong, Z. M., Zhu, S. Y., Zhuang, J. S., Wu, Q., and Chen, J. T. (2016). Reoperation after cervical disc arthroplasty versus anterior cervical discectomy and fusion: a meta-analysis. *Clin. Orthop. Relat. R.* 474, 1307–1316. doi: 10.1007/s11999-016-4707-5

Conflict of Interest: The authors declare that the research was conducted in the absence of any commercial or financial relationships that could be construed as a potential conflict of interest.

frontiers in Bioengineering and Biotechnology

ORIGINAL RESEARCH
published: 29 July 2021
doi: 10.3389/fbioe.2021.688041

The Influence of Kinematic Constraints on Model Performance During Inverse Kinematics Analysis of the Thoracolumbar Spine

Mohammad Mehdi Alemi[1,2], *Katelyn A. Burkhart*[1,2], *Andrew C. Lynch*[1], *Brett T. Allaire*[1], *Seyed Javad Mousavi*[1,2], *Chaofei Zhang*[3], *Mary L. Bouxsein*[1,2] *and Dennis E. Anderson*[1,2]*

[1] Center for Advanced Orthopaedic Studies, Beth Israel Deaconess Medical Center, Boston, MA, United States, [2] Department of Orthopaedic Surgery, Harvard Medical School, Boston, MA, United States, [3] Department of Automotive Engineering, Tsinghua University, Beijing, China

OPEN ACCESS

Edited by:
Fabio Galbusera, Galeazzi Orthopedic Institute (IRCCS), Italy

Reviewed by:
Sai Wei Yang, National Yang-Ming University, Taiwan
Riza Bayoglu, NuVasive, United States

***Correspondence:**
Dennis E. Anderson
danders7@bidmc.harvard.edu

Specialty section:
This article was submitted to Biomechanics, a section of the journal Frontiers in Bioengineering and Biotechnology

Received: *30 March 2021*
Accepted: *28 June 2021*
Published: *29 July 2021*

Citation:
Alemi MM, Burkhart KA, Lynch AC, Allaire BT, Mousavi SJ, Zhang C, Bouxsein ML and Anderson DE (2021) The Influence of Kinematic Constraints on Model Performance During Inverse Kinematics Analysis of the Thoracolumbar Spine. Front. Bioeng. Biotechnol. 9:688041. doi: 10.3389/fbioe.2021.688041

Motion analysis is increasingly applied to spine musculoskeletal models using kinematic constraints to estimate individual intervertebral joint movements, which cannot be directly measured from the skin surface markers. Traditionally, kinematic constraints have allowed a single spinal degree of freedom (DOF) in each direction, and there has been little examination of how different kinematic constraints affect evaluations of spine motion. Thus, the objective of this study was to evaluate the performance of different kinematic constraints for inverse kinematics analysis. We collected motion analysis marker data in seven healthy participants (4F, 3M, aged 27–67) during flexion–extension, lateral bending, and axial rotation tasks. Inverse kinematics analyses were performed on subject-specific models with 17 thoracolumbar joints allowing 51 rotational DOF (51DOF) and corresponding models including seven sets of kinematic constraints that limited spine motion from 3 to 9DOF. Outcomes included: (1) root mean square (RMS) error of spine markers (measured vs. model); (2) lag-one autocorrelation coefficients to assess smoothness of angular motions; (3) maximum range of motion (ROM) of intervertebral joints in three directions of motion (FE, LB, AR) to assess whether they are physiologically reasonable; and (4) segmental spine angles in static ROM trials. We found that RMS error of spine markers was higher with constraints than without ($p < 0.0001$) but did not notably improve kinematic constraints above 6DOF. Compared to segmental angles calculated directly from spine markers, models with kinematic constraints had moderate to good intraclass correlation coefficients (ICCs) for flexion–extension and lateral bending, though weak to moderate ICCs for axial rotation. Adding more DOF to kinematic constraints did not improve performance in matching segmental angles. Kinematic constraints with 4–6DOF produced similar levels of smoothness across all tasks and generally improved smoothness compared to 9DOF or unconstrained (51DOF) models. Our results also revealed that the maximum joint ROMs predicted using 4–6DOF constraints were largely within physiologically acceptable ranges throughout the spine and in all directions of motions. We conclude that a kinematic constraint with 5DOF

can produce smooth spine motions with physiologically reasonable joint ROMs and relatively low marker error.

Keywords: spine motion, degrees of freedom, dynamic movement, smoothness of motion, optoelectronic motion capture

INTRODUCTION

Spinal disorders, particularly low back pain (LBP), are key global health problems in both workplace and clinical settings with devastating effects on functional independence and work capacity, leading to disability and high medical and societal costs. For instance, LBP accounts for ∼40% of lost workdays with an estimated direct healthcare expenditure of $50–90 billion annually in the US (Guo et al., 1999; Yang et al., 2016). Many spinal disorders, including idiopathic back pain, degenerative disc disease, lumbar spinal stenosis, vertebral fractures (traumatic or osteoporotic), spine deformity, and muscle imbalance (e.g., myopathy, muscle dystrophy), can alter the kinematics and posture of the trunk (Al-Eisa et al., 2006; Briggs et al., 2007; Mahaudens et al., 2009; Galvis et al., 2016; Kuwahara et al., 2016; Schmid et al., 2016; Basques et al., 2017; Christe et al., 2017; Chun et al., 2017; Crawford et al., 2018; Igawa et al., 2018). Therefore, objective measurements of trunk kinematics and posture are useful in evaluating the functional impacts of spinal disorders and the development of novel clinical treatments. Typically, spine alignment and posture are studied as an overall trunk angle. However, direct measurement of individual vertebral movement is possible and can provide added information on spine biomechanics in health and disease. For instance, *in vivo* measurements of intervertebral motion can be obtained using various techniques such as biplane fluoroscopy (Lin et al., 2014; Wang et al., 2020), videofluoroscopy (Wong et al., 2006; Cheng et al., 2016), standard radiographs (Cheng et al., 2016), CT scans (Cheng et al., 2016), and MRI (Fujii et al., 2007). However, such methods are costly and highly invasive, making them impractical for widespread use for either clinical or research purposes.

Optoelectronic motion analysis is a standard technique to measure body kinematics and is often implemented in studies of upper and lower extremity motions. Several studies have already reported the use of optoelectronic motion capture systems (such as Vicon Nexus) for measurement of trunk posture and motion (Rast et al., 2016; Sung et al., 2016; Ignasiak et al., 2017; Marich et al., 2017; Zwambag et al., 2019). However, there is no standardized approach for measurement of trunk posture and spinal motion due to the methodological differences [e.g., different marker location, marker set (single or clusters), and the number of markers on the spine] involved in generating reproducible spinal kinematics (Mason et al., 2016). Some studies have addressed the between-session reliability of motion capture for trunk posture and range of motion (ROM) measurements (Dunk et al., 2004, 2005; O'Sullivan et al., 2010; Fortin et al., 2012; Hidalgo et al., 2012; Harsted et al., 2016; Rast et al., 2016; Muyor et al., 2017; Mousavi et al., 2018). Overall, these studies provide some evidence that optoelectronic motion capture data may provide an indirect but reliable approach to non-invasively assess the kinematics of the spine.

Although optoelectronic motion analysis systems allow overall measurement of trunk posture and motion, it does not directly measure individual vertebral joint movement. However, such motions may be estimated by imposing kinematic constraints on a spine model. Kinematic constraints apply interconnections between articulating segments which consequently reduce the degrees of freedom (DOF) and restrict the relative motions. Musculoskeletal models of the spine often rely on kinematic constraints to distribute overall motion to specific levels because skin-surface markers are unable to directly measure the motion of individual intervertebral joints (Lu and O'Connor, 1999; Roux et al., 2002; Andersen et al., 2010; El Habachi et al., 2015; Mason et al., 2016; Rajagopal et al., 2016; Cazzola et al., 2017; Kuo et al., 2018). Applying appropriate kinematic constraints on spine motion can minimize the effect of soft tissue artifacts on segmental kinematics (Lu and O'Connor, 1999), restrict the motion between adjacent segments, and prevent unrealistic intervertebral motions (Leardini et al., 2005; Lu and Chang, 2012). Therefore, appropriate kinematic constraints can generate trajectories for individual vertebral bodies that closely mimic real spinal movement. To our knowledge, most studies using kinematic constraints in musculoskeletal models of the spine have limited the spine to single DOF in each direction (e.g., Lu and O'Connor, 1999; Roux et al., 2002; Anderst et al., 2013; Mason et al., 2016; Bayoglu et al., 2019; Beaucage-Gauvreau et al., 2019), and there has been no examination of how different kinematic constraints might affect the evaluations of spine motion. Fewer constraints (i.e., more DOF) would provide models with more freedom to follow subject-specific spinal motion with less error in tracking the experimental marker data. However, with more DOF, spine kinematics could be more susceptible to movement artifacts causing unrealistic spine angles or discontinuities that prevent a "smooth" motion.

Therefore, the objective of this study was to evaluate the effect of seven different kinematic constraint conditions (allowing three through nine spine DOF) on marker error, smoothness of angular motions and estimated segmental motions when performing inverse kinematics with a thoracolumbar spine model. This information could help identify appropriate kinematic constraints in producing realistic spine motions based on motion analysis data.

MATERIALS AND METHODS

Participants

A convenience sample of seven healthy adult volunteers (4 F, 3 M) was used for this study, drawn from participants in our

TABLE 1 | List of all studies used to estimate the intervertebral motion ratios in the thoracic and lumbar spines.

Study	Measurement technique	Thoracic			Lumbar		
		FE	LB	AR	FE	LB	AR
Cheng et al. (2016)	Standard bending radiographs/video fluoroscopy				X	X	
Fujii et al. (2007)	MRI						X
Fujimori et al. (2012)	CT-scan			X			
Fujimori et al. (2014)	CT-scan		X				
Mannion et al. (2004)	Spinal Mouse curvature measurement device	X			X		
Morita et al. (2014)	CT-scan	X					
Panjabi et al. (1994)	3D load-displacement curves				X	X	X
Pearcy and Tibrewal (1984)	Biplane radiography					X	X
Rozumalski et al. (2008)	Motion analysis marker clusters attached to vertebral spinous processes via Kirshner wires				X	X	X
Shin et al. (2013)	Biplane radiography						X
White and Panjabi (1978)	Literature review	X	X	X	X	X	X
Willems et al. (1996)	Electromagnetic motion analysis system	X					
Wong et al. (2006)	Video fluoroscopy				X		

FE, flexion–extension; LB, lateral bending; AR, axial rotation; MRI, magnetic resonance imaging.

prior study of the reliability of measuring spine range of motion with an optoelectronic motion analysis system (Mousavi et al., 2018). The mean (±SD) age, height, weight, and BMI of the participants were 42 (±14) years, 172 (±7) cm, 69.6 (±11.1) kg, and 23.3 (±2.3) kg/m^2, respectively. Exclusion criteria for enrollment included any history of recent back pain, spinal surgery, traumatic vertebral fractures, thoracic deformity, and/or conditions affecting balance, movement, or ability to stand. The study was approved by the Institutional Review Board of Beth Israel Deaconess Medical Center. Written informed consent was obtained from all participants.

Procedures

At the beginning of each experimental session, age, height, and weight were recorded. For proper placement of retroreflective markers, anatomical landmarks were carefully palpated and marked. Then, retroreflective markers were attached to the skin using double-adhesive tape. Specifically, seven rigid clusters, consisting of four 9.5 mm retroreflective markers, were attached to the skin overlying the T1, T4, T5, T8, T9, T12, and L1 spinous processes. Additional 14-mm markers were placed over the iliac crests, anterior (ASIS) and posterior (PSIS) superior iliac spines, head (using a headband with attached four retroreflective markers), C7, shoulders (bilaterally on the acromion), sternum, clavicles, elbows (lateral epicondyle of the humerus), wrist (radial styloid process), greater trochanter of the femur, lateral and medial aspects of the knee joint, lateral and medial aspects of the ankle joint, posterior heel and first metatarsophalangeal joint (Mousavi et al., 2018). Marker positions during activities were collected using a 10-camera motion analysis system (Vicon Motion Systems, Oxford, UK). All participants were instructed to stand upright and facing forward (as standard anatomical posture) with arms slightly abducted, palms facing anteriorly, and feet shoulder-width apart. Initially, 3-D marker data were collected in the neutral, upright standing posture and static poses held in self-selected maximum flexion, extension, lateral bending, and axial rotation positions for ∼5 s each. Participants were then asked to perform three separate dynamic tasks in the following order: spinal flexion–extension, lateral bending (i.e., first left and then right lateral bending), and axial rotation (i.e., first left and then right axial rotation). In each dynamic task, the participants moved to their self-selected maximum ROM in 2 s (following a metronome), returned to neutral in 2 s, moved to their self-selected maximum ROM in the opposite direction in 2 s, and returned to neutral in 2 s. Participants performed this full sequence at least three times for each dynamic task. For the dynamic tasks, participants began in neutral, upright standing with their arms down at their sides, and during the motions, they kept their feet on the ground but were allowed to move their arms as needed to fully complete each motion.

Development of Kinematic Constraints

Ratios of Intervertebral Motion to Overall Spine Motion

For each direction of static and dynamic motion [i.e., flexion–extension (FE), lateral bending (LB), and axial rotation (AR)], we estimated the proportion of each intervertebral level motion from previous work that provided values for FE, LB, and AR in the thoracic and lumbar spines (**Table 1**). These studies evaluated segmental ranges of motion *in vivo* using a wide variety of techniques, including standard radiographs (Cheng et al., 2016), videofluoroscopy (Wong et al., 2006; Cheng et al., 2016), biplane radiography (Pearcy and Tibrewal, 1984; Shin et al., 2013), MRI (Fujii et al., 2007), CT scans (Fujimori et al., 2012, 2014; Morita et al., 2014), a spinal mouse curvature measurement device (Mannion et al., 2004), motion analysis marker clusters attached to vertebral spinous processes via Kirshner wires (Rozumalski et al., 2008), and an electromagnetic motion analysis system (Willems et al., 1996). We also included reported physiological ROM from the works of White and Panjabi (1978) and Panjabi et al. (1994). The angular motions

TABLE 2 | Ratios of individual-level intervertebral motions to overall spine motion were used to create kinematic constraints in flexion–extension, lateral bending, and axial rotation tasks.

Joint level	Flexion–extension	Lateral bending	Axial rotation
L5/S1	0.132	0.037	0.039
L4/L5	0.155	0.082	0.040
L3/L4	0.150	0.104	0.040
L2/L3	0.160	0.101	0.038
L1/L2	0.118	0.081	0.036
T12/L1	0.037	0.067	0.020
T11/T12	0.039	0.073	0.035
T10/T11	0.039	0.057	0.060
T9/T10	0.030	0.050	0.073
T8/T9	0.019	0.045	0.085
T7/T8	0.017	0.051	0.087
T6/T7	0.015	0.041	0.079
T5/T6	0.015	0.036	0.078
T4/T5	0.009	0.038	0.074
T3/T4	0.016	0.046	0.070
T2/T3	0.024	0.045	0.074
T1/T2	0.028	0.046	0.072

*The value in each cell is the median value of the rotational motion ratio assessed for each intervertebral level (based on all studies listed in **Table 1**).*

TABLE 3 | Summary of kinematic constraint conditions tested, indicating the total spine DOF and DOF in each rotational direction, plus the spine sections for each DOF and rotational direction.

Condition/Total DOF	FE DOF/Spine sections	LB DOF/Spine sections	AR DOF/Spine sections
3DOF	1 [T1-S1]	1 [T1-S1]	1 [T1-S1]
4DOF	2 [T1–T9, T9-S1]	1 [T1-S1]	1 [T1-S1]
5DOF	2 [T1–T9, T9-S1]	2 [T1-L1, L1-S1]	1 [T1-S1]
6DOF	2 [T1–T9, T9-S1]	2 [T1-L1, L1-S1]	2 [T1-L1, L1-S1]
7DOF	2 [T1–T9, T9-S1]	2 [T1-L1, L1-S1]	3 [T1–T9, T9-L1, L1-S1]
8DOF	2 [T1–T9, T9-S1]	3 [T1–T5, T5-L1, L1-S1]	3 [T1–T9, T9-L1, L1-S1]
9DOF	3 [T1–T9, T9-L1, L1-S1]	3 [T1–T5, T5-L1, L1-S1]	3 [T1–T9, T9-L1, L1-S1]

FE, flexion–extension; LB, lateral bending; AR, axial rotation; DOF, degrees of freedom.

at each intervertebral joint were converted to ratios relative to overall thoracic or lumbar motion. Because of inconsistencies in the methods used to estimate the intervertebral motions, we used the median value of the reported rotational motion ratio assessed for each level in the current study. The median values determined for thoracic and lumbar spines were then combined and expressed as ratios proportional to overall spine motion (**Table 2**). Percentage values of intervertebral joint motions to overall thoracic and lumbar spine motions in different studies (i.e., listed studies in **Table 1**) were shown in Tables 1–4 in Appendix A (**Supplementary Material**).

Kinematic Constraints Employed in Models

The ratios presented in **Table 2** were applied as kinematic constraints in subject-specific models. The ratios shown in **Table 2** reduced the overall spine kinematics to a single DOF in each orthogonal direction of spine motion or three DOF overall. Segmental motion data from our prior study suggests that some segments of the spine act differently than others during certain motions (Mousavi et al., 2018). For example, the upper thorax may extend during full lumbar flexion in some individuals, while the lumbar and thoracic spines may display different behaviors, particularly during axial rotation motions. Thus, we created multiple kinematic constraint conditions allowing three through nine DOF, as shown in **Table 3**. The total spine DOF in models with kinematic constraints refers to the number of independent rotational coordinates, which link the motions within specific sections of the spine. In these models, motion occurs at all levels, but the individual rotations at each level are dependent on the corresponding independent coordinate. For example, for the 3DOF model, the spine has only three independent coordinates, which describe FE, LB, and AR for the entire spine (T1-S1), and the motion of each intervertebral joint is defined as a proportion of the overall motion of the spine. However, in the 4DOF model, the FE motion of the spine has two independent coordinates, applied to sections T1-T9 and T9-S1, respectively, but still just a single independent coordinate in each of the LB and AR directions of motion (see **Table 3**). We also included a baseline condition (i.e., with no kinematic constraint), allowing 51 combined rotational DOF for the 17 thoracolumbar joints. The ratios of individual-level intervertebral motions to the overall spine for all kinematic constraints (3-9DOF) are shown in Table 1 of Appendix B (**Supplementary Material**).

Subject-Specific Modeling and Inverse Kinematics Using OpenSim

For each participant, we created a subject-specific musculoskeletal model based on our previously validated models of the thoracolumbar spine (Bruno et al., 2015, 2017). Models were scaled according to subject height and weight, with body segment lengths and spine curvature adjusted based on marker data recorded in a neutral static standing position (Burkhart et al., 2020). For each subject, we created one model without kinematic constraints applied (allowing 51 spine DOF). Seven additional models were created with the seven sets of kinematic constraints described earlier to limit spine motion to 3–9DOF. For each model and activity measured, we performed inverse kinematics (IK) in OpenSim [version 3.3; Delp et al. (2007)] to compute the joint angles that would best match the model to the measured marker positions. In all models, FE, LB, and AR are independent motions and are determined simultaneously in the inverse kinematics analysis. The marker

positions used for IK analyses were first low-pass filtered (6 Hz, fourth-order Butterworth filter, bidirectional). After completing IK analyses, OpenSim generated motion files containing the relative angles between adjacent vertebrae in each direction of motion (FE, LB, AR). The kinematic results were additionally used to evaluate Euler angles for particular spine segments of interest.

Outcome Measures and Statistical Analyses

The primary outcomes for this study were: (1) root mean square (RMS) error of recorded vs. tracked spine markers; (2) lag-one autocorrelation coefficient of the segmental (i.e., T1-T5, T5-T9, T9-L1, L1-S1) angular motions for each primary direction of tasks (FE, LB, and AR); (3) maximum ROM of intervertebral joint angles across three dynamic tasks (flexion–extension, lateral bending, axial rotation) for all combinations of kinematic constraints and directions of motion (i.e., FE, LB, AR); and (4) segmental spine angles in the static range of motion trials for four spine sections (i.e., T1–T5, T5–T9, T9-L1, L1-S1). Statistical analyses for the first three primary outcomes were performed using JMP Pro 15 (SAS, Cary, NC), using the restricted maximum likelihood method, with a statistical significance level of 0.05. Analyses of static segmental spine angles were performed in Stata/IC 13.1 (StataCorp LP, College Station, TX).

RMS Error of Spine Markers

We defined the RMS error of spine markers for each subject within each task and kinematic constraint as the square root of the sum of marker errors squared (measured vs. model) divided by the number of markers (e.g., 28 markers = 7 clusters × 4 markers on each cluster). For each task, we calculated the mean ± SD of RMS error of markers for each set of kinematic constraints [baseline or no constraint (51DOF) and seven sets of kinematic constraints (3–9DOF)]. We used a two-way repeated-measures analyses of variance (ANOVA) to examine the effects of *Task* and *Constraint* on RMS error of spine markers. Because the interaction effect *Task* × *Constraint* was not statistically significant, we simplified the model by employing separate one-way ANOVA for each task to assess the effect of *Constraint* (as an independent variable) on RMS marker error. Significant effects were followed by pairwise comparisons [Tukey's honest significance difference (HSD)] and simple effects testing, where relevant.

Lag-One Autocorrelation Coefficient of the Segmental Angular Motions

The lag-one autocorrelation coefficient reflects the correlation between values that are one time-step apart and thereby quantifies how much a point in a signal is predictable based on the previous point. Therefore, it can be used as an index to assess the smoothness of the angular motions. We computed the lag-one autocorrelation coefficients of the segmental angular motions for each primary direction of tasks (i.e., FE for flexion–extension, LB for lateral bending, and AR for axial rotation). We performed logit transformation on the autocorrelation coefficients as they were between 0 (least smooth) and 1 (smoothest) and had exhibited a skewed distribution. A one-way repeated measure of ANOVA for each primary task direction was applied to determine the effect of different kinematic constraints (as an independent variable) on the transformed autocorrelation coefficients. Statistically significant effects were followed by pairwise comparisons (Tukey's HSD) and simple effects testing, where relevant.

Maximum ROM of Intervertebral Joint Angles

To determine if the intervertebral joint angles are in a physiologically realistic range, we calculated the maximum ROM of the 17 intervertebral joint angles (i.e., T1/T2, T2/T3, …, L5/S1) grouped in three spine regions (T1–T9, T9-L2, L2-S1), for all combinations of kinematic constraints [3–9DOF and no constraint (51DOF)] and directions of motion (FE, LB, AR). Note that the maximum ROM for each intervertebral joint in each direction of motion was defined using the maximum angles recorded across all three dynamic tasks (i.e., maximum flexion angle–maximum extension angle, maximum left lateral bending angle – maximum right lateral bending angle, maximum left axial rotation angle – maximum right axial rotation angle). These ROMs were compared with the estimated limits of normal ROMs for intervertebral joints presented by White and Panjabi (1978). Because joints within the same part of the spine are expected to have similar ROMs, we combined results within three regions of the spine to simplify comparisons. Specifically, boxplots of ROMs created for thoracic (T1-T2 through T8-T9), thoracolumbar (T9-T10 through L1-L2), and lumbar (L2-L3 through L5-S1) joints and compared to the corresponding expected ranges of joint ROM.

Segmental Spine Angles in the Static Range of Motion Trials

To evaluate whether various kinematic constraints applied to a spine model allow the model to reasonably match measured positions, we compared segmental angles calculated directly from marker cluster orientations to those produced in the model after IK analysis. Marker data were collected for six static standing trials, specifically, while subjects held the position at their full ranges of motion for flexion, extension, left and right lateral bending, and left and right axial rotation. As previously described (Mousavi et al., 2018), Euler angles were calculated between marker clusters to provide rotations for segments T1–T5, T5–T9, T9-L1, and L1-S1.

Agreement between model segmental angles and corresponding cluster angles was evaluated with intra-class correlation coefficients (ICCs) and RMS differences. ICC results were deemed weak (ICC < 0.5), moderate ($0.5 \leq$ ICC < 0.75), good ($0.75 \leq$ ICC < 0.9), or excellent ($0.9 \leq$ ICC) (Koo and Li, 2016), including their 95% CIs. One-way repeated measures ANOVAs were used to examine whether model angles were different from the corresponding cluster angles. Analyses were performed separately for flexion–extension, lateral bending, and axial rotation angles, grouping all segments and trials to provide an overall evaluation of agreement of segmental angles for each direction of spine motion.

RESULTS

RMS Error of Spine Markers

The mean and standard deviation of RMS error of spine markers for different sets of kinematic constraints [3–9DOF and no constraint (51DOF)] in three tasks are summarized in **Figure 1**. Our first statistical analysis demonstrated that although there were significant main effects of *Task* ($p < 0.0001$) and *Constraint* ($p < 0.0001$) on RMS error of spine markers, we did not observe a *Task* × *Constraint* interaction effect ($p \sim 0.499$). The Tukey HSD *post-hoc* analyses showed that RMS error of spine markers was significantly different for all pairs of different tasks [i.e., flexion–extension greater than lateral bending ($p < 0.0001$), flexion–extension greater than axial rotation ($p < 0.0001$), and lateral bending smaller than axial rotation ($p < 0.0001$)]. Additionally, the results of our second statistical analysis revealed that a significant effect of *Constraint* within each task was observed for RMS marker errors. All other pairwise comparisons for the constraints within each task are presented in **Table 4**. Across all tasks, the RMS errors of spine markers for 51DOF were significantly lower than other constraints (p-values ≤ 0.0002).

For the flexion–extension, there were no differences in RMS errors between any pair of kinematic constraints with 4–9DOF, whereas the RMS errors for kinematic constraints with 4–9DOF were all significantly lower than the 3DOF model (p-values ≤ 0.0291) and higher than the 51DOF model (p-values < 0.0001). In the lateral bending, there were significant differences between models with lower and higher DOF [i.e., 3DOF >5–9DOF, and 4DOF >8–9DOF, (p-values < 0.05); **Table 4**], but there were no significant differences between any sequential pairs of constraints from 5 to 9DOF. Further, for axial rotation, 6DOF or higher kinematic constraints improved the RMS error of spine markers vs. 3–4DOF. However, no differences between any constraints from 6 to 9DOF were found.

Lag-One Autocorrelation Coefficient of the Angular Motions

The lag-one autocorrelation coefficients varied significantly by *Task* ($p < 0.0001$) and *Constraint* ($p < 0.0001$). The box plot of logit transformed autocorrelation coefficients for different tasks and constraints is shown in **Figure 2**, with larger values indicative of "smoother" joint motion [transformed autocorrelation values on y-axis extend from 0 (*least smoothness*) to 10 (*smoothest*)]. For the flexion–extension task, the lag-one autocorrelation coefficients for all but the 9DOF constraint showed significantly smoother motion than the 51DOF model ($p < 0.0001$; **Table 5**). Additionally, the motion was significantly smoother for the 3DOF model than for all other constraints. The lag-one autocorrelation coefficient did not differ between sequential constraints for flexion–extension, except for smoother motion in the 3DOF model than the 4DOF model ($p = 0.0138$). For lateral bending tasks, the lag-one autocorrelation coefficient differed for three pairs of constraints [3DOF vs. 9DOF, 3DOF vs. 51DOF, and 6DOF vs. 51DOF ($p < 0.05$)], but the differences in lag-one autocorrelation coefficients between sequential constraints were not significant. Finally, motion during all axial rotations was smoother for all constrained models than the 51DOF model ($p < 0.0001$) but was similar for all other constraint comparisons.

Maximum ROM of Intervertebral Joint Angles

Boxplots of maximum ROM of intervertebral joint angles (grouped in three spine regions: thoracic: T1–T9, thoracolumbar: T9-L2, lumbar: L2-S1) for all kinematic constraints [3–9DOF and no constraint (51DOF)] and directions of motion (FE, LB, AR) are depicted in **Figures 3** (FE), **4** (LB), and **5** (AR). To further compare our findings with the results reported in White and Panjabi (1978), we overlaid solid black horizontal lines in **Figures 3–5**, representing the minimum and maximum ROM of intervertebral joints in each spine region and direction of motion. The corresponding values of black horizontal lines in each panel plot in **Figures 3–5** have been calculated based on the results in **Table 2** of conducted study by White and Panjabi (1978). Readers of this paper are referred to Tables 1, 2 in Appendix C (**Supplementary Material**) for the range of maximum ROM of all individual intervertebral joint angles across four tasks (i.e., flexion, extension, lateral bending, axial rotation) for each combination of kinematic constraints [3–9DOF and no constraint (51DOF)] and direction of motion (FE, LB, AR). In Tables 1, 2 in Appendix C (**Supplementary Material**), the flexion–extension tasks were divided into flexion and extension separately.

As seen in **Figures 3–5**, on average, the range and interquartile ranges of the maximum ROM of intervertebral joint angles for 51DOF are often much larger than with constraints and findings in White and Panjabi (1978). For FE direction of motion (**Figure 3**), the medians of the ROM for constraints with 4–9DOF were close to each other and were largely within the reported range of White and Panjabi (1978) for the thoracic (T1–T9) region, while 3DOF underestimated the expected ROM. The medians for most constraints fell slightly below the reported range in the thoracolumbar region (T9-L2) and more so for the lumbar region (L2-S1), but the maximum ROMs found fell within the reported range. For LB direction (**Figure 4**), medians with 3–5DOF fell within the range reported by White and Panjabi (1978) in all spinal regions, although the maximum ROMs exceeded the maximum reported ROM in the lumbar region (L2-S1). Median LB ROMs with 6–51DOF exceeded the maximum reported ROM from White and Panjabi for the lumbar region (L2-S1). For AR direction (**Figure 5**), the medians of the ROM for all constraints were within the ranges reported by White and Panjabi for thoracic (T1–T9) and lumbar (L2-S1) regions. But only 5 and 6DOF had medians within the range for the thoracolumbar (T9-L2) region, although the maximum ROMs exceeded the maximum reported ROM. Overall, it seems that constraints 4DOF through 9DOF all produced similar and largely reasonable ROMs in FE, and similarly constraints 3DOF through 5DOF for LB, and constraints 5DOF and 6DOF for AR.

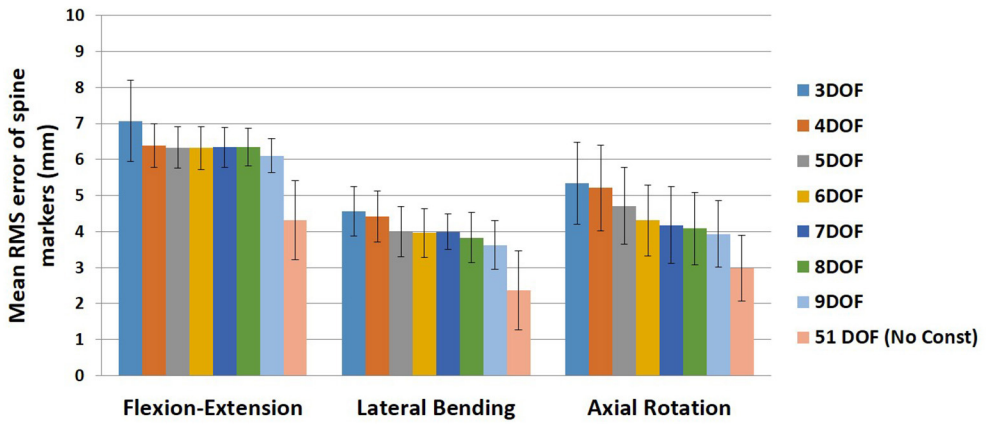

FIGURE 1 | Mean RMS error of spine markers for all kinematic constraints (3–9DOF) and no constraint condition (51DOF) in all tasks (flexion–extension, lateral bending, and axial rotation). Error bars indicate the SDs. RMS, root mean square; DOF, degrees of freedom.

TABLE 4 | Significant *post-hoc* pairwise comparisons (Tukey's HSD) of kinematic constraints for RMS error of spine markers in each task shown in **Figure 1**.

Kinematic constraint	Flexion-extension	Lateral bending	Axial rotation
3DOF	4–9DOFs and 51DOF	5–9DOFs and 51DOF	6–9DOFs and 51DOF
4DOF	3DOF and 51DOF	8–9DOF and 51DOF	6–9DOFs and 51DOF
5DOF	3DOF and 51DOF	3DOF and 51DOF	9DOF and 51DOF
6DOF	3DOF and 51DOF	3DOF and 51DOF	3–4DOFs and 51DOF
7DOF	3DOF and 51DOF	3DOF and 51DOF	3–4DOFs and 51DOF
8DOF	3DOF and 51DOF	3–4DOF and 51DOF	3–4DOFs and 51DOF
9DOF	3DOF and 51DOF	3–4DOFs and 51DOF	3–5DOFs and 51DOF

The constraint(s) in each cell are the constraint(s) significantly different from the corresponding constraint listed in the first column. HSD, honest significance difference; RMS, root mean square; DOF, degrees of freedom.

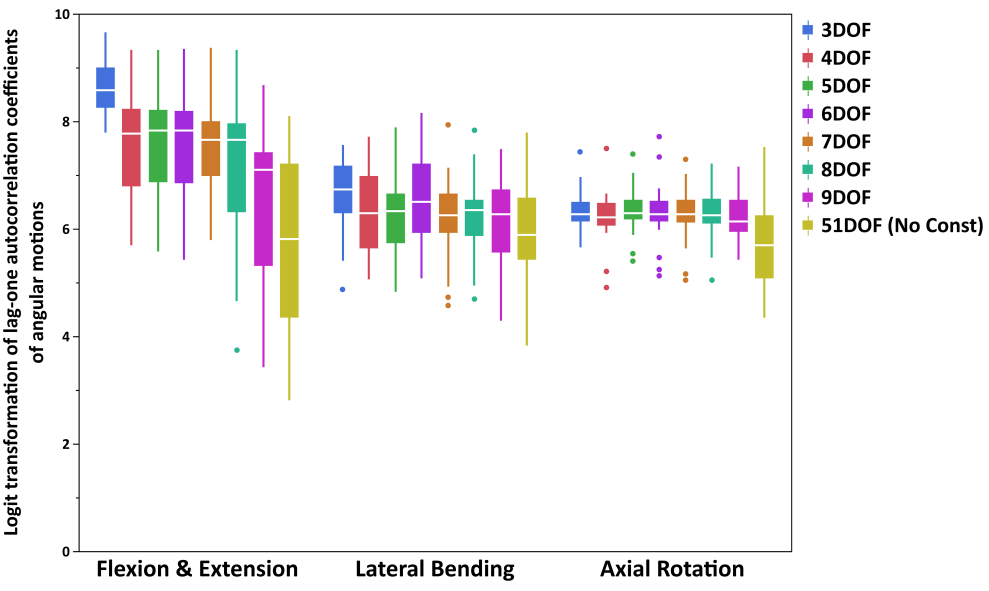

FIGURE 2 | Boxplot of logit transformed lag-one autocorrelation coefficients of angular motions for each primary direction of tasks (FE, LB, and AR). Note that logit transformed autocorrelation values extend from 0 *(least smoothness)* to 10 (*smoothest*). FE, flexion–extension; LB, lateral bending; AR, axial rotation.

TABLE 5 | Pairwise comparisons (Tukey's HSD) of kinematic constraints for lag-one autocorrelation coefficients of angular motions for each primary direction of tasks (FE, LB, and AR).

Kinematic constraint	Flexion-extension	Lateral bending	Axial rotation
3DOF	4–9DOFs and 51DOF	9DOF and 51DOF	51DOF
4DOF	3DOF, 9DOF and 51DOF	NS	51DOF
5DOF	3DOF, 9DOF and 51DOF	NS	51DOF
6DOF	3DOF, 9DOF and 51DOF	51DOF	51DOF
7DOF	3DOF and 51DOF	NS	51DOF
8DOF	3DOF and 51DOF	NS	51DOF
9DOF	3–6DOFs	3DOF	51DOF

The constraint(s) in each cell is the constraint(s) that were significantly different from the corresponding constraint in the first column. NS, no significant differences; HSD, honest significance difference; FE, flexion–extension; LB, lateral bending; AR, axial rotation; DOF, degrees of freedom.

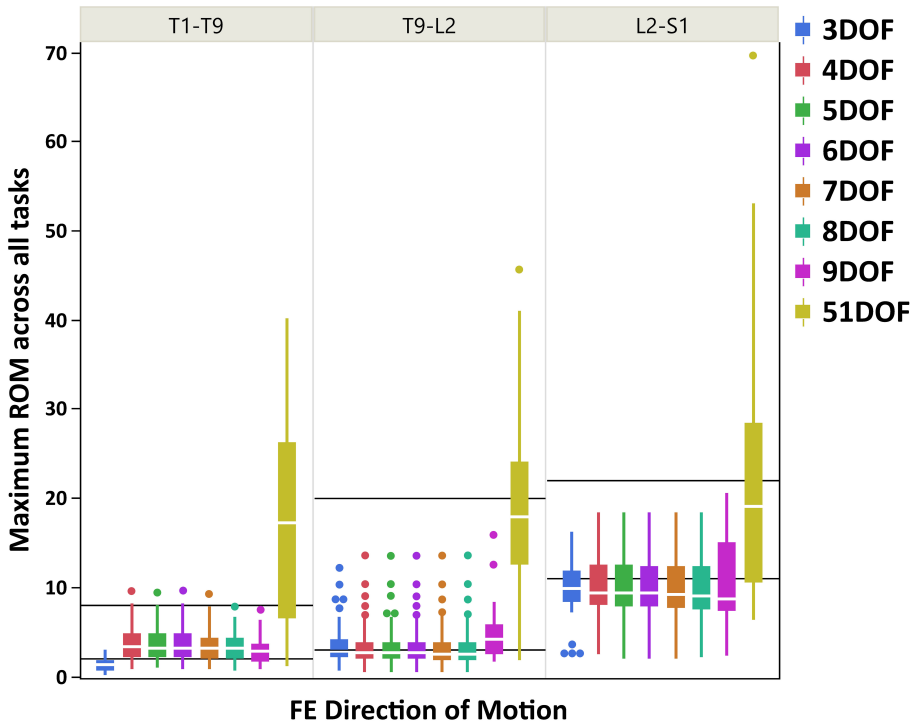

FIGURE 3 | Boxplot of maximum ROM of 17 intervertebral joint angles, grouped in three spine regions [i.e., "T1-T9": T1/T2 to T8/T9; "T9-L2": T9/T10 to L1/L2; "L2-S1": L2/L3 to L5/S1)], for all kinematic constraints [3–9DOF and no constraint (51DOF)] in FE direction of motion. The black lines horizontally overlaid on each panel plot are minimum and maximum ROM of intervertebral joints for the corresponding spine regions in FE direction of motion, reported by White and Panjabi (1978). ROM, range of motion; DOF, degrees of freedom; FE, flexion–extension.

Segmental Spine Angles in the Static Range of Motion Trials

The segmental angle RMS differences ranged from 9.1 to 10.0° for flexion–extension, 8.4–10.5° for lateral bending, and 10.3–12.1° for axial rotation angles (**Table 6**). Models with kinematic constraints had moderate to good ICCs for flexion–extension and lateral bending, though weak to moderate ICCs for axial rotation. The statistical results of ANOVAs indicated a significant effect of the angle evaluation approach (marker cluster orientations, models with kinematic constraints, model without kinematic constraints) for flexion–extension angles ($p = 0.022$), but not for lateral bending or axial rotation angles. However, *post-hoc* testing showed that none of the flexion–extension segmental angles evaluated by the models differed from those evaluated from marker cluster orientations (i.e., any differences were between different models).

DISCUSSION

This study explored the effect of different kinematic constraints on model performance during IK analysis of the thoracolumbar spine. This novel examination addresses a gap in knowledge

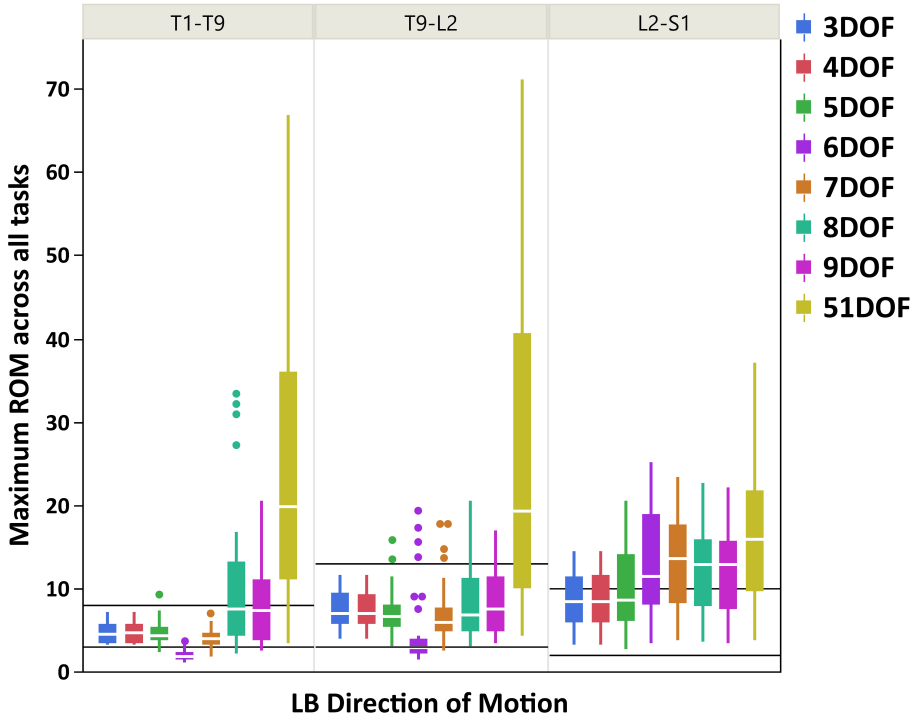

FIGURE 4 | Boxplot of maximum ROM of 17 intervertebral joint angles, grouped in three spine regions [i.e., "T1-T9": T1/T2 to T8/T9; "T9-L2": T9/T10 to L1/L2; "L2-S1": L2/L3 to L5/S1], for all kinematic constraints [3–9DOF and no constraint (51DOF)] in LB direction of motion. The black lines horizontally overlaid on each panel plot are minimum and maximum ROM of intervertebral joints for the corresponding spine regions in LB direction of motion, reported by White and Panjabi (1978). ROM, range of motion; DOF, degrees of freedom; LB, lateral bending.

regarding the influence of kinematic constraints with multiple DOFs on spine motion assessments. Most kinematic constraints previously imposed in musculoskeletal modeling have assumed a single DOF for each direction of spinal bending or rotation. We evaluated the effect of kinematic constraints with four main outcome measurements, including (1) RMS error of spine markers (measured vs. model); (2) lag-one autocorrelation coefficients to quantify the smoothness of angular motions; (3) maximum ROMs of 17 intervertebral joint angles, grouped in three spine regions, and whether they are in a physiologically realistic range; and (4) segmental spine angles in the static range of motions trials to verify if the spine models with different kinematic constraints reasonably match measurements directly from marker clusters.

RMS Error of Spine Markers

On average, the RMS error of spine markers for flexion–extension was higher than lateral bending and axial rotation across all kinematic constraints and no-constraint conditions. It is possible that the skin-surface spine markers are more sensitive to flexion–extension motions as they are largely aligned with the spine in the sagittal plane. RMS error of spine markers in axial rotation appeared to be slightly larger than lateral bending, perhaps because the more complex nature of spine movement in axial rotation (i.e., combination of rotational and coupled bending movement) causes a larger difference between the modeled and experimental position coordinates. Any differences in RMS error of spine markers should be checked for practical significance, as they might not be meaningful if less than the precision of the optoelectronic motion capture system. Merriaux et al. (2017) investigated the positioning performance of the Vicon motion capture system. They reported that the optimal position performance depends on the sampling rate of the system and the marker size, but with optimized performance, the mean absolute error for static and dynamic tasks could be as low as 0.15 and 0.3 mm, respectively. Thus, to define the practical importance of the RMS error of spine markers in our study, we compared the reduction in RMS error of markers between pairs of sequential constraints with the dynamic error estimate of 0.3 mm. Based on this comparison (**Figure 6**), no meaningful improvements in RMS error of spine markers were observed for the flexion–extension task after 4DOF. For lateral bending and axial rotation tasks, meaningful improvements in mean RMS error of spine markers were observed when changing from 4 to 5DOF, and for axial rotation, an additional meaningful improvement was seen in changing from 5 to 6DOF. In sum, depending on the type of the task, the results suggest that kinematic constraints with 4, 5, or 6 DOF may be beneficial, but additional DOF above 6 would not produce meaningful improvements on the RMS error of spine markers. **Figure 6** also includes the change in mean RMS error of spine markers from 9 to 51DOF, showing meaningful improvements in all tasks. It is expected that 51DOF

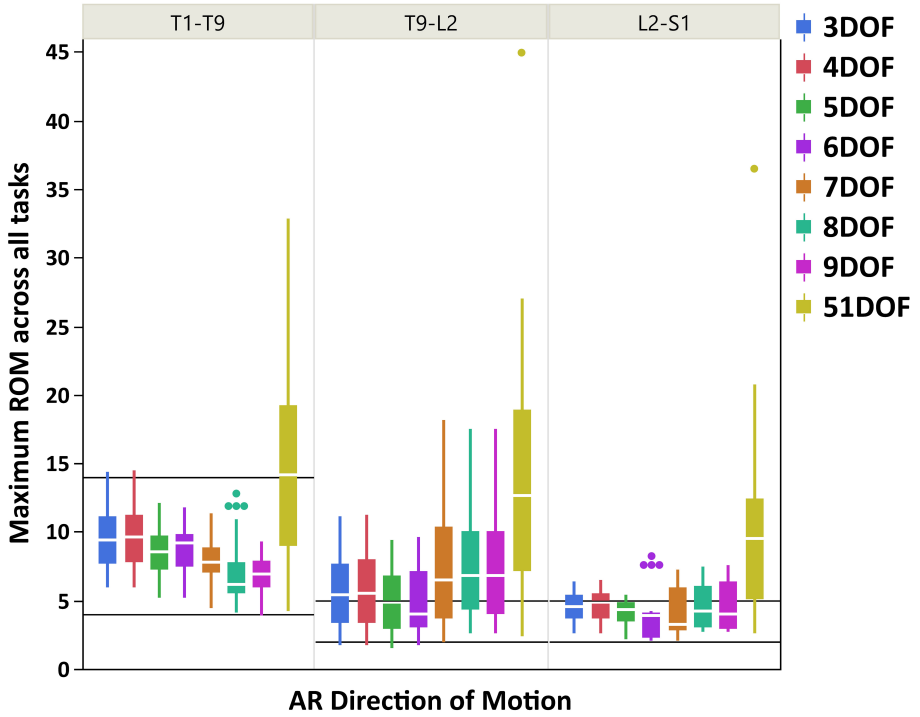

FIGURE 5 | Boxplot of maximum ROM of 17 intervertebral joint angles, grouped in three spine regions [i.e., "T1-T9": T1/T2 to T8/T9; "T9-L2": T9/T10 to L1/L2; "L2-S1": L2/L3 to L5/S1], for all kinematic constraints [3–9DOF and no constraint (51DOF)] in AR direction of motion. The black lines horizontally overlaid on each panel plot are minimum and maximum ROM of intervertebral joints for the corresponding spine regions in AR direction of motion, reported by White and Panjabi (1978). ROM, range of motion; DOF, degrees of freedom; AR, axial rotation.

would produce the smallest RMS error of spine markers among the conditions tested since the spine model with higher DOF can theoretically better adapt to the variation in subject motion. However, it is worth noting that the 1.8 mm improvement in RMS error (seen in flexion–extension) between the 9DOF and the 51DOF model comes by adding 42 more DOF. Thus, each additional DOF improves the RMS error by an average of 0.04 mm, seemingly well below any meaningful value.

Lag-One Autocorrelation Coefficient of the Angular Motions

The lag-one autocorrelation coefficients showed that kinematics in axial rotation were smoother with any constraint from 3 to 9DOF than without constraints (51DOF). This could also be visually inspected from Figure 3 in Appendix B (**Supplementary Material**), where the averaged angular motions of T9-L1 and L1-S1 spine segments for 51DOF were much less smooth than with kinematic constraints. Similarly, kinematics in flexion–extension was smoother with any constraint from 3 to 8DOF than 51DOF, where these findings suggested that moving from 2 to 3 FE DOF would lead the spinal angular motions to be less smooth compared to no-constraint conditions. For the lateral bending, in addition to 3DOF, the 6DOF constraint produced smoother angular motions compared with the 51DOF. This might be partially explained through interactions between LB and AR motions, as the 6DOF constraint is the only constraint with two AR DOF. Overall, the 3DOF constraint produced the smoothest motions during flexion–extension and lateral bending, and this is theoretically expected as the 3DOF constraint has the lowest DOF compared to all other constraints. The constraints 4–6DOF showed similar smoothness behavior in flexion–extension, and all produced smoother kinematics than the 9DOF constraint. Notably, flexion–extension tasks showed higher RMS error of spine markers and higher autocorrelation values (i.e., higher level of smoothness) than lateral bending or axial rotation tasks, indicating limiting DOF in flexion–extension may improve kinematic smoothness at the expense of accuracy. Overall, the lag-one autocorrelation results indicate that constraints between 4 and 6DOF produced similar levels of smoothness for angular motions across all tasks and generally improved smoothness compared to 9DOF or unconstrained models.

Maximum ROM of Intervertebral Joint Angles

The main objective of this section is to assess whether various constraint conditions produce maximum joint ROMs that fall within a physiologically reasonable range. Results in **Figures 3**–**5** demonstrated that maximum ROMs without constraints (51DOF) were notably larger than with constraints for all directions of motion and all regions of the spine and exceeded reasonable physiological ranges. Thus, performing

TABLE 6 | RMSD and ICCs for segmental spine angles from models with various spine DOFs vs. segmental angles calculated directly from the corresponding marker clusters.

Kinematic constraints (DOF)	Flexion-extension		Lateral bending		Axial rotation	
	RMSD	ICC (95% CI)	RMSD	ICC (95% CI)	RMSD	ICC (95% CI)
3	9.3	0.779 (0.712–0.833)	8.5	0.787 (0.720–0.839)	11.5	0.514 (0.391–0.612)
4	9.1	0.796 (0.732–0.846)	8.5	0.787 (0.720–0.839)	11.6	0.516 (0.392–0.621)
5	9.4	0.795 (0.730–0.845)	9.0	0.776 (0.707–0.830)	11.8	0.470 (0.340–0.582)
6	9.2	0.803 (0.740–0.852)	10.1	0.728 (0.647–0.794)	11.2	0.531 (0.410–0.633)
7	9.6	0.784 (0.716–0.837)	9.4	0.766 (0.693–0.823)	11.4	0.530 (0.409–0.633)
8	10.0	0.783 (0.716–0.836)	10.5	0.704 (0.617–0.774)	12.1	0.515 (0.391–0.620)
9	9.8	0.795 (0.730–0.845)	10.3	0.710 (0.624–0.779)	11.7	0.541 (0.422–0.642)
51	9.8	0.789 (0.723–0.841)	9.1	0.785 (0.718–0.838)	10.3	0.687 (0.596–0.761)

RMSD, root mean square differences; ICC, intraclass correlation coefficient; DOF, degrees of freedom.

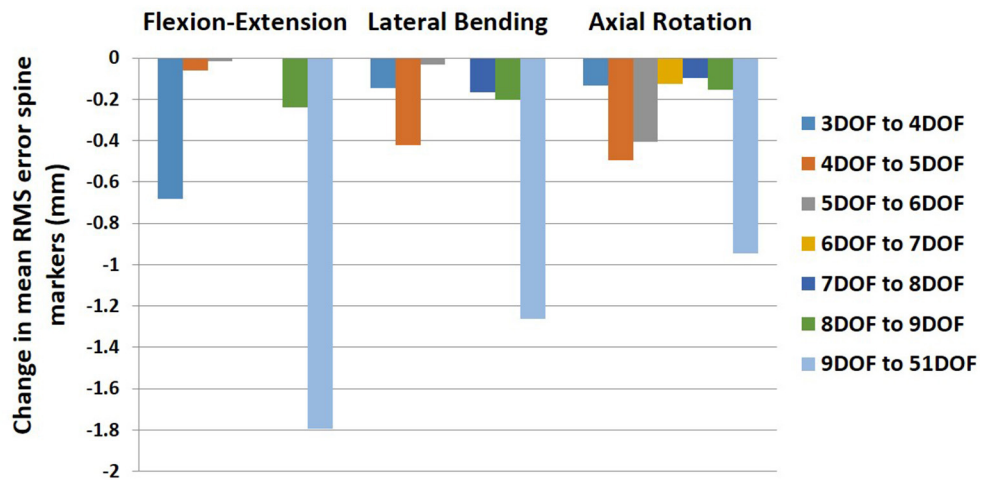

FIGURE 6 | Change in mean RMS error of spine markers for all pairs of sequential kinematic constraints in all tasks (flexion–extension, lateral bending, and axial rotation). RMS, root mean square.

inverse kinematics without kinematic constraints (51DOF) is unsuitable for characterizing *in vivo* spine motion.

On average, results in **Figure 3** suggested that for the FE direction of motion, kinematic constraints 4–9DOF produced quite similar maximum ROMs across all tasks and in all spine regions. The maximum ROM with these constraints did not exceed a physiologically reasonable value. However, the ROMs tended to underestimate the expected values of White and Panjabi (1978) in the thoracolumbar and especially the lumbar regions of the spine. It is possible that the participants tested for this study did not reach their maximum lumbar ROM during the flexion–extension task, which could explain this result. Nonetheless, our results revealed higher maximum ROM of the lumbar intervertebral joints than the thoracic and thoracolumbar joints, in agreement with the trend of expected ROM across different parts of the spine (White and Panjabi, 1978).

For LB direction of motion, larger maximum ROMs were observed for the thoracolumbar and lumbar regions than the thoracic region, consistent with the expected ROMs reported by White and Panjabi (1978). **Figure 4** also indicated that ROMs for kinematic constraints with 3–5DOF were largely within the physiologically acceptable range as reported by White and Panjabi (1978), except that the maximum ROMs with these kinematic constraints could exceed the expected maximum ROM of the lumbar region. The 6DOF constraint uniquely appeared to underestimate LB ROM in the thoracic spine. Interestingly, 8 and 9DOF kinematic constraints demonstrated much higher variability in the thoracic region than 3–7DOF constraints. This is likely because these kinematic constraints have three LB DOF, while the other constraints have only one or two LB DOF.

For AR direction of motion, the maximum ROMs for kinematic constraints with 3–6DOF were largely within the reported physiologically acceptable range from White and Panjabi (1978) for thoracic and lumbar regions. However, all constraints tended to overestimate the expected ROM in the

thoracolumbar region, where the lowest differences belonged to constraints with 5 and 6DOF. Our results generally found thoracolumbar joint ROMs to fall between thoracic and lumbar values, while the expected thoracolumbar ROM from White and Panjabi (1978) was identical to the lumbar values. Nonetheless, the maximum ROM of the thoracic intervertebral joints was notably larger than the lumbar intervertebral joints, following the expected trend reported in White and Panjabi (1978). Overall, it seems that kinematic constraints 5 and 6DOF produced the most consistent AR joint ROM results compared with the expected values of White and Panjabi (1978).

In sum, our findings suggest that the maximum ROM predicted using 4DOF through 6DOF constraints were within the physiologically acceptable range for the majority of spine regions, and directions of motions, based on comparison with the representative values reported in White and Panjabi (1978). The 5DOF kinematic constraint on balance seemed to provide the best and most stable result for all directions of motion. The 4DOF median ROM for thoracolumbar AR slightly exceeded the expected maximum value but was, in fact on quite similar to the 5DOF value. The 6DOF produced unusual LB motion patterns, underestimating expected thoracic ROM while exceeding expected lumbar ROM. It is important to note that the expected ranges of ROM reported by White and Panjabi (1978) are representative values based on a review of experimental data and expert opinion, thus should not be considered a "gold standard." The observed discrepancies between our results and the expected ROM of White and Panjabi (1978) are not out of line with discrepancies between that and various other studies (e.g., Pearcy and Tibrewal, 1984; Pearcy et al., 1984; Li et al., 2009) reporting intervertebral joint ROM. These discrepancies can be explained by implementing different methodological approaches to measure the intervertebral joint angles and evaluate the ranges of motion.

Segmental Spine Angles in the Static Range of Motion Trials

Overall, the results suggest that all models predicted similar segmental angles to those calculated directly from the marker data. Introducing different kinematic constraints in the models had no discernable effect on the RMS differences or ICCs for flexion–extension and lateral bending angles. For axial rotations, the models with kinematic constraints had uniformly higher RMS differences than the unconstrained model and lower ICCs (though generally with some overlap in the confidence intervals). In sum, all models with kinematic constraints appear equally valid, and adding more DOF did not improve performance, matching segmental angles calculated directly from spine marker clusters. It is important to note that the segmental angles calculated directly from markers do not represent a gold standard measurement of the underlying spine motion. Thus, this analysis does not directly address the accuracy of the models in predicting underlying spine motion but shows that model-predicted values should have similar validity as marker-based spine motion directly.

Study Limitations

A few potential limitations should be noted for this study. First, the study had a small sample size of seven healthy participants, so it is possible that the range of healthy normal spine motions was not fully represented. Moreover, it is unclear to what extent our results would be applicable for patients with spinal disorders. Therefore, further studies with larger and more heterogeneous sample sizes are needed to verify the generalizability of our findings. Second, during the data collection, the retroreflective markers were placed on bony landmarks by multiple experimenters, consequently adding some errors to our study (Della Croce et al., 1999). Third, we used marker sets with clusters in our study, and the generalizability to the use of different marker sets was not examined. Fourth, passive structure contributions such as spinal ligaments and intervertebral discs are not currently considered, nor are muscle forces or vertebral loading. Additionally, vertebral joints were modeled as ball joints with 3DOF and did not explicitly introduce within joint motion coupling or allow for any joint translational motion. Coupled intervertebral motion has been established in cadaveric testing studies (Panjabi et al., 1976; Gardner-Morse and Stokes, 2004), including between axial and lateral bend rotational motions, but it remains unclear how to characterize such coupling in kinematic constraints for kinematics analyses appropriately. However, as the FE, LB, and AR directions of motion remained independent in all analyses, the models can adopt coupled motions to best match the marker data. Thus, the model neither requires nor precludes coupled motion. A few studies have proposed optimization methods to adjust individual-level spinal kinematics to minimize passive structure forces–called force-dependent kinematics (Meng et al., 2015; Ignasiak et al., 2016) or minimize muscle mass and spine loading (Shojaei et al., 2015). These approaches may ultimately help to assign vertebral kinematics more accurately than kinematic constraints uniquely. They may even incorporate coupling and translational motion, but they pose significant challenges, including the need to characterize passive structure properties accurately and increased computational cost. Fifth, there are numerous possibilities for reasonable kinematic constraint conditions beyond the seven examined here, both in terms of the ratios used and the number and distribution of spinal DOF. There is no assurance that the kinematic constraints examined here are optimal, and indeed the optimal constraint would likely vary for different conditions and individuals. Undoubtedly, more research on different sets of kinematic constraints will shed light on how they can affect the spine motion during different activities.

CONCLUSIONS

Taken together, our findings suggest that adding more spinal DOF up to 6DOF produces meaningful improvements in marker error and that kinematic constraints from 4 to 6DOF provide similar levels of kinematic smoothness that are better than unconstrained models. Moreover, all the constraint conditions examined were similarly valid in matching separately determined

static segmental angles. Thus, adding more DOF (up to 9DOF) did not enhance the model's kinematic validity. Finally, on average, the joint ROMs produced the kinematic constraints from 4 to 6DOF were generally within physiologically reasonable ranges. These results indicate that the 5DOF model produces the best overall balance between the smoothness, realism of movement, and error of spine markers. The 6DOF model can provide a slight improvement in marker error during AR motions but at the expense of possibly less realistic LB motion patterns. It should be noted that most of the previous model validations focused on kinetic validations (e.g., Han et al., 2012; Bruno et al., 2015; Ignasiak et al., 2016), assessing whether a model can accurately predict musculoskeletal forces and muscle activations, by static optimization. These analyses require spinal kinematics to be specified as an input and are appropriately performed in models without kinematic constraints. However, our current work is a novel study that, for the first time, addresses the kinematic validity, whether a model precisely estimates the spine kinematics from inverse kinematics analysis through marker motion data. Our findings showed that this analysis is better performed in a model with kinematic constraints. Therefore, it is appropriate to utilize different versions of a model (with and without kinematic constraints) to evaluate kinematic and kinetic outcomes, respectively. In the future, additional research is warranted to understand the influence of kinematic constraints on the evaluation of spine motion during functional tasks and activities of daily living and in patients with spine disorders.

DATA AVAILABILITY STATEMENT

The raw data supporting the conclusions of this article will be made available by the authors, without undue reservation.

ETHICS STATEMENT

The studies involving human participants were reviewed and approved by Institutional Review Board of Beth Israel Deaconess Medical Center, Boston, United States. The patients/participants provided their written informed consent to participate in this study.

AUTHOR CONTRIBUTIONS

DA, MB, and MA substantially contributed to the conception and design of the study. DA and SM contributed to the collection and processing of data and static pose analyses using marker clusters. AL processed marker data for dynamic trials. CZ and DA performed a literature review and analysis to specify the kinematic constraints used. KB, AL, and BA created subject-specific models, implemented kinematic constraints in the models, and performed inverse kinematics analyses. MA and DA performed statistical analyses. MA wrote the first draft of the manuscript. All authors critically revised the manuscript and approved the version to be published.

FUNDING

This work was funded by grants from the National Institute on Aging (R00AG042458) and the National Institute of Arthritis and Musculoskeletal and Skin Diseases (R01AR073019) of the National Institutes of Health, with support from the Department of Orthopaedic Surgery at Beth Israel Deaconess Medical Center, and Harvard Catalyst, The Harvard Clinical and Translational Science Center (National Center for Advancing Translational Sciences, National Institutes of Health Award UL1 TR001102), and financial contributions from Harvard University and its affiliated academic healthcare centers. Other sources of funding included a grant from the National Institute on Aging (F32AG071308), the NRSA Institutional Research Training Grants (T32AR55885), and the Office of the Assistant Secretary of Defense for Health Affairs through the Peer Reviewed Medical Research Program (W81XWH-20-1-0608).

ACKNOWLEDGMENTS

The authors would like to acknowledge Rebecca Tromp for her contributions to subject recruitment and data collection.

SUPPLEMENTARY MATERIAL

The Supplementary Material for this article can be found online at: https://www.frontiersin.org/articles/10.3389/fbioe.2021.688041/full#supplementary-material

REFERENCES

Al-Eisa, E., Egan, D., Deluzio, K., and Wassersug, R. (2006). Effects of pelvic asymmetry and low back pain on trunk kinematics during sitting: a comparison with standing. *Spine* 31, E135–E143. doi: 10.1097/01.brs.0000201325.89493.5f

Andersen, M. S., Benoit, D. L., Damsgaard, M., Ramsey, D. K., and Rasmussen, J. (2010). Do kinematic models reduce the effects of soft tissue artefacts in skin marker-based motion analysis? An in vivo study of knee kinematics. *J Biomech* 43, 268–273. doi: 10.1016/j.jbiomech.2009.08.034

Anderst, W. J., Lee, J. Y., Donaldson, W. F., and Kang, J. D. (2013). Six-degrees-of-freedom cervical spine range of motion during dynamic flexion–extension after single-level anterior arthrodesis. *J. Bone Joint Surg.* 95, 497–506. doi: 10.2106/JBJS.K.01733

Basques, B. A., Espinoza Orías, A. A., Shifflett, G. D., Fice, M. P., Andersson, G. B., An, H. S., et al. (2017). The kinematics and spondylosis of the lumbar spine vary depending on the levels of motion segments in individuals with low back pain. *Spine* 42, E767–E774. doi: 10.1097/BRS.0000000000001967

Bayoglu, R., Galibarov, P. E., Verdonschot, N., Koopman, B., and Homminga, J. (2019). Twente Spine Model: a thorough investigation of the spinal loads in a complete and coherent musculoskeletal model of the human spine. *Med. Eng. Phys.* 68, 35–45. doi: 10.1016/j.medengphy.2019.03.015

Beaucage-Gauvreau, E., Robertson, W. S. P., Brandon, S. C. E., Fraser, R., Freeman, B. J. C., Graham, R. B., et al. (2019). Validation of an OpenSim full-body model with detailed lumbar spine for estimating lower lumbar spine loads during symmetric and asymmetric lifting tasks. *Comput. Methods Biomech. Biomed. Eng.* 22, 451–464. doi: 10.1080/10255842.2018.1564819

Briggs, A. M., van Dieon, J. H., Wrigley, T. V., Greig, A. M., Phillips, B., Lo, S. K., et al. (2007). Thoracic kyphosis affects spinal loads and trunk muscle force. *Phys. Ther.* 87, 595–607. doi: 10.2522/ptj.20060119

Bruno, A. G., Bouxsein, M. L., and Anderson, D. E. (2015). Development and validation of a musculoskeletal model of the fully articulated thoracolumbar spine and rib cage. *J. Biomech. Eng.* 137:4030408. doi: 10.1115/1.4030408

Bruno, A. G., Burkhart, K., Allaire, B., Anderson, D. E., and Bouxsein, M. L. (2017). Spinal loading patterns from biomechanical modeling explain the high incidence of vertebral fractures in the thoracolumbar region. *J. Bone Mineral Res.* 32, 1282–1290. doi: 10.1002/jbmr.3113

Burkhart, K., Grindle, D., Bouxsein, M. L., and Anderson, D. E. (2020). Between-session reliability of subject-specific musculoskeletal models of the spine derived from optoelectronic motion capture data. *J. Biomech.* 112:110044. doi: 10.1016/j.jbiomech.2020.110044

Cazzola, D., Holsgrove, T. P., Preatoni, E., Gill, H. S., and Trewartha, G. (2017). Cervical spine injuries: a whole-body musculoskeletal model for the analysis of spinal loading. *PLoS ONE* 12:e0169329. doi: 10.1371/journal.pone.0169329

Cheng, B., Castellvi, A. E., Davis, R. J., Lee, D. C., Lorio, M. P., Prostko, R. E., et al. (2016). Variability in flexion extension radiographs of the lumbar spine: a comparison of uncontrolled and controlled bending. *Int. J. Spine Surg.* 10:20. doi: 10.14444/3020

Christe, G., Kade, F., Jolles, B. M., and Favre, J. (2017). Chronic low back pain patients walk with locally altered spinal kinematics. *J. Biomech.* 60, 211–218. doi: 10.1016/j.jbiomech.2017.06.042

Chun, S.-W., Lim, C.-Y., Kim, K., Hwang, J., and Chung, S. G. (2017). The relationships between low back pain and lumbar lordosis: a systematic review and meta-analysis. *Spine J.* 17, 1180–1191. doi: 10.1016/j.spinee.2017.04.034

Crawford, R., Gizzi, L., Dieterich, A., Ni Mhuiris, Á., and Falla, D. (2018). Age-related changes in trunk muscle activity and spinal and lower limb kinematics during gait. *PLoS ONE* 13:e0206514. doi: 10.1371/journal.pone.0206514

Della Croce, U., Cappozzo, A., and Kerrigan, D. C. (1999). Pelvis and lower limb anatomical landmark calibration precision and its propagation to bone geometry and joint angles. *Med. Biol. Eng. Comput.* 37, 155–161. doi: 10.1007/BF02513282

Delp, S. L., Anderson, F. C., Arnold, A. S., Loan, P., Habib, A., John, C. T., et al. (2007). OpenSim: open-source software to create and analyze dynamic simulations of movement. *IEEE Trans. Biomed. Eng.* 54, 1940–1950. doi: 10.1109/TBME.2007.901024

Dunk, N. M., Chung, Y. Y., Sullivan Compton, D., and Callaghan, J. P. (2004). The reliability of quantifying upright standing postures as a baseline diagnostic clinical tool. *J. Manipulative Physiol. Ther.* 27, 91–96. doi: 10.1016/j.jmpt.2003.12.003

Dunk, N. M., Lalonde, J., and Callaghan, J. P. (2005). Implications for the use of postural analysis as a clinical diagnostic tool: reliability of quantifying upright standing spinal postures from photographic images. *J. Manipulative Physiol. Ther.* 28, 386–392. doi: 10.1016/j.jmpt.2005.06.006

El Habachi, A., Duprey, S., Cheze, L., and Dumas, R. (2015). A parallel mechanism of the shoulder—application to multi-body optimisation. *Multibody Syst. Dyn.* 33, 439–451. doi: 10.1007/s11044-014-9418-7

Fortin, C., Feldman, D. E., Cheriet, F., Gravel, D., Gauthier, F., and Labelle, H. (2012). Reliability of a quantitative clinical posture assessment tool among persons with idiopathic scoliosis. *Physiotherapy* 98, 64–75. doi: 10.1016/j.physio.2010.12.006

Fujii, R., Sakaura, H., Mukai, Y., Hosono, N., Ishii, T., Iwasaki, M., et al. (2007). Kinematics of the lumbar spine in trunk rotation: *in vivo* three-dimensional analysis using magnetic resonance imaging. *Eur. Spine J.* 16, 1867–1874. doi: 10.1007/s00586-007-0373-3

Fujimori, T., Iwasaki, M., Nagamoto, Y., Ishii, T., Kashii, M., Murase, T., et al. (2012). Kinematics of the thoracic spine in trunk rotation. *Spine* 37, E1318–E1328. doi: 10.1097/BRS.0b013e318267254b

Fujimori, T., Iwasaki, M., Nagamoto, Y., Matsuo, Y., Ishii, T., Sugiura, T., et al. (2014). Kinematics of the thoracic spine in trunk lateral bending: *in vivo* three-dimensional analysis. *Spine J.* 14, 1991–1999. doi: 10.1016/j.spinee.2013.11.054

Galvis, S., Burton, D., Barnds, B., Anderson, J., Schwend, R., Price, N., et al. (2016). The effect of scoliotic deformity on spine kinematics in adolescents. *Scoliosis Spinal Disord.* 11:42. doi: 10.1186/s13013-016-0103-x

Gardner-Morse, M. G., and Stokes, I. A. F. (2004). Structural behavior of human lumbar spinal motion segments. *J. Biomech.* 37, 205–212. doi: 10.1016/j.jbiomech.2003.10.003

Guo, H. R., Tanaka, S., Halperin, W. E., and Cameron, L. L. (1999). Back pain prevalence in US industry and estimates of lost workdays. *Am. J. Public Health* 89, 1029–1035. doi: 10.2105/AJPH.89.7.1029

Han, K.-S., Zander, T., Taylor, W. R., and Rohlmann, A. (2012). An enhanced and validated generic thoraco-lumbar spine model for prediction of muscle forces. *Med. Eng. Phys.* 34, 709–716. doi: 10.1016/j.medengphy.2011.09.014

Harsted, S., Mieritz, R. M., Bronfort, G., and Hartvigsen, J. (2016). Reliability and measurement error of frontal and horizontal 3D spinal motion parameters in 219 patients with chronic low back pain. *Chiropract. Manual Ther.* 24:13. doi: 10.1186/s12998-016-0092-0

Hidalgo, B., Gilliaux, M., Poncin, W., and Detrembleur, C. (2012). Reliability and validity of a kinematic spine model during active trunk movement in healthy subjects and patients with chronic non-specific low back pain. *J. Rehabil. Med.* 44, 756–763. doi: 10.2340/16501977-1015

Igawa, T., Katsuhira, J., Hosaka, A., Uchikoshi, K., Ishihara, S., and Matsudaira, K. (2018). Kinetic and kinematic variables affecting trunk flexion during level walking in patients with lumbar spinal stenosis. *PLoS ONE* 13:e0197228. doi: 10.1371/journal.pone.0197228

Ignasiak, D., Dendorfer, S., and Ferguson, S. J. (2016). Thoracolumbar spine model with articulated ribcage for the prediction of dynamic spinal loading. *J. Biomech.* 49, 959–966. doi: 10.1016/j.jbiomech.2015.10.010

Ignasiak, D., Rüeger, A., and Ferguson, S. J. (2017). Multi-segmental thoracic spine kinematics measured dynamically in the young and elderly during flexion. *Hum. Mov. Sci.* 54, 230–239. doi: 10.1016/j.humov.2017.05.011

Koo, T. K., and Li, M. Y. (2016). A guideline of selecting and reporting intraclass correlation coefficients for reliability research. *J. Chiropr. Med.* 15, 155–163. doi: 10.1016/j.jcm.2016.02.012

Kuo, C., Fanton, M., Wu, L., and Camarillo, D. (2018). Spinal constraint modulates head instantaneous center of rotation and dictates head angular motion. *J. Biomech.* 76, 220–228. doi: 10.1016/j.jbiomech.2018.05.024

Kuwahara, W., Deie, M., Fujita, N., Tanaka, N., Nakanishi, K., Sunagawa, T., et al. (2016). Characteristics of thoracic and lumbar movements during gait in lumbar spinal stenosis patients before and after decompression surgery. *Clin. Biomech.* 40, 45–51. doi: 10.1016/j.clinbiomech.2016.10.016

Leardini, A., Chiari, L., Croce, U., Della, and Cappozzo, A. (2005). Human movement analysis using stereophotogrammetry. *Gait Posture* 21, 212–225. doi: 10.1016/j.gaitpost.2004.05.002

Li, G., Wang, S., Passias, P., Xia, Q., Li, G., and Wood, K. (2009). Segmental *in vivo* vertebral motion during functional human lumbar spine activities. *Eur. Spine J.* 18, 1013–1021. doi: 10.1007/s00586-009-0936-6

Lin, C.-C., Lu, T.-W., Wang, T.-M., Hsu, C.-Y., Hsu, S.-J., and Shih, T.-F. (2014). *In vivo* three-dimensional intervertebral kinematics of the subaxial cervical spine during seated axial rotation and lateral bending via a fluoroscopy-to-CT registration approach. *J. Biomech.* 47, 3310–3317. doi: 10.1016/j.jbiomech.2014.08.014

Lu, T.-W., and Chang, C.-F. (2012). Biomechanics of human movement and its clinical applications. *Kaohsiung J. Med. Sci.* 28, S13–S25. doi: 10.1016/j.kjms.2011.08.004

Lu, T.-W., and O'Connor, J. J. (1999). Bone position estimation from skin marker coordinates using global optimisation with joint constraints. *J. Biomech.* 32, 129–134. doi: 10.1016/S0021-9290(98)00158-4

Mahaudens, P., Banse, X., Mousny, M., and Detrembleur, C. (2009). Gait in adolescent idiopathic scoliosis: kinematics and electromyographic analysis. *Eur. Spine J.* 18, 512–521. doi: 10.1007/s00586-009-0899-7

Mannion, A. F., Knecht, K., Balaban, G., Dvorak, J., and Grob, D. (2004). A new skin-surface device for measuring the curvature and global and segmental ranges of motion of the spine: reliability of measurements and comparison with data reviewed from the literature. *Eur Spine J.* 13, 122–136. doi: 10.1007/s00586-003-0618-8

Marich, A. V., Hwang, C.-T., Salsich, G. B., Lang, C. E., and Van Dillen, L. R. (2017). Consistency of a lumbar movement pattern across functional activities in people with low back pain. *Clin. Biomech.* 44, 45–51. doi: 10.1016/j.clinbiomech.2017.03.004

Mason, D. L., Preece, S. J., Bramah, C. A., and Herrington, L. C. (2016). Reproducibility of kinematic measures of the thoracic spine,

lumbar spine and pelvis during fast running. *Gait Posture* 43, 96–100. doi: 10.1016/j.gaitpost.2013.11.007

Meng, X., Bruno, A. G., Cheng, B., Wang, W., Bouxsein, M. L., and Anderson, D. E. (2015). Incorporating six degree-of-freedom intervertebral joint stiffness in a lumbar spine musculoskeletal model—method and performance in flexed postures. *J. Biomech. Eng.* 137:101008. doi: 10.1115/1.4031417

Merriaux, P., Dupuis, Y., Boutteau, R., Vasseur, P., and Savatier, X. (2017). A study of vicon system positioning performance. *Sensors* 17:1591. doi: 10.3390/s17071591

Morita, D., Yukawa, Y., Nakashima, H., Ito, K., Yoshida, G., Machino, M., et al. (2014). Range of motion of thoracic spine in sagittal plane. *Eur. Spine J.* 23, 673–678. doi: 10.1007/s00586-013-3088-7

Mousavi, S. J., Tromp, R., Swann, M. C., White, A. P., and Anderson, D. E. (2018). Between-session reliability of opto-electronic motion capture in measuring sagittal posture and 3-D ranges of motion of the thoracolumbar spine. *J. Biomech.* 79, 248–252. doi: 10.1016/j.jbiomech.2018.08.033

Muyor, J. M., Arrabal-Campos, F. M., Martínez-Aparicio, C., Sánchez-Crespo, A., and Villa-Pérez, M. (2017). Test-retest reliability and validity of a motion capture (MOCAP) system for measuring thoracic and lumbar spinal curvatures and sacral inclination in the sagittal plane. *J. Back Musculoskelet. Rehabil.* 30, 1319–1325. doi: 10.3233/BMR-169750

O'Sullivan, K., Clifford, A., and Hughes, L. (2010). The reliability of the CODA motion analysis system for lumbar spine analysis: a pilot study. *Physiother. Pract. Res.* 31, 16–22. doi: 10.3233/PPR-2010-31104

Panjabi, M. M., Brand, R. A., and White, A. A. (1976). Three-dimensional flexibility and stiffness properties of the human thoracic spine. *J. Biomech.* 9, 185–192. doi: 10.1016/0021-9290(76)90003-8

Panjabi, M. M., Oxland, T. R., Yamamoto, I., and Crisco, J. J. (1994). Mechanical behavior of the human lumbar and lumbosacral spine as shown by three-dimensional load-displacement curves. *J. Bone Joint Surg.* 76, 413–424. doi: 10.2106/00004623-199403000-00012

Pearcy, M., Portek, I., and Shepherd, J. (1984). Three-dimensional X-ray analysis of normal movement in the lumbar spine. *Spine* 9, 294–297. doi: 10.1097/00007632-198404000-00013

Pearcy, M., and Tibrewal, S. B. (1984). Axial rotation and lateral bending in the normal lumbar spine measured by three-dimensional radiography. *Spine* 9, 582–587. doi: 10.1097/00007632-198409000-00008

Rajagopal, A., Dembia, C. L., DeMers, M. S., Delp, D. D., Hicks, J. L., and Delp, S. L. (2016). Full-body musculoskeletal model for muscle-driven simulation of human gait. *IEEE Trans. Biomed. Eng.* 63, 2068–2079. doi: 10.1109/TBME.2016.2586891

Rast, F. M., Graf, E. S., Meichtry, A., Kool, J., and Bauer, C. M. (2016). Between-day reliability of three-dimensional motion analysis of the trunk: a comparison of marker based protocols. *J. Biomech.* 49, 807–811. doi: 10.1016/j.jbiomech.2016.02.030

Roux, E., Bouilland, S., Godillon-Maquinghen, A.-P., and Bouttens, D. (2002). Evaluation of the global optimisation method within the upper limb kinematics analysis. *J. Biomech.* 35, 1279–1283. doi: 10.1016/S0021-9290(02)00088-X

Rozumalski, A., Schwartz, M. H., Wervey, R., Swanson, A., Dykes, D. C., and Novacheck, T. (2008). The *in vivo* three-dimensional motion of the human lumbar spine during gait. *Gait Posture* 28, 378–384. doi: 10.1016/j.gaitpost.2008.05.005

Schmid, S., Studer, D., Hasler, C.-C., Romkes, J., Taylor, W. R., Lorenzetti, S., et al. (2016). Quantifying spinal gait kinematics using an enhanced optical motion capture approach in adolescent idiopathic scoliosis. *Gait Posture* 44, 231–237. doi: 10.1016/j.gaitpost.2015.12.036

Shin, J.-H., Wang, S., Yao, Q., Wood, K. B., and Li, G. (2013). Investigation of coupled bending of the lumbar spine during dynamic axial rotation of the body. *Eur. Spine J.* 22, 2671–2677. doi: 10.1007/s00586-013-2777-6

Shojaei, I., Arjmand, N., and Bazrgari, B. (2015). An optimization-based method for prediction of lumbar spine segmental kinematics from the measurements of thorax and pelvic kinematics. *Int. J. Numer. Method. Biomed. Eng.* 3:e02729. doi: 10.1002/cnm.2729

Sung, P. S., Danial, P., and Lee, D. C. (2016). Comparison of the different kinematic patterns during lateral bending between subjects with and without recurrent low back pain. *Clin. Biomech.* 38, 50–55. doi: 10.1016/j.clinbiomech.2016.08.006

Wang, H., Zhou, C., Yu, Y., Wang, C., Tsai, T.-Y., Han, C., et al. (2020). Quantifying the ranges of relative motions of the intervertebral discs and facet joints in the normal cervical spine. *J. Biomech.* 112:110023. doi: 10.1016/j.jbiomech.2020.110023

White, A. A., and Panjabi, M. M. (1978). The basic kinematics of the human spine. *Spine* 3, 12–20. doi: 10.1097/00007632-197803000-00003

Willems, J., Jull, G., and Ng, J.-F. (1996). An *in vivo* study of the primary and coupled rotations of the thoracic spine. *Clin. Biomech.* 11, 311–316. doi: 10.1016/0268-0033(96)00017-4

Wong, K. W. N., Luk, K. D. K., Leong, J. C. Y., Wong, S. F., and Wong, K. K. Y. (2006). Continuous dynamic spinal motion analysis. *Spine* 31, 414–419. doi: 10.1097/01.brs.0000199955.87517.82

Yang, H., Haldeman, S., Lu, M.-L., and Baker, D. (2016). Low back pain prevalence and related workplace psychosocial risk factors: a study using data from the 2010 national health interview survey. *J. Manipulative Physiol. Ther.* 39, 459–472. doi: 10.1016/j.jmpt.2016.07.004

Zwambag, D. P., Beaudette, S. M., Gregory, D. E., and Brown, S. H. M. (2019). Distinguishing between typical and atypical motion patterns amongst healthy individuals during a constrained spine flexion task. *J. Biomech.* 86, 89–95. doi: 10.1016/j.jbiomech.2019.01.047

Author Disclaimer: The content is solely the responsibility of the authors and does not necessarily represent the official views of Harvard Catalyst, Harvard University, and its affiliated academic healthcare centers, the National Institutes of Health, or the Department of Defense. The study sponsors had no role in the study design, data collection, analysis, manuscript preparation, or the decision to submit the manuscript for publication.

Conflict of Interest: The authors declare that the research was conducted in the absence of any commercial or financial relationships that could be construed as a potential conflict of interest.

Publisher's Note: All claims expressed in this article are solely those of the authors and do not necessarily represent those of their affiliated organizations, or those of the publisher, the editors and the reviewers. Any product that may be evaluated in this article, or claim that may be made by its manufacturer, is not guaranteed or endorsed by the publisher.

frontiers in Bioengineering and Biotechnology

ORIGINAL RESEARCH
published: 31 August 2021
doi: 10.3389/fbioe.2021.718996

Biomechanical Evaluation of Different Surgical Approaches for the Treatment of Adjacent Segment Diseases After Primary Anterior Cervical Discectomy and Fusion: A Finite Element Analysis

*Wencan Ke†, Chao Chen†, Bingjin Wang†, Wenbin Hua, Saideng Lu, Yu Song, Rongjin Luo, Zhiwei Liao, Gaocai Li, Liang Ma, Yunsong Shi, Kun Wang, Shuai Li, Xinghuo Wu, Yukun Zhang and Cao Yang**

Department of Orthopaedics, Union Hospital, Tongji Medical College, Huazhong University of Science and Technology, Wuhan, China

OPEN ACCESS

Edited by:
Marwan El-Rich, Khalifa University, United Arab Emirates

Reviewed by:
Mohammad Nikkhoo, Islamic Azad University, Iran
Abdelwahed Barkaoui, International University of Rabat, Morocco

***Correspondence:**
Cao Yang
caoyangunion@hust.edu.cn

†These authors have contributed equally to this work

Specialty section:
This article was submitted to Biomechanics, a section of the journal Frontiers in Bioengineering and Biotechnology

Received: *03 June 2021*
Accepted: *13 August 2021*
Published: *31 August 2021*

Citation:
Ke W, Chen C, Wang B, Hua W, Lu S, Song Y, Luo R, Liao Z, Li G, Ma L, Shi Y, Wang K, Li S, Wu X, Zhang Y and Yang C (2021) Biomechanical Evaluation of Different Surgical Approaches for the Treatment of Adjacent Segment Diseases After Primary Anterior Cervical Discectomy and Fusion: A Finite Element Analysis. Front. Bioeng. Biotechnol. 9:718996. doi: 10.3389/fbioe.2021.718996

Symptomatic adjacent segment disease (ASD) is a common challenge after anterior cervical discectomy and fusion (ACDF). The objective of this study was to compare the biomechanical effects of a second ACDF and laminoplasty for the treatment of ASD after primary ACDF. We developed a finite element (FE) model of the C2-T1 based on computed tomography images. The FE models of revision surgeries of ACDF and laminoplasty were simulated to treat one-level and two-level ASD after primary ACDF. The range of motion (ROM) and intradiscal pressure (IDP) of the adjacent segments, and stress in the cord were analyzed to investigate the biomechanical effects of the second ACDF and laminoplasty. The results indicated that revision surgery of one-level ACDF increased the ROM and IDP at the C2–C3 segment, whereas two-level ACDF significantly increased the ROM and IDP at the C2–C3 and C7-T1 segments. Furthermore, no significant changes in the ROM and IDP of the laminoplasty models were observed. The stress in the cord of the re-laminoplasty model decreased to some extent, which was higher than that of the re-ACDF model. In conclusion, both ACDF and laminoplasty can relieve the high level of stress in the spinal cord caused by ASD after primary ACDF, whereas ACDF can achieve better decompression effect. Revision surgery of the superior ACDF or the superior and inferior ACDF after the primary ACDF increased the ROM and IDP at the adjacent segments, which may be the reason for the high incidence of recurrent ASD after second ACDF.

Keywords: adjacent segment degeneration, finite element analysis, revision surgery, anterior cervical discectomy and fusion, laminoplasty

INTRODUCTION

Anterior cervical discectomy and fusion (ACDF) is generally accepted as the standard surgical treatment for cervical degenerative diseases (Oglesby et al., 2013; Kelly et al., 2018). ACDF is recognized as a comparatively safe procedure associated with few complications. However, adjacent segment disease (ASD), defined as new symptoms at nerve roots or myelopathy and

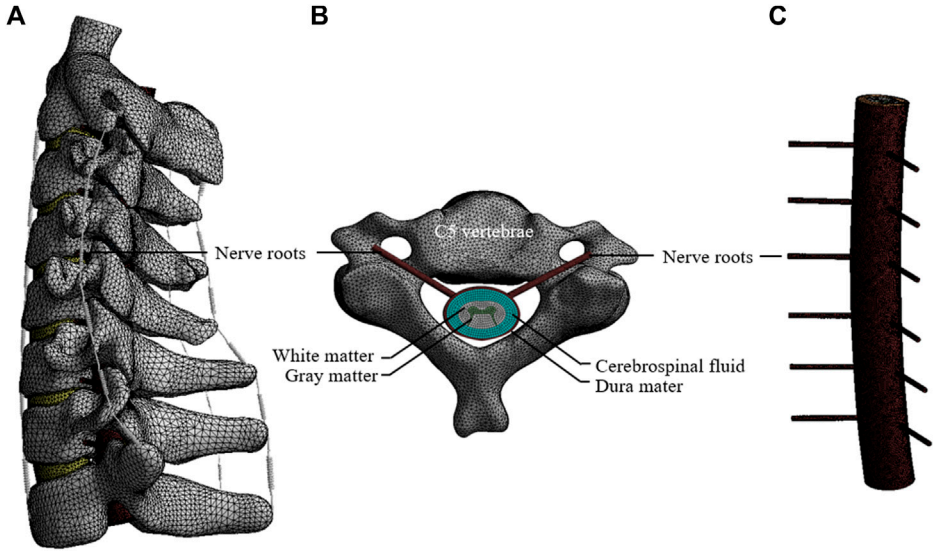

FIGURE 1 | The FE model of the C2–T1. **(A)** The FE model of the cervical spine and spinal cord. **(B)** Axial view of the spinal cord at the C5 vertebrae. **(C)** Lateral view of the spinal cord model.

TABLE 1 | Material properties of the spinal structures.

Component/materials	Young's modulus E (MPa)	Poisson's ratio	Element type
Cortical bone	12000	0.29	Shell93
Cancellous bone	450	0.29	Solid187
Posterior element	3500	0.29	Solid187
Facet cartilage	10.4	0.4	Solid187
Endplate	500	0.4	Shell93
Nucleus pulposus	1	0.49	Solid187
Annulus fibrosus	3.4	0.4	Solid187
Anterior longitudinal Ligament	30	0.3	Spring (tension only)
Posterior longitudinal Ligament	20	0.3	Spring (tension only)
Ligamentum flavum	1.5	0.3	Spring (tension only)
Capsular Ligament	20	0.3	Spring (tension only)
Interspinous Ligament	1.5	0.3	Spring (tension only)
Supraspinous Ligament	1.5	0.3	Spring (tension only)
Intertransverse Ligament	20	0.3	Spring (tension only)
PEEK	3000	0.3	Solid187
Bone graft	450	0.29	Solid187
Titanium alloy	110,000	0.3	Solid187
Degenerative annulus fibrosus	4	0.45	Solid187
Degenerative nucleus pulposus	4	0.49	Solid187
Osteophytes	450	0.23	Solid187

new radiographic evidence of degenerative changes at adjacent segments of previously fused segments, is one of the major problems after ACDF (Hilibrand and Robbins, 2004). In a retrospective study of 177 patients who underwent ACDF, radiographic and clinical ASD were found in 92.1 and 19.2% of patients, respectively; approximately 7% of the patients required revision surgery (Chung et al., 2014). Another study reported an incidence of 2.4% per year of revision surgery at adjacent segments after primary surgery, and the authors estimated that 22% of patients would require second surgery due to symptomatic ASD within a decade (Lee et al., 2015).

ASD can occur in the superior, inferior, or both adjacent levels, depending on the levels affected. Considering the clinical situation and secondary preoperative imaging findings, ASD can be treated by second ACDF, laminoplasty, and posterior fusion (Wang F. et al., 2017; Cao et al., 2020). ACDF decompresses the nerve roots and myelopathy by removing the herniated disc and posterior osteophytes, followed by

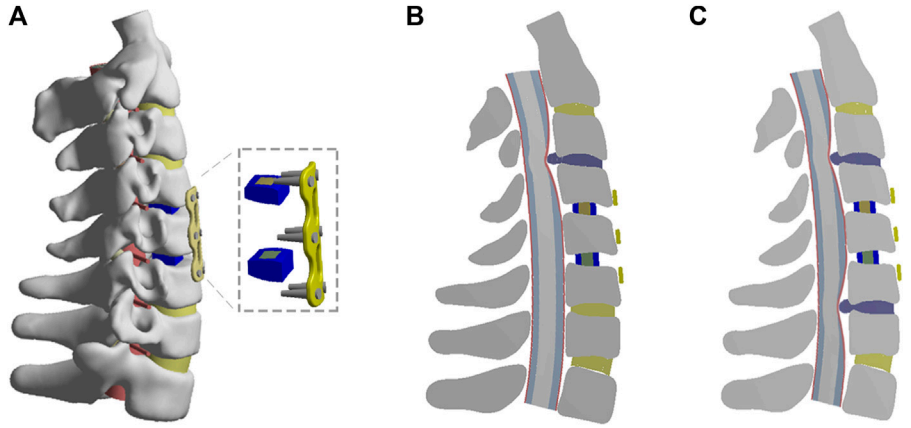

FIGURE 2 | The FE models of C4-C6 ACDF and one-level or two-level ASD after primary ACDF. **(A)** The FE model of C4-C6 ACDF. **(B)** Cross-sectional views of the FE model of one-level ASD. **(C)** Cross-sectional views of the FE model of two-level ASD.

TABLE 2 | Material properties of the spinal cord.

Materials	Material model	Material parameters
White matter	Hyperelastic (Ogden)	μ = 4.0 kPa, α= 12.5
Gray matter	Hyperelastic (Ogden)	μ = 4.1 kPa, α= 14.7
Dura mater and nerve roots	Elastic	E = 80 MPa, ν= 0.49
Cerebrospinal fluid	Newtonian fluid	Viscosity = 0.001 Pa s

restoration of the disc height and cervical lordosis by cages and bone graft (Schroeder et al., 2016; Muzević et al., 2018). Cervical laminoplasty was considered to be an effective method for the treatment of cervical degenerative stenosis as it expands the stenosed spinal canal (Yeh et al., 2014; Kurokawa and Kim, 2015). Posterior decompression and fusion can decompress the spinal cord and achieve immediate stabilization, thereby, preventing the occurrence of kyphotic (Du et al., 2014). Therefore, the appropriate surgical approaches for the treatment of ASD after ACDF still need to be studied.

The finite element (FE) analysis is an important method to study the spinal biomechanics (Nikkhoo et al., 2019; Cai et al., 2020b; Mesbah and Barkaoui, 2020). The range of motion (ROM), intradiscal pressure (IDP), facet joint stress, and stress in the cord can be calculated and analyzed to evaluate the biomechanical effects of different spine surgeries (Mesbah et al., 2020; Nikkhoo et al., 2020; Srinivasan et al., 2021). FE analysis can also be used to assess the risk of complications of spinal surgery, such as degeneration and internal implants fractures. However, the biomechanical evaluation of different surgical approaches for the treatment of ASD after ACDF has not been reported. In the present study, FE models with superior and two-level ASD after C4-C6 ACDF were conducted. The aim of this study was to compare the biomechanical effects of a second ACDF and laminoplasty for the treatment of ASD after primary ACDF.

MATERIALS AND METHODS

Construction of Intact Cervical Model (C2–T1)

In this study, a three-dimensional FE model of C2–T1 segments was developed based on the computed tomography (CT) images of a healthy volunteer (male, 25 years old, 64 kg, and 176 cm). This study was approved by the ethics committee of Tongji Medical College, Huazhong University of Science and Technology. Written informed consent was obtained from the volunteer. The CT images of the participant were obtained at intervals of 0.625 mm (Dual Source CT; Siemens, Munich, Germany). Mimics Research 20.0 software (Materialize, Leuven, Belgium) was used to reconstruct the geometric structure of the vertebrae. Hypermesh (Altair Engineering, Troy, Michigan, United States) was used to mesh and build the FE models of C2-T1 vertebrae. Afterwards, the FE models were analyses by ANSYS (ANSYS Ltd., Canonsburg, Pennsylvania, United States). This C2–T1 FE model could be divided into cancellous bone, cortical bone, intervertebral disc (IVD), facet joints, and ligaments (**Figure 1A**). The cortical bone was constructed as a shell with the thickness of 0.4 mm (Mo et al., 2017). The IVD consisted of annulus fibrosus and nucleus pulposus with the volume ratio to be 6:4. The IVD was considered as an elastic material referring to the previous studies (Wu et al., 2019; Li et al., 2021). The endplates were constructed as a shell with the thickness of 0.5 mm. The facet joints were assumed with 0.5-mm thick cartilage with nonlinear, surface-to-surface, frictionless sliding contact (Li et al., 2017). The ligaments consisted of anterior longitudinal ligament, posterior longitudinal ligament, ligamentum flavum, interspinous ligament, supraspinous ligament, capsular ligament, and intertransverse ligament. These ligaments were established using nonlinear tension-only Spring element (Guo et al., 2021; Lin et al., 2021). The material properties of the model are listed in **Table 2** (Cai et al., 2020a; Hua et al., 2020).

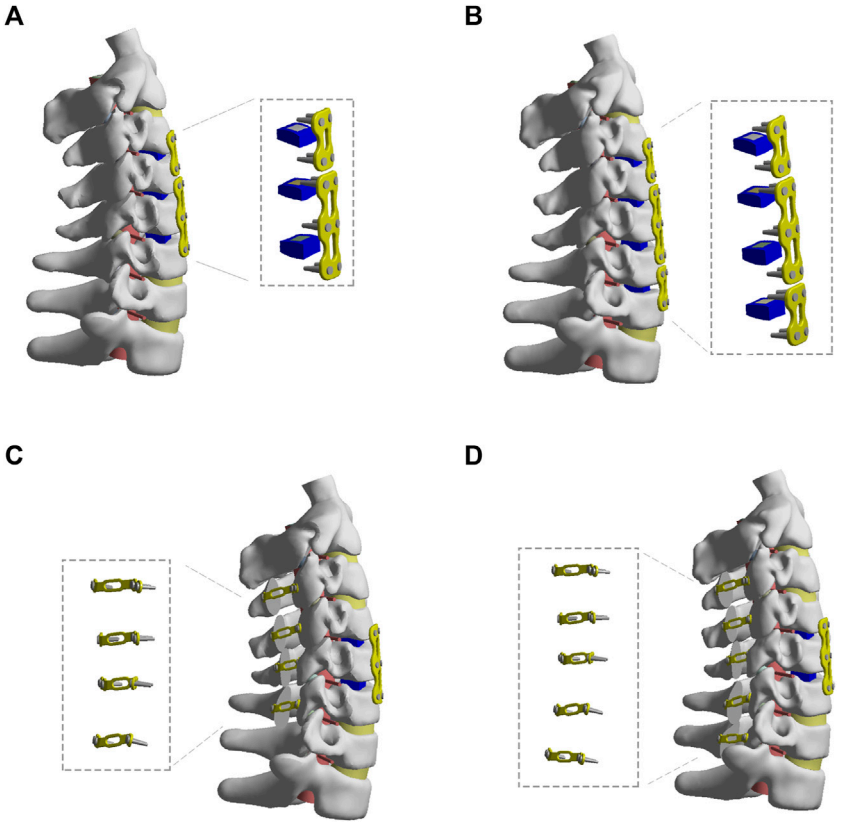

FIGURE 3 | The FE models of different revision surgeries after C4-C6 ACDF. **(A)** The revision surgery of C2-C3 ACDF. **(B)** The revision surgery of C3-C4 and C6-C7 ACDF. **(C)** The revision surgery of C3-C6 laminoplasty. **(D)** The revision surgery of C3-C7 laminoplasty.

In addition, the spinal cord was reconstructed according to the geometry of the cervical column and human spinal cord. The spinal cord model included white matter, gray matter, dura mater, nerve roots, and cerebrospinal fluid (CSF) layers (**Figures 1B,C**). The dural sheath was placed approximately 2.5 mm from the cord, since the CSF layer in the human cervical spine was reported to be 1.5–4.0 mm in a previous literature (Holsheimer et al., 1994). The white and gray matter were assumed as Hyperelastic element based on study (Ichihara et al., 2001). The dura mater and nerve roots were constructed with elastic element according to study (Persson et al., 2010). CSF was assumed as Newtonian fluid according to the viscosity of CSF (Brydon et al., 1995). A one-way Fluid-Solid Interaction analysis method was used to couple the interaction between the fluid and solid material. Material properties of the spinal cord model are listed in **Table 1**.

One-Level and Two-Level ASD Models After C4-C6 ACDF

A recent study demonstrated that patients treated with one- or two-segment anterior cervical arthrodesis were more likely to develop ASD than those treated with three or more segments (Lee et al., 2015). Therefore, the ASD models after primary surgery were based on the C4-C6 ACDF model (**Figure 2A**). The C4-C6 ACDF model was constructed according to a previous study (Hua et al., 2020). In brief, annulus fibrosus and nucleus pulposus were partly resected and the polyetheretherketone (PEEK) cages with bone graft were placed in the intervertebral space. Then, solid fusion was achieved with anterior titanium alloy plates and titanium alloy screws. The one-level and two-level ASD models after C4-C6 ACDF were shown in **Figures 2B,C**. A moderate degeneration in the adjacent segment was modified to simulate ASD according to study (Cai et al., 2020a). The disc height was reduced by 50% relative to the height of the normal model. An osteophyte, one quarter of the size of the herniated disc, was constructed to simulate intervertebral disc calcification. An occupying ratio of 40% was assumed to simulate the spinal cord compression by ASD. The occupying ratio was defined as the ratio of the thickness of herniated disc to the anterior–posterior diameter of the spinal canal. The material properties of PEEK cages, bone graft, titanium alloy and degenerative intervertebral disc were also listed in **Table 2**.

Anterior Surgical Models for One-Level or Two-Level ASD After C4-C6 ACDF

As shown in **Figure 3A**, for the treatment of one-level ASD after C4-C6 ACDF, an additional ACDF (re-ACDF) at C3-C4 level was constructed. As shown in **Figure 3B**, the second ACDF at C3-C4 and C6-C7 levels was simulated to treat two-level ASD after C4-C6 ACDF. The steps of ACDF are described above.

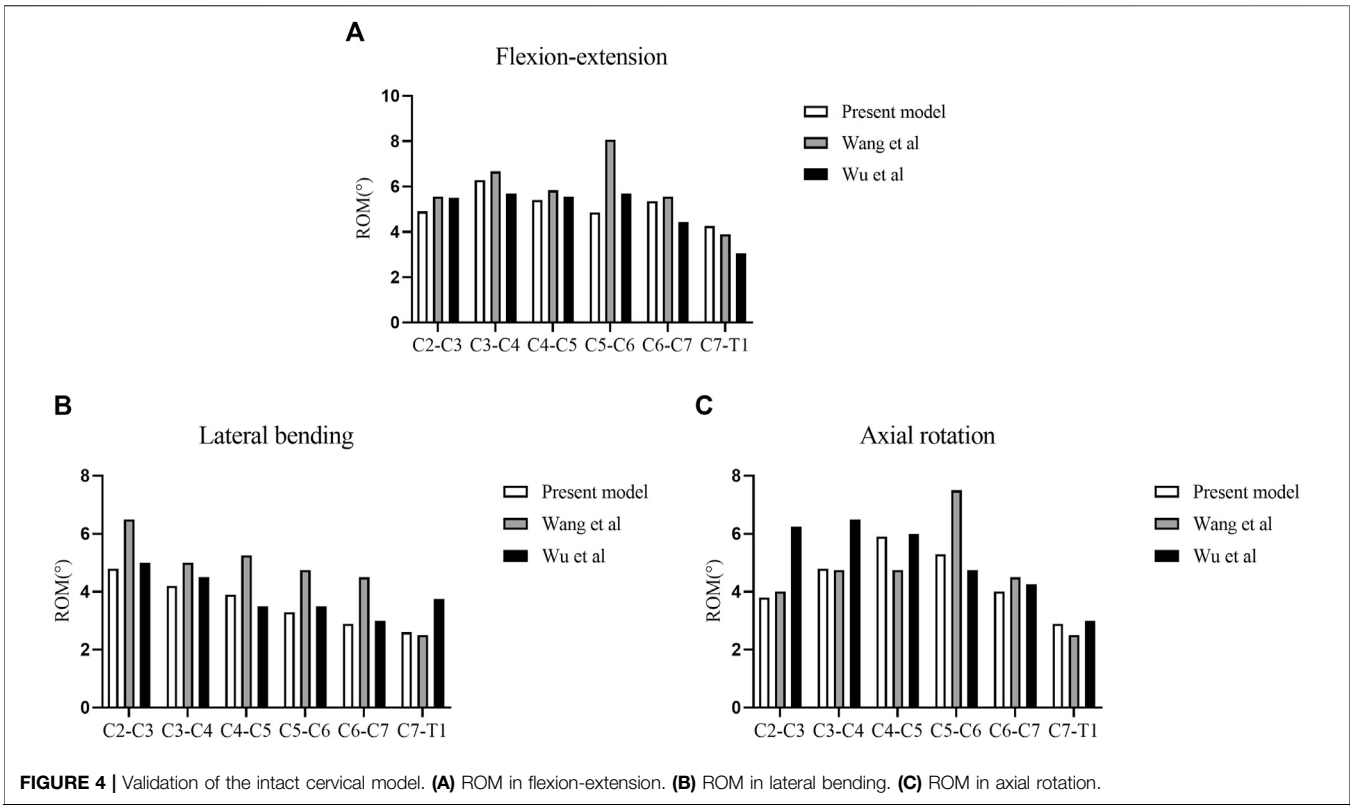

FIGURE 4 | Validation of the intact cervical model. **(A)** ROM in flexion-extension. **(B)** ROM in lateral bending. **(C)** ROM in axial rotation.

Posterior Surgical Models for One-Level or Two-Level ASD After C4-C6 ACDF

As shown in **Figures 3C,D**, C3-C6 or C3-C7 laminoplasty (re-laminoplasty) was simulated to treat one-level or two-level ASD after C4-C6 ACDF, respectively. The laminoplasty models were developed based on conventional surgical protocols (Hirabayashi et al., 2010). Firstly, a longitudinal groove of 3 mm width was constructed between the lamina and lateral mass at hinge side of the lamina. Then, an opening width of 12 mm was made at the open side. The lamina was fixed using titanium alloy plates and screws.

Boundary and Loading Conditions

All models were fixed at the inferior surface of the T1 vertebrae. A follower load of 73.6 N combined with a moment of 1.0 Nm was applied over the superior surface of C2 to simulate the spinal motions of flexion, extension, lateral bending, and axial rotation (Mo et al., 2017; Zhao et al., 2018). The ROM, IDP, and maximum von-Mises stress in the cord were analyzed to investigate the biomechanical effects of the second ACDF and laminoplasty for the treatment of ASD after primary ACDF.

RESULTS

Model Validation

The FE model of the intact cervical spine used in this study was validated by comparison with previous biomechanical models (Wang K. et al., 2017; Wu et al., 2018). The ROM and IDP of each segment were consistent with those of previous studies (**Figure 4**; **Supplementary Figure S1**).

Analyses of the Biomechanical Effects of Different Surgical Approaches for the Treatment of One-Level ASD After Primary ACDF

The segmental ROM and IDP of the FE models of different surgical approaches for the treatment of one-level ASD after primary ACDF were shown in **Figure 5**. The ROM at the C2–C3 segment of re-ACDF model increased than that of the one-level ASD model (**Figures 5A,B**). Similarly, the IDP at the C2–C3 segment of re-ACDF model was larger than that of the one-level ASD model (**Figures 5C,D**). Furthermore, no significant changes in the ROM and IDP of re-laminoplasty model were observed compared to the one-level ASD model (**Figure 5**).

Analyses of the Biomechanical Effects of Different Surgical Approaches for the Treatment of Two-Level ASD After Primary ACDF

The segmental ROM and IDP of the FE models of different surgical approaches for the treatment of two-level ASD after primary ACDF were shown in **Figure 6**. The ROM at the C2–C3 and C7-T1 segments of re-ACDF model increased significantly than that of the two-level ASD model (**Figures 6A,B**). Similarly, the IDP at the C2–C3 and C7-T1 segments of re-ACDF model

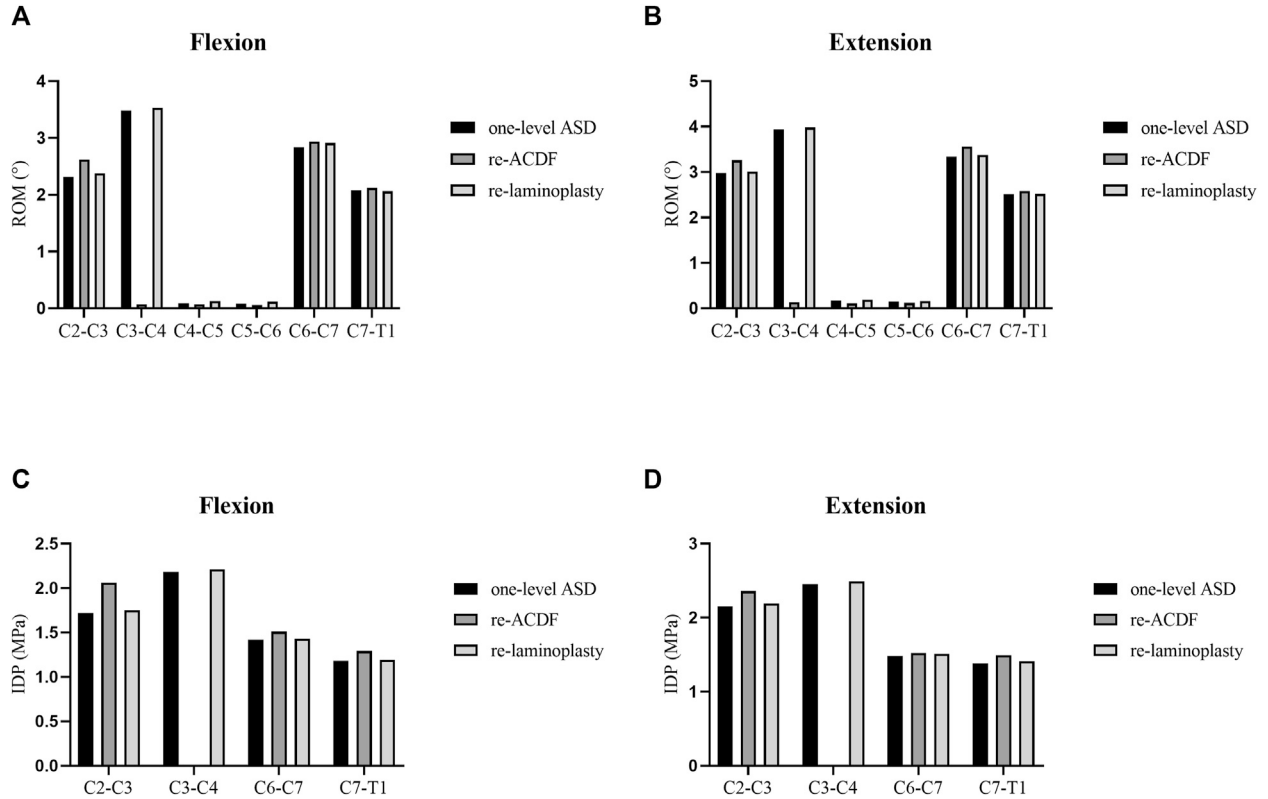

FIGURE 5 | ROM and IDP of different revision surgeries for the treatment of one-level ASD. **(A)** ROM in flexion. **(B)** ROM in extension. **(C)** IDP in flexion. **(D)** IDP in extension.

was significantly larger than that of the two-level ASD model (**Figures 6C,D**). The ROM and IDP of re-laminoplasty model increased slightly but the difference was not statistically significant (**Figure 6**).

Analyses of the Stress in the Spinal Cord of Different Surgical Approaches for the Treatment of One-Level or Two-Level ASD After Primary ACDF

The maximum von-Mises stress in the spinal cord of the FE models of different surgical approaches for the treatment of one-level or two-level ASD after primary ACDF were shown in **Figure 7**. The maximum von-Mises stress in the cord of the re-ACDF model was greatly reduced compared to the one-level or two-level ASD model. The stress in the cord of the re-laminoplasty model decreased to some extent, although it was higher than that of the re-ACDF model. The stress distribution in the spinal cord in the sagittal plane of different surgical approaches for the treatment of one-level or two-level ASD after primary ACDF were shown in **Figures 8**, **9**. The peak stress occurred where the cord and dural sheath attached. Anterior and posterior surgical approaches all decreased the stress in the spinal cord caused by ASD after the first surgery.

DISCUSSION

The purpose of this study was to compare the biomechanical effects of second ACDF and laminoplasty for the treatment of one-level or two-level ASD after primary ACDF. The biomechanical results indicated that both ACDF and laminoplasty can relieve the increased stress in the spinal cord caused by ASD after primary ACDF, whereas ACDF can achieve a better decompression effect than laminoplasty regardless of the level of ASD. Revision surgery of the superior ACDF or the superior and inferior ACDF after primary ACDF both increased the ROM and IDP at the adjacent segments. Furthermore, laminoplasty after primary ACDF had no significant effect on the biomechanical stability of the spine.

Recently, symptomatic ASD has become a major problem after spinal fusion surgeries Some experts think that ASD is the result of a natural history, while others believe that ASD is due to compensatory pressure on adjacent discs following vertebral fusion (Hilibrand and Robbins, 2004; Kavadi and Badve, 2019). If ASD occurs, conservative treatment is often the first choice for many patients. However, a revision surgery should be considered for the patients with obvious clinical manifestation and poor effect of conservative treatment. There remains some debate on the appropriate surgical approaches for the treatment of ASD after ACDF. Revision surgery via anterior approach was reported to be effective for patients who underwent primary ACDF for

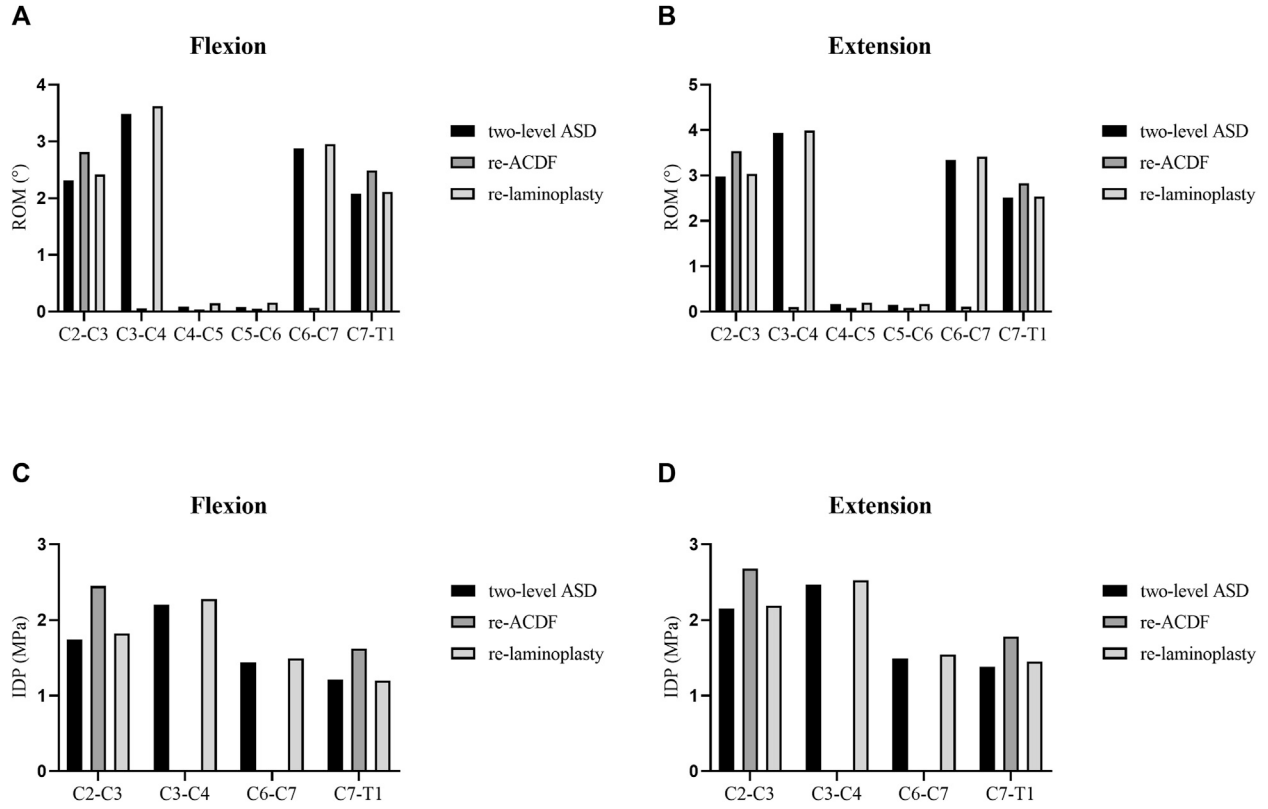

FIGURE 6 | ROM and IDP of different revision surgeries for the treatment of two-level ASD. **(A)** ROM in flexion. **(B)** ROM in extension. **(C)** IDP in flexion. **(D)** IDP in extension.

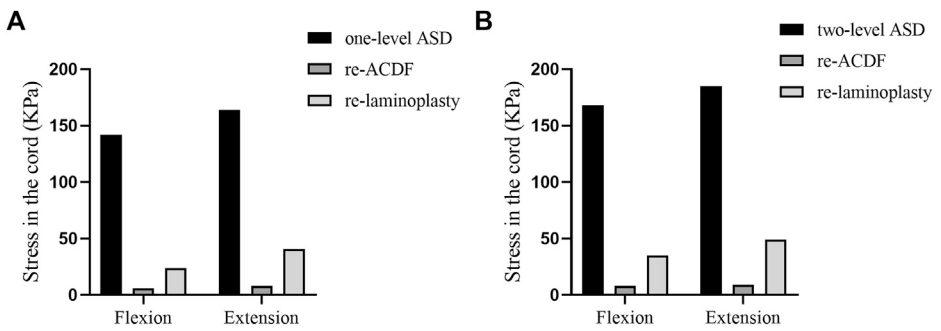

FIGURE 7 | Maximum von-Mises stress in the cord of re-ACDF and re-laminoplasty models. **(A)** Stress in the cord of different revision surgeries for the treatment of one-level ASD. **(B)** Stress in the cord of different revision surgeries for the treatment of two-level ASD.

symptomatic ASD (Li et al., 2016; O'Neill et al., 2016). However, the incidence of radiculopathy and ASD recurrence after anterior revision surgery was higher than that undergoing posterior approached (Xu et al., 2014). Furthermore, posterior revision surgery could result in greater blood loss and a longer hospital stay (Steinhaus et al., 2020). When patients developed spinal stenosis at the initial surgical levels or ossification of the posterior longitudinal ligament, a revision surgery with an anterior approach cannot easily resolve the issue, but a posterior approach can achieve extensive decompression (Cabraja et al., 2010; Cole et al., 2015).

ACDF and laminoplasty were reported to be effective in treating ASD after primary ACDF (Wang and Green, 2003; Basques et al., 2017). The clinical outcomes of the two surgical approaches have also been compared. The ACDF was reported to reduce intraoperative bleeding and better preserve cervical lordosis, while laminoplasty retained more ROM (Montano et al., 2019). Recently, Mohamed et al. reported a higher incidence of dysphagia, new-onset

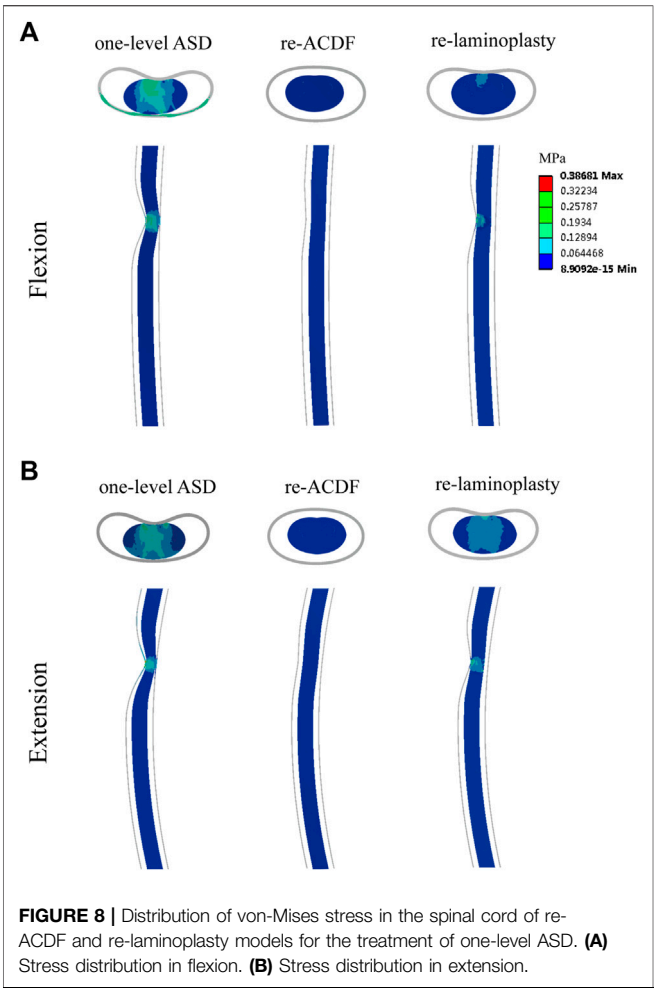

FIGURE 8 | Distribution of von-Mises stress in the spinal cord of re-ACDF and re-laminoplasty models for the treatment of one-level ASD. **(A)** Stress distribution in flexion. **(B)** Stress distribution in extension.

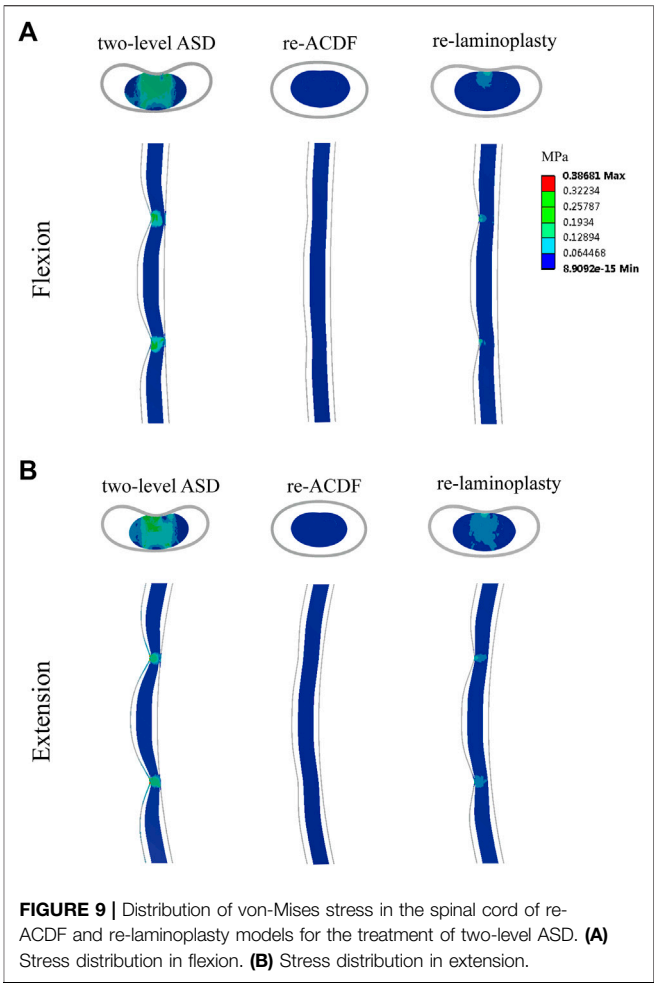

FIGURE 9 | Distribution of von-Mises stress in the spinal cord of re-ACDF and re-laminoplasty models for the treatment of two-level ASD. **(A)** Stress distribution in flexion. **(B)** Stress distribution in extension.

cervicalgia, and increased incidence of recurrence in patients with ACDF compared to those with laminoplasty (Mesregah et al., 2021). In a prospective cohort study of 60 patients with lordotic cervical spine, Liang et al. reported similar sagittal alignment results between ACDF and laminoplasty, while ACDF was associated with poor cervical lordosis preservation (Liang et al., 2019). Another study reported that both ACDF and laminoplasty can achieve favorable clinical results in patients with multilevel cervical spondylotic myelopathy (Chen et al., 2019). Compared with laminoplasty, ACDF has the advantage of less trauma and may be more suitable for elderly patients with poor surgical tolerance. However, the biomechanical evaluation of ACDF and laminoplasty for the treatment of ASD after ACDF is limited.

In the present study, the FE models of the one-level and two-level ASD based on C4-C6 ACDF were constructed to simulate the postoperative degeneration after primary ACDF. Revision surgeries of ACDF and laminoplasty were stimulated to compare the biomechanical effect of different surgical approaches for the treatment of ASD after primary ACDF. The biomechanical results suggested that revision surgery of the superior ACDF or the superior and inferior ACDF after the primary ACDF both increased the ROM and IDP at the adjacent segments. Increased IDP at the adjacent segments of the fused surgeries was supposed to be an important factor in the development of ASD (Eck et al., 2002). Xu et al. (2014) reported that patients who underwent a second ACDF after primary ACDF had a higher chance of developing recurrent ASD, up to 25%. The increased ROM and IDP at the adjacent segments of the re-ACDF model in our study may be a possible reason for the high incidence of recurrent ASD after second ACDF. Furthermore, no significant changes in the ROM and IDP of the re-laminoplasty model were observed, which is similar to the finding of a previous study (Xu et al., 2014). Decompression of the spinal cord is the main objective of revision surgery and it determines the outcome. The biomechanical results indicated that both ACDF and laminoplasty can decrease the stress in the spinal cord caused by ASD after primary ACDF, but ACDF can achieve a better decompression effect than laminoplasty regardless of the level of ASD. Compared with ACDF, laminoplasty serves as a motion-preserving procedure that allows for indirect decompression, which may be safer than direct decompression (Bakhsheshian et al., 2017).

Taken together, our results suggested that both ACDF and laminoplasty were effective for the treatment of ASD after primary ACDF. Although ACDF can achieve a better decompression effect, laminoplasty retained more ROM of the surgical segments. For decompression of one-level ASD after primary ACDF, both ACDF and laminoplasty were feasible and open to consideration. As for

the superior and inferior ASD, multilevel laminoplasty may be a suitable choice, while ACDF could significantly increase the ROM and IDP at the adjacent segments. The biomechanical results of this study provided guidance for surgical decisions for the treatment ASD after primary ACDF, but the actual situation should also be considered in clinical practice.

There are some limitations in the present study. First, only linear elastic materials were used for the vertebral body and IVD, which ignored the anisotropic properties of materials. Second, the muscles and collagen fibers were not considered in this study, which may affect the stability of cervical spine. Third, the ligaments were considered as nonlinear Spring element with no effect on compression. Furthermore, the model was constructed based on the data from a single volunteer. Although it had the advantage of making comparisons between different conditions and treatments, the results were somewhat haphazard. However, the simplified model can objectively reflect the biomechanics of the spine and has certain clinical guiding value for the evaluation of different surgical methods. Meanwhile, more accurate FE model and clinical studies are needed to explore the effect of different surgical methods in the future.

CONCLUSION

In conclusion, ACDF and laminoplasty can relieve the high level of stress in the spinal cord caused by ASD after primary ACDF, whereas ACDF can achieve a better decompression effect than laminoplasty regardless of the level of ASD. Revision surgery of the superior ACDF or the superior and inferior ACDF after primary ACDF increased the ROM and IDP at the adjacent segments, which may be the reason for the high incidence of recurrent ASD after second ACDF. Due to some defects in finite element analysis, it may not fully represent the real situation *in vivo*. The biomechanical results of this study provided guidance for surgical decisions for the treatment ASD after primary ACDF, but the actual situation should also be considered in clinical practice.

DATA AVAILABILITY STATEMENT

The original contributions presented in the study are included in the article/**Supplementary Material**, further inquiries can be directed to the corresponding author.

ETHICS STATEMENT

The studies involving human participants were reviewed and approved by the ethics committee of Tongji Medical College, Huazhong University of Science and Technology. Written informed consent was obtained from the volunteer.

AUTHOR CONTRIBUTIONS

WCK, CC, and BJW designed the study, analyzed the data, and wrote the manuscript. WBH, LM, YSS, KW, and SL participated in the design of the study and analyzed the data. SDL, YS, RJL, ZWL, and GCL helped in revising the manuscript. CY, YKZ, and XHW collected the clinical data, helped in writing the manuscript, and instructed on the surgical technique. All authors read and approved the final manuscript.

FUNDING

This work was supported by the National Key Research and Development Program of China (2018YFB1105700), National Natural Science Foundation of China (Grant no. 81904020, 81772401, and 81803917), Natural Science Foundation of Hubei Province (2019CFB305), and the Fundamental Research Funds for the Central Universities (2019kfyXMBZ063).

ACKNOWLEDGMENTS

We would like to thank SDL, YS, RJL, ZWL, and GCL for their help in revising the manuscript.

SUPPLEMENTARY MATERIAL

The Supplementary Material for this article can be found online at: https://www.frontiersin.org/articles/10.3389/fbioe.2021.718996/full#supplementary-material

Supplementary Figure S1 | Validation of IDP of the intact cervical model.

REFERENCES:

Bakhsheshian, J., Mehta, V. A., and Liu, J. C. (2017). Current Diagnosis and Management of Cervical Spondylotic Myelopathy. *Glob. Spine J.* 7, 572–586. doi:10.1177/2192568217699208

Basques, B. A., Ondeck, N. T., Geiger, E. J., Samuel, A. M., Lukasiewicz, A. M., Webb, M. L., et al. (2017). Differences in Short-Term Outcomes between Primary and Revision Anterior Cervical Discectomy and Fusion. *Spine (Phila Pa 1976)* 42, 253–260. doi:10.1097/brs.0000000000001718

Brydon, H. L., Hayward, R., Harkness, W., and Bayston, R. (1995). Physical Properties of Cerebrospinal Fluid of Relevance to Shunt Function. 1: The Effect of Protein upon CSF Viscosity. *Br. J. Neurosurg.* 9, 639–644. doi:10.1080/02688699550040927

Cabraja, M., Abbushi, A., Koeppen, D., Kroppenstedt, S., and Woiciechowsky, C. (2010). Comparison between Anterior and Posterior Decompression with Instrumentation for Cervical Spondylotic Myelopathy: Sagittal Alignment and Clinical Outcome. *Foc* 28, E15. doi:10.3171/2010.1.focus09253

Cai, X.-Y., Sang, D., Yuchi, C.-X., Cui, W., Zhang, C., Du, C.-F., et al. (2020a). Using Finite Element Analysis to Determine Effects of the Motion Loading Method on Facet Joint Forces after Cervical Disc Degeneration. *Comput. Biol. Med.* 116, 103519. doi:10.1016/j.compbiomed.2019.103519

Cai, X.-Y., Yuchi, C.-X., Du, C.-F., and Mo, Z.-J. (2020b). The Effect of Follower Load on the Range of Motion, Facet Joint Force, and Intradiscal Pressure of the Cervical Spine: a Finite Element Study. *Med. Biol. Eng. Comput.* 58, 1695–1705. doi:10.1007/s11517-020-02189-7

Cao, J., Qi, C., Yang, Y., Lei, T., Wang, L., and Shen, Y. (2020). Comparison between Repeat Anterior and Posterior Decompression and Fusion in the Treatment of

Two-Level Symptomatic Adjacent Segment Disease after Anterior Cervical Arthrodesis. *J. Orthop. Surg. Res.* 15, 308. doi:10.1186/s13018-020-01834-z

Chen, Q., Qin, M., Chen, F., Ni, B., Guo, Q., and Han, Z. (2019). Comparison of Outcomes between Anterior Cervical Decompression and Fusion and Posterior Laminoplasty in the Treatment of 4-Level Cervical Spondylotic Myelopathy. *World Neurosurg.* 125, e341–e347. doi:10.1016/j.wneu.2019.01.075

Chung, J.-Y., Kim, S.-K., Jung, S.-T., and Lee, K.-B. (2014). Clinical Adjacent-Segment Pathology after Anterior Cervical Discectomy and Fusion: Results after a Minimum of 10-year Follow-Up. *Spine J.* 14, 2290–2298. doi:10.1016/j.spinee.2014.01.027

Cole, T., Veeravagu, A., Zhang, M., Azad, T. D., Desai, A., and Ratliff, J. K. (2015). Anterior versus Posterior Approach for Multilevel Degenerative Cervical Disease. *Spine* 40, 1033–1038. doi:10.1097/brs.0000000000000872

Du, W., Zhang, P., Shen, Y., Zhang, Y.-Z., Ding, W.-Y., and Ren, L.-X. (2014). Enlarged Laminectomy and Lateral Mass Screw Fixation for Multilevel Cervical Degenerative Myelopathy Associated with Kyphosis. *Spine J.* 14, 57–64. doi:10.1016/j.spinee.2013.06.017

Eck, J. C., Humphreys, S. C., Lim, T.-H., Jeong, S. T., Kim, J. G., Hodges, S. D., et al. (2002). Biomechanical Study on the Effect of Cervical Spine Fusion on Adjacent-Level Intradiscal Pressure and Segmental Motion. *Spine* 27, 2431–2434. doi:10.1097/00007632-200211150-00003

Guo, X., Zhou, J., Tian, Y., Kang, L., and Xue, Y. (2021). Biomechanical Effect of Different Plate-To-Disc Distance on Surgical and Adjacent Segment in Anterior Cervical Discectomy and Fusion - a Finite Element Analysis. *BMC Musculoskelet. Disord.* 22, 340. doi:10.1186/s12891-021-04218-4

Hilibrand, A. S., and Robbins, M. (2004). Adjacent Segment Degeneration and Adjacent Segment Disease: the Consequences of Spinal Fusion?. *Spine J.* 4, 190S–194S. doi:10.1016/j.spinee.2004.07.007

Hirabayashi, S., Yamada, H., Motosuneya, T., Watanabe, Y., Miura, M., Sakai, H., et al. (2010). Comparison of Enlargement of the Spinal Canal after Cervical Laminoplasty: Open-Door Type and Double-Door Type, *European Spine Journal*, 19, 1690–1694. doi:10.1007/s00586-010-1369-y

Holsheimer, J., Den Boer, J. A., Struijk, J. J., and Rozeboom, A. R. (1994). MR Assessment of the normal Position of the Spinal Cord in the Spinal Canal. *AJNR Am. J. Neuroradiol* 15, 951–959.

Hua, W., Zhi, J., Ke, W., Wang, B., Yang, S., Li, L., et al. (2020). Adjacent Segment Biomechanical Changes after One- or Two-Level Anterior Cervical Discectomy and Fusion Using Either a Zero-Profile Device or Cage Plus Plate: A Finite Element Analysis. *Comput. Biol. Med.* 120, 103760. doi:10.1016/j.compbiomed.2020.103760

Ichihara, K., Taguchi, T., Shimada, Y., Sakuramoto, I., Kawano, S., and Kawai, S. (2001). Gray Matter of the Bovine Cervical Spinal Cord Is Mechanically More Rigid and Fragile Than the white Matter. *J. neurotrauma* 18, 361–367. doi:10.1089/08977150151071053

Kavadi, N., and Badve, S. (2019). Commentary on: Risk Factors of Second Surgery for Adjacent Segment Disease Following Anterior Cervical Discectomy and Fusion: A 16-year Cohort Study. *Int. J. Surg.* 69, 165. doi:10.1016/j.ijsu.2019.07.010

Kelly, M. P., Eliasberg, C. D., Riley, M. S., Ajiboye, R. M., and Soohoo, N. F. (2018). Reoperation and Complications after Anterior Cervical Discectomy and Fusion and Cervical Disc Arthroplasty: a Study of 52,395 Cases. *Eur. Spine J.* 27, 1432–1439. doi:10.1007/s00586-018-5570-8

Kurokawa, R., and Kim, P. (2015). Cervical Laminoplasty: The History and the Future, *Neurol. Med. Chir.(Tokyo)*, 55, 529–539. doi:10.2176/nmc.ra.2014-0387

Lee, J. C., Lee, S.-H., Peters, C., and Riew, K. D. (2015). Adjacent Segment Pathology Requiring Reoperation after Anterior Cervical Arthrodesis. *Spine* 40, E571–E577. doi:10.1097/brs.0000000000000846

Li, J., Tong, T., Niu, R., and Shen, Y. (2016). A Study on the Clinical Outcomes of Patients with Revision Surgery for Adjacent Segment Disease after 10-year's Anterior Cervical Spine Surgery. *J. Orthop. Surg. Res.* 11, 5. doi:10.1186/s13018-016-0341-x

Li, Y., Fogel, G. R., Liao, Z., Tyagi, R., Zhang, G., and Liu, W. (2017). Biomechanical Analysis of Two-Level Cervical Disc Replacement with a Stand-Alone U-Shaped Disc Implant. *Spine (Phila Pa 1976)* 42, E1173–E1181. doi:10.1097/brs.0000000000002128

Li, Z., Liu, H., Yang, M., and Zhang, W. (2021). A Biomechanical Analysis of Four Anterior Cervical Techniques to Treating Multilevel Cervical Spondylotic Myelopathy: a Finite Element Study. *BMC Musculoskelet. Disord.* 22, 278. doi:10.1186/s12891-021-04150-7

Liang, G., Liang, C., Zheng, X., Xiao, D., Zeng, S., Yin, D., et al. (2019). Sagittal Alignment Outcomes in Lordotic Cervical Spine. *Spine (Phila Pa 1976)* 44, E882–E888. doi:10.1097/brs.0000000000003016

Lin, M., Shapiro, S. Z., Doulgeris, J., Engeberg, E. D., Tsai, C.-T., and Vrionis, F. D. (2021). Cage-screw and Anterior Plating Combination Reduces the Risk of Micromotion and Subsidence in Multilevel Anterior Cervical Discectomy and Fusion-A Finite Element Study. *Spine J.* 21, 874–882. doi:10.1016/j.spinee.2021.01.015

Mesbah, M., and Barkaoui, A. (2020). Biomechanical Investigation of the Effect of Pedicle-Based Hybrid Stabilization Constructs: A Finite Element Study. *Proc. Inst. Mech. Eng. H* 234, 931–941. doi:10.1177/0954411920934956

Mesbah, M., Barkaoui, A., Chiali, H., and Bendoukha, M. (2020). Posterior Dynamic Topping-Off Fusion Stabilization System in Lumbosacral Spine: a Review of Different Instrumentation Techniques. *Ser. Biomech.* 34, 41–47.

Mesregah, M. K., Formanek, B., Liu, J. C., Buser, Z., and Wang, J. C. (2021). Perioperative Complications of Surgery for Degenerative Cervical Myelopathy: A Comparison between 3 Procedures. *Glob. Spine J* 2192568221998306, 2192568221998306. doi:10.1177/2192568221998306

Mo, Z., Li, Q., Jia, Z., Yang, J., Wong, D. W.-C., and Fan, Y. (2017). Biomechanical Consideration of Prosthesis Selection in Hybrid Surgery for Bi-level Cervical Disc Degenerative Diseases. *Eur. Spine J.* 26, 1181–1190. doi:10.1007/s00586-016-4777-9

Montano, N., Ricciardi, L., and Olivi, A. (2019). Comparison of Anterior Cervical Decompression and Fusion versus Laminoplasty in the Treatment of Multilevel Cervical Spondylotic Myelopathy: A Meta-Analysis of Clinical and Radiological Outcomes. *World Neurosurg.* 130, 530–536. doi:10.1016/j.wneu.2019.06.144

Muzević, D., Splavski, B., Boop, F. A., and Arnautović, K. I. (2018). Anterior Cervical Discectomy with Instrumented Allograft Fusion: Lordosis Restoration and Comparison of Functional Outcomes Among Patients of Different Age Groups. *World Neurosurg.* 109, e233–e243. doi:10.1016/j.wneu.2017.09.146

Nikkhoo, M., Cheng, C.-H., Wang, J.-L., Khoz, Z., El-Rich, M., Hebela, N., et al. (2019). Development and Validation of a Geometrically Personalized Finite Element Model of the Lower Ligamentous Cervical Spine for Clinical Applications. *Comput. Biol. Med.* 109, 22–32. doi:10.1016/j.compbiomed.2019.04.010

Nikkhoo, M., Cheng, C.-H., Wang, J.-L., Niu, C.-C., Parnianpour, M., and Khalaf, K. (2020). The Biomechanical Response of the Lower Cervical Spine Post Laminectomy: Geometrically-Parametric Patient-specific Finite Element Analyses. *J. Med. Biol. Eng.* 41, 59–70. doi:10.1007/s40846-020-00579-8

O'neill, K. R., Wilson, R. J., Burns, K. M., Mioton, L. M., Wright, B. T., Adogwa, O., et al. (2016). Anterior Cervical Discectomy and Fusion for Adjacent Segment Disease: Clinical Outcomes and Cost Utility of Surgical Intervention. *Clin. Spine Surg.* 29, 234–241. doi:10.1097/BSD.0b013e31828ffc54

Oglesby, M., Fineberg, S. J., Patel, A. A., Pelton, M. A., and Singh, K. (2013). Epidemiological Trends in Cervical Spine Surgery for Degenerative Diseases between 2002 and 2009. *Spine* 38, 1226–1232. doi:10.1097/brs.0b013e31828be75d

Persson, C., Evans, S., Marsh, R., Summers, J. L., and Hall, R. M. (2010). Poisson's Ratio and Strain Rate Dependency of the Constitutive Behavior of Spinal Dura Mater. *Ann. Biomed. Eng.* 38, 975–983. doi:10.1007/s10439-010-9924-6

Schroeder, G. D., Kurd, M. F., Millhouse, P. W., Vaccaro, A. R., and Hilibrand, A. S. (2016). Performing an Anterior Cervical Discectomy and Fusion. *Clin. Spine Surg.* 29, 186–190. doi:10.1097/bsd.0000000000000383

Srinivasan, S., Kumar S, D., R, S., Jebaseelan D, D., Yoganandan, N., and Rajasekarans (2021). Effect of Heterotopic Ossification after bryan-cervical Disc Arthroplasty on Adjacent Level Range of Motion: A Finite Element Study. *J. Clin. Orthopaedics Trauma* 15, 99–103. doi:10.1016/j.jcot.2020.10.027

Steinhaus, M. E., York, P. J., Bronheim, R. S., Yang, J., Lovecchio, F., and Kim, H. J. (2020). Outcomes of Revision Surgery for Pseudarthrosis after Anterior Cervical Fusion: Case Series and Systematic Review. *Glob. Spine J.* 10, 559–570. doi:10.1177/2192568219863808

Wang, F., Wang, P., Miao, D.-C., Du, W., and Shen, Y. (2017a). Different Surgical Approaches for the Treatment of Adjacent Segment Diseases after Anterior Cervical Fusion. *Medicine (Baltimore)* 96, e7042. doi:10.1097/md.0000000000007042

Wang, K., Wang, H., Deng, Z., Li, Z., Zhan, H., and Niu, W. (2017b). Cervical Traction Therapy with and without Neck Support: A Finite Element Analysis. *Musculoskelet. Sci. Pract.* 28, 1–9. doi:10.1016/j.msksp.2017.01.005

Wang, M. Y., and Green, B. A. (2003). Laminoplasty for the Treatment of Failed Anterior Cervical Spine Surgery. *Neurosurg. Focus* 15, E7. doi:10.3171/foc.2003.15.3.7

Wu, T. K., Meng, Y., Liu, H., Wang, B. Y., Hong, Y., Rong, X., et al. (2019). Biomechanical Effects on the Intermediate Segment of Noncontiguous Hybrid Surgery with Cervical Disc Arthroplasty and Anterior Cervical Discectomy and Fusion: a Finite Element Analysis. *Spine J.* 19, 1254-–1263. doi:10.1016/j.spinee.2019.02.004

Wu, W.-k., Yan, Z. j., Zhang, T.-f., Liao, C.-g., Liang, K.-l., Chen, L., et al. (2018). Biomechanical Influences of Transcorporeal Tunnels on C4 Vertebra under Physical Compressive Load under Flexion Movement: A Finite Element Analysis. *World Neurosurg.* 114, e199–e208. doi:10.1016/j.wneu.2018.02.140

Xu, R., Bydon, M., Macki, M., De La Garza-Ramos, R., Sciubba, D. M., Wolinsky, J.-P., et al. (2014). Adjacent Segment Disease after Anterior Cervical Discectomy and Fusion. *Spine* 39, 120–126. doi:10.1097/brs.0000000000000074

Yeh, K.-T., Yu, T.-C., Chen, I.-H., Peng, C.-H., Liu, K.-L., Lee, R.-P., et al. (2014). Expansive Open-Door Laminoplasty Secured with Titanium Miniplates Is a Good Surgical Method for Multiple-Level Cervical Stenosis. *J. Orthop. Surg. Res.* 9, 49. doi:10.1186/s13018-014-0049-8

Zhao, L., Chen, J., Liu, J., Elsamaloty, L., Liu, X., Li, J., et al. (2018). Biomechanical Analysis on of Anterior Transpedicular Screw-Fixation after Two-Level Cervical Corpectomy Using Finite Element Method. *Clin. Biomech.* 60, 76–82. doi:10.1016/j.clinbiomech.2018.09.008

Conflict of Interest: The authors declare that the research was conducted in the absence of any commercial or financial relationships that could be construed as a potential conflict of interest.

Publisher's Note: All claims expressed in this article are solely those of the authors and do not necessarily represent those of their affiliated organizations, or those of the publisher, the editors and the reviewers. Any product that may be evaluated in this article, or claim that may be made by its manufacturer, is not guaranteed or endorsed by the publisher.

frontiers in Bioengineering and Biotechnology

ORIGINAL RESEARCH
published: 12 October 2021
doi: 10.3389/fbioe.2021.746902

Surgical Outcome Prediction Using a Four-Dimensional Planning Simulation System With Finite Element Analysis Incorporating Pre-bent Rods in Adolescent Idiopathic Scoliosis: Simulation for Spatiotemporal Anatomical Correction Technique

Hiroyuki Tachi[1,2†], *Koji Kato*[3†], *Yuichiro Abe*[2], *Terufumi Kokabu*[1], *Katsuhisa Yamada*[1], *Norimasa Iwasaki*[1] *and Hideki Sudo*[1,4*]

[1]Department of Orthopaedic Surgery, Faculty of Medicine and Graduate School of Medicine, Hokkaido University, Sapporo, Japan, [2]Department of Orthopaedic Surgery, Eniwa Hospital, Eniwa, Japan, [3]Department of Systems Information Science, Future University Hakodate, Hakodate, Japan, [4]Department of Advanced Medicine for Spine and Spinal Cord Disorders, Faculty of Medicine and Graduate School of Medicine, Hokkaido University, Sapporo, Japan

An optimal surgical strategy for adolescent idiopathic scoliosis (AIS) is to provide maximal deformity correction while preserving spinal mobile segments as much as possible and obtaining a balanced posture. From a spatiotemporal deformity correction standpoint, we recently showed that anatomical four-dimensional (4D) spinal correction could be accomplished by curving the rod. In the surgical procedure, two rods are bent identically to confirm spinal anatomical alignment without referring to the intraoperative alignment of the deformity. Therefore, anatomically designed rods have been developed as notch-free, pre-bent rods for easier anatomical reconstruction. In addition to providing the best spinal instrumentation configurations as pre-bent rods, prediction of surgical outcome along with its biomechanical impact can be obtained by simulation of the surgical procedures with computer modeling. However, an objective model that can simulate the surgical outcome in patients with AIS has not been completely elucidated. The present study aimed to compare simulated deformity corrections based on our newly developed spatiotemporal morphological 4D planning simulation system incorporating pre-bent rods and actual deformity corrections in patients with AIS. A consecutive series of 47 patients who underwent anatomical posterior correction for AIS curves were prospectively evaluated. After multilevel facetectomy, except for the lowest instrumented segment, 11 types of pre-bent rods were used. Patient demographic data, radiographic measurements, and sagittal rod angles were analyzed within 1 week of surgery. Our simulation system incorporating pre-bent rods showed a significant correlation with the actual postoperative spinal alignment. The present study demonstrated the feasibility of our simulation system and the ability to simulate the surgical procedure using the pre-bent rods. The simulation system can be used to minimize the differences between the optimal and

OPEN ACCESS

Edited by:
Fabio Galbusera, Galeazzi Orthopedic Institute (IRCCS), Italy

Reviewed by:
Sebastiano Caprara, ETH Zürich, Switzerland
Luigi La Barbera, Politecnico di Milano, Italy

***Correspondence:**
Hideki Sudo
hidekisudo@yahoo.co.jp

[†]These authors have contributed equally to this work and share first authorship

Specialty section:
This article was submitted to Biomechanics, a section of the journal Frontiers in Bioengineering and Biotechnology

Received: *25 July 2021*
Accepted: *09 September 2021*
Published: *12 October 2021*

Citation:
Tachi H, Kato K, Abe Y, Kokabu T, Yamada K, Iwasaki N and Sudo H (2021) Surgical Outcome Prediction Using a Four-Dimensional Planning Simulation System With Finite Element Analysis Incorporating Pre-bent Rods in Adolescent Idiopathic Scoliosis: Simulation for Spatiotemporal Anatomical Correction Technique. Front. Bioeng. Biotechnol. 9:746902. doi: 10.3389/fbioe.2021.746902

possible outcomes related to the instrumentation levels and rod shapes. Preoperative assumption of rod shape and length can contribute to a reduction in operative time which decreases blood loss and risk of infection. The results of the finite element analysis in the simulation system measured for each individual patient would also provide a more realistic representation of the surgical procedures.

Keywords: surgical outcome, simulation system, finite element analysis, pre-bent rods, adolescent idiopathic scoliosis

INTRODUCTION

Adolescent idiopathic scoliosis (AIS) is the most commonly encountered pediatric musculoskeletal disease presenting a three-dimensional (3D) deformity of the spine. Standard measurement in scoliosis is the Cobb angle, which is the coronal plane angle measured between the vertebrae at the upper and lower bounds of the curve on a standing radiograph. Patients with severe (Cobb angle >40°–50°) or progressive curves may require surgery to correct the deformity.

An optimal surgical strategy is to provide maximal deformity correction while preserving spinal mobile segments to the best extent and obtaining a balanced posture. For instance, inadequate selection for instrumentation length may lead to a postoperative postural imbalance. In addition, although surgical technique as well as spinal instrumentation has been developed in which the 3D correction is achieved, there is still a possibility of implant-related complications such as pedicle screw loosening, screw or spinal rod breakage, and pedicle fracture. Load levels of the screws and rods are important concerns in surgical outcomes. Furthermore, although a rod shape considerably affects postoperative spinal alignment (Salmingo et al., 2014; Kokabu et al., 2016; Sudo et al., 2016; Le Navéaux, et al., 2017), the rod-bending maneuver relies excessively on surgeons' experience. If the rod curvature does not match the patient's deformity and does not allow for deformity correction, such situations will lead to an inadequate correction or implant-related complications due to the overstress on the implant and spine (Sudo et al., 2018). These issues require some innovative systems to assist surgery or predict the most probable outcome of surgery (Aubin et al., 2008; Sudo et al., 2021).

The typical thoracic AIS presents itself with thoracic hypokyphosis. Therefore, the surgical goal should be a correction of the thoracic kyphosis (TK) and achieves an anatomically correct thoracic curve. Post-surgery hypokyphosis can occur after using pedicle screw instrumentation. Several posterior surgical techniques have been developed to maintain and/or improve the TK (Clement et al., 2008; Sudo et al., 2014). However, next-generation surgical techniques are required in order to achieve true anatomical correction. In a healthy human population, the apex of the TK is typically located at T6–T8, when viewing standing sagittal films (Hasegawa et al., 2017). However, for some AIS, the postoperative apex of the TK is almost identical with the apex of the preoperative thoracic scoliosis (Sudo et al., 2018), which is not anatomically correct. This insufficient correction resulting in a postoperative non-anatomical TK is thought to be, because the spinal rods are being bent to match the curvature of scoliosis. From the standpoint of spatiotemporal deformity correction, we recently showed that anatomical four-dimensional (4D) spinal correction could be accomplished by curving the rod (**Figure 1**) (Sudo et al., 2018; Sudo et al., 2021). In the surgical procedure, two rods are bent in a nearly identical fashion to confirm spinal anatomical alignment without reference to the intraoperative alignment of the deformity (Sudo et al., 2018; Sudo et al., 2021). Consequently, pre-bent rod geometries were obtained from intraoperative tracings of the rod shapes, and optimized rod shapes were derived using iterative closest point method followed by hierarchical cluster analysis (Kokabu et al., 2018). Currently, 11 types of pre-bent cobalt-chrome (CoCr) alloy rods are available based on the deformity types and its lengths in Japan that can guide anatomical spinal correction regardless of the surgeons' experience (**Figure 1**, Sudo et al., 2021).

In addition to providing the best spinal instrumentation configurations as pre-bent rods, prediction of surgical outcome along with its biomechanical impact can be obtained by simulation of the surgical procedures with computer modeling (Aubin et al., 2008). However, an objective model that can simulate the 3D outcome of the AIS surgery by considering the preoperative spinal alignment and the surgical intervention has not been completely elucidated (Pasha and Flynn, 2018). In addition, most planning tools in AIS surgery only simulate morphology-based changes of the spinal alignment, lacking the biomechanical analysis (Ferrero et al., 2008; Pasha and Flynn, 2018; Shao et al., 2018). A planning simulator based on spatiotemporal morphological postoperative 4D changes with a patient-specific finite element analysis (FEA) can allow surgeons to predict postoperative outcomes and effectively assist in performing AIS surgery (Galbusera et al., 2015; Wang et al., 2016; Le Navéaux et al., 2016; Cobetto et al., 2020; La Barbera et al., 2021; Galbusera et al., 2021).

The hypothesis of the present study was that our newly developed 4D planning simulation system incorporating pre-bent rods would significantly correlate with the actual postoperative spinal alignment after anatomical 4D spinal correction surgery. The current study aimed to compare simulated and actual deformity corrections in patients with AIS.

MATERIALS AND METHODS

Patient Selection

After institutional review board approval, data from a consecutive series of 47 patients who underwent 4D anatomical correction surgery for AIS curves between 2019 and 2021 were prospectively evaluated; all patients had a Cobb angle of ≤90°. We did not define

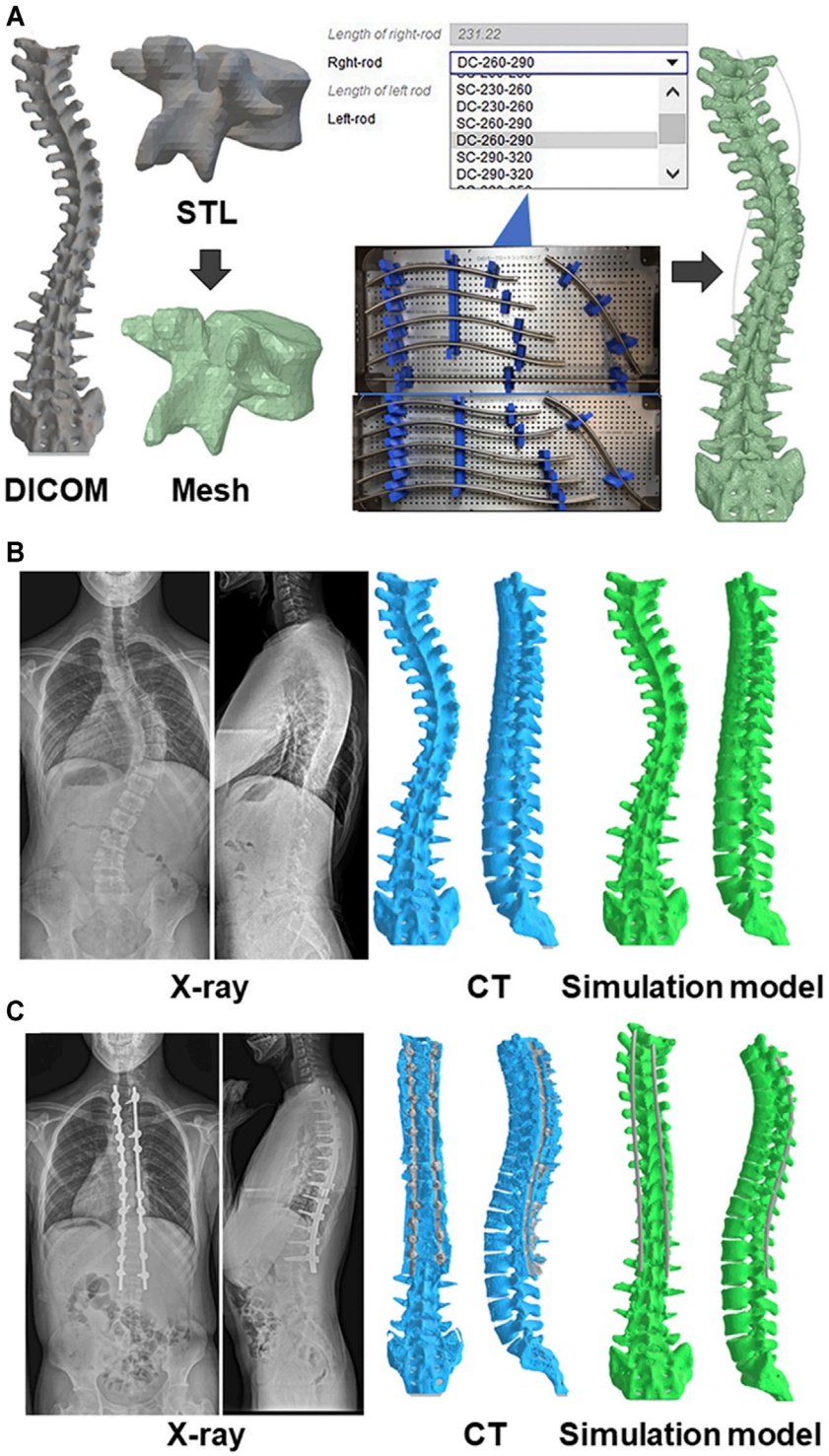

FIGURE 1 | Biomechanical model of the spine **(A)** A custom spinal finite element model was constructed based on the preoperative computed tomography (CT) data. The collected raw data in the Digital Imaging and Communications in Medicine (DICOM) format were imported in a standard triangle language (STL). Subsequently, the STL data were converted to a solid structure, which were built of 10-node tetrahedral element meshes. Eleven types of beam element rods were selected based on the deformity types and its lengths, and positioned for the screws. Representative pre**(B)**- and post**(C)**operative images of radiograph, CT, and simulation model.

the lower limit of the Cobb angle. However, patients with severe (Cobb angle >40°–50°) and/or progressive curves were included. The Ethics Committee of Hokkaido University Hospital approved this research including any relevant details. All methods were performed in accordance with the relevant guidelines and regulations. Written consents were obtained from all the subjects, and when applicable from their guardians. The exclusion criteria were neuromuscular, congenital, and other syndromic scoliosis.

Standing posteroanterior radiographs were recorded preoperatively and within 1 week after surgery. Regarding Cobb measurements, the end vertebrae levels were determined on preoperative radiographs and measured on subsequent radiographs to maintain consistency for statistical comparisons (Cidambi et al., 2012; Sudo et al., 2013). The angle of rotation of the main thoracic (MT) and/or thoracolumbar/lumbar (TL/L) apical vertebra was determined on computed tomography (CT) images (Cidambi et al., 2012; Silvestre et al., 2013; Sudo et al., 2014). Internal studies of the present interrater and intrarater reliability have demonstrated high kappa statistics for all continuous measures (0.90–0.98).

Surgical Procedures

While the end vertebrae were to be considered part of the instrumentation levels, the selection of the upper or lower instrumented vertebrae was dependent on several preoperative anatomical conditions. Shoulder balance and anatomical TK determine the vertebra that was selected for the upper instrumented vertebra (UIV); T2 was selected if the radiographic shoulder height (RSH) was positive, T3 if RSH was between −5 and 0 mm, and T4 if RSH was < −5 mm (Sudo et al., 2018). However, in case with TK < 20° and T5 or T6 upper-end vertebra, the UIV selected was T4 to create anatomical TK (Sudo et al., 2018). The lowest instrumented vertebra (LIV) depends on the lumbar modifiers. For a lumbar modifier A or B, the last vertebra touching the center sacral vertebral line was the LIV (Matsumoto et al., 2013). In the case of lumbar modifier C, LIV was determined at L3 (Sudo et al., 2021).

Side-loading polyaxial pedicle screws (CVS spinal system; Robert Reid, Tokyo, Japan) were inserted. Our previous studies have shown that multilevel facetectomy and screw density on the concave side rather than the convex side significantly impact scoliosis correction and TK restoration (Sudo et al., 2016). This means it is important to place as many screws as possible on the concave side. On the convex side, screws should be placed at 1) the UIV, 2) the upper-end vertebra, 3) the lower-end vertebra, 4) the LIV, and 5) at the apex of scoliosis and its periapical lesions. All-level facetectomy was performed in all patients except for the lowest instrumented segment to avoid pseudoarthrosis at this site (Sudo et al., 2018). For pre-bent rods, CoCr alloy rods (φ 5.5 mm) were bent identically to duplicate the postoperative anatomical TK (Sudo et al., 2018; Sudo et al., 2021). The apex was anticipated to be at T6–T8 for the postoperative TK (Sudo et al., 2018). The rod configurations were split into two types of shapes: single curve and double curves. In the case that LIV was L1 or above, the single-curve rods were applied (Sudo et al., 2018; Sudo et al., 2021), and the TL/L region remained straight. When the LIV was L2 or L3, the double-curve rods were applied (Sudo et al., 2018; Sudo et al., 2021). Each shape was provided by increments of 3 cm. After connecting to the screw heads, the rods were simultaneously rotated. During the rod derotation maneuver, the present technique helped prevent the hypokyphotic deformation of the rod compared with the simple single-rod derotation maneuver or direct vertebral rotation technique (Sudo et al., 2014). The simultaneous rod rotation maneuver does not intend to manipulate vertebral rotation at each level separately and works to correct the rotational deformity not at each segment separately but in the entire instrumentation area simultaneously (Sudo et al., 2014). After 90° rod rotation, several screw heads were tightened to lock the rods. The presence of a mark on the rod helped confirm 90° rotation. Distraction force was first applied on each screw head on the concave side of the thoracic curve, so that not only scoliosis but also TK could be corrected more effectively by lengthening the posterior column. Subsequently, compression force was applied segmentally on the convex curve. *In situ* rod-bending procedure was not performed (Sudo et al., 2014; Sudo et al., 2016; Sudo et al., 2018).

Biomechanical Model of the Spine

For each patient, a custom spinal finite element model (FEM) was constructed based on the preoperative CT Digital Imaging and Communications in Medicine (DICOM) data (**Figure 1**). The software ANSYS 19.2 (ANSYS JAPAN, Tokyo, Japan) was used to model the spine and perform surgical simulations. The collected raw data in the DICOM format were imported into Mimics research 19.0 (Materialize, Leuven, Belgium) to generate 3D vertebral models in a standard triangle language (STL). Subsequently, the STL data generated were imported into ANSYS 19.2 in the form of solid 3D structure (Peng et al., 2020; Zhou et al., 2020), which was built of 10-node tetrahedral element meshes (Ulrich et al., 1998). Screws were positioned and oriented in the desired locations. A new triangulated surface of the instrumented vertebra was generated by Boolean subtraction between the original vertebral surface and the surface of the screws to represent the insertion of screws into the vertebrae. Tetrahedral finite element meshes of the vertebrae and screws were then automatically generated (Galbusera et al., 2015). Eleven types of beam element rods were selected based on the deformity types and its lengths, and positioned for the screws.

Vertebrae were considered as rigid elements in the model to avoid penetration of bone structures. Spinal rods were modeled with a cross-sectional diameter of 5.5 mm, Young's modulus of 420 GPa, and Poisson's ratio of 0.3 according to CoCr alloy properties (Yamada et al., 2020). The screws were modeled as cylinders with a length of 30 mm, cross-sectional diameter of 5.5 mm, Young's modulus of 5,000 MPa, and Poisson's ratio of 0.3 (Zhou et al., 2020). Rods and screws were modeled with materials of isotropic elastic linear material properties. The number of elements in the implants was 790 in the rod and 88 in each screw (Shin et al., 2018).

Connections between the geometries were defined to simulate spatiotemporal morphological postoperative 4D changes. For

TABLE 1 | Stiffness matrix components used in this study.

	Force [N/mm] (with facetectomy)			Moment [N· mm/deg] (with facetectomy)		
	Antero-posterior	Medio-lateral	Cranial-caudal	Antero-posterior	Medio-lateral	Cranial-caudal
T1/2-L4/5	1,392 (696)	294 (188)	341 (188)	448 (224)	644 (406)	738 (406)
L5/S	700	190	190	222	410	410

stability of simulation, intervertebral discs were completely removed, and each vertebra was connected with joint element having intervertebral stiffness (Galbusera et al., 2015). The stiffness matrix components used in this study (**Table 1**) were using the ANSYS software. We set the stiffness matrix components based on the literature (Argoubi and Shirazi-Adi, 1996). The intervertebral stiffness was calculated from reaction forces and moments according to the relative amount of translational and rotational displacements between two vertebrae (Senteler et al., 2016). The values were same through T1/2 to L4/5. However, the value of stiffness matrix component was reduced to be representative of facetectomy (Oda et al., 2002) where facetectomy was performed. The connection between vertebra and screw was set as a joint where boundary condition was defined with all translational and rotational degrees constrained. A spring contact model was defined between screw head and rod to simulate the rod being captured in the screws. Finally, a spring contact model was defined between the concave and convex rods to simulate the rotation of rods simultaneously. In this study, distractioncompression force was not applied on each screw head.

Surgical Simulations

During the whole simulation process, boundary conditions were imposed on the spinal FEM to mimic conditions observed in a surgical setting and ensure simulation convergence. Boundary conditions of the spinal FEM were defined with the sacrum fixed and T1 free to rotate and to translate in the caudocranial direction, allowing possible lengthening of the spine during the simulation of the correction process. For multilevel facetectomy simulation, contacts between posterior facets were neglected at instrumented levels except for the lowest instrumented segment to mimic their surgical removal. Regarding rod rotation maneuver, connecting concave and convex rods to screw head was simulated by setting the spring length between the rod and the screw to zero. Furthermore, the power delivered to the concave rod was gradually increased towards concave (66 ± 106 N; range, 0–300 N) and dorsal sides of scoliosis (922 ± 169 N; range, 400–1,000 N) to perform a 90° rotation of the rod. Then, final locking of the screws was simulated. For each screw, null relative translations and rotations between the appropriate rod node and the screw head were imposed. Therefore, the rods could not slide or rotate anymore into the screw heads. Moreover, all external constraints (displacement or forces) were released at this step, and the new equilibrium state was computed. The model was left free to reach equilibrium at the end of the simulation. In this surgical simulation, distractioncompression force was not applied on each screw head. Hence, intraoperative surgical steps described in the simulation included precisely the same as actual surgery except for distractioncompression procedure and screw length and diameter. However, the stiffness matrix does not correctly describe the real condition because this model did not consider preoperative curve flexibility.

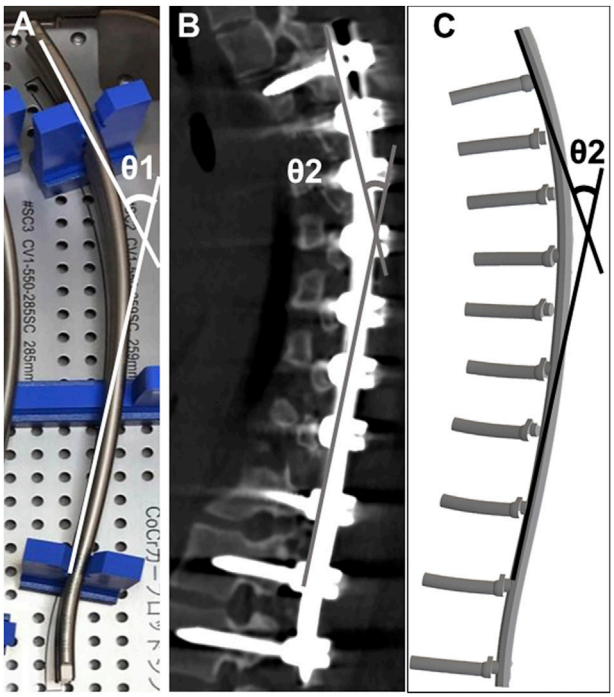

FIGURE 2 | Rod angle before and after implantation **(A)** Prior to implantation, the angle between the proximal and distal tangential line was measured (θ1). Postoperative implant rod geometry (θ2) was obtained after the surgery using computed tomography **(B)** and the simulation model **(C)**.

Simulation Data Analysis

The spinal profile, quantified in terms of coronal MT Cobb angle, TK and TL/L lordosis, and apical vertebral rotation angle, was monitored over the course of the surgery simulation process. Von Mises stress, which is an equivalent stress, was shown as the reaction forces on the concave and convex rods at the end of the correction (Shin et al., 2018; Peng et al., 2020). Axial forces at the bonescrew interface were analyzed for all the pedicle screws with respect to their simulated final positions and the postoperative ones. The direction of these forces was along the direction of the

TABLE 2 | Patient demographic data.

	Mean ± standard deviation (range)
Number of patients	47
Age at surgery (yr.)	14.7 ± 2.5 (10–19)
Gender (no. and % of woman)	42 (89%)
Risser sign (grade)	3.9 ± 1.3 (0–5)
Lenke type (no.)	
1	31
2	3
3	1
4	1
5	5
6	6
Lumbar modifier (no.)	
A	23
B	3
C	21
Number of instrumented vertebrae (segments)	11.2 ± 1.5 (8–14)

screw's shaft. They were supposed to be responsible for the pull-out phenomenon; therefore, the expression "pull-out forces" was used to describe them. This first phase study did not analyze other forces and moments components such as medio-lateral forces and screw bending moments (responsible for pedicle wall breach and screw breakage, respectively) because the pull-out phenomenon is likely observed compared to the other phenomena in actual AIS surgery (Abul-Kasim and Ohlin, 2014; Oda et al., 2021).

Analysis of Rod Configuration

The angle between the cranial and caudal tangential lines was obtained before implantation (θ1) (**Figure 2**). Similarly, the postoperative rod angle was obtained (θ2) using reconstructed sagittal CT images and simulation models (Cidambi et al., 2012; Kokabu et al., 2016; Sudo et al., 2021). The angle of rod deformation was defined as the difference between θ1 and θ2 (θ1–θ2) (Kokabu et al., 2016; Sudo et al., 2021).

Statistical Analysis

All data were presented as means ± standard deviation and range. The entire cohort was first analyzed and then further assessed based on selective thoracic fusion to L1 in ten Lenke 1 A patients to confirm the feasibility of our simulation system and the ability to simulate the uninstrumented lumbar segments. Repeated-measures analysis of variance was used to compare differences among the standing radiographs, CT images, and simulation data. Data were checked for normality and equality of variances, and Bonferroni post-hoc analysis was used to set the significance level at 0.05. Comparisons of radiographic quantitative variables and rod angles were performed using MannWhitney *U* test or paired *t*-test. Spearman's correlation coefficient analysis was used to assess relationships between CT images and simulation models. Data analyses were performed using JMP statistical software for Windows (version 14; SAS, Inc, Cary, NC, United States). $p < 0.05$ was considered statistically significant.

RESULTS

Patient Demographic Data

Demographic data are summarized in **Tables 2**, **3**. The cephalad-instrumented vertebrae ranged from T2 to T6, and the caudal-instrumented vertebrae ranged from T12 to L3. Preoperative standing radiographic MT and TL/L curves averaged 52° and 37°, respectively, and TK angle was 17°, whereas the lumbar lordosis angle was of 47°. Postoperatively, MT and TL/L curves averaged 11° and 9°, respectively, and TK angle was 30°, whereas the lumbar lordosis angle was 48°. The average MT and TL/L curve correction rate was 81% (range, 64–98%) and 75% (range, 36–98%), respectively. The average preoperative MT and TL/L vertebral rotation angles measured on CT images were 18° each, which decreased after surgery to an average of 11° each.

Comparison Among Standing Radiographs, CT Images, and Simulation Models

Preoperatively, there were significant differences between standing radiographs and CT images or simulation models in both coronal and sagittal plane data ($p < 0.05$). However, there were no significant differences among postoperative standing radiographs, CT images, and simulation models in both coronal and sagittal plane data ($p > 0.05$). Regarding postoperative vertebral rotation angle, there was no significant difference between CT images and simulation model ($p > 0.05$).

Correlation Analysis and Accuracy Evaluation

Spearman's correlation coefficient analysis showed that simulated coronal and sagittal plane data as well as vertebral rotation angle were significantly correlated with those of data on postoperative CT images ($p < 0.001$, **Figure 3**). Mean absolute error and root mean squared error between CT images and simulation model are summarized in **Table 4**. Simulated coronal and sagittal plane data as well as vertebral rotation angle were predicted within 5° compared to actual postoperative measurements.

Subgroup Analysis

There were no significant differences between postoperative CT images and simulation models in all coronal, sagittal, and axial plane data in Lenke 1 A patients (**Table 5**, $p > 0.05$). Regarding mean absolute error and root mean squared error between CT images and simulation model, the simulated coronal and sagittal plane data as well as vertebral rotation angle were predicted within 5° compared to actual postoperative measurements (**Table 6**).

Analysis of Rod Stress and Screw Forces

We estimated rod stress and screw force in simulation models. The models showed that peak stress was located near the apex of the curve in both single and double curve

TABLE 3 | Radiographic and CT parameters.

	Standing radiographs (range)	CT (range)	Simulation model (range)	Repeated-measures analysis of variance	Bonferroni *p*		
				p	Standing radiographs to CT	Standing radiographs to simulation model	CT to simulation model
Preoperative coronal plane data							
Main thoracic curve (°)	52 ± 11 (28–82)	45 ± 11 (20–83)	45 ± 11 (20–83)	<0.001	0.011	0.011	1.000
Thoracolumbar/lumbar curve (°)	37 ± 13 (16–72)	32 ± 13 (8–65)	32 ± 13 (8–65)	0.008	0.022	0.022	1.000
Preoperative sagittal plane data							
Thoracic kyphosis (°)	17 ± 9 (2–42)	13 ± 7 (3–32)	13 ± 7 (3–32)	0.037	0.042	0.042	1.000
Lumbar lordosis (°)	47 ± 10 (18–69)	42 ± 10 (24–72)	42 ± 10 (24–72)	0.012	0.024	0.024	1.000
Preoperative vertebral rotation angle							
Main thoracic apical vertebra (°)	NA	18 ± 8 (3–35)	18 ± 8 (3–35)	1.000			
Thoracolumbar/ lumbar apical vertebra (°)	NA	18 ± 9 (4–41)	18 ± 9 (4–41)	1.000			
Postoperative coronal plane data							
Main thoracic curve (°)	11 ± 7 (1–28)	13 ± 6 (3–30)	14 ± 6 (2–30)	0.916			
Thoracolumbar/lumbar curve (°)	9 ± 6 (1–27)	12 ± 8 (1–30)	11 ± 6 (2–26)	0.782			
Postoperative sagittal plane data							
Thoracic kyphosis (°)	30 ± 4 (19–38)	28 ± 4 (20–39)	28 ± 4 (20–36)	0.632			
Lumbar lordosis (°)	48 ± 9 (36–69)	48 ± 8 (35–68)	47 ± 7 (33–65)	0.811			
Postoperative vertebral rotation angle							
Main thoracic apical vertebra (°)	NA	11 ± 6 (1–21)	11 ± 6 (0–23)	0.719			
Thoracolumbar/lumbar apical vertebra (°)	NA	11 ± 7 (1–30)	10 ± 6 (1–26)	1.000			

All data expressed as means ± SD and range.

type rods (**Figure 4**). In addition, another peak was located near the extremities of the instrumented segments. **Table 7** shows estimated rod stress and screw force in one simulation model. The rod stress was significantly higher at the concave side compared to the convex side ($p < 0.05$). Regarding pull-out forces on screws, peak forces were located near the apex of the MT curve at the concave side in both single and double curves. In addition, another peak was located near the LIV at both concave and convex sides in double curve. The pull-out forces on screws were significantly higher at the concave side compared to the convex side ($p < 0.05$).

Implant-Rod Angles of Curvature

The rod deformation angle was significantly higher on the concave side than on the convex side ($p < 0.001$; **Table 8**). There were no significant differences between postoperative CT images and simulation model in the rod deformation angle at both concave and convex sides ($p = 0.129$ and $p = 0.237$, respectively).

DISCUSSION

Our personalized finite element spinal biomechanical model and its simulated response to surgical instrumentation allowed to evaluate the effect of the 4D anatomical correction technique on AIS deformity correction and on loads in the instrumentation. Not only geometric aspects of the deformity correction but also biomechanical results were simulated using existing pre- and postoperative information of 47 patients and 11 types of pre-bent rods. Despite the heterogeneity in the cohort of patients with various Lenke types, this study analyzed a cohort of patient-specific surgery models and found that our newly developed 4D planning simulation system incorporating pre-bent rods showed a significant correlation with the actual postoperative spinal alignment after anatomical 4D spinal correction surgery. The simulated measurements were all within 5° agreement with the clinical values, equivalent to the generally accepted clinical error of 5° (Majdouline et al., 2009).

The present study demonstrated the feasibility of our simulation system and the ability to simulate the surgical procedure using the pre-bent rods. The preoperative assumption for rod shape and length will help reduce operative time, thereby decreasing blood loss and risk of infection. However, in this model, the values of intervertebral stiffness matrix components were same through thoracic to lumbar spines and not personalized. We consider this as a main factor that may justify imperfect correlations of the slope and intercept. It may be important to consider the personal stiffness matrix for improving the capability of the model in predicting the perfect values. Other factors affecting the

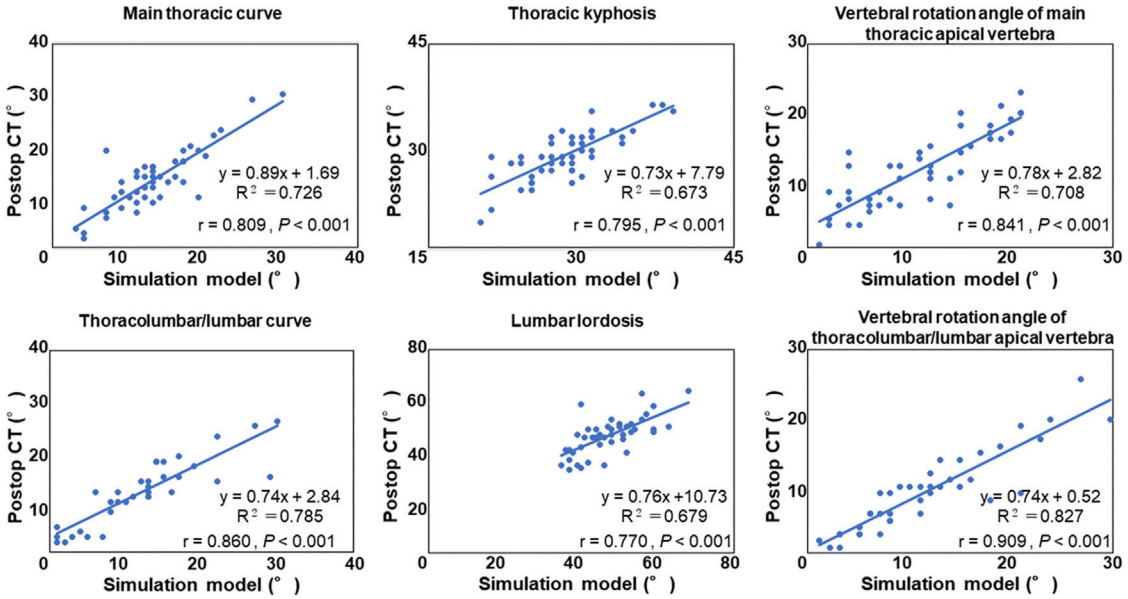

FIGURE 3 | Correlation analysis between the postoperative computed tomography (CT) measurement and the simulation model.

TABLE 4 | MAE and RMSE between CT images and simulation model.

	MAE	RMSE
Coronal plane data		
Main thoracic curve (°)	3.1	4.1
Thoracolumbar/lumbar curve (°)	2.3	3.5
Sagittal plane data		
Thoracic kyphosis (°)	2.0	2.4
Lumbar lordosis (°)	3.7	4.7
Vertebral rotation angle		
Main thoracic apical vertebra (°)	2.5	3.3
Thoracolumbar/lumbar apical vertebra (°)	2.7	3.6

MAE, mean absolute error; RMSE, root mean squared error.

correlations could be that boundary conditions applied during simulation were not the same as during the actual surgery for each patient, and there was an issue that clinical measurements of the parameters of interest were not perfect. In addition, we cannot provide a quantitative justification regarding the prediction accuracy because no steps were used to ensure the credibility of our model in predicting the right values. Although computational models are increasingly used to support surgical planning, varying levels of model verification and validation limit the level of confidence in their predictive potential (Poncelas et al., 2021). Recently, Poncelas et al. performed a credibility assessment of their model to investigate proximal junctional failure in clinical cases with adult spine deformity using ASMEV&V40 standard (Poncelas et al., 2021). We should also assess the credibility of our model for AIS surgery using the recommended strategies in the future.

In the present study, the surgical simulations were conducted using the DICOM CT scans in a supine position and approximated with the surgical procedures performed on patients lying prone. In addition, the postoperative corrected angles were measured clinically using the DICOM CT data in a supine position. Consequently, supine CT scans were obtained after surgery, while the patient was still recovering; therefore, it was not yet load-bearing, and provided a better comparison

TABLE 5 | Postoperative CT and simulation model parameters in patients with Lenke type 1 A.

	CT (range)	Simulation model (range)	*p*
Coronal plane data			
Main thoracic curve (°)	14 ± 5 (3–22)	14 ± 6 (4–23)	0.909
Thoracolumbar/lumbar curve (°)	9 ± 5 (1–16)	8 ± 4 (3–12)	0.629
Sagittal plane data			
Thoracic kyphosis (°)	28 ± 3 (24–31)	28 ± 3 (23–32)	0.848
Lumbar lordosis (°)	48 ± 9 (37–68)	49 ± 6 (41–64)	1.000
Vertebral rotation angle			
Main thoracic apical vertebra (°)	13 ± 5 (6–20)	12 ± 4 (5–19)	0.424
Thoracolumbar/lumbar apical vertebra (°)	6 ± 3 (1–12)	5 ± 3 (1–10)	0.445

All data expressed as means ± SD and range.

TABLE 6 | MAE and RMSE between CT images and simulation model.

	MAE	RMSE
Coronal plane data		
Main thoracic curve (°)	2.1	3.4
Thoracolumbar/lumbar curve (°)	2.0	2.4
Sagittal plane data		
Thoracic kyphosis (°)	1.4	1.7
Lumbar lordosis (°)	3.5	4.3
Vertebral rotation angle		
Main thoracic apical vertebra (°)	1.6	2.0
Thoracolumbar/lumbar apical vertebra (°)	1.4	1.7

In patients with Lenke type 1 A.
MAE, mean absolute error; RMSE, root mean squared error.

between the clinical and simulated measurements (Little et al., 2013). The difference between the present simulation model and reality was small in the instrumented segments. Conversely, there is a possibility that the results for the uninstrumented regions are not accurate because the gravity and postural control were not simulated in the standing posture (Robitaille et al., 2009). Due to the aforementioned reasons, we performed comparisons using standing radiographs. Consequently, while there were significant differences in preoperative measurement values between standing radiographs and simulation model, there were no significant differences in postoperative measurement values between the standing radiographs and simulation model, indicating that the simulation model can predict postoperative spinal alignment in standing position including uninstrumented lumbar segments in the case with selective thoracic instrumentation for Lenke 1 A curves.

There have been computational studies that similarly predicted 3D correction and implant loads (Wang et al., 2016; Le Navéaux et al., 2016; La Barbera et al., 2021; Galbusera et al., 2021). These studies determined how several instrumentation parameters such as screw density and rod contouring angle affected correction and stress in the instrumentation. Because our previous studies have shown that multilevel facetectomy and screw density on the concave side significantly impact the amount of scoliosis correction and also TK restoration, especially in preoperative hypokyphotic (TK <15°) thoracic spine (Kokabu et al., 2016; Sudo et al., 2016), we currently attempt on inserting the screw as much as possible on the concave side. Also, rod curvatures were limited to up to 11 types. We have analyzed the correlation between preoperative rod angle and rod stress in the apex of the MT curve or TL/L curve. In addition, the correlation between postoperative TK in the simulation model and screw density on the concave side or preoperative rod angle in patients with hypothoracic (TK <15°) Lenke one curves was analyzed. The results showed that there were no significant correlations between the simulated correction and rod stress and instrumentation parameters (**Supplementary figures S1, S2**). Therefore, we could not confirm that clinical observation reported by Sudo et al. (2016) and Kokabu et al. (2016) was confirmed by the present biomechanical models. Because there was no range of numbers for the screw density and rod curvature, as well as sufficient quantity of sample numbers, there may be limitations in statistical analysis.

However, because both pre- and postoperative rod measurements were available in the current study, it was possible to utilize the initial rod shape and simulate its elastic deformation precisely. In this simulation model, the maximum power delivered to the rod was 1,000 N. We previously documented that the notch-free, pre-bent CoCr alloy rod (φ5.5 mm) showed an approximated linear loaddisplacement curve under 1000 N of load (Yamada et al., 2020). Due to these reasons, we opine that almost only elastic deformation occurred. However, elastoplastic phenomena involved in rod contouring may be considered in future studies to better elucidate whether both elastic and plastic deformation may be involved *in vivo* to explain any change in rod shape *in vivo*.

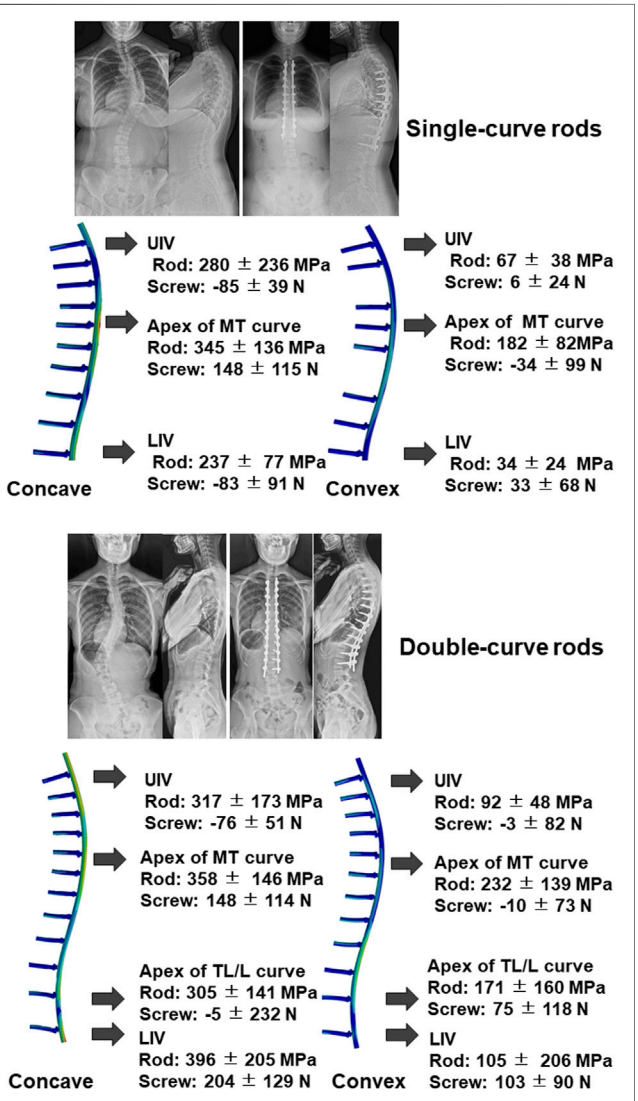

FIGURE 4 | Representative images of radiograph and simulation model using single-curve rod **(upper)** and double-curve rods. Results of rod stress and screw forces analysis of all 47 cases were also presented. Positive value in the screw force means pull-out force. UIV; upper instrumented vertebra, MT; main thoracic, LIV; lowest instrumented vertebra, TL/L; thoracolumbar/lumbar.

TABLE 7 | Estimated rod stress (MPa) and screw forces (N) in simulation model.

	Rods			Screws		
	Concave	Convex	*p*	Concave	Convex	*p*
Single-curve rods (N = 15)						
UIV	280 ± 236 (52–931)	67 ± 38 (21–172)	0.002	−85 ± 39 (−179 to −20)	6 ± 24 (−33–57)	<0.001
Apex of MT curve	345 ± 136 (127–527)	182 ± 82 (24–312)	0.001	148 ± 115 (48–432)	−34 ± 99 (−220 to 220)	<0.001
LIV	233 ± 77 (113–358)	34 ± 24 (11–109)	<0.001	−83 ± 91 (−239 to 95)	33 ± 68 (−52–214)	0.004
Double-curve rods (N = 32)						
UIV	317 ± 173 (105–856)	92 ± 48 (20–220)	<0.001	−76 ± 51 (−188 to 35)	−3 ± 82 (−157–224)	<0.001
Apex of MT curve	358 ± 146 (69–840)	232 ± 139 (43–580)	<0.001	148 ± 114 (−134–416)	−10 ± 73 (−242 to 135)	<0.001
Apex of TL/L curve	305 ± 141 (126–586)	171 ± 160 (21–773)	<0.001	−5 ± 232 (−411 to 395)	75 ± 118 (−153–307)	0.109
LIV	396 ± 205 (50–1,002)	105 ± 206 (43–580)	<0.001	204 ± 129 (7–497)	103 ± 90 (−60–307)	0.001

All data expressed as means ± SD and range. Positive value in the screw force means pull-out force. UIV, upper instrumented vertebra; MT, main thoracic; LIV, lowest instrumented vertebra, TL/L, thoracolumbar/lumbar.

TABLE 8 | Implant-rod angle of curvature.

	Concave	Convex	*p*
Preoperative rod angle (θ1) (°)			
CT	39.3 ± 5.7 (29.1–46.1)	39.3 ± 5.7 (29.1–46.1)	1.000
Simulation model	39.3 ± 5.7 (29.1–46.1)	39.3 ± 5.7 (29.1–46.1)	1.000
Postoperative rod angle (θ2) (°)			
CT	32.2 ± 4.2 (24.2–40.0)	36.2 ± 4.9 (27.2–43.0)	<0.001
Simulation model	33.2 ± 4.2 (26.8–41.3)	36.8 ± 5.0 (28.0–44.7)	<0.001
Rod deformation angle (Δθ) (°)			
CT	7.1 ± 3.1 (1.3–13.8)	3.2 ± 2.5 (−1.8–8.9)	<0.001
Simulation model	6.5 ± 3.2 (0.2–12.6)	2.5 ± 2.9 (−3.9–7.6)	<0.001

All data expressed as means ± SD and range. Δθ was defined as the difference between θ1 and θ2 (θ1–θ2).

Although it has been demonstrated that the amount of curvature incorporated into the rods before their insertion impacts TK restoration (Salmingo et al., 2014; Kokabu et al., 2016; Sudo et al., 2016; Le Navéaux, et al., 2017), there are a few studies that have estimated the loads in the rod during and after deformity collection (Galbusera et al., 2015). To our knowledge, this is the first study to show that the simulation model can predict the deformation of the implanted rod. The simulation model determined significant changes in the rod contours, especially on the concave side which has been clinically reported (Sudo et al., 2021). In addition, based on the changes in rod geometry and FEA, the highest stress was found at the apex of the rod curvature and the extremities of the instrumented levels, which is in agreement with previous results (Belmont et al., 2001; Aubin et al., 2008; Abe et al., 2015). Qualitative understanding of the stress in the rods is useful to estimate the risk of implant failure and loosening intraoperatively and/or postoperatively, which currently depends on the surgeon's experience (Galbusera et al., 2015).

Further understanding of bonescrew forces in AIS instrumentation is essential as high-stresses at the bonescrew interface can cause screw loosening or breakage. Shear forces on the screws are more relevant to be reported rather than only pull-out values. In addition, because we did not observe intraoperative complications such as screw pull-out and bending, we could not analyze the predicted forces in cases with complications. However, in this study, the forces generated at the bonescrew interface (peak 497 N) were lower than the thoracic pedicle screws pull-out forces of approximately 800 N reported in experimental studies (Liljenqvist et al., 2001). The present study validated only the geometrical aspects, and more investigations are needed to validate the model in terms of forces at the bonescrew interfaces. However, the implants tested by Liljenquist et al. were monoaxial pedicle screws which were different from the screws in the current study (poly-axial screws). Bonescrew forces were higher for monoaxial screws than polyaxial screws, indicating that in patients with large and stiff spinal deformities or in patients with compromised bone quality, screws with more degrees of freedom would offer better perspective to reduce bonescrew connection failure (Wang et al., 2012). Although the thresholds may serve as a comparison in the present study, therefore, those simulated cases exceeding the threshold may not be considered necessarily unsafe, it is likely that the anatomical correction technique may be used safely.

Our study has some limitations. First, we applied boundary conditions only to the pelvis and did not include the cervical spine, ribs, and scapulae. Although this simplification of the real spine represents a condition wherein the vertebral levels are not entirely fixed, including the cervical vertebrae could demonstrate a more naturalistic behavior of the uninstrumented spinal segment (Majdouline et al., 2012). Second, we only simulated one diameter although the screw diameter is known to have the highest effect on the force to failure compared to screw length (Cho et al., 2010; Bianco et al., 2019). Since this was a first phase study to simulate the surgical procedure, the simulation was maintained as simple as possible. Additionally, model validation was purely based on the final rod geometry and the main spinal curves. However, to ensure that the simulation model can predict postoperative alignment, a more detailed validation on single vertebra position and rotation, together with individualized screw's models and trajectories, would be needed. Third, this study did not analyze other forces and moments such as medio-lateral forces and screw bending moments. The other loading components may play a role in other clinically relevant failure modes and may be addressed in the future. Finally, in this surgical simulation, preoperative curve flexibility was not considered, and distractioncompression force was not applied on each screw head. Nonetheless, the simulation model can predict postoperative surgical alignments. However,

we are currently improving the model to incorporate both preoperative curve flexibility based on bending radiographs and distractioncompression procedures, as well as actual screw length and diameter. There may be a limit to improve the comparison between model prediction and actual postoperative correction; however, the incorporation may further improve the estimation of rod stress and screw force because this information will contribute to set stiffness matrix components and connections between the geometries.

CONCLUSION

Our newly developed 4D planning simulation system incorporating pre-bent rods showed a significant correlation with the actual postoperative spinal alignment after anatomical 4D spinal correction surgery. The present study demonstrated the feasibility of our simulation system and the ability to simulate the surgical procedure using pre-bent rods. The FEA results in the simulation system measured for each individual patient would also provide a more realistic representation of the surgical procedures.

DATA AVAILABILITY STATEMENT

The raw data supporting the conclusion of this article will be made available by the authors, without undue reservation.

ETHICS STATEMENT

The studies involving human participants were reviewed and approved by the Hokkaido University Hospital. Written informed consent to participate in this study was provided by the participants' legal guardian/next of kin.

AUTHOR CONTRIBUTIONS

HS conceived and designed the study. HT, KK, YA, TK, KY, and HS. performed the experiment. HT, KK, YA, and HS. analysed the results. HT, KK, YA, NI, and HS. contributed to discussions throughout the study. HS. wrote and edited the manuscript. All authors have read and approved the final submitted manuscript.

FUNDING

This work was supported by the Japan Agency for Medical Research and Development (JP18he1302026h0003).

SUPPLEMENTARY MATERIAL

The Supplementary Material for this article can be found online at: https://www.frontiersin.org/articles/10.3389/fbioe.2021.746902/full#supplementary-material

REFERENCES

Abe, Y., Ito, M., Abumi, K., Sudo, H., Salmingo, R., and Tadano, S. (2015). Scoliosis Corrective Force Estimation from the Implanted Rod Deformation Using 3D-FEM Analysis. *Scoliosis* 10, S2. doi:10.1186/1748-7161-10-S2-S2

Abul-Kasim, K., and Ohlin, A. (2014). Evaluation of Implant Loosening Following Segmental Pedicle Screw Fixation in Adolescent Idiopathic Scoliosis: a 2 Year Follow-Up with Low-Dose CT. *Scoliosis* 9, 13, 2014 . eCollection 2014. doi:10.1186/1748-7161-9-13

Argoubi, M., and Shirazi-Adl, A. (1996). Poroelastic Creep Response Analysis of a Lumbar Motion Segment in Compression. *J. Biomech.* 29, 1331–1339. doi:10.1016/0021-9290(96)00035-8

Aubin, C. E., Labelle, H., Chevrefils, C., Desroches, G., Clin, J., and Eng, A. B. M. (2008). Preoperative Planning Simulator for Spinal Deformity Surgeries. *Spine* 33, 2143–2152. doi:10.1097/BRS.0b013e31817bd89f

Belmont, P. J., Jr, Klemme, W. R., Dhawan, A., and Polly, D. W., Jr (2001). *In Vivo* Accuracy of Thoracic Pedicle Screws. *Spine* 26, 2340–2346. doi:10.1097/00007632-200111010-00010

Bianco, R.-J., Arnoux, P.-J., Mac-Thiong, J.-M., and Aubin, C.-E. (2019). Thoracic Pedicle Screw Fixation under Axial and Perpendicular Loadings: A Comprehensive Numerical Analysis. *Clin. Biomech.* 68, 190–196. doi:10.1016/j.clinbiomech.2019.06.010

Cho, W., Cho, S. K., and Wu, C. (2010). The Biomechanics of Pedicle Screw-Based Instrumentation. *The J. Bone Jt. Surg. Br. volume* 92-B, 1061–1065. doi:10.1302/0301-620X.92B8.24237

Cidambi, K. R., Glaser, D. A., Bastrom, T. P., Nunn, T. N., Ono, T., and Newton, P. O. (2012). Postoperative Changes in Spinal Rod Contour in Adolescent Idiopathic Scoliosis. *Spine* 37, 1566–1572. doi:10.1097/BRS.0b013e318252ccbe

Clement, J.-L., Chau, E., Kimkpe, C., and Vallade, M.-J. (2008). Restoration of Thoracic Kyphosis by Posterior Instrumentation in Adolescent Idiopathic Scoliosis. *Spine* 33, 1579–1587. doi:10.1097/BRS.0b013e31817886be

Cobetto, N., Aubin, C.-E., and Parent, S. (2020). Anterior Vertebral Body Growth Modulation. *Spine (Phila Pa 1976)* 45, E1203–E1209. doi:10.1097/BRS.0000000000003533

Di Silvestre, M., Lolli, F., Bakaloudis, G., Maredi, E., Vommaro, F., and Pastorelli, F. (2013). Apical Vertebral Derotation in the Posterior Treatment of Adolescent Idiopathic Scoliosis: Myth or Reality? *Eur. Spine J.* 22, 313–323. doi:10.1007/s00586-012-2372-2

Galbusera, F., Bassani, T., La Barbera, L., Ottardi, C., Schlager, B., Brayda-Bruno, M., et al. (2015). Planning the Surgical Correction of Spinal Deformities: Toward the Identification of the Biomechanical Principles by Means of Numerical Simulation. *Front. Bioeng. Biotechnol.* 3, 178. doi:10.3389/fbioe.2015.00178

Galbusera, F., Cina, A., Panico, M., and Bassani, T. (2021). The Importance of Curve Severity, Type and Instrumentation Strategy in the Surgical Correction of Adolescent Idiopathic Scoliosis: an In Silico Clinical Trial on 64 Cases. *Sci. Rep.* 11, 1799. doi:10.1038/s41598-021-81319-z

Hasegawa, K., Okamoto, M., Hatsushikano, S., Shimoda, H., Ono, M., Homma, T., et al. (2017). Standing Sagittal Alignment of the Whole Axial Skeleton with Reference to the Gravity Line in Humans. *J. Anat.* 230, 619–630. doi:10.1111/joa.12586

Kokabu, T., Kanai, S., Abe, Y., Iwasaki, N., and Sudo, H. (2018). Identification of Optimized Rod Shapes to Guide Anatomical Spinal Reconstruction for Adolescent Thoracic Idiopathic Scoliosis. *J. Orthop. Res.* 36, 3219–3224. doi:10.1002/jor.24118

Kokabu, T., Sudo, H., Abe, Y., Ito, M., Ito, Y. M., and Iwasaki, N. (2016). Effects of Multilevel Facetectomy and Screw Density on Postoperative Changes in Spinal Rod Contour in Thoracic Adolescent Idiopathic Scoliosis Surgery. *PLoS One* 11, e0161906. doi:10.1371/journal.pone.0161906

La Barbera, L., Larson, A. N., Rawlinson, J., and Aubin, C.-E. (2021). In Silico patient-specific Optimization of Correction Strategies for Thoracic Adolescent Idiopathic Scoliosis. *Clin. Biomech.* 81, 105200. doi:10.1016/j.clinbiomech.2020.105200

Le Navéaux, F., Aubin, C.-E., Parent, S., O. Newton, P., and Labelle, H. (2017). 3D Rod Shape Changes in Adolescent Idiopathic Scoliosis Instrumentation: How Much Does it Impact Correction? *Eur. Spine J.* 26, 1676–1683. doi:10.1007/s00586-017-4958-1

Le Navéaux, F., Larson, A. N., Labelle, H., Wang, X., and Aubin, C.-É. (2016). How Does Implant Distribution Affect 3D Correction and Bone-Screw Forces in Thoracic Adolescent Idiopathic Scoliosis Spinal Instrumentation? *Clin. Biomech.* 39, 25–31. doi:10.1016/j.clinbiomech.2016.09.002

Liljenqvist, U., Hackenberg, L., Link, T., and Halm, H. (2001). Pullout Strength of Pedicle Screws versus Pedicle and Laminar hooks in the Thoracic Spine. *Acta Orthop. Belg.* 67, 157–163.

Little, J. P., Izatt, M. T., Labrom, R. D., Askin, G. N., and Adam, C. J. (2013). An FE Investigation Simulating Intra-operative Corrective Forces Applied to Correct Scoliosis Deformity. *Scoliosis* 8, 9. doi:10.1186/1748-7161-8-9

Lopez Poncelas, M., La Barbera, L., Rawlinson, J. J., Crandall, D., and Aubin, C. E. (2021). Credibility Assessment of Patient-specific Biomechanical Models to Investigate Proximal Junctional Failure in Clinical Cases with Adult Spine Deformity Using ASME V&V40 Standard. *Comput. Methods Biomech. Biomed. Eng.* 24, 1–11. doi:10.1080/10255842.2021.1968380

Majdouline, Y., Aubin, C.-E., Sangole, A., and Labelle, H. (2009). Computer Simulation for the Optimization of Instrumentation Strategies in Adolescent Idiopathic Scoliosis. *Med. Biol. Eng. Comput.* 47, 1143–1154. doi:10.1007/s11517-009-0509-1

Majdouline, Y., Aubin, C.-E., Wang, X., Sangole, A., and Labelle, H. (2012). Preoperative Assessment and Evaluation of Instrumentation Strategies for the Treatment of Adolescent Idiopathic Scoliosis: Computer Simulation and Optimization. *Scoliosis* 7, 21. doi:10.1186/1748-7161-7-21

Matsumoto, M., Watanabe, K., Hosogane, N., Kawakami, N., Tsuji, T., Uno, K., et al. (2013). Postoperative Distal Adding-On and Related Factors in Lenke Type 1A Curve. *Spine* 38, 737–744. doi:10.1186/1471-2474-15-36610.1097/brs.0b013e318279b666

Oda, I., Abumi, K., Cunningham, B. W., Kaneda, K., and McAfee, P. C. (2002). An *In Vitro* Human Cadaveric Study Investigating the Biomechanical Properties of the Thoracic Spine. *Spine* 27, E64–E70. doi:10.1097/00007632-200202010-00007

Oda, K., Ohba, T., Hiroshi, Y., Fujita, K., Tanaka, N., Koyma, K., et al. (2021). Factors Affecting Pedicle Screw Insertional Torque in Spine Deformity Surgery. *Spine (Phila Pa 1976)* 46, E932–E938. doi:10.1097/BRS.0000000000004021

Pasha, S., and Flynn, J. (2018). Data-driven Classification of the 3D Spinal Curve in Adolescent Idiopathic Scoliosis with an Applications in Surgical Outcome Prediction. *Sci. Rep.* 8, 16296. doi:10.1038/s41598-018-34261-6

Peng, Y. X., Zheng, Z. Y., Wang, Md, W. g., Liu, L., Chen, Md, F., Xu, Md, H. t., et al. (2020). Relationship between the Location of Ligamentum Flavum Hypertrophy and its Stress in Finite Element Analysis. *Orthop. Surg.* 12, 974–982. doi:10.1111/os.12675

Robitaille, M., Aubin, C.-É., and Labelle, H. (2009). Effects of Alternative Instrumentation Strategies in Adolescent Idiopathic Scoliosis: a Biomechanical Analysis. *J. Orthop. Res.* 27, 104–113. doi:10.1002/jor.20654

Salmingo, R. A., Tadano, S., Abe, Y., and Ito, M. (2014). Influence of Implant Rod Curvature on Sagittal Correction of Scoliosis Deformity. *Spine J.* 14, 1432–1439. doi:10.1016/j.spinee.2013.08.042

Senteler, M., Weisse, B., Rothenfluh, D. A., and Snedeker, J. G. (2016). Intervertebral Reaction Force Prediction Using an Enhanced Assembly of OpenSim Models. *Comput. Methods Biomech. Biomed. Eng.* 19, 538–548. doi:10.1080/10255842.2015.1043906

Shao, K., Wang, H., Li, B., Tian, D., Jing, J., Tan, J., et al. (2018). Morphology-based Realization of a Rapid Scoliosis Correction Simulation System. *Comput. Biol. Med.* 94, 85–98. doi:10.1016/j.compbiomed.2018.01.004

Shin, J. K., Lim, B.-Y., Goh, T. S., Son, S. M., Kim, H.-S., Lee, J. S., et al. (2018). Effect of the Screw Type (S2-Alar-Iliac and Iliac), Screw Length, and Screw Head Angle on the Risk of Screw and Adjacent Bone Failures after a Spinopelvic Fixation Technique: A Finite Element Analysis. *PLoS One* 13, e0201801. doi:10.1371/journal.pone.0201801

Sudo, H., Abe, Y., Kokabu, T., Ito, M., Abumi, K., Ito, Y. M., et al. (2016). Correlation Analysis between Change in Thoracic Kyphosis and Multilevel Facetectomy and Screw Density in Main Thoracic Adolescent Idiopathic Scoliosis Surgery. *Spine J.* 16, 1049–1054. doi:10.1016/j.spinee.2016.04.014

Sudo, H., Abe, Y., Kokabu, T., Kuroki, K., Iwata, A., and Iwasaki, N. (2018). Impact of Multilevel Facetectomy and Rod Curvature on Anatomical Spinal Reconstruction in Thoracic Adolescent Idiopathic Scoliosis. *Spine (Phila Pa 1976)* 43, E1135–E1142. doi:10.1097/BRS.0000000000002628

Sudo, H., Ito, M., Abe, Y., Abumi, K., Takahata, M., Nagahama, K., et al. (2014). Surgical Treatment of Lenke 1 Thoracic Adolescent Idiopathic Scoliosis with Maintenance of Kyphosis Using the Simultaneous Double-Rod Rotation Technique. *Spine* 39, 1163–1169. doi:10.1097/BRS.0000000000000364

Sudo, H., Ito, M., Kaneda, K., Shono, Y., and Abumi, K. (2013). Long-Term Outcomes of Anterior Dual-Rod Instrumentation for Thoracolumbar and Lumbar Curves in Adolescent Idiopathic Scoliosis. *J. Bone Jt. Surg.* 95, e49. doi:10.2106/JBJS.L.0078110.2106/JBJS.L.00781

Sudo, H., Tachi, H., Kokabu, T., Yamada, K., Iwata, A., Endo, T., et al. (2021). *In Vivo* deformation of Anatomically Pre-bent Rods in Thoracic Adolescent Idiopathic Scoliosis. *Sci. Rep.* 11, 12622. doi:10.1038/s41598-021-92187-y

Ulrich, D., van Rietbergen, B., Weinans, H., and Rüegsegger, P. (1998). Finite Element Analysis of Trabecular Bone Structure: a Comparison of Image-Based Meshing Techniques. *J. Biomech.* 31, 1187–1192. doi:10.1016/s0021-9290(98)00118-3

Wang, X., Aubin, C.-E., Crandall, D., Parent, S., and Labelle, H. (2012). Biomechanical Analysis of 4 Types of Pedicle Screws for Scoliotic Spine Instrumentation. *Spine* 37, E823–E835. doi:10.1097/BRS.0b013e31824b7154

Wang, X., Boyer, L., Le Navéaux, F., Schwend, R. M., and Aubin, C.-E. (2016). How Does Differential Rod Contouring Contribute to 3-dimensional Correction and Affect the Bone-Screw Forces in Adolescent Idiopathic Scoliosis Instrumentation? *Clin. Biomech.* 39, 115–121. doi:10.1016/j.clinbiomech.2016.10.002

Yamada, K., Sudo, H., Iwasaki, N., and Chiba, A. (2020). Mechanical Analysis of Notch-free Pre-bent Rods for Spinal Deformity Surgery. *Spine (Phila Pa 1976)* 45, E312–E318. doi:10.1097/BRS.0000000000003269

Zhou, Q.-k., Zeng, F.-h., Tu, J.-l., Dong, Z.-q., and Ding, Z.-H. (2020). Influence of Cement-Augmented Pedicle Screw Instrumentation in an Osteoporotic Lumbosacral Spine over the Adjacent Segments: a 3D Finite Element Study. *J. Orthop. Surg. Res.* 15, 132. doi:10.1186/s13018-020-0165010.1186/s13018-020-01650-5

Conflict of Interest: The authors declare that the research was conducted in the absence of any commercial or financial relationships that could be construed as a potential conflict of interest.

Publisher's Note: All claims expressed in this article are solely those of the authors and do not necessarily represent those of their affiliated organizations, or those of the publisher, the editors and the reviewers. Any product that may be evaluated in this article, or claim that may be made by its manufacturer, is not guaranteed or endorsed by the publisher.

frontiers in Bioengineering and Biotechnology

ORIGINAL RESEARCH
published: 01 November 2021
doi: 10.3389/fbioe.2021.760498

Biomechanics of Lumbar Spine Injury in Road Barrier Collision–Finite Element Study

L. Pachocki[1], *K. Daszkiewicz*[1], *P. Łuczkiewicz*[2]* *and W. Witkowski*[1]

[1]Department of Mechanics of Materials and Structures, Faculty of Civil and Environmental Engineering, Gdansk University of Technology, Gdansk, Poland, [2]2nd Division of Orthopedics and Kinetic Organ Traumatology, Faculty of Medicine, Medical University of Gdansk, Gdansk, Poland

Literature and field data from CIREN database have shown that lumbar spine injuries occur during car crashes. There are multiple hypotheses regarding how they occur; however, there is no biomechanical explanation for these injuries during collisions with road safety barriers (RSBs). Therefore, the objective of this study was to investigate the mechanics of vertebral fractures during car collisions with concrete RSBs. The finite element method was used for the numerical simulations. The global model of the car collision with the concrete RSB was created. The lumbar spine kinematics were extracted from the global simulation and then applied as boundary conditions to the detailed lumbar spine model. The results showed that during the collision, the occupant was elevated, and then dropped during the vehicle landing. This resulted in axial compression forces 2.6 kN with flexion bending moments 34.7 and 37.8 Nm in the L2 and L3 vertebrae. It was shown that the bending moment is the result of the longitudinal force on the eccentricity. The lumbar spine index for the L1–L5 section was 2.80, thus indicating a lumbar spine fracture. The minimum principal strain criterion of 7.4% and damage variable indicated L2 and L3 vertebrae and the inferior part of L1, as those potentially prone to fracture. This study found that lumbar spine fractures could occur as a consequence of vehicle landing during a collision with a concrete RSB mostly affecting the L1–L3 lumbar spine section. The fracture was caused by a combination of axial forces and flexion bending moments.

Keywords: car crash, numerical modeling, road safety, spine fracture, spine injury

OPEN ACCESS

Edited by:
Marwan El-Rich, Khalifa University, United Arab Emirates

Reviewed by:
Elisabetta M. Zanetti, University of Perugia, Italy
Bharath Koya, Wake Forest Baptist Medical Center, United States

***Correspondence:**
P. Łuczkiewicz
plucz@gumed.edu.pl

Specialty section:
This article was submitted to Biomechanics, a section of the journal Frontiers in Bioengineering and Biotechnology

Received: *18 August 2021*
Accepted: *18 October 2021*
Published: *01 November 2021*

Citation:
Pachocki L, Daszkiewicz K, Łuczkiewicz P and Witkowski W (2021) Biomechanics of Lumbar Spine Injury in Road Barrier Collision–Finite Element Study. Front. Bioeng. Biotechnol. 9:760498. doi: 10.3389/fbioe.2021.760498

1 INTRODUCTION

Road barriers are used to prevent road injuries and fatalities. However, these barriers can cause severe or fatal injuries by transferring impact forces on vehicle occupants during crashes (Karim et al., 2012). According to the report of National Police Headquarters in Poland (2020), 1.4% of all road injuries were associated with vehicle crashes against road safety barriers (RSBs). The most serious consequences of those accidents are vertebral fractures and spinal cord injuries (Muller et al., 2014). Wang et al. (2009) revealed that front-seat occupants involved in crashes sustained spinal fractures in 12.5% of the considered cases. Adolph et al. (2013) showed that 15% of crashes with MAIS 2 + injuries included lumbar and/or thoracic spine injuries. Moreover, lumbar spine fractures occurred more frequently in late model vehicles than in early ones in frontal crashes (Pintar et al., 2012; Kaufman et al., 2013). None of the regulated or consumer information crash tests (US-NCAP, IIHS) considered lumbar spine injury as a part of their safety evaluation process, which is a cause of

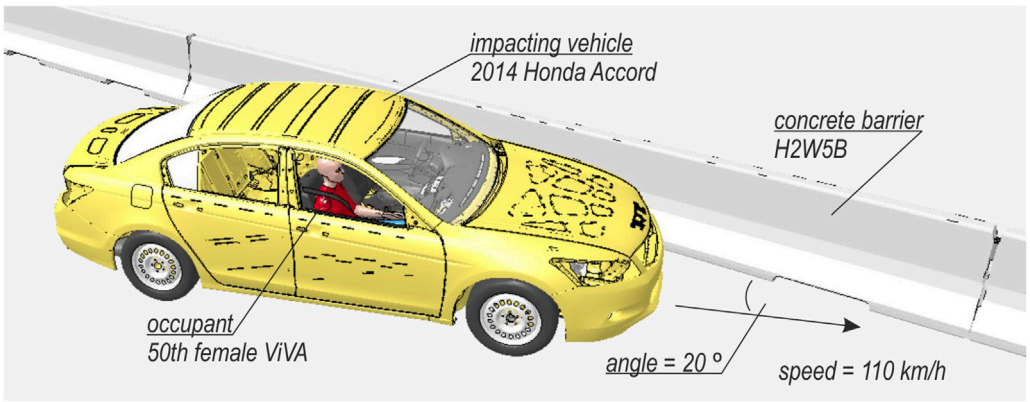

FIGURE 1 | Setup of the global collision FE model.

concern. The primary mechanism of lumbar spine fractures is caused by high-energy axial compression forces with resultant bending moments (Richards et al., 2006; Ivancic, 2013). Begeman et al. (1973) showed that the compression force was transferred from the seat pan to the lumbar spine. Munjin et al. (2011) reported that a fracture at the Th12 or L1 vertebra occurred when the patient was launched from the seat or when the patient fell back down into the seat after being launched. It is unclear how an axial compression force can act on the lumbar spine in frontal crashes. Huelke et al. (1995) hypothesized that three-point-belted occupants sustained lumbar fracture due to "submarining" of the pelvis under the lap belts. However, Tang et al. (2020) found that features that prevented submarining increased the lumbar spine forces, and as a consequence, the risk of fracture.

In previous studies, the authors demonstrated the ability to reconstruct real-world crashes using finite element method (FEM) and various types of FE human body models (HBMs) or FE models of anthropomorphic test devices (ATDs). For instance, a 50th percentile male Hybrid III ATD model was used in the work of (Li et al., 2015; Tang et al., 2020). In the research by (Arun et al., 2017), they used the HBM developed by Global Human Body Model Consortium (GHBMC). However, THUMS was used by (Golman et al., 2014; Gaewsky et al., 2015; Jones et al., 2016; Ye et al., 2018), and ViVA – open source HBM was adopted by (Östh et al., 2015; Östh et al., 2016a; Östh et al., 2016b; Östh et al., 2017a; Östh et al., 2017b). The latter model was chosen for this study because it was an open source project, and it was a model of 50th percentile female, for whom there was evidence that they could be more vulnerable during vehicle collisions (Pintar et al., 2012; Kaufman et al., 2013; Östh et al., 2017b).

The analysis of spine biomechanics during impacts was limited to frontal and side crash simulations in previous numerical studies. Although the Crash Injury Research and Engineering Network (CIREN) database described the spine fractures as a result of a vehicle collision with concrete barriers, the biomechanics has not been yet clarified. Because of lack of data required to simulate a specific barrier collision from CIREN database, the objective was to investigate the mechanism of vertebral fracture during a normative TB32 crash test (BSI, 2010) with a concrete road safety barrier using FEM.

2 MATERIALS AND METHODS

2.1 Global Model of Vehicle Collision

A global FE model was created in the LS-DYNA environment (Hallquist, 2006; LSTC, 2017a). The global model consisted of a concrete RSB, an impacting vehicle, and an occupant. The setup of the global model is illustrated in **Figure 1**. The simulation accounts for geometric and material nonlinearities and contact effects in explicit time-integration dynamics. Because the impact angle and impact speed were difficult to infer, the TB32 crash test (BSI, 2010) was selected as a representative case (see **Figure 1**), i.e., a velocity of 110 km/h and an impact angle of 20°. The vehicle was positioned to hit the barrier after 0.05 s of the simulation. The selected barrier was a concrete safety system of a H2W5B class (BSI, 2010). The model of this barrier has been validated and successfully used in previous studies (Pachocki and Wilde, 2018; Pachocki and Bruski, 2020). The impacting vehicle was a 2014 Honda Accord, developed and validated by the NHTSA (Singh et al., 2018). The NHTSA's model contained seats, seatbelts with pretensioners, and required compartment elements. It weighs approximately 1,600 kg without an occupant. For the occupant, the ViVA HBM was adopted (Östh et al., 2017a; 2016b), a 50th percentile female located on the passenger side of the vehicle. The entire simulation covered 1 s of the collision. Once the global simulation was terminated, the translations and rotations of the Th12 and L5 vertebrae from the model were extracted and then imposed as boundary conditions for the detailed lumbar spine model. Specifically, the displacements were extracted from a node above Th12 and a node below L5 of the ViVA HBM.

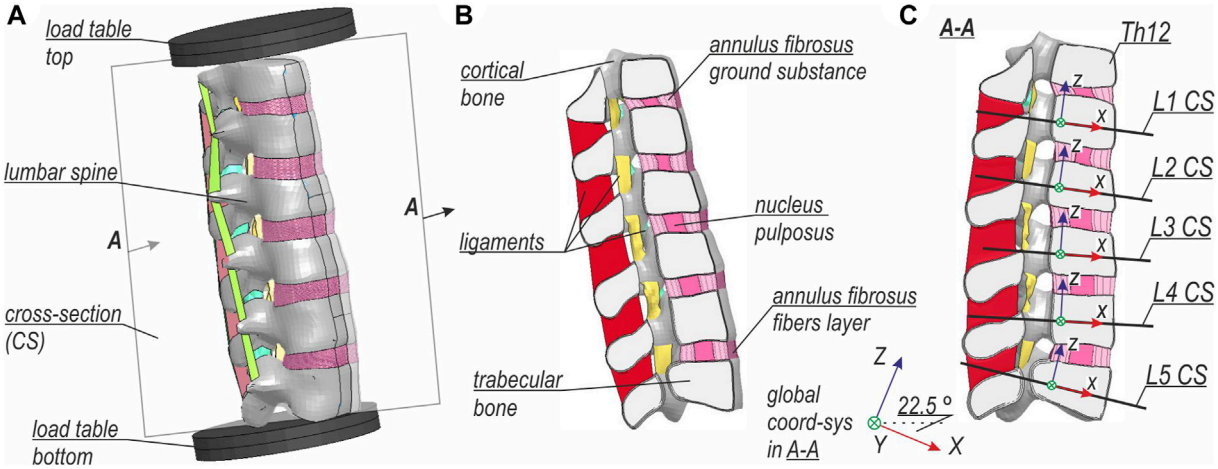

FIGURE 2 | Setup of the detailed lumbar spine FE model: **(A)** general view, **(B)** half-section view, and **(C)** view on cross-sections with global and local coordinate systems.

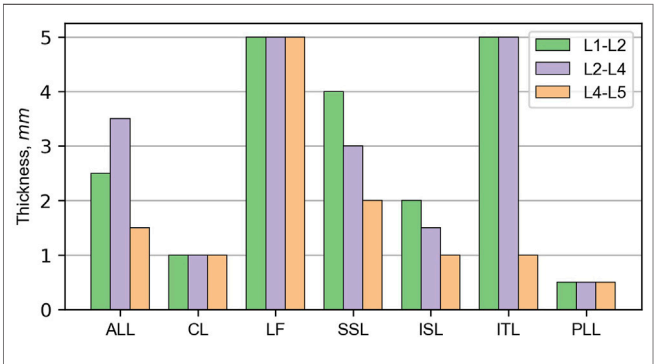

FIGURE 3 | Thickness of ligaments in the lumbar spine model.

Those nodes were also used for the definition of 6-degree of freedom springs that connected adjacent vertebras.

2.2 Detailed Lumbar Spine Section Model

The detailed lumbar spine model was based on the section from the 50th percentile Total HUman Model for Safety v6.1 (THUMS) developed by Toyota Motor Corporation, and it was used e.g. in research by (Mendoza-Vazquez et al., 2015; Jones et al., 2016). The setup of the model is shown in **Figure 2A**. The comparison between the global and the local model of L-spine is provided in **Supplementary Appendix A**. As in the global model, a nonlinear dynamic analysis with time integration of an explicit scheme was performed. The boundary conditions from the global model were imposed on load tables that were constrained to the adjacent parts of the vertebrae: Th12 and L5. The load tables were positioned so that their centers of gravity coincided with the nodes in the global model that were used for the extraction of boundary conditions. Furthermore, the detailed model setup was rotated 25.5° in sagittal plane, which is based on the positioning of L-spine in the global model. **Figure 2B** presents the half-section A-A with the names of specific parts of the lumbar spine model. The internal forces in the respective vertebras were calculated in the cross-sections (CSs) located at the height of their center of gravity (CG), as shown in **Figure 2C**. The normal directions of the CSs planes were calculated as an average of the normal directions of the planes created on the superior and inferior endplates of the given vertebra.

To pass several validation tests described in the works by (Demetropoulos et al., 1998; Renner et al., 2007; Xu et al., 2017) some parts and parameters of the THUMS model were modified. The FE mesh of the THUMS model was refined to a size of 1.5–2.0 mm. The detailed model consisted of 111,457 nodes comprising 37,740 shells, 503,712 solids, and 17,478 seatbelt elements (LSTC, 2017b). The properties of vertebras remained unchanged, however, the thicknesses and material properties of ligaments were modified according to the experimental data from research by (Chazal et al., 1985; Pintar et al., 1992). **Figure 3** depicts the thickness of ligaments in specified sections of the L-spine. The material data for nucleus pulposus (NP) and annulus fibrosus (AF) ground substance of lumbar discs were taken from the experimental work (Schmidt et al., 2006; Schmidt et al., 2007). Additionally, NP was separated from the surrounding bones and ground substance of AF, and appropriate contact was defined. Fibers of AF were rearranged into five layers and their direction was modified to be closer to 30°. The volume content of the fibers was equal to 16% of the volume of AF's ground substance. Their material characteristics were based on the work by Shirazi-Adl (1986). Material characteristics of soft tissues in the lumbar spine model are summarized in **Table 1**.

Several criteria from the literature were applied to capture the possible fractures in the detailed model. The first was a lumbar spine index (LSI) proposed by (Ye et al., 2018). This index is based

TABLE 1 | Material properties of soft tissues in the lumbar spine model.

Soft tissue	Modulus, MPa	ρ, $\frac{t}{mm^3}$	ν, –	Material law	References
Annulus fibrosus–ground substance	L1-L2 → C_1 = 0.36; C_2 = 0.09 L2-L4 → C_1 = 0.24; C_2 = 0.06 L4-L5 → C_1 = 0.18; C_2 = 0.045	1.0 e-9	0.45	Mooney-Rivlin	Schmidt et al., 2006; Schmidt et al., 2007
Annulus fibrosus–collagen fibers	nonlinear stress-strain curves	—	—	1-D nonlinear stress-strain	Shirazi-Adl (1986)
Nucleus pulposus	C_1 = 0.12; C_2 = 0.03	1.0 e-9	0.4999	Mooney-Rivlin	Schmidt et al., 2006; Schmidt et al., 2007
Ligaments	nonlinear stress-strain curves	1.0 e-9	0.3	orthotropic nonlinear stress-strain	Chazal et al., 1985; Pintar et al., 1992

on the combined load of an axial compression force and the resultant bending moment in each vertebra of the lumbar spine. They proposed a threshold value for the L1–L4 LSI that indicated a fracture as 2.29. Another fracture criterion was based on experimental research by (Hansson et al., 1986). They described the material characteristics of a trabecular bone in the lumbar spine for compressive loads. The mean value of ultimate compressive stress equaled 1.55 ± 1.11 MPa with corresponding strain 7.4 ± 2.4%. Thus, the value of 7.4% minimum principal strain was selected as the injury criterion. The two remaining criteria of the Huber–von Mises–Hencky (HMH) effective stress and the damage variable were based on the material properties available in THUMS. For the trabecular bone, the yield stress was set as 1.8 MPa. The damage variable criterion, based on the continuum damage mechanics model, had no specific threshold assigned; thus, we proposed our own interpretation of its value.

3 RESULTS

3.1 Global Model

The views of the vehicular crash with the H2W5B concrete RSB are presented in **Figure 4** for the selected time instances. In the simulation, the vehicle hits the barrier in the connection between two segments of the barrier (0.05 s). The front left wheel of the car drove over a segment of the barrier (0.15 s), which resulted in an elevation of the entire vehicle (0.33 s). The vehicle remained in contact with the barrier, moved along the barrier, finally landed (0.65 s), and separated from the RSB (0.76 s). Owing to inertia forces, the passenger of the vehicle, after the initial impact, was forced to move forward (0.15 s). The chest and pelvis of the occupant were restrained by a three-point seatbelt system. However, because of the force vector of the impact acting in the front-left direction, the occupant bent laterally, and the shoulder belt slipped down from the upper torso. Then, the head of the passenger flexed and missed the deployed passenger airbag. While the vehicle was still elevated (0.33 s), the entire chest was placed above the shoulder belt, and the entire body of the occupant was floating over the bottom seat. The body position was maintained until the vehicle landed. Then, the upper torso wrapped above the shoulder belt, resulting in flexion of the spine, and the pelvic region dropped on the seat. The specific displacements and rotations extracted from the global model are provided in **Figure 5**. Those results are presented in the global coordinate system XYZ, as in **Figure 2C**.

3.2 Detailed Model

The compression force and the flexion moment were the highest internal forces in the lumbar spine. They occurred during the landing of the vehicle at 0.65 s. Consequently, a time instance of 0.65 s was selected for the analysis of the detailed model. A comparison of the passenger positions between the initial configuration and the configuration during landing is depicted in **Figure 6**. The hands and legs of the occupant from the global model (**Figures 6A–C**) were switched off for clarity, and the location of the lumbar spine section was highlighted. The detailed model results of the lumbar spine (**Figures 6B–D**) are presented only for the left half-section A-A. **Figure 6D** shows a simplified version of the trajectory of the compressive forces (denoted by the red line) during landing. The normal force and bending moments determined for each CS vertebra are listed in **Table 2**. Then, the longitudinal compressive force acting on the eccentricity, calculated as the bending moment divided by the normal force, was determined. For clarity, the eccentricity is shown in **Figure 6D** only in the local *x*-direction (see **Figure 2**), and it was calculated relative to the CG of the cross-section. The longitudinal force in the lumbar spine was approximately 2.6 kN, and the differences between vertebras were under 10%. The highest resultant bending moment and the greatest x-eccentricity was observed for L3. The eccentricities for each vertebra in both directions are listed in **Table 2**. As seen in **Table 2**, the moments in flexion were dominant in relation to the lateral bending moments.

The criterion used to estimate the risk of lumbar spine fracture was the LSI. The age-adjusted L1-L5 LSI was 2.76, and the age-adjusted L1-L4 LSI was 2.80. The threshold was 2.29; hence, the index indicated a fracture in the lumbar spine section. The LSI values for specific vertebras are presented in **Table 2**.

The other results from the detailed lumbar spine model are presented in **Figure 7** only for the trabecular bone. **Figure 7A** presents the map of the minimum principal strain, where the criterion of ultimate compressive strain of 7.4% was assumed. **Figure 7B** shows the fringe plot of effective stresses according to the HMH hypothesis, and **Figure 7C** shows the isosurfaces of the damage variable. The eccentric force that acted on the lumbar spine during landing resulted in kyphosis in sections Th12–L5 (see **Figure 7**). The largest stress and strain

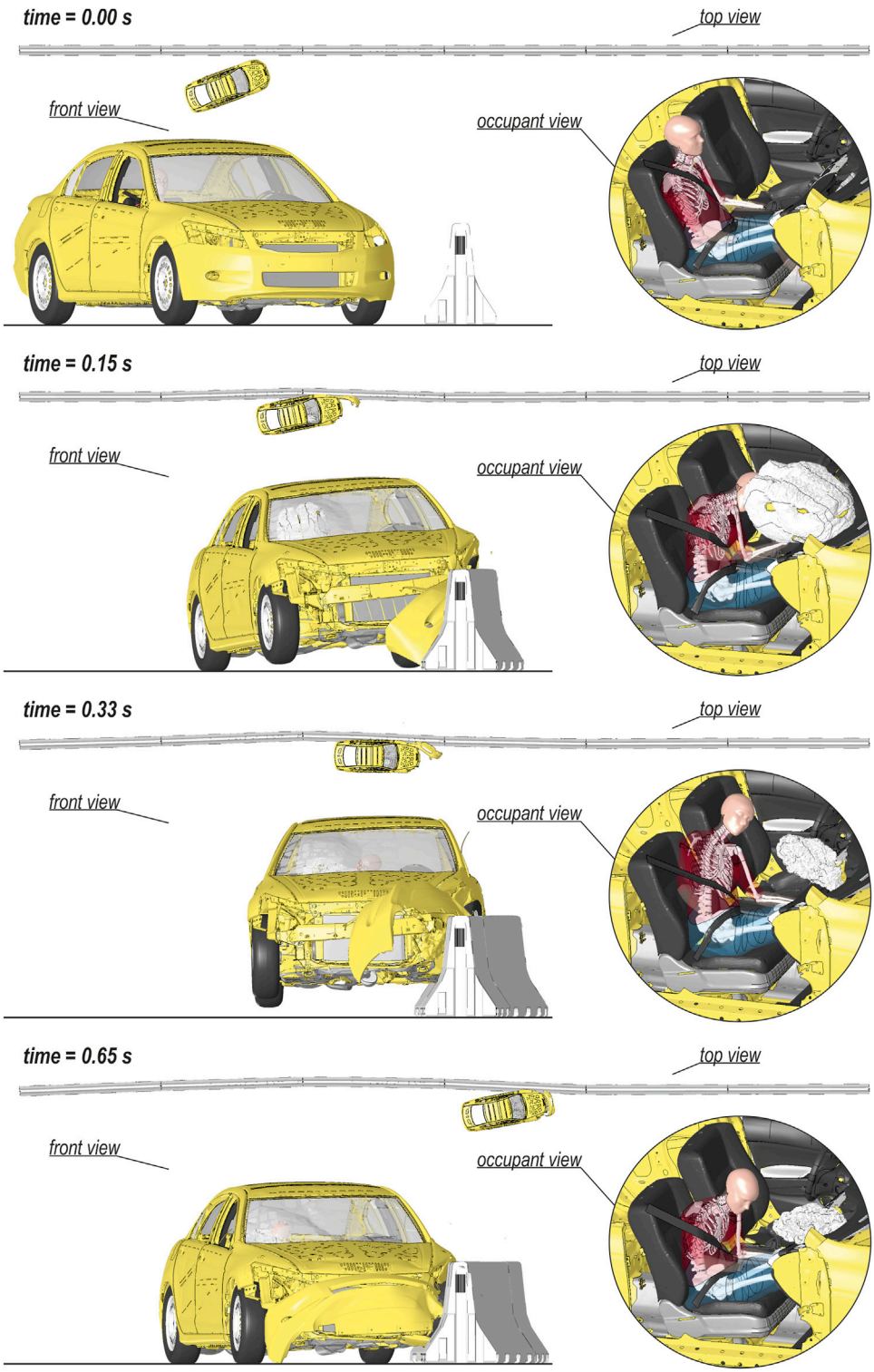

FIGURE 4 | Different views on the selected time instances of the car collision with the H2W5B concrete RSB.

concentrations were found in L2 and L3 vertebras, where the highest x-eccentricities of normal forces were found. An area of high strain and HMH stress was observed in the inferior part of L1. The distribution of the damage variable indicated similar locations of potential vertebral fractures as the two previous indicators (see **Figure 7C**).

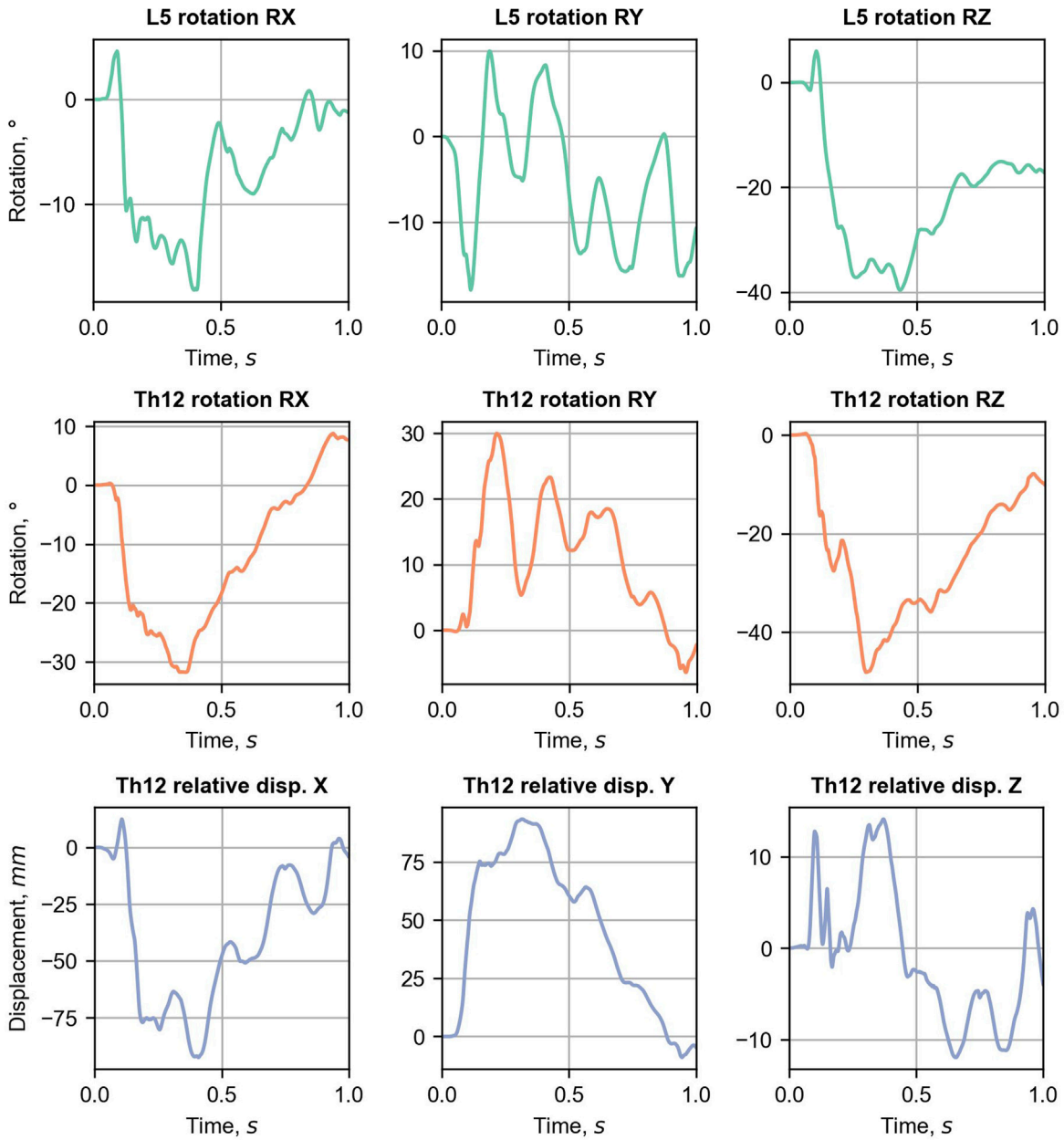

FIGURE 5 | Displacement and rotation curves extracted from the global L-spine model.

4 DISCUSSION

This study aimed to analyze the possible injury mechanism of the lumbar spine during a car crash against concrete RSBs. FEM proved to be a useful tool for creating a complex description of a spine injury and analyzing the influence of different parameters on the risk of vertebral fracture (Fradet et al., 2014). Thus, FEA was selected to determine the physical components that appeared to be associated with lumbar spine fractures. Numerical modeling of the whole collision of the vehicle versus the concrete road barrier allowed consideration of potential risk factors indicated by other researchers, such as submarining (Huelke et al., 1995; Richards et al., 2006), belt loading on the thorax (Kaufman et al., 2013) and high-energy axial loads in the lumbar spine (Ivancic, 2013; Yoganandan et al., 2013). Apart from the global analysis of the vehicle crash, we also used a detailed model of the lumbar spine to assess the injury risk in this section. Because the essential step for the FEM is the validation of numerical results, we confirmed that our results of the concrete barrier crash test simulation were consistent with the data available in the literature (Zain and Mohammed, 2015; Pachocki and Bruski, 2020). Furthermore, the detailed model of the lumbar spine section was an improvement over the original THUMS.

Several phases of the accident can be distinguished by focusing on the occupant's response. First, when the car hit the barrier, the

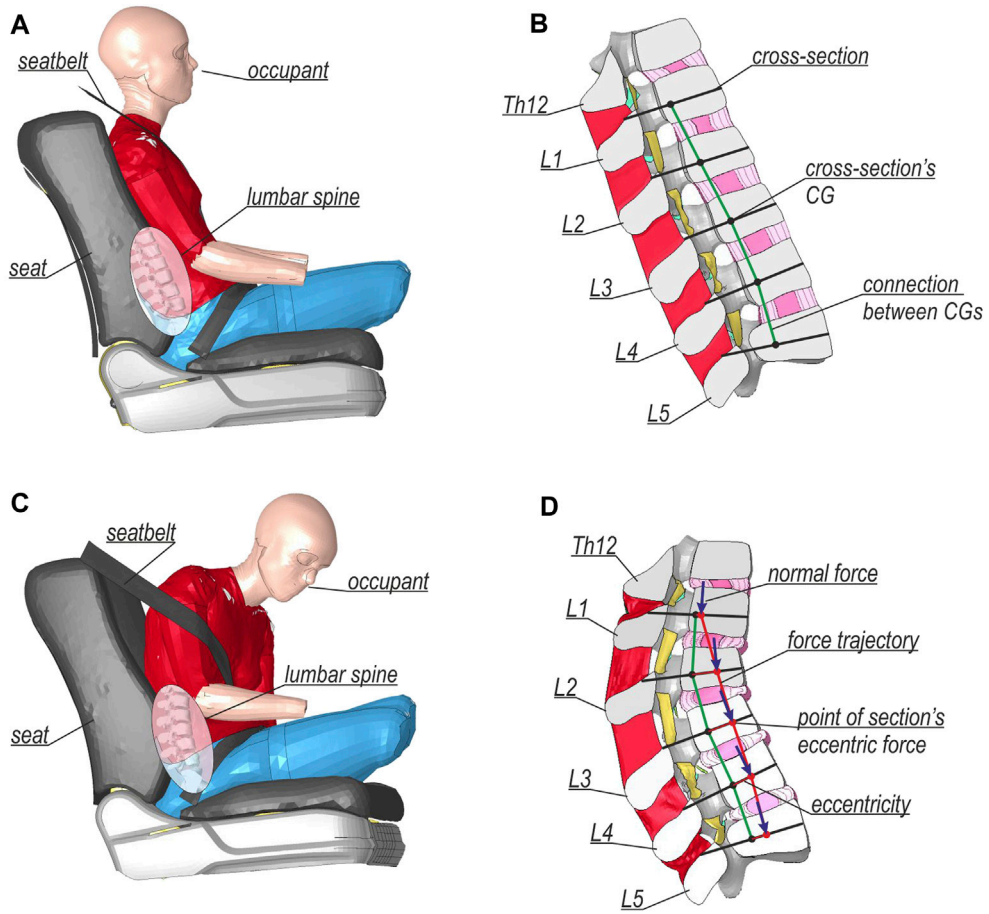

FIGURE 6 | Comparison between the results for initial configurations of **(A)** global and **(C)** detailed models, and landing configurations of **(B)** global and **(D)** detailed models.

TABLE 2 | The internal forces, eccentricities and LSIs of specific vertebras during landing.

	Vertebrae				
	L1	**L2**	**L3**	**L4**	**L5**
Longitudinal force, kN	−2.44	−2.61	−2.72	−2.66	−2.59
Lateral bending moment (x-x), Nm	1.22	−8.35	−11.57	−6.21	2.54
Flexion moment (y-y), Nm	6.95	34.72	37.77	28.86	21.36
Resultant bending moment, Nm	7.05	35.71	39.50	29.52	21.51
Eccentricity (x-local), mm	2.85	13.31	13.90	10.86	8.25
Eccentricity (y-local), mm	−0.50	3.20	4.26	2.34	−0.98
LSI, -	2.07	3.03	3.22	2.89	2.60

passenger moved forward and was restrained by the seat belts. Subsequently, the elevated vehicle moved along the barrier. This change in the direction of the vehicle's movement caused the occupant to lean to the left and flex over the shoulder belt. This position of the occupant during the vehicle landing might have caused the deepening of flexion of the whole spine, thereby increasing the flexion moment. Some researchers have described how axial loading with spine flexion during frontal crashes can act on the lumbar spine of a belted occupant. Begeman et al. (1973) presented experimental evidence that an axial force along the lumbar spine did exist during frontal crashes, and they hypothesized that it was transferred through a seat pan. Huelke et al. (1995) postulated that three-point belted occupants could still sustain a spinal fracture due to "submarining" of the pelvis of the occupant under the lap belt. The lumbar spine injury mechanism similar to that in the current work was described by (Munjin et al., 2011), who presented a "catapult effect". However, Munjin et al. (2011) only indicated the influence of an axial force that was generated in the spine during the landing of the occupant. Our results showed that flexion moment could also contribute to some types of lumbar spine injuries. The described phenomenon occurred even without apparent malfunctions of vehicle interiors, as e.g. buckling of the floor or bulging of the seat that were described by (Kaufman et al., 2013).

During vehicle landing, the compression force in the lumbar spine was calculated to be approximately equal to 2.6 kN. The force acting on the eccentricities caused bending moments in the CG of the analyzed cross-section. The largest eccentricity was found at the height of vertebrae L2 and L3, which also corresponded to the highest flexion moments of 34.7 Nm and

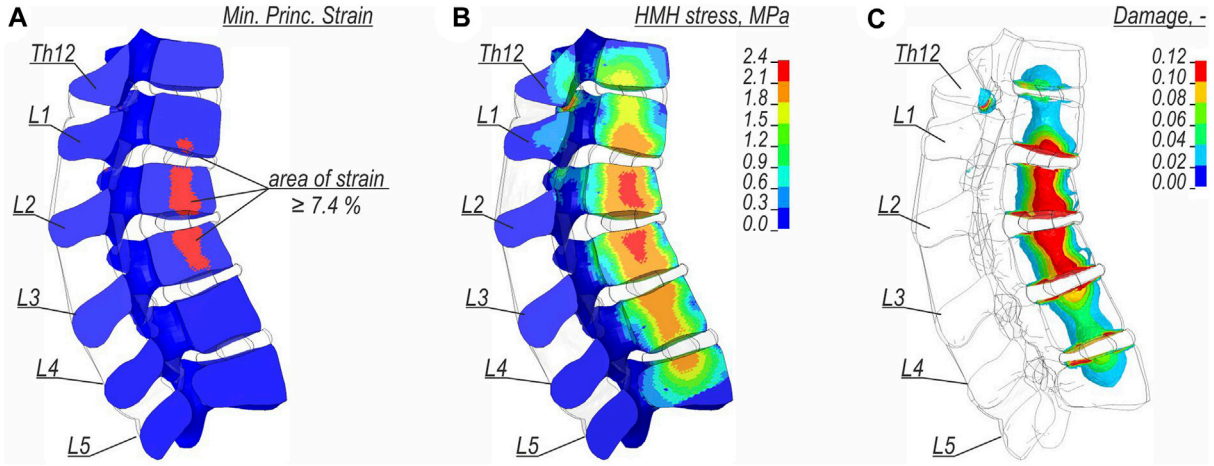

FIGURE 7 | Results for the detailed lumbar spine model: **(A)** the map of minimum principal strain, **(B)** the fringe plot of HMH stresses, and **(C)** the isosurfaces of the damage variable.

37.8 Nm respectively. In the work by (Yoganandan et al., 2013), they proposed a fracture probability assessment based on an axial force. Authors used a drop tower tests and found a peak force of 3.7 kN that corresponded to a 50% risk of a fracture for both, thoracic and lumbar spine. In our study, the proposed method indicated a fracture probability of 11%, which led to the conclusion that some additional factors should be considered. As our research showed, flexion bending should be considered in the evaluation of injury risk as it might highly contribute to lumbar spine fractures. The combined load of an axial compression force and bending moment was investigated by (Ye et al., 2018). They proposed LSI which in our study indicated that a fracture may occur in the lumbar section; however, the index was not able to indicate the specific location of the injury. Thus, we tried other injury metrics.

In a study by (Hansson et al., 1986), based on 231 specimens, the authors described the material characteristics of trabecular bone in lumbar spines for compressive loads. The strength of Hansson's study was a relatively large sample of simple compressive tests. Based on this research, we selected the value of 7.4% minimum principal strain as the injury criterion. This criterion indicated that the L2 and L3 vertebrae were most prone to injury. A small area of the inferior part of L1 is also marked. The distribution of HMH stress in the trabecular bone showed a large area of plastic yielding during the landing of the vehicle. The highest stress concentrations were observed in L2 and L3. This criterion also indicated a risk of yielding in other vertebrae of the lumbar spine. However, as a plasticity-based criterion, it did not immediately indicate complete failure of the material of the bone. Another criterion used was the damage variable. There are no specific usage guidelines for the damage variable for the current application. It was found that letting the damage variable equal to 10% revealed similar locations of potential injury as the strain criterion that was used.

The simulations in the current study could be associated with real-life accident cases. Querying CIREN database, accidents were filtered to cases where a vehicle impacted a concrete RSB and the belted occupant sustained a lumbar spine injury. Three cases that met these criteria were found: 100,113,783, 340,863,218, and 431,438,444. In 1st case, the occupant sustained a L1 burst fracture with a major compression (>20% loss of anterior height) and disc herniation in L1–L2. In 2nd case, the occupant sustained a L3 burst fracture with minor compression (≤20% loss of anterior height). In 3rd case, the occupant sustained a L1 burst fracture with major compression. The locations of the potential injury obtained in the detailed model agreed with the data from the selected CIREN cases. Moreover, they were also consistent with the results available in the literature, where the authors indicated that most injuries occurred in the L1–L3 section (Begeman et al., 1973; Munjin et al., 2011; Pintar et al., 2012; Kaufman et al., 2013). Our study showed that lumbar spine injuries, most common in the frontal vehicle crashes (Pintar et al., 2012), could also occur in collisions with concrete RSBs. Moreover, to the best of the authors' knowledge, this particular fracture mechanism was described for the first time, and it was important, e.g., in the context of the design of vehicles and road safety equipment.

The current study has its limitations as follows.

- The numerical simulation was limited to a single case study. The selected conditions were set to a TB32 crash test for a single vehicle, occupant, and RSB. However, the current approach was sufficient to explain the specific mechanism of lumbar spine injury during a car collision against the concrete RSB. The future studies should discuss the influence of impact conditions, vehicle model and passenger anatomy on the presented injury mechanism. It can be done using the methodology from e.g. Pascoletti et al., 2019a, Pascoletti et al., 2019b, where authors generated human body model, basing on the weight and height, and then using the design of experiment, they

limited the number of simulations required to draw conclusion.
- The analysis of injury risk was limited to compression injuries of the lumbar spine only, because this was the injury mechanism indicated in the CIREN database. Therefore, the analysis focused only on the injuries during the landing of the vehicle; for example, a potential flexion-distraction injury from the initial impact was omitted from consideration. Further studies could investigate the potential risk of damage in other phases of collisions with RSBs.
- The detailed lumbar spine model used in this study has its limitations. Similar to THUMS v6.1, the model assumed the homogeneity of the material properties and did not describe the bone microstructure. Next, strain-rate-dependent properties were applied only to the cortical part of the vertebra. Our detailed model did not account for muscle contribution during the impact, which was justified when analyzing passenger responses. Hence, we were not able to demonstrate the specific fracture morphology, and we focused only on fracture risk assessment.

5 CONCLUSION

The current study confirmed that during a car crash with the H2W5B concrete RSB, there was a potential risk of a lumbar spine fracture at the height of vertebrae L1–L3. The fracture occurred as a consequence of a high eccentric compression force during the landing of the vehicle that was lifted by the concrete RSB. The highest eccentricity and flexion bending moments were found in vertebras L2 and L3. The largest effective stresses and minimum principal strains were also observed at L2 and L3, and the inferior part of L1. The material damage variable also indicated same location where a potential fracture could occur.

DATA AVAILABILITY STATEMENT

The raw data supporting the conclusion of this article will be made available by the authors, without undue reservation.

AUTHOR CONTRIBUTIONS

Study concept and design were performed by KD, PŁ, ŁP, WW; model preparation and simulations were carried out by ŁP; analysis and interpretation by ŁP, KD; drafting of manuscript by ŁP, KD; critical revision of manuscript by KD, PŁ, WW; and study supervision was done by PŁ, WW.

FUNDING

This work was supported by the National Science Centre of Poland under grant number 2020/37/B/ST8/03231.

ACKNOWLEDGMENTS

The authors would also like to acknowledge the contribution of Prof. Jacek Chróścielewski for his advice during the preparation of the models and the analysis of the results. The calculation were carried out at the Academic Computer Centre in Gdansk, Gdansk University of Technology, Poland.

SUPPLEMENTARY MATERIAL

The Supplementary Material for this article can be found online at: https://www.frontiersin.org/articles/10.3389/fbioe.2021.760498/full#supplementary-material

REFERENCES

Adolph, T., Wisch, M., Eggers, A., Johannsen, H., Cuerden, R., Carroll, J., Hynd, D., and Sander, U. (2013). "Analyses of Thoracic and Lumbar Spine Injuries in Frontal Impacts," in International Research Council on the Biomechanics of Injury (IRCOBI) 2013 Sep 11-13, Gothenburg, Sweden, 91–102.

Arun, M. W. J., Hadagali, P., Driesslein, K., Curry, W., Yoganandan, N., and Pintar, F. A. (2017). Biomechanics of Lumbar Motion-Segments in Dynamic Compression. *Stapp Car Crash J.* 61, 1–25. doi:10.4271/2017-22-0001

Begeman, P. C., King, A. I., and Prasad, P. (1973). Spinal Loads Resulting from -Gx Acceleration. *Pap* 5, 343–360. doi:10.4271/730977

BSI (2010). *EN 1317-Part1: Terminology and General Criteria for Test Methods*. Great Britan: British Standard Institution in Great Britan

Chazal, J., Tanguy, A., Bourges, M., Gaurel, G., Escande, G., Guillot, M., et al. (1985). Biomechanical Properties of Spinal Ligaments and a Histological Study of the Supraspinal Ligament in Traction. *J. Biomech.* 18 (3), 167–176. doi:10.1016/0021-9290(85)90202-7

Demetropoulos, C. K., Yang, K. H., Grimm, M. J., Khalil, T. B., and King, A. I. (1998). Mechanical Properties of the Cadaveric and Hybrid III Lumbar Spines. *SAE Tech. Paper 983160*. doi:10.4271/983160

Fradet, L., Petit, Y., Wagnac, E., Aubin, C.-E., and Arnoux, P.-J. (2014). Biomechanics of Thoracolumbar junction Vertebral Fractures from Various Kinematic Conditions. *Med. Biol. Eng. Comput.* 52 (1), 87–94. doi:10.1007/s11517-013-1124-8

Gaewsky, J. P., Weaver, A. A., Koya, B., and Stitzel, J. D. (2015). Driver Injury Risk Variability in Finite Element Reconstructions of Crash Injury Research and Engineering Network (CIREN) Frontal Motor Vehicle Crashes. *Traffic Inj. Prev.* 16, S124–S131. doi:10.1080/15389588.2015.1061666

Golman, A. J., Danelson, K. A., Miller, L. E., and Stitzel, J. D. (2014). Injury Prediction in a Side Impact Crash Using Human Body Model Simulation. *Accid. Anal. Prev.* 64, 1–8. doi:10.1016/j.aap.2013.10.026

Hallquist, J. O. (2006). *LS-DYNA Theory Manual*. Livermore, CA: Livermore Software Technology Corporation (LSTC)

Hansson, T., Keller, T. S., and Panjabi, M. M. (1986). A Study of the Compressive Properties of Lumbar Vertebral Trabeculae: Effects of Tissue Characteristics. *Spine (Phila. Pa. 1976)* 11 (10), 1–7.

Huelke, D. F., Mackay, G. M., and Morris, A. (1995). Vertebral Column Injuries and Lap-Shoulder Belts. *J. Trauma Inj. Infect. Crit. Care* 38 (4), 547–556. doi:10.1097/00005373-199504000-00014

Ivancic, P. C. (2013). Hybrid Cadaveric/surrogate Model of Thoracolumbar Spine Injury Due to Simulated Fall from Height. *Accid. Anal. Prev.* 59, 185–191. doi:10.1016/j.aap.2013.05.024

Jones, D. A., Gaewsky, J. P., Kelley, M. E., Weaver, A. A., Miller, A. N., and Stitzel, J. D. (2016). Lumbar Vertebrae Fracture Injury Risk in Finite Element

Reconstruction of CIREN and NASS Frontal Motor Vehicle Crashes. *Traffic Inj. Prev.* 17, 109–115. doi:10.1080/15389588.2016.1195495

Karim, H., Magnusson, R., and Wiklund, M. (2012). Assessment of Injury Rates Associated with Road Barrier Collision. *Proced. - Soc. Behav. Sci.* 48, 52–63. doi:10.1016/j.sbspro.2012.06.987

Kaufman, R. P., Ching, R. P., Willis, M. M., Mack, C. D., Gross, J. A., and Bulger, E. M. (2013). Burst Fractures of the Lumbar Spine in Frontal Crashes. *Accid. Anal. Prev.* 59, 153–163. doi:10.1016/j.aap.2013.05.023

Li, N., Fang, H., Zhang, C., Gutowski, M., Palta, E., and Wang, Q. (2015). A Numerical Study of Occupant Responses and Injuries in Vehicular Crashes into Roadside Barriers Based on Finite Element Simulations. *Adv. Eng. Softw.* 90, 22–40. doi:10.1016/j.advengsoft.2015.06.004

LSTC (2017a). *Volume 1, in: LS-DYNA R10.0 Keyword User's Manual*. Livermore, CA: Livermore Software Technology Corporation (LSTC)

LSTC (2017b). *Volume 2, in: LS-DYNA R10.0 Keyword User's Manual. International Research Council on the Biomechanics of Injury (IRCOBI), 2016 Sep 13-15, Antwerp, Belgium*. Livermore, CA: Livermore Software Technology Corporation (LSTC).

Mendoza-Vazquez, M., Davidsson, J., and Brolin, K. (2015). Construction and Evaluation of Thoracic Injury Risk Curves for a Finite Element Human Body Model in Frontal Car Crashes. *Accid. Anal. Prev.* 85, 73–82. doi:10.1016/j.aap.2015.08.003

Müller, C. W., Otte, D., Decker, S., Stübig, T., Panzica, M., Krettek, C., et al. (2014). Vertebral Fractures in Motor Vehicle Accidents-A Medical and Technical Analysis of 33,015 Injured Front-Seat Occupants. *Accid. Anal. Prev.* 66, 15–19. doi:10.1016/j.aap.2014.01.003

Munjin, M. A., Zamorano, J. J., Marré, B., Ilabaca, F., Ballesteros, V., Martínez, C., et al. (2011). Speed Hump Spine Fractures. *Tech* 24 (6), 386–389. doi:10.1097/bsd.0b013e3182019dda

Östh, J., Brolin, K., and Bråse, D. (2015). A Human Body Model with Active Muscles for Simulation of Pretensioned Restraints in Autonomous Braking Interventions. *Traffic Inj. Prev.* 16 (3), 304–313. doi:10.1080/15389588.2014.931949

Östh, J., Brolin, K., Svensson, M. Y., and Linder, A. (2016a). A Female Ligamentous Cervical Spine Finite Element Model Validated for Physiological Loads. *J. Biomech. Eng.* 138, 061005. doi:10.1115/1.4032966

Östh, J., Mendoza-Vazquez, M., Linder, A., Svensson, M. Y., and Brolin, K. (2017a). "The VIVA OpenHBM Finite Element 50th Percentile Female Occupant Model: Whole Body Model Development and Kinematic Validation," in International Research Council on the Biomechanics of Injury (IRCOBI), 2016 Sep 14-16, Malaga, Spain, 173–181.

Östh, J., Mendoza-Vazquez, M., Sato, F., Svensson, M. Y., Linder, A., and Brolin, K. (2017b). A Female Head-Neck Model for Rear Impact Simulations. *J. Biomech.* 51, 49–56. doi:10.1016/j.jbiomech.2016.11.066

Östh, J., Vazquez, M. M., Svensson, M. Y., Linder, A., and Brolin, K. (2016b). "Development of a 50th Percentile Female Human Body Model," in IRCOBI Conference, 573–575.

Pachocki, Ł., and Bruski, D. (2020). Modeling, Simulation, and Validation of a TB41 Crash Test of the H2/W5/B concrete Vehicle Restraint System. *Archiv.Civ.Mech.Eng* 20, 62. doi:10.1007/s43452-020-00065-7

Pachocki, Ł., and Wilde, K. (2018). Numerical Simulation of the Influence of the Selected Factors on the Performance of a concrete Road Barrier H2/W5/B. *MATEC Web Conf.* 231, 01014. doi:10.1051/matecconf/201823101014

Pascoletti, G., Catelani, D., Conti, P., Cianetti, F., and Zanetti, E. M. (2019a). A Multibody Simulation of a Human Fall: Model Creation and Validation. *Proced. Struct. Integrity* 24, 337–348. doi:10.1016/j.prostr.2020.02.031

Pascoletti, G., Catelani, D., Conti, P., Cianetti, F., and Zanetti, E. M. (2019b). Multibody Models for the Analysis of a Fall from Height: Accident, Suicide, or Murder? *Front. Bioeng. Biotechnol.* 7, 1–12. doi:10.3389/fbioe.2019.00419

Pintar, F. A., Yoganandan, N., Maiman, D. J., Scarboro, M., and Rudd, R. W. (2012). Thoracolumbar Spine Fractures in Frontal Impact Crashes. *Ann. Adv. Automot Med.* 56, 277–283.

Pintar, F. A., Yoganandan, N., Myers, T., Elhagediab, A., and Sances, A. (1992). Biomechanical Properties of Human Lumbar Spine Ligaments. *J. Biomech.* 25 (11), 1351–1356. doi:10.1016/0021-9290(92)90290-h

National Police Headquarters in Poland (2020). Road accidents in Poland in 2020. Available at: https://statystyka.policja.pl/st/ruch-drogowy/76562,Wypadki-drogowe-raporty-roczne.html (in Polish).

Renner, S. M., Natarajan, R. N., Patwardhan, A. G., Havey, R. M., Voronov, L. I., Guo, B. Y., et al. (2007). Novel Model to Analyze the Effect of a Large Compressive Follower Pre-load on Range of Motions in a Lumbar Spine. *J. Biomech.* 40 (6), 1326–1332. doi:10.1016/j.jbiomech.2006.05.019

Richards, D., Carhart, M., Raasch, C., Pierce, J., Steffey, D., and Ostarello, A. (2006). Incidence of Thoracic and Lumbar Spine Injuries for Restrained Occupants in Frontal Collisions. *Annu. Proc. Assoc. Adv. Automot Med.* 50, 125–139.

Schmidt, H., Heuer, F., Simon, U., Kettler, A., Rohlmann, A., Claes, L., et al. (2006). Application of a New Calibration Method for a Three-Dimensional Finite Element Model of a Human Lumbar Annulus Fibrosus. *Clin. Biomech.* 21 (4), 337–344. doi:10.1016/j.clinbiomech.2005.12.001

Schmidt, H., Kettler, A., Heuer, F., Simon, U., Claes, L., and Wilke, H.-J. (2007). Intradiscal Pressure, Shear Strain, and Fiber Strain in the Intervertebral Disc under Combined Loading. *Spine* 32 (7), 748–755. doi:10.1097/01.brs.0000259059.90430.c2

Shirazi-Adl, A. (1986). Mechanical Response of A Lumbar Motion Segment in Axial Torque Alone and Combined with Compression. *Spine (Phila. Pa. 1976)* 11, 914. doi:10.1097/00007632-198611000-00012

Singh, H., Ganesan, V., Davies, J., and Paramasuwom, M.Gradisching (2018). *Vehicle interior and Restraints Modeling Development of Full Vehicle Finite Element Model Including Vehicle interior and Occupant Restraints Systems for Occupant Safety Analysis Using THOR Dummies (Report No. DOT HS 812 545)*. Washington, DC: National Highway Traffic Safety Administration.

Tang, L., Zheng, J., and Hu, J. (2020). A Numerical Investigation of Factors Affecting Lumbar Spine Injuries in Frontal Crashes. *Accid. Anal. Prev.* 136, 105400. doi:10.1016/j.aap.2019.105400

Wang, M. C., Pintar, F., Yoganandan, N., and Maiman, D. J. (2009). The Continued burden of Spine Fractures after Motor Vehicle Crashes. *J. Neurosurg. Spine* 10 (2), 86–92. doi:10.3171/SPI.2008.10.08279

Xu, M., Yang, J., Lieberman, I. H., and Haddas, R. (2017). Lumbar Spine Finite Element Model for Healthy Subjects: Development and Validation. *Comput. Methods Biomech. Biomed. Eng.* 20 (1), 1–15. doi:10.1080/10255842.2016.1193596

Ye, X., Gaewsky, J. P., Jones, D. A., Miller, L. E., Stitzel, J. D., and Weaver, A. A. (2018). Computational Modeling and Analysis of Thoracolumbar Spine Fractures in Frontal Crash Reconstruction. *Traffic Inj. Prev.* 19, S32–S39. doi:10.1080/15389588.2018.1498090

Yoganandan, N., Arun, M. W., Stemper, B. D., Pintar, F. A., and Maiman, D. J. (2013). Biomechanics of Human Thoracolumbar Spinal Column Trauma from Vertical Impact Loading. *Ann. Adv. Automot Med.* 57, 155–166.

Zain, M. F. B. M., and Mohammed, H. J. (2015). Concrete Road Barriers Subjected to Impact Loads: An Overview. *Lat. Am. J. Solids Struct.* 12 (10), 1824–1858. doi:10.1590/1679-78251783

Conflict of Interest: The authors declare that the research was conducted in the absence of any commercial or financial relationships that could be construed as a potential conflict of interest.

frontiers in Bioengineering and Biotechnology

ORIGINAL RESEARCH
published: 02 November 2021
doi: 10.3389/fbioe.2021.750862

Sex-Dependent Estimation of Spinal Loads During Static Manual Material Handling Activities—Combined *in vivo* and *in silico* Analyses

Ali Firouzabadi[1], *Navid Arjmand*[2], *Fumin Pan*[1], *Thomas Zander*[1] *and Hendrik Schmidt*[1]*

[1]*Julius Wolff Institute, Berlin Institute of Health at Charité—Universitätsmedizin Berlin, Berlin, Germany,* [2]*Department of Mechanical Engineering, Sharif University of Technology, Tehran, Iran*

Manual material handling (MMH) is considered as one of the main contributors to low back pain. While males traditionally perform MMH tasks, recently the number of females who undertake these physically-demanding activities is also increasing. To evaluate the risk of mechanical injuries, the majority of previous studies have estimated spinal forces using different modeling approaches that mostly focus on male individuals. Notable sex-dependent differences have, however, been reported in torso muscle strength and anatomy, segmental mass distribution, as well as lifting strategy during MMH. Therefore, this study aimed to use sex-specific models to estimate lumbar spinal and muscle forces during static MHH tasks in 10 healthy males and 10 females. Motion-capture, surface electromyographic from select trunk muscles, and ground reaction force data were simultaneously collected while subjects performed twelve symmetric and asymmetric static lifting (10 kg) tasks. AnyBody Modeling System was used to develop base-models (subject-specific segmental length, muscle architecture, and kinematics data) for both sexes. For females, female-specific models were also developed by taking into account for the female's muscle physiological cross-sectional areas, segmental mass distributions, and body fat percentage. Males showed higher absolute L5-S1 compressive and shear loads as compared to both female base-models (25.3% compressive and 14% shear) and female-specific models (41% compressive and 23.6% shear). When the predicted spine loads were normalized to subjects' body weight, however, female base-models showed larger loads (9% compressive and 16.2% shear on average), and female-specific models showed 2.4% smaller and 9.4% larger loads than males. Females showed larger forces in oblique abdominal muscles during both symmetric and asymmetric lifting tasks, while males had larger back extensor muscle forces during symmetric lifting tasks. A stronger correlation between measured and predicted muscle activities was found in females than males. Results indicate that female-specific characteristics affect the predicted spinal loads and must be considered in musculoskeletal models. Neglecting sex-specific parameters in these models could lead to the overestimation of spinal loads in females.

Keywords: manual material handling, spinal loads, trunk muscle forces, sex differences, musculoskeletal models

OPEN ACCESS

Edited by:
Tarun Goswami,
Wright State University, United States

Reviewed by:
Tao Liu,
University of Alberta, Canada
Francesco Travascio,
University of Miami, United States

****Correspondence:***
Hendrik Schmidt
hendrik.schmidt@charite.de

Specialty section:
This article was submitted to Biomechanics, a section of the journal Frontiers in Bioengineering and Biotechnology

Received: *31 July 2021*
Accepted: *13 October 2021*
Published: *02 November 2021*

Citation:
Firouzabadi A, Arjmand N, Pan F, Zander T and Schmidt H (2021) Sex-Dependent Estimation of Spinal Loads During Static Manual Material Handling Activities—Combined in vivo *and* in silico *Analyses. Front. Bioeng. Biotechnol. 9:750862. doi: 10.3389/fbioe.2021.750862*

INTRODUCTION

Manual material handling (MMH) activities are regularly performed in daily life as well as in occupational workstations (Craig et al., 2015). These activities could expose the worker to external forces/moments under various postures such as trunk bending and twisting or a combination thereof. During MMH activities, trunk muscles demonstrate high levels of activation/coactivation thus imposing large loads on the spine passive structures (Zander et al., 2015; Corbeil et al., 2019). While several studies have indicated an association between MMH tasks and increased spinal loads thus identifying MMH as a risk factor for low back pain (Hoogendoorn et al., 2000; Palmer et al., 2003; Davis et al., 2005), this association remains debatable (Swain et al., 2020). The knowledge of spinal loads under various MMH conditions can therefore provide appropriate insight into the mechanism of such a likely association. An accurate estimation of trunk muscle forces and spinal loads during MMH activities is also required to design safer workplaces and effective injury prevention programs.

In an effort to gain an in-depth evaluation of spinal loads during MMH tasks, multiple *in vivo* and *in silico* methods have been used (Cruz et al., 2019; Dreischarf et al., 2016). Although *in vivo* studies provide valuable knowledge on spinal loading (Nachemson, 1981; Rohlmann et al., 2014; Wilke et al., 2001), these measurements are challenging, complex, costly and invasive. As alternatives, biomechanical models have therefore been developed to predict internal spinal loads. In this context, a number of musculoskeletal models (open-source/commercial software), regression equation, and artificial neural networks have emerged as robust and relatively accurate options (Damsgaard et al., 2006; Delp et al., 2007; Arjmand et al., 2011; Dreischarf et al., 2016; Aghazadeh et al., 2020). Electromyography (EMG)-driven (Marras and Granata, 1997; McGill and Norman, 1986), optimization-driven (Brown and Potvin, 2005; Damsgaard et al., 2006) and hybrid (EMG-Assisted Optimization) (Cholewicki and McGill, 1994; Mohammadi et al., 2015; Gagnon et al., 2016; Samadi and Arjmand, 2018) models have been used. These models predict joint loads and muscle forces through *in vivo* kinematics and/or EMG data. However, to account for the differences between individuals, models should be personalized or scaled based on individuals' kinematics and anthropometric data.

Anybody Modeling (AB) System (Anybody® Technology, Aalborg, Denmark), an optimization-driven model, is a scalable full-body model with a highly detailed musculature for the lumbar spine. This model has been used in many studies to predict spinal loads (Arshad et al., 2017; Asadi and Arjmand, 2020; Behjati and Arjmand, 2019; Ignasiak et al., 2016b; Rajaee et al., 2015; Zander et al., 2015) and could be applied to simulate a wide range of MMH activities. Spinal compressive loads predicted by the AB full-body model during different activities, including the MMH, have been validated versus *in vivo* intradiscal pressure data (Wilke et al., 2001) by several studies (Bassani et al., 2017; Ignasiak et al., 2016a; Rajaee et al., 2015; Rasmussen et al., 2009). These studies have indicated that the AB model is a robust tool for accurately evaluating spinal loads in physiological activities.

For the biomechanical risk assessment, the majority of previous studies have evaluated spinal loads while focusing on male individuals. However, notable sex-dependent kinematic differences in joint movements (Plamondon et al., 2017; Sheppard et al., 2016), lumbo-pelvic coordination (Pan et al., 2020; Pries et al., 2015), and lifting style (Haddas et al., 2015; Lindbeck and Kjellberg, 2001) have been reported. Furthermore, muscle cross-sectional areas (Anderson et al., 2012; Marras et al., 2001), body anthropometric measures, and mass distribution in upper body (Shan and Bohn, 2003; Davis et al., 2005) are also significantly different between sexes. These sex differences may influence muscle activities and spinal loads during MMH tasks (Marras et al., 2003; Plamondon et al., 2017) thereby suggesting that the previous model findings for male workers cannot be generalized to female ones. In accordance with recent greater participations of females in physically demanding jobs, epidemiological studies have reported higher work-related physical injuries (Hansen et al., 2018) and prevalence of low back pain in females than males (Wu et al., 2020).

To date, only few studies have investigated the role of sex and differences in spinal loads between males and females during common lifting tasks (Ghezelbash et al., 2016; Ghezelbash et al., 2018; Kumar, 1990; Marras et al., 2003). Marras et al. (2003), using a single level EMG-driven model without a comprehensive scaling approach, showed that males had significantly greater compression spine forces than females. Ghezelbash et al. (2016) investigated the effect of sex differences and other personalized factors (age, body height (BH), and body weight (BW)) on spinal loads using a kinematics/optimization-driven musculoskeletal trunk finite element model and found that sex has small effects on spinal loads during symmetric lifting tasks. For their model simulations, they used available kinematics data in the literature (Pries et al., 2015) that had been collected during maximal upper body flexion with no loads in hands. It has, however, been shown that lifting/holding external loads in hands influences trunk kinematic (Davis and Marras, 2000; Granata and Sanford, 2000). In addition, identical segmental mass distributions were used for both sexes despite the fact that the mass distribution of the upper body is significantly different between males and females (Davis et al., 2005).

All the sex-related differences findings in the literature and epidemiology studies highlight the urgent need to account for inherent sex differences when predicting spinal loads via biomechanical modeling approaches. Therefore, the current study aimed to predict spinal loads and trunk muscle forces during different MMH tasks, using the full-body, subject- and sex-specific models driven by *in vivo* kinematic and ground

TABLE 1 | Demographic data (mean ± standard deviation) of the participants. Bold values show that males have a significantly greater body height, weight, and body mass index (BMI) ($p < 0.05$) than females.

	Female	Male	*p*-value
Number of participants	10	10	-
Age (year)	31.9 ± 7.6	33.0 ± 7.4	0.724
Height (cm)	168.5 ± 3.5	176.9 ± 8.8	**0.009**
Weight (kg)	56.4 ± 4.5	77.3 ± 9.8	**<0.001**
BMI (kg/m^2)	19.92 ± 1.9	24.7 ± 2.2	**<0.001**

reaction data. Absolute and normalized (to BW) L5-S1 loads were compared between males and females. It was hypothesized that including sex-specific parameters into the musculoskeletal model markedly affect their predictions for spinal loads during MMH tasks.

MATERIALS AND METHODS

Participants

Twenty healthy volunteers (10 males and 10 females) with no professional lifting experience participated in the study. Males had a significantly greater body height, weight, body mass index (BMI) ($p < 0.05$) but not age ($p = 0.724$) than females (**Table 1**). Participants had no history of pain in the back, pelvis, and hip in the 12 months prior to the measurements and no spinal or pelvic surgery history. The study was approved by the Ethics Committee of the Charité—Universitätsmedizin Berlin (EA1/059/21). After explaining the tests to each participant, he/she signed a written informed consent.

Measurement Devices

Three-dimensional motion analysis was carried out using the Vicon Motion Capturing System (Vicon Motion Systems, Inc., Oxford, United Kingdom). The system consisted of 10 high-speed infrared cameras to track retro-reflective skin markers placed over participant's body with a sampling rate of 200 Hz. Ground reaction forces (GRFs) were measured by two floor-embedded force plates (AMTI, model OR6-6, Watertown, MA, USA) sampling at 1,000 Hz. A wireless EMG device (Delsys, Inc., Boston, MA) was used to record muscle activities at 2000 Hz. EMG and force plate data were integrated into the Vicon Nexus system and synchronized with the Vicon data.

In vivo Data Collections

A marker set consisting of 47 reflective markers (12 mm diameter) was used to capture body motion during gait and different lifting tasks. According to our previous study (Arshad et al., 2017), markers were placed on the anatomical landmarks of different body segments (head–neck, trunk, pelvis, arms, forearms, thighs, and feet) based on the Vicon Plug-in gait

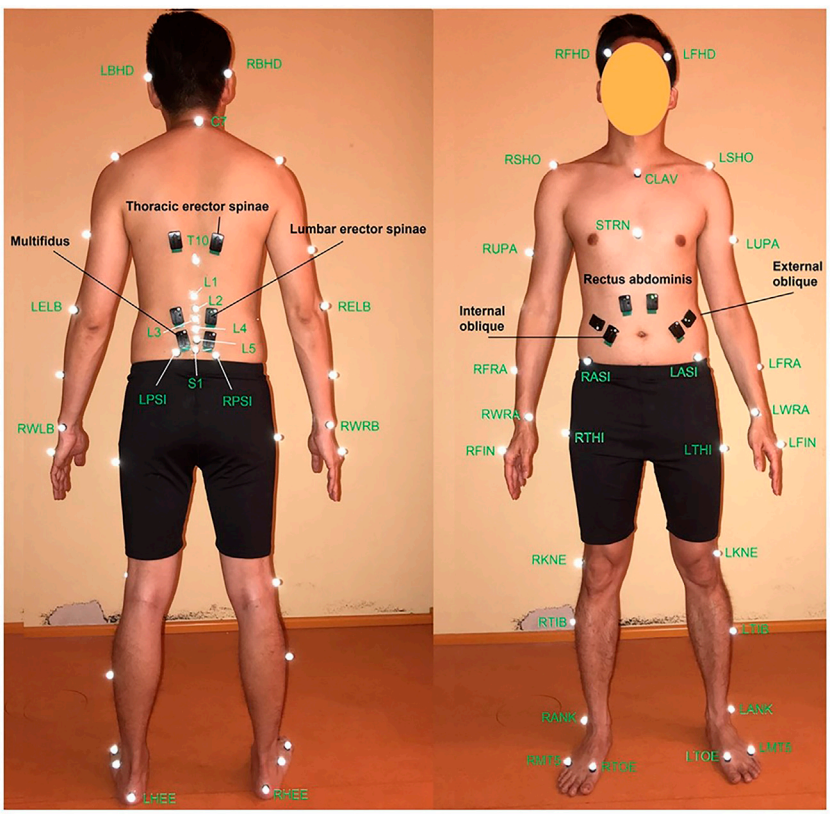

FIGURE 1 | Position of VICON markers (white ones) (Arshad et al., 2017) and EMG sensors (black ones) (McGill, 1991) from **(left)** back and **(right)** front views.

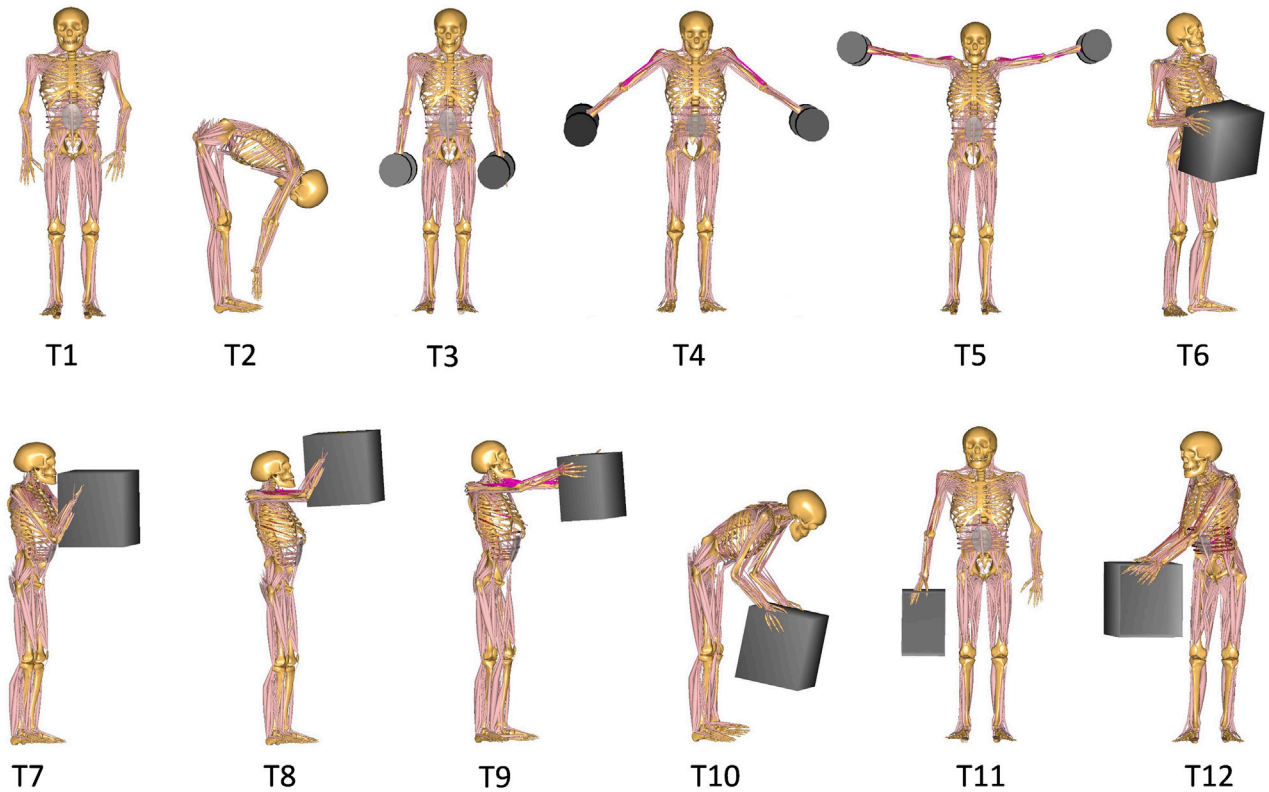

FIGURE 2 | Different lifting tasks performed by participants and simulated by the model.

marker configuration. Six additional markers were placed on the superior spinal process of the lumbar vertebrae and the sacrum (**Figure 1**). Twelve surface EMG electrodes recorded trunk muscle activities. Electrodes were positioned bilaterally on six superficial back and abdominal muscles as follows (McGill, 1991): multifidus (~2 cm lateral to midline at the L5), lumbar erector spinae (~3 cm lateral to midline at the L3), thoracic erector spinae (~5 cm lateral to midline at the T9), external oblique (~10 cm lateral to midline above umbilicus and aligned with muscle fibers), internal oblique (below to the external oblique sensors and superior to the inguinal ligament), and rectus abdominis (~3 cm lateral to midline above the umbilicus) (**Figure 1**). Participants performed 3 trails of Maximal Voluntary Contractions (MVC) for back and abdominal muscles (Konard, 2006). During MVC measurements, subjects were verbally encouraged to exert their maximum efforts. Their hands were held crossed on the chest while the hip and legs were fully constrained.

To prepare the kinematics data for model simulations, motion capture data were pre-processed in Vicon Nexus 2.8.1 (Vicon Motion System, Oxford Metrics Inc., Oxford, UK) for marker labeling and gap-filling. Missing or occluded markers were reconstructed *via* the spline fill, pattern fill, or rigid body fill algorithms (Vicon Nexus 2, 2018). A zero-lag 2nd order low-pass Butterworth filter was used with the cut-off frequency of 6 Hz for trajectories of the reflective markers, and the cut-off frequency of 20 Hz for measured GRFs. A band-pass filter (30–450 Hz) was applied to the EMG signals to reduce the effect of artifacts and noises. Subsequently, the signals were rectified, low-pass filtered (cut off frequency 3 Hz), and normalized relative to their MVC peak values.

Tasks

Participants performed a dynamic lifting task that started from the moment they touched the weight, lifted it, held it in the final position for 3 s and finally ended with putting it back on the ground. For our analyses here, we only considered the 3 s of static holding of the weight (**Figure 2**). They performed a total of twelve symmetric and asymmetric static load-handling tasks in a randomized order (**Figure 2**). These tasks have been selected so that different parameters that might influence spinal loads, such as postures, lifting techniques, horizontal distance of the hand load, and lifting height could be included in the analyses (Rajaee et al., 2015). The end (static) position of each lifting task differs as follows:

Reference Postures:

➢Task 1 (T1): relaxed upright standing
➢Task 2 (T2): full upper body flexion with straight knees and without loads in hand

Symmetric holding of two 5 kg dumbbells on each side of the body with:

TABLE 2 | PCSAs (cm^2) of trunk muscles for male and female base-models as well as female-specific model.

Muscle	Male and female base-models	Female-specific model
Multifidus	14.07	9.49
Erector Spinae	27.89	16.14
Quadratus Lumborum	4.41	2.44
Psoas Major	14.63	10.67
Internal Oblique	6.24	6.30
External Oblique	6.24	7.08
Rectus Abdominis	7.80	6.37

TABLE 3 | Mass distribution of body segments for male and female base-models as well as female-specific model. Values are expressed as the percentage of total body mass (% of BW).

Segments	Male and female base-models	Female-specific model
Head	8.10	7.97
Thorax	21.60	20.25
Lumbar	13.90	12.43
Pelvis	14.20	11.54
Thighs	20.00	26.62
Shanks	9.30	10.24
Feet	2.90	2.60
Upper arms	5.60	4.70
Lower arms	3.20	2.60
Hands	1.20	1.04

➢ Task 3 (T3): arms close to the trunk at the thigh height
➢ Task 4 (T4): arms abducted 45° at the hip height
➢ Task 5 (T5): arms abducted 90° at the shoulder height

Symmetric holding of a 10 kg box in front of and close to the body at the:

➢ Task 6 (T6): hip height
➢ Task 7 (T7): chest height
➢ Task 8 (T8): head height

Symmetric holding of a 10 kg box in front of the body:

➢ Task 9 (T9): at the chest height with extended elbows
➢ Task 10 (T10): with flexed back and extended knee

Asymmetric holding of a 10 kg box:

➢ Task 11 (T11): by one hand in the favored side
➢ Task 12 (T12): in front of the body and twisting the trunk to the right side

Musculoskeletal Model

Base Models

In this study, a commercially available MoCap-FullBody musculoskeletal model from the AnyBody Managed Model Repository v.1.6.2 of the AnyBody Modeling System software v. 6.0.4 (AnyBody Technology A/S, Aalborg, Denmark) was used as the base-model. This validated model for males (Bassani et al., 2017) included the Twente Lower Extremity Model (TLEM) (Klein Horsman et al., 2007) and a detailed lumbar spine model (Zee et al., 2007). The spine model consisted of 7 rigid-bodies, including the pelvis, lumbar, and a rigid thoracic segment. In the lumbar part, each vertebra was modeled as a rigid segment with 3-DoF spherical joints in between. All significant muscles related to the trunk, arms and legs were included in the model. A total of 188 muscle fascicles were used to represent the muscular architecture of the lumbar spine model. Trunk muscles were grouped as global (attached to thoracic spine) and local (attached to lumbar spine) (El-Rich et al., 2004). Intervertebral joint stiffnesses were considered as linear in flexion, extension, lateral bending, and axial rotation. Intra-abdominal pressure was modeled as an abdominal volume wrapped by the transverse muscles with the maximum upper bound limitation of 26.6 kPa (Essendrop, 2004). During body movements, these muscles acted on the abdominal volume, and due to the change in the volume, the intra-abdominal pressure was generated. The spine curvature was adjusted based on the markers on the hip and thorax. Intersegmental lumbar rotations (lumbar spine movement rhythm) were prescribed as a function of the 3D angle between pelvis and trunk. This lumbar spine rhythm was taken from (White and Panjabi, 1990), which provides the representative rotation of each lumbar joint in flexion/extension, lateral bending, and axial rotation from several *in vivo* and *in vitro* studies. A 10 kg box and two 5 kg dumbbells were added in the model with the same size, mass, location, and orientation as those used in the experiments while also considering the hand-load contact reaction forces. Three markers captured the motion trajectories of the hand load during the tasks. Markers were defined in the model precisely as they were placed on the weight during the motion capturing.

For each subject, the model was adjusted in terms of body height, body weight, and segmental lengths according to the subject's body measures. Distribution of segmental body masses and body fats were also adjusted (Frankenfield et al., 2001; Winter, 2009). Simulations by an AnyBody motion-captured model required the subject-specific kinematic data as input, and consisted of the following two steps: parameter optimization and inverse dynamic. In the first step, the model was adjusted subject-specifically. The segmental lengths were scaled using a linear method through an optimization procedure that minimized the least-square errors for virtual markers on the model according to the position of corresponding experimental reflective markers placed on the subject (Andersen et al., 2010). Besides, muscle strengths were also scaled using length-mass-fat scaling law by taking the body fat percentage into account (Rasmussen et al., 2005). The optimized and scaled model was then used in kinematic analysis to calculate joint angles from an over-determinate kinematic solver.

In the second step, individual joint angles together with the measured GRFs were used as input for the inverse dynamics analysis. In the course of an inverse dynamics simulation, joints and muscle forces were estimated from known kinematics by solving Newton's equations. As muscles outnumbered the Newton's equations for a given movement (i.e., joint kinetic redundancy), an optimization algorithm was applied to estimate muscle forces (Damsgaard et al., 2006). In this study, a third-order polynomial

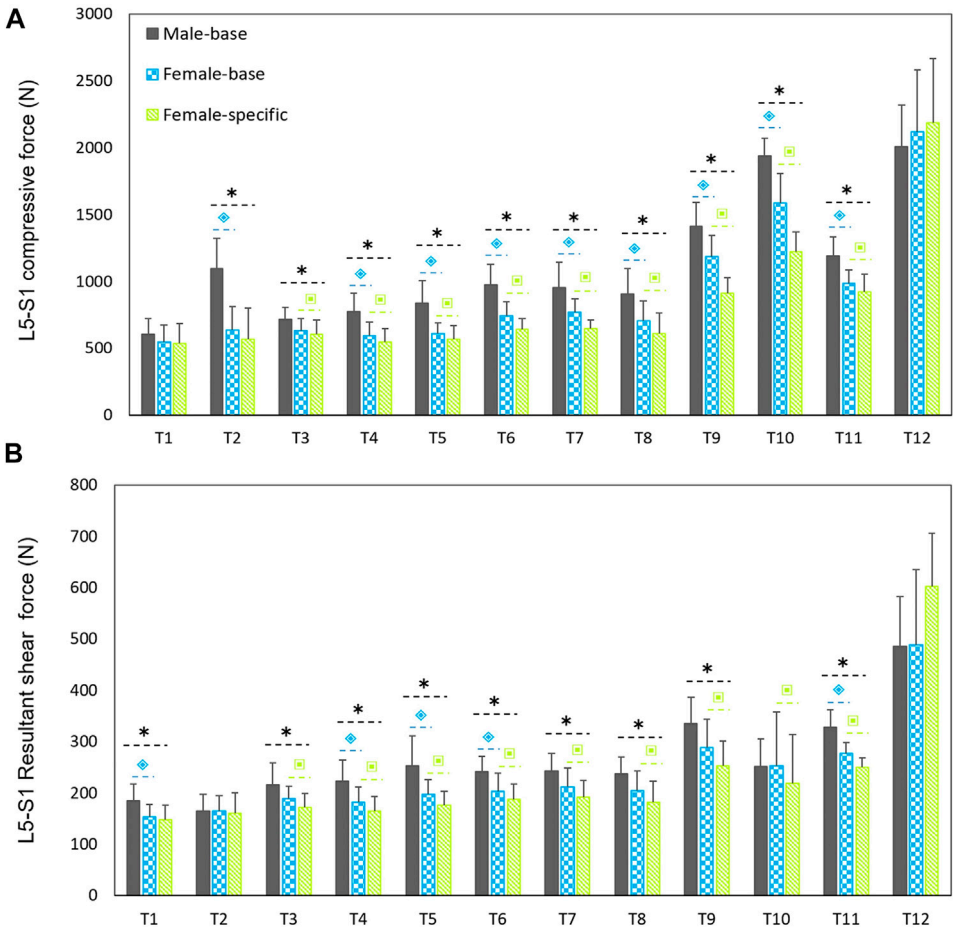

FIGURE 3 | Predicted mean (standard deviations as error bars) absolute L5-S1 compressive **(A)** and shear **(B)** forces by the base-models for both sexes and female-specific models for females. ⊠ indicates a significant difference ($p < 0.05$) between males and females load predicted by base-models. * indicates a significant difference ($p < 0.05$) between loads predicted by male models and female-specific models. ⊠ indicates a significant difference ($p < 0.05$) between loads predicted by female-base models and female-specific models.

objective function minimizing the sum of cubed muscle stresses was employed (Arjmand and Shirazi-Adl, 2006).

Female-specific Models

To develop female-specific models, the anatomical attributes that vary as a function of sex were taken into account, and the base-models were modified for females. Muscle physiological cross-sectional areas (PCSAs), segmental mass distributions, and body fat percentage were modified based on available *in vivo* data. PCSAs of trunk muscles were taken from (Marras et al., 2001; Stokes et al., 2005) (**Table 2**). Mass distribution of each segment was calculated from (Shan and Bohn, 2003) based on a regression equation that estimates the segmental mass distribution based on the body mass and height (**Table 3**). Moreover, body fat percentage for females was calculated using a regression equation (Frankenfield et al., 2001) based on BMI.

A base-model was developed for each male and two models were developed for each female participant to consider the sex differences into account; female base-model (before applying sex-specific parameters) and female-specific model that was a modified version of the base-model according to the abovementioned female-specific parameters. First, both male and female participants were simulated by the base-model for all the tasks then females were simulated with the corresponding developed female-specific model. Total of 360 model simulations (10 male base-models + 10 female base-models + 10 female-specific models times 12 tasks) were carried out in AnyBody.

Data Analyses

The resulting forces were calculated over the 3 s of the holding period. Global and local trunk muscle forces as well as L5-S1 compressive and shear (resultant of mediolateral and anteroposterior) loads were computed. Statistical analyses were performed in MATLAB R2019b (The Math Work, Inc.). Pearson analysis was used to analyze anthropometric data. Independent (unpaired) student t-test was applied to assess the sex-dependent difference between males and females. A p-value < 0.05 was considered statistically significant. Paired student t-test was applied to assess loads predicted by models for females before

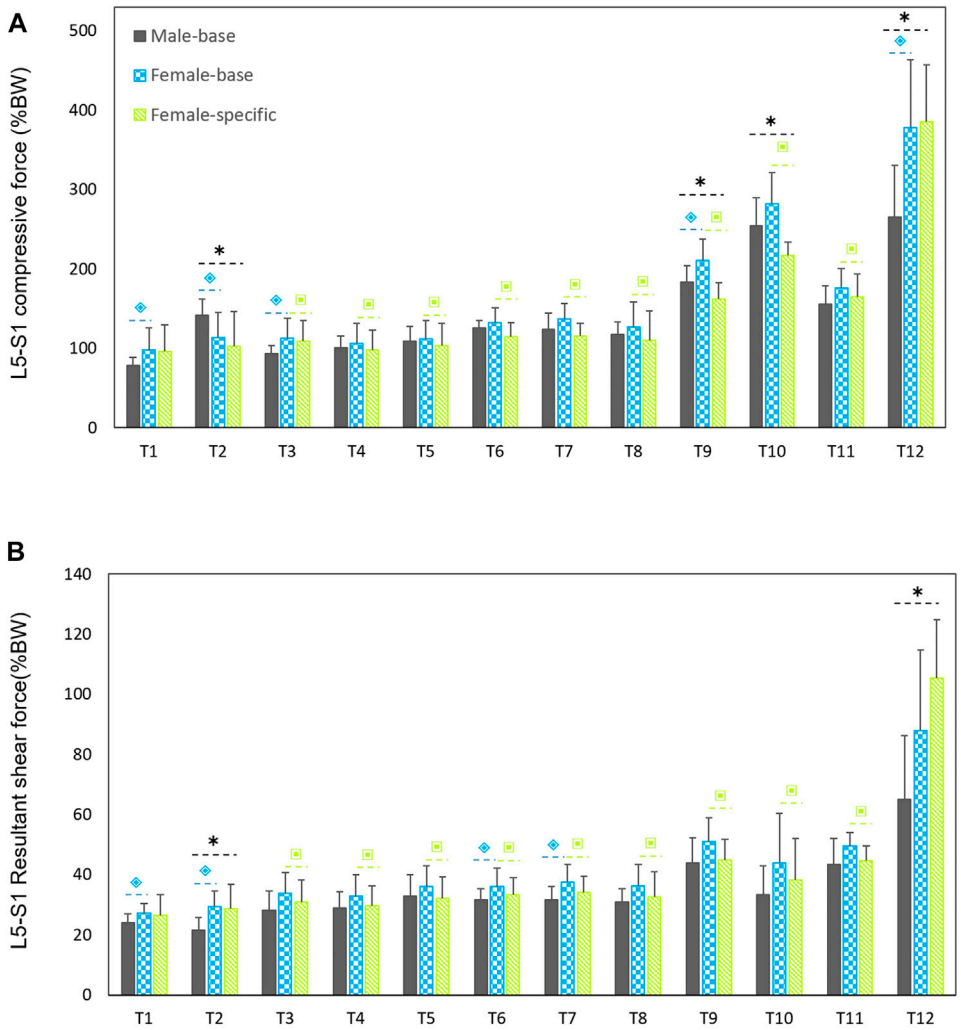

FIGURE 4 | Predicted mean (standard deviations as error bars) L5-S1 compressive **(A)** and shear **(B)** forces normalized to body weight (%BW) by the base-models for both sexes and female-specific models for females. ⊠ indicates a significant difference ($p < 0.05$) between males and females load predicted by base-models. * indicates a significant difference ($p < 0.05$) between loads predicted by male models and female-specific models. ⊠ indicates a significant difference ($p < 0.05$) between loads predicted by female-base models and female-specific models.

and after applying the sex-dependent parameters. Pearson correlation analysis was applied to determine the correlation between normalized measured EMG and model predicted muscle activities (muscle force divided by muscle strength).

RESULTS

Spinal Loads in Male's vs. Female's Base-Models

Males had considerably larger L5-S1 compressive and resultant shear loads than females in average (25.3% compressive and 14% shear loads) for all the simulated tasks but T12 (**Figure 3**). The lowest and highest loads, without significant differences between males and females (base-models), were predicted for, respectively, task T1 (upright standing posture) and T12 (trunk axial rotation with 10 kg load in hands). Interestingly, in females, the compressive forces for symmetric lifting tasks in the sagittal plane only slightly varied in T1 through T8 tasks despite the fact that a 10 kg weight was held in hands for some of these activities; i.e., only T9 to T12 tasks caused a substantial load increase as compared to T1 task in females. For males, flexion task (T2) resulted in a significant increase in L5-S1 compressive loads (**Figure 3A**). When the predicted loads were normalized to the BW, the large differences between the base-models of males and females disappeared and even for some tasks the predicted loads in females became slightly larger than those in males (**Figure 4**). That is, female base-models predicted, in average (of all tasks), larger compressive (9%) and shear (16.2%) normalized loads than males' based-models.

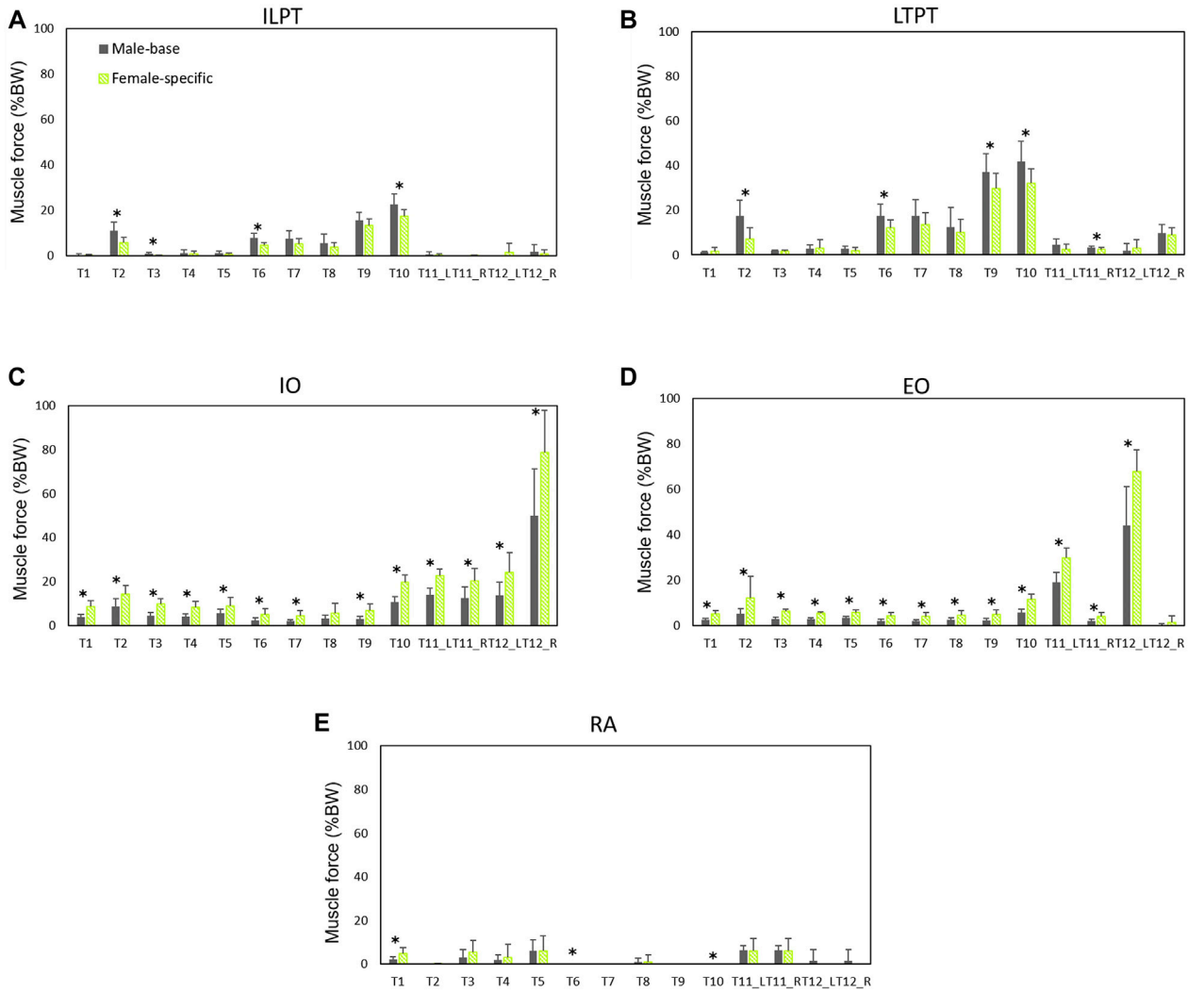

FIGURE 5 | Global muscle forces **(average of left and right)** as predicted by males' models and female-specific models: **(A)** iliocostalis lumborum pars thoracic (ILPT), **(B)** longissimus thoracis pars thoracic (LTPT), **(C)** internal oblique (IO), **(D)** external oblique (EO), and **(E)** rectus abdominis (RA). * indicates a significant difference ($p < 0.05$) between males and females.

Spinal Loads in Female-Specific Models

On average (of all tasks), the predicted absolute forces by males' models were considerably larger than the female-specific models (41% compressive and 23.6% shear loads). However, the normalized (to BW) compressive and shear loads in female-specific models were, respectively, 2.4% smaller and 9.4% larger than males in average. Moreover, the predicted loads by the female-specific models were significantly smaller than those predicted by the female based-models except for T12 task (**Figure 3**) ($p < 0.05$ in most of the simulated tasks). The largest effect of female-specific parameters on the predicted L5-S1 loads was 22.7% reduction in the predicted compressive load (task T9) and 18.6% increase in the predicted shear load (task T12) (**Figure 3**). Such an effect was in average (all tasks) 11.4 and 9.8% reduction for the predicted compressive and shear loads, respectively.

Muscle Forces

Normalized (to BW) muscle forces predicted by males' models and female-specific models are shown in **Figures 5**, **6**. Females showed larger oblique muscle forces ($p < 0.05$ in most of the simulated tasks) while males had larger trunk extensor muscle (global) forces during most of the symmetric lifting tasks ($p < 0.05$). The maximum global force for symmetric lifting tasks in both groups was predicted for the longissimus thoracis pars thoracic (LTPT) muscle in task T10 (41.8 %BW for males and 32.2 %BW for females) (**Figure 5**). In asymmetric tasks, maximum global muscle forces were predicted in T12 for the internal oblique muscle (50 %BW for males and 78 %BW for females) (**Figure 5**).

For the local muscles, the highest forces for symmetric lifting tasks were predicted in T10 for iliocostalis lumborum (ILPL) muscle (24.8 %BW for males and 23 %BW for females) (**Figure 6**). For asymmetric

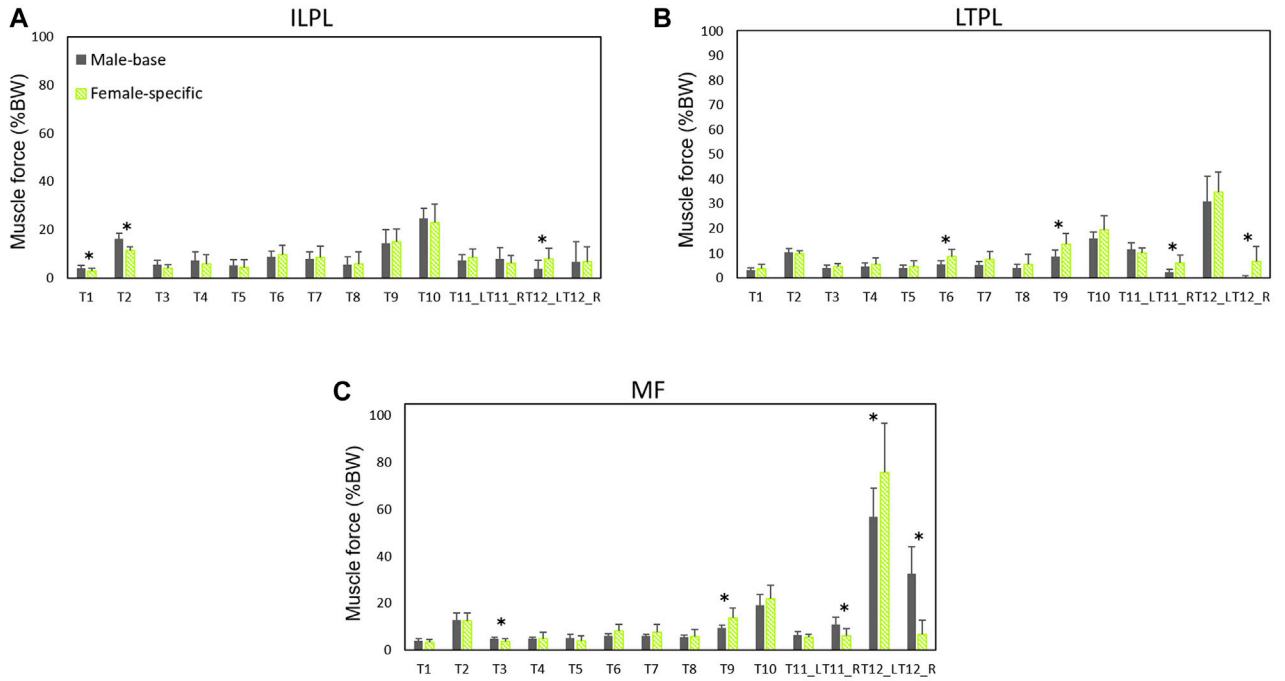

FIGURE 6 | Local muscle forces **(average of left and right)** as predicted by males' models and female-specific models: **(A)** iliocostalis lumborum pars lumborum (ILPL), **(B)** longissimus thoracis pars lumborum (LTPL), and **(C)** multifidius (MF). * indicates a significant difference ($p < 0.05$) between males and females.

TABLE 4 | Pearson correlations between muscle activities predicted by models and EMG signals recorded from participants' muscles during lifting tasks. The bolded values indicate a linear relationship between measured and predicted muscle activity ($p < 0.05$).

	Male base-model		Female base-model		Female-specific model	
	r	p-vale	r	p-vale	r	p-vale
multifidus (left)	0.38	0.22	0.35	0.26	0.40	0.20
multifidus (right)	0.38	0.22	0.54	0.07	0.68	**0.02**
Lumbar erector spinae (left)	0.31	0.32	0.35	0.27	0.52	0.08
lumbar erector spinae (right)	0.76	**0.00**	0.47	0.13	0.81	**0.00**
thoracic erector spinae (left)	0.65	**0.02**	0.70	**0.01**	0.81	**0.00**
thoracic erector spinae (right)	0.54	0.07	0.77	**0.00**	0.75	**0.01**
internal oblique (left)	0.67	**0.02**	0.92	**0.00**	0.79	**0.00**
internal oblique (right)	0.02	0.95	0.67	**0.02**	0.66	**0.02**
external oblique (left)	0.36	0.25	0.90	**0.00**	0.90	**0.00**
external oblique (right)	0.03	0.92	-0.26	0.42	-0.38	0.22
rectus abdominis (left)	-0.22	0.50	0.03	0.91	-0.05	0.87
rectus abdominis (right)	-0.27	0.39	-0.24	0.45	-0.30	0.34

lifting tasks, multifidus showed the largest force (56.7 %BW for males and 75.7 %BW for females) (**Figure 6**).

Predicted vs. Measured Muscle Activities

The measured EMGs collected from twelve back and abdominal muscles and their corresponding model predicted muscle activities (female base-model, female-specific model, and male base-model) were compared (**Table 4**). As compared to female base-model, female-specific model improved the correlations for back extensor muscles. The erector spinae muscles (iliocostalis and longissimus) showed a strong correlation (r = 0.72) in females, and a moderate correlation in males (r = 0.57). For abdominal oblique muscles, the correlation was moderate for females (r = 0.50) and weak for males (r = 0.27). For both sexes, internal oblique muscles showed a higher correlation than external oblique muscles. The small measured and predicted activities in rectus abdominis (**Figure 5**) were poorly correlated for both sexes (**Table 4**).

DISCUSSION

The present study aimed to predict spinal loads and trunk muscle forces at the lumbosacral (L5-S1) joint during a number of

manual material handling tasks using full-body, subject- and sex-specifics models driven by subject-specific *in vivo* kinematic data. Literature has demonstrated notable sex-dependent differences in joint angles during lifting activities (Plamondon et al., 2017; Sheppard et al., 2016), lumbo-pelvic coordination (Pan et al., 2020; Pries et al., 2015), lifting style (Haddas et al., 2015; Lindbeck and Kjellberg, 2001), muscle cross-sectional area (Marras et al., 2001; Anderson et al., 2012), anthropometry measures, and mass distribution (Shan and Bohn, 2003). These sex-specific parameters influence spinal loads and can explain sex-dependent differences in the predicted spinal loads.

Comparing the predicted L5-S1 loads in females with and without applying sex-specific parameters showed a maximum of ~23% reduction for the L5-S1 compressive forces in tasks T9 and T10 (**Figure 3**). Our results showed that sex could significantly affect predicted spinal loads and revealed that the differences in spine loads between males and females were not only a function of body size. In contradiction with earlier findings (Ghezelbash et al., 2016) that showed sex had a small effect on spinal loads, in our study sex-specific parameters for females significantly affected the predicted loads in almost all tasks. On average (all the simulated tasks), the compressive and shear forces were 11.4 and 9.8%, respectively, smaller in female-specific models than female-base models. Ghezelbash et al. (2016), assumed identical body weight, height, and age for their males' and females' models and showed that during symmetric lifting activities the effect of sex on spinal loads was small (0.7% for compression and 2.1% for shear). In the present study, however, the effect of sex was found to be much larger (18% for compression and 10.9% for shear) during symmetric lifting tasks (T6-T10). This could be explained by the fact that (Ghezelbash et al., 2016) neglected proper sex/subject-specific kinematics. Moreover, they used kinematics data of unloaded motion (Pries et al., 2015) to simulate lifting tasks while holding external loads in hands influences trunk kinematics (Davis and Marras, 2000; Granata and Sanford, 2000). Altogether, these assumptions in the study of Ghezelbash et al. (2016) may explain their findings as to the small effect of sex on spinal loads. Our findings showed that spinal loads in females and for almost all the simulated tasks except T12 were in average smaller (11.8% for compressive and 9% for shear forces) when the female-specific models were used. Note that the PCSA's values of back muscles in the base-models were larger (39%) than corresponding values in female-specific models.

Both sexes showed large L5-S1 compressive and shear forces in task T12. Combination of trunk axial rotation and load-handling is a significant risk factor for back injuries. External and internal oblique muscles have been identified as prime trunk rotators. It has been shown that during axial rotation, compared to movements in the coronal or sagittal planes, higher co-contractions are produced in these muscles (Ng et al., 2001), resulting in increased spinal loads (Granata and Marras, 1995). In agreement, in our study lifting a 10 kg hand load while also twisting the trunk (task T12) showed the highest L5-S1 loads and muscle forces of the contralateral external oblique and ipsilateral internal oblique (**Figures 3–5**). In the female base-models, the PCSAs of oblique abdominal muscles was, in average, 7.2% smaller than PCSAs of female reported in the literature (Marras et al., 2001) that used in female-specific model. This could be the reason for the increase of the predicted spinal loads (7.3% compressive, 18.6% shear) in task T12 (lifting while twisting the back) for females after applying sex-specific parameters. Therefore, it is important to consider sex-specific parameters, especially when simulating tasks with a large trunk axial rotation.

In agreement with previous EMG-assisted biomechanical model (Marras et al., 2002; Marras et al., 2003), and subject-specific kinematics driven models (Ghezelbash et al., 2018), in our study males showed larger absolute compressive (41%) and shear (23.6%) loads. In these studies, however, other confounding parameters such as BW and body height were not controlled. It has been shown that BW markedly affects spinal loads (Ghezelbash et al., 2016; Hajihosseinali et al., 2015), thus larger absolute spinal loads in males could partially be due to their larger body masses. Marras et al. (2002), during two lifting conditions (isolated torso and whole-body free-dynamic), showed that even when differences in body weight were accounted for, sex differences in spine loading persisted. He showed when lifting motions were confined to torso (i.e., having the same lifting style), the sex differences in the spine loading were directly due to the variations in BW. However, when greater kinematics freedom was permitted, females' spinal loads increased as compared to those in males. According to their findings, it became complicated to relate spinal load differences between males and females to their BW alone. Spinal load differences also are linked to the degree of control required during exertion (Marras et al., 2002; Marras et al., 2003). Females adopt different lifting kinematics in demanding lifting activities. While females perform these tasks by mainly relying on their hips, males rely more on their lumbar spine. The larger motion in females' hip is attributable to their lower trunk strength. In our study, during task T12 (lifting and twisting the trunk), which is a demanding task, larger absolute and normalized spinal forces were predicted in females, despite their smaller body mass as compared to male participants. However, when the predicted loads were normalized to BW, the difference in spinal loads between males and females almost disappeared (males had 2.4% larger compressive, and 9.4% smaller shear loads than females). By assuming identical BWs in males' and females' models, (Ghezelbash et al., 2016) also found small differences in spinal load between both sexes; females had slightly larger (4.7% for compression and 8.7% for shear) loads than males. Moreover, we compared the predicted relative loads for four matched participants [2 males (weight: 61.9 kg, height: 166.3 cm) and 2 females (weight: 60.8 kg, height: 165.5 cm)]. Males had, in average, ~%6 larger relative compressive forces than females thus confirming the general finding of our study.

Our previous *in vivo* study on a large asymptomatic population (141 males and 179 females) indicated that BMI did not affect lumbar range of flexion or spine rhythm (Zander et al., 2018) as long as BMI remains below a threshold of 26 kg/cm^2. More importantly, another recent study of our group (Ghasemi and Arjmand, 2021) found that BMI had no significant effects on the three-dimensional spine

(trunk, lumbar, and pelvis) kinematics of males during various symmetric and asymmetric load-handling activities. Moreover, some studies reported remarkable effects of sex on lifting kinematics (Lindbeck and Kjellberg, 2001; Plamondon et al., 2014). Similarly, significant lumbo-pelvic movement differences between females and males were reported in our previous study (Pries et al., 2015); larger contribution of the pelvis and less trunk flexion in females compared to males. Altogether, these findings indicate that spine kinematics are mainly affected by sex rather than BMI.

It has been shown that during identical lifting activities, females produce higher levels of muscle activities (Marras et al., 2003). In agreement, our models (on average) predicted slightly higher muscle forces in females. Measured and predicted muscle activities showed a stronger correlation for females. A linear correlation between AB predicted muscle activities and measured EMGs for erector spinae muscles has been found during lifting activities at two different heights ($r = 0.62$ and $r = 0.70$) (Stambolian et al., 2016). In agreement, our study showed a strong correlation ($r = 0.72$) in females and moderate ($r = 0.57$) correlation in males for the erector spinae muscles.

Females on average are smaller in size and have lower muscular strength than males (Lindbeck and Kjellberg, 2001; Plamondon et al., 2014). Significantly smaller muscle PCSAs in females (Anderson et al., 2012; Marras et al., 2001) could, at least partly, be responsible for their smaller muscular strength. Females' lifting strength ranges between 48 and 70% of that of males (Kumar and Garand, 1992; Marras et al., 2002; Plamondon et al., 2014), and therefore they have lower spine tolerant limits. Sex differences in strength have an impact on their lumbo-pelvic coordination and their muscle activity patterns. Larger contribution of the pelvis in females during lifting tasks might be a compensation mechanism to help them flex less their trunk due to the lower trunk strength capacity in the lumbar region (Marras et al., 2002). Furthermore, females tend to increase their muscle activities to stabilize the trunk and flex it less (Lindbeck and Kjellberg, 2001). Subramaniyam et al. (2019) showed sex-dependent muscle activity patterns during identical lifting tasks. Abdominal coactivities increase spinal stability during lifting (El-Rich et al., 2004), and significantly contribute to spine shear forces (Marras et al., 2002). *In vivo* studies, in agreement with our simulation results, showed that females had more active trunk stabilizer muscles, MF, IO, and EO, during symmetric and asymmetric lifting tasks (Marras et al., 2002; Subramaniyam et al., 2019). Although the higher activity of nonprimary extensor muscles during lifting plays a stabilization role for the trunk by providing greater stiffness, it could adversely increase spinal loads (El-Rich et al., 2004). A comparison of spine loads relative to the tolerance limits indicated that females were 25% closer to their expected tolerance (Marras et al., 2003). Having higher muscular coactivities and smaller strength capacity, cause females to experience greater muscle fatigue and be more vulnerable to muscle strain and injury. This is supported by findings of the epidemiological studies that report higher work-related physical injuries (Hansen et al., 2018) and a higher prevalence of low back pain (Wu et al., 2020) in females than males. Under different lifting conditions in the work environment, female workers also behave differently than males in terms of kinematics and muscle activities (Plamondon et al., 2014). Altogether, and taking into account the sex-specific differences, males and females are to be treated differently while designing their work environments (Lindbeck and Kjellberg, 2001).

This study had some limitations. The BMI of male and female participants was not controlled. Unequal body masses influence absolute spinal loads (Ghezelbash et al., 2016; Hajihosseinali et al., 2015). Although loads normalized to a subject's BW account for certain anthropometric differences, it would be preferable to consider matched male-female subjects (in terms of BW and BH) when sex-dependent spinal load differences are investigated during identical lifting activities. Soft tissue artifacts are the main source of errors in skin marker-based motion analysis (Benoit et al., 2006; Leardini et al., 2005; Stagni et al., 2005). In order to minimize such errors, a local optimization method (Andersen et al., 2010) was used to update the initial segment lengths and marker locations on the model with respect to the experimental ones. As motion capture data do not provide individual lumbar vertebrae kinematics, a pre-defined 3D lumbar spine rhythm was used to define intervertebral rotations during upper body inclination; the likely inter-individual differences in lumbar spine rhythm were overlooked (Arshad et al., 2016; Pearcy, 1985; Zander et al., 2018). Recorded skin EMGs were limited to select muscles subjected also to the cross-talk issue. As to the model itself, force-length-velocity relationships were neglected. Spinal ligaments and facet articulations were not considered and intervertebral joints were modeled as spherical joints with fixed centers of rotation. The moment arms of muscles were not sex-dependent in the model. AnyBody Modeling System (Damsgaard et al., 2006) uses a general linear scaling approach to adjust the segment-fixed insertion nodes of muscles based on subject's anthropometric characteristics. This is in accordance with the MRI imaging study (Jorgensen et al., 2001) that showed the distance of the muscles from the spine (e.g., moment arm) depends upon anthropometric characteristics such as torso depth/breadth, body mass, and stature. Finally, while sex-dependent parameters influenced spinal loads, their distinct effects remains to be investigated.

CONCLUSION

The present study aimed to predict spinal loads and trunk muscle forces at the lumbosacral (L5-S1) joint during a number of manual material handling tasks using full-body, subject- and sex-specifics models driven by subject-specific *in vivo* kinematic data. Base-models (subject-specific segmental length, muscle architecture, and kinematics data) used for both sexes. For females, female-specific models were also developed by taking into account the female-specific parameters (muscle physiological cross-sectional areas, segmental mass distributions, and body fat percentage). Males showed significantly larger absolute compressive and shear spinal loads than females for almost all

the simulated tasks in this study. When the spine loads were normalized to BW, differences between the predicted spinal load for males and females became less pronounced. Female-specific models predicted significantly smaller L5-S1 loads as compared to female base-model. Neglecting sex-specific parameters in musculoskeletal models of the spine could result in overestimation of the spinal loads in females.

DATA AVAILABILITY STATEMENT

The raw data supporting the conclusion of this article will be made available by the authors, without undue reservation.

ETHICS STATEMENT

The studies involving human participants were reviewed and approved by Ethics Committee of the Charité Universitätsmedizin Berlin (EA1/059/21). The patients/participants provided their written informed consent to participate in this study.

AUTHOR CONTRIBUTIONS

AF, NA, and HS contributed to the conception and design of the study. AF developed the models and performed simulations. AF and PF performed the data acquisitions and conducted the statistical analysis. All authors contributed in preparing the manuscript and approved the submission.

FUNDING

This study was financed by the German Academic Exchange Service (DAAD, No. 57320205) and by the German Research Foundation (DFG, SCHM 2572/12-1).

REFERENCES

Aghazadeh, F., Arjmand, N., and Nasrabadi, A. M. (2020). Coupled Artificial Neural Networks to Estimate 3D Whole-Body Posture, Lumbosacral Moments, and Spinal Loads during Load-Handling Activities. *J. Biomech.* 102, 109332. doi:10.1016/j.jbiomech.2019.109332

Andersen, M. S., Damsgaard, M., MacWilliams, B., and Rasmussen, J. (2010). A Computationally Efficient Optimisation-Based Method for Parameter Identification of Kinematically Determinate and Over-determinate Biomechanical Systems. *Comput. Methods Biomech. Biomed. Eng.* 13, 171–183. doi:10.1080/10255840903067080

Anderson, D. E., D'Agostino, J. M., Bruno, A. G., Manoharan, R. K., and Bouxsein, M. L. (2012). Regressions for Estimating Muscle Parameters in the Thoracic and Lumbar Trunk for Use in Musculoskeletal Modeling. *J. Biomech.* 45, 66–75. doi:10.1016/j.jbiomech.2011.10.004

Arjmand, N., Plamondon, A., Shirazi-Adl, A., Larivière, C., and Parnianpour, M. (2011). Predictive Equations to Estimate Spinal Loads in Symmetric Lifting Tasks. *J. Biomech.* 44, 84–91. doi:10.1016/j.jbiomech.2010.08.028

Arjmand, N., and Shirazi-Adl, A. (2006). Sensitivity of Kinematics-Based Model Predictions to Optimization Criteria in Static Lifting Tasks. *Med. Eng. Phys.* 28, 504–514. doi:10.1016/j.medengphy.2005.10.001

Arshad, R., Angelini, L., Zander, T., Di Puccio, F., El-rich, M., and Schmidt, H. (2018). Spinal Loads and Trunk Muscles Forces during Level Walking - A Combined *In Vivo* and In Silico Study on Six Subjects. *J. Biomech.* 70, 113–123. doi:10.1016/j.jbiomech.2017.08.020

Arshad, R., Zander, T., Dreischarf, M., and Schmidt, H. (2016). Influence of Lumbar Spine Rhythms and Intra-abdominal Pressure on Spinal Loads and Trunk Muscle Forces during Upper Body Inclination. *Med. Eng. Phys.* 38, 333–338. doi:10.1016/j.medengphy.2016.01.013

Asadi, F., and Arjmand, N. (2020). Marker-less versus Marker-Based Driven Musculoskeletal Models of the Spine during Static Load-Handling Activities. *J. Biomech.* 112, 110043. doi:10.1016/j.jbiomech.2020.110043

Bassani, T., Stucovitz, E., Qian, Z., Briguglio, M., and Galbusera, F. (2017). Validation of the AnyBody Full Body Musculoskeletal Model in Computing Lumbar Spine Loads at L4L5 Level. *J. Biomech.* 58, 89–96. doi:10.1016/j.jbiomech.2017.04.025

Behjati, M., and Arjmand, N. (2019). Biomechanical Assessment of the NIOSH Lifting Equation in Asymmetric Load-Handling Activities Using a Detailed Musculoskeletal Model. *Hum. Factors* 61, 191–202. doi:10.1177/0018720818795038

Benoit, D. L., Ramsey, D. K., Lamontagne, M., Xu, L., Wretenberg, P., and Renström, P. (2006). Effect of Skin Movement Artifact on Knee Kinematics during Gait and Cutting Motions Measured *In Vivo*. *Gait & Posture* 24, 152–164. doi:10.1016/j.gaitpost.2005.04.012

Brown, S. H. M., and Potvin, J. R. (2005). Constraining Spine Stability Levels in an Optimization Model Leads to the Prediction of Trunk Muscle Cocontraction and Improved Spine Compression Force Estimates. *J. Biomech.* 38, 745–754. doi:10.1016/J.JBIOMECH.2004.05.011

Cholewicki, J., and McGill, S. M. (1994). EMG Assisted Optimization: A Hybrid Approach for Estimating Muscle Forces in an Indeterminate Biomechanical Model. *J. Biomech.* 27, 1287–1289. doi:10.1016/0021-9290(94)90282-8

Corbeil, P., Plamondon, A., Handrigan, G., Vallée-Marcotte, J., Laurendeau, S., Ten Have, J., et al. (2019). Biomechanical Analysis of Manual Material Handling Movement in Healthy Weight and Obese Workers. *Appl. Ergon.* 74, 124–133. doi:10.1016/j.apergo.2018.08.018

Craig, B. N., Congleton, J. J., Beier, E., Kerk, C. J., Amendola, A. A., and Gaines, W. G. (2015). Occupational Risk Factors and Back Injury. *Int. J. Occup. Saf. Ergon.* 19, 335–345. doi:10.1080/10803548.2013.11076992

Cruz, J., Yang, J., and Xiang, Y. (2019). "Approaches to Study Spine Biomechanics: A Literature Review," in *Advances in Intelligent Systems and Computing* (Springer-Verlag), 453–462. doi:10.1007/978-3-319-94223-0_43

Damsgaard, M., Rasmussen, J., Christensen, S. T., Surma, E., and de Zee, M. (2006). Analysis of Musculoskeletal Systems in the AnyBody Modeling System. *Simulation Model. Pract. Theor.* 14, 1100–1111. doi:10.1016/j.simpat.2006.09.001

Davis, K. G., Jorgensen, M. J., Davis, K. G., and Jorgensen, M. J. (2005). Biomechanical Modeling for Understanding of Low Back Injuries: A Systematic Review. *Oer* 5, 57–76. doi:10.3233/oer-2005-5106

Davis, K. G., and Marras, W. S. (2000). Assessment of the Relationship between Box Weight and Trunk Kinematics: Does a Reduction in Box Weight Necessarily Correspond to a Decrease in Spinal Loading. *Hum. Factors* 42, 195–208. doi:10.1518/001872000779656499

de Zee, M., Hansen, L., Wong, C., Rasmussen, J., and Simonsen, E. B. (2007). A Generic Detailed Rigid-Body Lumbar Spine Model. *J. Biomech.* 40, 1219–1227. doi:10.1016/j.jbiomech.2006.05.030

Delp, S. L., Anderson, F. C., Arnold, A. S., Loan, P., Habib, A., John, C. T., et al. (2007). OpenSim: Open-Source Software to Create and Analyze Dynamic Simulations of Movement. *IEEE Trans. Biomed. Eng.* 54, 1940–1950. doi:10.1109/TBME.2007.901024

Dreischarf, M., Shirazi-Adl, A., Arjmand, N., Rohlmann, A., and Schmidt, H. (2016). Estimation of Loads on Human Lumbar Spine: A Review of *In Vivo* and Computational Model Studies. *J. Biomech.* 49, 833–845. doi:10.1016/j.jbiomech.2015.12.038

El-Rich, M., Shirazi-Adl, A., and Arjmand, N. (2004). Muscle Activity, Internal Loads, and Stability of the Human Spine in Standing Postures: Combined Model and *In Vivo* Studies. *Spine* 29, 2633–2642. doi:10.1097/01.brs.0000146463.05288.0e

Essendrop, M. (2004). Significance of Intra-abdominal Pressure in Work Related Trunk-Loading. vailable online: http//www.arbejdsmiljoforskning.dk/da/projekter/sosu/laes-mere-om-arbejdsmiljoeet-i-aeldreplejen/\\sim/media/Boeger-og-rapporter/me-phd.pdf (accessed May 2, 2017).

Frankenfield, D. C., Rowe, W. A., Cooney, R. N., Smith, J. S., and Becker, D. (2001). Limits of Body Mass index to Detect Obesity and Predict Body Composition. *Nutrition* 17, 26–30. doi:10.1016/S0899-9007(00)00471-8

Gagnon, D., Plamondon, A., and Larivière, C. (2016). A Biomechanical Comparison between Expert and Novice Manual Materials Handlers Using a Multi-Joint EMG-Assisted Optimization Musculoskeletal Model of the Lumbar Spine. *J. Biomech.* 49, 2938–2945. doi:10.1016/j.jbiomech.2016.07.009

Ghasemi, M., and Arjmand, N. (2021). Spinal Segment Ranges of Motion, Movement Coordination, and Three-Dimensional Kinematics during Occupational Activities in normal-weight and Obese Individuals. *J. Biomech.* 123, 110539. doi:10.1016/J.JBIOMECH.2021.110539

Ghezelbash, F., El Ouaaid, Z., Shirazi-Adl, A., Plamondon, A., and Arjmand, N. (2018). Trunk Musculoskeletal Response in Maximum Voluntary Exertions: A Combined Measurement-Modeling Investigation. *J. Biomech.* 70, 124–133. doi:10.1016/j.jbiomech.2017.11.007

Ghezelbash, F., Shirazi-Adl, A., Arjmand, N., El-Ouaaid, Z., Plamondon, A., and Meakin, J. R. (2016). Effects of Sex, Age, Body Height and Body Weight on Spinal Loads: Sensitivity Analyses in a Subject-specific Trunk Musculoskeletal Model. *J. Biomech.* 49, 3492–3501. doi:10.1016/J.JBIOMECH.2016.09.026

Granata, K. P., and Marras, W. S. (1995). The Influence of Trunk Muscle Coactivity on Dynamic Spinal Loads. *Spine.* 20, 913–919. doi:10.1097/00007632-199504150-00006

Granata, K. P., and Sanford, A. H. (2000). Lumbar-pelvic Coordination Is Influenced by Lifting Task Parameters. *Spine* 25, 1413–1418. doi:10.1097/00007632-200006010-00014

Haddas, R., Sizer, P., and Yang, J., (2015). Effects of Gender and Recurrent Low Back Pain on Lifting Style. *Cent. Eur. J. Sport Sci. Med.* 11, 15–28. doi:10.18276/cej.2015.3-02

Hajihosseinali, M., Arjmand, N., and Shirazi-Adl, A. (2015). Effect of Body Weight on Spinal Loads in Various Activities: A Personalized Biomechanical Modeling Approach. *J. Biomech.* 48, 276–282. doi:10.1016/J.JBIOMECH.2014.11.033

Hansen, M. C., Aagaard, T., Christensen, H. W., and Hartvigsen, J. (2018). Work-related Acute Physical Injuries, Chronic Overuse Complaints, and the Psychosocial Work Environment in Danish Primary Care Chiropractic Practice - a Cross-Sectional Study. *Chiropr Man. Therap* 26, 4. doi:10.1186/s12998-018-0174-2

Hoogendoorn, W. E., Bongers, P. M., De Vet, H. C. W., Douwes, M., Koes, B. W., Miedema, M. C., et al. (2000). Flexion and Rotation of the Trunk and Lifting at Work Are Risk Factors for Low Back Pain: Results of a Prospective Cohort Study. *Spine.* 25, 3087–3092. doi:10.1097/00007632-200012010-00018

Ignasiak, D., Dendorfer, S., and Ferguson, S. J. (2016a). Thoracolumbar Spine Model with Articulated Ribcage for the Prediction of Dynamic Spinal Loading. *J. Biomech.* 49, 959–966. doi:10.1016/j.jbiomech.2015.10.010

Ignasiak, D., Ferguson, S. J., and Arjmand, N. (2016b). A Rigid Thorax assumption Affects Model Loading Predictions at the Upper but Not Lower Lumbar Levels. *J. Biomech.* 49, 3074–3078. doi:10.1016/j.jbiomech.2016.07.006

Jorgensen, M. J., Marras, W. S., Granata, K. P., and Wiand, J. W. (2001). MRI-derived Moment-Arms of the Female and Male Spine Loading Muscles. *Clin. Biomech.* 16, 182–193. doi:10.1016/S0268-0033(00)00087-5

Klein Horsman, M. D., Koopman, H. F. J. M., van der Helm, F. C. T., Prosé, L. P., and Veeger, H. E. J. (2007). Morphological Muscle and Joint Parameters for Musculoskeletal Modelling of the Lower Extremity. *Clin. Biomech.* 22, 239–247. doi:10.1016/j.clinbiomech.2006.10.003

Konard, P. (2006). "The ABC of EMG," in *A Practical Introduction to Kinsesiological Electromyography* (USA: Noraxon INC.).

Kumar, S. (1990). Cumulative Load as a Risk Factor for Back Pain. *Spine* 15, 1311–1316. doi:10.1097/00007632-199012000-00014

Kumar, S., and Garand, D. (1992). Static and Dynamic Lifting Strength at Different Reach Distances in Symmetrica] and Asymmetrical Planes. *Ergonomics* 35, 861–880. doi:10.1080/00140139208967367

Leardini, A., Chiari, L., Croce, U. D., and Cappozzo, A. (2005). Human Movement Analysis Using Stereophotogrammetry. *Gait & Posture* 21, 212–225. doi:10.1016/j.gaitpost.2004.05.002

Lindbeck, L., and Kjellberg, K. (2001). Gender Differences in Lifting Technique. *Ergonomics* 44, 202–214. doi:10.1080/00140130120142

Marras, W. S., Davis, K. G., and Jorgensen, M. (2003). Gender Influences on Spine Loads during Complex Lifting. *Spine J.* 3, 93–99. doi:10.1016/S1529-9430(02)00570-3

Marras, W. S., Davis, K. G., and Jorgensen, M. (2002). Spine Loading as a Function of Gender. *Spine* 27, 2514–2520. doi:10.1097/01.BRS.0000031264.74555.1D10.1097/00007632-200211150-00017

Marras, W. S., and Granata, K. P. (1997). The Development of an EMG-Assisted Model to Assess Spine Loading during Whole-Body Free-Dynamic Lifting. *J. Electromyogr. Kinesiol.* 7, 259–268. doi:10.1016/S1050-6411(97)00006-0

Marras, W. S., Jorgensen, M. J., Granata, K. P., and Wiand, B. (2001). Female and Male Trunk Geometry: Size and Prediction of the Spine Loading Trunk Muscles Derived from MRI. *Clin. Biomech.* 16, 38–46. doi:10.1016/S0268-0033(00)00046-2

McGill, S. M. (1991). Electromyographic Activity of the Abdominal and Low Back Musculature during the Generation of Isometric and Dynamic Axial Trunk Torque: Implications for Lumbar Mechanics. *J. Orthop. Res.* 9, 91–103. doi:10.1002/jor.1100090112

McGill, S. M., and Norman, R. W. (1986). 1986 Volvo Award in Biomechanics: Partitioning of the L4 - L5 Dynamic Moment into Disc, Ligamentous, and Muscular Components during Lifting. *Spine* 11, 666–678. doi:10.1097/00007632-198609000-00004

Mohammadi, Y., Arjmand, N., and Shirazi-Adl, A. (2015). Comparison of Trunk Muscle Forces, Spinal Loads and Stability Estimated by One Stability- and Three EMG-Assisted Optimization Approaches. *Med. Eng. Phys.* 37, 792–800. doi:10.1016/j.medengphy.2015.05.018

Nachemson, A. L. (1981). Disc Pressure Measurements. *Spine* 6, 93–97. doi:10.1097/00007632-198101000-00020

Ng, J. K.-F., Parnianpour, M., Richardson, C. A., and Kippers, V. (2001). Functional Roles of Abdominal and Back Muscles during Isometric Axial Rotation of the Trunk. *J. Orthop. Res.* 19, 463–471. doi:10.1016/S0736-0266(00)90027-5

Palmer, K. T., Griffin, M. J., Syddall, H. E., Pannett, B., Cooper, C., and Coggon, D. (2003). The Relative Importance of Whole Body Vibration and Occupational Lifting as Risk Factors for Low-Back Pain. *Occup. Environ. Med.* 60, 715–721. doi:10.1136/oem.60.10.715

Pan, F., Firouzabadi, A., Zander, T., and Schmidt, H. (2020). Sex-dependent Differences in Lumbo-Pelvic Coordination for Different Lifting Tasks: A Study on Asymptomatic Adults. *J. Biomech.* 102, 109505. doi:10.1016/j.jbiomech.2019.109505

Pearcy, M. J. (1985). Stereo Radiography of Lumbar Spine Motion. *Acta Orthopaedica Scand.* 56, 1–45. doi:10.3109/17453678509154154

Plamondon, A., Larivière, C., Denis, D., Mecheri, H., and Nastasia, I. (2017). Difference between Male and Female Workers Lifting the Same Relative Load when Palletizing Boxes. *Appl. Ergon.* 60, 93–102. doi:10.1016/j.apergo.2016.10.014

Plamondon, A., Larivière, C., Denis, D., St-Vincent, M., and Delisle, A. (2014). Sex Differences in Lifting Strategies during a Repetitive Palletizing Task. *Appl. Ergon.* 45, 1558–1569. doi:10.1016/j.apergo.2014.05.005

Pries, E., Dreischarf, M., Bashkuev, M., Putzier, M., and Schmidt, H. (2015). The Effects of Age and Gender on the Lumbopelvic Rhythm in the Sagittal Plane in 309 Subjects. *J. Biomech.* 48, 3080–3087. doi:10.1016/j.jbiomech.2015.07.030

Rajaee, M. A., Arjmand, N., Shirazi-Adl, A., Plamondon, A., and Schmidt, H. (2015). Comparative Evaluation of Six Quantitative Lifting Tools to Estimate Spine Loads during Static Activities. *Appl. Ergon.* 48, 22–32. doi:10.1016/j.apergo.2014.11.002

Rasmussen, J., de Zee, M., and Carbes, S. (2009). "Validation of a Biomechanical Model of the Lumbar Spine," in Proceedings, XXIInd Congress of the International Society of Biomechanics, Cape Town, South Africa, 5-9 July 2009.

Rasmussen, J., De Zee, M., Damsgaard, M., Tørholm Christensen, S., Marek, C., and Siebertz, K. (2005). "A General Method for Scaling Musculo-Skeletal Models," in Int. Symp. Comput. Simul. Biomech. Cleveland, Ohio, United States, 3.

Rohlmann, A., Pohl, D., Bender, A., Graichen, F., Dymke, J., Schmidt, H., et al. (2014). Activities of Everyday Life with High Spinal Loads. *PLoS One* 9, e98510–9. doi:10.1371/journal.pone.0098510

Samadi, S., and Arjmand, N. (2018). A Novel Stability-Based EMG-Assisted Optimization Method for the Spine. *Med. Eng. Phys.* 58, 13–22. doi:10.1016/j.medengphy.2018.04.019

Shan, G., and Bohn, C. (2003). Anthropometrical Data and Coefficients of Regression Related to Gender and Race. *Appl. Ergon.* 34, 327–337. doi:10.1016/S0003-6870(03)00040-1

Sheppard, P. S., Stevenson, J. M., and Graham, R. B. (2016). Sex-based Differences in Lifting Technique under Increasing Load Conditions: A Principal Component Analysis. *Appl. Ergon.* 54, 186–195. doi:10.1016/j.apergo.2015.12.002

Stagni, R., Fantozzi, S., Cappello, A., and Leardini, A. (2005). Quantification of Soft Tissue Artefact in Motion Analysis by Combining 3D Fluoroscopy and

Stereophotogrammetry: A Study on Two Subjects. *Clin. Biomech.* 20, 320–329. doi:10.1016/j.clinbiomech.2004.11.012

Stambolian, D., Eltoukhy, M., and Asfour, S. (2016). Development and Validation of a Three Dimensional Dynamic Biomechanical Lifting Model for Lower Back Evaluation for Careful Box Placement. *Int. J. Ind. Ergon.* 54, 10–18. doi:10.1016/j.ergon.2015.12.005

Stokes, M., Rankin, G., and Newham, D. J. (2005). Ultrasound Imaging of Lumbar Multifidus Muscle: normal Reference Ranges for Measurements and Practical Guidance on the Technique. *Man. Ther.* 10, 116–126. doi:10.1016/j.math.2004.08.013

Subramaniyam, M., Kim, S. E., Park, J., and Nam, S. (2019). Trunk Muscle Activities during Lifting in Upright and Stooped Postures. *Int. J. Eng. Res. Technol.* 12 (2), 245–254.

Swain, C. T. V., Pan, F., Owen, P. J., Schmidt, H., and Belavy, D. L. (2020). No Consensus on Causality of Spine Postures or Physical Exposure and Low Back Pain: A Systematic Review of Systematic Reviews. *J. Biomech.* 102, 109312. doi:10.1016/j.jbiomech.2019.08.006

Vicon Nexus 2 (2018). Fill Gaps in Trial Data - Nexus 2.12 Documentation - Vicon Documentation. [WWW Document]. URL: https://docs.vicon.com/display/Nexus212/Fill+gaps+in+trial+data (accessed Jun 6, 2021).

White, A. A., and Panjabi, M. M. (1990). *Clinical Biomechanics of the Spine*. Lippincott.

Wilke, H.-J., Neef, P., Hinz, B., Seidel, H., and Claes, L., (2001). Intradiscal Pressure Together with Anthropometric Data-Aa Data Set for the Validation of Models. 16 Suppl. 1:S111–S126. doi:10.1016/s0268-0033(00)00103-0

Winter, D. (2009). *Biomechanics and Motor Control of Human Movement*. New York: Wiley.

Wu, A., March, L., Zheng, X., Huang, J., Wang, X., Zhao, J., et al. (2020). Global Low Back Pain Prevalence and Years Lived with Disability from 1990 to 2017: Estimates from the Global Burden of Disease Study 2017. *Ann. Transl. Med.* 8, 299. doi:10.21037/atm.2020.02.175

Zander, T., Bashkuev, M., and Schmidt, H. (2018). Are There Characteristic Motion Patterns in the Lumbar Spine during Flexion. *J. Biomech.* 70, 77–81. doi:10.1016/j.jbiomech.2017.09.006

Zander, T., Dreischarf, M., Schmidt, H., Bergmann, G., and Rohlmann, A. (2015). Spinal Loads as Influenced by External Loads: A Combined *In Vivo* and In Silico Investigation. *J. Biomech.* 48, 578–584. doi:10.1016/j.jbiomech.2015.01.011

Conflict of Interest: The authors declare that the research was conducted in the absence of any commercial or financial relationships that could be construed as a potential conflict of interest.

Publisher's Note: All claims expressed in this article are solely those of the authors and do not necessarily represent those of their affiliated organizations, or those of the publisher, the editors and the reviewers. Any product that may be evaluated in this article, or claim that may be made by its manufacturer, is not guaranteed or endorsed by the publisher.

frontiers in Bioengineering and Biotechnology

ORIGINAL RESEARCH
published: 05 November 2021
doi: 10.3389/fbioe.2021.749914

Stability Evaluation of Different Oblique Lumbar Interbody Fusion Constructs in Normal and Osteoporotic Condition – A Finite Element Based Study

Ferenc Bereczki[1,2], *Mate Turbucz*[1,2], *Rita Kiss*[3], *Peter Endre Eltes*[1,4*†] *and Aron Lazary*[1,4†]

[1]*In Silico Biomechanics Laboratory, National Center for Spinal Disorders, Budapest, Hungary,* [2]*School of PhD Studies, Semmelweis University, Budapest, Hungary,* [3]*Department of Mechatronics, Optics and Mechanical Engineering Informatics, Budapest University of Technology and Economics, Budapest, Hungary,* [4]*Department of Spine Surgery, Semmelweis University, Budapest, Hungary*

OPEN ACCESS

Edited by:
Marwan El-Rich, Khalifa University, United Arab Emirates

Reviewed by:
Kaushik Mukherjee, Indian Institute of Technology Delhi, India
Shuqiao Xie, Imperial College London, United Kingdom

***Correspondence:**
Peter Endre Eltes
eltespeter@yahoo.com

[†]*These authors have contributed equally to this work*

Specialty section:
This article was submitted to Biomechanics, a section of the journal Frontiers in Bioengineering and Biotechnology

Received: *30 July 2021*
Accepted: *11 October 2021*
Published: *05 November 2021*

Citation:
Bereczki F, Turbucz M, Kiss R, Eltes PE and Lazary A (2021) Stability Evaluation of Different Oblique Lumbar Interbody Fusion Constructs in Normal and Osteoporotic Condition – A Finite Element Based Study. Front. Bioeng. Biotechnol. 9:749914. doi: 10.3389/fbioe.2021.749914

Introduction: In developed countries, the age structure of the population is currently undergoing an upward shift, resulting a decrease in general bone quality and surgical durability. Over the past decade, oblique lumbar interbody fusion (OLIF) has been globally accepted as a minimally invasive surgical technique. There are several stabilization options available for OLIF cage fixation such as self-anchored stand-alone (SSA), lateral plate-screw (LPS), and bilateral pedicle screw (BPS) systems. The constructs' stability are crucial for the immediate and long-term success of the surgery. The aim of this study is to investigate the biomechanical effect of the aforementioned constructs, using finite element analysis with different bone qualities (osteoporotic and normal).

Method: A bi-segmental (L2–L4) finite element (FE) model was created, using a CT scan of a 24-year-old healthy male. After the FE model validation, CAD geometries of the implants were inserted into the L3–L4 motion segment during a virtual surgery. For the simulations, a 150 N follower load was applied on the models, then 10 Nm of torque was used in six general directions (flexion, extension, right/left bending, and right/left rotation), with different bone material properties.

Results: The smallest segmental (L3–L4) ROM (range of motion) was observed in the BPS system, except for right bending. Osteoporosis increased ROMs in all constructs, especially in the LPS system (right bending increase: 140.26%). Osteoporosis also increased the caudal displacement of the implanted cage in all models (healthy bone: 0.06 ± 0.03 mm, osteoporosis: 0.106 ± 0.07 mm), particularly with right bending, where the displacement doubled in SSA and LPS constructs. The displacement of the screws inside the L4 vertebra increased by 59% on average (59.33 ± 21.53%) due to osteoporosis (100% in LPS, rotation). BPS-L4 screw displacements were the least affected by osteoporosis.

Conclusions: The investigated constructs provide different levels of stability to the spine depending on the quality of the bone, which can affect the outcome of the surgery. In our

model, the BPS system was found to be the most stable construct in osteoporosis. The presented model, after further development, has the potential to help the surgeon in planning a particular spinal surgery by adjusting the stabilization type to the patient's bone quality.

Keywords: degenerative disc disease, spine surgery, finite element analysis, osteoporosis, oblique lateral interbody fusion, stand-alone

INTRODUCTION

Lumbar interbody fusion (LIF) is a gold-standard surgical treatment option for a range of spinal disorders, including degenerative pathologies, infection, trauma, and neoplasia (Mobbs et al., 2015; Resnick et al., 2005). LIF can be achieved via different approaches and techniques, each with its own unique instruments, implants (exp. cages), advantages, disadvantages, indications, and limitations. The age structure of the global population is currently undergoing an upward shift due to decreasing fertility rates and increasing life expectancy (Fuster, 2017), resulting in the changing epidemiology of diseases and spinal disorders (Fehlings et al., 2015). Advancement in minimally invasive spinal fusion technology (Yue et al., 2010) can provide an answer for the challenges posed by the ageing population (Shamji et al., 2015). The minimally invasive anterior approach to the lumbar spine through retroperitoneal access was first described by Mayer (1997). Silvestre et al. (2012) used Mayer's minimally invasive retroperitoneal anterior approach for LIF, and it was referred to as oblique lumbar interbody fusion (OLIF). The OLIF technique is widely accepted (Mobbs et al., 2015; Phan et al., 2016) and provides, from the patient's left side, a safe access corridor from L2 to L5 vertebra between the psoas and the aorta. Through the corridor, the surgeon can resect the disc, remove the cartilage endplate, insert a large intervertebral cage, and achieve the goal of intervertebral fusion and indirect decompression (Mehren et al., 2016) by keeping the lumbosacral plexus safe (Phan et al., 2016; Mehren et al., 2016; Chung et al., 2017). During the OLIF procedure, different additional fixation methods can be applied, and there is no consensus about the indication for choosing a particular type. Self-anchored stand-alone (SSA) OLIF cages contain a screw fixation part besides the intervertebral spacer. Lateral plate-screw (LPS) fixation has a longer history in spinal trauma, but a new plate design has recently emerged, dedicated for OLIF. Percutaneous bilateral pedicle screw (BPS) fixation can be used after turning the patient to prone position, which, in general, increases the operation time (Li et al., 2020) and the invasiveness by the posterior incisions used to insert the pedicle screws. For experienced spine surgeons, there is no difference in the complexity of the 3 procedures. Several other fixation methods and a combination of these have been reported considering their technical specifications. However, only a few studies have investigated the biomechanical characteristics of OLIF with various fixation options (Hah and Kang, 2019), especially focusing on the effect of osteoporosis, which is widely present in the ageing population (Fehlings et al., 2015). Biomechanical characteristics of the different OLIF constructs can significantly influence the short- and long-term implant-related complication rate, as well as the possibility of achieving bony fusion, thus the therapeutic outcome.

The first application of finite element analysis (FEA) in biomechanics was published by Brekelmans et al. (1972). In the last decades, FEA contributed to the understanding of the spine, its components, and its behavior in healthy, diseased, or damaged conditions (Fagan et al., 2002), complementing the *in vitro* experiments. FEA has become a common research method in the field of *in silico* medicine (Viceconti et al., 2008).

To the best knowledge of the authors, there is no study comparing the 3 aforementioned OLIF implants with different bone material properties in the current literature. The aim of this study was to use FE analysis to evaluate the stability of different OLIF fusion constructs (BPS, LPS, and SSA) in normal and osteoporotic conditions. While a direct validation of the outputs of the models for this specific application was not the goal of this study, the present comparative computational approach enables to highlight the importance of bone material strength and stiffness reduction (ageing, metabolic bone diseases, etc.) in the surgeon's decision-making process of choosing between different fixation options.

MATERIALS AND METHODS

Generation of L2–L4 Lumbar Spine Bi-Segment Finite Element Model

A CT scan (Hitachi Presto, Hitachi Medical Corporation, Tokyo, Japan) of a 24-year-old patient's lumbar spine was selected from a study of 270 patients who underwent different treatments due to lower back pain in our clinic (MySPINE, Project ID: 269909, Funded under: FP7-ICT). The imaging protocol was previously defined in the MySPINE project (Castro-Mateos et al., 2015), (Rijsbergen et al., 2018), and the images were reconstructed with a voxel size of $0.6 \times 0.6 \times 0.6\,mm^3$. The L2–L3 and L3–L4 segments were not affected by any musculoskeletal pathology. The data were extracted from the hospital PACS in DICOM file format. To comply with the ethical approval of the patient data protection, de-identification of the DICOM data was performed using Clinical Trial Processor software (Radiological Society of North America, https://www.rsna.org/ctp.aspx) (Aryanto et al., 2015). In order to define the 3D geometry, we performed a segmentation procedure using Mimics image analysis software (Mimics Research, Mimics Innovation Suite v23. 0, Materialise, Leuven, Belgium) via the Hounsfield

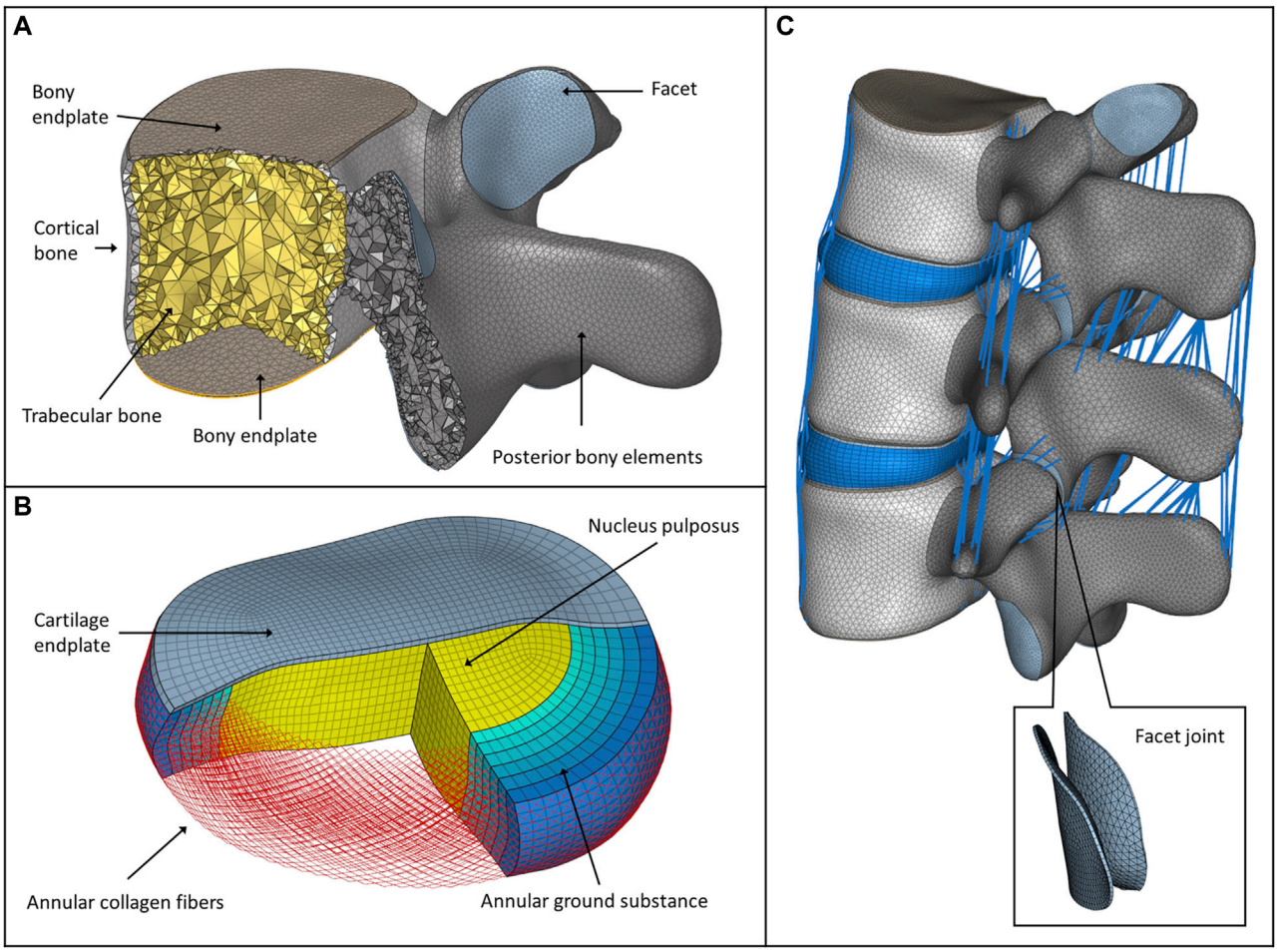

FIGURE 1 | FE model of the intact L2–L4 spine bi-segment. **(A)** Model of the vertebral body, bony endplates, cortical shell, trabecular core, posterior elements, and articular facet. **(B)** Model of the intervertebral disc, nucleus pulposus, annular collagen fibers, and ground substance. **(C)** Intact L2–L4 lumbar spine bi-segment FE model, with facet joints and ligaments from a left posterior-lateral view.

thresholding algorithm and manual segmentation tools. To evaluate the accuracy of the segmentation process, we calculated the Dice Similarity Index (DSI) (Zou et al., 2004; Bharatha et al., 2001) based on two segmentation sessions of the same geometry.

From the segmented masks, a triangulated surface mesh was automatically generated in STL (Stereolithography) format. In 3-Matic (Mimics Research, Mimics Innovation Suite v21.0, Materialise, Leuven, Belgium) software, surface smoothing (iteration: 6, smoothing factor: 0.7, with shrinkage compensation) and uniform remeshing (target triangle edge length 0.6 mm, sharp edge preservation, sharp edge angle 60°) were applied on the 3D geometries.

In 3-Matic, the vertebrae were divided into posterior and anterior parts (Shirazi-adl et al., 1984). The anterior parts were divided into a cortical shell (thickness: 1 mm), vertebral bony endplates (thickness: 0.5 mm), and a cancellous core. Facet joints were modeled manually, with 0.25 mm cartilage height and a minimum 0.5 mm gap between the two facets (Dreischarf et al., 2014) (**Figure 1A**). The intersection-based non-manifold assembly was exported to Hypermesh software (Altair Engineering, Inc., Troy, Michigan, United States), and all of the surfaces were remeshed with a uniform triangulated surface mesh (target tringle edge length: 1 mm). From the resulting 3D surfaces, an adaptive tetrahedral volume mesh was generated, with the exception of the bony endplates, where pyramid elements were used (**Table 1**).

The annulus fibrosus (AF) and the nucleus pulposus (NP) defining the intervertebral disc were modelled manually according to the literature (**Figure 1B**) (Shirazi-Adl et al., 1986), (Schmidt et al., 2007). The NP accounted for 45% of the intervertebral volume and was moved in the posterior direction, so that the sagittal thickness of the posterior AF substance became 80% of the anterior AF (Shirazi-Adl et al., 1986). The fluid-like behavior of the NP was modeled using an isotropic, hyperelastic Mooney-Rivlin formulation (hexahedral mesh) (Schmidt et al., 2007). The AF consisted of 2 times 6 annulus fiber sets embedded into a hexahedral ground substance matrix of six layers with alternating orientations about ±30° to the mid-cross-sectional area of the disc (Lu et al., 1996). The fiber

TABLE 1 | Material properties and mesh type assigned to the FE model.

Material	Element type	Constitutive law	Young's modulus (MPa)	Poisson ratio (-)	References
Normal cortical bone	C3D4	Linear elastic	12,000	0.3	Shirazi-adl et al. (1984)
Osteoporotic cortical bone	C3D4	Linear elastic	8,040 (67% of normal)	0.3	(Polikeit et al., 2003), (Zhang et al., 2010), (Salvatore et al., 2018)
Normal cancellous bone	C3D4	Linear elastic	100	0.2	Shirazi-adl et al. (1984)
Osteoporotic cancellous bone	C3D4	Linear elastic	34 (34% of normal)	0.2	(Polikeit et al., 2003), (Zhang et al., 2010), (Salvatore et al., 2018)
Normal post. elements	C3D4	Linear elastic	3,500	0.25	Shirazi-Adl et al. (1986)
Osteoporotic post. elements	C3D4	Linear elastic	2,345 (67% of normal)	0.25	(Polikeit et al., 2003), (Zhang et al., 2010), (Salvatore et al., 2018)
Normal bony endplate	C3D4,C3D5, C3D8	Linear elastic	1,000	0.4	Silva et al. (1997)
Osteoporotic bony endplate	C3D4,C3D5, C3D8	Linear elastic	670 (67% of normal)	0.4	(Polikeit et al., 2003), (Zhang et al., 2010), (Salvatore et al., 2018)
Cartilaginous endplate	C3D8	Linear elastic	23.8	0.4	Lu et al. (1996)
Facet cartilage	C3D6	Neo-Hooke	C10 = 5.36; D1 = 0.04		Finley et al. (2018)
AF ground substance	C3D8	Neo-Hooke	C10 = 0.3448; D1 = 0.3		Rohlmann et al. (2009)
AF fibre	T3D2	Nonlinear stress–strain curve	Cross-sectional areas were calculated by a layer from volume fractions; 23% at the outermost layer to 5% at the innermost fibre layer		Shirazi-Adl et al. (1986), Lu et al. (1996)
Nucleus pulposus (NP)	C3D8H	Mooney–Rivlin	C10 = 0.12; C01 = 0.03; v = 0.4999		Schmidt et al. (2007)
Ligaments	SPRINGA	Nonlinear stress–strain curve (**Table 2**)	NA	NA	Rohlmann et al. (2006)
Bone graft	C3D4	Linear elastic	100	0.2	Akamaru et al. (2005)
PEEK cage	C3D4	Linear elastic	3,600	0.3	Zhang et al. (2018)
Titanium (screw, plate, and rod)	C3D4	Linear elastic	110,000	0.3	Zhang et al. (2018)

TABLE 2 | Properties of the ligaments (Rohlmann et al., 2006).

Ligament	Stiffness (N/mm)	Strains between (%)	Stiffness (N/mm)	Strains between (%)	Stiffness (N/mm)	Strains higher than (%)
ALL	347	0–12.2	787	12.2–20.3	1864	20.3
PLL	29.5	0–11.1	61.7	11.1–23	236	23
LF	7.7	0–5.9	9.6	5.9–49	58.2	49
CL	36	0–25	159	25–30	384	30
ITL	1.4	0–13.9	1.5	13.9–20	14.7	20
SSL	2.5	0–20	5.3	20–25	34	25
ISL	0.3	0–18.2	1,8	18.2–23.3	10.7	23.3

cross-sectional areas were calculated using the assumed collagen fiber volume fractions: 23% at the outermost layer, gradually decreasing to 5% at the innermost layer (Shirazi-Adl et al., 1986; Lu et al., 1996). The cartilaginous endplate thickness was set to 0.5 mm with hexahedral elements (**Table 1**), (Finley et al., 2018).

In total, seven ligaments were modeled as tension-only spring elements with non-linear material properties, namely, the ALL (anterior longitudinal ligament), PLL (posterior longitudinal ligament), LF (ligamentum flavum), ISL (interspinal ligament), SSL (supraspinal ligament), ITL (intertransverse ligament), and CL (capsular ligament) (**Table 2**). The attachment points, orientation and the element number of the ligaments were adopted from a previous study (MySPINE, Project ID: 269909, FP7-ICT), (**Figure 1C**). The material properties were adopted from the literature (Rohlmann et al., 2006). The facet cartilage material was described by using a Neo-Hookean model, and a surface-to-surface contact without friction was set between the facet surfaces (Lu et al., 1996).

Cage, Implant Construct and Surgical FE Model Development

A PEEK (polyether-ether-ketone) OLIF cage (EMERALD™, Sanatmetal, Eger, Hungary, 45 mm × 22 mm × 12 mm, with 6° lordosis) was scanned using a ScanBox 3D scanner (Smart Optics Sensortechnik GmbH, Bochum, Germany). The obtained point cloud was used to reconstruct the virtual 3D cage model using 3-Matic software. The model was exported in STL format to Autodesk Fusion 360 (Autodesk Inc., San Rafael, CA, United States) CAD (Computer Aided Design) software and served as a base for creating a simplified cage mesh (**Figure 2A**). The resulting geometry was used in all three (BPS, LPS, and

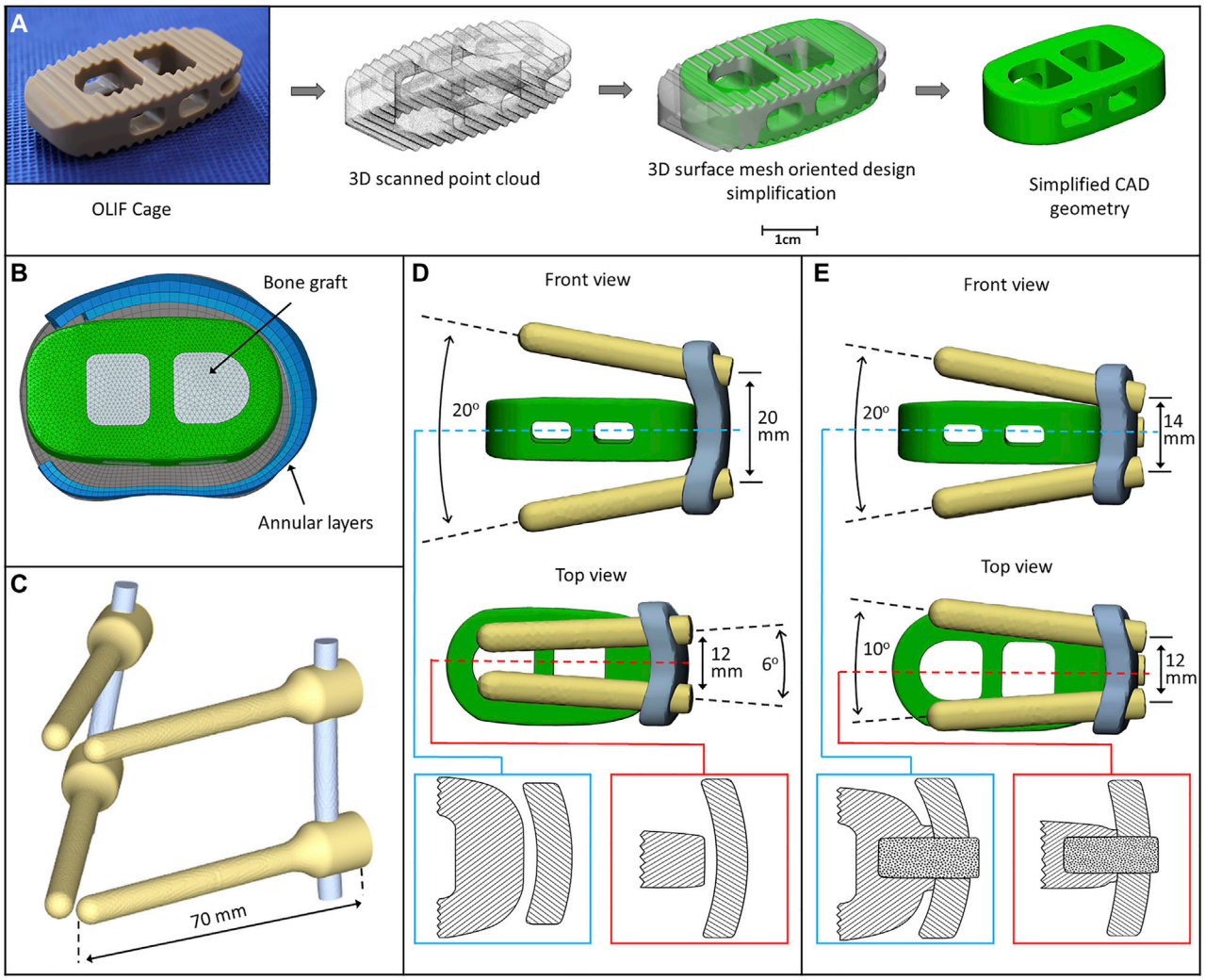

FIGURE 2 | 3D models of the implants. **(A)** Physical OLIF cage and virtually simplified CAD geometry obtained via 3D scanning (point cloud). The 3D surface mesh model oriented the design simplification process. **(B)** Position of the cage inside the intervertebral space. The internal space of the cage is filled with bone graft. **(C)** Bilateral pedicle screw fixation (BPS) model. **(D)** Cage model and lateral plate fixation system with screws (LPS). The cage is not connected to the plate (blue box: axial plane section, red box: sagittal plane section). **(E)** Cage connects to the plate with a screw (SSA) forming a self-anchoring mechanism (blue box: axial plane section, red box: sagittal plane section).

SSA) FE models in the same central position. In order to simulate the surgical nucleotomy, the NP, 4 inner layers of the AF, and the cartilage endplates were removed from the investigated motion segment (L3–L4), and a window was created to insert the cage from the left side of the disc (**Figure 2B**). For the BPS model, 4 identical simplified transpedicular screws (5.5 mm × 70 mm) were placed inside the L3 and L4 pedicles. The screwheads were connected using a 5.5-mm titanium rod (**Figure 2C**). A lateral plate (32 mm × 23 mm × 4 mm) was designed to match the geometry of the L3 and L4 vertebrae with a coronal and an axial curvature for the LPS model, and 4 simplified lateral screws (40 mm × 5.5 mm) were inserted to fix the plate. There was no connection between the plate and the inserted cage (**Figure 2D**). For the SSA model, a smaller bicurved plate (26 mm × 23 mm × 4 mm) was anchored to the cage using a simplified screw (15 mm × 5.5 mm), and the 4 lateral screws were inserted at a different (diverging) axial angle compared to the LPS model (**Figure 2E**). "Tie constraint" was defined between bone–titanium, titanium–titanium, and PEEK–titanium contact surfaces to simulate rigid fixation, and in order to model the knurled surface of the PEEK cage, a 0.2-friction coefficient was set for the bony endplate–PEEK contact surfaces (Ambati et al., 2015). The material properties used in the intact and surgical models can be seen in **Table 1**. Osteoporotic bone mineral density was modeled by decreasing Young's modulus of elasticity by a set amount (**Table 1**), (Polikeit et al., 2003), (Salvatore et al., 2018). **Figure 3**

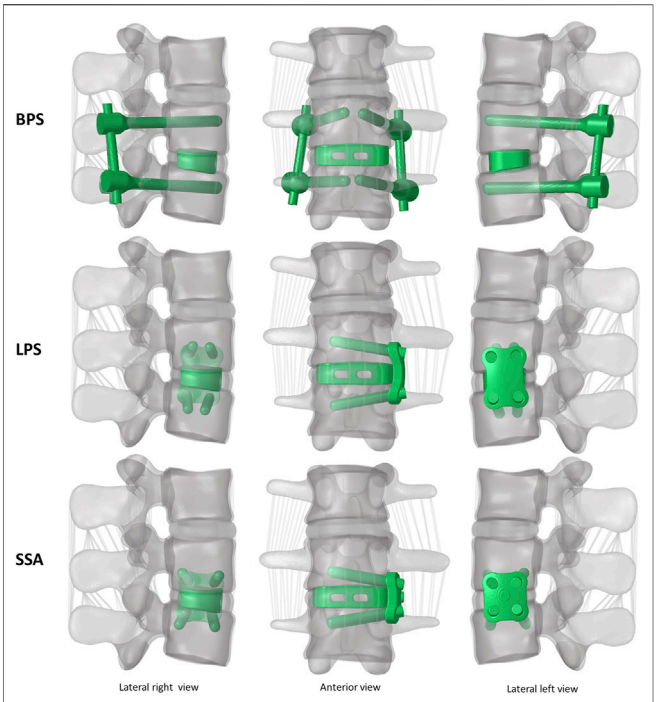

FIGURE 3 | 3D geometry of the bi-segment (L2–L4) model with the three investigated (OLIF) fixation constructs: OLIF cage with bilateral pedicle screws (BPS), OLIF cage with lateral plate system (LPS), OLIF cage with self-anchoring stand-alone system (SSA). Lateral left–right, and frontal view.

presents the construction of OLIF models with various fixation options (BPS, LPS, SSA).

Material Properties, Boundary and Loading Conditions, FE Model Validation

The intact L2–L4 and the six surgical bi-segment FE models (3 normal and 3 osteoporotic) were exported to Abaqus/CAEv11 (Dassault Systemes, Simulia Corp, Providence, RI, United States) software. Material properties and mesh types assigned to the FE models are summarized in **Tables 1**, **2**. In order to validate the created L2–L4 intact model, a pure torque of 7.5 Nm was applied to the L2 vertebral body upper endplate in 3 general directions (flexion-extension, right/left bending, and right/left rotation), while the lower endplate of the L4 vertebra was fixed in place. The intact L2–L3 and L3–L4 segmental range of motions was compared to a cadaveric study (Ilharreborde et al., 2011). The lower endplate of the L4 vertebra was fixed in the case of the six surgical models as well. The simulations were conducted in two steps: first, a 150 N follower load was applied between the vertebral bodies; second, a pure 10 Nm torque was applied to the L2 vertebral body's upper endplate in the three general directions used for the validation process.

RESULTS

Model Validation

In order to evaluate the accuracy of the L2–L4 segmentation process, two investigators created the 3D geometries of the L2–L4 bony structures separately. The obtained DSI value for the vertebrae was 94%, indicating the high accuracy of the segmented models (Yao et al., 2016). The FE mesh quality was evaluated by defining the aspect ratio (AR) of the volume elements (**Supplementary Table S1**) and interpreted according to the literature (Burkhart et al., 2013), (Zhu et al., 2017).

The resulting ROMs were in accordance with the findings of a previous cadaveric study by Ilharreborde et al., 2011 (Ilharreborde et al., 2011), (**Figure 4**). The ROM of the L2–L3 segment in flexion–extension, lateral bending, and axial rotation was 5.86°, 9.01°, and 4.59° respectively. In the cadaveric experiment, the corresponding ROM of the L2–L3 segment was 6.8° ± 2.5°, 7.3° ± 2.3°, and 4.7° ± 2.7°, respectively. For the L3–L4 segment, the ROM for flexion–extension, lateral bending, and axial rotation was 6.19°, 7.92°, 4.72°, respectively in our model and 6.6° ± 3.5°, 7.9° ± 4.5°, and 5.5° ± 3.9° for the cadaveric experiment, respectively.

The ROM comparison's results suggested that the intact L2–L4 FE model in the present study was successfully constructed and could be used for further investigation.

ROM, Displacement, and Cortical Endplate Stress Distribution

In order to compare the primary stabilizing properties of the 3 investigated implants, the ROMs of the virtually operated motion segments were compared. To evaluate the interaction between the inserted cage and the bony endplate below it, the cage's caudal displacement and the endplate's surface stress distribution were investigated. Additionally, the osteoporosis-induced increase in L4 screw displacement was studied to better understand which implant's screws are the least affected by osteoporosis. A total of six surgical constructs were modeled and analyzed, corresponding to the BPS, LPS, and SSA fixation options with normal and osteoporotic bone material properties. The ROM of the surgical models under a combined load of 150 N follower load and 10 Nm torque is shown in **Figure 5A**. After the OLIF cage was inserted, the predicted ROM at the surgical level (L3–L4) decreased under all motion conditions compared with the intact model (**Figures 4**, **5A**). Osteoporosis increased the ROM in all directions compared to the normal bone material property models. The highest impact caused by osteoporosis on the ROM occurred in the LPS fixation construct, where the ROM increased by 97.3% in flexion, 86.3% in extension, 30.14% in left bending, 140.26% in right bending, 50.96% in left rotation, and 53.38% in right rotation. The BPS provided the most stable primary fixation with low ROM values in normal and osteoporotic conditions with the exception of the right-bending scenario. The highest difference between the BPS and lateral plate systems (LPS, SSA) was found in the left- and right-side rotations. For normal bone, the difference in

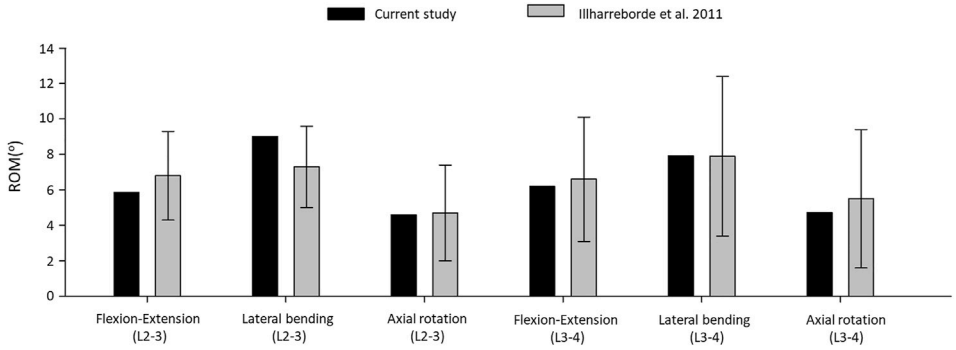

FIGURE 4 | Comparison of the computed range of motions given by the intact L2–L4 bi-segmetal model with experimental results for 7.5-Nm pure moments.

BPS vs LPS was 99% and BPS vs SSA was 119.73%, and for the porotic bone, BPS vs LPS was 158.94% and BPS vs SSA was 145.49%.

Osteoporosis increased the cage's displacement in the caudal direction (U3) for all of the fixation constructs (**Figure 5B**). The highest increase in displacement was found in right bending for the LPS (from 0.115 to 0.24 mm, 109%) and for the SSA (from 0.113 to 0.237 mm, 110%) fixation. With the exception for flexion and left bending, the BPS fixation had lower displacement values both for normal and osteoporotic conditions compared to the LPS and SSA fixation. Overall, the cage displacement values were similar for the SSA and LPS fixation.

The von Mises stress peaks on the L4 upper cortical endplate are shown in **Figure 5C**. Compared to the normal bone, the stress peaks increased in the osteoporotic models for extension, right bending, and right rotation. In flexion and left bending, the stress peaks for the BPS model were much higher compared to the other models (LPS, SSA) regardless of the bone material properties (Von Mises stress peaks for BPS were 10.92 and 13.31 MPa for flexion and left bending in normal bone, respectively, and 14.43 and 16.06 MPa in osteoporotic condition, respectively). To investigate this phenomenon, the von Mises stress distribution on the L4 upper cortical endplates was visualized using contour plots (**Figure 6**). This showed that the exceeding von Mises stress peaks in flexion and left bending for the BPS models are stress concentrations at the place of the fenestration made on the AF and the OLIF cage border.

The screw displacement was measured by highlighting the screw tips inside the L4 vertebra in the 3 constructs. The distance between two points were measured: Point 1: screw tip location before applying the forces. Point 2: screw tip location after the last "step" ("step" is a basic concept in Abaqus FE solver software) (Manual, 2020) of the simulation in a direction, and the result was the average of the 2 values (there were always 2 screws inside the L4 vertebra).

Osteoporosis increased the screw displacement in the L4 vertebra in all motion conditions compared to the normal bone models (**Figure 5D**). The highest increase was found in the case of LPS fixation for left (100%) and right (100%) rotation. The impact of osteoporosis on the BPS fixation's screw displacement was lower in all of the six modeled motions, compared to the other two implants (screw displacement increase in the BPS model for flexion: 61.38%, extension: 40.38%, left bending: 31%, right bending: 39%, left rotation: 36.32%, and right rotation: 33.48%).

DISCUSSION

In the past decade, due to the advancement in minimally invasive spinal fusion technologies (Yue et al., 2010), the OLIF procedure has emerged, and it has been used ever more often by spine surgeons. The advantages of the OLIF surgical technique include the preservation of the posterior structures of the lumbar spine, reduced blood loss, and shorter hospital stay (Phan et al., 2016). Despite the fact that OLIF has been successfully adopted in the clinical environment, the risks of cage subsidence and screw loosening are possible postoperative complications related to this technique (Quillo-Olvera et al., 2018). Biomechanical failure of the stabilization construct (cage subsidence and loosening of the screws) is a multifactorial phenomenon (damage to endplates during preparation, overdistraction, cage design, etc.) (Quillo-Olvera et al., 2018). Bone quality as well as the biomechanical stability of the whole fusion construct can play a significant role in the development of this complication, possibly influencing the short- and long-term therapeutic outcome. The present study aimed to investigate the effect of bone quality on the stability of a fused segment with the aid of FEA models in 3 different fixation options.

First, an intact L2–L4 bi-segment FE model was developed and validated by comparing the ROMs (ante-retroflexion, lateral flexion, and rotation) under a pure 7.5 Nm torque to the findings of a previous cadaveric study by Ilharreborde et al. (Ilharreborde et al., 2011). The adequate validation results (**Figure 4**) allowed us to take a step further and modify the FE model to establish different OLIF construct models: BPS, LPS, and SSA with normal and osteoporotic bone material properties (**Figure 3**).

The ROM of the surgical models under a combined load of 150 N follower load and 10 Nm torque (**Figure 5A**) showed different behaviors based on the fixation type and bone material properties (normal/osteoporotic). The BPS fixation provided the most stable primary fixation in both

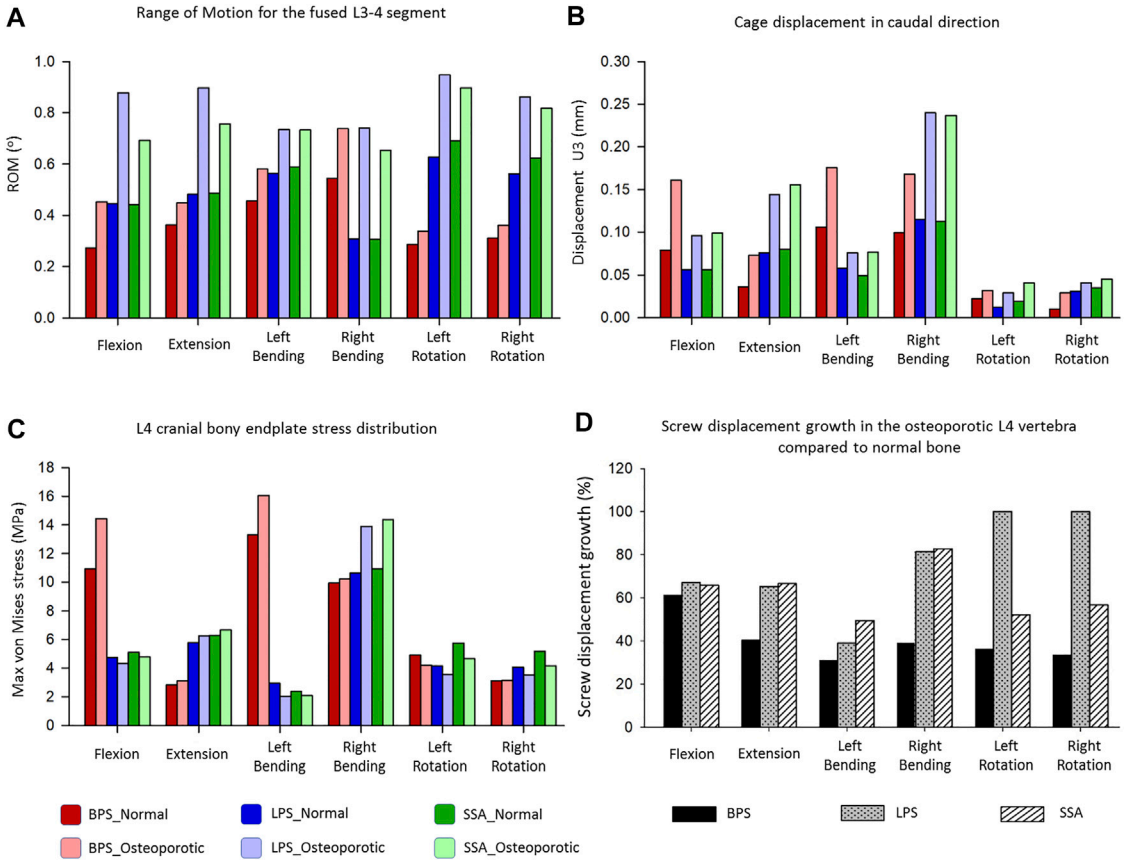

FIGURE 5 | Results of the simulations extracted from the surgically reconstructed bi-segmental FEA model according to the six loading scenarios in normal and osteoporotic conditions. **(A)** Range of motion (ROM) values for the operated L3–L4 segment containing the investigated implant constructs (BPS: bilateral pedicle screw, LPS: lateral plate-screw, SSA: self-anchored stand-alone). **(B)** Cage displacement in the caudal direction (U3 in Abaqus). **(C)** Von Mises stress peaks on the L4 cranial bony endplate. **(D)** Measured L4 screw displacement increase (%) caused by osteoporotic bony conditions compared to L4 screw displacements inside the normal bone.

normal and osteoporotic conditions. These findings are in accordance with the study by Guo et al. (Guo et al., 2020) who used a L3–L5 bi-segment FE model to evaluate OLIF constructs with various fixation options under the same combined loading of 150 N follower load and 10 Nm torque. They applied normal bone material properties and found similar results for the ROMs and also found that the BPS fixation provides the highest stability compared to lateral-only fixations.

To our knowledge, the first study to apply FE models to establish an osteoporotic spine model (L1–S1) to research the single-segment (L3–L4) biomechanical stability of OLIF with different fixation methods was recently published by Song et al. (Song et al., 2021). They found a similar trend in their results that the BPS fixation provides a more stable fixation than lateral plates in normal and osteoporotic conditions despite the differences between their (boundary conditions: axial compressive preload of 400 N, and torsional moment of 10 Nm) and our models. Song's lateral plate fixation design concept differed from our model (the lateral plate was fixed to the vertebral body with 2 screws in their model, while 4 screws were used in our constructs), and his investigation did not include the SSA OLIF cage concept. Based on our results, osteoporosis increased the ROM in all motion conditions compared to the normal bone material property models. The highest impact caused by osteoporosis on the ROM occurred in the LPS fixation construct. The highest difference between the BPS and lateral plate systems (LPS, SSA) was found in rotational movements.

Osteoporosis increased the cage displacement in the caudal direction (U3 in Abaqus) for all of the fixation options (**Figure 5B**). Overall, the cage displacement values were similar for the SSA and LPS systems. The highest increase in displacement was found in right bending for the LPS and SSA implants. With the exception of flexion, and left bending BPS fixation had lower displacement values both for normal and osteoporotic conditions. Parallel to the caudal displacement, the opposite side of the cages can move in the cranial direction (**Supplementary Figure S1**). The complex mechanism of subsidence involving the upper and lower endplates supported by radiologic findings is still widely investigated (Quillo-Olvera et al., 2018).

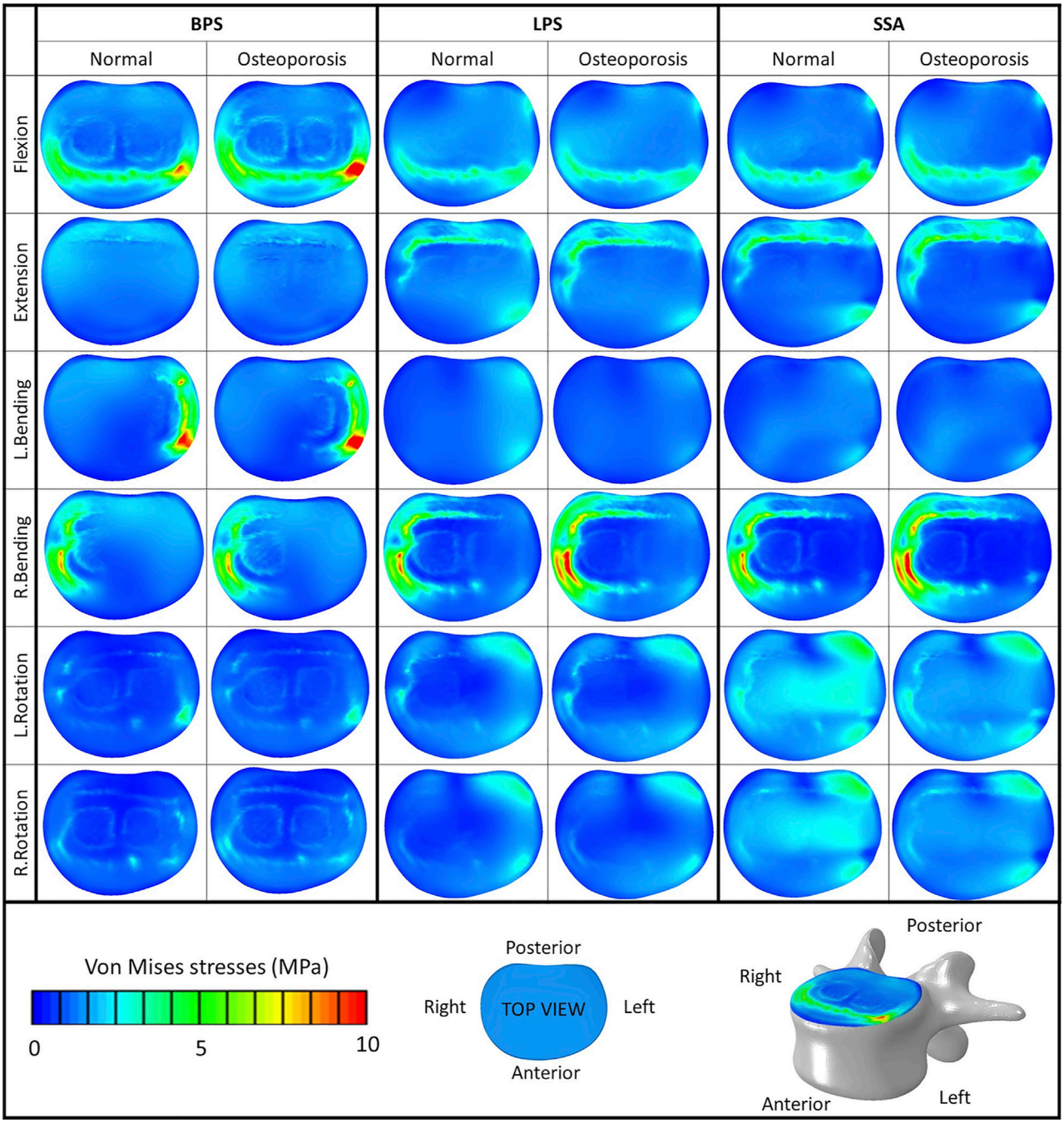

FIGURE 6 | Von Mises stress distribution on the cranial bony endplate of the L4 vertebra, with various fixation options (BPS: bilateral pedicle screw, LPS: lateral plate-screw, SSA: self-anchored stand-alone) in normal and osteoporotic conditions under six loading scenarios. Color bar (blue/green/red), scale (0–10 MPa), top view.

Compared to normal bone, in the osteoporotic models we have measured increased values for the von Mises stress peaks on the L4 upper cortical endplate (**Figure 5C**) for extension, right bending, and right rotation. In flexion and left bending, the BPS model's peek stress values were much higher compared to the other models (LPS, SSA) regardless of the bone material properties. Stress concentrations at the place of the AF fenestration and the OLIF cage border occurred in the BPS model in flexion and left bending (**Figure 6**). In the other loading scenarios, higher stresses can be observed on the endplate surface for the LPS and SSA models compared to the BPS model. Song's study found that on the investigated L4 endplate, the stress increases with osteoporosis, but it is lower for the BPS implants compared to lateral plate fixation (Song et al., 2021).

Osteoporosis increased the screw displacement in the L4 vertebra in all motion conditions compared to normal bone models (**Figure 5D**). The highest increase was found in the case of LPS fixation for left (100%) and right (100%) rotation. The impact of osteoporosis on the BPS fixation screw displacement was lower in all of the six modeled motions compared to the other fixations.

The results of this study highlight that the possible advantages of the LPS and SSA fixations (e.g., lower operation time and invasiveness due to the lack of the posterior–percutaneous–fixation steps) could be hindered in osteoporotic patients. In osteoporotic patients, the BPS fixation provides a more stable fixation than the LPS and SSA fixation, which is important to avoid mechanical complications and provide optimal therapeutic outcome.

Although the FE analysis has many advantages over *in vitro* experiments, it has limitations as well, for example, its inability to "perfectly" mimic the human tissue mechanics. In order to simulate certain biomechanical processes inside the human body, simplifications need to be performed due to the limitations of *in silico* software. Osteoporotic and normal bone qualities are not uniformly distributed within the human skeleton. There can be vertebrae and regions inside the vertebrae that are more affected by osteoporosis and can lead to weaker spots. This line of thought leads to an infinite amount of bone material property distribution models, so we have chosen the path of creating a uniform bone material model for our investigations. The osteoporosis FE model was constructed by decreasing the elastic modulus of the normal uniform cortical and cancellous bone by a certain proportion. However, in the literature, more complex approaches are described to model osteoporosis, by integrating micro-level trabecular structural mechanics (McDonald et al., 2010). With ageing, degenerative changes can occur in the spine not only affecting the vertebral bone material properties but also the geometry (exp. stabilizing osteophytes) (Margulies et al., 1996) and the internal structure of the intervertebral disc as well. Therefore, in an osteoporotic model, the non-surgically treated discs and bony structures should be altered accordingly.

In this study, the osteoporotic model had the same bony geometry and intervertebral disc material properties as the normal bony model.

The developed model investigated the primary stability of the constructs right after the surgery, not taking into consideration the expected fusion process because long-term bony fusion is often the desired result of an adequately chosen implant and correctly executed surgery.

CONCLUSION

Bilateral pedicle screw (BPS) and rod fixation provided superior primary biomechanical stability for OLIF cages, compared to self-anchored stand-alone (SSA) or lateral plate-screw fixated (LPS) cages in both normal and osteoporotic conditions. Osteoporosis amplified the difference between the stability of the bilateral pedicle screw fixation and the two other investigated fixation methods. Clinically, in the case of decreased bone quality (primary or secondary osteoporosis), the surgeon has to take into consideration the limits of the SSA and LPS fixations, despite the advantage that there is no need for a second step in the surgery by turning the patient to the prone position to perform the percutaneous pedicle screw fixation. This study highlights the need for further investigation (experimental and clinical trials) to adjust the indication of the fixation methods in OLIF to the patient's bone quality.

DATA AVAILABILITY STATEMENT

The original contributions presented in the study are included in the article/**Supplementary Material**; further inquiries can be directed to the corresponding author.

ETHICS STATEMENT

The studies involving human participants were reviewed and approved by the National Ethics Committee of Hungary and the National Institute of Pharmacy and Nutrition (reference number: OGYÉI/163-4/2019). The patients/participants provided their written informed consent to participate in this study.

AUTHOR CONTRIBUTIONS

PE, RK, and AL: research design; FB, MT, PE, and AL: acquisition of data. All were involved in the analysis and/or interpretation of data and drafting the article or revising it critically. All approved the submitted and final version.

FUNDING

The project leading to the scientific results was supported by the Hungarian Scientific Research Fund grant Budapest, Hungary, (award number: OTKA FK123884), and by the Doctoral Student Scholarship Program of the Co-operative Doctoral Program of the Ministry of Innovation and Technology, Hungary, financed from the National Research, Development and Innovation Fund (C1014064). The financial support from these funding bodies are gratefully acknowledged.

SUPPLEMENTARY MATERIAL

The Supplementary Material for this article can be found online at: https://www.frontiersin.org/articles/10.3389/fbioe.2021.749914/full#supplementary-material

REFERENCES

Akamaru, T., Kawahara, N., Sakamoto, J., Yoshida, A., Murakami, H., Hato, T., et al. (2005). The Transmission of Stress to Grafted Bone inside a Titanium Mesh Cage Used in Anterior Column Reconstruction after Total Spondylectomy: A Finite-Element Analysis. *Spine* 30, 2783–2787. doi:10.1097/01.brs.0000192281.53603.3f

Ambati, D. V., Wright, E. K., Lehman, R. A., Kang, D. G., Wagner, S. C., and Dmitriev, A. E. (2015). Bilateral Pedicle Screw Fixation Provides superior Biomechanical Stability in Transforaminal Lumbar Interbody Fusion: A Finite Element Study. *Spine J.* 15, 1812–1822. doi:10.1016/j.spinee.2014.06.015

Aryanto, K. Y. E., Oudkerk, M., and van Ooijen, P. M. A. (2015). Free DICOM De-identification Tools in Clinical Research: Functioning and Safety of Patient Privacy. *Eur. Radiol.* 25, 3685–3695. doi:10.1007/s00330-015-3794-0

Bharatha, A., Hirose, M., Hata, N., Warfield, S. K., Ferrant, M., Zou, K. H., et al. (2001). Evaluation of Three-Dimensional Finite Element-Based Deformable Registration of Pre- and Intraoperative Prostate Imaging. *Med. Phys.* 28, 2551–2560. doi:10.1118/1.1414009

Brekelmans, W. A. M., Poort, H. W., and Slooff, T. J. J. H. (1972). A New Method to Analyse the Mechanical Behaviour of Skeletal Parts. *Acta Orthopaedica Scand.* 43, 301–317. doi:10.3109/17453677208998949

Burkhart, T. A., Andrews, D. M., and Dunning, C. E. (2013). Finite Element Modeling Mesh Quality, Energy Balance and Validation Methods: A Review with Recommendations Associated with the Modeling of Bone Tissue. *J. Biomech.* 46, 1477–1488. doi:10.1016/j.jbiomech.2013.03.022

Castro-Mateos, I., Pozo, J. M., Lazary, A., and Frangi, A. (2015). "3D Vertebra Segmentation by Feature Selection Active Shape Model," in *Recent Advances in Computational Methods and Clinical Applications for Spine Imaging* (Springer), 241–245.

Chung, N.-S., Jeon, C.-H., Lee, H.-D., and Kweon, H.-J. (2017). Preoperative Evaluation of Left Common Iliac Vein in Oblique Lateral Interbody Fusion at L5-S1. *Eur. Spine J.* 26, 2797–2803. doi:10.1007/s00586-017-5176-6

Dreischarf, M., Zander, T., Shirazi-Adl, A., Puttlitz, C. M., Adam, C. J., Chen, C. S., et al. (2014). Comparison of Eight Published Static Finite Element Models of the Intact Lumbar Spine: Predictive Power of Models Improves when Combined Together. *J. Biomech.* 47, 1757–1766. doi:10.1016/j.jbiomech.2014.04.002

Fagan, M. J., Julian, S., and Mohsen, A. M. (2002). Finite Element Analysis in Spine Research. *Proc. Inst. Mech. Eng. H* 216, 281–298. doi:10.1243/09544110260216568

Fehlings, M. G., Tetreault, L., Nater, A., Choma, T., Harrop, J., Mroz, T., et al. (2015). The Aging of the Global Population. *Neurosurgery* 77, S1–S5. doi:10.1227/neu.0000000000000953

Finley, S. M., Brodke, D. S., Spina, N. T., DeDen, C. A., and Ellis, B. J. (2018). FEBio Finite Element Models of the Human Lumbar Spine. *Comp. Methods Biomech. Biomed. Eng.* 21, 444–452. doi:10.1080/10255842.2018.1478967

Fuster, V. (2017). *Changing Demographics: A New Approach to Global Health Care Due to the Aging Population*.

Guo, H.-z., Tang, Y.-c., Guo, D.-q., Luo, P.-j., Li, Y.-x., Mo, G.-y., et al. (2020). Stability Evaluation of Oblique Lumbar Interbody Fusion Constructs with Various Fixation Options: A Finite Element Analysis Based on Three-Dimensional Scanning Models. *World Neurosurg.* 138, e530–e538. doi:10.1016/j.wneu.2020.02.180

Hah, R., and Kang, H. P. (2019). Lateral and Oblique Lumbar Interbody Fusion-Current Concepts and a Review of Recent Literature. *Curr. Rev. Musculoskelet. Med.* 12, 305–310. doi:10.1007/s12178-019-09562-6

Ilharreborde, B., Shaw, M. N., Berglund, L. J., Zhao, K. D., Gay, R. E., and An, K.-N. (2011). Biomechanical Evaluation of Posterior Lumbar Dynamic Stabilization: An *In Vitro* Comparison between Universal Clamp and Wallis Systems. *Eur. Spine J.* 20, 289–296. doi:10.1007/s00586-010-1641-1

Li, R., Li, X., Zhou, H., and Jiang, W. (2020). Development and Application of Oblique Lumbar Interbody Fusion. *Orthop. Surg.* 12, 355–365. doi:10.1111/os.12625

Lu, Y. M., Hutton, W. C., and Gharpuray, V. M. (1996). Do Bending, Twisting, and Diurnal Fluid Changes in the Disc Affect the Propensity to Prolapse? A Viscoelastic Finite Element Model. *Spine (Phila Pa 1976)* 21, 2570–2579. doi:10.1097/00007632-199611150-00006

Manual, A. U. (2020). *Abaqus User Manual*. Johnston, RI: Abacus.

Margulies, J. Y., Payzer, A., Nyska, M., Neuwirth, M. G., Floman, Y., and Robin, G. C. (1996). The Relationship between Degenerative Changes and Osteoporosis in the Lumbar Spine. *Clin. Orthop. Relat. Res.* 324, 145–152. Available at:. doi:10.1097/00003086-199603000-00017

Mayer, H. M. (1997). A New Microsurgical Technique for Minimally Invasive Anterior Lumbar Interbody Fusion. *Spine (Phila Pa 1976)* 22, 691–700. doi:10.1097/00007632-199703150-00023

McDonald, K., Little, J., Pearcy, M., and Adam, C. (2010). Development of a Multi-Scale Finite Element Model of the Osteoporotic Lumbar Vertebral Body for the Investigation of Apparent Level Vertebra Mechanics and Micro-level Trabecular Mechanics. *Med. Eng. Phys.* 32, 653–661. doi:10.1016/j.medengphy.2010.04.006

Mehren, C., Mayer, M. H., Zandanell, C., Siepe, C. J., and Korge, A. (2016). The Oblique Anterolateral Approach to the Lumbar Spine Provides Access to the Lumbar Spine with Few Early Complications. *Clin. Orthop. Relat. Res.* 474, 2020–2027. doi:10.1007/s11999-016-4883-3

Mobbs, R. J., Phan, K., Malham, G., Seex, K., and Rao, P. J. (2015). Lumbar Interbody Fusion: Techniques, Indications and Comparison of Interbody Fusion Options Including PLIF, TLIF, MI-TLIF, OLIF/ATP, LLIF and ALIF. *J. Spine Surg.* 1, 2–18. doi:10.3978/j.issn.2414-469X.2015.10.05

Phan, K., Maharaj, M., Assem, Y., and Mobbs, R. J. (2016). Review of Early Clinical Results and Complications Associated with Oblique Lumbar Interbody Fusion (OLIF). *J. Clin. Neurosci.* 31, 23–29. doi:10.1016/j.jocn.2016.02.030

Polikeit, A., Nolte, L. P., and Ferguson, S. J. (2003). The Effect of Cement Augmentation on the Load Transfer in an Osteoporotic Functional Spinal Unit. *Spine* 28, 991–996. doi:10.1097/01.BRS.0000061987.71624.17

Quillo-Olvera, J., Lin, G. X., Jo, H. J., and Kim, J. S. (2018). Complications on Minimally Invasive Oblique Lumbar Interbody Fusion at L2-L5 Levels: a Review of the Literature and Surgical Strategies. *Ann. Transl Med.* 6, 101. doi:10.21037/atm.2018.01.22

Resnick, D. K., Choudhri, T. F., Dailey, A. T., Groff, M. W., Khoo, L., Matz, P. G., et al. (2005). Guidelines for the Performance of Fusion Procedures for Degenerative Disease of the Lumbar Spine. Part 7: Intractable Low-Back Pain without Stenosis or Spondylolisthesis. *J. Neurosurg. Spine* 2, 670–672. doi:10.3171/spi.2005.2.6.0670

Rijsbergen, M. v., van Rietbergen, B., Barthelemy, V., Eltes, P., Lazáry, Á., Lacroix, D., et al. (2018). Comparison of Patient-specific Computational Models vs. Clinical Follow-Up, for Adjacent Segment Disc Degeneration and Bone Remodelling after Spinal Fusion. *PLoS One* 13, e0200899. doi:10.1371/journal.pone.0200899

Rohlmann, A., Bauer, L., Zander, T., Bergmann, G., and Wilke, H.-J. (2006). Determination of Trunk Muscle Forces for Flexion and Extension by Using a Validated Finite Element Model of the Lumbar Spine and Measured *In Vivo* Data. *J. Biomech.* 39, 981–989. doi:10.1016/j.jbiomech.2005.02.019

Rohlmann, A., Zander, T., Rao, M., and Bergmann, G. (2009). Applying a Follower Load Delivers Realistic Results for Simulating Standing. *J. Biomech.* 42, 1520–1526. doi:10.1016/j.jbiomech.2009.03.048

Salvatore, G., Berton, A., Giambini, H., Ciuffreda, M., Florio, P., Longo, U. G., et al. (2018). Biomechanical Effects of Metastasis in the Osteoporotic Lumbar Spine: A Finite Element Analysis. *BMC Musculoskelet. Disord.* 19, 38. doi:10.1186/s12891-018-1953-6

Schmidt, H., Kettler, A., Heuer, F., Simon, U., Claes, L., and Wilke, H.-J. (2007). Intradiscal Pressure, Shear Strain, and Fiber Strain in the Intervertebral Disc under Combined Loading. *Spine* 32, 748–755. doi:10.1097/01.brs.0000259059.90430.c2

Shamji, M. F., Goldstein, C. L., Wang, M., Uribe, J. S., and Fehlings, M. G. (2015). Minimally Invasive Spinal Surgery in the Elderly. *Neurosurgery* 77, S108–S115. doi:10.1227/neu.0000000000000941

Shirazi-Adl, A., Ahmed, A. M., and Shrivastava, S. C. (1986). Mechanical Response of a Lumbar Motion Segment in Axial Torque Alone and Combined with Compression. *Spine* 11, 914–927. doi:10.1097/00007632-198611000-00012

Shirazi-adl, S. A., Shrivastava, S. C., and Ahmed, A. M. (1984). Stress Analysis of the Lumbar Disc-Body Unit in Compression A Three-Dimensional Nonlinear Finite Element Study. *Spine* 9, 120–134. doi:10.1097/00007632-198403000-00003

Silva, M. J., Keaveny, T. M., and Hayes, W. C. (1997). Load Sharing between the Shell and Centrum in the Lumbar Vertebral Body. *Spine (Phila Pa 1976)* 22, 140–150. doi:10.1097/00007632-199701150-00004

Silvestre, C., Mac-Thiong, J.-M., Hilmi, R., and Roussouly, P. (2012). Complications and Morbidities of Mini-Open Anterior Retroperitoneal Lumbar Interbody Fusion: Oblique Lumbar Interbody Fusion in 179 Patients. *Asian Spine J.* 6, 89–97. doi:10.4184/asj.2012.6.2.89

Song, C., Chang, H., Zhang, D., Zhang, Y., Shi, M., and Meng, X. (2021). Biomechanical Evaluation of Oblique Lumbar Interbody Fusion with Various Fixation Options: A Finite Element Analysis. *Orthop. Surg.* 13, 517–529. doi:10.1111/os.12877

Viceconti, M., Clapworthy, G., and Van Sint Jan, S. (2008). The Virtual Physiological Human - a European Initiative for In Silico Human Modelling -. *J. Physiol. Sci.* 58, 441–446. doi:10.2170/physiolsci.RP009908

Yao, J., Burns, J. E., Forsberg, D., Seitel, A., Rasoulian, A., Abolmaesumi, P., et al. (2016). A Multi-center Milestone Study of Clinical Vertebral CT Segmentation. *Comput. Med. Imaging Graphics* 49, 16–28. doi:10.1016/j.compmedimag.2015.12.006

Yue, J. J., Guyer, R., Johnson, J. P., Khoo, L. T., and Hochschuler, S. H. (2010). *The Comprehensive Treatment of the Aging Spine E-Book: Minimally Invasive and Advanced Techniques-Expert Consult*. Elsevier Health Sciences.

Zhang, L., Yang, G., Wu, L., and Yu, B. (2010). The Biomechanical Effects of Osteoporosis Vertebral Augmentation with Cancellous Bone Granules or Bone Cement on Treated and Adjacent Non-treated Vertebral Bodies: A Finite Element Evaluation. *Clin. Biomech.* 25, 166–172. doi:10.1016/j.clinbiomech.2009.10.006

Zhang, Z., Fogel, G. R., Liao, Z., Sun, Y., and Liu, W. (2018). Biomechanical Analysis of Lateral Lumbar Interbody Fusion Constructs with Various Fixation Options: Based on a Validated Finite Element Model. *World Neurosurg.* 114, e1120–e1129. e1129. doi:10.1016/j.wneu.2018.03.158

Zhu, R., Niu, W.-x., Zeng, Z.-l., Tong, J.-h., Zhi-wei, Z., Zhou, S., et al. (2017). The Effects of Muscle Weakness on Degenerative Spondylolisthesis: A Finite Element Study. *Clin. Biomech.* 41, 34–38. doi:10.1016/j.clinbiomech.2016.11.007

Zou, K. H., Warfield, S. K., Bharatha, A., Tempany, C. M. C., Kaus, M. R., Haker, S. J., et al. (2004). Statistical Validation of Image Segmentation Quality Based on a Spatial Overlap index1. *Acad. Radiol.* 11, 178–189. doi:10.1016/S1076-6332(03)00671-8

Conflict of Interest: The authors declare that the research was conducted in the absence of any commercial or financial relationships that could be construed as a potential conflict of interest.

frontiers in Bioengineering and Biotechnology

BRIEF RESEARCH REPORT
published: 22 November 2021
doi: 10.3389/fbioe.2021.745703

The Simulation of Muscles Forces Increases the Stresses in Lumbar Fixation Implants with Respect to Pure Moment Loading

Matteo Panico[1,2]*, *Tito Bassani*[2], *Tomaso Maria Tobia Villa*[1,2] and *Fabio Galbusera*[2]

[1]Department of Chemistry, Materials and Chemical Engineering "Giulio Natta", Politecnico di Milano, Milan, Italy, [2]IRCCS Istituto Ortopedico Galeazzi, Milan, Italy

Simplified loading conditions such as pure moments are frequently used to compare different instrumentation techniques to treat spine disorders. The purpose of this study was to determine if the use of realistic loading conditions such as muscle forces can alter the stresses in the implants with respect to pure moment loading. A musculoskeletal model and a finite element model sharing the same anatomy were built and validated against *in vitro* data, and coupled in order to drive the finite element model with muscle forces calculated by the musculoskeletal one for a prescribed motion. Intact conditions as well as a L1-L5 posterior fixation with pedicle screws and rods were simulated in flexion-extension and lateral bending. The hardware stresses calculated with the finite element model with instrumentation under simplified and realistic loading conditions were compared. The ROM under simplified loading conditions showed good agreement with *in vitro* data. As expected, the ROMs between the two types of loading conditions showed relatively small differences. Realistic loading conditions increased the stresses in the pedicle screws and in the posterior rods with respect to simplified loading conditions; an increase of hardware stresses up to 40 MPa in extension for the posterior rods and 57 MPa in flexion for the pedicle screws were observed with respect to simplified loading conditions. This conclusion can be critical for the literature since it means that previous models which used pure moments may have underestimated the stresses in the implants in flexion-extension and in lateral bending.

Keywords: muscles forces, pure moments, spinal fixation, lumbar fixation, realistic loading conditions, simplified loading conditions

OPEN ACCESS

Edited by:
Ron Noah Alkalay,
Beth Israel Deaconess Medical Center, United States

Reviewed by:
Isador Lieberman,
Texas Back Institute, United States
Dennis E. Anderson,
Harvard Medical School, United States

***Correspondence:**
Matteo Panico
matteo.panico@polimi.it

Specialty section:
This article was submitted to Biomechanics, a section of the journal Frontiers in Bioengineering and Biotechnology

Received: *22 July 2021*
Accepted: *05 November 2021*
Published: *22 November 2021*

Citation:
Panico M, Bassani T, Villa TMT and Galbusera F (2021) The Simulation of Muscles Forces Increases the Stresses in Lumbar Fixation Implants with Respect to Pure Moment Loading. Front. Bioeng. Biotechnol. 9:745703. doi: 10.3389/fbioe.2021.745703

INTRODUCTION

Spinal fixation has become a consolidated treatment for severe degenerative spinal disorders such as adult scoliosis, fixed sagittal imbalance, and high-grade spondylolisthesis (Ha et al., 2008; Casaroli et al., 2019; Galbusera et al., 2020). Despite the generally high success rates of spine surgeries nowadays, biomechanical complications such as hardware failure and loosening are relatively frequent (Kuklo et al., 2001; Tsuchiya et al., 2006; Kebaish, 2010). The literature indeed includes several studies in which different spinal fixation techniques have been investigated in terms of stresses and strains in the instrumentation (Fleischer et al., 2012; Burns et al., 2016; Sutterlin et al., 2016; Casaroli et al., 2019; Cunningham et al., 2019; Zhang and Zhu, 2019), which can be considered as indicators of the risk of biomechanical complications.

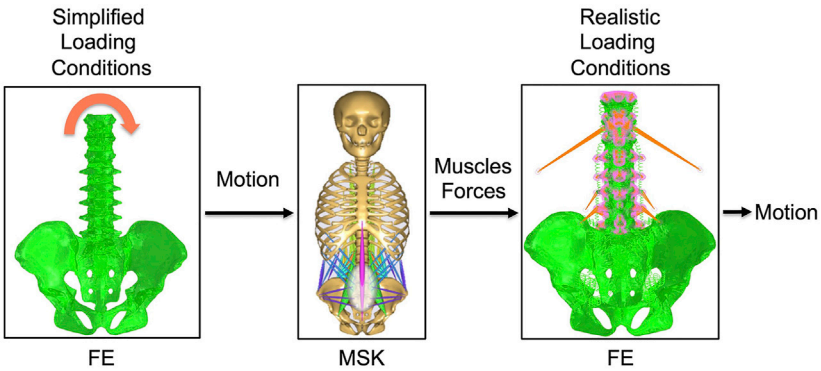

FIGURE 1 | The combination of the intact FE model with the intact MSK model. Simplified loading conditions are applied to the FE model in order to obtain the motion. This motion is imposed as input to the MSK model and muscles forces that contribute to give that motion are predicted by this model. Muscles forces are then applied to the FE model to realistically simulate the loading conditions. The motion under realistic loading conditions is then obtained.

Most of the *in vitro* and finite element (FE) studies have been conducted using simplified loading conditions, usually consisting of pure moments, in some cases in combination with compressive forces, which are easier to implement than more realistic conditions involving muscle forces (Stokes and Gardner-Morse, 1995; Wilke et al., 2001; Kim et al., 2014; Zhang and Zhu, 2019). Although several studies confirmed that applying simplified or realistic loading conditions provides the same motion in intact spines (Rohlmann et al., 2009; Han et al., 2011; Zhang and Zhu, 2019), the effect on the instrumentation stresses has never been documented.

As regards the identification of realistic loads, software for musculoskeletal (MSK) modelling such as AnyBody (AnyBody Technology, Aalborg, Denmark) and OpenSim (Stanford University, Stanford, US) provide pre-built models able to predict the muscle forces for any imposed motion of the body segments using algorithms based on inverse dynamics (Bruno et al., 2015; Bassani et al., 2017; Benditz et al., 2018; Liu et al., 2018; Liu et al., 2019). Such models are based on the equations of motion of rigid bodies and cannot therefore be used to estimate the stresses in the implants or in biological structures (Zhu et al., 2013; Arshad et al., 2016; Liu et al., 2018; Bassani et al., 2019). However, the computed muscle forces can be applied as loading condition from the MSK model to the FE model, from which detailed information regarding the hardware stresses can be extracted (Bassani et al., 2017; Liu et al., 2018; Bassani et al., 2019; Liu et al., 2019). Such strategy, coupling FE and MSK models, has never been used to investigate the instrumentation stresses after spinal fixation, and can represent an advantageous approach to determine if the simplified loading conditions consisting of pure moments used in the majority of the available studies are good enough to accurately estimate the hardware stresses in physiological conditions. The aim of this study is therefore to develop and validate coupled FE-MSK models with and without instrumentation and to explore the differences, in terms of hardware stresses, between simplified (pure moment without follower load) and realistic loading conditions.

MATERIALS AND METHODS

Intact Model

The three-dimensional (3D) geometry of T10-T12 thoracic vertebrae, lumbar vertebrae, and pelvis of the body model from the AnyBody Managed Model Repository (AMMR, version 2.0.0) in the standing posture was used to construct a FE model (**Figure 1**) made of linear tetrahedral elements after the surfaces were cleaned using MeshLab software (http://www.meshlab.net). Then, the triangular elements of the surfaces of the vertebral endplates were extruded in order to obtain a volume made by tetrahedral elements representing the discs, which were divided into nucleus pulposus and annulus fibrosus based on anatomical data from the literature (Zhong et al., 2014). The annulus included collagen fibers modeled with nonlinear springs; ligaments were also modelled with the same type of elements. The material properties of the bones, intervertebral discs and ligaments were obtained with a calibration procedure based on data reported in the literature (Schmidt et al., 2007). Pure moments of 7.5 Nm in extension, flexion, lateral bending, and axial rotation were applied as simplified loading condition to the upper endplate of T10 through a set of rigid beam elements (**Figure 1**). The acetabula were completely fixed during all the simulation. The range of motion (ROM) calculated at all levels were then compared to *in vitro* data in order to validate the FE model under simplified loading conditions (Cook et al., 2015; Lindsey et al., 2018).

Then, the obtained ROMs were used as inputs for the MSK model of the thoracolumbar spine with articulated ribcage (**Figure 1**) developed and validated by Ignasiak et al. (Ignasiak et al., 2016). The muscles simulated in this MSK model were transversus, spinalis, semispinalis, erector spinae, obliquus internus, obliquus externus, psoas major, multifidi, and quadratus lumborum. In this model, the rotational stiffness of the intervertebral joints was calibrated in order to match the linear moment-rotation behavior of the FE model, including the effects of all the joint structures (including facet joint and ligaments). This stiffness does not account for compressive

loading or coupling. The pelvis was constrained to the ground. Extension, flexion, and left and right lateral bending movements were simulated by imposing intervertebral rotations matching those calculated with the validated FE model under simplified loading conditions. The muscle forces were calculated for each simulated motion by inverse static analysis (**Figure 1**).

After that, the obtained muscles forces were modelled at each level (from T10 to the pelvis) in the FE model as concentrated loads to simulate the realistic loading condition (**Figure 1**), removing the pure moment which implemented the simplified loading conditions; the upper endplate of the T10 vertebra was subjected to a 3D translation equal to that predicted by the MSK model, using a set of rigid beam elements. Moreover, reaction loads from the MSK model were applied to the upper endplate of the T10. Such loading conditions were applied to the FE model for all the investigated motions: extension, flexion, left and right lateral bending. Finally, a validation of the FE model under realistic loading conditions was performed by comparing the ROMs obtained under realistic loading conditions (**Figure 1**) and the one imposed as input for the MSK model. Ideally, for the validation the ROMs values had to be equal. Moreover, the reaction moment at the upper endplate of T10 was compared between MSK model and FE model in order to provide an extra validation.

Instrumented Model

From the intact FE model, an instrumented model was derived. This model included a posterior lumbar fixation in which pedicle screws and rods were inserted in the lumbar region between L1 and L5 vertebrae. 3D models of rods and screws were created with commercial software Solidworks (Dassault Systèmes, Waltham, MA, USA). Rods had a circular section with a diameter of 5.5 mm. Pedicle screws had a length of 45 mm and a diameter of 6 mm. The instrumentation was modelled in titanium with an elastic modulus of 110 GPa and a Poisson coefficient of 0.3. Simplified loading conditions and boundary conditions were the same as in the intact model (**Figure 1**).

Similarly, an instrumented MSK model was created from the intact one. Spinal fusion was modeled by introducing rigid kinematic and kinetic constraints from L1 to L5 vertebrae, guaranteeing rigid connection (no relative motion between vertebrae) and full force and moment transmission (Ignasiak et al., 2018; Ignasiak, 2020). The validation of this model was performed against an *in vivo* study by Rohlmann (Rohlmann et al., 1997), in which bending moments in the posterior rods were measured by means of instrumented implants. Extension, flexion, and left and right lateral bending movements were simulated imposing the intervertebral rotations calculated with the instrumented FE model under simplified loading conditions. From this model, muscle forces were obtained for the four different motions, as for the intact model (**Figure 1**).

Realistic loading conditions were then simulated in the instrumented model as for the intact model (**Figure 1**). The FE model under realistic loading conditions was then validated by comparing the intervertebral motion calculated with it with the one imposed as input for the MSK model. As for the intact model, the reaction moment at the upper endplate of T10 was compared between those predicted by the MSK and the FE models in order to provide an extra validation.

Validation and Output

The outputs of the intact models that were calculated for two types of loading conditions were: 1) the ROM of L1-S1 vertebrae and SIJ; 2) the reaction moment at the upper endplate of T10 joint. The 1) values were used to validate the intact FE model under simplified loading conditions (Cook et al., 2015; Lindsey et al., 2018). 1) and 2) values were used to validate the intact FE model under realistic loading conditions.

The outputs of the instrumented models that were calculated for two types of loading conditions were, in addition to those of the intact model, also: 3) the maximal von Mises stresses in L1-L5 pedicle screws; 4) the maximal von Mises stresses in the posterior rods between the pedicle screws in L1 and L5. The 1) values were used to validate the instrumented FE model under simplified loading conditions. The 1) and 2) values were used to validate the instrumented FE model under realistic loading conditions. The 3) and 4) values were used to compare the hardware stresses between the finite element model under simplified loading conditions and those under realistic loading conditions.

RESULTS

Validation of the Intact Model

The ROMs calculated with the intact FE model under simplified loading conditions showed a tendency toward a higher rigidity with respect to the literature (Cook et al., 2015; Lindsey et al., 2018) (**Figure 2**); despite this, the predicted values were inside the standard deviations of the *in vitro* data in flexion-extension and axial rotation, except for the L1-L2 ROM in axial rotation which was higher than the corresponding experimental finding. In lateral bending, the ROM was approximately equal to the lower limit of the standard deviations of the *in vitro* studies, except for the SIJ ROM which was in agreement with the value found in the literature.

The ROM calculated with the intact model under realistic loading conditions revealed values similar to those calculated with the intact model under simplified loading conditions in flexion-extension and lateral bending, as expected (**Figure 3A**); nevertheless, some relatively small differences were observed. For instance, negligible differences up to 0.7° were found in lateral bending. The reaction moment at the upper endplate of T10 showed a maximal relative difference of 3.5% between the FE model and the MSK model.

Validation of the Instrumented Model

The instrumented FE model showed that the ROM of instrumented levels was negligible with respect to the case without instrumentation, as seen in computational and *in vitro* studies (Rohlmann et al., 2007; Dmitriev et al., 2008). The reaction moments at the instrumented levels obtained with the MSK model were inside the range of fixator load measurements assessed *in vivo* (Rohlmann et al., 1997), demonstrating the plausibility of the results.

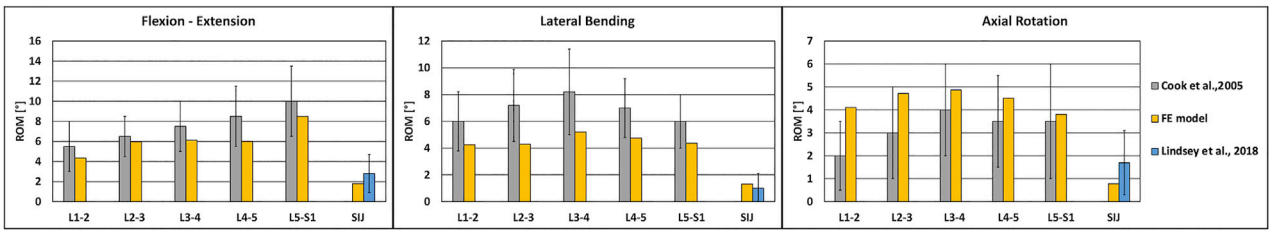

FIGURE 2 | Validation of the intact FE model under simplified loading conditions. Predicted ranges of motion of L1-S1 and sacroiliac joints of the intact model under simplified loading conditions in flexion-extension **(left),** lateral bending (middle) and axial rotation **(right),** as compared with data from *in vitro* experiments, shown as mean and standard deviation (Cook et al., 2015; Lindsey et al., 2018).

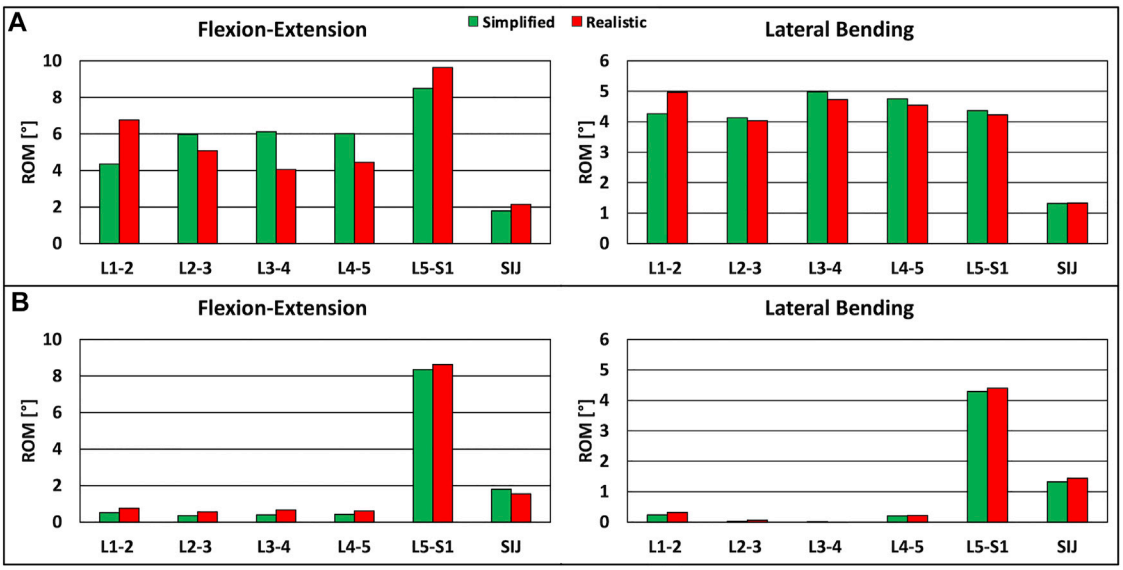

FIGURE 3 | Predicted ranges of motion of L1-S1 and sacroiliac joints under simplified loading conditions and under realistic loading conditions. **(A)** For the intact model in flexion-extension **(left)** and lateral bending **(right). (B)** For the instrumented model, in flexion-extension **(left)** and lateral bending **(right)**.

The comparison of the ROMs under simplified and realistic loading conditions revealed very similar values in the two cases, with small differences up to 0.3° in flexion-extension (**Figure 3B**). The reaction moment at the upper endplate of T10 showed a negligible difference between the FE model and the MSK model.

Stresses in the Pedicle Screws

In extension, flexion, lateral bending on the left side, and lateral bending on the right side, the maximum stresses on the L1-L5 pedicle screws were higher when realistic loading conditions were applied to the model (**Figures 4A,B**). In extension, the maximum stresses for the L1-L4 pedicle screws were higher than the values found with simplified loading conditions. With respect to simplified loading conditions, an increase of 44 MPa (5.6% with respect to the yield stress) for the right pedicle screw in L1 was found under realistic loading conditions. The maximum stresses for the L5 pedicle screws showed more comparable values, with changes up to up to 3 MPa. In flexion, results similar to the extension case were found, but with bigger differences; the highest difference was found for the left pedicle screw in L3 (7.2% with respect to the yield stress) (**Figure 4A**). For lateral bending, higher stresses on all pedicle screws were predicted when realistic loading conditions were used; the maximal difference resulted to be 45 MPa (5.7% with respect to the yield stress) (**Figure 4B**).

Stresses in the Posterior Rods

The maximal stresses on the left and right posterior rods had similar values among simplified and realistic loading conditions (**Figures 4A,B**). Similar to the pedicle screws, the maximal stresses on the posterior rods were highest when realistic loading conditions were simulated. In flexion-extension, increases exceeding 99% were found with a maximal difference of 40 MPa in extension (5.1% with respect to the yield stress) (**Figure 4A**). The same trend was observed in lateral bending, but with smaller differences up to 33 MPa (4.2% with respect to the yield stress) (**Figure 4B**).

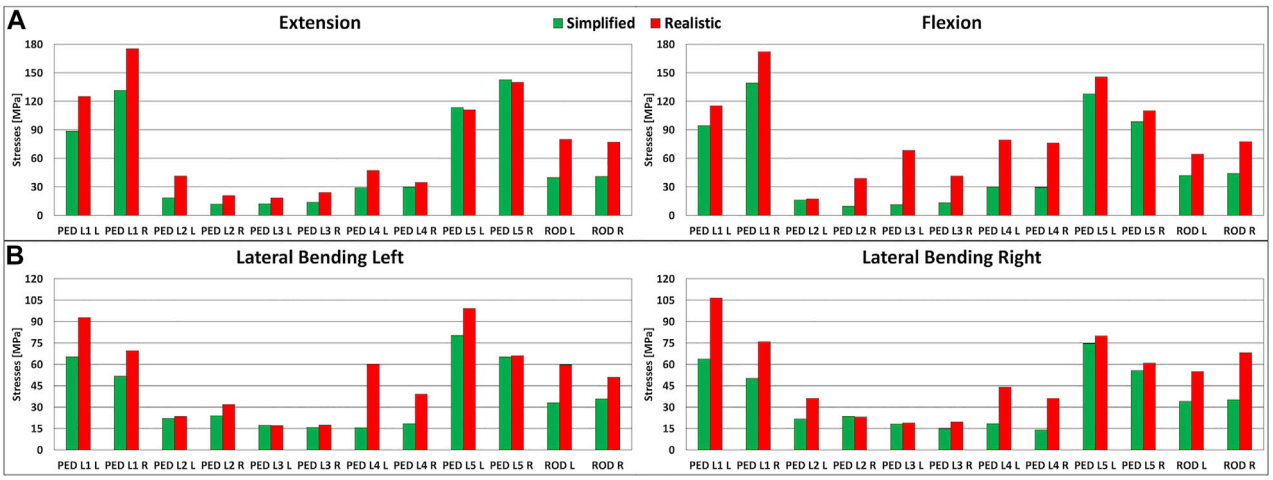

FIGURE 4 | Stresses in the left and right lumbar instrumentation and in the left and right posterior rods. **(A)** Maximal stresses in the L1-L5 pedicle screws and posterior rods in extension **(left)** and in flexion **(right). (B)** Maximal stresses in the L1-L5 pedicle screws and posterior rods in lateral bending on the left side **(left)** and on the right side **(right).**

DISCUSSION

This paper presents a preliminary biomechanical comparison between simplified and realistic loading conditions to determine the hardware stresses in a spinal fixation model, aimed at investigating if the implementation of a more realistic loading scenario has the potential to significantly affect the results. Simplified loading conditions consisting of pure bending moments, in some cases combined with compressive loads, are often preferred for *in vitro* and computational testing of spine specimens being easier to implement than more realistic conditions involving muscle forces, while ensuring better reproducibility. Nevertheless, this study demonstrated that applying simplified loads can result in an underestimation of the hardware stresses in the instrumented models, with potential implications about the safety of the implants (Wilke et al., 2001).

In this study, the metrics used to evaluate the importance of the loading conditions were the stresses in the L1-L5 pedicle screws and those in the posterior rods. The results showed that realistic loading conditions increase the stresses in the hardware, up to 57 MPa in flexion (**Figures 4A,B**). For the pedicle screws in L1-L5, the stresses were higher for all four motions when realistic loading conditions were used. For the posterior rods, higher stresses were found for all conditions with realistic loading conditions (**Figures 4A,B**). This is a very interesting result because the most common type of biomechanical failure of the fixation is indeed rod breakage (Yamanaka et al., 2015).

Since this approach (coupling FE and MSK modelling) is reported here for the first time for an instrumented spine model, no comparison of the current results with similar existing data can be performed. Despite this, previous studies investigated the validity of simplified loading conditions by comparing *in vivo* measurements with *in vitro* experimental tests. Wilke et al. compared the loads acting on an internal spinal fixator in 10 patients (*in vivo*) with an equivalent *in vitro* simulator under the application of pure bending moments (Wilke et al., 2001). They found good agreement for the loads acting in the internal fixator for axial rotation and lateral bending. For flexion ad extension, reasonable agreement was found only for the healthy spines instrumented with fixators, while for specimens in which a bone graft was implanted in the intervertebral space a lower agreement between *in vivo* and *in vitro* data was found. As regards the proposed FE-MSK approach, other studies in the literature have exploited such combination, but not to investigate instrumented scenarios. For instance, in a computational study by Liu and colleagues a coupled FE-MSK model was used to investigate the load-sharing in the lumbosacral spine, where muscle forces, as predicted by a MSK model, were used as loading conditions for the FE model (Liu et al., 2018; Liu et al., 2019).

This present study has some limitations. Axial rotation was not investigated; however, it is worth considering that the previous papers exploiting coupled FE-MSK models only considered flexion-extension motion, therefore the simulation of lateral bending motion still constitutes an advance with respect to the state-of-the-art (Rohlmann et al., 2006; Liu et al., 2018; Liu et al., 2019). Another limitation was the translation imposed to the most cranial vertebra, which was chosen as boundary condition after verifying that a pure load-controlled simulation driven by muscle forces and the reaction force calculated by the MSK model at the most cranial joint did not lead to convergence. This is however an improvement with respect to the method used by Liu et al., in which the L1 vertebra was subjected to a translation in the direction of the force equal to the one predicted by the MSK model in order to ensure quick convergence of the FE model, but the applied translation was adjusted if the difference of the reaction force in the MSK model and in the FE model was greater than predefined tolerances (Liu et al., 2018; Liu et al., 2019); in the present study, no adjustment was necessary. Besides, only one instrumented configuration was

presented in this study while various instrumentation strategies are used in the clinical practice, depending on the condition of the spine of the patient; the simulation of other common configurations is indeed ongoing. Another limitation was that the simplified loading conditions included only pure bending moments without a compressive load mimicking the body weight, such as for example a follower load (Patwardhan et al., 2003). This simplification could justify the difference found in the hardware stresses between the two types of loading conditions, but it should be said that the use of pure moment without compressive loads is very common *in vitro* and computational studies investigating the stresses in the implants (e.g., Wilke et al., 2001; Galbusera et al., 2020), and pure moments have been recommended as the preferred method to test spinal implants in standardized laboratory tests (Wilke et al., 1998). However, we acknowledge that additional studies should be done using a follower load in combination with pure moments in order to simulate another commonly implemented set of simplified loading conditions. Moreover, it should be noted that the motion imposed as input for the MSK model was equal to the validated output of the corresponding FE model under simplified loading conditions, being therefore possibly different from the physiological motion of the spine. In this respect, gait analysis and fluoroscopy can be potential alternatives to determine the motion of the spine to be used as input for the MSK model (Haddas et al., 2018; Breen and Breen, 2020). Finally, it should be noted that the stiffness imposed to the MSK model does not account for compressive loading, but only for the pure moment applied to the FE model.

In conclusion, hardware stresses resulted markedly higher when realistic loading conditions, consisting of muscles forces applied to several vertebrae from T10 to the pelvis, are used instead of simplified loading conditions. This conclusion has relevant biomechanical implications since it means that previous models which used pure moments may have underestimated the stresses in the implants in flexion-extension and in lateral bending. Further studies, using different spinal fixation techniques and follower load, need to be done in order to understand if this combined method is more useful than a simplified one to predict implants failure.

DATA AVAILABILITY STATEMENT

The raw data supporting the conclusions of this article will be made available by the authors, without undue reservation.

AUTHOR CONTRIBUTIONS

MP, TB, and FG contributed to the conception and design of the study. MP, TB, and FG performed the analysis and interpretation of data; MP wrote the first draft of the manuscript; MP, TB, TV, and FG contributed to manuscript revision and approved the submitted version; MP, TB, TV, and FG contributed to an administrative, technical, or material support.

FUNDING

The study was supported by the Italian Ministry of Health ("Ricerca Corrente").

REFERENCES

Arshad, R., Zander, T., Dreischarf, M., and Schmidt, H. (2016). Influence of Lumbar Spine Rhythms and Intra-abdominal Pressure on Spinal Loads and Trunk Muscle Forces during Upper Body Inclination. *Med. Eng. Phys.* 38 (4), 333–338. doi:10.1016/j.medengphy.2016.01.013

Bassani, T., Stucovitz, E., Qian, Z., Briguglio, M., and Galbusera, F. (2017). Validation of the AnyBody Full Body Musculoskeletal Model in Computing Lumbar Spine Loads at L4L5 Level. *J. Biomech.* 58, 89–96. doi:10.1016/j.jbiomech.2017.04.025

Bassani, T., Casaroli, G., and Galbusera, F. (2019). Dependence of Lumbar Loads on Spinopelvic Sagittal Alignment: An Evaluation Based on Musculoskeletal Modeling. *PloS one* 14 (3), e0207997. doi:10.1371/journal.pone.0207997

Benditz, A., Auer, S., Spörrer, J. F., Wolkerstorfer, S., Grifka, J., Suess, F., et al. (2018). Regarding Loads after Spinal Fusion, Every Level Should Be Seen Separately: a Musculoskeletal Analysis. *Eur. Spine J.* 27 (8), 1905–1910. doi:10.1007/s00586-018-5476-5

Breen, A., and Breen, A. (2020). Dynamic Interactions between Lumbar Intervertebral Motion Segments during Forward Bending and Return. *J. Biomech.* 102, 109603. doi:10.1016/j.jbiomech.2020.109603

Bruno, A. G., Bouxsein, M. L., and Anderson, D. E. (2015). Development and Validation of a Musculoskeletal Model of the Fully Articulated Thoracolumbar Spine and Rib Cage. *J. Biomech. Eng.* 137 (8), 081003. doi:10.1115/1.4030408

Burns, C. B., Dua, K., Trasolini, N. A., Komatsu, D. E., and Barsi, J. M. (2016). Biomechanical Comparison of Spinopelvic Fixation Constructs: Iliac Screw versus S2-Alar-Iliac Screw. *Spine Deformity* 4 (1), 10–15. doi:10.1016/j.jspd.2015.07.008

Casaroli, G., Galbusera, F., Chande, R., Lindsey, D., Mesiwala, A., Yerby, S., et al. (2019). Evaluation of Iliac Screw, S2 Alar-Iliac Screw and Laterally Placed Triangular Titanium Implants for Sacropelvic Fixation in Combination with Posterior Lumbar Instrumentation: a Finite Element Study. *Eur. Spine J.* 28 (7), 1724–1732. doi:10.1007/s00586-019-06006-0

Cook, D. J., Yeager, M. S., and Cheng, B. C. (2015). Range of Motion of the Intact Lumbar Segment: a Multivariate Study of 42 Lumbar Spines. *Int. J. Spine Surg.* 9, 5. doi:10.14444/2005

Cunningham, B. W., Sponseller, P. D., Murgatroyd, A. A., Kikkawa, J., and Tortolani, P. J. (2019). A Comprehensive Biomechanical Analysis of Sacral Alar Iliac Fixation: an *In Vitro* Human Cadaveric Model. *J. Neurosurg. Spine* 30 (3), 367–375. doi:10.3171/2018.8.SPINE18328

Dmitriev, A. E., Gill, N. W., Kuklo, T. R., and Rosner, M. K. (2008). Effect of Multilevel Lumbar Disc Arthroplasty on the Operative- and Adjacent-Level Kinematics and Intradiscal Pressures: an *In Vitro* Human Cadaveric Assessment. *Spine J.* 8 (6), 918–925. doi:10.1016/j.spinee.2007.10.034

Fleischer, G. D., Kim, Y. J., Ferrara, L. A., Freeman, A. L., and Boachie-Adjei, O. (2012). Biomechanical Analysis of Sacral Screw Strain and Range of Motion in Long Posterior Spinal Fixation Constructs. *Spine* 37 (3), E163–E169. doi:10.1097/BRS.0b013e31822ce9a7

Galbusera, F., Casaroli, G., Chande, R., Lindsey, D., Villa, T., Yerby, S., et al. (2020). Biomechanics of Sacropelvic Fixation: a Comprehensive Finite Element Comparison of Three Techniques. *Eur. Spine J.* 29 (2), 295–305. doi:10.1007/s00586-019-06225-5

Ha, K.-Y., Lee, J.-S., and Kim, K.-W. (2008). Degeneration of Sacroiliac Joint after Instrumented Lumbar or Lumbosacral Fusion: a Prospective Cohort Study Over Five-Year Follow-Up. Spine. *Spine* 33 (11), 1192–1198. doi:10.1097/BRS.0b013e318170fd35

Haddas, R., Ju, K. L., Belanger, T., and Lieberman, I. H. (2018). The Use of Gait Analysis in the Assessment of Patients Afflicted with Spinal Disorders. *Eur. Spine J.* 27 (8), 1712–1723. doi:10.1007/s00586-018-5569-1

Han, K.-S., Rohlmann, A., Yang, S.-J., Kim, B. S., and Lim, T.-H. (2011). Spinal Muscles Can Create Compressive Follower Loads in the Lumbar Spine in a Neutral Standing Posture. *Med. Eng. Phys.* 33 (4), 472–478. doi:10.1016/j.medengphy.2010.11.014

Ignasiak, D., Dendorfer, S., and Ferguson, S. J. (2016). Thoracolumbar Spine Model with Articulated Ribcage for the Prediction of Dynamic Spinal Loading. *J. Biomech.* 49 (6), 959–966. doi:10.1016/j.jbiomech.2015.10.010

Ignasiak, D., Peteler, T., Fekete, T. F., Haschtmann, D., and Ferguson, S. J. (2018). The Influence of Spinal Fusion Length on Proximal junction Biomechanics: a Parametric Computational Study. *Eur. Spine J.* 27 (9), 2262–2271. doi:10.1007/s00586-018-5700-3

Ignasiak, D. (2020). A Novel Method for Prediction of Postoperative Global Sagittal Alignment Based on Full-Body Musculoskeletal Modeling and Posture Optimization. *J. Biomech.* 102, 109324. doi:10.1016/j.jbiomech.2019.109324

Kebaish, K. M. (2010). Sacropelvic Fixation: Techniques and Complications. *Spine* 35 (25), 2245–2251. doi:10.1097/BRS.0b013e3181f5cfae

Kim, B. S., Lim, T.-H., Kwon, T. K., and Han, K.-S. (2014). Feasibility of Compressive Follower Load on Spine in a Simplified Dynamic State: a Simulation Study. *Bio-Med. Mater. Eng.* 24 (6), 2319–2329. doi:10.3233/BME-141045

Kuklo, T. R., Bridwell, K. H., Lewis, S. J., Baldus, C., Blanke, K., Iffrig, T. M., et al. (2001). Minimum 2-year Analysis of Sacropelvic Fixation and L5-S1 Fusion Using S1 and Iliac Screws. *Spine* 26 (18), 1976–1983. doi:10.1097/00007632-200109150-00007

Lindsey, D. P., Parrish, R., Gundanna, M., Leasure, J., Yerby, S. A., and Kondrashov, D. (2018). Biomechanics of Unilateral and Bilateral Sacroiliac Joint Stabilization: Laboratory Investigation. *J. Neurosurg. Spine* 28 (3), 326–332. doi:10.3171/2017.7.SPINE17499

Liu, T., Khalaf, K., Naserkhaki, S., and El-Rich, M. (2018). Load-sharing in the Lumbosacral Spine in Neutral Standing & Flexed Postures - A Combined Finite Element and Inverse Static Study. *J. Biomech.* 70, 43–50. doi:10.1016/j.jbiomech.2017.10.033

Liu, T., Khalaf, K., Adeeb, S., and El-Rich, M. (2019). Effects of Lumbo-Pelvic Rhythm on Trunk Muscle Forces and Disc Loads during Forward Flexion: A Combined Musculoskeletal and Finite Element Simulation Study. *J. Biomech.* 82, 116–123. doi:10.1016/j.jbiomech.2018.10.009

Patwardhan, A. G., Havey, R. M., Carandang, G., Simonds, J., Voronov, L. I., Ghanayem, A. J., et al. (2003). Effect of Compressive Follower Preload on the Flexion-Extension Response of the Human Lumbar Spine. *J. Orthop. Res.* 21 (3), 540–546. doi:10.1016/S0736-0266(02)00202-4

Rohlmann, A., Bergmann, G., Graichen, F., and Weber, U. (1997). Comparison of Loads on Internal Spinal Fixation Devices Measured *In Vitro* and *In Vivo*. *Med. Eng. Phys.* 19 (6), 539–546. doi:10.1016/s1350-4533(97)00018-0

Rohlmann, A., Bauer, L., Zander, T., Bergmann, G., and Wilke, H.-J. (2006). Determination of Trunk Muscle Forces for Flexion and Extension by Using a Validated Finite Element Model of the Lumbar Spine and Measured *In Vivo* Data. *J. Biomech.* 39 (6), 981–989. doi:10.1016/j.jbiomech.2005.02.019

Rohlmann, A., Burra, N. K., Zander, T., and Bergmann, G. (2007). Comparison of the Effects of Bilateral Posterior Dynamic and Rigid Fixation Devices on the Loads in the Lumbar Spine: a Finite Element Analysis. *Eur. Spine J.* 16 (8), 1223–1231. doi:10.1007/s00586-006-0292-8

Rohlmann, A., Zander, T., Rao, M., and Bergmann, G. (2009). Applying a Follower Load Delivers Realistic Results for Simulating Standing. *J. Biomech.* 42 (10), 1520–1526. doi:10.1016/j.jbiomech.2009.03.048

Schmidt, H., Heuer, F., Drumm, J., Klezl, Z., Claes, L., and Wilke, H.-J. (2007). Application of a Calibration Method Provides More Realistic Results for a Finite Element Model of a Lumbar Spinal Segment. *Clin. Biomech.* 22 (4), 377–384. doi:10.1016/j.clinbiomech.2006.11.008

Stokes, I. A. F., and Gardner-Morse, M. (1995). Lumbar Spine Maximum Efforts and Muscle Recruitment Patterns Predicted by a Model with Multijoint Muscles and Joints with Stiffness. *J. Biomech.* 28 (2), 173–186. doi:10.1016/0021-9290(94)e0040-a

Sutterlin, C. E., 3rd, Field, A., Ferrara, L. A., Freeman, A. L., and Phan, K. (2016). Range of Motion, Sacral Screw and Rod Strain in Long Posterior Spinal Constructs: a Biomechanical Comparison between S2 Alar Iliac Screws with Traditional Fixation Strategies. *J. Spine Surg.* 2 (4), 266–276. doi:10.21037/jss.2016.11.01

Tsuchiya, K., Bridwell, K. H., Kuklo, T. R., Lenke, L. G., and Baldus, C. (2006). Minimum 5-year Analysis of L5-S1 Fusion Using Sacropelvic Fixation (Bilateral S1 and Iliac Screws) for Spinal Deformity. *Spine* 31 (3), 303–308. doi:10.1097/01.brs.0000197193.81296.f1

Wilke, H.-J., Wenger, K., and Claes, L. (1998). Testing Criteria for Spinal Implants: Recommendations for the Standardization of *In Vitro* Stability Testing of Spinal Implants. *Eur. Spine J.* 7 (2), 148–154. doi:10.1007/s005860050045

Wilke, H.-J., Rohlmann, A., Neller, S., Schulthei, M., Bergmann, G., Graichen, F., et al. (2001). Is it Possible to Simulate Physiologic Loading Conditions by Applying Pure Moments? *Spine* 26 (6), 636–642. doi:10.1097/00007632-200103150-00014

Yamanaka, K., Mori, M., Yamazaki, K., Kumagai, R., Doita, M., and Chiba, A. (2015). Analysis of the Fracture Mechanism of Ti-6Al-4V Alloy Rods that Failed Clinically after Spinal Instrumentation Surgery. *Spine* 40 (13), E767–E773. doi:10.1097/BRS.0000000000000881

Zhang, H., and Zhu, W. (2019). The Path to Deliver the Most Realistic Follower Load for a Lumbar Spine in Standing Posture: A Finite Element Study. *J. Biomech. Eng.* 141 (3), 031010. Advance online publication. doi:10.1115/1.4042438

Zhong, W., Driscoll, S. J., Wu, M., Wang, S., Liu, Z., Cha, T. D., et al. (2014). *In Vivo* morphological Features of Human Lumbar Discs. *Medicine* 93 (28), e333. doi:10.1097/MD.0000000000000333

Zhu, R., Zander, T., Dreischarf, M., Duda, G. N., Rohlmann, A., and Schmidt, H. (2013). Considerations when Loading Spinal Finite Element Models with Predicted Muscle Forces from Inverse Static Analyses. *J. Biomech.* 46 (7), 1376–1378. doi:10.1016/j.jbiomech.2013.03.003

Conflict of Interest: The authors declare that the research was conducted in the absence of any commercial or financial relationships that could be construed as a potential conflict of interest.

The reviewer DEA declared a past co-authorship with with several of the authors FG and TB to the handling editor.

frontiers | Frontiers in Bioengineering and Biotechnology

ORIGINAL RESEARCH
published: 27 April 2022
doi: 10.3389/fbioe.2022.751291

Sensitivity of the Cervical Disc Loads, Translations, Intradiscal Pressure, and Muscle Activity Due to Segmental Mass, Disc Stiffness, and Muscle Strength in an Upright Neutral Posture

Rizwan Arshad[1]*, *Hendrik Schmidt*[2], *Marwan El-Rich*[3] and *Kodjo Moglo*[1]

[1]Biomechanics Laboratory, Department of Mechanical and Aerospace Engineering, Royal Military College of Canada, Kingston, ON, Canada, [2]Julius Wolff Institute, Berlin Institute of Health, Charité—Universitätsmedizin Berlin, Berlin, Germany, [3]Healthcare Engineering Innovation Center, Department of Mechanical Engineering, Khalifa University, Abu Dhabi, United Arab Emirates

OPEN ACCESS

Edited by:
Yang Liu,
Hong Kong Polytechnic University,
Hong Kong SAR, China

Reviewed by:
Sabine Bauer,
University of Koblenz and Landau,
Germany
Eric Wagnac,
École de Technologie Supérieure
(ÉTS), Canada

***Correspondence:**
Rizwan Arshad
rizwan.arshad@rmc.ca

Specialty section:
This article was submitted to
Biomechanics,
a section of the journal
Frontiers in Bioengineering and
Biotechnology

Received: 31 July 2021
Accepted: 21 March 2022
Published: 27 April 2022

Citation:
Arshad R, Schmidt H, El-Rich M and
Moglo K (2022) Sensitivity of the
Cervical Disc Loads, Translations,
Intradiscal Pressure, and Muscle
Activity Due to Segmental Mass, Disc
Stiffness, and Muscle Strength in an
Upright Neutral Posture.
Front. Bioeng. Biotechnol. 10:751291.
doi: 10.3389/fbioe.2022.751291

Musculoskeletal disorders of the cervical spine have increased considerably in recent times. To understand the effects of various biomechanical factors, quantifying the differences in disc loads, motion, and muscle force/activity is necessary. The kinematic, kinetic, or muscle response may vary in a neutral posture due to interindividual differences in segmental mass, cervical disc stiffness, and muscle strength. Therefore, our study aimed to develop an inverse dynamic model of the cervical spine, estimate the differences in disc loads, translations, intradiscal pressure, and muscle force/activity in a neutral posture and compare these results with data available in the literature. A head–neck complex with nine segments (head, C1–T1) was developed with joints having three rotational and three translational degrees of freedom, 517 nonlinear ligament fibers, and 258 muscle fascicles. A sensitivity analysis was performed to calculate the effect of segmental mass (5th to 95th percentile), translational disc stiffness (0.5–1.5), and muscle strength (0.5–1.5) on the cervical disc loads (C2–C3 to C7–T1), disc translations, intradiscal pressure, and muscle force/activity in a neutral posture. In addition, two axial external load conditions (0 and 40 N) were also considered on the head. The estimated intradiscal pressures (0.2–0.56 MPa) at 0 N axial load were comparable to *in vivo* measurements found in the literature, whereas at 40 N, the values were 0.39–0.93 MPa. With increased segmental mass (5th to 95th), the disc loads, translations, and muscle forces/activities increased to 69% at 0 N and 34% at 40 N axial load. With increased disc stiffness (0.5–1.5), the maximum differences in axial (<1%) and shear loads (4%) were trivial; however, the translations were reduced by 67%, whereas the differences in individual muscle group forces/activities varied largely. With increased muscle strength (0.5–1.5), the muscle activity decreased by 200%. For 40 vs. 0 N, the differences in disc loads, translations, and muscle forces/activities were in the range of 52–129%. Significant differences were estimated in disc loads, translations, and muscle force/activity in the normal population, which could help distinguish between normal and pathological cervical spine conditions.

Keywords: cervical spine, musculoskeletal model, inverse dynamics, intervertebral disc loads, intradiscal pressure

INTRODUCTION

Musculoskeletal disorders such as neck pain are frequent across all age and sex groups. Globally, neck pain prevalent cases were 288.7 million in 2017 (Safiri et al., 2020). Several factors could contribute to neck pain, such as sedentary lifestyle, sustained or awkward posture, vibration, and psychological or socioeconomic factors (Linton, 2000; Charles et al., 2018). Not all but several causes may be linked with a biomechanical condition of the cervical spine (Kong et al., 2017). For example, neck pain may arise from spinal cord compression due to degenerative changes in the spinal structures (Cohen, 2015; McCormick et al., 2020).

To distinguish between asymptomatic (pain-free) population with physiologically intact structures and symptomatic population with a pathomorphological condition, knowledge of the variation in the cervical spine loads, motion, and muscle activity in asymptomatic population is crucial. Previously, experimental studies (Panjabi et al., 1986, 2001; Wheeldon et al., 2006; Ackland et al., 2011; Suderman and Vasavada, 2017) measured load-displacement behavior, muscle moment arm, or the range of motion in flexion, extension, lateral bending, or axial rotation. In addition, computational studies either based on the finite element (Mesfar and Moglo, 2013; Bredbenner et al., 2014; Mustafy et al., 2014; Lasswell et al., 2017), inverse dynamic (Anderst et al., 2013; Diao et al., 2018, 2017), or forward dynamic models (Sartori et al., 2014; Silvestros et al., 2019) investigated the effect of variation in geometrical or material properties on the cervical spine loads, motion, or muscle force. However, in an asymptomatic population, quantification of the differences in spinal loads, segment translations, or muscle activity in a neutral posture needs further attention. Such data provided could help improve the prognosis and outcome of the interventions applied to prevent or treat pathological conditions of the cervical spine.

The anthropometric and biomechanical characteristics in the general population are subject-specific (Vasavada et al., 2008; Winter 2009). Such interindividual variations may lead to significant differences in segmental kinematics, disc loads, or muscle force/activity in a neutral posture. Therefore, we hypothesize that parameters such as segment mass, intervertebral disc stiffness, and muscle strength significantly affect the kinematic, kinetic, or muscle response of the cervical spine in a neutral posture. For example, the cervical segments and head mass vary considerably among the general population. The head has the largest mass, which could vary due to differences in head circumference (Ching, 2007). In addition, the head mass could differ significantly in a specific percentile population of a certain height and body mass (Nguyen et al., 2012). The disc stiffness plays a vital role in flexibility and load-bearing mechanism. Previously, *in vitro* studies showed a large variation in cervical disc axial and shear stiffness (Moroney et al., 1988; Yoganandan et al., 2001; Dowling-Medley et al., 2020). These differences may influence the local kinematics, the initial contact mechanics between the facet joints (Yoganandan et al., 2003; Jaumard et al., 2011), and the cervical spine's overall motion and load sharing mechanism (Cripton, 1999; Patwardhan et al., 2000). In addition, neck muscle strengths vary widely among the population (Ikai and Fukunaga, 1968; Maganaris et al., 2001; Catenaccio et al., 2017), leading to significant differences in the level of muscle activity required to stabilize the cervical spine in a neutral posture.

In the asymptomatic population, quantification of the differences in the cervical disc loads, disc translations, and neck muscle force/activity due to variation in segmental mass, disc stiffness, and muscle strength still requires more consideration. Therefore, the aim of this study was 1) to develop an inverse dynamic musculoskeletal model of the cervical spine, 2) calculate the differences in cervical disc loads, disc translations, intradiscal pressure, and the muscle force/activity due to segmental mass, translational disc stiffness, and muscle strength in a neutral posture, and 3) compare these results with data available in the literature.

METHODS

Model Development

For developing an inverse dynamic musculoskeletal model, the 3D geometry for the head and neck complex was acquired from a previous study (Mesfar and Moglo, 2013) (**Figure 1**), where they used data from the Visible Human Project (Spitzer et al., 1996; Ackerman, 1998). The male subject's measured height was 180 cm, which is close to the 50th percentile of Caucasian populations (Cassola et al., 2011).

The center of mass for each vertebral segment was computed for uniform density across the segment volume. The spherical joints were defined between the head–neck complex with three rotational degrees of freedom and were placed at the geometric centroids of the cervical discs. Furthermore, three translational degrees of freedom using force-dependent kinematics (FDK) were added from C2–C3 to C7–T1, allowing soft constraints defined by the stiffness given in the local x, y, and z directions. During inverse analysis, the system resolves the equilibrium equations quasi-statically and computes translations so that the forces in these directions are in equilibrium (Andersen et al., 2011).

The cervical spine ligaments (**Figure 1A**) such as apical, alar, transverse, anterior longitudinal, posterior longitudinal, supraspinous, interspinous, intertransverse, capsular, ligament flavum, and anterior and posterior atlanto-occipital membranes were added (**Table 1**). The origin and insertion points for ligaments were taken from a previously developed finite element model of the cervical spine (Mesfar and Moglo, 2013). The nonlinear ligament stiffness properties at a slow strain rate were defined based on previously published experimental data (Shim et al., 2006). The ligament fibers were calibrated for no stress in a neutral posture. The forces did not exceed the maximum computed for 75 percent of the failure strain for the physiological ranges of motion.

The head and neck muscles were added (**Figure 1B**) based on the previously published dataset of muscle parameters (Borst et al., 2011). In total, 34 muscle groups and 129 muscle fascicles were included (**Figure 1C**) on each side. These muscle groups were further grouped as anterior/anterolateral, posterior/

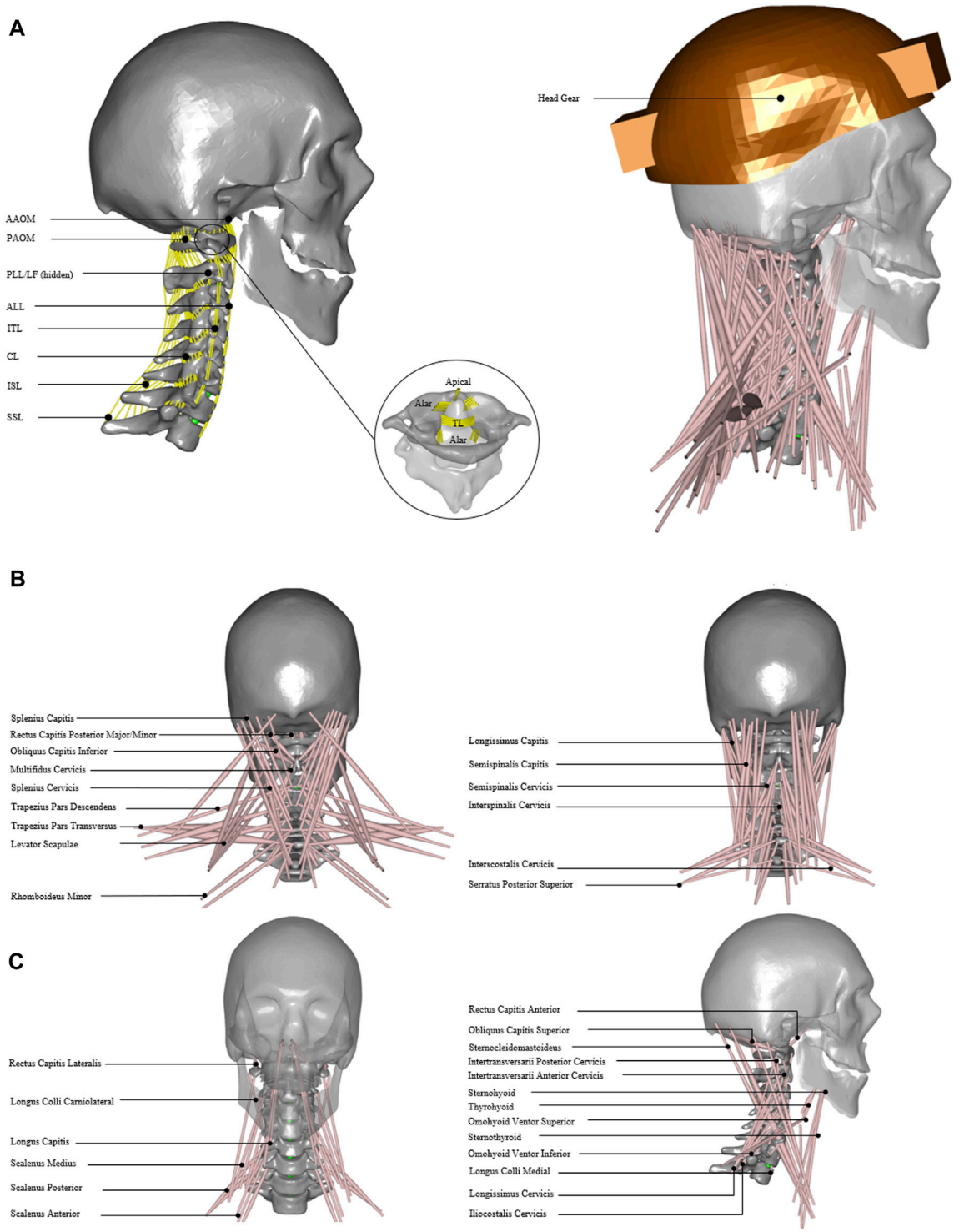

FIGURE 1 | Head and neck model. **(A)** Model with cervical ligament fibers. Apical, alar, TL; transverse ligament, AAOM and PAOM; anterior and posterior atlantooccipital membranes, ALL; anterior longitudinal ligament, PLL; posterior longitudinal ligament, SSL; supraspinous ligament, ISL; interspinous ligament, ITL; intertransverse ligament, CL; capsular ligament, and LF; ligament flavum. **(B)** Model with 34 muscle groups and headgear. **(C)** Detailed front, back, and side view of 34 muscle groups added in the model.

TABLE 1 | Cervical ligament fibers included in the musculoskeletal model.

Type/Level	C0-C1	C0-C2	C1-C2	C2-C3	C3-C4	C4-C5	C5-C6	C6-C7	C7-T1
ALAR		10	6						
APICAL		3							
TL			5						
AAM Ant	13		9						
AAM Pos	13		11						
ALL			5	5	5	5	5	5	5
PLL				5	5	5	5	5	5
SSL			1	1	1	1	1	1	1
ISL			5	5	5	5	5	5	5
ITLL			2	2	2	2	2	2	
ITRR			2	2	2	2	2	2	
CLL	14		14	15	16	16	16	16	15
CLR	14		14	15	16	16	16	16	15
LF				12	12	12	12	12	12
Total	**54**	**13**	**74**	**62**	**64**	**64**	**64**	**64**	**58**

The apical, alar, TL; transverse ligament, AAOM; anterior atlantooccipital membrane, POAM; posterior atlantooccipital membrane, ALL; anterior longitudinal ligament, PLL; posterior longitudinal ligament, SLL; supraspinous ligament, ISL; interspinous ligament, ITLL; intertransverse ligament left, ITRR; intertransverse ligament right, CLL; capsular ligament left, CLR; capsular ligament right and LF; ligament flavum.

TABLE 2 | Head and neck muscle groups and the number of fascicles (sum of left and right) included in the musculoskeletal model.

Anterior/anterolateral (no)	Posterior/posterolateral (no)	Lateral (no)
1. Rectus capitis anterior (2)	1. Rectus capitis posterior major (2)	1. Rectus capitis lateralis (2)
2. Longus capitis (8)	2. Rectus capitis posterior minor (2)	2. Intertransversarii anterior cervicis (12)
3. Longus colli craniolateral (4)	3. Obliquus capitis inferior (2)	3. Intertransversarii posterior cervicis (12)
4. Longus colli medial (10)	4. Obliquus capitis superior (2)	
5. Sternocleidomastoideus (8)	5. Semispinalis capitis (18)	
6. Scalenus anterior (6)	6. Splenius capitis (14)	
7. Scalenus medius (14)	7. Longissimus capitis (12)	
8. Scalenus posterior (4)	8. Iliocostalis cervicis (6)	
9. Omohyoid venter inferior (2)	9. Intercostalis cervicis (2)	
10. Omohyoid venter superior (2)	10. Interspinalis cervicis (10)	
11. Sternohyoid (4)	11. Splenius cervicis (4)	
12. Thyrohyoid (2)	12. Semispinalis cervicis (20)	
13. Sternothyroid (4)	13. Longissimus cervicis (16)	
	14. Multifidus cervicis (20)	
	15. Levator scapulae (8)	
	16. Rhomboideus minor (4)	
	17. Trapezius Pars descendens (8)	
	18. Trapezius Pars transversus (4)	
	19. Serratus posterior superior (8)	

posterolateral, or lateral muscles (**Table 2**). The muscle behavior was defined by a simple contractile element with constant specific muscle strength.

Sensitivity Analysis

Three parameters were considered for sensitivity analysis, namely, 1) segmental mass, 2) cervical disc stiffness in compression and shear, and 3) muscle strength. In addition, two external load (EL) conditions (0 and 40 N axial loads on the head) were considered to simulate the head without or with typical headgear, such as in the case of a helicopter pilot wearing a helmet with night vision goggles (NVGs) (**Figure 1B**). The segmental masses were computed using a scaling function for the 5th, 50th, and 95th percentile implemented in the AnyBody Standing Model (AMMR v. 2.2.3). The axial and shear stiffness were adapted from previous studies (Yoganandan et al., 2001; Dowling-Medley et al., 2020), which were varied as 0.5, 1, and 1.5 of the disc stiffness. For quasi-static inverse analysis, simple muscles were considered with three specific muscle strengths of 30, 60, and 90 N/cm^2, whereas these values were within the normal range as published in previous literature (Ikai and Fukunaga, 1968; Maganaris et al., 2001). The values set for the three parameters are given in **Table 3**. In total, 54 simulations were performed for two external load conditions and with parameter settings for 27 models (**Supplementary Table S1**).

Inverse Analysis

In AnyBody, the muscle and joint forces were calculated by inverse analysis while taking known inertia and external forces into account. To estimate muscle forces in the model, a

TABLE 3 | Model parameter values for segmental mass (M), disc stiffness (DS), and muscle strength (MS).

Segment	Head and Neck Segment Mass (M) (kg)			Disc level	Disc Stiffness (DS) (N/mm)			Disc level	Shear			Specific Muscle Strength (MS) (N/cm^2)		
	5^{th}	50^{th}	95^{th}		Compression				0.5DS	1.0DS	1.5DS	0.5MS	1.0MS	1.5MS
	(Estimated from AnyBody Standing Model, AMMR version 2.2.3)				(Yoganandan et al. 2001)				(Dowling-Medley et al. 2020)					
C0	3.305092	4.434112	5.566028	C2C3	318.75	637.5	956.25							
C1	0.1567685	0.2103207	0.2640103	C3C4	382.65	765.3	1147.95							
C2	0.177671	0.2383635	0.2992116	C4C5	392.3	784.6	1176.9							
C3	0.1707035	0.2290159	0.2874778	C5C6	400.1	800.2	1200.3	C2-C3 to C7-T1	41	82	123	30	60	90
C4	0.163736	0.2196683	0.2757441	C6C7	414.85	829.7	1244.55							
C5	0.163736	0.2196683	0.2757441	C7T1	486.8	973.6	1460.4							
C6	0.1707035	0.2290159	0.2874778											
C7	0.1567685	0.2103207	0.2640103											

polynomial-based muscle recruitment criterion was considered that minimizes the muscle stresses with better synergism between neck muscles, which is given in **Eq. 1**.

$$Minimize\, G = \sum_{i=1}^{N} \left(\frac{F_i}{F_{i,max}} \right)^3, 0 \le F_i \le F_{i,max},\ Cf = r. \quad (1)$$

Here, G represents the cost function, i represents the muscle number, N represents the total number of muscles, F_i represents the actual muscle force at any instant of the simulation, and $F_{i,max}$ represents the strength of the muscle. The system of equilibrium equations was represented by $Cf = r$, where f represents a vector of the muscle and joint forces, C represents a matrix of equation coefficients, and r represents a vector of known inertia and external forces.

Results and Validation/Verification

The intradiscal pressure (IDP) for the cervical discs was estimated as given in **Eq. 2**.

$$IDP_{model} = \frac{F_{c\ model}}{Area_{disc} \times CF}. \quad (2)$$

$F_{c\ model}$ is the estimated axial force from inverse analysis, and $Area_{disc}$ is the cross-sectional area of the cervical discs taken from the literature (Pooni et al., 1986). No studies were available that, in particular, presented the correction factor (CF) to estimate IDP in the cervical spine; however, we used the typical CF range (0.55–0.77), with a mean value of 0.66 recommended for the lumbar spine (Dreischarf et al., 2013). The estimated IDP from the model for the 5th, 50th, and 95th percentile population was compared with *in vivo* measurements found in the literature (Kambin et al., 1980; Hattori et al., 1981).

The axial load and translation were taken perpendicular to the surface, and shear force or translation was taken parallel to the surface of the lower segment. The axial and shear loads estimated were compared with the findings in the literature (Barrett et al., 2020). In addition, the estimated 34 group muscle forces and activities were also compared qualitatively with data found in the literature (Assi et al., 2005; Ibrahim, 2015; Van den Abbeele et al., 2018).

RESULTS

IDP

The estimated IDP for C2–C3 to C7–T1 discs and its comparison with *in vivo* measurements are given in **Figure 2**. With 0 N axial load, the range of average IDP was 0.2–0.56 MPa with a mean correction factor of 0.66 (**Figure 2A**). These estimations were comparable to *in vivo* measurements (0.3–0.45 MPa). At 40 N axial load, the values increased to 104% (5th percentile mass) and 62% (95th percentile mass), with values in the range of 0.39–0.93 MPa (**Figure 2B**). Higher values of IDP were estimated in the upper than the lower-level cervical discs. The IDP for the 5th, 50th, and 95th percentile mass showed noticeable differences; however, no significant differences were seen due to disc stiffness and muscle strength. Due to segmental mass, the estimated IDP showed a difference of about 68% at 0 N and 33% at 40 N axial load.

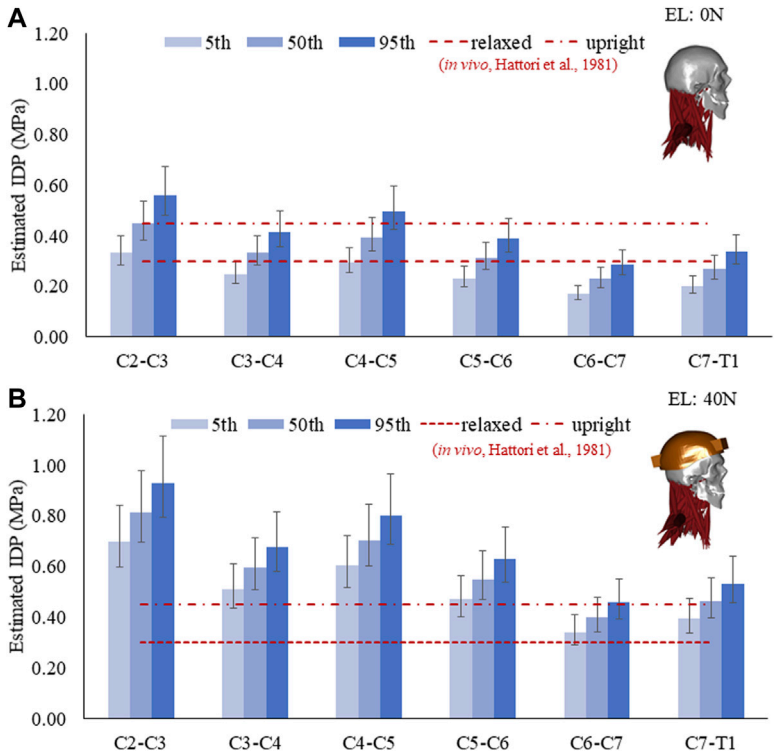

FIGURE 2 | Estimated IDP in a neutral posture for the 5th, 50th, and 95th percentile segmental mass with a mean correction factor of 0.66. Error bars show the range of IDP with a correction factor of 0.55–0.77. **(A)** IDP at 0 N and **(B)** IDP at 40 N external load (EL).

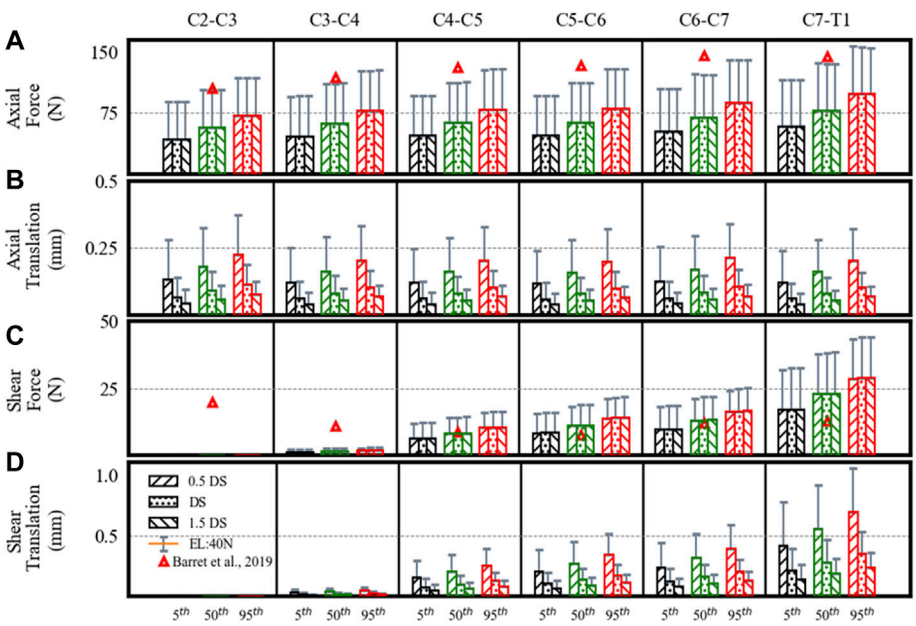

FIGURE 3 | Estimated disc loads and translations in a neutral posture showing differences for the 5th, 50th, and 95th percentile segmental mass, 0.5DS, DS, and 1.5DS disc stiffness (DS). **(A)** Axial force. **(B)** Axial translation. **(C)** Shear force. **(D)** Shear translation. Bars and error bars show disc loads and translations at 0N and 40N external load (EL).

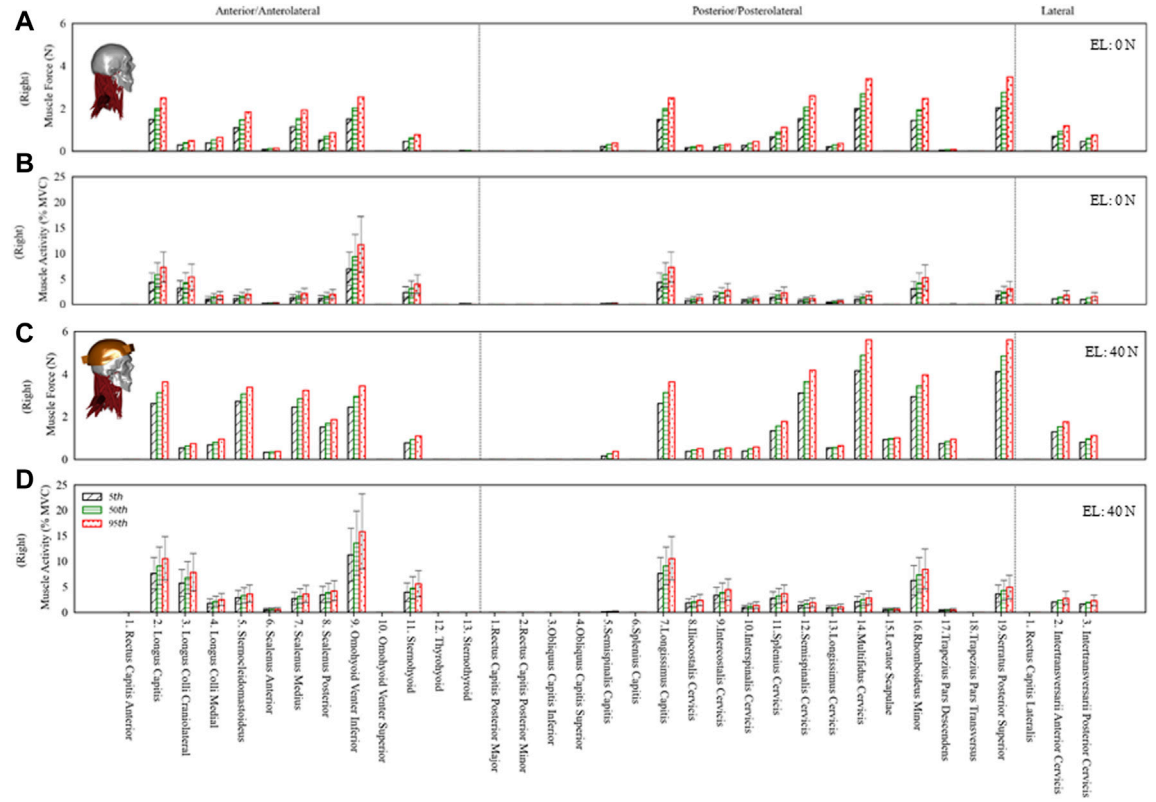

FIGURE 4 | The estimated muscle force and activity of the right side anterior/anterolateral, posterior/posterolateral, and lateral muscle groups for the 5th, 50th and 95th percentile segmental mass at 0N and 40N external load (EL). Error bars show variation in muscle activity due to differences in muscle strength from 30 to 90 N/cm^2. **(A)** Muscle force at 0N EL. **(B)** Muscle activity at 0N EL. **(C)** Muscle force at 40N EL. **(D)** Muscle activity at 40N EL.

Disc Loads and Translations

From C2–C3 to C7–T1, the estimated axial loads and their comparison (Barrett et al., 2020) are given in **Figure 3A**. Barret et al. recorded EMG measurements from eight healthy males wearing a helmet for a helicopter pilot. Furthermore, they predicted the cervical joint loads using an EMG-driven inverse model of a 50th percentile male. In our study, the estimated axial loads for the 50th percentile mass with 40 N external load were comparable to those mentioned in the work by Barret et al.

The axial loads increased from upper to lower levels. At 0 N axial load, the axial loads increased about 68% from the 5th to 95th percentile segmental mass for C2–C3 (43–72 N), C3–C4 (46–78 N), C4–C5 (47–79 N), C5–C6 (47–80 N), C6–C7 (52–88 N), and C7–T1 (58–98 N) segments. For the 40 N axial load, the estimated loads increased by 33% due to segmental mass in C2–C3 (89–119 N), C3–C4 (95–127 N), C4–C5 (96–128 N), C5–C6 (96–128 N), C6–C7 (104–140 N), and C7–T1 (116–156 N) segments. For the 40 N vs. 0 N load condition, axial loads increased by 104–62% for the 5th to 95th percentile mass. No significant differences were found in axial loads due to disc stiffness and muscle strength.

The estimated shear loads are given in **Figure 3C**. Though the estimated shear loads were small and comparable to those in the work by Barret et al., the shear loads increased from the upper (C2–C3) to the lower level (C7–T1) in our results, which is different from their study (a decrease from C2–C3 to C5–C6, followed by an increase to C7–T1).

Due to segmental mass, the estimated shear loads increased up to 67% for C3–C4 (1–2 N), C4–C5 (6–11 N), C5–C6 (8–14 N), C6–C7 (10–17 N), and C7–T1 (17–29 N) segments. The shear forces computed for level C2–C3 were nearly 0 N. Under 40 N axial load, the estimated loads increased by 33% in C2–C3 (0.2–0.4 N), C3–C4 (2–3 N), C4–C5 (12–16 N), C5–C6 (16–21 N), C6–C7 (19–25 N), and C7–T1 (33–44 N) segments. For the 40 N vs. 0 N load condition, the shear loads increased by 91–52% for the 5th to 95th percentile mass. No notable differences were found due to disc stiffness and muscle strength.

The axial translations at different spine levels were almost similar (**Figure 3B**), whereas shear translations increased from upper to lower levels (**Figure 3D**). With an increase in segmental mass, the axial translations increased by 68%. With a decrease in disc stiffness from 1.5 to 0.5, axial and shear translations increased by 67% for each percentile mass. From C2–C3 to C7–T1, the range of axial translations was 0.04–0.22 mm and 0.08–0.37 mm at 0 N and 40 N axial loads, whereas shear translations were between 0 and 0.7 mm and 0–1 mm. For 40 N vs. 0 N load condition, axial translations

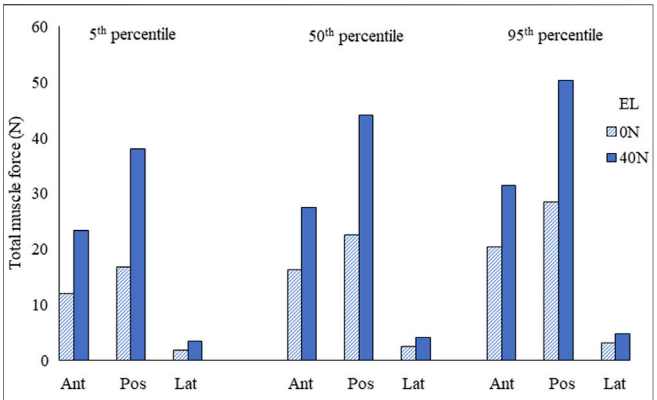

FIGURE 5 | Total muscle force in anterior/anterolateral (Ant), posterior/posterolateral (Pos), and lateral (Lat) muscle groups for the 5th, 50th, and 95th percentile segmental mass at 0 N and 40 N external load (EL).

increased by 104–62% and shear translations increased by 91–52% for the 5th to 95th percentile. No differences were found in disc translations due to muscle strength.

Muscle Force and Activity

The estimated muscle force in individual muscle groups for the right side (**Figures 4A,C**) and the total muscle force in anterior, posterior, and lateral muscle groups (left and right) are given in **Figure 5**. The maximum muscle forces reached in any individual muscle group were from 3 (0 N axial load) to 5.9 N (40 N axial load). These estimated muscle forces were within the range (approx. 3.2–6 N) found in other studies (Assi et al., 2005; Van den Abbeele et al., 2018).

The total muscle force in posterior muscles was greater than that in anterior muscle groups, whereas the total muscle force in lateral muscles was the least. The muscle forces increased by 69% due to segmental mass under 0 N axial load and 34% under 40 N axial load. Due to 40 N vs. 0 N axial load, the estimated difference in muscle forces was between 103% (5th percentile) and 60% (95th percentile).

The muscle activity for anterior, posterior, and lateral muscle groups is given in **Figure 4B,D** under 0 N and 40 N axial loads. The average muscle activities were mostly less than 5% of maximum voluntary contraction (MVC), with few up to 10% MVC for 0 N axial load and about 15% MVC for 40 N axial load. The muscle activities estimated in this study with 0 and 40 N axial load for sternocleidomastoid, erector spinae, and trapezius muscles were comparable to the EMG measurements in the study of Ibrahim (2015), where 16 young subjects were measured in a neutral posture with no load and a loaded condition on the head (3.68 kg). Some of the infrahyoid muscle groups showed higher activity in the range of 5–25% MVC. The maximum difference due to segmental mass was about 69 and 34% for 0 and 40 N axial load, whereas the activity varied by 200% due to specific muscle strength. The differences estimated in muscle activity due to disk stiffness varied largely among individual muscle groups.

DISCUSSION

Due to interindividual differences, the IDP, cervical disc loads, translations, and neck muscle response varies considerably. Quantifying such differences among the general population is necessary for better treatment of musculoskeletal disorders related to the cervical spine. Understanding such differences may help differentiate between healthy and symptomatic population. Sensitivity analysis was performed to investigate the effect of segmental mass, disc stiffness, and muscle strength variation on the axial and shear disc loads, translations, IDP, and muscle force/activity under 0 N and 40 N axial loads in a neutral posture. *In vivo* studies measuring IDP in the cervical discs are rare. We could find two studies in the literature (Kambin et al., 1980; Hattori et al., 1981). Kambin et al. performed intraoperative measurements on 19 patients before a discectomy was undertaken. The disadvantage of intraoperative measurements was the elimination of muscle tone due to the applied anesthetics and relaxants, making it impossible to determine the intradiscal pressure under realistic muscle stress. Therefore, they analyzed the pressure–volume relationship after intradiscal injection of defined fluid measurements. In 62% of the discs, they found normal results with pressure values between 0.6 and 1.2 MPa after injection of 0.2–0.4 ml of fluid. On the other hand, degenerated intervertebral discs with partial rupture of the annulus fibrosus and destroyed nucleus pulposus developed maximum pressures between 0.1 and 0.4 MPa after injection of 1.5 ml of fluid. In analogy, reduced pressures are considered in advanced degenerative changes already proven for the lumbar intervertebral disc (Nachemson, 1966).

Hattori et al. determined the cervical intradiscal pressure *in vivo* in patients who were awake. In 48 patients undergoing treatment for degenerative cervical spine problems, they performed discographic pressure measurements in 80 cervical discs. They took measures in a neutral position on the sitting patient and during flexion/extension, axial rotation, and lateral inclination. In a relaxed, tucked-back position, the values averaged 0.3 MPa, while in a sitting position, they rose to 0.45 MPa in the neutral position.

In addition, a couple of *in vitro* studies (Cripton, 1999; Pospiech et al., 1999) also provided some insight into the cervical IDP under different loading conditions. Pospiech et al. found IDP similar to that found by Hattori et al. in a neutral position from seven specimens (C3–C4 and C5–C6). Cripton, 1999 found a linear relationship between compression and the IDP from a sample of four specimens, including C2–C3 (2), C3–C4 (1), and C4–C5 (1). They found peak IDP of 2.4–3.5 MPa under 800 N. Based on their findings, Cripton et al. suggested a thumb rule that for every 1000 N of axial load, an IDP of 3.75 MPa is expected in cervical discs, which is much higher than that in the lumbar region (1 MPa for every 1000 N). However, in these *in vitro* studies, the sample size was limited and technical difficulties were reported in acquiring IDP for small cervical discs (Cripton, 1999). Numerous biomechanical parameters can affect the cervical disc loads and IDP. In this study, we estimated the change in

IDP due to segmental mass in a neutral posture, which was found in a similar range as reported in experimental studies (Kambin et al., 1980; Hattori et al., 1981). The estimated IDP was higher in upper-level discs than in the lower-level discs, possibly due to the smaller size of the upper cervical discs (Pooni et al., 1986).

The estimated cervical disc loads in compression and shear increased from upper to lower cervical levels as the total mass above each level increased naturally. The axial and shear load increased in a neutral posture due to segmental mass; however, it did not change significantly due to disc stiffness and muscle strength. Shear loads were comparatively much less than axial loads, with the highest values at the lowest level and almost no shear load at the upper level of the spine. Here, segmental masses from 5th to 95th percentiles were considered. One may note that even within a specific percentile of the population, the head mass can vary significantly. However, the variation of head mass within a certain percentile was not considered in this study. Due to the small size of cervical discs, the increase in segmental mass and external axial loading showed a considerable rise in IDP. With 40 N axial loading, which is close to a normal auxiliary weight of a helicopter pilot due to a helmet worn with the NVG, our study showed that the IDP could increase two-fold. Previous studies reported the association of a helmet worn with NVG with neck pain in helicopter pilots (Karakolis et al., 2015). High IDP and cumulative loading for persistent long hours might cause tissue damage and, therefore, neck pain.

The cervical disc translations showed significant differences due to segmental mass and disc stiffness. Quantifying the differences in disc translations of the spinal segment may prove helpful in understanding the initial contact mechanics and loading of the facet joints in the neutral posture. The axial translation almost remained similar for different segment levels, which is per increased axial stiffness of the discs that could have compensated the effect of additional mass at progressively lower spine levels. On the contrary, shear translations increased from upper to lower levels as the shear stiffness considered in the model was similar at all levels.

The muscle forces stabilize the head and neck complex in a neutral posture. Here, the sensitivity analysis showed that the activity is much higher with low muscle strength to maintain the neutral posture. While the strength of neck muscles can vary among the normal population, the neck muscles with lower strength can get fatigued earlier for sustaining a posture for a prolonged time. Studies measuring EMG activity reported significant interindividual variations in sternocleidomastoid, erector spinae, and trapezius muscles (Villanueva et al., 1997; Caneiro et al., 2010; Newell et al., 2013; Callaghan et al., 2014; Ibrahim, 2015; Cheon and Park, 2017; Lee et al., 2017). The muscle activities estimated in this study were within a similar range. The estimated muscle activity in neutral posture showed noticeable differences. The maximum muscle activity calculated under 0 N and 40 N axial load was up to 10 and 15% MVC for most muscle groups, respectively. Some infrahyoid muscles showed higher activity (5–25% MVC), which may be associated with their significant contribution in flexion moment. A previous study by Mortensen et al. (2018) showed substantial contribution of hyoid muscles to stabilize the cervical spine by providing increased flexion moment in their model compared to others without hyoid muscles (Vasavada et al., 1998).

The predicted muscle forces in individual groups were approximately in the range of 3–6 N. These values were comparable with those in other studies found in the literature (Assi et al., 2005; Van den Abbeele et al., 2018). Here, we also presented the sum of forces in anterior, posterior, and lateral muscles. The total force in posterior muscles was comparatively higher than that in anterior muscles. Since the overall center of mass was located about C1 and slightly anterior, more extensor moment would be required to keep the spine stable in a neutral posture. With the addition of 40 N axial load, the total muscle forces increased almost two-fold.

This study investigated the differences in cervical disc loads, disc translations, IDP, and muscle force/activity due to segmental mass, disc stiffness, and muscle strength in the general population. However, the study has its limitations. Apart from the effects of the parameters shown in this study, interactions among the parameters may exist. For example, in our preliminary analysis, we noticed negligible or no interaction among the parameters for the disc loads and total muscle forces in a neutral posture; however, for disc translations, nonlinear interaction may exist between the disc stiffness versus segmental mass and the external load. Estimating a full range of variation was not within the scope of this study. Other biomechanical parameters may affect these estimations. Here, we considered only one set of the geometric musculoskeletal model; therefore, differences due to morphological/geometrical parameters were not considered. For example, cervical spine shape varies among the general population as previous studies showed that one-third of the asymptomatic population has cervical kyphosis rather than commonly perceived cervical lordosis (Le Huec et al., 2019, 2014), whereas some studies showed gender differences in the spine shape (Been et al., 2017). In addition, the nonsymmetric geometric features in vertebra shape or bifid in spinous processes may lead to differences in muscle attachments and muscle moment arms. In this study, facet contact mechanics was not considered as it may be sensitive to the definition of facet joint gap and other geometrical parameters. The current model estimated the joint loads, translations, and muscle force/activity in a neutral posture. In our future work, we aim to validate the model for flexion, extension, lateral bending, and axial rotation and include facet joints for simulating these large motions.

CONCLUSION

The cervical disc loads, motion, and muscle force/activity vary significantly in a neutral posture. Quantifying such differences due to various parameters is necessary to

better evaluate the cervical spine's normal or pathological condition.

DATA AVAILABILITY STATEMENT

The original contributions presented in the study are included in the article/**Supplementary Material**, further inquiries can be directed to the corresponding author.

AUTHOR CONTRIBUTIONS

RA: concept and design of the study, model development, simulations, sensitivity analysis, data evaluation, interpretation of the results, writing, and editing of the manuscript. HS: review, discussion, and editing of the manuscript. ME-R: review and editing of the manuscript. KM: funding acquisition, supervision, concept and design of the study, and review and editing of the manuscript.

FUNDING

This study was sponsored by the Directorate of Aerospace Engineering Support (DTAES 7), National Defense Headquarters, Ottawa, Canada, K1A 0K2.

SUPPLEMENTARY MATERIAL

The Supplementary Material for this article can be found online at: https://www.frontiersin.org/articles/10.3389/fbioe.2022.751291/full#supplementary-material

Supplementary Table 1 | Model parameters settings for segmental mass (M), disc stiffness (DS), muscle strength (MS) and external load (EL) for sensitivity analysis.

REFERENCES

Ackerman, M. J. (1998). The Visible Human Project. *Proc. IEEE* 86, 504–511. doi:10.1109/5.662875

Ackland, D. C., Merritt, J. S., and Pandy, M. G. (2011). Moment Arms of the Human Neck Muscles in Flexion, Bending and Rotation. *J. Biomech.* 44, 475–486. doi:10.1016/j.jbiomech.2010.09.036

Andersen, M. S., Damsgaard, M., and Rasmussen, J. (2011). "Force-Dependent Kinematics: A New Analysis Method for Non-Conforming Joints," in 13th Biennial International Symposium on Computer Simulation in Biomechanics, Belgium, 30 Jun 2011, 2 Jul 2011 (Leuven: Int. Symp. Comput. Simul. Biomech.).

Anderst, W. J., Donaldson, W. F., Lee, J. Y., and Kang, J. D. (2013). Subject-Specific Inverse Dynamics of the Head and Cervical Spine During *In Vivo* Dynamic Flexion-Extension. *J. Biomech. Eng.* 135, 1–8. doi:10.1115/1.4023524

Assi, A., Pomero, V., Bonneau, D., Saintonge, R., and Skalli, W. (2005). Cervical Muscles Forces and Spinal Loads Estimation in Standing Position: Asymptomatic Cases. *Comp. Methods Biomech. Biomed. Eng.* 8, 9–10. doi:10.1080/10255840512331388001

Barrett, J. M., McKinnon, C., and Callaghan, J. P. (2020). Cervical Spine Joint Loading with Neck Flexion. *Ergonomics* 63, 101–108. doi:10.1080/00140139.2019.1677944

Been, E., Shefi, S., and Soudack, M. (2017). Cervical Lordosis: the Effect of Age and Gender. *Spine J.* 17, 880–888. doi:10.1016/j.spinee.2017.02.007

Borst, J., Forbes, P. A., Happee, R., and Veeger, D. (2011). Muscle Parameters for Musculoskeletal Modelling of the Human Neck. *Clin. Biomech.* 26, 343–351. doi:10.1016/j.clinbiomech.2010.11.019

Bredbenner, T. L., Eliason, T. D., Francis, W. L., McFarland, J. M., Merkle, A. C., and Nicolella, D. P. (2014). Development and Validation of a Statistical Shape Modeling-Based Finite Element Model of the Cervical Spine Under Low-Level Multiple Direction Loading Conditions. *Front. Bioeng. Biotechnol.* 2, 1–12. doi:10.3389/fbioe.2014.00058

Callaghan, J. P., Laing, A. C., and Dickerson, C. R. (2014). The Influence of Neck Posture and Helmet Configuration on Neck Muscle Demands. Technical Report. Available at: https://apps.dtic.mil/sti/citations/AD1000883 (Accessed March 1, 2021).

Caneiro, J. P., O'Sullivan, P., Burnett, A., Barach, A., O'Neil, D., Tveit, O., et al. (2010). The Influence of Different Sitting Postures on Head/neck Posture and Muscle Activity. *Man. Ther.* 15, 54–60. doi:10.1016/j.math.2009.06.002

Cassola, V. F., Milian, F. M., Kramer, R., De Oliveira Lira, C. A. B., and Khoury, H. J. (2011). Standing Adult Human Phantoms Based on 10th, 50th and 90th Mass and Height Percentiles of Male and Female Caucasian Populations. *Phys. Med. Biol.* 56, 3749–3772. doi:10.1088/0031-9155/56/13/002

Catenaccio, E., Mu, W., Kaplan, A., Fleysher, R., Kim, N., Bachrach, T., et al. (2017). Characterization of Neck Strength in Healthy Young Adults. *PM&R* 9, 884–891. doi:10.1016/j.pmrj.2017.01.005

Charles, L. E., Ma, C. C., Burchfiel, C. M., and Dong, R. G. (2018). Vibration and Ergonomic Exposures Associated with Musculoskeletal Disorders of the Shoulder and Neck. *Saf. Health Work* 9, 125–132. doi:10.1016/j.shaw.2017.10.003

Cheon, S., and Park, S. (2017). Changes in Neck and Upper Trunk Muscle Activities According to the Angle of Movement of the Neck in Subjects with Forward Head Posture. *J. Phys. Ther. Sci.* 29, 191–193. doi:10.1589/jpts.29.191

Ching, R. P. (2007). Relationship Between Head Mass and Circumference in Human Adults. Technical Brief. Available at: https://smf.org/docs/articles/pdf/chingtechbrief.pdf (Accessed March 1, 2021).

Cohen, S. P. (2015). Epidemiology, Diagnosis, and Treatment of Neck Pain. *Mayo Clinic Proc.* 90, 284–299. doi:10.1016/j.mayocp.2014.09.008

Cripton, P. A. (1999). *Load-Sharing in the Human Cervical*. Canada: Queen's University at Kingston.

Diao, H., Xin, H., Dong, J., He, X., Li, D., and Jin, Z. (20171976). Prediction of Cervical Spinal Joint Loading and Secondary Motion Using a Musculoskeletal Multibody Dynamics Model via Force-Dependent Kinematics Approach. *Spine (Phila. Pa.* 42, E1403–E1409. doi:10.1097/BRS.0000000000002176

Diao, H., Xin, H., and Jin, Z. (2018). Prediction of *In Vivo* Lower Cervical Spinal Loading Using Musculoskeletal Multi-Body Dynamics Model During the Head Flexion/Extension, Lateral Bending and Axial Rotation. *Proc. Inst. Mech. Eng. H* 232, 1071–1082. doi:10.1177/0954411918799630

Dowling-Medley, J. J., Doodkorte, R. J., Melnyk, A. D., Cripton, P. A., and Oxland, T. R. (2020). Shear Stiffness in the Lower Cervical Spine: Effect of Sequential Posterior Element Injury. *Proc. Inst. Mech. Eng. H* 234, 141–147. doi:10.1177/0954411919889194

Dreischarf, M., Rohlmann, A., Zhu, R., Schmidt, H., and Zander, T. (2013). Is it Possible to Estimate the Compressive Force in the Lumbar Spine From Intradiscal Pressure Measurements? A Finite Element Evaluation. *Med. Eng. Phys.* 35, 1385–1390. doi:10.1016/j.medengphy.2013.03.007

Hattori, S., Oda, H., and Kawai, S. (1981). Cervical Intradiscal Pressure in Movernents and Traction of the Cervical Spine. *Z. Orthop.* 119, 568–569.

Ibrahim, E. (2015). The Effects of Neck Posture and Head Load on the Cervical Spine and Upper Extremities. Canada: McMaster University. M.Sc Thesis. Avaliable at: http://hdl.handle.net/11375/18088.

Ikai, M., and Fukunaga, T. (1968). Calculation of Muscle Strength Per Unit Cross-Sectional Area of Human Muscle by Means of Ultrasonic Measurement. *Int. Z. Angew. Physiol. Einschl. Arbeitsphysiol.* 26, 26–32. doi:10.1007/BF00696087

Jaumard, N. V., Welch, W. C., and Winkelstein, B. A. (2011). Spinal Facet Joint Biomechanics and Mechanotransduction in Normal, Injury and Degenerative Conditions. *J. Biomech. Eng.* 133, 071010. doi:10.1115/1.4004493

Kambin, P., Abda, S., and Kurpicki, F. (1980). Intradiskal Pressure and Volume Recording. *Clin. Orthopaedics Relat. Res.* 146, 144–147. doi:10.1097/00003086-198001000-00019

Karakolis, T., Farrell, P., and Fusina, G. (2015). Neck Overuse Injury in CH-146 Griffon Helicopter Aircrews. *Proced. Manufacturing* 3, 4205–4212. doi:10.1016/j.promfg.2015.07.396

Kong, L., Tian, W., Cao, P., Wang, H., Zhang, B., and Shen, Y. (2017). Predictive Factors Associated with Neck Pain in Patients with Cervical Disc Degeneration. *Medicine (Baltimore)* 96, e8447. doi:10.1097/MD.0000000000008447

Lasswell, T. L., Cronin, D. S., Medley, J. B., and Rasoulinejad, P. (2017). Incorporating Ligament Laxity in a Finite Element Model for the Upper Cervical Spine. *Spine J.* 17, 1755–1764. doi:10.1016/j.spinee.2017.06.040

Le Huec, J. C., Demezon, H., and Aunoble, S. (2014). Sagittal Parameters of Global Cervical Balance Using EOS Imaging: Normative Values from a Prospective Cohort of Asymptomatic Volunteers. *Eur. Spine J.* 24, 63–71. doi:10.1007/s00586-014-3632-0

Le Huec, J. C., Thompson, W., Mohsinaly, Y., Barrey, C., and Faundez, A. (2019). Sagittal Balance of the Spine. *Eur. Spine J.* 28, 1889–1905. doi:10.1007/s00586-019-06083-1

Lee, S., Lee, Y., and Chung, Y. (2017). Effect of Changes in Head Postures during Use of Laptops on Muscle Activity of the Neck and Trunk. *Ptrs* 6, 33–38. doi:10.14474/ptrs.2017.6.1.33

Linton, S. J. (2000). A Review of Psychological Risk Factors in Back and Neck Pain. *Spine* 25, 1148–1156. doi:10.1097/00007632-200005010-00017

Maganaris, C. N., Baltzopoulos, V., Ball, D., and Sargeant, A. J. (2001). *In Vivo* Specific Tension of Human Skeletal Muscle. *J. Appl. Physiol.* 90, 865–872. doi:10.1152/jappl.2001.90.3.865

McCormick, J. R., Sama, A. J., Schiller, N. C., Butler, A. J., and Donnally, C. J. (2020). Cervical Spondylotic Myelopathy: A Guide to Diagnosis and Management. *J. Am. Board Fam. Med.* 33, 303–313. doi:10.3122/jabfm.2020.02.190195

Mesfar, W., and Moglo, K. (2013). Effect of the Transverse Ligament Rupture on the Biomechanics of the Cervical Spine Under a Compressive Loading. *Clin. Biomech.* 28, 846–852. doi:10.1016/j.clinbiomech.2013.07.016

Moroney, S. P., Schultz, A. B., Miller, J. A. A., and Andersson, G. B. J. (1988). Load-Displacement Properties of Lower Cervical Spine Motion Segments. *J. Biomech.* 21, 769–779. doi:10.1016/0021-9290(88)90285-0

Mortensen, J. D., Vasavada, A. N., and Merryweather, A. S. (2018). The Inclusion of Hyoid Muscles Improve Moment Generating Capacity and Dynamic Simulations in Musculoskeletal Models of the Head and Neck. *PLoS One* 13, e0199912–14. doi:10.1371/journal.pone.0199912

Mustafy, T., El-Rich, M., Mesfar, W., and Moglo, K. (2014). Investigation of Impact Loading Rate Effects on the Ligamentous Cervical Spinal Load-Partitioning Using Finite Element Model of Functional Spinal Unit C2-C3. *J. Biomech.* 47, 2891–2903. doi:10.1016/j.jbiomech.2014.07.016

Nachemson, A. (1966). The Load on Lumbar Disks in Different Positions of the Body. *Clin. Orthopaedics Relat. Res.* 45, 107–122. doi:10.1097/00003086-196600450-00014

Newell, R. S., Blouin, J.-S., Street, J., Cripton, P. A., and Siegmund, G. P. (2013). Neck Posture and Muscle Activity Are Different When Upside Down: A Human Volunteer Study. *J. Biomech.* 46, 2837–2843. doi:10.1016/j.jbiomech.2013.08.013

Nguyen, A. K. D., Simard-Meilleur, A. A., Berthiaume, C., Godbout, R., and Mottron, L. (2012). Head Circumference in Canadian Male Adults: Development of a Normalized Chart. *Int. J. Morphol.* 30, 1474–1480. doi:10.4067/s0717-95022012000400033

Panjabi, M. M., Crisco, J. J., Vasavada, A., Oda, T., Cholewicki, J., Nibu, K., et al. (2001). Mechanical Properties of the Human Cervical Spine as Shown by Three-Dimensional Load-Displacement Curves. *Spine* 26, 2692–2700. doi:10.1097/00007632-200112150-00012

Panjabi, M. M., Summers, D. J., Pelker, R. R., Videman, T., Friedlaender, G. E., and Southwick, W. O. (1986). Three-Dimensional Load-Displacement Curves Due to Froces on the Cervical Spine. *J. Orthop. Res.* 4, 152–161. doi:10.1002/jor.1100040203

Patwardhan, A. G., Havey, R. M., Ghanayem, A. J., Diener, H., Meade, K. P., Dunlap, B., et al. (2000). Load-Carrying Capacity of the Human Cervical Spine in Compression Is Increased Under a Follower Load. *Spine (Phila. Pa. 1976)* 25, 1548–1554. doi:10.1097/00007632-200006150-00015

Pooni, J., Hukins, D., Harris, P., Hilton, R., and Davies, K. (1986). Comparison of the Structure of Human Intervertebral Discs in the Cervical, Thoracic and Lumbar Regions of the Spine. *Surg. Radiol. Anat.* 8, 175–182. doi:10.1007/BF02427846

Pospiech, J., Stolke, D., Wilke, H. J., and Claes, L. E. (1999). Intradiscal Pressure Recordings in the Cervical Spine. *Neurosurgery* 44, 379–384. doi:10.1097/00006123-199902000-00078

Safiri, S., Kolahi, A.-A., Hoy, D., Buchbinder, R., Mansournia, M. A., Bettampadi, D., et al. (2020). Global, Regional, and National Burden of Neck Pain in the General Population, 1990-2017: Systematic Analysis of the Global Burden of Disease Study 2017. *BMJ* 368, m791. doi:10.1136/bmj.m791

Sartori, M., Farina, D., and Lloyd, D. G. (2014). Hybrid Neuromusculoskeletal Modeling to Best Track Joint Moments Using a Balance Between Muscle Excitations Derived from Electromyograms and Optimization. *J. Biomech.* 47, 3613–3621. doi:10.1016/j.jbiomech.2014.10.009

Shim, V. P. W., Liu, J. F., and Lee, V. S. (2006). A Technique for Dynamic Tensile Testing of Human Cervical Spine Ligaments. *Exp. Mech.* 46, 77–89. doi:10.1007/s11340-006-5865-2

Silvestros, P., Preatoni, E., Gill, H. S., Gheduzzi, S., Hernandez, B. A., Holsgrove, T. P., et al. (2019). Musculoskeletal Modelling of the Human Cervical Spine for the Investigation of Injury Mechanisms During Axial Impacts. *PLoS One* 14, e0216663–20. doi:10.1371/journal.pone.0216663

Spitzer, V., Ackerman, M. J., Scherzinger, A. L., and Whitlock, D. (1996). The Visible Human Male: A Technical Report. *J. Am. Med. Inform. Assoc.* 3, 118–130. doi:10.1136/jamia.1996.96236280

Suderman, B. L., and Vasavada, A. N. (2017). Neck Muscle Moment Arms Obtained *In-Vivo* From MRI: Effect of Curved and Straight Modeled Paths. *Ann. Biomed. Eng.* 45, 2009–2024. doi:10.1007/s10439-017-1830-8

Van den Abbeele, M., Li, F., Pomero, V., Bonneau, D., Sandoz, B., Laporte, S., et al. (2018). A Subject-Specific Biomechanical Control Model for the Prediction of Cervical Spine Muscle Forces. *Clin. Biomech.* 51, 58–66. doi:10.1016/j.clinbiomech.2017.12.001

Vasavada, A. N., Danaraj, J., and Siegmund, G. P. (2008). Head and Neck Anthropometry, Vertebral Geometry and Neck Strength in Height-Matched Men and Women. *J. Biomech.* 41, 114–121. doi:10.1016/j.jbiomech.2007.07.007

Vasavada, A. N., Li, S., and Delp, S. L. (1998). Influence of Muscle Morphometry and Moment Arms on the Moment-Generating Capacity of Human Neck Muscles. *Spine* 23, 412–422. doi:10.1097/00007632-199802150-00002

Villanueva, M. B. G., Jonai, H., Sotoyama, M., Hisanaga, N., Takeuchi, Y., and Saito, S. (1997). Sitting Posture and Neck and Shoulder Muscle Activities at Different Screen Height Settings of the Visual Display Terminal. *Ind. Health* 35, 330–336. doi:10.2486/indhealth.35.330

Wheeldon, J. A., Pintar, F. A., Knowles, S., and Yoganandan, N. (2006). Experimental Flexion/Extension Data Corridors for Validation of Finite Element Models of the Young, Normal Cervical Spine. *J. Biomech.* 39, 375–380. doi:10.1016/j.jbiomech.2004.11.014

Winter, D. A. (2009). *Biomechanics and Motor Control of Human Movement, Biomechanics and Motor Control of Human Movement*. Hoboken: John Wiley & Sons.

Yoganandan, N., Knowles, S. A., Maiman, D. J., and Pintar, F. A. (2003). Anatomic Study of the Morphology of Human Cervical Facet Joint. *Spine* 28, 2317–2323. doi:10.1097/01.BRS.0000085356.89103.A5

Yoganandan, N., Kumaresan, S., and Pintar, F. A. (2001). Biomechanics of the Cervical Spine Part 2. Cervical Spine Soft Tissue Responses and Biomechanical Modeling. *Clin. Biomech.* 16, 1–27. doi:10.1016/S0268-0033(00)00074-7

Conflict of Interest: The authors declare that the research was conducted in the absence of any commercial or financial relationships that could be construed as a potential conflict of interest.

Advantages of publishing in Frontiers

OPEN ACCESS
Articles are free to read for greatest visibility and readership

FAST PUBLICATION
Around 90 days from submission to decision

HIGH QUALITY PEER-REVIEW
Rigorous, collaborative, and constructive peer-review

TRANSPARENT PEER-REVIEW
Editors and reviewers acknowledged by name on published articles

Frontiers
Avenue du Tribunal-Fédéral 34
1005 Lausanne | Switzerland

Visit us: www.frontiersin.org
Contact us: frontiersin.org/about/contact

REPRODUCIBILITY OF RESEARCH
Support open data and methods to enhance research reproducibility

DIGITAL PUBLISHING
Articles designed for optimal readership across devices

FOLLOW US
@frontiersin

IMPACT METRICS
Advanced article metrics track visibility across digital media

EXTENSIVE PROMOTION
Marketing and promotion of impactful research

LOOP RESEARCH NETWORK
Our network increases your article's readership